Version 2.1
June 25, 2010

Wide Field Camera 3 Instrument Handbook for Cycle 18

(Version 2.1 is an Update to WFC3 Cycle 18 Instrument Handbook)

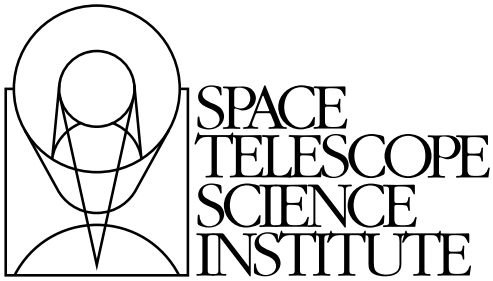

Space Telescope Science Institute
3700 San Martin Drive
Baltimore, Maryland 21218
help@stsci.edu

Operated by the Association of Universities for Research in Astronomy, Inc., for the National Aeronautics and Space Administration

User Support

For prompt answers to any question, please contact the STScI Help Desk.

- **E-mail:** help@stsci.edu
- **Phone:** (410) 338-1082
  (800) 544-8125 (U.S., toll free)

World Wide Web

Information and other resources are available on the WFC3 World Wide Web site at STScI:

http://www.stsci.edu/hst/wfc3

WFC3 Instrument Handbook Revision History

Version	Date	Editors
2.1	June 25, 2010	Linda Dressel, Michael H. Wong, Cheryl Pavlovsky, Knox S. Long
2.0	January 2010	Michael H. Wong, Cheryl Pavlovsky, Knox S. Long
1.0	December 2007	Howard E. Bond and Jessica Kim Quijano

Contributors:

Bruce Balick, Sylvia Baggett, Howard Bond, Tiffany Borders, Ray Boucarut, Tom Brown, Howard Bushouse, Nicholas Collins, Colin Cox, Ilana Dashevsky, Linda Dressel, Susana Deustua, Michael Dulude, Mauro Giavalisco, Ron Gilliland, George Hartig, Bryan Hilbert, Robert J. Hill, Jason Kalirai, Diane Karakla, Jessica Kim Quijano, Randy Kimble, Martin Kümmel, Harald Kuntschner, Matt Lallo, Knox Long, Olivia Lupie, Brian McLean, Peter McCullough, John MacKenty, Eliot Malumuth, André Martel, Cheryl Pavlovsky, Larry Petro, Nor Pirzkal, Vera Kozhurina-Platais, Elizabeth Polidan, Manuel Quijada, Abhijith Rajan, Neill Reid, Adam Riess, Massimo Robberto, Elena Sabbi, Massimo Stiavelli, Randal Telfer, Alex Viana, Nolan Walborn, Jeremy Walsh, Tom Wheeler, and Mike Wong.

Citation:

In publications, refer to this document as:
Dressel, L., Wong, M.H., Pavlovsky, C., and Long, K. et al., 2010. “Wide Field Camera 3 Instrument Handbook, Version 2.1” (Baltimore: STScI)

Send comments or corrections to:
Space Telescope Science Institute
3700 San Martin Drive
Baltimore, Maryland 21218
E-mail:help@stsci.edu

Table of Contents

List of Updates

(last updated June 25, 2010)

Table 5.1: Value and description of UVIS CCD full well changed in table and note to table.

Section 5.4.5: Discussion of saturation, bleeding, and CCD full well modified.

Section 6.9.1: Discussion of CCD full well, use of ETC, and photometry of saturated targets modified.

Section 7.7.3: More accurate title; differences between sample sequences for full arrays and subarrays emphasized.

Section 7.7.4: More accurate title; dependence of times in sample sequences on subarray size emphasized.

Appendix C: Values of b11 and b10 for UVIS changed.

Acknowledgments

The WFC3 Science Integrated Product Team (2009)

Sylvia Baggett
Tiffany Borders
Howard Bushouse
Linda Dressel
Susana Deustua
Michael Dulude
George Hartig
Bryan Hilbert
Robert Hill (GSFC)
Jason Kalirai
Jessica Kim Quijano
Randy Kimble (Instrument Scientist, GSFC)
Vera Kozhurina-Platais
Knox Long
John MacKenty (Deputy Instrument Scientist)
Brian McLean
Peter McCullough
Cheryl Pavlovsky
Larry Petro
Nor Pirzkal
Abhijith Rajan
Adam Riess
Elena Sabbi
Alex Viana
Michael Wong

Past Science IPT Members

Wayne Baggett
Howard Bond
Tom Brown
Laura Cawley
Ed Cheng (GSFC, now Conceptual Analytics)
Ilana Dashevsky
Don Figer
Mauro Giavalisco

Shireen Gonzaga
Christopher Hanley
Ron Henry
Pat Knezek
Ray Kutina
Casey Lisse
Olivia Lupie (GSFC)
André Martel
Neill Reid
Massimo Robberto
Michael Robinson
Megan Sosey
Massimo Stiavelli

The WFC3 Scientific Oversight Committee

Bruce Balick, University of Washington
Howard E. Bond, Space Telescope Science Institute
Daniela Calzetti, Space Telescope Science Institute
C. Marcella Carollo, Institute of Astronomy, ETH, Zurich
Michael J. Disney, Cardiff University
Michael A. Dopita, Mt Stromlo and Siding Spring Observatories
Jay Frogel, AURA
Donald N. B. Hall, University of Hawaii
Jon A. Holtzman, New Mexico State University
Randy Kimble, NASA Goddard Space Flight Center (ex officio)
Gerard Luppino, University of Hawaii
Patrick J. McCarthy, Carnegie Observatories
John MacKenty, Space Telescope Science Institute (ex officio)
Robert W. O'Connell, University of Virginia (Chair)
Francesco Paresce, European Southern Observatory
Abhijit Saha, National Optical Astronomy Observatory
Joseph I. Silk, Oxford University
John T. Trauger, Jet Propulsion Laboratory
Alistair R. Walker, Cerro Tololo Interamerican Observatory
Bradley C. Whitmore, Space Telescope Science Institute
Rogier A. Windhorst, Arizona State University
Erick T. Young, University of Arizona

Thanks

The editors thank the authors who prepared major revisions regarding on-orbit performance evaluation and Cycle 18 plans: Sylvia Baggett (Chapter 5), Howard Bushouse (Chapters 5, 8, E), Bryan Hilbert (Chapters 5, 6, 7), Jason Kalirai (Chapters 6, 9, A), George Hartig (Chapters 6, 7, B), Mike Wong (Chapter 6), Martin Kümmel, Harald Kuntschner, and Jeremy Walsh (Chapter 8), Linda Dressel (Appendices B, C), Vera Kozhurina-Platais (Appendix B). Many others provided valuable assistance.

The contributions of Alan Welty, Tom Wheeler, and Susan Rose (Technical Editor) to the editing and production of this *Instrument Handbook* are greatly appreciated.

CHAPTER 1:

Introduction to WFC3

In this chapter . . .

1.1 Overview

The **Wide Field Camera 3** (**WFC3**) is a fourth-generation imaging instrument. It was installed in the *Hubble Space Telescope* (*HST*) during Servicing Mission 4 (SM4) in May 2009. WFC3 saw first light on June 24, 2009, following the cooling of its detectors. Servicing Mission 4 Observatory Verification (SMOV) activities were completed in late August 2009.

This *WFC3 Instrument Handbook* has been prepared by the WFC3 team at STScI. It is the basic technical reference manual for WFC3 observers. The information in this *Handbook* is intended to be useful for Cycle 18 Phase I proposers, for the subsequently selected General Observers (GOs) as they prepare their Phase II specifications, and for those analyzing WFC3 data. The *HST Primer* and the *Call for Proposals* also contain valuable information for proposers, and the *Call for Proposals* is the final authority on *HST* policy.

This edition of the *WFC3 Instrument Handbook* (Version 2) was written near the end of the SMOV data analysis phase of instrument commissioning. It supersedes Version 1, and includes results from an *initial* analysis of on-orbit performance.

The WFC3 instrument occupies *HST*'s radial scientific-instrument bay, from where it obtains on-axis direct images. During SM4 the shuttle astronauts installed WFC3 in place of the long-serving Wide Field Planetary Camera 2 (WFPC2). WFPC2, in turn, was installed during SM1 in December 1993, to replace the original Wide Field/Planetary Camera (WF/PC1). WFC3, like WFPC2, contains optics that correct

for the spherical aberration discovered in the *HST* primary mirror following launch of the telescope in April 1990.

WFC3 is designed to ensure that *HST* maintains its powerful imaging capabilities until the end of its mission, while at the same time advancing its survey and discovery capability through WFC3's combination of broad wavelength coverage, wide field of view, and high sensitivity. WFC3 also provides a good degree of redundancy for the Wide Field Channel of the Advanced Camera for Surveys (ACS) as well as for the Near-Infrared Camera and Multi-Object Spectrometer (NICMOS) cameras.

A key feature of WFC3 is its panchromatic wavelength coverage. By combining two optical/ultraviolet CCDs with a near-infrared HgCdTe array, WFC3 is capable of direct, high-resolution imaging over the entire wavelength range from 200 to 1700 nm. Equipped with a comprehensive range of wide-, intermediate-, and narrow-band filters, WFC3 has broad applicability to a variety of new astrophysical investigations.

WFC3 is a facility instrument. It was developed, constructed, characterized, and calibrated by an Integrated Product Team (IPT) led by NASA's Goddard Space Flight Center (GSFC), and composed of staff astronomers and engineers from GSFC, STScI, Ball Aerospace & Technologies Corp., the Jet Propulsion Laboratory (JPL), and other industrial contractors.

A Scientific Oversight Committee (SOC), selected by NASA from the international astronomical community and appointed in 1998, provided scientific advice for the design and development of WFC3. The SOC's activities were in a range of areas, including: definition of the key scientific goals and success criteria for WFC3; participation in project reviews; recommending an optimum set of filters and grisms for the instrument and the pixel scale and field of view of the detectors; participation in the selection of flight detectors; and advice on technical trade-off decisions in the light of the scientific goals of the instrument.

1.2 Key Features of WFC3

The optical design of WFC3 features two independent channels, one sensitive at ultraviolet (UV) and optical wavelengths, approximately 200 to 1000 nm (the **UVIS channel**), and the other sensitive at near-infrared (near-IR) wavelengths, approximately 800 to 1700 nm (the **IR channel**). A channel-selection mirror directs on-axis light from the *HST* optical telescope assembly (OTA) to the IR channel, or the mirror can be removed from the beam to allow light to enter the UVIS channel. This means that *simultaneous* observations with the UVIS and IR detectors are not possible. However, both UVIS and IR observations can be made *sequentially*, even during the same *HST* orbit.

The extended wavelength range, combined with high sensitivity, high spatial resolution, large field of view, and a wide selection of spectral elements, makes WFC3 an extremely versatile instrument. Key features of WFC3 include:

- **UVIS channel:** two 2k×4k CCDs; pixel scale 0.04 arcsec/pix; field of view 162×162 arcsec; wavelength range 200-1000 nm; S/N=10 in a 10-hour exposure (F606W filter) for a point source with V=29.2 (ABMAG).

- **IR channel:** 1k×1k HgCdTe array; pixel scale 0.13 arcsec/pix; field of view 136×123 arcsec; wavelength range 800-1700 nm; S/N=10 in a 10-hour exposure (F160W) for a point source with *H*=27.9 (ABMAG).
- 62 wide-, medium-, and narrow-band filters in the UVIS channel.
- 15 wide-, medium-, and narrow-band filters in the IR channel.
- 1 grism in the UVIS channel, and 2 grisms in the IR channel.

A "White Paper," prepared by the SOC and the Science IPT, outlines some scientific areas that will especially benefit from the capabilities of WFC3. These include searches for galaxies at redshifts up to z~10; studies of the physics of star formation in distant and nearby galaxies; investigations of resolved stellar populations down to faint levels in the UV, optical, and near-IR; and high-resolution imaging of objects in the solar system. WFC3's panchromatic capabilities allow investigations of the assembly and evolution of galaxies; star birth, evolution, and death and its relation to the interstellar medium; individual and collective properties of small solar system bodies; and aurorae and meteorology of the outer planets. The White Paper (Stiavelli, M., & O'Connell, R.W., eds., 2000, "*Hubble Space Telescope* Wide Field Camera 3, Capabilities and Scientific Program") can be found at:

http://www.stsci.edu/hst/wfc3/documents/published/WFC3-WhitePaper-2001.pdf

1.3 WFC3 Quick Reference Guide

The most important basic information about WFC3 can be found in this Handbook at the following locations:

- Table 5.1: Instrument Characteristics (field of view, pixel scale, detector parameters, etc.)
- Table 6.2: UVIS Channel Filters and Grism
- Figures 6.3-6.6: Plots of system throughput for UVIS Filters
- Table 7.2: IR Channel Filters and Grisms
- Figures 7.5.2-7.3: Plots of system throughput for IR Filters

1.4 Special Considerations for Cycle 18

1.4.1 Current Instrument Status

WFC3 is operating as expected on *HST*, with its detectors at nominal setpoints of –83°C (UVIS) and –128°C (IR). There are no significant anomalies in its performance.

1.4.2 Ongoing Calibration

At the time of this writing, SMOV4 calibration activities are complete and a large number of WFC3 Instrument Science Reports discussing the results (WFC3 ISRs 2009-15 through 2009-34) are published on the WFC3 Web site.

During Cycle 17, about 250 "external" orbits have been allocated for the calibration of WFC3. Also allocated were about 2000 "internal" orbits—in which *HST* is pointed at the Earth or conducting observations with other instruments, so that the WFC3 detectors are not exposed to the sky. The overall Cycle 17 calibration plan is discussed in WFC3 ISR 2009-06, with more details available concerning the photometric calibration of WFC3 (WFC3 ISR 2009-05) and the detector monitoring campaign (WFC3 ISR 2009-07). Galactic cluster observations are a cornerstone of the Cycle 17 calibration effort (WFC3 ISR 2009-06).

Proposers and users of WFC3 should monitor the Cycle 18 announcement Web site for the latest information:

`http://www.stsci.edu/hst/proposing/docs/cycle18announce`

Additional information will be released as part of WFC3 Space Telescope Analysis Newsletters (STANs) and other updates posted directly to the WFC3 Web site:

`http://www.stsci.edu/hst/wfc3`

Throughout this handbook, a special "Online" symbol indicates information that is especially likely to be updated on the WFC3 Web site.

Information especially likely to be updated on the WFC3 Web site is indicated by this symbol.

1.5 Sources of Further Information

Table 1.1 provides a guide to online documents containing further information about *HST*, the proposal process, and data analysis.

Table 1.1: Useful documents.

Purpose	Document or resource
General observatory information	*HST* Primer http://www.stsci.edu/hst/proposing/documents/primer/primer_cover.html
Phase I proposals	Proposing Overview http://www.stsci.edu/hst/proposing/docs/proposingOverview Call for Proposals http://www.stsci.edu/hst/proposing/documents/cp/cp_cover.html
Phase II programs	Phase II Proposal Instructions http://www.stsci.edu/hst/programs/hst/proposing/docs/p2pi.html Astronomer's Proposal Tool (APT) for Phase I and II preparations http://apt.stsci.edu/
Data analysis and instrument characteristics	General WFC3 Information and Updates http://www.stsci.edu/hst/wfc3 WFC3 Data Handbook http://www.stsci.edu/hst/wfc3/documents/handbooks/currentDHB/WFC3_longdhbcover.html Dither Handbook http://www.stsci.edu/hst/HST_overview/documents/dither_handbook Space Telescope Analysis Newsletter http://www.stsci.edu/hst/wfc3/documents/newsletters WFC3 Instrument Science Reports (ISRs) http://www.stsci.edu/hst/wfc3/documents/ISRs Calibration and Pipeline Information http://www.stsci.edu/hst/Post-observation

Proposers who desire more detailed information about WFC3 capabilities should refer to the WFC3 Instrument Science Reports (ISRs; see link in Table 1.1), which contain extensive details about all aspects of the instrument. Proposers may also seek further assistance as described in the next section.

1.6 The WFC3 Instrument Team at STScI

STScI's team of Instrument Scientists, Data Analysts, Engineers, and Scientific Programmers support the design, development, operation, calibration, and documentation of WFC3. STScI also maintains a "Help Desk" to provide answers quickly to any WFC3- and *HST*-related questions. Please refer all questions regarding WFC3 and *HST* to the Help Desk, as follows:

- E-mail: help@stsci.edu
- Phone: (410) 338-1082

The Team Lead for WFC3 is John Mackenty:

- E-mail: mackenty@stsci.edu
- Phone: (410) 338-4559

Additional STScI contact info can be found in the *Cycle 18 Call for Proposals*.

CHAPTER 2:

WFC3 Instrument Description

In this chapter . . .

2.1 Optical Design and Detectors

The optical design of WFC3 was driven by the need to provide a large field of view and high sensitivity over a broad wavelength range, excellent spatial resolution, and stable and accurate photometric performance. WFC3 features two independent imaging cameras: the **UV/Visible channel** (**UVIS**) and the **near-infrared channel** (**IR**). Figure 2.1 shows a schematic diagram of the instrument's optical and mechanical layout.

On-axis light coming from the *HST* optical telescope assembly (OTA) is intercepted by the flat 45° WFC3 pick-off mirror (POM) and is directed into the instrument. For IR observations, the channel select mechanism (CSM) then diverts the light into the IR channel; for UVIS observations, the CSM mirror is simply removed, which allows the light to enter the UVIS channel. Because of this design, only a single channel, either UVIS or IR, can be used at any one time, although it is possible to switch between them fairly quickly.

Optical elements in each channel (anamorphic aspherical correctors) correct separately for the ~1/2 wave spherical aberration of the *HST* primary mirror. Both channels also have internal flat-field illumination sources.

WFC3 uses two different types of detectors. The UVIS channel uses two butted 4096×2051 thinned, back-illuminated e2v Ltd. (formerly Marconi) CCD detectors to support imaging between 200 and 1000 nm. The IR channel uses a 1024×1024

Teledyne (formerly Rockwell Scientific) HgCdTe detector array, with the central 1014×1014 pixels useful for imaging, and covering the near-infrared between 800 and 1700 nm.

The primary characteristics of the two channels are summarized in Table 2.1.

Table 2.1: Characteristics of the two WFC3 channels.

Channel	*f*-ratio	Detector type	Spectral range (nm)	Detector pixel format	Pixel scale (arcsec)	Field of view (arcsec)
UVIS	31	CCD	200-1000	2×2051×4096	0.0395×0.0395	162×162
IR	11	HgCdTe	800-1700	1014×1014	0.135×0.121	136×123

Figure 2.1: Schematic optical layout of the WFC3 instrument. Note that for schematic simplicity, the incoming OTA beam and POM have been rotated into the plane of the optical diagram. The actual incoming OTA beam direction is into the page and then reflected by the POM into the instrument. Yellow indicates light from the OTA, which is sent into the camera by the pick-off mirror. The Channel Select Mechanism then either allows light to pass into the UVIS channel (blue path), or directs light into the IR channel (red path). Mechanisms and optics in both channels allow for focus and alignment, and correct for the OTA spherical aberration. Filters and grisms are contained in the UVIS SOFA and the IR FSM. The UVIS channel has a mechanical shutter, while the IR channel is shuttered electronically by the detector. Light is detected by either the UVIS CCDs or the IR focal-plane array. A separate subsystem provides flat- field illumination for both channels.

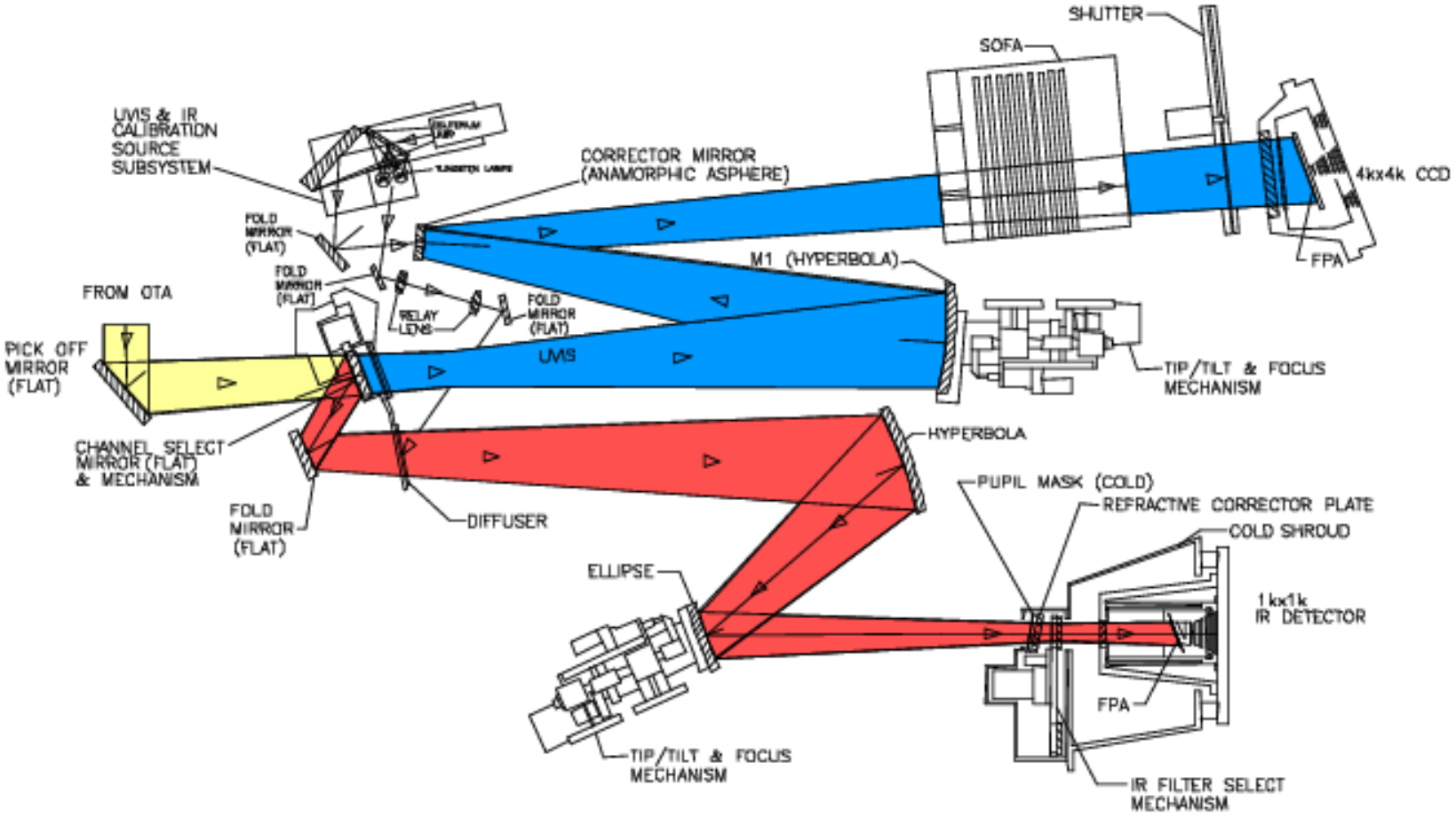

2.2 Field of View and Geometric Distortions

WFC3 replaces WFPC2, *Hubble*'s first large-area camera that included corrections for the spherical aberration of the *HST* primary mirror. The appearance of the *HST* focal plane following SM4 is shown in Figure 2.2.

Figure 2.2: The *HST* focal-plane layout, showing the instrument complement following SM4. Although the WFC3 IR and UVIS detectors appear co-aligned in this figure, IR alignment activities have confirmed that the two detector centers are actually offset by 4.8 arcsec. The diameter of the outer black circle, projected onto the sky, is about 28 arcminutes.

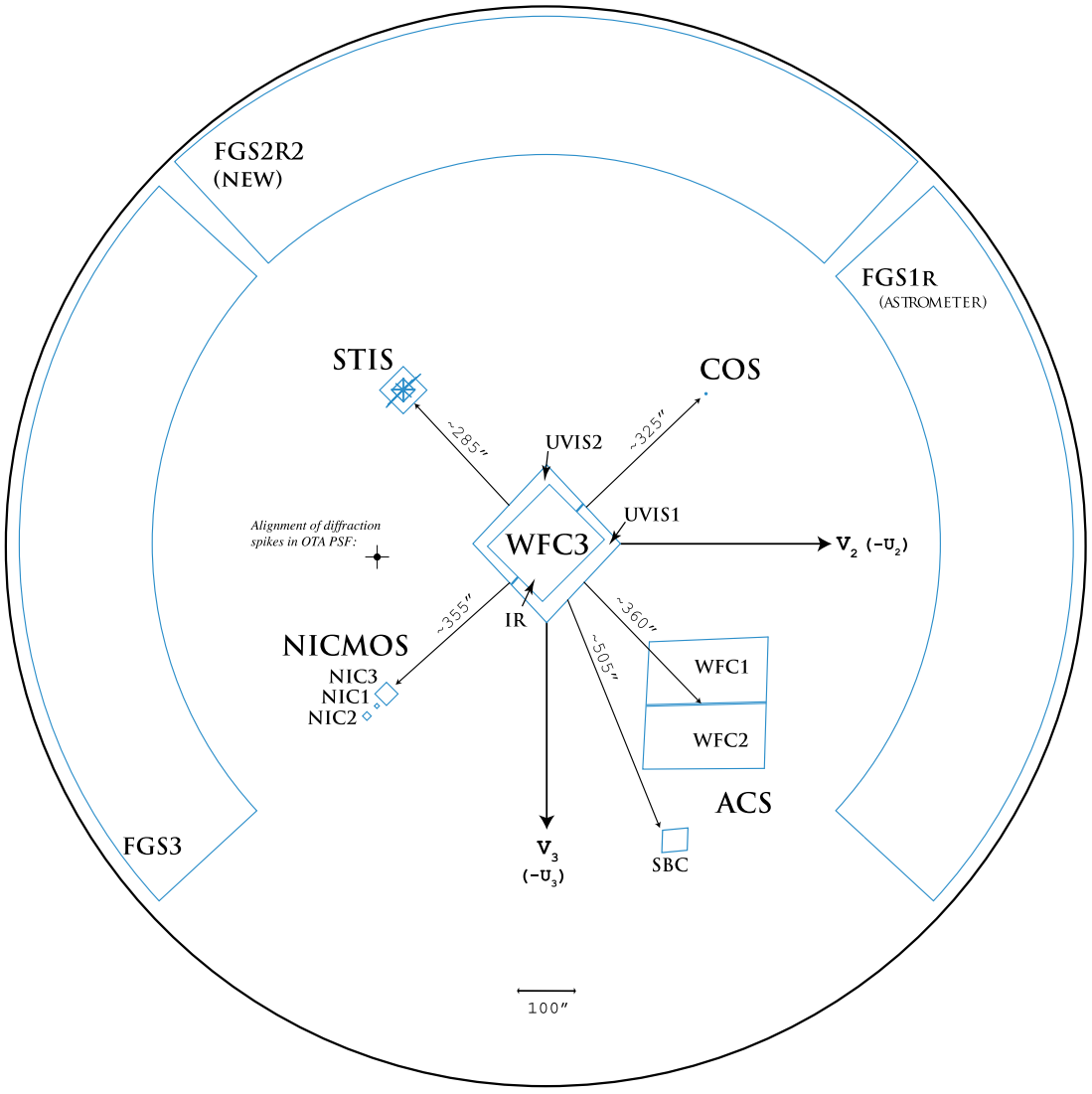

WFC3 images are subject to significant geometric distortions. These result primarily from the tilt of the focal plane relative to the optical axis (required for constant focus across the detectors; see Figure 2.1), which leads to a modest

elongation of the field of view in both channels. In the UVIS detector, most of the distortion runs approximately parallel to the diagonal direction of the CCD, while in the IR channel the distortion is parallel to the sides of the detector. As a result, the UVIS field projected onto the sky is shaped like a rhombus, with an acute angle between the *x*- and *y*-axes of the detector of approximately 86.1°. The IR channel projected onto the sky is rectangular, with an aspect ratio of about 0.90. Individual pixels projected onto the sky have the same geometry; thus the UVIS pixels are rhomboidal, measuring 0.0395 arcsec on each side, while the IR pixels are rectangular, measuring 0.135×0.121 arcsec.

For further discussion of geometric distortions in WFC3, see Appendix B.

2.3 Spectral Elements

2.3.1 The Filter Selection Process

Both WFC3 channels are equipped with a broad selection of spectral elements. These elements were chosen on recommendation of the WFC3 SOC, following a lengthy process with wide scientific and community input. Initial community suggestions and advice were considered at the WFC3 Filter Selection Workshop, held at STScI on July 14, 1999. Other input came from the WFC3 Science White Paper (see Section 1.2), from a suite of SOC-developed test proposals representing a broad range of current astronomical investigations, and from statistics of historical filter use in previous *HST* imaging instruments. The filter sets were chosen to fully cover the wavelength regimes of both WFC3 channels with a range of bandwidths, while complementing the filter sets available in ACS and NICMOS.

Based upon the SOC recommendations, the WFC3 IPT (see Section 1.1) developed detailed specifications for the vendors who designed and manufactured the filters. The final flight spectral elements were fully characterized, evaluated by the IPT and SOC, approved for flight, and installed into the filter wheels.

2.3.2 Filter and Grism Summaries

The UVIS channel has a selectable optical filter assembly (SOFA) that contains a stack of 12 filter wheels housing a total of 48 elements: 42 full-frame filters, 5 quad filters, and 1 UV grism. Each wheel also has an open, or empty, slot. For UVIS observations, the appropriate wheel is rotated to place the chosen filter into the light path, and the other eleven wheels are rotated to place the open slot in the light path. Only a single filter can be used at a time. Since the simultaneous insertion of two filters would result in significant defocus, the ground system does not provide the capability of crossing two filters.

The IR channel has a single filter wheel (FSM, or Filter Select Mechanism) housing 17 elements: 15 filters and 2 grisms; an 18th slot contains an opaque element

(or BLANK). For IR observations, the requested single element is rotated into the light beam. The FSM is a bidirectional wheel and always takes the shortest path to a new filter position. The filter wheel and all of its filters are housed, along with the HgCdTe detector package, in a cold shroud maintained at –30°C, a thermally-isolated enclosure which reduces the thermal loads and background emission onto the detector.

The filter sets in both channels include wide-, medium-, and narrow-band filters, as well as low-dispersion grisms (one in the UVIS channel, two in the IR channel) for slitless spectroscopy. The wide- and medium-band filters include popular passbands used in extragalactic, stellar, and solar-system astronomy, as well as passbands similar to those already used in other *HST* instruments for photometric consistency and continuity. The classical *UBVRIJH*, Strömgren, and Washington systems are reproduced, along with the filters of the Sloan Digital Sky Survey (SDSS). In addition, several extremely wide-band filters have been included in both channels, for ultra-deep imaging.

There are also a total of 36 different narrow-band passbands in the UVIS channel, consisting of 16 full-field filters and 5 quad filters. Quad filters are 2×2 mosaics occupying a single filter slot; each one provides four different bandpasses, at the cost of each one covering only about 1/6 of the field of view. The narrow-band filters provide the capability for high-resolution emission-line imaging in many of the astrophysically important transitions, as well as the methane absorption bands seen in planets, cool stars, and brown dwarfs.

In addition to the wide-band filters, the IR channel includes six narrow-band filters, which likewise sample the most important planetary, stellar, and nebular spectral features in the near-IR.

Finally, wide-band filters with similar wavelength coverages to those of the grism dispersers are available. These allow direct images in the same spectral ranges covered by the grisms. They are used to accurately identify spectroscopic sources and for wavelength calibration. WFC3 contains no ramp filters or polarizers, unlike ACS or WFPC2.

Table 6.2 and Table 7.2 provide a complete summary of the filters available for imaging with the UVIS and IR channels, respectively. Individual filter transmission curves as well as filter+WFC3+HST system throughput curves are presented in Appendix A. Graphical representations of the UVIS and IR filter wheels are shown in Figure 2.3 and Figure 2.4. Figure 3.2 shows the overall integrated system throughputs of WFC3 compared to other instruments.

Figure 2.3: UVIS Filter Wheels

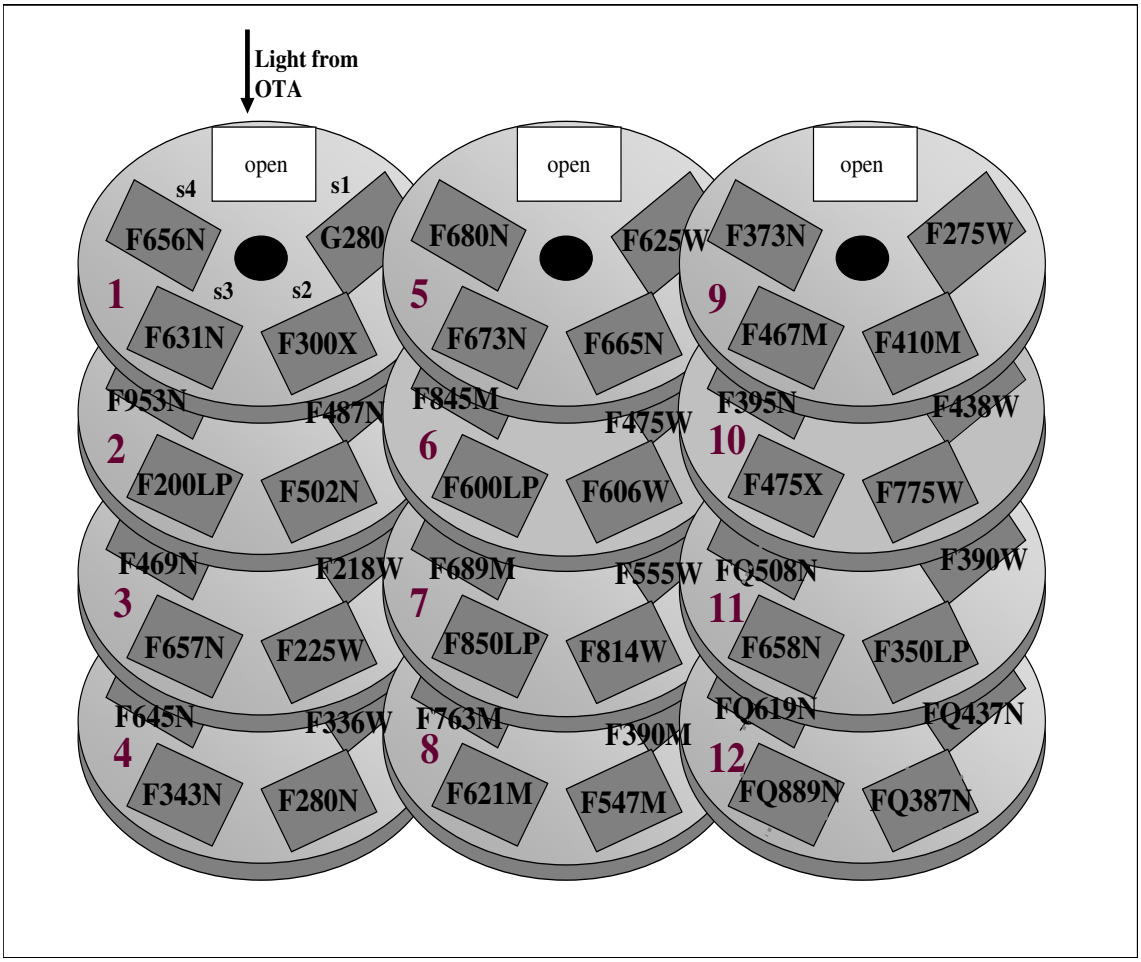

Figure 2.4: IR Filter Wheel

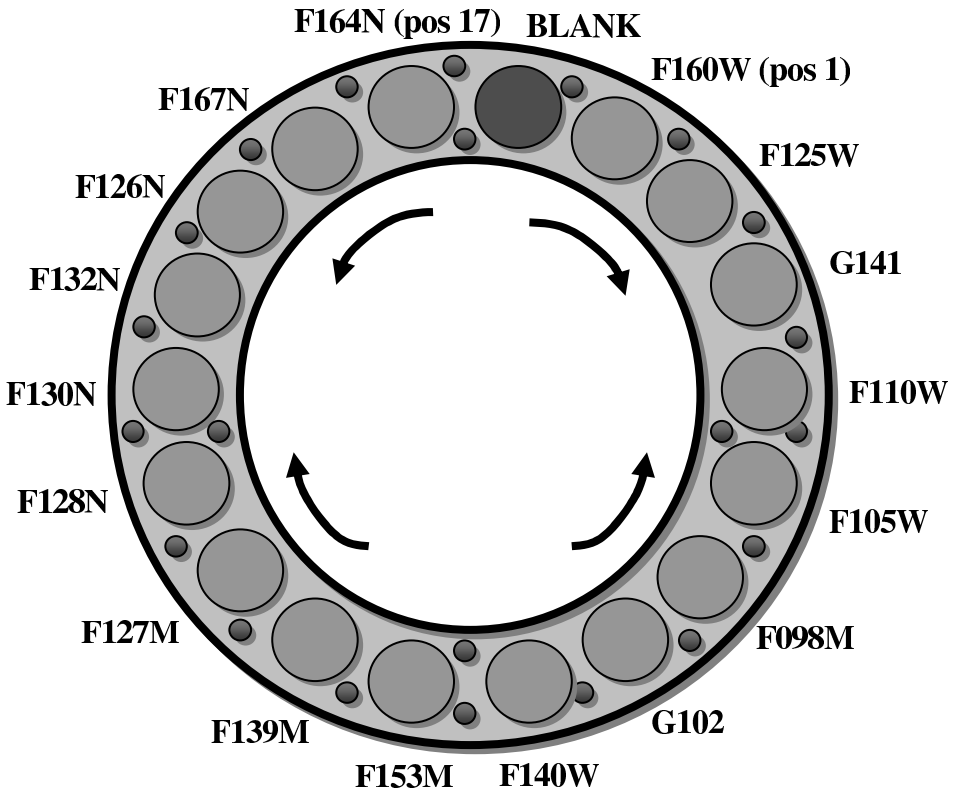

2.3.3 Shutter Mechanism

Integration times in the UVIS channel are controlled via a mechanical shutter blade very similar in design to the ACS/WFC shutter. Sitting directly behind the SOFA, the WFC3 UVIS shutter is a rotating disk about 12 inches in diameter; it is divided into four 90° quadrants, with alternating quadrants providing the blocking (i.e., there are two open and two closed positions). When the shutter is in the closed position initially, a commanded move of 90° places it into an open configuration; at the end of the exposure, another move of 90° places the shutter back into a closed position. Although the shutter can be operated in either a clockwise or counterclockwise direction, the current flight software always moves the blade in the same direction.

For very short exposure times in the UVIS channel, there are minor issues with exposure time non-uniformity (Section 6.7.1) and blurring due to shutter-induced vibration (Section 6.9.5).

There is no mechanical shutter in the IR channel; instead, the detector provides electronic shuttering. Dark-current measurements are obtained by using the BLANK, an opaque blocker in the filter wheel, which also is used to prevent the detector from viewing the Earth during occultations.

2.4 Detector Read-Out Modes and Dithering

The detectors in both channels offer subarray readout capability; see Section 6.4.4 (UVIS) and Section 7.4.4 (IR) for full details. The UVIS channel also allows 2×2 and 3×3 on-chip binning of full-frame images. Finally, a variety of dithering patterns can be requested using the Astronomer's Proposal Tool (APT) software. Predefined patterns have been established to address common requirements, such as sub-pixel dithering to improve PSF sampling or dithering to achieve large areal coverage while also sampling the inter-chip gap (Appendix C). The post-observation pipeline software (see Appendix E, the *WFC3 Data Handbook*, and the *MultiDrizzle Handbook*) carries out appropriate calibration of data taken in all of these configurations, and offers the option of reconstructing dithered images with a drizzling algorithm. If the dither pattern incorporates non-integer pixel offsets, it can effectively improve the sampling of the point-spread function (PSF). The software can also handle mosaicked images according to a set of rules or associations, rectifying them onto a cartesian pixel coordinate system.

CHAPTER 3:

Choosing the Optimum *HST* Instrument

In this chapter . . .

3.1 Overview

This chapter addresses the general questions that arise when observers choose between proposing to use WFC3 or one or more of the other imaging instruments that are available on *HST*. Following SM4, the observatory is at its highest level of capability: new instruments have been installed, both STIS and ACS/WFC have been repaired, and NICMOS has been reactivated.

In choosing between instruments for their particular projects, observers should carefully evaluate the capabilities of WFC3 and compare them to those of the other *HST* instruments, in the context of their own scientific goals. There is some intentional redundancy between WFC3, ACS, STIS and NICMOS, to provide a degree of protection against degradation or failure of the instruments. However, the instruments largely complement one another, and therefore it is likely that one instrument will be preferred for any science program. Therefore, observers do need to give careful consideration to instrument capabilities in order to optimize their observations. They should refer to the *HST Call for Proposals* for any policy issues, and the *HST Primer* for additional comparison information.

3.2 Choosing Between Instruments

The primary factors to consider in choosing the preferred instrument are areal coverage, spatial resolution, wavelength coverage, sensitivity, and availability of specific spectral elements. Table 3.3.3 lists the primary characteristics of the imaging instruments currently available on *HST*.

For some research programs, the instrument choice may be dictated by the need for a particular spectral element. In this regard, WFC3 offers considerable capability because of its broad complement of wide-, medium-, and narrow-band filters both at UV/optical and near-IR wavelengths, as well as one UV grism and two near-IR grisms for slitless spectroscopy.

For studies at optical wavelengths, the trade-offs to consider when deciding between WFC3/UVIS and ACS/WFC include pixel size, field of view and, to some extent, throughput. WFC3 is generally preferable when angular resolution has higher priority than field of view, because of its finer pixel size. On the other hand, ACS/WFC has higher throughput than WFC3/UVIS at wavelengths longward of ~400 nm (see Figure 3.2), and hence may be the best choice when the highest possible sensitivity at such wavelengths is crucial. However, considerations of degraded charge-transfer efficiency (CTE) should be kept in mind, since ACS has endured the high-radiation space environment for more than seven years longer than has WFC3.

At UV wavelengths, WFC3/UVIS is the only imager on *HST* to offer a large field of view combined with high throughput. However, its spectral coverage does not extend shortward of 200 nm, whereas ACS/SBC and STIS/FUV-MAMA both reach down to 115 nm (STIS/NUV-MAMA reaches 160 nm), and also offer finer spatial sampling (see Table 3.3.3). Thus, WFC3 will be the choice whenever both large field of view and coverage down to 200 nm are required (e.g., multi-wavelength surveys). However, if observations at extreme far-UV wavelengths are necessary, or if the highest available spatial sampling at UV wavelengths is a primary requirement, then ACS/SBC or the STIS UV channels should be considered. Because ACS/HRC could not be repaired during SM4, WFC3 offers imaging at the finest pixel scale of any *HST* instrument at optical wavelengths.

At near-IR wavelengths WFC3/IR offers a much larger field of view and, generally, higher throughput than NICMOS. It also offers greatly improved sensitivity and ease of data reduction and calibration, due to its more uniform flat field and the accurate bias subtraction made possible by the presence of reference pixels. However, WFC3 sensitivity is limited to wavelengths shortward of ~1700 nm, and WFC3 has coarser pixel sizes than NIC1 and NIC2, and does not offer a coronagraph or polarizers. For IR observations of bright targets, NICMOS may also be preferred because observations may be obtained with the instrument intentionally defocused to avoid saturation. This is not permitted with WFC3.

Table 3.1: Comparison of wavelength coverage, pixel scales, and fields of view of *HST*'s imaging instruments.

Instrument	Wavelength coverage (nm)	Pixel size (arcsec)	Field of View (arcsec)
WFC3 UVIS	**200 – 1000**	**0.04**	**162×162**
ACS WFC	370 – 1100	0.05	202×202
ACS SBC	115 – 170	0.032	34×31
STIS FUV-MAMA	115 – 170	0.024	25×25
STIS NUV-MAMA	165 – 310	0.024	25×25
STIS CCD	250 – 1100	0.05	52×52
WFC3 IR	**800 – 1700**	**0.13**	**136×123**
NICMOS NIC1	800 – 1900	0.043	11×11
NICMOS NIC2	800 – 2500	0.076	19×19
NICMOS NIC3	800 – 2500	0.20	51×51

3.3 Comparison of WFC3 with Other *HST* Imaging Instruments

3.3.1 Wavelength Coverage

The WFC3 UVIS channel is similar in design to the Wide Field Channel (WFC) of the ACS. There are, however, a few differences. While ACS/WFC is blind at wavelengths shorter than about 370 nm (i.e., shortward of the *B* band), WFC3/UVIS has excellent sensitivity extending down to 200 nm. The design trade-offs adopted to achieve this extended UV wavelength coverage (primarily the CCD coating and the use of aluminum coatings for the reflective optics) lead to a reduced sensitivity of WFC3 at longer optical wavelengths compared to that of ACS/WFC. WFC3/UVIS has no sensitivity in the far-UV region below 200 nm. The far-UV is covered by three MAMA detectors in ACS and STIS.

The WFC3 IR channel provides nearly a factor of 2 improvement in sensitivity over NICMOS. However, its wavelength coverage is shorter, ending at about 1700 nm (compared with 2500 nm for NICMOS). The WFC3/IR cutoff at 1700 nm greatly reduces the instrument's sensitivity to the thermal background. Unlike NICMOS, the WFC3 IR channel does not have a cryogenic dewar or mechanical cryocooler for cooling of instrument components; instead, all optical components of the IR channel are actively cooled by a thermal-control subsystem. Although much simpler than the NICMOS cryocooler, this design allows the IR detector to be cooled only to ~145 K; also, the view of warmer components along the optical path precludes suppression of the thermal background at wavelengths longer than ~1700 nm.

3.3.2 Field of View

Figure 3.1 illustrates the fields of view, at the same scale, for all of the *HST* imaging instruments currently available on *HST*.

Figure 3.1: Schematic diagram comparing relative sizes of the fields of view for all available *HST* imaging instruments. Successive lines of text underneath each field of view give the field size in pixels, the pixel scale in arcsec/pixel, and the field size in arcsec. Detector footprints are rendered as rectangular in the diagram and thus do not include the effects of geometric distortion. For a more accurate depiction of detector footprints including geometric distortions and relative *HST* focal plane locations, see Figure 2.2.

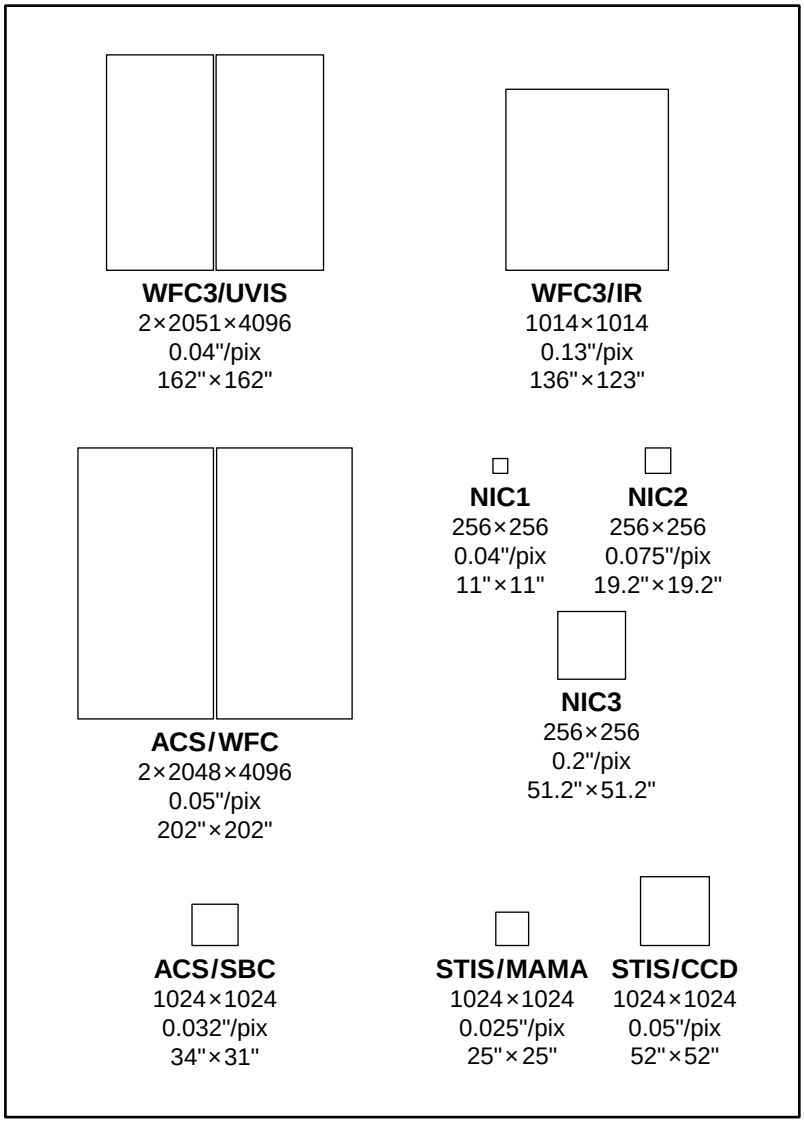

The pixel scale of the WFC3 UVIS channel is 20% finer in comparison to the ACS/WFC, obtained at the cost of covering only about 66% of the area of the ACS field of view.

The WFC3 IR channel covers about 6.4 times the area of the NICMOS NIC3 channel, with almost 2-times better spatial sampling, but it lacks the very high spatial

samplings offered by the NICMOS/NIC1 and NIC2 channels. Further, the WFC3/IR channel covers 45 times the area of NICMOS/NIC2 channel with slightly coarser sampling, but arguable better photometric precision.

Table 3.1 presents a comparison of the wavelength coverage, pixel scale, and field of view of WFC3 and of the other *HST* imaging instruments that are currently available.

3.3.3 Detector Performance

Table 3.2 summarizes the on-orbit measurements of read-out noise and dark current for the WFC3 detectors, and compares them with the parameters for the other currently available *HST* imaging detectors. Chapter 5 gives more detailed information about the detectors in both channels. Chapter 9 discusses sensitivities, limiting magnitudes, and exposure times.

Table 3.2: Characteristics of *HST* CCD and HgCdTe imaging detectors currently available. The WFC3/IR dark current includes the instrument thermal background.

Detector	Read-out noise (e^- rms)	Dark current (e^-/pix/s)	Mean well Depth (e^-)
WFC3/UVIS	**3.1–3.2**	**0.0003–0.0006**	**75,000-80,000**
ACS/WFC	4.8	0.0062	84,700
STIS/CCD	5.4 (gain=1), 7.7 (gain=4)	0.009	114,000
WFC3/IR	**~12.0[1]**	**0.05**	**77,900**
NICMOS/NIC1	26	0.3	145,000
NICMOS/NIC2	26	0.3	152,000
NICMOS/NIC3	29	0.3	213,000

1. WFC3/IR read noise is for a 16-read linear fit; NICMOS read noise is for a pair of reads (double sampling). WFC3/IR double sampling read noise is 20.2–21.4 e^-.

3.3.4 System Throughputs and Discovery Efficiencies

Figure 3.2 plots the measured on-orbit system throughputs of the two WFC3 channels as functions of wavelength, compared to those of ACS, NICMOS, and WFPC2. These curves include the throughput of the OTA, all of the optical elements of the instruments themselves, and the sensitivities of the detectors. Throughputs were calculated at the central wavelength (the "pivot wavelength"; see Footnote [3] to Table 6.2) of each wide-band filter of each instrument.

As Figure 3.2 shows, WFC3 offers a unique combination of high sensitivity and wide spectral coverage ranging from the UV to the near-IR. WFC3 extends and complements, over a large field of view, the optical performance of ACS/WFC at wavelengths shorter than ~400 nm and longer than 1000 nm. The good degree of

functional redundancy with ACS and NICMOS will help ensure that the unique scientific capabilities of *HST* will remain available until the end of its mission.

Another quantity that is useful when comparing different instruments, especially in the context of wide-angle surveys, is the "discovery efficiency," defined as system throughput times area of the field of view as projected onto the sky. In Figure 3.3 we plot the discovery efficiencies of the *HST* imaging instruments, again vs. wavelength. Note that the *y*-axis is now logarithmic. This figure dramatically illustrates the enormous gains that WFC3 offers, compared to previous *HST* instruments, both in the optical/UV below 400 nm, and in the near-IR.

Finally, we present WFC3's strengths by including detector noise and thus showing how its efficiency, wide wavelength coverage, and large field of view apply to general problems: the limiting point-source magnitude reached in 10 hours of observing time (Figure 3.4); and the time needed to survey a sky area about 9 times larger than the Hubble Ultra Deep Field, to a limiting ABMAG of 26 (Figure 3.5).

Figure 3.2: System throughputs of optical/infrared imaging instruments on *HST* as functions of wavelength. The plotted quantities are end-to-end throughputs, including filter transmissions, calculated at the pivot wavelength of each wide-band filter of each camera.

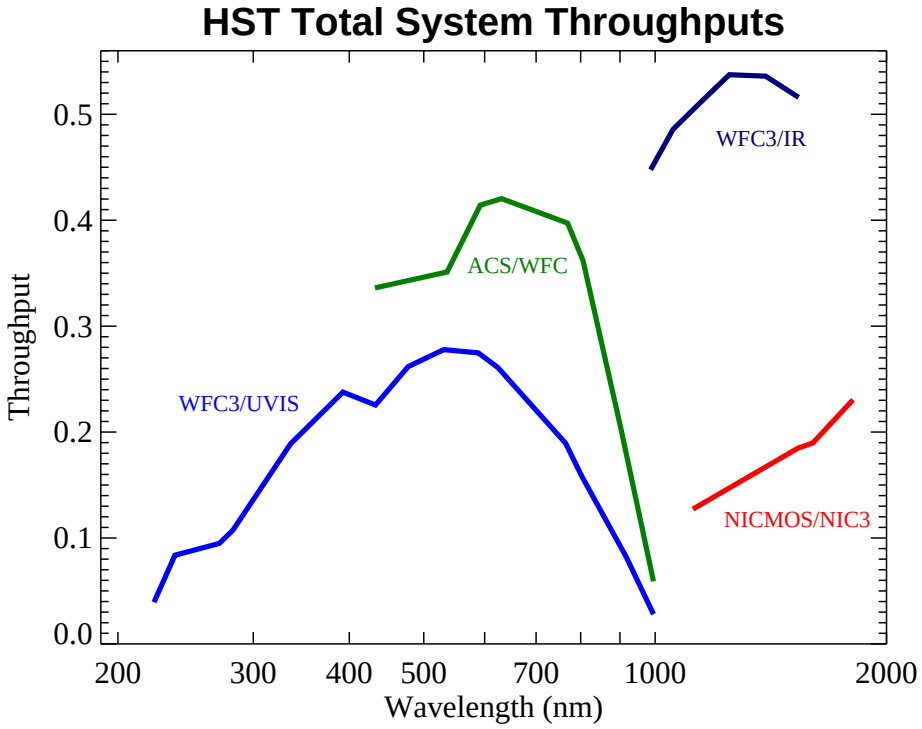

Figure 3.3: Discovery efficiencies of optical/infrared *HST* imaging instruments, including those verified on-orbit for WFC3. Discovery efficiency is defined as the system throughput (plotted in Figure 3.2) multiplied by the area of the field of view. Note that the *y*-axis is now logarithmic.

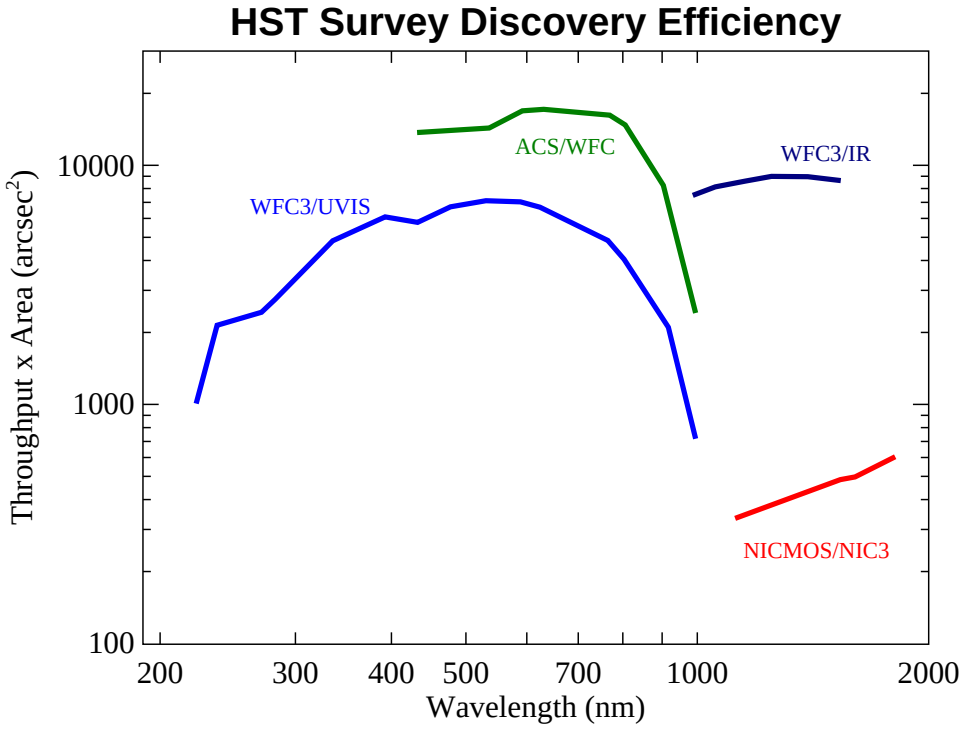

Figure 3.4: Limiting point-source magnitudes reached by optical/infrared *HST* imaging instruments in 10 hours.

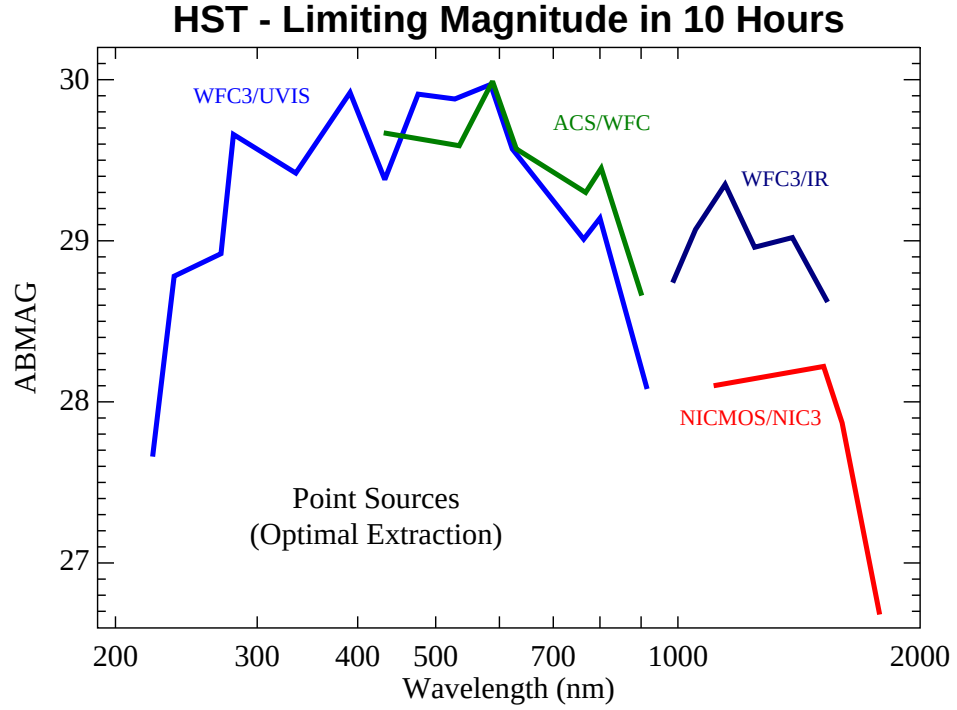

Figure 3.5: Time needed for optical/infrared *HST* imaging instruments to survey a wide sky area to a limiting extended (1 arcsec^2) ABMAG of 26.

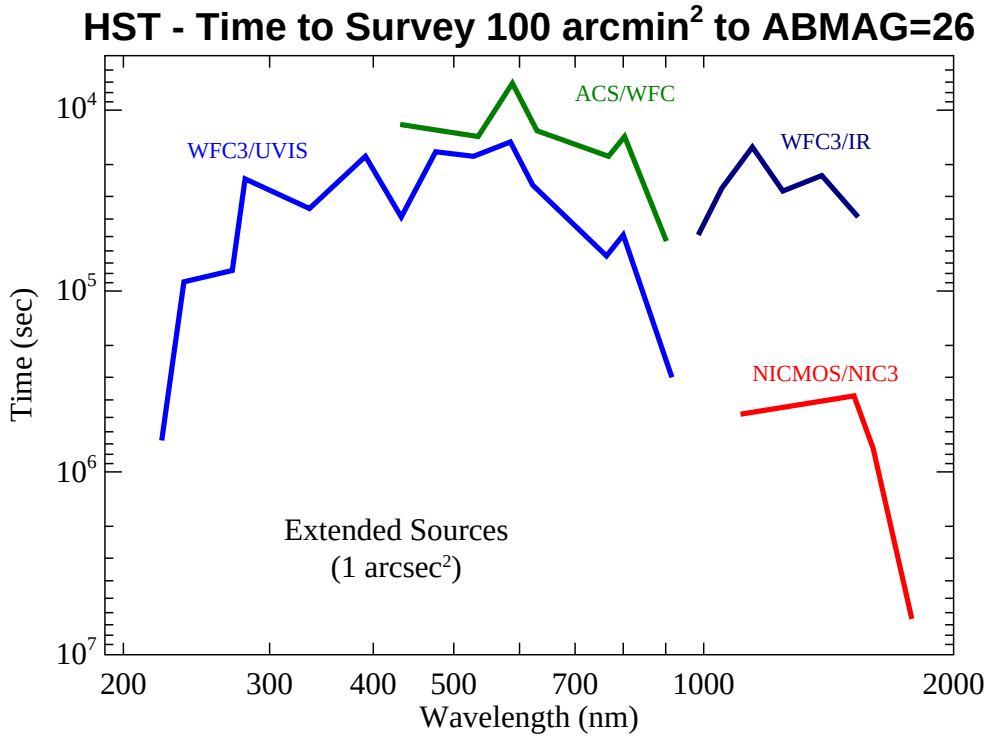

CHAPTER 4:

Designing a Phase I WFC3 Proposal

In this chapter . . .

4.1 Phase I and Phase II Proposals

The first steps in preparing an *HST* program are to establish a set of science goals and to explore whether *HST* can be used to achieve those science goals (using the information provided in the *HST Call for Proposals*, the *HST Primer* and the instrument handbooks). Once an observer has decided that *HST* can achieve the science goals, they must prepare a formal proposal.

In this Chapter we give an overview of the steps that are taken in preparing an *HST* observing proposal that involves WFC3 observations. "**Phase I**" refers to the initial proposal that is reviewed by the Telescope Allocation Committee (TAC). The Phase I proposal presents the scientific justification for the project, lists the targets to be observed and the instrument(s) and spectral elements to be used, and includes a request for a specific number of spacecraft orbits. (See the *HST Call for Proposals* and *HST Primer* for a full discussion of all policy issues and additional guidance.)

The Phase I proposal does not contain many of the details that are actually required to carry out observations with *HST*. These are included in a "**Phase II**" proposal that will be needed if and after the proposal is recommended by the TAC and approved by the STScI Director. The *Phase II Proposal Instructions* are a vital resource at that time.

The actual submission of proposals in both Phase I and Phase II is accomplished using the **Astronomer's Proposal Tool** (**APT**); see http://apt.stsci.edu.

This Chapter focuses on the steps for assembling the information needed to prepare a Phase I WFC3 proposal for submission using APT**.**

4.2 Preparing a Phase I Proposal

An *HST* program is a set of exposures specified so as to achieve one or more scientific objectives. We can break down the development of a WFC3 observing program, imaging and/or spectroscopic, into a six-step process. Often there is not a unique way in which to achieve the scientific objectives, and you must assess the trade-offs and feasibilities of multiple approaches. Furthermore, you will wish to use *HST* and WFC3 efficiently, in order to obtain as much science within as small an orbit allocation as possible. Therefore, you may need to iterate these steps in order to achieve a final feasible program that is also optimal.

In this chapter we introduce issues that you may need to consider in designing your observations. Later chapters in this *Handbook* will present detailed information for your use. These six steps, and the considerations they entail, are described in the following subsections.

4.2.1 Which WFC3 Channel(s) and Filter(s)?

First, from your science requirements, determine the desired wavelength(s) of observation. Those requirements may include considerations of the spectral energy distribution (SED) of the target, or the required angular resolution, which also varies as a function of wavelength. Typically, if the wavelength of observation is less than 900 nm, then the WFC3 UVIS channel will be used; or if the wavelength is greater than 900 nm, then the WFC3 IR channel will be used. Your program may involve use of both channels.

The angular resolution, field of view, and sensitivity of the two channels differ appreciably, and may also influence your selection of the WFC3 channel(s) to use (see Chapter 2 for an overview of the UVIS and IR channels). Features of interest in the target's SED can be matched to the spectral resolution of the observation by selecting appropriate filters (see Chapter 6 for the UVIS channel, Chapter 7 for the IR channel, and Appendix A.1 for detailed filter passbands), or grisms (see Chapter 8).

To match continuum features, wide-, medium-, and/or narrow-band filters may be selected, presenting the possibility of a trade-off between detector signal and spectral resolution. Note that the UVIS quad filters limit the field of view to about one sixth of the full field.

4.2.2 What Exposure Times?

Second, you should determine the exposure time and exposure sequences needed to achieve the required signal-to-noise (S/N) with the chosen filter(s) or grism(s). A full discussion of exposure time calculation is presented in Chapter 9, but, as mentioned in that chapter, in most cases you will use the online Exposure Time Calculator (ETC). The S/N depends upon the target's incident flux and the noise from

the background and detector sources. These sources include zodiacal light, detector dark current, and stray light from both Earth and bright targets in the field of view.

Having determined the basic exposure time necessary to achieve the required S/N, you will in most cases find it necessary to achieve that total exposure time through a sequence of shorter exposures. For instance, if the exposure time is greater than the maximum orbital target visibility, it will be necessary to obtain a sequence of exposures. UVIS exposures exceeding 3,600 s require more than one exposure as do IR exposures greater than 2,800 s (see Chapter 6 and Chapter 7 for a fuller discussion).

Additional reasons to structure the total exposure time are described in the following paragraphs, as well as considerations peculiar to each of the two WFC3 channels.

Dithering and Mosaicking

A sequence of exposures obtained in a dither pattern of *HST* pointings will often be used to reduce the noise from flat-field calibration error, cosmic rays, and residual images. Including sub-pixel displacements in the dither pattern will allow better sampling of the point-spread function (PSF). You may design and specify a dither pattern, or use one of the pre-defined patterns already designed to sub-sample the PSF, to cover the UVIS inter-chip gap, or to mosaic a large field. The pre-defined sequences and information on designing your own patterns, are presented in Appendix C of this *Handbook* and in the Phase II Proposal Instructions.

Bright Targets

For bright targets, a sequence of shorter exposures may be needed to avoid entering the non-linear or saturation regimes of the detectors (see Chapters 5, 6, and 7).

Bright objects do not cause safety concerns for either UVIS or IR observations with WFC3. Image persistence can be a concern for IR observations (as discussed in Section 7.9.4 and Appendix D) but is not generally a problem with the UVIS channel.

UVIS Exposures

For UVIS observations, it will almost always also be desirable to use a sequence of exposures, in order to remove cosmic-ray impacts. For observations with the UVIS channel of faint targets, the effects of charge-transfer efficiency (CTE) during readout of the detector must be considered (see Chapters 5 and 6). Charge injection for such images will mitigate the non-ideal CTE, but are not necessary at present and will not be offered in Cycle 18.

IR Exposures

For observations with the IR channel you must choose a readout method from the 11 available kinds of sample sequences, each of which may comprise from 1 to 15 non-destructive readouts. These include RAPID, linear (SPARS), and log-linear (STEP) sequences (see Chapter 7). The exposure time is dictated by the sequence chosen. The ability to remove cosmic-ray impacts will depend upon the sequence chosen.

4.2.3 What Aperture or Subarray?

Next, from considerations of the target's angular size and structure, and of data volume, you should determine the WFC3 aperture or subarray you will use. The available UVIS apertures and subarrays are presented in Chapter 6, and those for the IR channel in Chapter 7.

In some cases, correct placement of an extended target within an aperture may require you to specify a special *HST* pointing and possibly the orientation of the field of view (which is determined by the spacecraft roll angle). Additional considerations may include detector imperfections such as the UVIS inter-chip gap (Chapter 5), diffraction spikes (Chapters 6 & 7), filter ghost images (see Chapters 6 & 7), detector saturation (i.e., for bleeding in a UVIS image along a detector column; Chapter 5), detector charge transfer (Chapter 5), distortion of the image (Appendix B), or dispersion direction of the grism (see Chapter 8). However, most of these only need to be considered at the Phase II stage, unless they affect the number of orbits needed for the proposal.

Note that selection of a WFC3 aperture without specifying further constraints implicitly specifies: (1) the full image will be read out; (2) the target coordinates will be placed at a default location on the detector (see Chapters 6 & 7; generally the target will be placed at the center of the chosen field of view); and (3) the telescope roll angle will be unspecified, as it will depend on the date the exposure is executed. You may override any of these defaults, however.

You can reduce the size of the image read out and thus the volume of data obtained by selecting a subarray. For the UVIS detector, on-chip binning of the pixels will also reduce the data volume, but at the expense of angular resolution (see Chapters 5 & 6). Reducing the data volume will reduce the overhead to read out and transfer images, which may be desirable in order to allow more images of the target of interest to be obtained during an *HST* orbit. During Phase II preparation, the location of the target can be specified with the POS TARG Special Requirement and the rotation of the image can be specified with the ORIENT Special Requirement (see Chapters 6 & 7).

4.2.4 What Overheads and How Many *HST* Orbits?

Fourth, determine the overhead times required, in addition to the exposure times, in order to operate the spacecraft and the camera (see Chapter 10).

The spacecraft overhead includes the time needed for guide-star acquisition or re-acquisition at the beginning of each orbit. The camera overheads include time needed to change filters, change between the UVIS and IR channels, read out the exposure to the WFC3 data buffer, and transfer the images from the buffer to the *HST* science data storage. Note that overheads are especially severe for sequences of short exposures, but these can sometimes be mitigated by using small subarrays or by alternating short and long exposures. For Phase II proposals, the APT provides tools for detailed modeling of complete observation sequences.

Finally, you will add the overhead times to the exposure times to find the total time needed for your program, which is what you will request in your Phase I proposal.

This total time is expressed as the (integer) number of *HST* orbits required to obtain the observations.

4.2.5 Any Special Calibration Observations?

Most observers will not need to worry about special calibration observations. As a result of ground based and SMOV testing, WFC3 is fairly well-characterized as described in this Handbook and in more detail in WFC3 Instrument Science Reports. Instrument characterization and calibration will be maintained and improved as part of the ongoing calibration program conducted by STScI (Appendix E).

The main reasons an observer would need to consider special observations are situations where a program requires greater precision than is provided through the standard calibration program. These additional observations must be justified in your Phase I proposal submission, and the orbits required to carry out the special observations must be included in the overall orbit allocation requested. Proposers are advised to discuss their need for special observations with the helpdesk.

4.2.6 What is the Total Orbit Request?

Having determined the content of the science and supporting observations necessary to achieve your scientific objectives, you must finally determine the total amount of *HST* time to carry out those activities by including the appropriate amount of time for spacecraft and instrument overheads.

Detailed procedures for determining the total amount of time to request in your Phase I proposal are presented in Chapter 10.

CHAPTER 5:

WFC3 Detector Characteristics and Performance

In this chapter . . .

5.1 Overview of this Chapter

The science return on any data can typically be enhanced if observers acquire a basic understanding of how the detectors operate, and of their individual characteristics and limitations. For the most demanding observations, such as imaging very faint or extremely bright sources, or for exposures using non-default parameters, an even deeper understanding of the detectors and their operation may be required. This chapter aims to provide both basic and in-depth information on the detectors used in both WFC3 channels. Sections 5.2-5.4 discuss the CCD detectors used in the UVIS channel, and Sections 5.5-5.7 discuss the infrared detector used in the IR channel.

Table 5.1 summarizes the basic characteristics of the flight CCD and IR detectors. For the CCDs, the information is either an average for the two chips, or the range of values for both of them. Results are based on ground measurements as well as data taken during the 2009 Servicing Mission Observatory Verification program run after WFC3 was installed in *HST*.

Table 5.1: WFC3 Detector Characteristics

Characteristic	UVIS Channel CCDs	IR Channel Detector
Architecture	e2v CCD detectors. Thinned, backside illuminated, UV optimized, multi-phase pinned, buried/mini-channel, charge injection capability.	Teledyne HgCdTe infrared detector. MBE-grown, substrate removed, on Si CMOS Hawaii-1R multiplexer.
Wavelength Range	200 to 1000 nm	800 to 1700 nm
Pixel Format	2 butted 2051 × 4096, 31-pixel gap	1024 × 1024 (1014 × 1014 active)
Pixel Size	15 μm × 15 μm	18 μm × 18 μm
Plate Scale	0.040"/pixel	0.13"/pixel
Field of View on Sky	Rhomboidal, 162" × 162"	Rectangular, 136" × 123"
Quantum Efficiency	50–59% @ 250 nm[1] 68–69% @ 600 nm 47–52% @ 800 nm	77% @ 1000 nm 79% @ 1400 nm 79% @ 1650 nm
Dark Count	1–2 e^-/hr/pixel (median)	0.048 e^-/s/pixel (median)
Readout Noise	3.1–3.2 e^-	20.2–21.4 e^- (pair of reads) 12.0 e^- (16-read linear fit)
Full Well[2]	63,000–72,000 e^-	77,900 e^- (mean saturation level)
Gain	1.60–1.63 e^-/DN	2.28–2.47 e^-/ADU
ADC Maximum	65,535 DN	65,535 DN
Operating Temperature	–83°C	145 K

1. Quantum efficiency at 250 nm does not include multiple-electron events, which lead to larger apparent efficiency in e.g., Figure 5.2.
2. The IR full well value is based on fully-integrated instrument ground testing. Other CCD and IR parameters are derived from on-orbit data.

5.2 The WFC3 UVIS Channel CCD Detectors

5.2.1 Basics of CCD Operation

A charge-coupled device (CCD) is a silicon-based detector containing a two-dimensional array of summing wells called pixels, short for pixel elements. Each pixel accumulates electric charge in proportion to the number of photons striking that location on the detector. Physically, the summing wells are created by electric fields established at the depletion (charge-free) regions of the Si-SiO_2 metal-oxide-semiconductor (MOS) capacitors. In a typical three-phase CCD, the size

of the depletion region is controlled by the voltage of three gates. The gates are arranged in parallel, with every third gate connected together.

At the end of an exposure, the voltages of the gates are changed with an appropriate clocking pattern, causing all charge packets to be sequentially transferred to the adjacent pixel, until they reach the readout circuitry at the detector's edge. The transfer of charges between pixels occurs in parallel, row by row, whereas the extraction of the "zeroth" row at the edge occurs along an external serial register, where each packet is serially transferred to an output amplifier at the detector corner.

5.2.2 The WFC3 CCDs

The WFC3 UVIS channel uses two CCD detectors fabricated by e2v Ltd. (formerly Marconi Applied Technologies Ltd.). Both CCDs are 2051×4096 devices with 15×15 μm square pixels. There are 2051 rows by 4096 columns, where the row/columns definition follows the convention of having the parallel direction first and the serial direction second. Having the serial register along the long (4096 pixel) edge reduces the number of transfers required to read out a charge packet.

The WFC3 CCDs are three-phase devices, thinned and back-illuminated (back-thinned) to improve the sensitivity to UV light. Thinning refers to the removal of the thick substrate on which the chip is originally built and is done to improve shorter-wavelength efficiency (only those electrons generated in the vicinity of the gate structure can be collected efficiently). Back-illumination means that photons are focussed on the back side of the chip, rather than having to pass through the opaque gate structures implanted on the front side.

Similar to ACS, the WFC3 CCDs also have buried channels and are operated in multi-pinned phase (MPP) mode. This buried channel, or mini-channel, improves CTE for targets with relatively low signal levels (~10K e^- or less) and reduces the dark current as well. The buried channels have the capability of injecting charges to fill in the traps and improve the CTE. Further details of these features are given in Section 5.4.8.

The two WFC3 CCDs are butted together along their long dimension to create a 2×1 mosaic. Figure 5.1 shows a picture of a CCD assembly similar to the flight detector. The butted configuration is equivalent to a 4102×4096 array, but with a gap of 31 ± 0.1 pixels between the two chips (1.2 arcsec on the sky).

The CCDs are cooled by a four-stage thermoelectric cooler (TEC) to a nominal temperature of −83° C. The detectors are packaged inside a cold enclosure, which is nearly identical to the one used for ACS, itself a scaled-up version of the STIS design. The package includes a second cooled window to reduce the radiative heat load.

The CCD focal plane is assembled on a molybdenum (moly) base disk, which provides some shielding from cosmic rays and also serves as the thermal sink path from the hot side of the TEC stack to the heat pipes (which carry the heat to the external radiator). The "cover" with the external window is about 1 cm thick and is made of "alloy 42" steel; it provides some protection from CRs incident on the front side of the CCDs.

The WFC3 CCDs are quite similar to those used in the ACS Wide Field Channel (WFC). They have the same pixel size, nearly the same format (2051×4096 in WFC3, compared to 2048×4096 in ACS), the same orientation of the serial and parallel registers, similar technology (buried-channel, MPP operation), and nearly identical mechanical interfaces. The main differences of the WFC3 chips compared to those in ACS/WFC are:

- UV optimization of the WFC3 wavelength response
- Significantly lower readout noise for the WFC3 chips (~3.1- 3.2 e^- compared to ~5 e^-)
- 2051 rows instead of 2048
- Charge-injection capability
- 31-pixel gap instead of 50
- Manufactured by e2V (formerly Marconi); ACS has Site devices.

An overview of the WFC3 CCD performance was given above in Table 5.1.

Figure 5.1: Detector package similar to the WFC3/UVIS flight detector. The size of the 4kx4k array is approximately 6×6 cm, and it consists of two butted 2051×4096 CCDs with a 31-pixel gap between them.

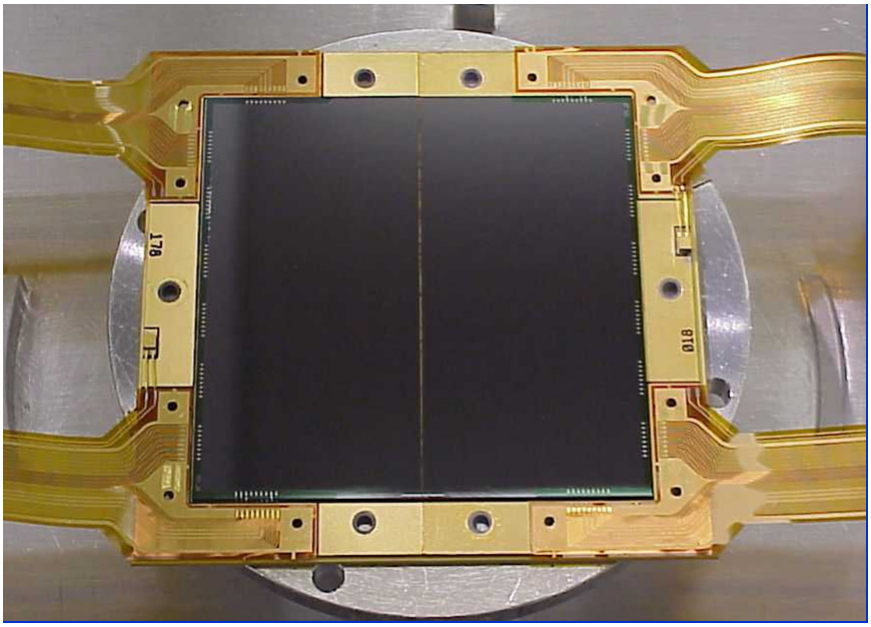

5.3 WFC3 CCD Readout Formats

5.3.1 Full-frame Readout

The WFC3 UVIS channel contains two CCD chips, each of which has two readout amplifiers. The amplifiers on chip 1 are designated A and B, and those on chip 2 as C and D. Although a chip (or part of a chip) may be read out through a single amplifier, the default and fastest readout mode employs all four amplifiers simultaneously, such that each amplifier reads out half of a chip.

A full-frame UVIS exposure produces a single FITS file in which the data from each of the two chips are stored in separate image extensions, along with associated error and data quality arrays for each image. For consistency with ACS, the image data from CCD chip 2 are stored in SCI array 1 (FITS extension 1) and the image data from CCD chip 1 are stored in SCI array 2 (FITS extension 4). Table 5.2 lists the chips, the associated amplifiers, and the FITS extensions of the science image data.

Each CCD chip contains 2051×4096 active pixels, but the raw images returned by the WFC3 electronics contain a larger number of pixels. This is due to the detector overscan: portions of the detector that are not exposed to light. Overscan regions are useful for characterizing detector electronics performance, and especially for measuring the bias level contained within an image. Serial overscan corresponds to a fixed number of unexposed pixels at each end of each serial shift register. Conversely, parallel overscan is generated by additional parallel shifting before or after all of the exposed rows of the detector have been read out. In principal, both serial and parallel overscan can be implemented either as physical overscan or virtual overscan. The physical overscan is a characteristic of the detector hardware, whereas virtual overscan is a software function, and the number of rows and columns of virtual overscan generated for an image is controllable via the readout timing pattern.

The WFC3 CCD overscan regions are described in more detail in Section 6.7.

Table 5.2: WFC3 CCD Naming Conventions.

CCD Chip	Amplifiers	Science Image FITS File Extension	Error Array FITS File Extension	Data Quality Array FITS File Extension
1	A, B	[SCI,2]=[4]	[ERR,2]=[5]	[DQ,2]=[6]
2	C, D	[SCI,1]=[1]	[ERR,1]=[2]	[DQ,1]=[3]

5.3.2 Subarrays

The default CCD readout mode is to read all pixels of both chips, including all available overscan regions. It is also possible to restrict the readout to rectangular subarray regions. Only data from the area within the subarray are stored in buffer memory, and the rest of the image is discarded. The subarray can be chosen from several pre-defined configurations.

UVIS subarray images contain no virtual overscan data and serial physical overscan is present only if the defined subarray boundaries overlap the physical overscan columns on either end of the chips. Thus all corner subarrays contain physical overscan data, while centered subarrays do not. (Table 6.1).

Subarrays are discussed in detail in Section 6.4.4.

5.3.3 On-Chip Binning

The UVIS CCDs also provide an on-chip binning capability, in which several adjacent pixels may be read out as a single pixel. The available choices are 2×2 and 3×3 on-chip binning. On-chip binning and subarrays can not be used simultaneously. See Section 6.4.4 for details on the use of on-chip binning in WFC3/UVIS observations. If on-chip binning is used, the overscan geometry is complicated by the need to truncate "odd" pixels, and each half of a row must be considered separately.

Some science data are binned together with overscan data. Details are given at the end of Section 6.7.2.

5.4 WFC3 CCD Characteristics and Performance

5.4.1 Quantum Efficiency

The quantum efficiencies (QEs) of the two WFC3 CCDs are plotted against wavelength in Figure 5.4.3. Here the QE is defined as electrons yielded per incident photon. The solid curves illustrate the QEs as measured at the Detector Characterization Laboratory (DCL) at Goddard Space Flight Center, slightly corrected downward by the TV3 ground tests. The plots demonstrate the high sensitivity of the CCDs in the UV down to 200 nm. On the other hand, the peak QE at ~600 nm is less than that of the ACS/WFC detectors which reach ~85% at their peaks. The QE measurements were made with the detectors perpendicular to the incident light. As installed in WFC3, the CCDs are tilted by 21 degrees with respect to the normal. The nominal change in optical thickness is ~6%, but the QE variations, as measured at the DCL on similar devices, turn out to be negligible.

The integrated system throughput of WFC3 depends on many factors including the *HST* OTA, pickoff mirror, filter transmission functions, QE, etc. Based on ground measurements of these components, the intergrated system throughput was calculated

and compared to the first on-orbit measurements during SMOV4. A 5 to 20% increase in the integrated system throughput was discovered, likely attributable to multiple components. The dashed curves represent the QE under the assumption that the entire flight correction is in the detector QE. For UV observations, UVIS2 achieves a higher sensitivity than UVIS1.

Figure 5.2: Quantum efficiency curves of the WFC3 UVIS1 and UVIS2 CCDs based on Goddard DCL measurements corrected (downward) by TV3 measurements (solid). The integrated system throughput of the UVIS detector was measured on-orbit to be higher than ground tests by 5–20%, and the dashed curves shows the QE under the assumption that this entire gain is due to the QE. In reality, some fraction of this gain is likely attributable to other *HST* and/or instrument components.

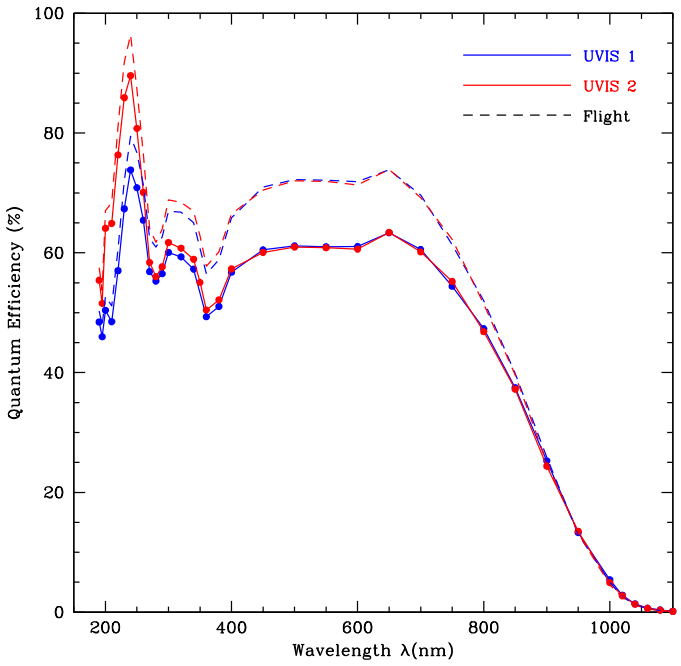

5.4.2 Multiple-Electron Events at Short Wavelengths

Like the ACS HRC and STIS CCDs (and unlike WFPC2), the WFC3 UVIS CCDs are directly sensitive to UV photons. In silicon, photons of energy higher than 3.65 eV (i.e., wavelength shorter than ~340 nm) can produce multiple electron-hole pairs when the energetic conduction-band electron collides with other valence-band electrons. At higher energies (energy above 3.65 eV, or wavelength below ~340 nm) the incident photons can directly extract more than one electron from the valence band. This effect (called "quantum yield") of a single photon producing more than one electron must be taken into account properly when estimating the noise level for short-wavelength observations.

Because the generation of multiple electrons is a random phenomenon, an extra noise term must be added to account for an observed variance larger than that

associated with the normal Poisson distribution of incoming photons. The correction is theoretically about 1.7 e^-/photon at 200 nm, decreasing linearly to 1.0 at 340 nm. Measurements of ground-based data, however, have indicated that the effect in the WFC3 chips is much less, 1.07 e^-/photon at 218 nm and 1.03 e^-/photon at 275 nm (WFC3 ISR 2008-47). The cause for this is unclear.

The QE curves presented in Figure 5.2 include the contribution from multiple electrons at UV wavelengths. The estimates generated by the WFC3 Exposure Time Calculator (ETC) are based on the measured WFC3 quantum yield. These estimates include the contribution from multiple electrons to the total counts, but do not include distortion of the Poissonian noise distribution by the multiple electrons. The noise distortion from multiple electrons is not large compared to other contributions to the signal-to-noise ratio in the ultraviolet (see Section 9.2).

5.4.3 Flat Fields

The flat fields needed for the reduction of WFC3 images combine information from two sources. Before launch, ground-based flats were obtained for all filters at a S/N of ~200 per pixel. To refine the low-frequency domain of the ground flats, in-flight observations of rich stellar fields (Omega Centauri and 47 Tucanae) are being obtained using large-scale dither patterns during SMOV and Cycle 17. Data acquired during SMOV indicate that the L-flat correction varies from 1.5% to 4.5%, from the long to the short wavelengths (see WFC ISR 2009-19). The resulting library of flat-field images is expected to support photometry to ~1% accuracy over the full WFC3 UVIS field of view at wavelengths longer than 350 nm, and to 2–3% accuracy at UV wavelengths.

Figure 5.3 shows examples of bias-corrected ground-based flats for two wide-band filters. Both are displayed with an inverse greyscale stretch chosen to highlight features; the vignetting in the upper-right corner is not instrument-related but an artifact of the optical stimulus. The crosshatch features in the UV flat field (F336W) are normal, due to the detection-layer structure in the CCDs; the level is typically <5% peak-to-peak compared to the rest of the flat.

Figure 5.3: WFC3/UVIS ground-based flat fields at F336W (top) and F555W (bottom).

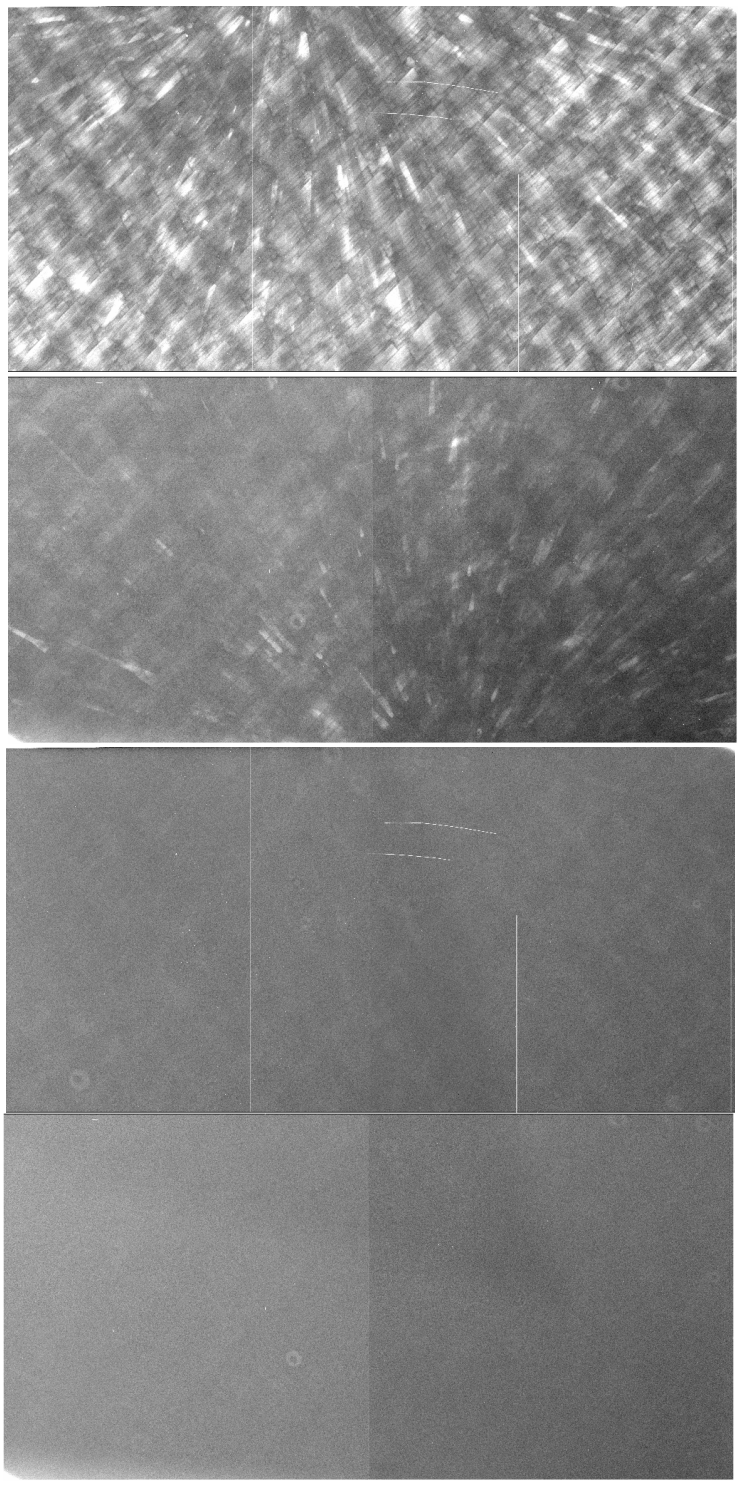

5.4.4 Long-Wavelength Fringing

Like most back-thinned CCDs, the WFC3 CCDs exhibit fringing at wavelengths longward of ~700 nm (see Figure 5.4). The amplitude of the flat-field signal for monochromatic input increases gradually with wavelength, and can reach levels of ±50% at the longest CCD wavelengths (fringe amplitude is the envelope of the curve shown in Figure 5.5).

Fringing results from interference due to multiple reflections between the layers of the CCD detector. The amplitude of the fringes is a strong function of the silicon detector layer thickness and the spectral energy distribution of the light source.

Detector thickness and wavelength modulate the phase of the fringing pattern. Broad-band illumination averages over wavelength-dependent phase, reducing the overall fringe amplitude. Likewise, narrow-band illumination samples a smaller range of fringe-pattern phase, producing a larger amplitude fringe pattern. Thus, although fringing is generally weak at wavelengths shorter than 700 nm, the very narrow Hα filter (F656N) still exhibited a fringe amplitude of about ±1% in flat fields acquired during ground testing (WFC3 ISRs 2008-17, 2008-46). The fringe pattern has been shown to be very stable, as long as the wavelength of light on a particular part of the CCD stays constant, so fringing can be corrected if an appropriate flat field is available.

The fringe pattern can also be modeled, either by interpolating between or combining monochromatic patterns previously obtained in the laboratory, or from theoretical calculations. For a detailed explanation of ongoing efforts to model the WFC3 fringe pattern, see Malumuth et al. (2003, *Proceedings of SPIE* 4854, Future EUV/UV and Visible Space Astrophysics Missions and Instrumentation, pp. 567–576).

Tools for modeling and correcting fringing effects are being developed. See http://www.stsci.edu/hst/wfc3/ins_performance/fringing/

Figure 5.4: UVIS chip 1 (top) and chip 2 (bottom) fringe pattern for monochromatic illumination at 977 nm.

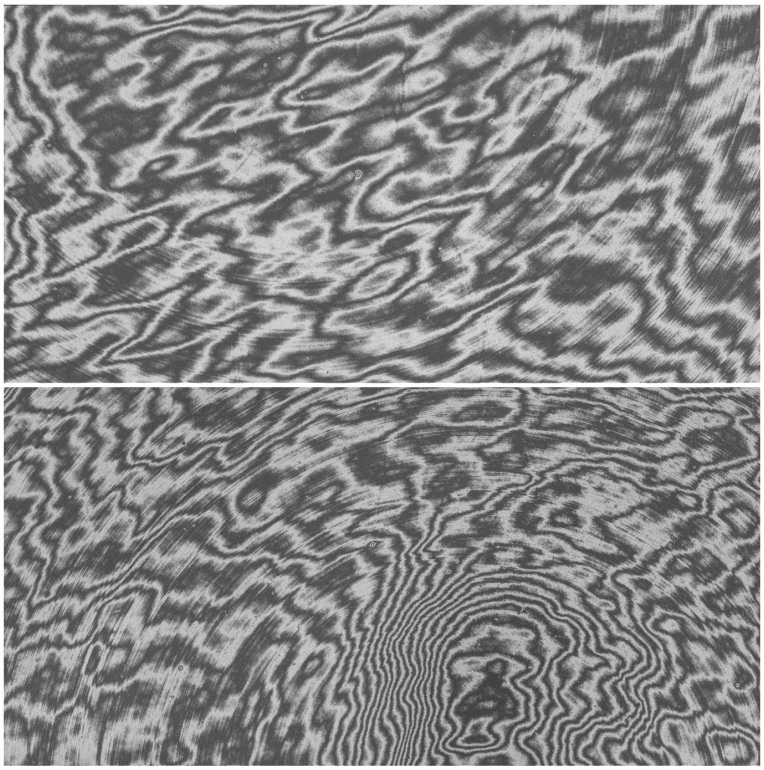

Figure 5.5: Flux (normalized to the mean of the image) as a function of wavelength for a single pixel, based on the Malumuth et al. (2003) model. Fringe phase (rapid oscillation) and fringe amplitude (curve envelope) vary as a function of wavelength. Due to wavelength averaging (even within narrow band filter bandpasses), actual WFC3 data exhibit peak to trough fringe amplitudes of < 30%.

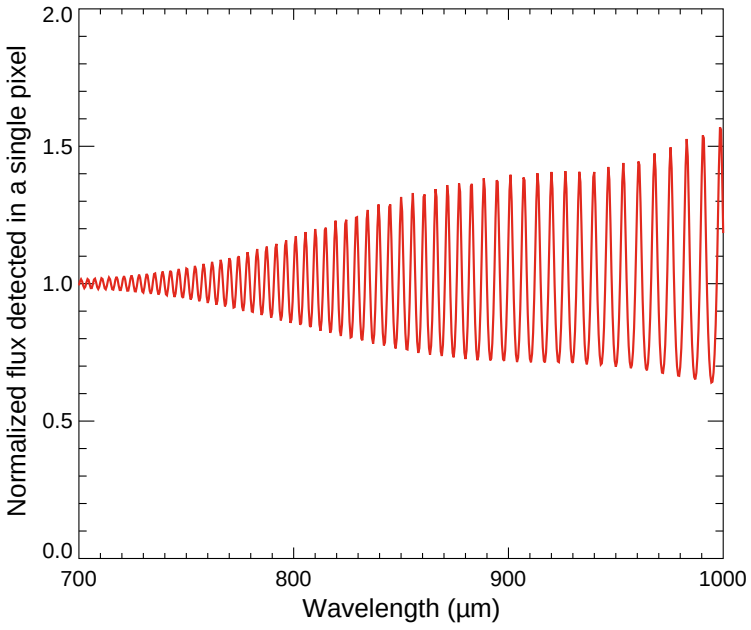

5.4.5 Linearity and Saturation

In general, the photometric response of CCDs is intrinsically linear up to and even well beyond the level at which saturation sets in, and beyond this bleeding along columns occurs as detailed further in Section 6.9.1. On-orbit observations have shown that on UVIS2 the onset of saturation varies from about 67000 to 72000 electrons over the CCD, and for UVIS1 this has a larger range of 63000 to 71000 electrons. Spatial information is, of course, lost once saturation and bleeding begins to occur.

Even extreme over-exposure is not believed to cause any long-term damage to the CCDs, so there are no bright-object limits for the WFC3 CCDs.

5.4.6 Gain

Electrons that accumulate in the CCD wells are read out and converted to data numbers (DNs), often called Analog-to-Digital Units (ADUs), by the analog-to-digital converter (ADC). The ADC output is a 16-bit number, producing a maximum of 65,535 DN for each pixel. A straightforward scheme in which one DN corresponded to one electron would make it impossible to measure signals larger than 65,535 electrons. Hence the conversion gain parameter provides a way of adjusting the scale so that multiple counts correspond to a single DN, allowing larger numbers of electrons to be measured. The conversion gain is defined as the number of electrons per DN.

Although it is possible to operate the WFC3 CCD detector at gains of 1, 1.5, 2, and 4 e^-/DN, only a gain of 1.5 e^-/DN is supported. This gain permits sampling of the entire dynamic range of the detectors, with negligible impact on the readout noise.

The gains for the WFC3 CCDs measured during SMOV are summarized in Table 5.3. Uncertainties in the measurements are about +/-0.01 e^-/DN.

Table 5.3: WFC3/UVIS Gains (from WFC3 ISR 2009-09).

CCD Chip	Amp	Gain (e^-/DN)
1	A	1.61
	B	1.61
2	C	1.63
	D	1.62

5.4.7 Read Noise

The read noise level in the science area pixels of bias frames for all of the amplifiers at the default gain setting was measured during SMOV (WFC3 ISR 2009-26). Table 5.4 shows the results obtained at the default gain setting of 1.5 e^-/DN. The read noise was found to be stable to 1%, 0.4%, 0.7%, and 0.8%, for amps A,B,C, & D, respectively (based on measurements through the end of August 2009).

Table 5.4: WFC3/UVIS readout noise (e^-) and uncertainty for normal and binned modes.

	Amplifier A			Amplifier B			Amplifier C			Amplifier D		
Binning	**1×1**	**2×2**	**3×3**	**1×1**	**2×2**	**3×3**	**1×1**	**2×2**	**3×3**	**1×1**	**2×2**	**3×3**
Mean	2.91	3.11	3.22	2.99	3.15	3.26	2.90	2.99	3.09	3.01	3.29	3.38
Uncertainty	0.03	0.02	0.04	0.01	0.01	<0.01	0.02	<0.01	0.01	0.02	0.02	<0.01

A preliminary analysis of the statistical behavior of the WFC3 ADCs shows some tendency for the least significant bit to be slightly biased at the readout speed adopted by the WFC3 electronics (see WFC3-ISR 2005-27). This minor effect should not degrade the photometric and noise characteristics of the WFC3/UVIS images.

5.4.8 Dark Current

The WFC3 CCDs, like most large-area scientific CCDs, operate with buried channels. Earlier generations of CCDs worked with surface channels, i.e., storing and transferring charges only along the surface of the semiconductor. In these earlier devices, the Si-SiO_2 interface between the detector material Si (p-doped conductor) and the surface layer of SiO_2 (isolator) created significant charge traps, which limited both the charge-transfer efficiency and the dark current. In buried-channel devices, a shallow (~0.5 micron thick) n-type Si layer is implanted just below the surface between the p-doped Si and the SiO_2 surface, to store and transfer the collected signal charge away from the traps at the interface.

Dark current in WFC3 detectors is further reduced using MPP technology. The dark current generated at the Si-SiO_2 interface ultimately depends on two factors: the density of interface states and the density of free carriers (holes and electrons) that populate the interface. Electrons can thermally "hop" from the valence band to an interface state (sometimes referred to as a "mid-band state") and from there to the conduction band, producing a dark electron-hole pair. Free carriers also fill interface states and, if these states were completely populated, can suppress hopping and conduction, reducing the surface dark current at levels comparable to the bulk dark. Unfortunately, normal CCD operations deplete the interface of free carriers, maximizing dark current generation.

In MPP technology, the Si-SiO_2 interface is populated with holes that suppress the hopping conduction process. MPP mode is applied to the CCD by significantly biasing the array clocks negatively to invert (push electrons away from) the n-buried channel and "pin" the surface potential beneath each phase to substrate potential (hence the name multi-pinned phase). Biasing the array clocks in this manner causes holes from the p+ channel stops to migrate and populate the Si-SiO_2 interface, eliminating surface dark-current generation. Note that it is not possible to invert conventional CCDs in this way, as the sensor's full-well capacity would be annihilated since the potential wells within a pixel all assume the same level. To circumvent this difficulty in MPP

CCD technology, an additional implant is included below one of the phases, allowing charge to accumulate in collecting sites when biased into inversion.

Besides eliminating surface dark current, MPP CCD technology offers additional advantages. For example, the charge-transfer efficiency of a CCD generally degrades with decreasing operating temperature. MPP technology assists in the charge-transfer process because it permits the use of higher operating temperatures.

The MPP CCD also eliminates residual image, a serious problem that has plagued low-signal-level CCD users for many years. Residual image, also known as quantum-efficiency hysteresis, results when the sensor is either overexposed or first powered up. Under these circumstances, electrons are found trapped at the Si-SiO_2 interface that slowly release into the pixel's potential well. Residual charge may take hours or even days before its level falls below the read-noise floor. Inverting the CCD causes holes to recombine immediately with the trapped residual electrons, eliminating remnant image effects during integration as well as readout.

During pre-flight tests, the CCD dark current was measured both in the cryogenic environment at the DCL, and in the instrument during thermal vacuum testing. The ground dark currents in Table 5.5, in units of e^-/pix/hr, are from the 2004 thermal vacuum testing (see WFC3 ISR 2005-13). On-orbit dark currents are derived from SMOV calibrations and are described in WFC3 ISR 2009-16.

Like all CCDs operated in a low-earth-orbit radiation environment, the WFC3 CCDs are subject to radiation damage by energetic particles trapped in the radiation belts. Ionization damage and displacement damage are two types of damage caused by protons in silicon. The MPP mode is very effective in mitigating the damage due to ionization, such as the generation of surface dark current due to the creation of new trapping states in the Si-SiO_2 interface. Although protons lose only a minor fraction of their total energy via non-ionizing energy loss, lattice displacement damage can cause significant performance degradation in CCDs by decreasing the charge transfer efficiency (CTE), increasing the average dark current, and introducing pixels with very high dark current (hot pixels). Displacement damage to the silicon lattice occurs mostly due to the interaction between low-energy protons and silicon atoms. The generation of phosphorous-vacancy centers introduces an extra level of energy between the conduction band and the valence band of the silicon. As described above, new energy levels in the silicon bandgap increase the dark current as they allow thermally generated charges to reach the conduction band. As a consequence, the dark current of CCDs operated in a radiative environment is predicted to increase with time. A preliminary rate of dark current increase of less than 1 e^-/sec/year based on SMOV data will be refined as part of the Cycle 17 calibration program.

Table 5.5: WFC3/UVIS dark current, in e^-/pix/hr.

	CCD Chip 1		CCD Chip 2	
	Amp A	**Amp B**	**Amp C**	**Amp D**
Ground	0.16 ± 0.09	0.32 ± 0.10	0.34 ± 0.10	0.41 ± 0.11
On-orbit	1.62 ± 0.29		1.70 ± 0.34	

5.4.9 Bad Pixels

Two types of bad pixels are routinely monitored using on-orbit WFC3 data: hot pixels and dead pixels. Hot pixels, i.e., those pixels with a higher than normal dark current, are identified in dark frames using a threshold of 54 e^-/hr. The cutoff was chosen based on the tail of the dark histogram (see Figure 5.6) as well as visual examination of the dark frames. The number of hot pixels increases over time due to on-orbit radiation damage; periodic anneal procedures, where the UVIS detector is warmed to ~20°C, successfully fix about 90% of the hot pixels. Hot pixel locations and levels are provided in the UVIS superdark reference files which are subtracted from science data. Dithering can also mitigate bad pixel effects and is recommended for most observations.

Dead pixels, specifically dead columns, are identified through visual inspection from both individual, and stacks of, internal frames. Bad pixel locations are propagated into the bad pixel mask which is applied by calwf3 in the standard data reduction pipeline.

Table 5.6 summarizes the number of hot and dead pixels in each chip. The hot pixel range is the number of hot pixels observed between a single anneal procedure conducted during Cycle 17, i.e., immediately after the August 2009 anneal and just preceding the September 2009 anneal. Typically, ~1000 new hot pixels appear every day.

Figure 5.6: Dark Histogram used to determine Hot Pixels using a 54 e^-/hr threshold.

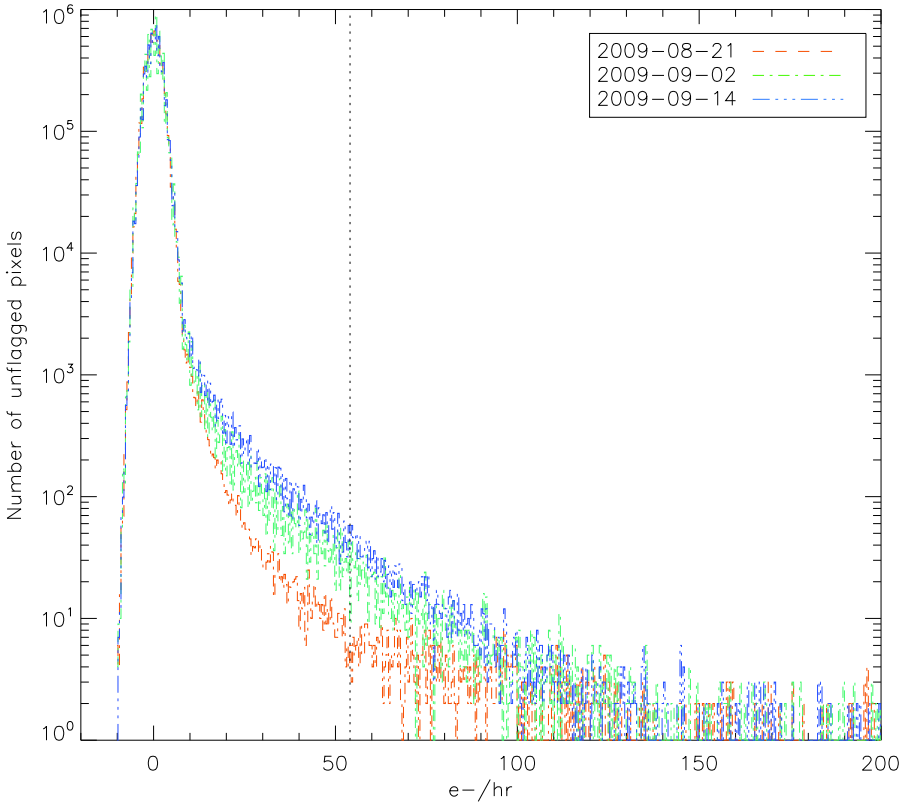

Table 5.6: Summary of bad pixels for Chip 1 and 2.

	Chip 1		Chip 2	
Bad Pixel Type	**Amp A & B**	**% of Chip**	**Amp C & D**	**% of Chip**
Hot Pixels				
• Before anneal 2009-08-21	39568	1.471%	40492	0.482%
• After anneal 2009-09-14	15626	0.186%	16382	0.195%
Dead Pixels	~8000	0.095%	~16000	0.190%

5.4.10 Cosmic Rays

The fraction of WFC3 pixels impacted by cosmic rays varies from 5% to 9% per chip during 1800 sec exposures in SAA-free orbits, providing a basis for assessing the risk that the target(s) in any set of exposures will be compromised. Observers seeking rare or serendipitous objects, as well as transients, may have stringent requirements on how many cosmic rays can be tolerated in an image stack. Assuming cosmic-rays affect 5-9% of a chip in 1800 sec, at least 4-5 images will be needed to ensure that fewer than 100 pixels will be hit in all images of the stack.

The flux deposited on a CCD from an individual cosmic ray depends less on the energy of the cosmic ray than on the distance it travels in the silicon substrate, and thus on its direction of incidence. The electron deposition due to individual cosmic rays measured with ACS/WFC has a well-defined cutoff, with negligible events of less than 500 e^- and a median of ~1000 e^- (see Figure 5.7). The overall characteristics of the cosmic ray population appear nominal in WFC3 but a more detailed analysis is currently underway.

Figure 5.7: Electron deposition by cosmic rays on ACS/WFC.

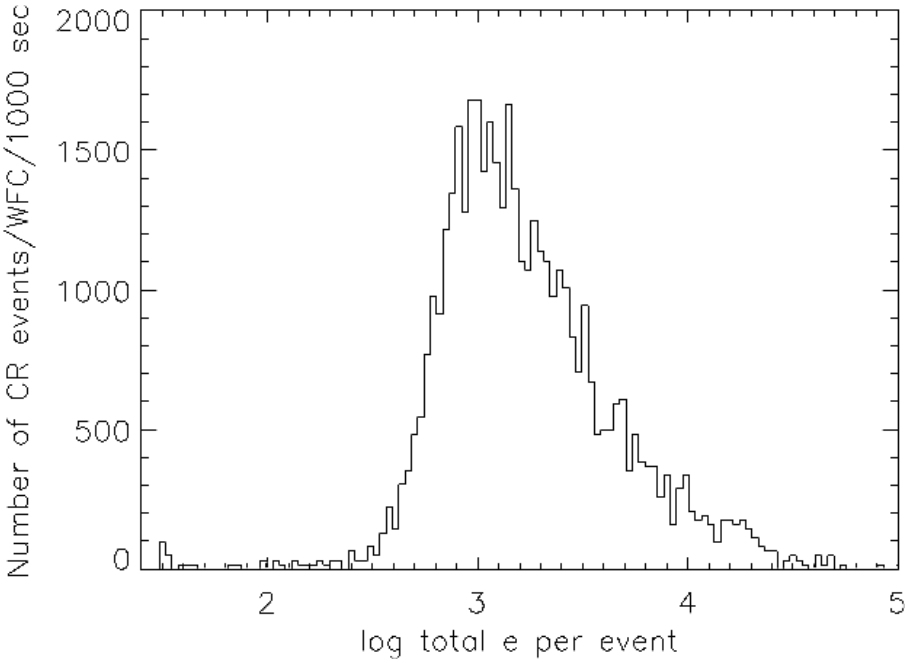

Online

Analysis of cosmic ray behavior in WFC3 is ongoing. Updates will be posted on the WFC3 Web page:
http://www.stsci.edu/hst/wfc3/ins_performance/cosmic_rays/

5.4.11 Charge-Transfer Efficiency

Uniform response within each pixel and excellent charge-transfer efficiency (CTE) are key to achieving accurate photometric performance. CTE is a measure of how effective the CCD is at moving charge from one pixel location to the next when reading out the chip. A perfect CCD would be able to transfer 100% of the charge as it is shunted across the chip and then out through the serial register. In practice, small traps in the silicon lattice compromise this process by retaining electrons, and then releasing them at a later time. (Depending on the trap type, the release time ranges from a few microseconds to several seconds.) For large charge packets (several thousand electrons), losing a few electrons along the way is not a serious problem, but for smaller (~100 e^- or less) signals, it can represent a substantial fraction.

CTE is typically measured as a pixel-transfer efficiency, and would be unity for a perfect CCD. The CTE numbers for the WFC3 CCDs were measured at the DCL using a ^{55}Fe source, and showed that charge loss is of the order of $3\text{-}5\times10^{-7}$ e^-/transfer, an excellent value for pre-flight devices.

The anticipated CTE performance of the UVIS detectors over WFC3's lifetime is expected to be better than previous *HST* instruments due to several factors. First, shielding (similar to ACS/WFC) has been used to protect the CCDs from the high-radiation space environment, thereby slowing the production of charge traps. Second, the WFC3 CCDs have been designed with a mini-channel (improved over ACS/WFC), which reduces the number of traps seen by small charge packets during read-out transfers. In addition, in future cycles the WFC3 CCDs will have the switchable option of charge injection, which, by filling traps, can mitigate the effects of CTE losses with an increased read noise level of about 10 e^-. Early indications from SMOV data show that the charge transfer degradation on-orbit, taking into account the lower dark current inWFC3, is following the ACS trend observed for the 200 days after its installation in *HST*. Charge injection is not available in Cycle 18, and its availability in Cycle 19 depends upon the rate of CTE decline measured during the next year.

5.4.12 Crosstalk

Anomalous features are found in some UVIS CCD images, including very low-level ghost images produced by crosstalk in the detector electronics. Point sources, extended targets, hot pixels, and cosmic rays generate a low-level mirror image in the quadrant adjoining the target quadrant, on the same chip. This residual crosstalk is linear, negative, and appears at the level of ~10^{-4} to 10^{-5}. Figure 5.8, from WFC3 ISR 2009-03, illustrates the crosstalk effect as observed during ground testing. Crosstalk ghost images are not to be confused with optical ghosts and stray light, as described in Sections 6.5.3 and 6.9.7.

Figure 5.8: Crosstalk test frame (left), and 20-line average cuts through the target and crosstalk images (right). The image is displayed with a hard inverted greyscale stretch. The target was placed in quadrant C, and the crosstalk appears in quadrant D. The faint large ring in C offset from the primary target is an optical window ghost.

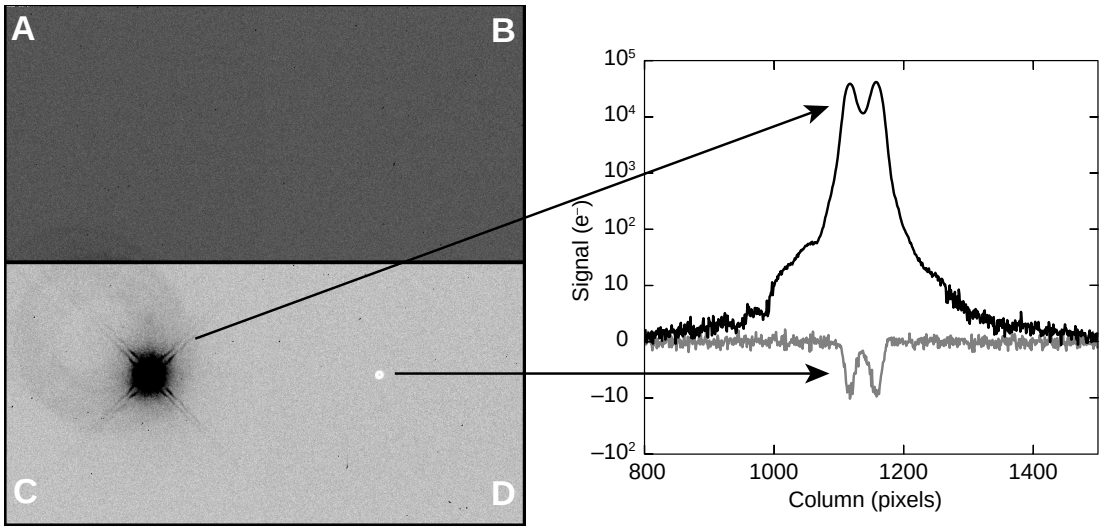

5.5 The WFC3 IR Channel Detector

5.5.1 Overview

The infrared channel of WFC3 employs a low-noise, high-QE, 1024×1024 pixel HgCdTe array manufactured by Teledyne Imaging Sensors (formerly Rockwell Science Center). The detector area sensitive to light is 1014×1014 pixels. Active cooling by a six-stage thermoelectric cooler (TEC) keeps the detector at a nominal operating temperature of 145 K. Although the IR detector is sensitive between 400 and 1700 nm, the detector coating is optimized for wavelengths longward of ~1000 nm, where the QE reaches its peak (Figure 5.14). The IR channel filter set is also limited to wavelengths above 900 nm, making the IR channel complementary to the UVIS channel.

Compared to CCD detectors, IR detectors like the one used in the WFC3 IR channel have higher read noise and dark current. Unlike CCDs, however, IR detectors allow the accumulated signal in each pixel to be measured non-destructively multiple times. The capability to sample the signal multiple times during the integration can be exploited to reduce the effective read-out noise significantly. IR exposures are called "ramps" due to this capability to sequentially read the detector as signal accumulates. IR detectors are also immune to the charge bleeding exhibited by CCDs at high signal levels. Saturation is still a concern, however, because pixels subject to the highest signal levels show higher dark-current rates ("image persistence") in subsequent exposures.

The capability of multiple readouts and the absence of bleeding makes IR detectors capable of very high dynamic-range observations. Non-destructive readouts also allow for the recovery of pixels affected by cosmic rays (CRs), because CR hits can be recognized and removed between adjacent reads. Unlike CCDs, IR detectors also show minimal long-term on-orbit CTE degradation, because they do not employ the charge-transfer mechanism used in CCDs. IR detectors, however, are intrinsically non-linear. Nevertheless, at low and intermediate signal levels, the departure from linearity is quite modest and can be well calibrated by a low-order polynomial fit, whose parameters can in principle be determined for each pixel.

5.5.2 IR Detector Basics

In this section, we briefly describe the operational principles of the WFC3/IR detector. Figure 5.9 (adapted from McLean 1997, Electronic Imaging in Astronomy: Detectors and Instrumentation) shows the basic physical structure of the photovoltaic HgCdTe detector used in WFC3.

Figure 5.9: Cross-section of a WFC3-IR detector (not to scale).

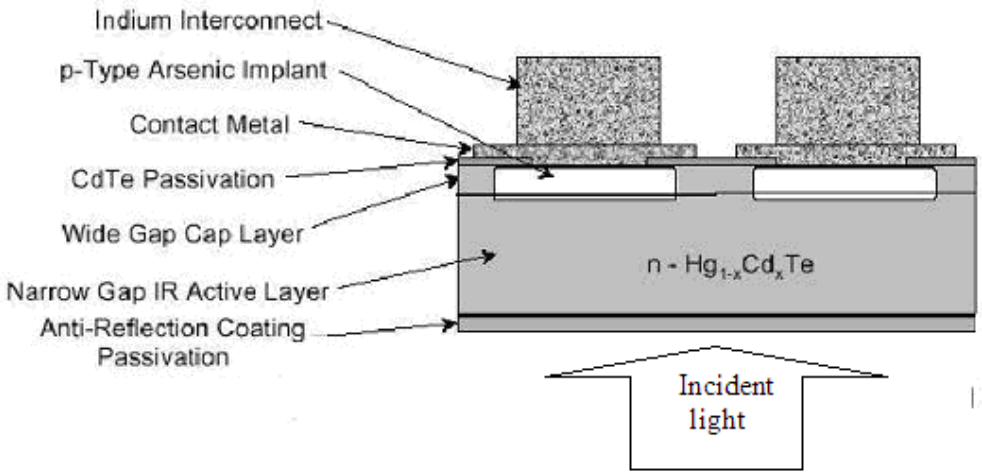

Infrared detectors used in astronomy today are basically two-dimensional arrays of p-n junctions working as photodetectors (photodiodes). In a p-n junction, negative charges migrate from the n-type doped material to saturate the unmatched covalent bonds of the adjacent p-type material. The displaced carriers establish an electric field across the junction, setting up an intermediate region depleted of free carriers. The depletion region is therefore both charged and highly resistive. The strength of the electric field and the size of the depletion region may be increased by applying an external electric field ("negative bias"). This biasing corresponds to the initial RESET applied at the beginning of the integration. When an incident IR photon is absorbed by the photosensitive material, it creates a free electron-hole pair. The two photo-generated charges drift in the material and would eventually recombine. However, if the mobility of the charge carrier (a hole in an n-type material) is high enough, it will reach the depletion region before recombining and be swept to the other side of the junction by the electric field. There, in the p-type region, it will recombine with one of the electrons of the ionized holes, causing a reduction of the voltage across the junction. This change of voltage can be measured and, being proportional to the number of photo-generated charges, provides a direct measure of the photons captured on each pixel.

In the case of the WFC3 IR detector, the photosensitive material is made of HgCdTe grown with a molecular beam epitaxial (MBE) process on a ZnCdTe substrate. The fraction (stoichiometric ratio) of Hg vs. Cd controls the long-wavelength cutoff of the material, whereas the doping material (As for the p-type, In for the n-type) creates the p-n junction. The MBE growth process is different from that used in the NICMOS detectors on *HST*, in which the HgCdTe was grown on sapphire in a liquid phase (PACE process). MBE growth on a ZnCdTe substrate is expected to provide a better lattice match to HgCdTe than sapphire, creating fewer defects and charge traps at the interface between the two materials. The

MBE growth process is followed by the processing phase, in which the implants and contacts of each pixel are manufactured.

As usual with IR arrays, the readout circuitry is made on a separate CMOS chip (multiplexer or MUX), which is eventually hybridized to the detector with an indium contact for each pixel (see Figure 5.10). After the two chips have been hybridized, the ZnCdTe substrate is removed to reduce the susceptibility of the device to cosmic-ray events and to increase the sensitivity at short wavelengths. The final chip therefore is a CMOS device connected through indium columns to a thin layer of HgCdTe photosensitive material.

Figure 5.10: Basic "hybrid" structure of infrared array detectors (not to scale).

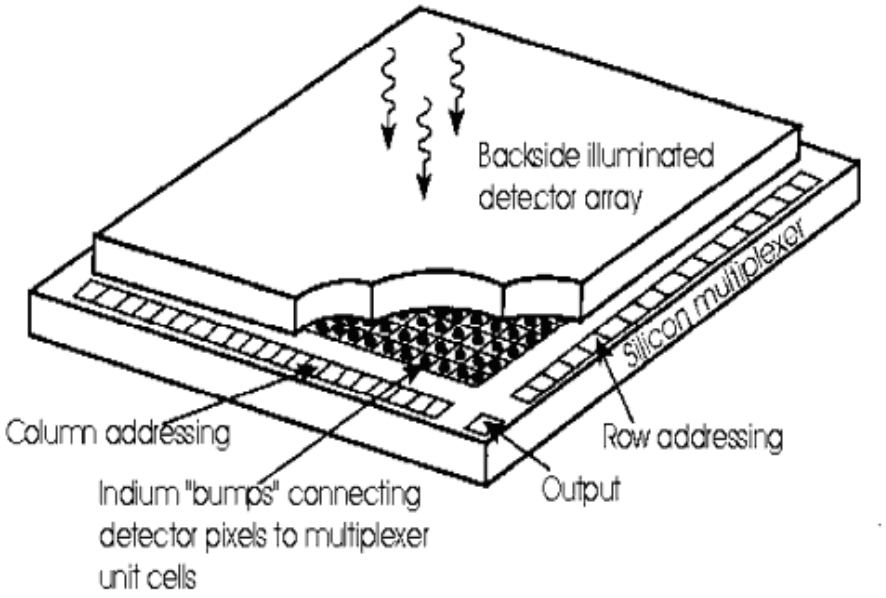

In the MUX, each pixel has its own dedicated readout circuitry (unit cell). In particular, the voltage change across the p-n junction is monitored by a field-effect transistor (FET) configured as a source-follower amplifier, which has gain of 1 and effectively decouples the detection process from the noisy readout circuitry. Two other FETs connect the pixel to the reset voltage and the output line. Figure 5.11 shows the equivalent circuit diagram for the WFC3 detector unit cell. Each WFC3 IR unit cell contains three transistors. For comparison, the NICMOS detectors have four transistors, whereas the latest generation of Hawaii-2RG detectors for JWST has seven transistors per unit cell. A higher number of transistors increases the versatility of the device. For example, on the NICMOS detectors it is possible to reset each individual cell, whereas on WFC3 detectors the reset is sent simultaneously to all cells on the same row. Note that since there are no potential barriers between pixels, pixels do not spill charges into nearby pixels when they reach a certain level ("blooming full well") of accumulated charges, as in typical multiphase CCDs. Therefore, IR detectors do not show "bleeding" along columns. Moreover, due to individual readout, bad pixels do not block the rest of the column as they do in a CCD.

Figure 5.11: Equivalent circuit diagram of the WFC3/IR unit cell.

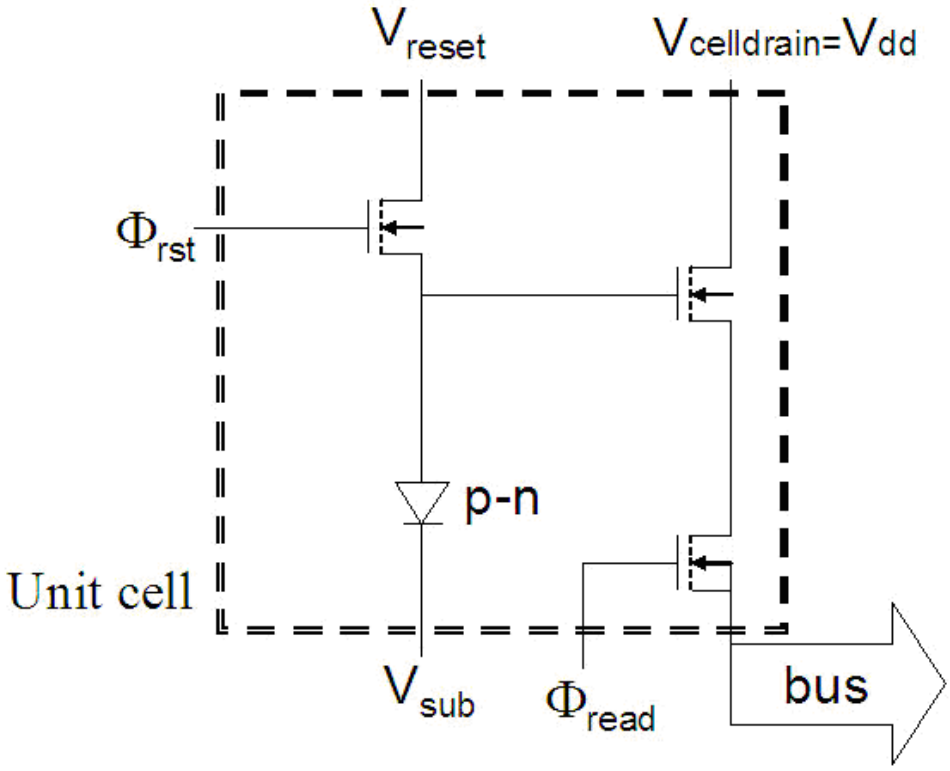

5.6 WFC3 IR Readout Formats

5.6.1 Full-Frame Readouts and Reference Pixels

The WFC3 IR detector contains 1024×1024 square pixels of 18×18 micron physical size. The detector is divided into four quadrants of 512×512 pixels, each of which is read out independently from its outer corner, as illustrated in Figure 5.12. The outermost rows are read first, proceeding along each row from the outermost column to the horizontal mid-point of the detector, and then continuing inwards on subsequent rows to the vertical mid-point.

Figure 5.12: Schematic layout of the WFC3 IR detector. The long (red) and short (blue) arrows indicate the direction of the fast and slow multiplexer clocking, respectively. In contrast to CCD "bucket-brigade" image-shifting to the output amplifier, the IR detector pixels are selected for readout in a raster pattern by multiplexer circuits.

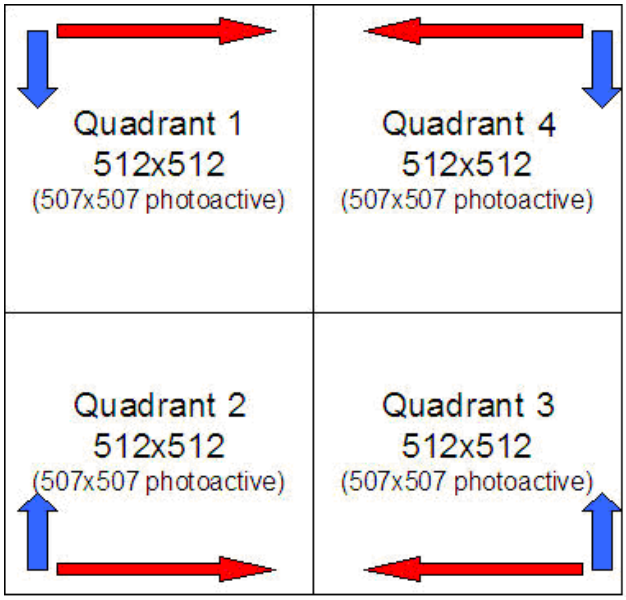

A major effort has been made to eliminate both the amplifier glow and bias drifts that have affected the NICMOS detectors.

To eliminate the amplifier glow entirely, WFC3 uses external amplifiers located in the immediate vicinity of the detector, rather than those directly on the multiplexer (which are also present, but are not activated in the WFC3 implementation).

In regard to bias drifts, the WFC3 IR class of detectors is the first to use reference pixels, configured as follows (see Figure 5.13). Of the 1024×1024 pixels, only the inner 1014×1014 pixels are light-sensitive. The five outer rows and columns of pixels all around the array use fixed capacitances to provide constant-voltage reference values. There are actually two types of reference pixels: (1) the pixels on the outermost columns/rows are connected to capacitors located outside of the unit cells. Their values follow a 4× periodic pattern, providing 4 sequentially increasing voltage levels all within the range of the detector output signal; (2) the 4 inner rows/columns are instead connected to capacitors created within their unit cells. These on-board capacitors are identical by design and all provide nearly the same reference signal. The current version of the WFC3/IR data reduction pipeline uses only the inner reference pixels, as they provide a more robust statistical estimate of the variable detector bias.

The reference pixels track the low-frequency drift of the readout electronics and efficiently remove the "pedestal" variations that affected, for example, NICMOS. Analysis of ground test data has shown that the reference pixel signal is also sensitive to the detector temperature and may therefore be used to assess the expected level of dark current during an exposure, independently from a reading of the detector temperature itself. Actual on-orbit experience indicates that detector temperature is very stable.

Full-frame exposures result in one raw 1024×1024 pixel image for each readout, which includes the 5 rows and columns of reference pixels on the periphery. After calibration, the reference pixels are trimmed off, leaving only the 1014×1014 arrays of light-gathering pixels.

Figure 5.13: Schematic layout of the active pixels (dark shading) and of the reference pixels at a corner of the WFC3/IR detector. The color coding represents different values of the reference pixel capacitance.

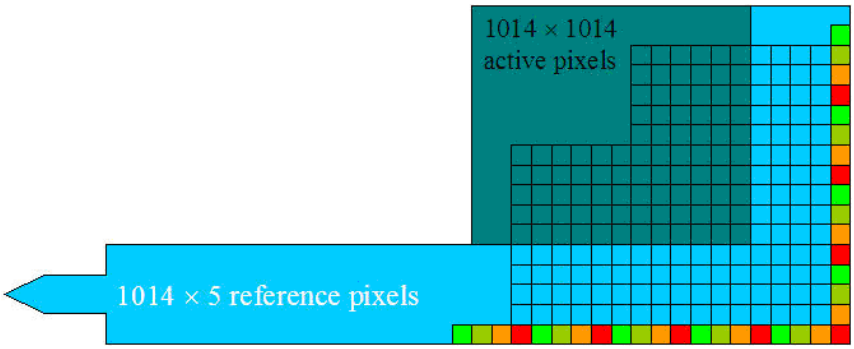

5.6.2 Subarrays

The default IR exposure mode is to read out the entire detector. It is also possible, however, to read out only a portion of the detector. WFC3 IR subarrays are implemented in four user-selectable sizes: 64×64, 128×128, 256×256, and 512×512 pixels. All subarrays are centered on the detector with an equal number of pixels in each quadrant, using each of the 4 detector amplifiers to read the subarray pixels contained in its quadrant (as with full-frame readouts).

The 5-pixel wide bands of reference pixels that share rows or columns with the subarray are also included in subarray readouts. The reference pixels therefore come from the same detector rows and columns as the “live” portion of the subarray, with the 5×5 pixels at the subarray corners filled by the reference pixels at the corresponding corner of the detector.

Certain combinations of IR subarrays and sample sequences give rise to images containing a sudden low-level jump in the overall background level of the image. The cause of the artifact is under investigation. The use of IR subarrays is discussed in more detail in Section 7.4.4.

5.7 WFC3/IR Detector Characteristics and Performance

5.7.1 Quantum Efficiency

The QE of the flight IR detector, as measured at the Goddard Detector Characterization Lab (DCL), is shown as a solid curve in Figure 5.14. The QE curve demonstrates very high sensitivity of the IR detector for wavelengths longer than 1000 nm. The actual total system throughput of WFC3 depends on many factors including the *HST* OTA, pickoff mirror, filter transmission functions, QE, etc. Based on ground measurements of these quantities, the total system throughput was calculated and compared to the first on-orbit measurements. A 5–20% increase in the total system throughput was discovered, which we attribute to multiple factors. The dashed curve represents the QE under the assumption that the entire flight correction is in the QE. This assumption is unphysical given the realities of anti-reflection coatings and interpixel capacitance.

Figure 5.14: QE curve of the WFC3/IR detector based on Goddard DCL measurements (solid). The total system throughput of the IR detector was measured on-orbit to be higher than ground tests by up to 20%, and the dashed curve shows the QE under the assumption that this entire gain is due to the QE. In reality, some fraction of this gain must be attributable to other *HST* and/or instrument components.

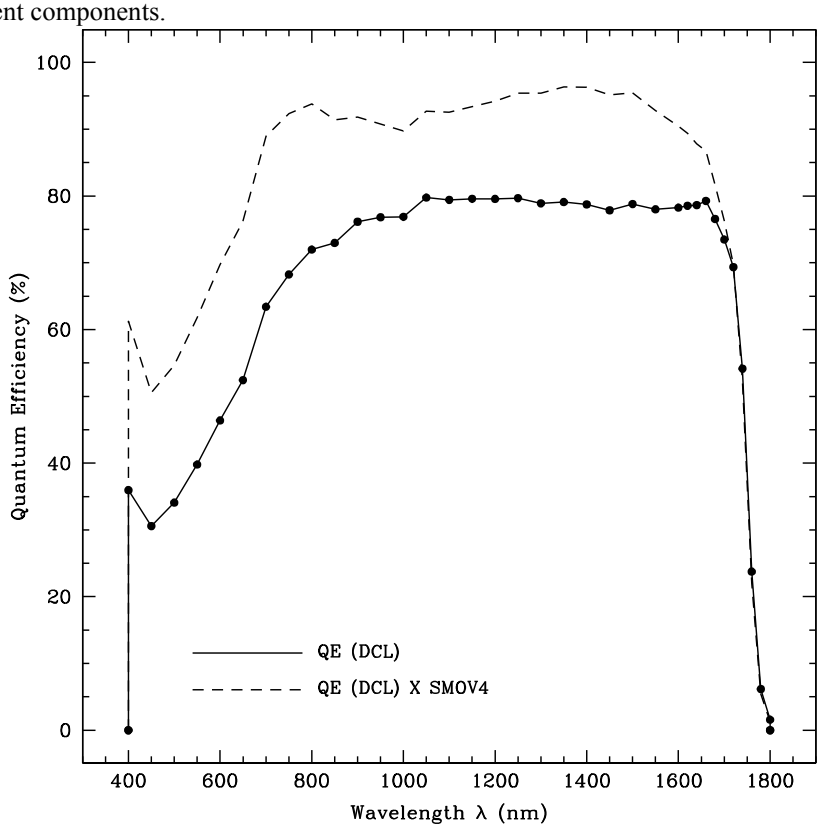

5.7.2 Dark Current

To avoid the complexity and limited lifetime of a stored-cryogen system, while at the same time providing the low operating temperatures required for dark-current and thermal-background reduction, the WFC3 IR detector is refrigerated with a six-stage TEC to a nominal operating temperature of 145 K. This is an unusually high temperature for near-IR detectors, and required tailoring the composition of the HgCdTe material for a long-wavelength cutoff at ~1700 nm. The higher band-gap associated with the short cutoff wavelength effectively limits both the intrinsic detector dark current and its sensitivity to the internal thermal background.

WFC3 IR exposures taken with an aluminum blank in place, rather than a filter, provide a measure of the detector dark current. The dark current of the flight array has a skewed distribution, with a mode, median, and mean of 0.045, 0.048, and 0.048 e^-/s/pixel respectively. The shifted mode is due to the asymmetry of the dark-current distribution among the pixels, characterized by a long tail of "hot pixels" randomly located across the detector. The histogram of dark current values, along with the cumulative dark-current distribution, i.e., the fraction of pixels with a dark current lower than a certain level, is shown in Figure 5.15. See WFC3 ISR 2009-21 for details on dark current calculations. For broad band filters, the detector dark current's contribution to the total noise is insignificant for most pixels. The background zodiacal light creates 0.3 to 1.0 e^-/s/pixel in wide filters.

Direct thermal control of the detector (via a sensor integrated in the MUX that controls the 6-stage TEC current) provides typical thermal stability of < 50 mK. Tests made on similar detectors indicate that the residual dark-current variations can be largely calibrated and subtracted out using reference pixels.

Figure 5.15: Histogram of the dark current level of WFC3/IR detector.

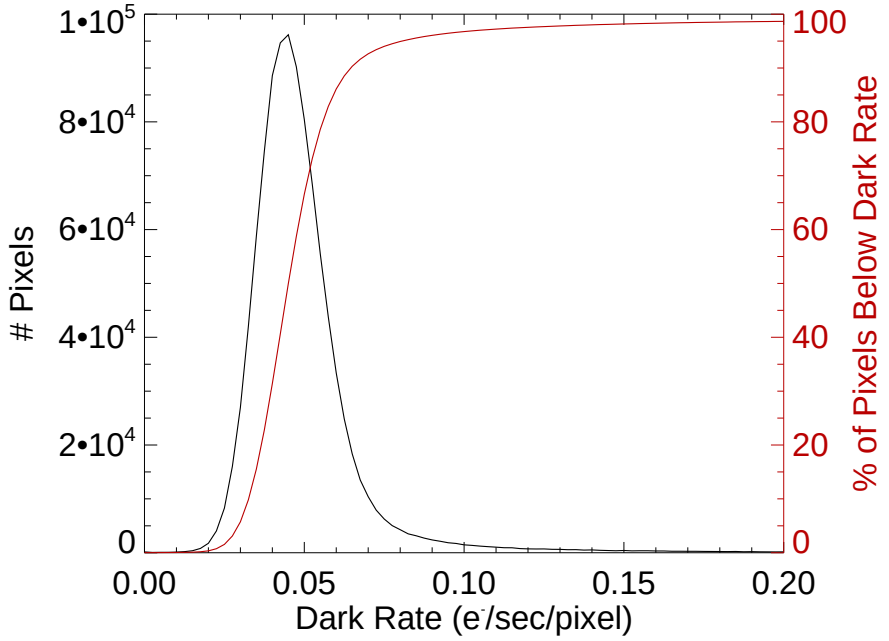

5.7.3 Read Noise

The IR detector has four independent readout amplifiers, each of which reads a 512×512 pixel quadrant. The four amplifiers generate very similar amounts of read noise. This is illustrated in Figure 5.16 (left), which compares the correlated double sampling (CDS) read noise levels for the four quadrants of the detector. CDS read noise refers to the noise associated with subtracting a single pair of reads. These read noise values were derived from a series of RAPID ramps from SMOV testing, providing a measure of the total noise in a difference image. For short ramps, such as these RAPID ramps, the contribution of shot noise due to dark current accumulation is less than 0.01 e^-. Figure 5.16 (left) therefore shows that the CDS read noise of the detector is between 20.2–21.4 e^-. These results are also shown in Table 5.1.

Using multiple reads, the effective noise of a final IR image can be averaged down. For example, by creating a final image from all 15 reads of a SPARS200 sample sequence, the effective noise decreases from the SPARS200 CDS value of ~20.0 e^- down to ~12.0 e^-. Similar decreases in noise can be gained with the other sample sequences. See WFC3 ISR 2009-23 for details on effective noise.

Figure 5.16: CDS read noise values measured for each quadrant in 40 RAPID ramps during SMOV testing (left). Effective noise versus the number of reads in the ramp for a SPARS200 ramp (right).

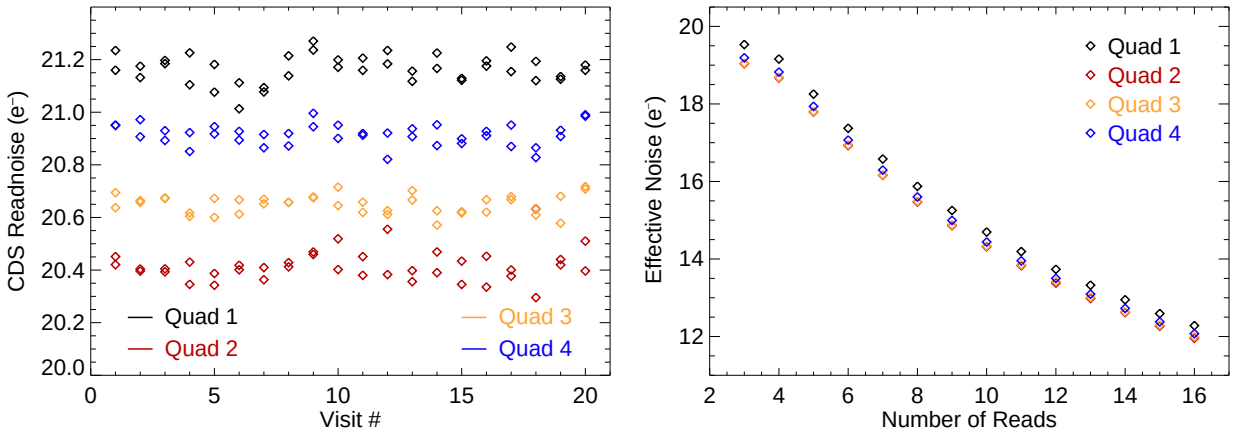

For some scientific programs, such as ultra-low-background observations, read noise becomes a non-negligible component of the noise floor. The relative contribution of read noise to the total noise depends on infrared background levels (see Section 7.9.5). The contribution to the read noise in WFC3 IR data due to digitization errors associated with the conversion from electrons to data numbers (DN) is negligible.

5.7.4 Flat Fields

Flat fields taken with the WFC3/IR array show response variations on both large and small scales. In Figure 5.17 we show the flat-field pattern through four filters: F105W, F125W, F160W, and F167N. These images were obtained during SMOV using WFC3's internal calibration lamp.

Figure 5.17: Internal flat field exposures obtained during SMOV, displayed on a linear scale from 0.8 to 1.25.

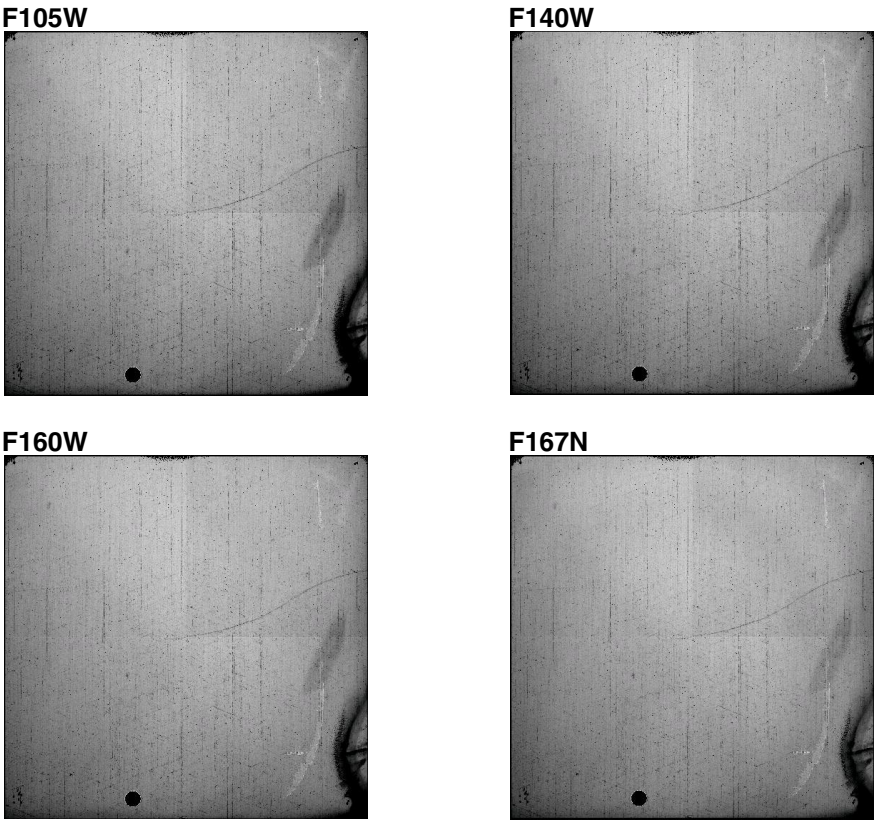

The high-frequency flat-field pattern contains a number of defects that are related to blemishes on the detector surface. Being on the focal plane, they show a very sharp profile. Defects in the optical path, especially particles on the cold enclosure window and filters, are out of focus and show a more diffuse, nearly circular pattern. Flat-field procedures are expected to remove these effects to better than 1%. At the end of SMOV, flat-fielding residuals have been reduced to ~1.5% (rms).

5.7.5 Linearity and Saturation

The WFC3 IR calibration program shows that the detector response is in fact (slightly) non-linear over the full dynamic range. This behavior is illustrated in Figure 5.18, which presents a plot of average counts as a function of time. The black diamonds are the measured average signal; a linear fit has been made to the signals up to ~25,000 electrons (solid red line). The dashed red line shows this best-fit line extended out to the total exposure time of the ramp. The blue horizontal line marks the level at which the counts deviate by more than 5% from linearity (about 78,000 electrons). For the purposes of non-linearity correction, the 5% nonlinearity level has been defined as “saturation.”

Figure 5.18: Non-linear response of mean signal as a function of time, measured in Thermal Vacuum 3 testing for the WFC3/IR detector.

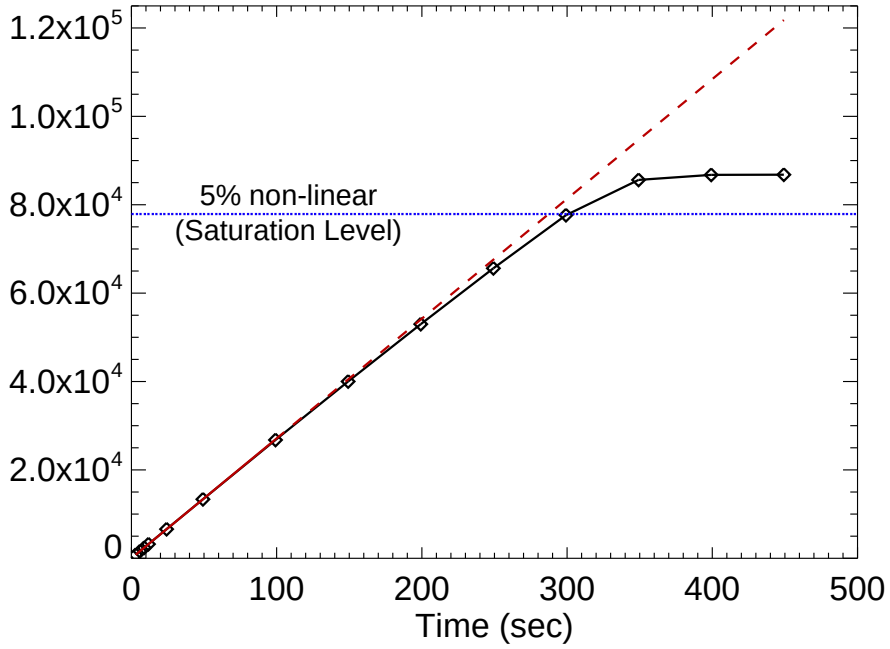

The linearity correction implemented in the WFC3/IR calibration pipeline corrects pixels over the entire dynamic range between zero and saturation. Once the pixel value exceeds the saturation threshold, the pixel is flagged as saturated in the data-quality array within the FITS file and no linearity correction is applied. Pixels driven heavily into saturation can begin to show decreasing readout values, such that their DN values fall back below the defined saturation threshold. To prevent a situation where a pixel is flagged as saturated in one or more readouts, but then not flagged in later readouts, the calibration processing system flags saturated pixels in all subsequent readouts for pixels that are found to be above the saturation threshold in any given readout.

5.7.6 Detector Cosmetics

The make-up of the WFC3/IR detector's pixel population includes several flavors of anomalously responsive pixels. So-called "hot" pixels have a more than 100 times the average dark current, and thus show excessive charge compared to the surrounding pixels. On the other hand, "cold pixels" are inversely sensitive to incident photons than the typical pixel and are defined as having a negative slope when measured up the ramp (i.e., pixel value is lower in last frame up the ramp compared to first frame). The anomalously low responsivity of a "cold" pixel could be due to a lower intrinsic QE of the pixel, or to surface defects. Some pixels do not respond at all ("dead pixels") to incoming light, while some pixels sporadically behave in an unpredictable fashion (non-repeatable pixels). The current bad pixel tables (BPIXTAB) identify about 1% of WFC3/IR pixels as "bad," and analysis of the pixel population is ongoing during Cycle 17.

In addition to randomly-distributed bad pixels, coherent regions of bad pixels exist in the IR detector (Figure 5.19). Unbonded pixels near the detector edges, and the circular "death star" feature, do not respond to light. Pixels in the wagon wheel have lower than normal quantum efficiency. WFC3 ISR 2008-28 describes the characterization of these defects based on ground-testing data.

Figure 5.19: IR detector cosmetic defects.

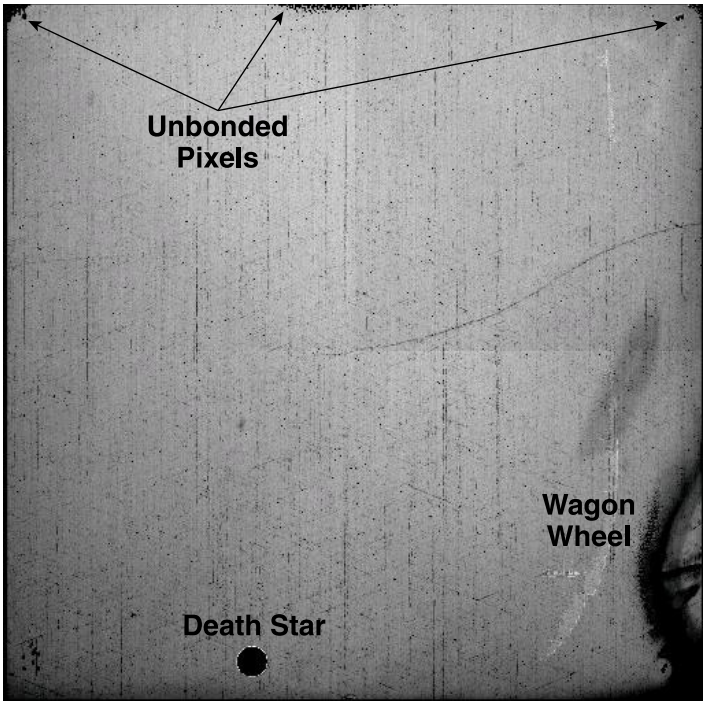

CHAPTER 6:

UVIS Imaging with WFC3

In this chapter . . .

6.1 WFC3 UVIS Imaging

As described in Chapter 2, the optical design of WFC3 features two independent channels, each with its own separate optics, filters and grisms, and detectors. The **UVIS channel** is sensitive to UV and optical wavelengths (200-1000 nm), and the **IR channel** is sensitive to near-infrared wavelengths (800-1700 nm).

Only a single channel, either UVIS or IR, can be used at any one time. Thus they cannot be used in parallel, but they can be used sequentially.

A schematic diagram showing the locations of the fields of view of the UVIS and IR detectors in the *HST* focal plane is shown in Figure 2.2.

This chapter describes the capabilities of the UVIS channel. The following chapter, Chapter 7, describes the IR channel. Detailed performance characteristics of the detectors used in both channels are given in Chapter 5 and summarized in Table 5.1.

6.2 Specifying a UVIS Observation

In the *HST* proposal system, it is relatively simple to specify the parameters for a UVIS observation. The parameters available to General Observers for the UVIS channel are the following:

1. **Configuration**: always **WFC3/UVIS**
2. **Mode**: always **ACCUM**
3. **Aperture:** must be specified; **UVIS** selects readout of the full area of both CCDs; other choices are discussed in Section 6.4.5
4. **Spectral Element:** must be specified for each exposure; see Section 6.5
5. **Optional Parameters:** the available options control splitting of the exposures for cosmic-ray removal (see the Phase II Instructions for the **CR-SPLIT** Optional Parameter), and the **BIN** Optional Parameter for on-chip binning (see Section 6.4.4)
6. **Special Requirements:** see the *Phase II Proposal Instructions* for details of Special Requirements related to the timing of visits and for dithering and mosaicking. Also available is the exposure-level Special Requirement **POS TARG** for offsetting the target from the default reference point of the aperture (see Section 6.4.3 for a discussion of the UVIS channel coordinate system).
7. **Number of Iterations** and **Time per Exposure:** the exposure time for the UVIS channel must be a multiple of 0.1 s, ranging from 0.5 to 3600 s, except that 0.6 s is not allowed; see Section 6.7.1 for details).

6.3 UVIS Channel Characteristics

In concept and functionality, as well as in many design details, the WFC3 UVIS channel is patterned after the ACS/WFC channel. The UVIS channel contains an optical train providing focus and alignment adjustments as well as a correction for the OTA spherical aberration, a filter-selection mechanism, a shutter mechanism, and a CCD detector assembly (which uses the same camera-head design as ACS/WFC). These are supported by a thermal-control subsystem and also by control and data-handling electronics subsystems.

As described in Section 5.2.2, the detectors in the WFC3 UVIS channel are two 4096×2051 pixel CCDs, butted together to yield a 4096×4102 array with a ~31 pixel (1.2 arcsec) gap. The gap can, of course, be filled in by using appropriate telescope dithering strategies (see Section 6.10.1 and Appendix C). The plate scale is approximately 0.04 arcsec per pixel, providing a good compromise between adequate sampling of the PSF and a wide field of view. Geometric distortions introduced by the

WFC3 optics cause the nominally square detector to map onto the sky as a skewed rhombus, about 162×162 arcsec in size.

The UVIS CCDs currently have excellent CTE. As discussed in Section 5.4.11, the CTE is expected to degrade slowly over WFC3's lifetime, and indeed the early indications are that the degradation is no more rapid than was anticipated. For this reason, charge injection is not available in Cycle 18.

6.4 UVIS Field Geometry

6.4.1 Field of View and Pixel Size

As described above, the UVIS channel uses two 4096×2051 CCDs, butted together to yield a 4096×4102 array with a ~31 pixel (1.2 arcsec) gap. Because the detector is tilted along its diagonal axis 21° with respect to the incident beam, the field of view projected onto the sky is rhombus-shaped, 162 arcsec on a side, with an angle of 86.1° between the sides. The pixels projected onto the sky are also rhomboidal, ~0.04 arcsec on a side.

6.4.2 Geometric Distortion

Distortions due to the WFC3 optics cause the nominally square field of view of the UVIS detector to map onto the sky as a skewed rhombus. Geometric distortions in both channels are discussed in more detail in Appendix B.

Distortion must be taken into account when exposures are flat-fielded, photometrically calibrated, used for astrometric measurements, or combined with other dithered exposures. The *MultiDrizzle* software appropriately carries out those operations using Calibration Database distortion polynomials (IDCTAB) and pixel area correction tables (PAM).

A pixel area map and coefficients for 4th-order polynomial coordinate transformations are available on the WFC3 Web site:
http://www.stsci.edu/hst/wfc3/pam/pixel_area_maps
http://www.stsci.edu/hst/wfc3/idctab_lbn

6.4.3 Coordinate Systems

There are three different coordinate systems defined for use with the CCDs in the UVIS channel, each tailored to specific purposes. They are shown in Figure 6.1 and are as follows:

- **FITS image-based system** (AXIS1, AXIS2; units of pixels)
- **Proposal POS TARG system** (X-POSTARG, Y-POSTARG; units of arcsec)
- ***HST*-based system** (V2, V3 or U2, U3; units of arcsec)

Figure 6.1: WFC3 CCD detector coordinate systems.

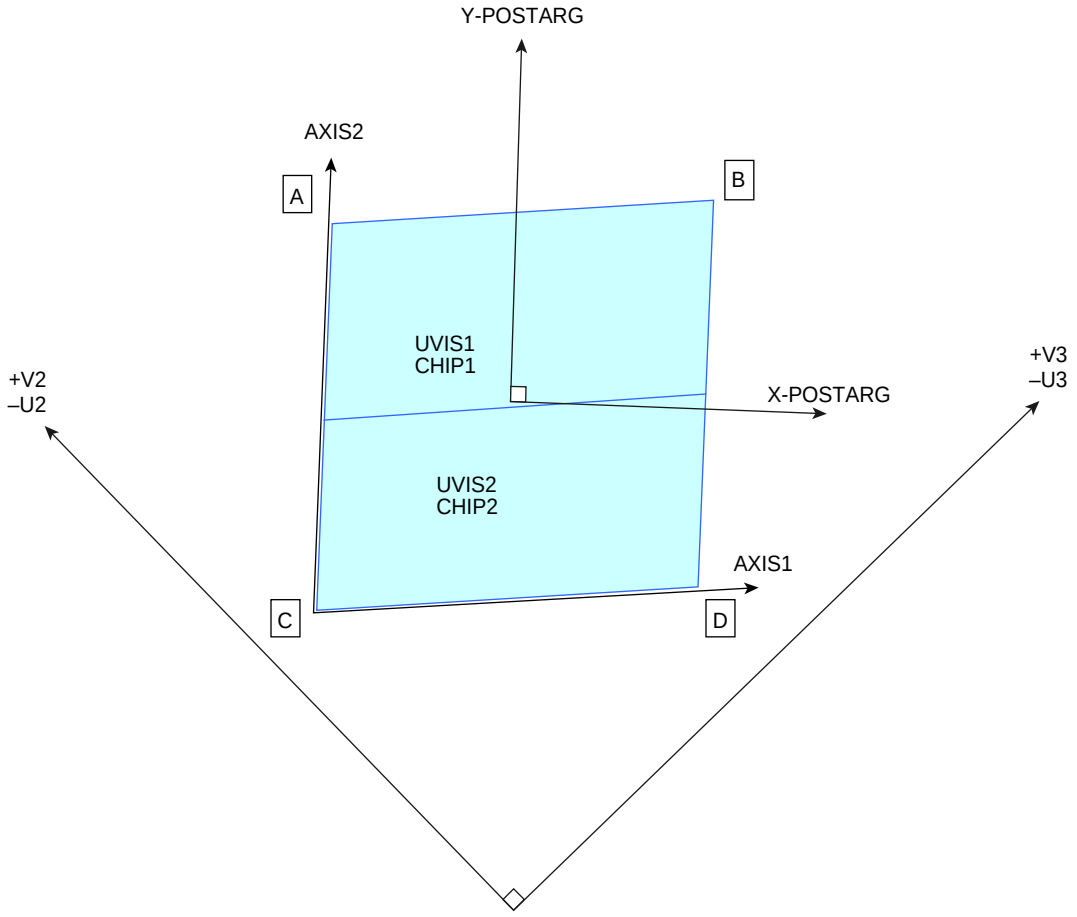

The **image-based coordinate system** (AXIS1, AXIS2, as shown in Figure 6.1) is an orthogonal system in pixel units. It is used by the calibration pipeline and other data-analysis software. Sometimes also referred to as the user frame, when an image is displayed on a computer screen, this system has the X-axis (AXIS1) increasing to the right and the Y-axis (AXIS2) increasing to the top of the screen, with 1 being the conventional index of the first pixel. The image-based coordinate system is used in most figures in this handbook, as well as in the aperture definitions available in the Science Instrument Aperture File.

The origin of this coordinate system is context specific. Logical or image coordinates have the origin at the lower left corner of the image, even for subarray images or images containing overscan data. These coordinates are shown as the "Image X,Y" coordinates in DS9. Physical or CCD coordinates have their origin at the lower left corner of the chip's science area. Thus, pixels to the left of the science area within the physical overscan area (see Figure 6.14) actually have negative coordinates in the physical image-based system. These physical coordinates are displayed as

"Physical X,Y" coordinates in DS9, which determines the coordinates using the LTV1 and LTV2 FITS header keywords. The lengths of the axes, in pixels, are stored in the FITS header keywords NAXIS1 and NAXIS2.

The **POS TARG reference frame**, sometimes referred to as the spacecraft system, is used for specifying the placement of an astronomical target relative to the aperture reference point in the instrument field of view. Its units are arcseconds. For the UVIS channel, the POS TARG system has been defined such that the Y-POSTARG axis is parallel to AXIS2 at the reference point of the aperture in use. The X-POSTARG axis is not parallel to AXIS1 due to geometric distortion.

As is the case for other *HST* instruments, the POS TARG origin is defined to be at the reference point of the user-selected UVIS aperture (such as the geometric center of a particular chip, or the optimum center of a quadrant, etc.; see Table 6.1 below for the names of the various UVIS channel apertures). Figure 6.1 illustrates the POS TARG reference frame for the "UVIS" aperture, whose center is near the middle of the WFC3 UVIS field of view; the POS TARG directions are indicated by arrows labeled X-POSTARG and Y-POSTARG.

The ***HST*-based**, or vehicle (V2, V3), system is an orthogonal reference frame tied to the telescope and is used operationally for alignment, pointing, and slewing purposes. The V1 axis lies along the optical axis while V2,V3 run parallel and perpendicular, respectively, to the solar-array rotation axis (see Figure 2.2). Note that the (undistorted) diagonals of the WFC3 CCD detector run along the V2,V3 directions. Because WFC3 is on-axis, the origin of the V2,V3 system lies near the center of the WFC3 field of view. However, the V2,V3 coordinate axes have been shifted for clarity in Figure 6.1.

HST observers may be more familiar with the U2,U3 coordinate system than V2,V3; for example, the specification of the ORIENT angle Special Requirement in APT uses the position angle of the U3 axis. The U2,U3 coordinates are defined as U2 = –V2 and U3 = –V3, and are marked in Figure 6.1 as well.

A fourth coordinate system (the **detector-based reference frame** in pixel units) is described here for completeness, but observers are unlikely to encounter this system other than in technical documents created during the development and ground-testing of WFC3. The detector-based system (Xdet, Ydet) is used by the flight software for commanding the detectors. It is a right-handed system based upon the orientation of the CCD serial registers, with its origin at Amplifier A (the four amplifiers are in the outer corners of the detectors, as shown in Figure 6.1). The +Xdet and +Ydet axes map to the –AXIS2 and +AXIS1 axes, respectively. Unlike the image-based AXIS1,AXIS2 system, the detector system is 0-indexed. Parallel shifting is performed along constant Xdet, and serial shifting is done along the constant Ydet direction (Section 6.7.2).

6.4.4 Subarrays and On-Chip Binning

While the default WFC3 UVIS readout mode is full-frame (both CCDs), subarrays may be employed to read out and store only a portion of the full field of view. Subarrays may be used, for example, in cases where the full-field data-volume and/or instrument-overhead requirements would constrain the observations unacceptably. There are also circumstances in which on-chip binning may be desirable. Both modes

have implications for the overscan information, as listed in Table 6.1 and discussed in Section 6.7.2.

Subarrays

Beginning in Cycle 18, a wider range of subarray sizes will be available: 512×512, 1k×1k, and 2k×2k. User-defined subarrays, and subarrays that span quadrant boundaries, will no longer be available. Subarrays are invoked via the appropriate Aperture parameter in the Phase II observing proposal; these apertures contain the string "SUB" in their names. Figure 6.2 shows the subarrays expected to be available in Cycle 18, but the names, positions, and number of subarrays may be changed slightly during the implementation process.

Online

For updates on subarray and aperture definitions, check the WFC3 Web site and the Science Instrument Aperture File (SIAF) page:
http://www.stsci.edu/hst/wfc3/ins_performance/subarrays/
http://www.stsci.edu/hst/observatory/apertures/

Figure 6.2: WFC3 UVIS subarrays available for Cycle 18. Full names of the subarrays are given in Table 6.1.

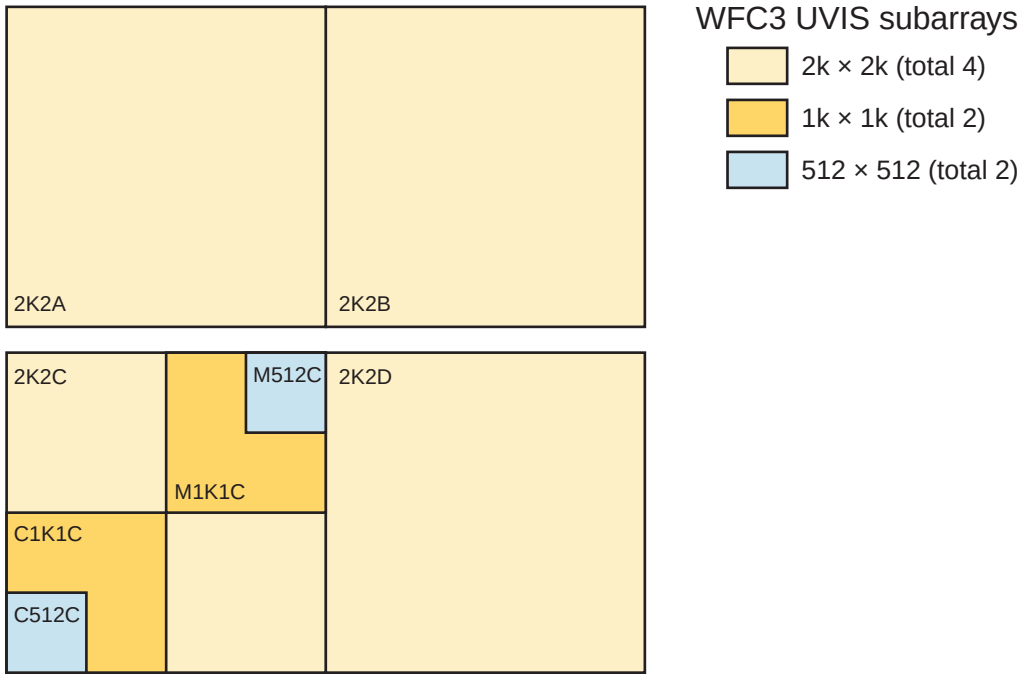

The WFC3 UVIS channel supports three pre-defined subarray sizes: 512×512, 1k×1k, and 2k×2k. Subarrays are invoked via the appropriate Aperture parameter in the Phase II observing proposal; these apertures contain the string "SUB" in their names.

For the special case of quad filters (which are optical elements that include four different bandpasses simultaneously, one bandpass per WFC3 UVIS quadrant), the observer must select one of the "QUAD" aperture values in the Phase II proposal, in conjunction with the desired quad filter via the filter parameter. This combination of quad aperture and quad filter ensures that the target is automatically placed in the correct quadrant for imaging with the requested quad bandpass. Furthermore, specification of the subarray quad aperture (UVIS-QUAD-SUB) instructs the ground system to read out only the 2k×2k quadrant of interest. If "-SUB" is omitted from the quad aperture name (i.e., UVIS-QUAD, UVIS-QUAD-FIX), the target is positioned in the proper quadrant for the bandpass requested in the filter parameter, but the entire frame, both CCDs, is still be read out.

Use of any quad filter aperture, full-frame or subarray, is fully supported. However, if data volume and overhead time are not an issue, the observer is encouraged to allow full-frame readouts of quad-filter exposures, enabling serendipitous discoveries in the other quadrants of the image as well as enrichment of the *HST* data archive.

On-Chip Binning

For greater sensitivity when observing very faint targets, or for acquiring full-frame images as rapidly as possible, the BIN optional parameter in the observing proposal may be used to specify that the CCDs be read out in binned mode. Legal values for the parameter are NONE (the default), or 2 or 3, for 2×2 and 3×3 on-chip binning, respectively. On-chip binning is only allowed with full-frame readouts; it may not be used in conjunction with any subarray mode. To perform on-chip binning, multiple rows are parallel-shifted into the serial register, which is shifted multiple pixels at a time into a single output pixel, which is then read once. This type of binning improves the signal-to-noise in an image by minimizing readout noise: a 2×2 or 3×3 binned pixel contains approximately the same amount of read noise as a single pixel in an unbinned readout (see Section 5.4.7).

In addition to the S/N improvement, on-chip binning results in a significant reduction of readout overhead time, not only because of the shorter time needed to read out 1/4 or 1/9 of the usual full-frame number of pixels (~50 and ~23 sec, for 2×2 and 3×3 binning respectively, compared to 93 sec for unbinned), but the image sizes are also smaller, i.e., more images will fit into the instrument image buffer before it must be dumped to the SSR. However, binning results in a loss of spatial resolution; the observer must weigh the benefit of binning against the cost of degraded resolution in the science images.

Binning affects the overscan data associated with an exposure. At the frame edges, some science and overscan pixels are binned together. Section 6.7.2 gives details concerning the rows and columns affected by binning mixed science and overscan data.

6.4.5 Apertures

The **APERTURE** parameter in the Phase II observing proposal defines two quantities: the active **region** of the detector to be read out (full frame or subarray), as

well as the positioning of the target within the region (**reference point**). The default is to center the target at the chosen reference point, but a **POS TARG** Special Requirement may be added to offset the target from this position.

There are two types of predefined apertures: "**fixed**" and "**optimum**." The fixed positions have reference points at the geometric center of the aperture in question; as the name implies, their locations will remain fixed in image-based coordinates for the life of the instrument. The "optimum" apertures have reference points near the geometric center of the region, but the precise location may be offset slightly from the geometric center so as to avoid any known CCD features (e.g., bad column, quad filter edge effects) that might compromise the observation of a target at that position. The locations of the "optimum" aperture reference points—in both the image-based coordinate system and the spacecraft V2,V3 coordinate system—may change over time as the characteristics and the characterization of the CCD evolve. For example, SMOV and Cycle 17 calibration data are being used to define the offset between the IR and UVIS channels, and the size of the gap between the UVIS1 and UVIS2 CCDs.

For updates on subarray and aperture definitions, check the Science Instrument Aperture File (SIAF) page:
http://www.stsci.edu/hst/observatory/apertures/

The choice of optimum or fixed aperture depends on the program's objectives and target. For a very small target, or one which easily fits into the aperture's field of view, the optimum aperture's reference point is defined to ensure that the target center does not fall on known problematic areas of the detector. The WFC3 Web site and STAN will announce changes in optimum aperture definitions. On the other hand, when the observer needs precise control of the position of the target on the detector, fixed apertures should be used. Fixed apertures are therefore appropriate when target position relative to detector edges is important, or when mosaics are being designed with edges requiring positional accuracies of better than 10 arcsec or so. The available WFC3 UVIS apertures (Table 6.1) include both fixed and optimum versions for the primary locations: the center of the full two-chip detector (UVIS and UVIS-FIX), and the center of each chip (UVIS1 and UVIS2, and UVIS1-FIX and UVIS2-FIX).

There are also fixed and optimum apertures for use with the quad filters. Because the filter wheel assembly is necessarily offset from the focal plane, the edges between quad filters are blurred at the focal plane, producing regions with contributions from multiple quad filter passbands (Figure 6.8). For Cycle 18, the "optimum" quad apertures have reference points centered within the useful single-passband regions, while the "fixed" quad apertures have reference points at the geometric centers of the quadrants (closer to the filter edge effects). In programs where targets are placed in different quadrants, the choice of quad aperture will affect the size of offsets and may require new guide star acquisition, as described in Section 10.2.

Subarray apertures pictured in Figure 6.2 are all "optimum," and no "fixed" apertures are available for these subapertures. UVIS-QUAD-SUB and

UVIS-QUAD-SUB-FIX are the only subapertures with fixed and optimum options, necessitated by the relatively large offsets (~15 arcsec) between the fixed and optimum reference points. For comparison, distances between fixed and optimum reference points for ACS/WFC3 are 4 arcsec or less.

Table 6.1: Predefined apertures available in Cycle 18 for WFC3/UVIS (details can be found in the Phase II Proposal Instructions).

Aperture	Over-scan[1]	Region	Reference point
UVIS	P, V	Full detector	Optimum center of full two-CCD field of view
UVIS-FIX	P, V	Full detector	Geometric center of full two-CCD field of view
UVIS1	P, V	Full detector	Optimum center of CCD Chip 1
UVIS1-FIX	P, V	Full detector	Geometric center of CCD Chip 1
UVIS2	P, V	Full detector	Optimum center of CCD Chip 2
UVIS2-FIX	P, V	Full detector	Geometric center of CCD Chip 2
G280-REF	P, V	Full detector	Grism reference aperture for undispersed exposures
UVIS-QUAD	P, V	Full detector	Optimum center of quadrant corresponding to selected quadrant filter
UVIS-QUAD-FIX	P, V	Full detector	Geometric center of quadrant corresponding to selected quadrant filter
UVIS-QUAD-SUB	P	2048×2050, quadrant corresponding to selected quadrant filter	Optimum center of the quadrant
UVIS-QUAD-SUB-FIX	P	2048×2050, quadrant corresponding to selected quadrant filter	Geometric center of the quadrant
UVIS1-2K2A-SUB **UVIS1-2K2B-SUB** **UVIS2-2K2C-SUB** **UVIS2-2K2D-SUB**	P	2048×2050	Optimum center of 2k × 2k subarray
UVIS2-M1K1C-SUB		1024×1024, quadrant C near detector center	Optimum center of 1k × 1k subarray
UVIS2-C1K1-SUB	P	1024×1024, near Amplifier C	Optimum center of 1k × 1k subarray
UVIS2-M512C-SUB		512×512, quadrant C near detector center	Optimum center of 512×512 subarray
UVIS2-C512C-SUB	P	512×512, near amplifier C	Optimum center of 512×512 subarray;

1. P indicates aperture includes physical overscan, V indicates aperture includes virtual overscan. Apertures with no symbol do not include any overscan data for bias level correction.

6.5 UVIS Spectral Elements

6.5.1 Filter and Grism Summary

An overview of the UVIS spectral elements was given in Section 2.3. This section gives further details of the UVIS filters and grism. Table 6.2 contains a complete listing of the available spectral elements in the UVIS channel. Figures 6.3 through 6.6 show the effective throughput curves, including the filter transmission convolved with the OTA, WFC3 optics, and detector response. All of the UVIS filters are contained in a multi-wheel mechanism—identical to the mechanism on WFPC2—called the Selectable Optical Filter Assembly (SOFA). Values in Table 6.2 have been calculated for UVIS chip 2, which has a higher UV sensitivity, except in the cases of quad filters which are restricted to the A and B quadrants.

More detailed information on the throughput curves of all of the filters is given in Appendix A; in particular, Section A.2.1 describes how to generate tabular versions of the throughput curves using ***synphot***. All measurements of the UVIS filters which involve wavelengths, as tabulated in Table 6.2 and plotted in Figures 6.3 through 6.6 and in Appendix A, were done in air. The data have been converted to vacuum wavelengths using the formula given by D. C. Morton (1991, *ApJS* **77**, 119). It should also be noted that the laboratory measurements were done at a temperature of 20°C, whereas the UVIS filters are operated on orbit at 0°C. The temperature difference may lead to wavelength shifts that are no more than 0.14 nm in the worst cases, according to the filter manufacturing specifications.

The UVIS filters have been chosen to cover a wide variety of scientific applications, ranging from color selection of distant galaxies to accurate photometry of stellar sources and narrow-band imaging of nebular gas. The set includes several very wide-band filters for extremely deep imaging, filters that match the most commonly used filters on WFPC2 and ACS (to provide continuity with previous observations), the SDSS filters, and filters that are optimized to provide maximum sensitivity to various stellar parameters (e.g., the Strömgren and Washington systems, and the F300X filter for high sensitivity to the stellar Balmer jump). There is a variety of narrow-band filters, which allow investigations of a range of physical conditions in the interstellar medium, nebulae, and solar system. A few of the narrow-band filters are also provided with slightly redshifted wavelengths, for use in extragalactic applications. Finally, there is a UV grism that provides slitless spectra with useful dispersion covering 200–400 nm (although the grism transmission spans the full wavelength range of the CCD).

Table 6.2: WFC3/UVIS Filters and Grism.

Name[1]	Description[2]	Pivot[3] λ_p (nm)	Width[4] (nm)	Peak System Throughput
UVIS Long-Pass (LP) and Extremely Wide (X) Filters				
F200LP	Clear	488.3	502.2	0.33
F300X	Extremely wide UV; grism reference	280.7	66.3	0.17
F350LP	Long pass	584.6	475.8	0.29
F475X	Extremely wide blue	493.9	205.6	0.28
F600LP	Long pass	744.4	229.2	0.29
F850LP	SDSS *z′*	916.6	118.2	0.09
UVIS Wide-Band (W) Filters				
F218W	ISM feature	222.4	32.2	0.05
F225W	UV wide	235.9	46.7	0.10
F275W	UV wide	270.4	39.8	0.13
F336W	*U*, Strömgren *u*	335.5	51.1	0.20
F390W	Washington *C*	392.1	89.6	0.25
F438W	WFPC2 *B*	432.5	61.8	0.24
F475W	SDSS *g′*	477.3	134.4	0.27
F555W	WFPC2 *V*	530.8	156.2	0.28
F606W	WFPC2 Wide *V*	588.7	218.2	0.29
F625W	SDSS *r′*	624.2	146.3	0.28
F775W	SDSS *i′*	764.7	117.1	0.23
F814W	WFPC2 Wide *I*	802.4	153.6	0.23
UVIS Medium-Band (M) Filters				
F390M	Ca II continuum	389.7	20.4	0.22
F410M	Strömgren *v*	410.9	17.2	0.27
FQ422M	Blue continuum	421.9	11.2	0.19
F467M	Strömgren *b*	468.3	20.1	0.28
F547M	Strömgren *y*	544.7	65.0	0.26
F621M	11% passband	621.9	60.9	0.28
F689M	11% passband	687.6	68.3	0.25
F763M	11% passband	761.2	70.4	0.21
F845M	11% passband	843.6	78.7	0.14
UVIS Narrow-Band (N) Filters				
FQ232N	C II] 2326	241.3	3.4	0.04
FQ243N	[Ne IV] 2425	246.8	3.6	0.05
F280N	Mg II 2795/2802	283.1	4.3	0.06
F343N	[Ne V] 3426	343.5	25.0	0.21
F373N	[O II] 3726/3728	373.0	5.0	0.18
FQ378N	*z* ([O II] 3726)	379.2	9.9	0.20
FQ387N	[Ne III] 3868	387.4	3.4	0.18
F395N	Ca II 3933/3968	395.5	8.5	0.22
FQ436N	Hγ 4340 + [O III] 4363	436.7	4.3	0.19
FQ437N	[O III] 4363	437.1	3.0	0.20
F469N	He II 4686	468.8	5.0	0.20
F487N	Hβ 4861	487.1	6.0	0.25

Name[1]	Description[2]	Pivot[3] λ_p (nm)	Width[4] (nm)	Peak System Throughput
FQ492N	*z* (Hβ)	493.3	11.4	0.25
F502N	[O III] 5007	501.0	6.5	0.26
FQ508N	*z* ([O III] 5007)	509.1	13.1	0.26
FQ575N	[N II] 5754	575.8	1.8	0.23
FQ619N	CH_4 6194	619.9	6.1	0.26
F631N	[O I] 6300	630.4	5.8	0.25
FQ634N	6194 continuum	634.9	6.4	0.26
F645N	Continuum	645.4	8.4	0.25
F656N	Hα 6562	656.1	1.8	0.24
F657N	Wide Hα + [N II]	656.7	12.1	0.26
F658N	[N II] 6583	658.4	2.8	0.26
F665N	*z* (Hα + [N II])	665.6	13.1	0.26
FQ672N	[S II] 6717	671.6	1.9	0.25
F673N	[S II] 6717/6731	676.6	11.8	0.25
FQ674N	[S II] 6731	673.1	1.8	0.19
F680N	*z* (Hα + [N II])	687.7	37.1	0.25
FQ727N	CH_4 7270	727.5	6.4	0.21
FQ750N	7270 continuum	750.3	7.0	0.18
FQ889N	CH_4 25 km-agt[5]	889.2	9.8	0.10
FQ906N	CH_4 2.5 km-agt	905.8	9.9	0.08
FQ924N	CH_4 0.25 km-agt	924.8	9.2	0.08
FQ937N	CH_4 0.025 km-agt	937.2	9.3	0.07
F953N	[S III] 9532	953.0	9.7	0.05
		UVIS Grism (G)		
G280[6]	UV grism	Useful range: 200–400 nm[6]		0.17

1. The spectral-element naming convention is as follows for both the UVIS and IR channels. All filter names begin with F, and grisms with G; if the filter is part of a four-element quad mosaic, a Q follows F. Then there is a three-digit number giving the nominal effective wavelength of the bandpass, in nm (UVIS channel) or nm/10 (IR channel). (For long-pass filters, the number is instead the nominal blue cut-off wavelength in nm.) Finally, for the filters, one or two letters indicate the bandpass width: X (extremely wide), LP (long pass), W (wide), M (medium), or N (narrow).
2. Filters intended for imaging in a red-shifted bandpass are given descriptions similar to the following: "*z* (Hα + [N II])".
3. "Pivot wavelength" is a measure of the effective wavelength of a filter (see Section 9.3 and Tokunaga & Vacca 2005, PASP, **117**, 421). It is calculated here based on the integrated system throughput. Filter transmissions were measured in air, but the equivalent vacuum wavelengths are reported in this table.
4. Widths listed are passband rectangular width, defined as the equivalent width divided by the maximum throughput within the filter bandpass. Equivalent width is the integral with respect to wavelength of the throughput across the filter passband.
5. km-agt (km-amagat) is a unit of vertical column density, equal to 2.69×10^{24} molecules/cm^2.
6. See Chapter 8 for UVIS Grism details.

Most of the UVIS filters, as well as the UVIS grism, are full-sized elements that cover the entire UVIS field of view. However, in order to provide a larger number of bandpasses, there are five sets of "quad" filters, identified with "FQ" in the filter name, where each bandpass covers ~1/6 of the WFC3 UVIS field of view (i.e., each bandpass covers less than half of a single CCD chip). The quad filters are discussed in more detail below.

The UVIS channel is designed to be used with a single filter or grism in the light path. Although possible in principle, unfiltered imaging, or imaging through a combination of two filters (from two different SOFA wheels), would lead to significantly degraded image quality and has not been tested; thus these options are not permitted. The F200LP filter provides a clear fused silica element that approximates unfiltered imaging.

While the red blocking in the WFC3 UV filters is generally very good, resulting in negligible red leaks for hot objects (typically <<1% for targets with effective temperature $T_{\rm eff}$ > 10,000 K), the red leak can become significant in some filters for cooler targets (e.g., ~10% in F225W for a star with $T_{\rm eff}$ = 5000 K). More details are available in Section 6.5.2; Table 6.5 in that section tabulates red-leak values as a function of stellar effective temperature.

Figure 6.3: Integrated system throughput of the WFC3 UVIS long-pass and extremely wide filters (top panel) and of the wide-band filters covering 2000-6000 Å (bottom panel). The throughput calculations include the *HST* OTA, WFC3 UVIS-channel internal throughput, filter transmittance, and the QE of the UVIS flight detector, and a correction factor to account for the gain sensitivity seen in SMOV4 on-orbit observations vs. TV3 ground tests. Throughputs in all plots below ~3200 Å contain contributions at the measured rate from all detected electrons, including UV multiple electrons.

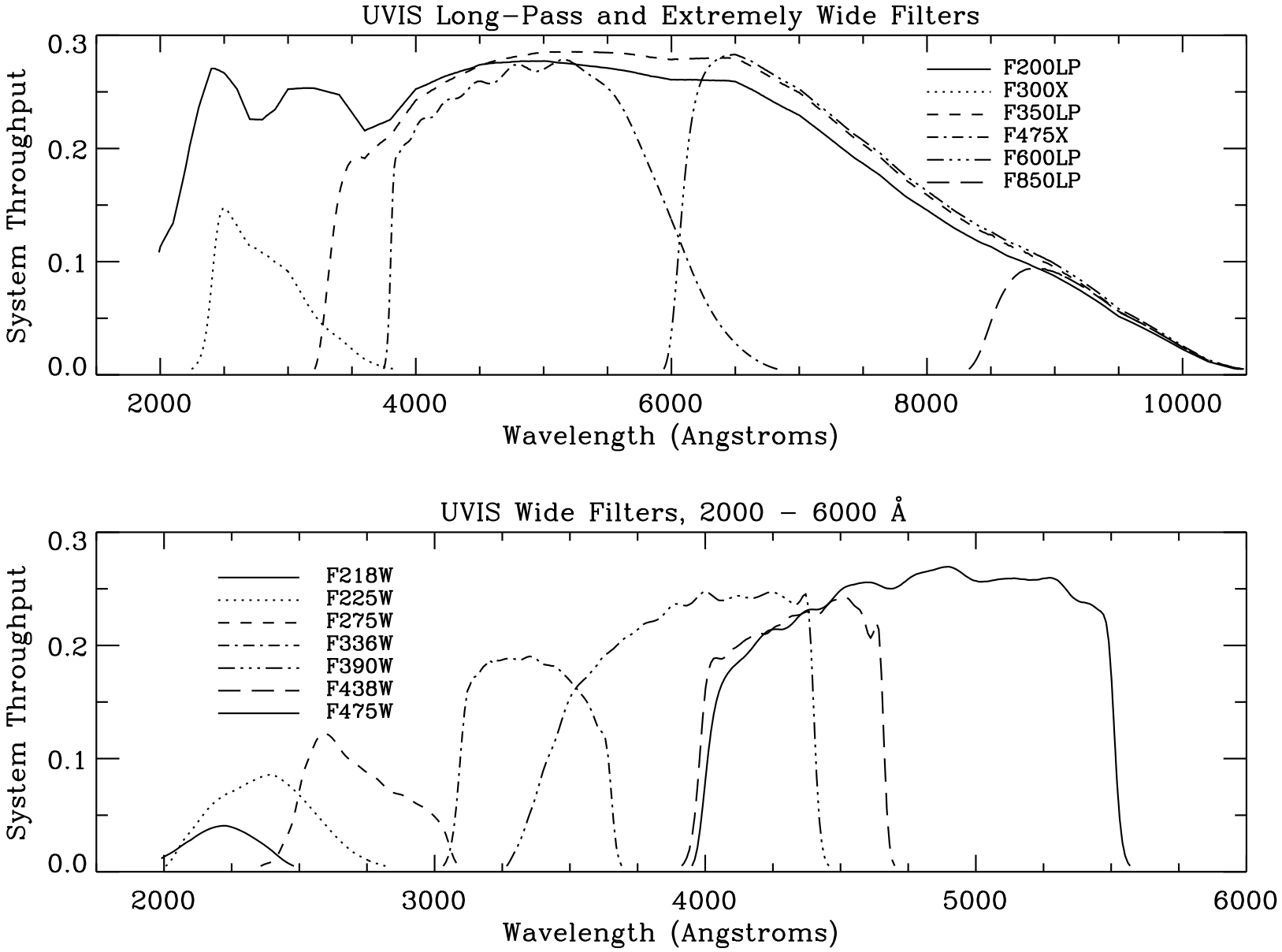

Figure 6.4: Integrated system throughput of the WFC3 UVIS wide-band filters covering 4000-10,000 Å (top panel) and the medium-band filters (bottom panel). The throughput calculations include the *HST* OTA, WFC3 UVIS-channel internal throughput, filter transmittance, and the QE of the UVIS flight detector, and a correction factor to account for the gain sensitivity seen in SMOV4 on-orbit observations vs. TV3 ground tests.

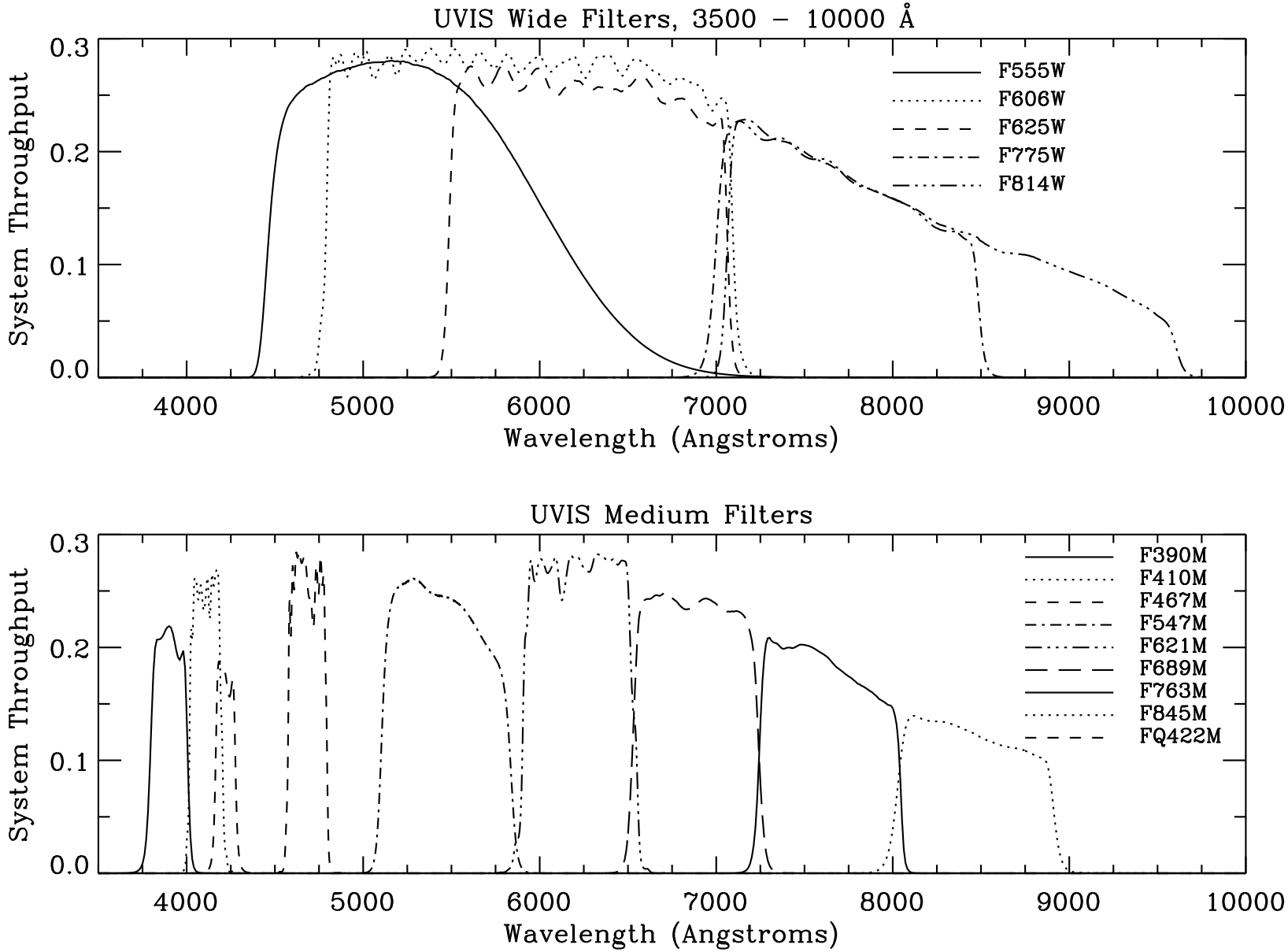

Figure 6.5: Integrated system throughput of the WFC3 UVIS narrow-band filters covering 2000-4500 Å (top panel) and the narrow-band filters covering 4500-6000 Å (bottom panel). The throughput calculations include the *HST* OTA, WFC3 UVIS-channel internal throughput, filter transmittance, and the QE of the UVIS flight detector, and a correction factor to account for the gain sensitivity seen in SMOV4 on-orbit observations vs. TV3 ground tests.

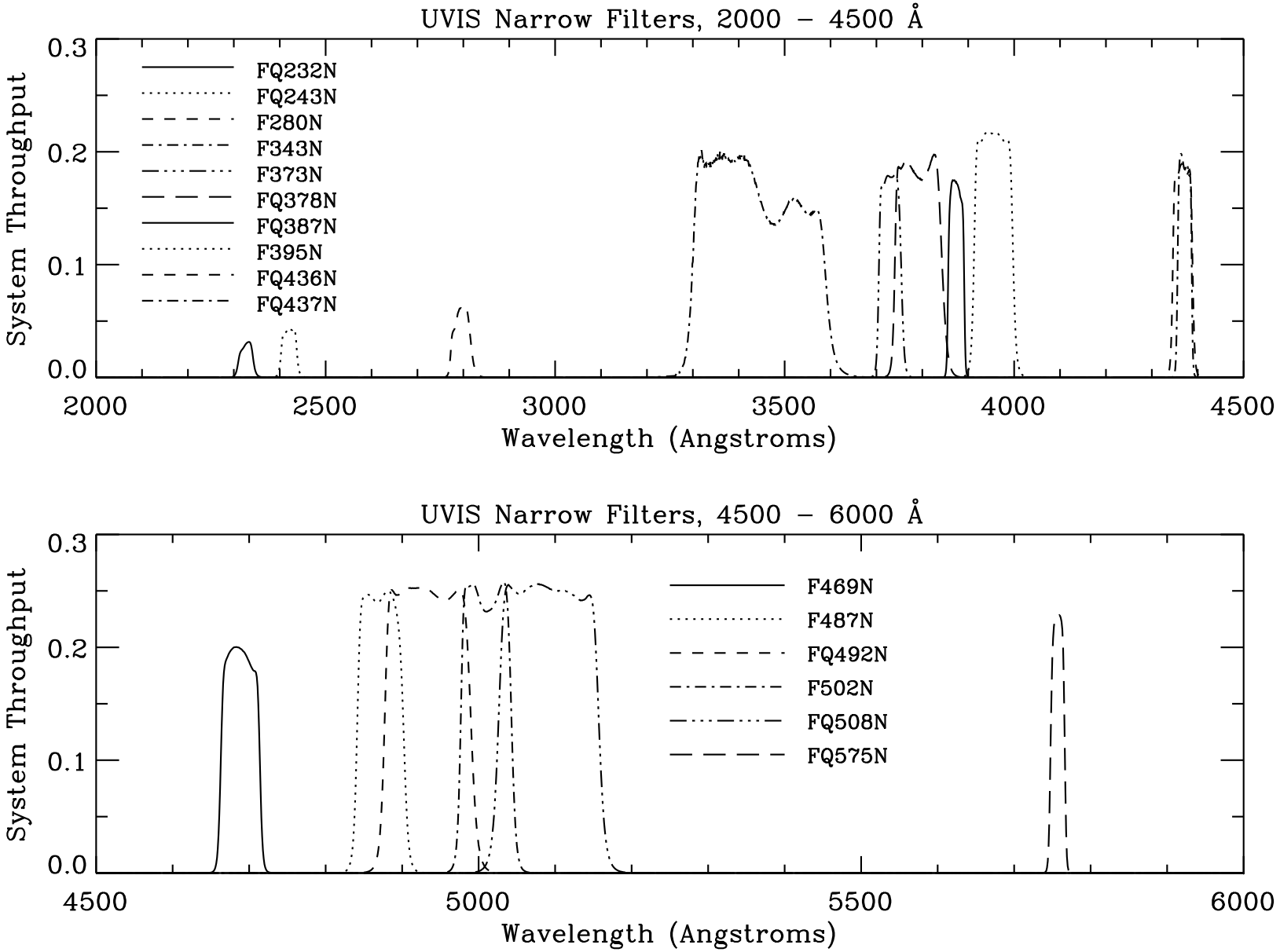

Figure 6.6: Integrated system throughput of the WFC3 UVIS narrow-band filters covering 6000-6800 Å (top panel) and the narrow-band filters covering 6600-9600 Å (bottom panel). The throughput calculations include the *HST* OTA, WFC3 UVIS-channel internal throughput, filter transmittance, and the QE of the UVIS flight detector, and a correction factor to account for the gain sensitivity seen in SMOV4 on-orbit observations vs. TV3 ground tests.

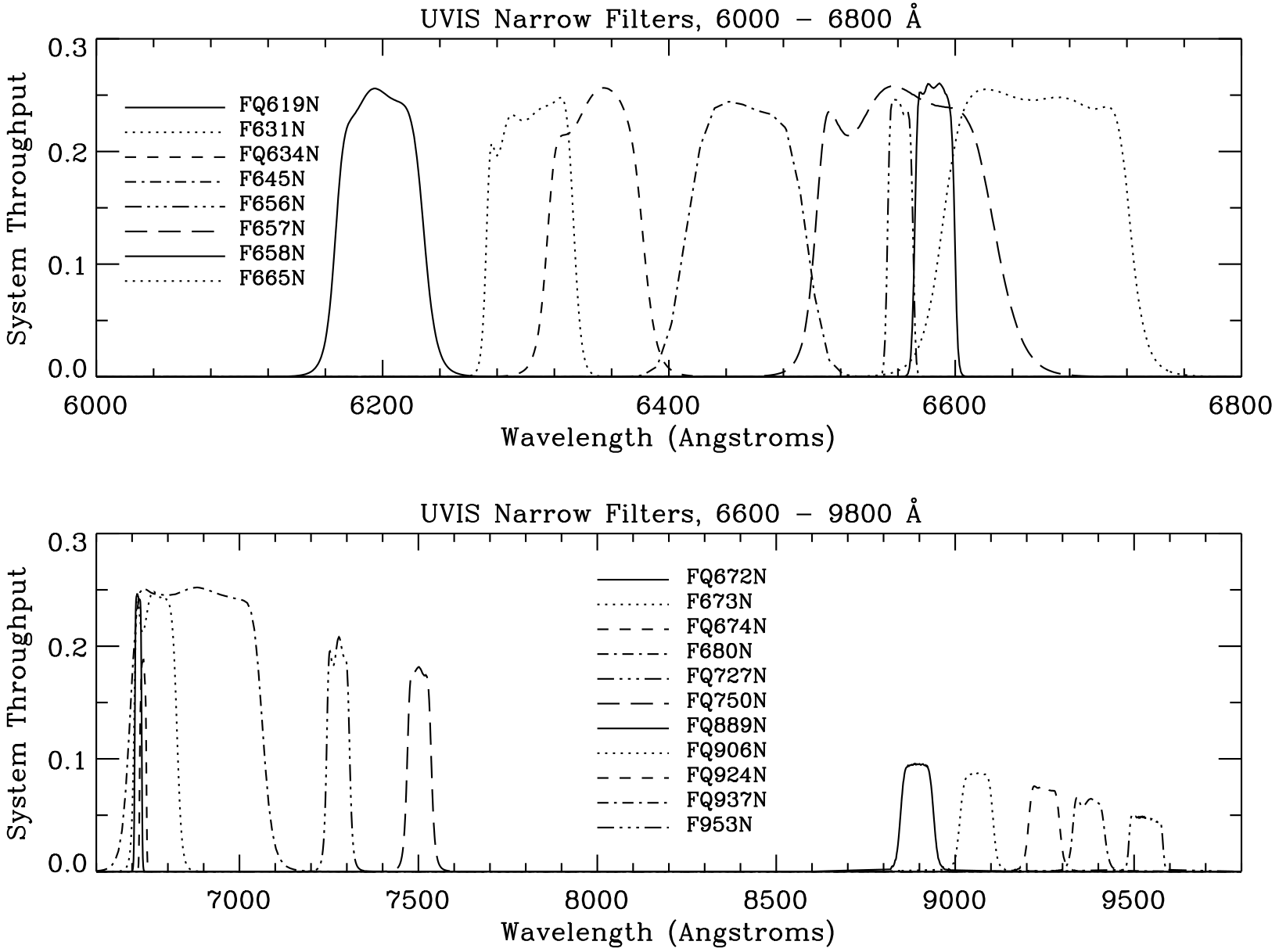

UV Filters

As mentioned earlier, the WFC3 UVIS optics and CCDs have been optimized for UV imaging. As such, the UV filters play a key role and considerable effort has been made to procure filters with the best possible characteristics, including maximum throughput, maximum out-of-band blocking, and minimal ghosts.

The UV filters include the shortest-wavelength F218W, intended for studies of the ISM absorption feature; the wide F225W and F275W for broad-band UV imaging; the Strömgren *u* (F336W) and Washington C (F390W) for stellar astrophysics; the extremely wide F300X for very deep imaging; and narrow bands such as F280N (Mg II) and the quad filters FQ232N and FQ243N (C II] and [Ne IV]).

Ultra-Wide Filters

The selection of extremely wide (X) and long-pass (LP) filters is suited for deep imaging of faint sources. The ultra-wide F200LP filter is simply a fused-silica element with a UV-optimized anti-reflection coating which covers the UVIS channel's entire spectral range (200-1000 nm). The F200LP filter is analogous to the clear filter on STIS.

WFC3's maximum sensitivity to hot sources can be obtained by subtracting an F350LP image from an F200LP, thereby creating a very broad ultraviolet bandpass. In Figure 6.7, the blue curve shows the filter transmission for the F200LP filter, and the black curve shows the effective transmission for a F200LP minus F350LP difference image. For redder targets, some additional calibration may be necessary to account for differences in the transmission of the two filters longward of ~450 nm.

The F850LP filter is part of the Sloan Digital Sky Survey (SDSS) *griz* filter set, and is the reddest of the ultra-wide filters.

Figure 6.7: Sensitivity of F200LP-F350LP compared to other UV filters (F225W, F275W and F300X). Light grey curves show blackbody functions for 20,000 and 50,000 K.

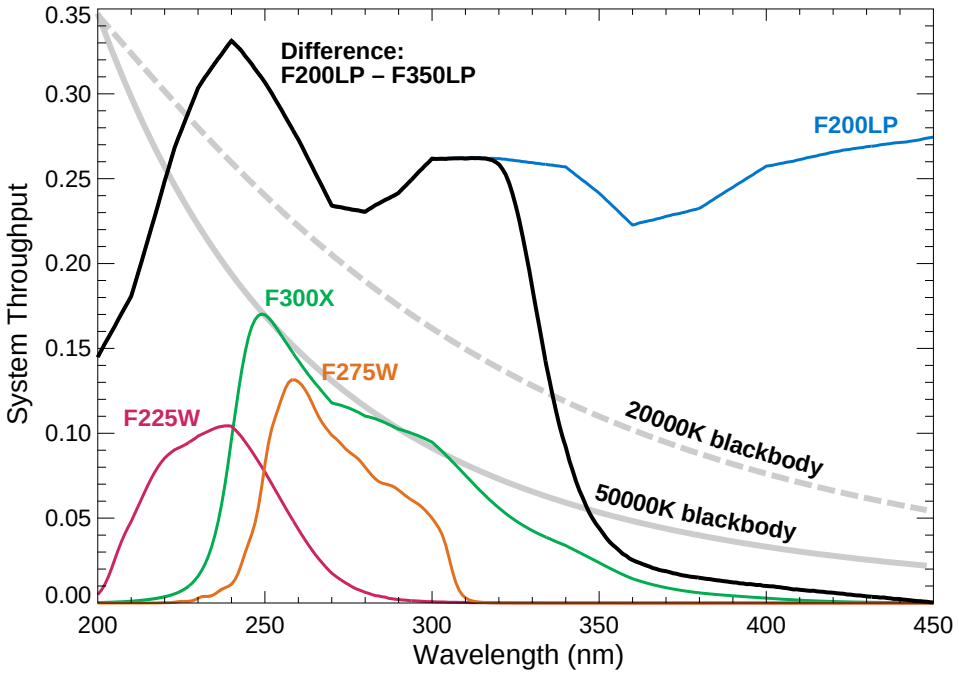

Wide-band Filters

The most commonly used WFPC2 and ACS wide filters are also included in the WFC3 filter set. In addition to a wide *V*-band filter (F606W), there is the Johnson-Cousins *BVI* set (F438W, F555W, F814W).

The Sloan Digital Sky Survey (SDSS) *griz* filter set (F475W, F625W, F775W, F850LP) is designed to provide high throughput for the wavelengths of interest and excellent rejection of out-of-band wavelengths. These filters provide wide, non-overlapping filter bands that cover the entire range of CCD sensitivity from blue to near-IR wavelengths.

Medium-band Filters

The medium-band filters include the Strömgren set (*u*, *v*, *b*, and *y*), as well as some continuum bands needed for use with narrow-band imaging (F390M, FQ422M). The four 11% passband filters were added to the WFC3 UVIS set in order to cover the ~600-900 nm wavelength region with equal-energy filters. The "11%" refers to the filter bandwidths, which are ~11% of the central wavelength.

Narrow-band Filters

The WFC3 UVIS channel contains 36 different narrow-band filters, covering a variety of species and most of the astrophysically interesting transitions, including Hα, Hβ, Hγ, He II, C II], [N II], [O I], [O II], [O III], [Ne IV], [Ne V], [S II], and Ca II. The methane absorption bands seen in planets, cool stars, and brown dwarfs are also covered.

Cosmological emission lines can be detected across a range of redshifts within the bandpasses of the narrow-band filters. Table 6.3 lists the redshifts that can be probed using the specified emission lines. These redshift ranges are offered as a guide; exact values depend on the wavelengths of the filter cutoffs. Filter cutoffs used in Table 6.3 were defined using the passband rectangular widths (defined in Footnote 3 of Table 6.2). However, passband cutoffs were not centered on the filter pivot wavelengths λ_p (defined in Section 9.3), because red leaks shift the pivot wavelengths to longer wavelengths by 1-9% in some of the ultraviolet filters. Instead, the central wavelength for each filter was determined by maximizing the wavelength-integrated product of a rectangular passband of the specified width with the actual system throughput for the filter. In the most extreme case (FQ232N), the pivot wavelength of 241.3 nm is more than two bandpass widths to the red of the rectangular passband equivalent central wavelength (232.6 nm).

Table 6.3: Nominal redshift ranges for WFC3/UVIS narrow-band filters.

Filter	Description	Filter λ_p (nm)	Filter Width (nm)	Line Rest Wavelength (nm)	Minimum *cz* (km/sec)	Maximum *cz* (km/sec)
FQ232N	C II] 2326	241.3	3.4	232.6	-2191	2191
FQ243N	[Ne IV] 2425	246.8	3.6	242.5	-2843	1607
F280N	MgII 2795/2802	283.1	4.3			
F343N	[Ne V] 3426	343.5	25.0	342.6	-10763	11113
F373N	[O II] 3726+29	373.0	5.0	372.7	-1689	2333
FQ378N	*z* ([O II]) or continuum	379.2	9.9	372.7	1247	9210
FQ387N	[Ne III] 3869	387.4	3.4	386.9	-907	1728
F395N	Ca II 3933+68	395.5	8.5			
FQ436N	Hγ 4340 + [OIII] 4363	436.7	4.3	434.0	414	3384
FQ437N	[O III] 4363	437.1	3.0	436.3	-412	1649
F469N	He II 4686	468.8	5.0	468.6	-1388	1811
F487N	Hβ 4861	487.1	6.0	486.1	-1252	2448
FQ492N	*z* (Hβ) or continuum	493.3	11.4	486.1	968	7998
F502N	[O III] 5007	501.0	6.5	500.7	-1754	2138
FQ508N	*z* ([O III]) or continuum	509.1	13.1	500.7	1120	8964
FQ575N	[N II] 5755	575.8	1.8	575.5	-344	594
FQ619N	CH_4 6194 on	619.9	6.1			
F631N	[O I] 6300	630.4	5.8	630.0	-1156	1604
FQ634N	CH_4 6194 off	634.9	6.4			
F645N	continuum	645.4	8.4			
F656N	Hα 6562	656.1	1.8	656.3	-448	375
F657N	wide Hα + [NII]	656.7	12.1	656.3	-2709	2818
F658N	[NII] 6583	658.4	2.8	658.3	-519	756
F665N	*z* (Hα + [NII]) or continuum	665.6	13.1	656.3	1311	7295
FQ672N	[S II] 6717	671.6	1.9	671.7	-402	446
F673N	[S II] 6717+31	676.6	11.8	672.5	-847	4413
FQ674N	[S II] 6731	673.1	1.8	673.1	-437	365
F680N	*z* (Hα + [NII]) or continuum	687.7	37.1	656.3	5833	22781

Filter	Description	Filter λ_p (nm)	Filter Width (nm)	Line Rest Wavelength (nm)	Minimum *cz* (km/sec)	Maximum *cz* (km/sec)
FQ727N	CH_4 7270 on	727.5	6.4			
FQ750N	CH_4 7270 off	750.3	7.0			
FQ889N	CH_4 25 km-agt	889.2	9.8			
FQ906N	CH_4 2.5 km-agt	905.8	9.9			
FQ924N	CH_4 0.25 km-agt	924.8	9.2			
FQ937N	CH_4 0.025 km-agt	937.2	9.3			
F953N	[S III] 9532	953.0	9.7	953.1	-1494	1557

Quad Filters

The WFC3 UVIS channel contains five quad filters: each is a 2×2 mosaic of filter elements occupying a single filter slot, with each quadrant providing a different bandpass (typically narrow-band, although there are also several bandpasses intended for continuum measurements). The five quad filter sets on WFC3 significantly increase the number of available narrow-band filters. The WFC3 quad filters are listed in Table 6.4 with their readout amplifiers.

A quadrant nominally covers only 1/4 of the WFC3 total field of view or about 80"×80", although edge effects (Figure 6.8) result in an unvignetted field of about 1/6 of the field of view. The filter edges are out of focus on the focal plane, so light from multiple passbands reaches the detector in those areas.

In programs where targets are placed in different quadrants during a single orbit, spacecraft maneuvers may be large enough to force a new guide star acquisition. Guide star acquisition overheads are described in Section 10.2.

Table 6.4: Quad filter names and positions (identified by readout amplifier).

Filter	Readout Amplifier	Filter	Readout Amplifier	Filter	Readout Amplifier	Filter	Readout Amplifier
FQ232N	C	FQ436N	D	FQ619N	A	FQ750N	B
FQ243N	D	FQ437N	A	FQ634N	C	FQ889N	A
FQ378N	B	FQ492N	B	FQ672N	D	FQ906N	C
FQ387N	A	FQ508N	A	FQ674N	B	FQ924N	D
FQ422M	C	FQ575N	C	FQ727N	D	FQ937N	B

Figure 6.8: Quad filter edge effects (indicated by brackets). QUAD-SUB-FIX and QUAD-FIX apertures have reference points *in the center of each quadrant*. For Cycle 18, QUAD-SUB and QUAD apertures have reference points *in the center of the areas unaffected by filter edge effects*.

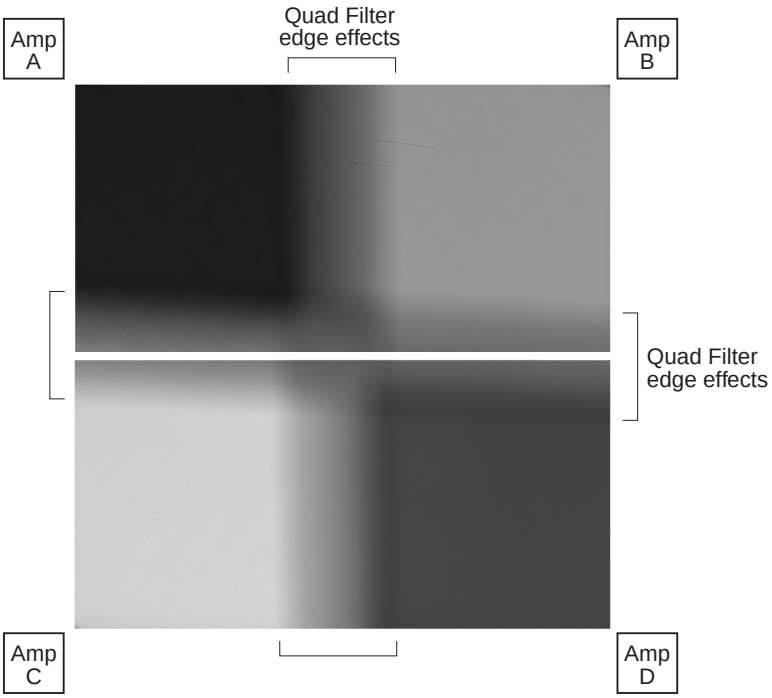

Grism

The UVIS channel has a UV grism (G280), the spare element from WF/PC-1. It provides slitless spectra with a dispersion of about 1.4 nm/pix and a spectral resolution of about 70, over the 200-400 nm wavelength range, but with transmission in the zeroth order over the entire response of the CCD (see Figure 8.2). Typically, a grism observation is accompanied by a direct image, for source identification and wavelength zero-point calibration; an ideal filter for the identification image is the F300X discussed above. Chapter 8 discusses WFC3 slitless spectroscopy in detail.

6.5.2 Filter Red Leaks

The design and manufacture of the UV filters was based on a careful balance of the in- and out-of-band transmissions: in general, higher in-band transmission results in poorer suppression of out-of-band transmission, and vice versa. The WFC3 filters represent an attempt to achieve an optimum result, maximizing the in-band transmission while keeping the out-of-band transmission as low as possible in order to minimize red leaks.

Table 6.5 below summarizes the red-leak levels for the WFC3 UV filters. The table lists the fraction of the total signal that is due to flux longward of 400 nm, as a function of effective temperature. This was calculated by convolving a blackbody of the given $T_{\rm eff}$ with the system throughput in the listed filter. As can be seen from the table, red leaks should not be an issue for observations of any objects taken with F275W or

F336W. The other UV filters have some red leaks, whose importance depends on stellar temperature. The red leaks in F218W and F300X, for example, exceed ~1% for objects cooler than ~6000 K, while in F225W the red leak reaches ~1% for objects with even cooler temperatures. The most extreme red leaks arise from F218W and F225W observations of objects with T_{eff} of ~4000 K or cooler, necessitating appropriate corrections.

Table 6.5: Fraction of flux longward of 400 nm as a function of effective temperature.

T_{eff} (K)	F218W	F225W	F275W	F300X	F336W
1000	1	1	1	1	1
2000	9.9E-01	9.9E-01	8.4E-01	5.5E-01	3.0E-02
3000	6.0E-01	2.7E-01	3.0E-02	8.9E-02	8.4E-04
4000	1.1E-01	1.8E-02	3.1E-03	3.3E-02	1.4E-04
5000	2.7E-02	3.2E-03	8.6E-04	1.7E-02	4.5E-05
6000	9.9E-03	1.0E-03	3.8E-04	1.0E-02	2.2E-05
7000	4.9E-03	4.6E-04	2.2E-04	7.3E-03	1.3E-05
8000	2.8E-03	2.5E-04	1.5E-04	5.5E-03	9.0E-06
9000	1.9E-03	1.6E-04	1.1E-04	4.4E-03	6.8E-06
10000	1.3E-03	1.1E-04	8.6E-05	3.7E-03	5.4E-06
11000	1.0E-03	8.6E-05	7.1E-05	3.2E-03	4.5E-06
12000	8.3E-04	6.9E-05	6.0E-05	2.8E-03	3.9E-06
13000	6.9E-04	5.7E-05	5.3E-05	2.6E-03	3.5E-06
14000	5.9E-04	4.8E-05	4.8E-05	2.3E-03	3.1E-06
15000	5.1E-04	4.2E-05	4.3E-05	2.2E-03	2.9E-06
20000	3.3E-04	2.6E-05	3.2E-05	1.7E-03	2.2E-06
30000	2.1E-04	1.7E-05	2.4E-05	1.3E-03	1.7E-06
40000	1.8E-04	1.4E-05	2.1E-05	1.2E-03	1.5E-06
50000	1.6E-04	1.3E-05	2.0E-05	1.1E-03	1.4E-06

6.5.3 Ghosts

The WFC3 UVIS channel exhibits three different types of optical ghosts: a) those due to reflections between the CCD front surface and the two detector package windows; b) those due to reflections between the window surfaces; and c) those due to reflections within the particular filter in use.

Window Ghosts

Window ghosts were predicted from early models of the UVIS detector (WFC3 IRS 2001-17) and were produced with an optical stimulus during ground testing (WFC3 IRS 2004-04).

When a point source is positioned in the lower right quadrant of the UVIS detector, out-of-focus reflections between the CCD and windows appear along a diagonal from the source towards the upper left, well removed from the source. These figure-eight shaped ghosts gradually move outside the field of view as the target moves out of the lower right corner. They contain a few percent of the flux of the target. The ghosts of several bright stars are visible in the exposure of 47 Tuc shown in Figure 6.9.

Smaller window ghosts appear closer to the target. They are due to reflections between the window surfaces. (See Figure 6.13 for an image showing these ghosts.)

To prevent the worst effects of window ghosts, avoid placing very bright targets on the D quadrant. Also, pay attention to the location of key science targets if bright sources are in the lower right area of the field of view. If necessary, ORIENT special requirements can be imposed within APT at the Phase II proposal preparation stage to control the positioning of bright sources on the detector.

Figure 6.9: UVIS figure-eight window ghosts. An F606W exposure of 47 Tuc (iabj01z7q_flt, display log stretched and saturated) shows figure-8 ghosts well removed along a diagonal from the bright stars in the lower right quadrant that produce them..

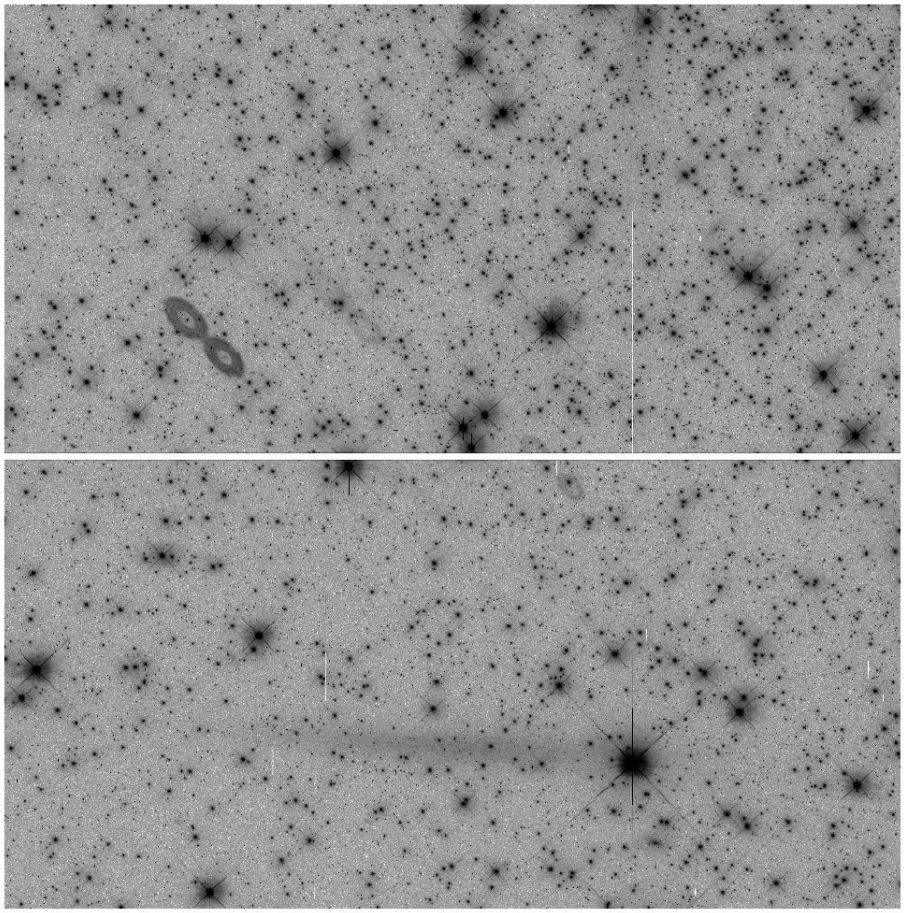

Filter Ghosts

Filter ghosts for the WFC3 filters were specified to be less than 0.2%, and in most cases were measured during ground testing to be less than 0.1%. A few filters however, were found during ground testing to have ghosts that exceeded the specification. Some of these, the ones deemed highest priority, were remanufactured and installed in the SOFA. Consequently, there are a relatively small number of filters that may be of concern for ghosts. These are listed in Table 6.6. They have been retained in the flight instrument either because they were of lower scientific priority, or because the ghost level was deemed acceptable in light of the otherwise excellent performance characteristics of the filters (e.g., in- and out-of-band transmission, sharpness of bandpass edges). While some scientific programs (e.g., stellar photometry) may be unaffected by filter ghosts, others (e.g., observations of extended targets or faint objects adjacent to bright ones) could be adversely affected. In such cases, extra planning and/or data-analysis efforts may be needed, e.g., combining images taken at different dither positions and/or roll angles, or applying a deconvolution algorithm.

Table 6.6: Filters exceeding the filter ghost requirement, measured during ground testing of the integrated instrument (see WFC3 ISR 2007-09).

Filter	Description	Ghost Level (% of total PSF flux)
F200LP	Clear	0.35[1]
F218W	ISM feature	1.3
F225W	UV wide	0.4
FQ232N	CII] 2326	7.0
FQ243N	[Ne IV] 2425	5.0
F280N	Mg II 2795/2802	0.6
F300X	Extremely wide UV; grism reference	0.3
F656N	Hα 6562	0.4
F658N	[N II] 6583	0.4
F673N	[S II] 6717/6731	0.3
F680N	*z* (Hα + [NII])	0.3

1. Laboratory measurement of stand-alone filter.

6.6 UVIS Optical Performance

Following its alignment to the OTA, a series of observations through a variety of filters were obtained to demonstrate the WFC3 optical performance. The WFC3 UVIS channel is meeting or exceeding all image quality specifications. The following subsections summarize the measured flight optical performance for the UVIS channel, as described by its point-spread function (PSF), i.e., the spatial distribution of the flux in an image of a point source. The results shown are produced using an optical model which has been adjusted and correlated to the PSFs measured on-orbit and represent mean values averaged over the field. This PSF model includes the pupil geometry, residual aberration, the mid-frequency wavefront error of the OTA, the effect of the detector charge diffusion, and first-order geometric distortion.

6.6.1 PSF Width and Sharpness

The PSFs over most of the UVIS wavelength range are well described by gaussian profiles. Two simple metrics of the size of the PSFs are the full width half maximum (FWHM) and the sharpness, defined as

$$S = \sum_{i,j} f_{ij}^2 \ ,$$

where f_{ij} is the fraction of the flux from a point source in pixel i, j. Sharpness measures the reciprocal of the number of pixels that the PSF "occupies," and can be used to determine the number of pixels for optimal photometric extraction.

Table 6.7 lists the FWHM of the model PSF core in units of pixel and arcsec and the sharpness parameter for 10 wavelengths. The sharpness range shown for each wavelength indicates the values for the PSF centered on the pixel corners and center. The degradation in image width and other performance measures in the near UV is due predominantly to the OTA mid-frequency, zonal polishing errors, which effectively move power from image core into progressively wider and stronger non-gaussian wings as wavelength decreases.

Figure 6.10 plots the azimuthally-averaged model OTA+WFC3 PSF at three different UVIS wavelengths, indicating the fractional PSF flux per pixel at radii from 1 pixel to 5 arcsec.

Table 6.7: WFC3/UVIS PSF FWHM (pixels and arcseconds), and sharpness, vs. wavelength.

Wavelength (nm)	FWHM (pix)	FWHM (arcsec)	Sharpness
200	2.069	0.083	0.040–0.041
300	1.870	0.075	0.051–0.056
400	1.738	0.070	0.055–0.061
500	1.675	0.067	0.055–0.061
600	1.681	0.067	0.053–0.058
700	1.746	0.070	0.050–0.053
800	1.844	0.074	0.047–0.048
900	1.960	0.078	0.042–0.043
1000	2.091	0.084	0.038–0.039
1100	2.236	0.089	0.034–0.035

Figure 6.10: Azimuthally averaged mean WFC3/UVIS PSF.

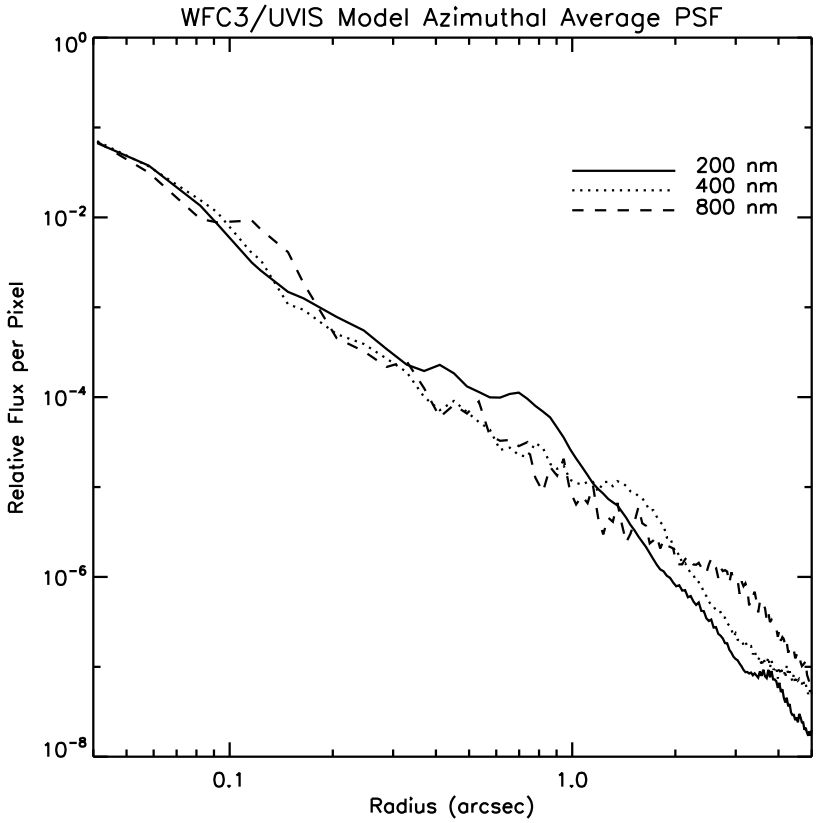

6.6.2 Encircled and Ensquared Energy

The **encircled energy** is the fraction of the total light from a point source that is contained within a circular aperture of a given radius. Since detectors have nominally square pixels, it is often more convenient to evaluate the energy falling within a certain number of pixels (**"ensquared energy"**) instead of the encircled energy, which requires interpolation to account for the fractional pixels intercepted by a circular aperture. Correlated model encircled and ensquared energy values are presented in Tables 6.6 and 6.7 and plotted in Figure 6.11 for 200, 400, and 800 nm.

Figure 6.11: Encircled Energy for the WFC3/UVIS channel.

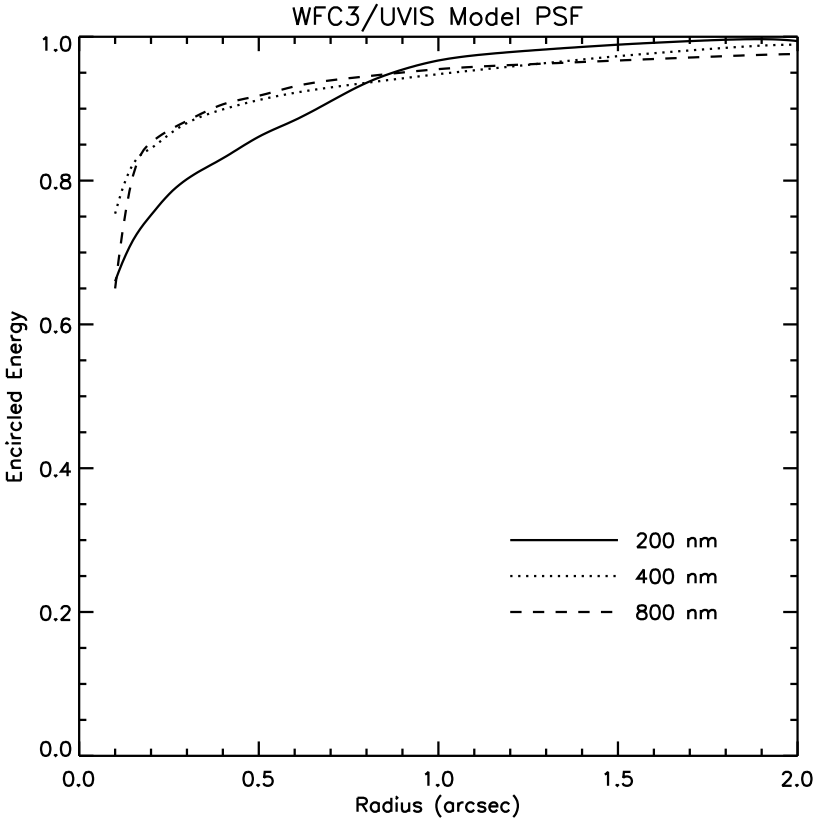

Table 6.8: WFC3/UVIS PSF Encircled Energy Fraction vs. Aperture radius (arcsec).

Aperture radius (arcsec)	Wavelength (nm)									
	200	300	400	500	600	700	800	900	1000	1100
0.10	0.660	0.739	0.754	0.745	0.720	0.687	0.650	0.623	0.612	0.605
0.15	0.717	0.793	0.823	0.834	0.832	0.823	0.807	0.778	0.742	0.699
0.20	0.752	0.822	0.845	0.859	0.859	0.857	0.853	0.847	0.844	0.829
0.25	0.781	0.844	0.864	0.875	0.877	0.874	0.870	0.867	0.868	0.864
0.30	0.802	0.858	0.880	0.888	0.890	0.889	0.883	0.879	0.879	0.876
0.40	0.831	0.880	0.899	0.911	0.910	0.907	0.906	0.904	0.900	0.894
0.50	0.861	0.894	0.912	0.923	0.925	0.923	0.918	0.915	0.918	0.917
0.60	0.884	0.906	0.922	0.932	0.934	0.933	0.931	0.927	0.927	0.923
0.80	0.936	0.928	0.936	0.944	0.947	0.946	0.945	0.942	0.944	0.942
1.00	0.967	0.946	0.948	0.954	0.955	0.955	0.955	0.952	0.955	0.952
1.50	0.989	0.984	0.973	0.970	0.970	0.969	0.967	0.966	0.970	0.968
2.00	0.994	0.992	0.989	0.985	0.980	0.977	0.976	0.975	0.978	0.976

Table 6.9: WFC3/UVIS PSF Ensquared Energy Fraction vs. Aperture size (pixels), where the target is centered on the aperture. Row 1 indicates the maximal (PSF centered on the pixel) peak pixel fraction, useful for determining the exposure time at which saturation may occur.

Aperture size (pixels)	Wavelength (nm)									
	200	300	400	500	600	700	800	900	1000	1100
1×1	0.126	0.165	0.184	0.188	0.180	0.166	0.149	0.132	0.117	0.103
2×2[1]	0.354	0.412	0.431	0.437	0.434	0.423	0.405	0.380	0.352	0.322
3×3	0.546	0.610	0.613	0.600	0.578	0.563	0.553	0.543	0.531	0.510
5×5	0.681	0.760	0.784	0.783	0.767	0.738	0.699	0.662	0.638	0.624
7×7	0.725	0.800	0.827	0.839	0.839	0.832	0.821	0.802	0.775	0.737
9×9	0.757	0.826	0.849	0.861	0.861	0.860	0.856	0.851	0.849	0.838
11×11	0.782	0.845	0.866	0.876	0.878	0.874	0.870	0.869	0.869	0.864
13×13	0.801	0.858	0.880	0.889	0.890	0.888	0.883	0.878	0.880	0.877
15×15	0.816	0.868	0.891	0.900	0.900	0.899	0.895	0.889	0.888	0.884
17×17	0.830	0.879	0.898	0.909	0.909	0.907	0.905	0.900	0.898	0.892
19×19	0.843	0.887	0.905	0.916	0.916	0.914	0.911	0.909	0.909	0.902
21×21	0.857	0.893	0.910	0.922	0.923	0.920	0.917	0.914	0.917	0.911
23×23	0.868	0.899	0.916	0.926	0.928	0.926	0.923	0.919	0.921	0.919
25×25	0.879	0.905	0.920	0.930	0.932	0.931	0.928	0.924	0.926	0.923
51×51	0.978	0.964	0.957	0.962	0.962	0.961	0.961	0.959	0.962	0.960
101×101	0.996	0.994	0.992	0.992	0.987	0.984	0.982	0.980	0.983	0.981

1. For the 2×2 aperture, the target is located at the center of the array.

6.6.3 Other PSF Behavior and Characteristics

Temporal Dependence of the PSF: *HST* Breathing

Short term variations in the focus of *HST* occur and affect all of the data obtained from all of the instruments on *HST*. A variety of terms, "OTA breathing", "*HST* breathing", "focus breathing", or simply "breathing" all refer to the same physical behavior. The focus changes are attributed to the contraction/expansion of the OTA due to thermal variations during an orbital period. Thermally induced *HST* focus variations also depend on the thermal history of the telescope. For example, after a telescope slew, the telescope temperature variation exhibits the regular orbital component plus a component associated with the change in telescope attitude. The focus changes due to telescope attitude are complicated functions of Sun angle and telescope roll. More information and models can be found on the "*HST* Thermal Focus Modeling" Web site at:

http://www.stsci.edu/hst/observatory/focus/thermal.html

For WFC3, breathing induces small temporal variations in the UVIS PSF. The variations of the UVIS PSF are expected to be as large as 8% at 200 nm, 3% at 400 nm and 0.3% at 800 nm, on typical timescales of one orbit. Some variation over the field of the PSF response to breathing is also expected, since the detector surface is not perfectly matched to the focal surface, and the optical design includes some field-dependent aberration.

Pixel Response Function

The point-spread function (PSF) is the distribution of light from a point source as spread over a number of pixels. Even with a very compact optical PSF, however, charge diffusion, or migration of charge from one pixel into adjacent neighbor pixels, can degrade the sharpness of a CCD PSF. The effect is usually described in terms of the pixel response function (PRF), which maps the response of the detector to light from a hypothetical very sharp PSF whose light all falls within an individual pixel. Observations using the integrated WFC3 instrument along with optical stimulus point-sources provided empirical PSFs for comparison with, and to provide constraints for, the models. Those models, which included an independent assessment of the low-order wavefront error, the pupil mask, and a reasonable estimate of the detector PRF, yield good agreement with the observed instrumental encircled-energy curves. The resulting best empirical fit to the pixel response convolution kernel is shown in Figure 6.12.

Figure 6.12: CCD Pixel Response functions at 250 nm (top) and 800 nm (bottom).

$$\begin{bmatrix} 0.023 & 0.105 & 0.023 \\ 0.105 & 0.488 & 0.105 \\ 0.023 & 0.105 & 0.023 \end{bmatrix}$$

$$\begin{bmatrix} 0.007 & 0.071 & 0.007 \\ 0.071 & 0.688 & 0.071 \\ 0.007 & 0.071 & 0.007 \end{bmatrix}$$

PSF Characteristics

The PSF of the UVIS channel was assessed during SMOV. As part of this assessment exposures of a field containing unsaturated data (highlighting the bright PSF core) were combined with highly saturated data (emphasizing the faint PSF wings). The results are illustrated in Figure 6.13, which shows the select portions of the composite image with a logarithmic stretch. No geometric distortion correction has been applied, so the images appear elongated along the diagonal, due to the 21 degree tilt of the detector to the chief ray. Although the target was chosen to be isolated, a number of field galaxies appear in the F625W image (right) but are absent in the F275W image; these galaxies are also seen in the IR channel images of the same target (Section 7.6.1). Some detector artifacts, including warm pixels and imperfectly removed cosmic ray hits are evident.

Figure 6.13: High dynamic range composite UVIS star images through F275W (left) and F625W (right) subtending ~20 arcsec on each side at different locations in the field. No distortion correction has been applied. Stretch is logarithmic from 1 to 10^6 e^-/pixel.

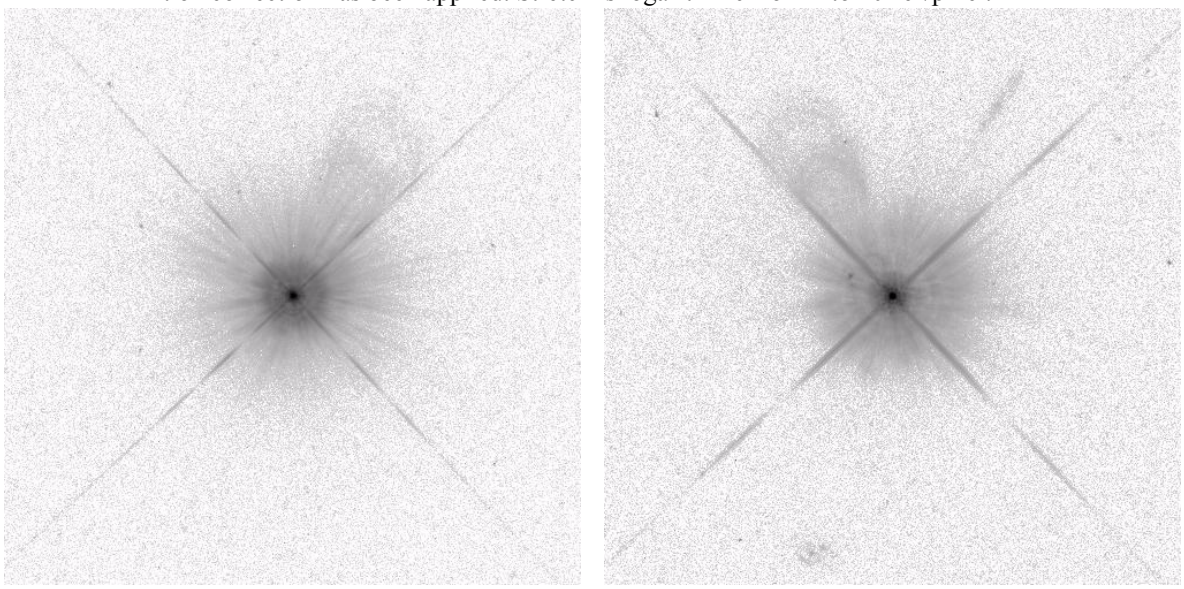

Two different types of "ghost" artifacts are visible in the images. As expected from the UVIS channel design, there are low-level ghosts due to reflections between the four surfaces of the two anti-reflection-coated detector windows: these are the sets of relatively large diameter, ring-shaped ghosts seen extending out at PA ~330° (left) and PA ~30° (right). Ghosts due to reflections from the CCD to the windows, as discussed above in Section 6.5.3, fall further from the PSF, along the diagonal from lower right to upper left of the field of view, and are not visible in these frames which image only subsections of the WFC3 field of view.

Also evident is a filter ghost, due to reflections between the surfaces of the F625W filter (right). In multi-substrate filters (a stack of two or more substrates bonded or laminated together with a layer of optical adhesive) filter ghosts appear as faint, point-like features, such as the ghost at PA ~65 degrees, radius 1.6 arcsec, in the F625W image, which contains much less than 0.1% of the stellar flux. In single-substrate or air-gap filters (the latter consisting of two substrates joined via thin spacers), filter ghosts appear as small extended shapes (typically rings), closer to the PSF centers than the window ghosts. For the F275W image in Figure 6.13 the filter ghost level is <0.1% and is not obvious. A small number of filters exhibit brighter ghosts and are discussed in detail in Section 6.5.3 and are tabulated in Table 6.6.

6.7 UVIS Exposure and Readout

6.7.1 Exposure Time

Exposure times in the UVIS channel are controlled by a rotating mechanical shutter blade (see Section 2.3.3). The time per UVIS exposure must be between 0.5 s and 3600 s, excluding 0.6 s, in steps of 0.1 s.[1] Pre-flight testing has verified that shutter exposure times deviate by less than 1% for exposure times of 0.5 s, as well as those greater than or equal to 1 s. For example, typical variations of 4 ms were measured in a set of 1 s exposures. For exposure times between 0.7 s and 0.9 s (inclusive), exposure-time deviations were measured to be 2.6% (see WFC3 ISR 2004-14). Additional analysis will take place during Cycle 17.

The shutter uniformity requirement specifies that any differences in exposure time across the field of view must be <0.01 s. Comparisons of long (30 s) and short (0.5 s) exposures taken during instrument-level ground tests have shown that the shutter provides a uniform exposure time across the field of view to ~0.004 s, easily meeting the requirement.

To allow for cosmic-ray removal during post-observation data processing, UVIS exposures can be split into multiple exposures. The Optional Parameter CR-SPLIT in the Phase II observing proposal can be used to equally divide the original exposure time into the specified number of subexposures (the default is 2, maximum of 8, subexposures). The exposure-splitting function may also be disabled by setting the CR-SPLIT parameter value to NO.

If CR-SPLIT is requested, the exposure time is first divided by the requested number of subexposures and the subexposure times are rounded down to the nearest multiple of 0.1 s. At the end of this process, if the resulting subexposure times are not legal values, the proposal software adjusts them so that they are allowed and reports those changes to the observer.

6.7.2 ACCUM Mode

"**ACCUM**" is the only observing mode for the UVIS channel. In ACCUM mode, the shutter is opened and photons strike the CCDs and generate charge, which is accumulated until the shutter is closed at the end of the requested exposure time and the charge is read out. During the readout, the analog-to-digital (A-to-D) converter translates the charge into data numbers (DN) via the gain setting. There are four gains (1.0, 1.5, 2.0, and 4.0 e^-/DN) that are possible in principle. However, the only gain setting offered to observers is the default value of 1.5 e^-/DN.

1. Under normal shutter operations, the 0.5 s exposure would not provide a sufficiently uniform exposure level. However, it has been implemented through a special "continuous sweep" operation, where the shutter disk moves smoothly through 180°, from one closed position to the next, thus meeting the uniformity requirement. All exposures longer than 0.5 s are obtained via pairs of closed-to-open and open-to-closed commands.

A full detector readout of both UVIS chips takes 96 s. The image contains all the exposed pixels from each CCD (2 times 2051×4096), as well as a variety of overscan pixels, described in more detail later in this section. Shorter readout times are possible by using smaller subarray readout sizes, as discussed in more detail in Section 6.4.4.

Each of the two CCD chips contains two on-chip amplifiers used for reading out. The fastest—and default—way to read out the entire detector, at full spatial resolution, is to use all four amplifiers simultaneously. Other full-detector readout modes are possible but take more time and involve more charge-transfer shifts. For example, two amplifier full frame readout takes more than twice as long as a four-amplifier readout (~193 sec vs. 96 sec). Non-default readout modes are not offered to General Observers.

Subarray frames, unlike full detector frames, are read out by a single amplifier (the closest amplifier to the subarray center).

Overscan Regions

The UVIS CCD detectors each have 4096×2051 pixels that are exposed to light. In addition, both chips have 25 extra columns at both ends that are not exposed to light; these 25 columns are *physical* overscan pixels. Moreover, during readout of the chips, extra pixels can be clocked in order to create *virtual* overscan pixels.

The location of the overscan regions in a raw image varies, depending upon the type of readout that is performed. The overscan regions are used to monitor the instrument, and are needed to measure the bias level. The bias level is subtracted from the raw image, normally through the BLEVCORR step in the WFC3 calibration pipeline (see Section E.1 and Section 3.2.2 of the *WFC3 Data Handbook*).

Figure 6.14 shows the format of a raw image obtained with full-chip unbinned four-amplifier readout. The raw image has 25 columns of physical overscan pixels and two areas of virtual overscan: 60 columns of serial overscan in the center of each row and 38 rows (19 per chip) of parallel overscan next to the inter-chip gap. The serial physical overscan pixels are also known as the serial prescan, or leading-edge, overscan; the serial virtual overscan pixels are also called the trailing-edge pixels.

Figure 6.14: Format of a Raw Full-Chip WFC3 UVIS Image.

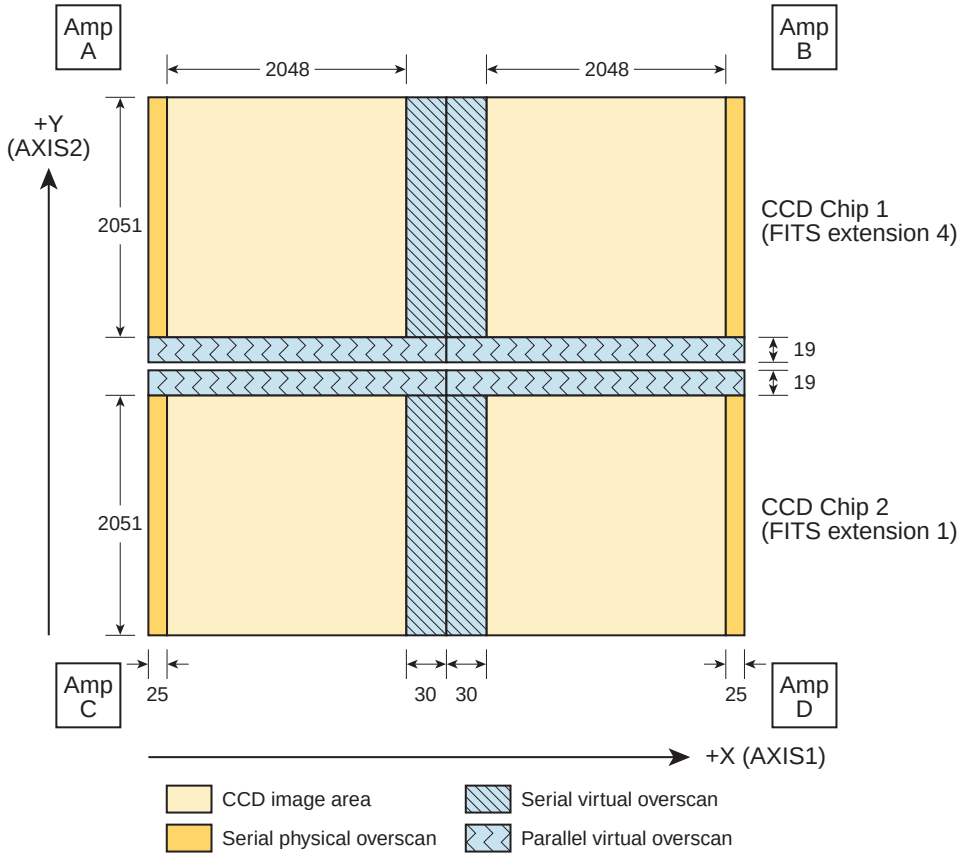

As Figure 6.14 illustrates, a raw image resulting from a default full-frame, four-amplifier readout of the UVIS channel contains 110 columns of serial overscan (25×2 physical and 30×2 virtual) plus 38 rows of parallel virtual overscan, which combined with the 4096×2051 science pixels, result in a raw image size of 4206×4140 pixels. Other types of readouts have differing amounts and/or locations of overscan. Subarrays contain no virtual overscan of either type (serial or parallel), although they can contain physical overscan if a subarray is chosen that overlaps the physical overscan region. Subarrays containing physical overscan data are listed in Table 6.1. In general, it is desirable to include some physical overscan in observations using subarrays for accurate bias level subtraction.

Exposures taken with on-chip binning are complicated by the need to truncate "odd" pixels and to treat each half of the chip's row separately. Also, due to the odd number of some overscan pixels, the boundary between the data and overscan pixels of a binned exposure can contain binned pixels resulting from a combination of both data and overscan pixels. A 2×2 binned frame readout, for example, contains 2070 rows × 2102 columns. That is, each binned chip readout has 1035 rows (9 binned virtual overscan + 1 combined data/virtual parallel overscan + 1025 data) and each binned chip readout contains 2102 columns (12 physical overscan + 1 combined data/overscan + 1023 columns of data + 1 combined data/virtual overscan column + 14 virtual overscan pixels for each of the two amps in a chip). A 3×3 binned image

contains 1402×1380 pixels (8 overscan + 1 combined overscan/data + 682 data + 10 overscan columns in each amplifier of each chip and 6 overscan + 1 combined overscan/data + 688 data rows in each chip).

For completeness, we mention here that WFC3 can also be commanded to take EPER (extended pixel edge response) readouts. This capability is intended for calibration/engineering purposes only. The EPER images are a way to measure and monitor charge-transfer inefficiency (CTI) effects using internal images, rather than external, pointed observations that would take *HST* observing time away from science observations. The EPER frame starts with an internal tungsten lamp flat field; any CTI present causes a fraction of charge from that flat field to be captured temporarily in traps. As the frame is read out, the trapped charge escapes and can appear in the overscan regions as an exponential tail of deferred charge. The EPER readout includes significantly larger areas of overscan so that the full extent of the exponential tail can be measured, ideally down to where it becomes indistinguishable from the nominal noise level of the detector. That is, the EPER image allows direct measurement of the charge losses during the readout since nearly all the lost electrons are expected to appear in the exponential tail.

6.8 UVIS Sensitivity

6.8.1 Limiting Magnitudes

Table 6.10 presents the predicted limiting-magnitude performance of WFC3 and compares it with that of the ACS camera. The calculations are based on optimal extraction of a point source. The limiting ABMAG at a S/N of 10 was calculated for a 1-hour and a 10-hour exposure. The WFC3 filters used are listed in column 2; for ACS, the most comparable wide-band filter was used and its name is given in column 3. The ACS/HRC camera was assumed for the NUV and *U*-band comparison, and ACS/WFC was assumed for *B*, *V*, and *I*.

Table 6.10: Limiting-magnitude performance of WFC3 compared with that of ACS based on on-orbit sensitivity from SMOV4. The table provides limiting ABMAGs at a S/N of 10 for the indicated WFC3 filters and for ACS with its most similar filters. WFC3 UVIS comparisons are with the ACS HRC channel (NUV and *U*) and the ACS WFC channel (*B*,*V*,*I*).

Band	Filter		Limiting magnitude in 1 hr		Limiting magnitude in 10 hrs	
	WFC3	ACS	WFC3	ACS	WFC3	ACS
NUV	F225W	F220W (HRC)	26.7	25.9	28.1	27.2
U	F336W	F330W (HRC)	27.3	26.4	28.7	27.8
B	F438W	F435W (WFC)	27.3	27.6	28.7	28.9
V	F606W	F606W (WFC)	27.9	27.9	29.2	29.2
I	F814W	F814W (WFC)	27.1	27.4	28.4	28.7

Chapter 9 gives further details on estimation of exposure times. More accurate estimates require use of the WFC3 Exposure Time Calculator (ETC), available online.

6.9 Other Considerations for UVIS Imaging

6.9.1 Gain and Full-well Saturation

The dynamic range of a detector is determined not only by the full-well capacity of the device but also by the analog-to-digital converter (ADC) and gain setting that are used during readout to convert the accumulated charge into data numbers (DN). The WFC3 UVIS channel detectors use 16-bit ADCs, so that the maximum DN that can be read out is 2^{16} - 1 or 65,535. If the charge accumulated in a given pixel exceeds the ADC maximum, any additional charge does not result in any further increase in the DN and may, in cases of extreme saturation, result in values of zero. The gain setting provides a mechanism for extending the scale to a larger maximum number of electrons by assigning a single DN to more than 1 electron. At the standard UVIS gain of ~1.6 e^-/DN, saturation always occurs on chip, not in the ADC, unless binning is used, in which case saturation occurs in the ADC and photometric information is therefore lost.

The ETC uses a representative full-well value of 70,000 e^- to determine saturation; users wishing to strictly avoid this occurrence should allow a buffer of at least 10% below this. During SMOV4, the on-orbit gain in the CCDs was measured to be ~1.62 e^-/DN, approximately 3% higher than the previously assumed value of 1.57 e^-/DN (see WFC3 ISR 2009-29). Thus, the detector full well of 63,000 to 72,000 e^- corresponds to DN values of 38,900 to 44,500. ADC saturation corresponds to 106,167 e^-.

A Cycle 17 calibration program will measure UVIS linearity on-orbit. See http://www.stsci.edu/hst/wfc3/ins_performance/linearity/

Once the charge exceeds the pixel full-well level, it can escape that pixel and spread into adjacent vertical pixels; as the signal continues to accumulate, these adjacent pixels themselves can accumulate charge up through the ADC/gain level to full-well and leak into further adjacent vertical pixels, resulting in the "blooming," or charge overflow, effect. The MPP (multi-phased pinned) operation of the detectors, used to minimize surface dark current, constrains the blooming along the detector columns, so the blooming is only vertical and not horizontal. Photometric information well beyond saturation can be recovered by defining a special aperture that encompasses all of the pixels that have been bled into. A forthcoming ISR will present an algorithm that needs to be invoked for UVIS1 to regain full linearity beyond saturation to near 1%. UVIS2 is linear with simple summation over the saturated pixels.

Whenever the pixel full-well capacity is exceeded, the linearity and dark current can be adversely affected (the large number of photoelectrons effectively fill all trap states), and there can be after-effects such as blooming and persistence artifacts. Residual or persistence effects have not been observed in orbit, either during SMOV4 or since science observations commenced. Long timescale residual images are not expected since the WFC3 CCDs are backside-illuminated, so the substrate layer (which can cause bulk residual images) was removed.

6.9.2 Cosmic Rays and Hot Pixels

The cosmic-ray fluxes for WFC3 UVIS are comparable to the levels seen in ACS, STIS CCD, and WFPC2. As with these previous *HST* instruments, typical WFC3 imaging observations need to be split or dithered to obtain adequate cosmic-ray removal (see Section 5.4.10).

The WFC3 CCDs have a small number of pixels with higher than normal dark current. On orbit the number of hot pixels increases with time due to radiation damage, but can be mitigated by annealing. For WFC3, we have chosen a limit of 54 e^-/hr (0.015 e^-/s/pix) as a threshold above which we consider a pixel to be "hot," based on the tail of the dark current distribution as well as a visual examination of 900 sec dark frames taken during Cycle17. Figure 6.15 shows a histogram of CR-free pixels from 900 sec darks taken at three different times after the August 2009 anneal procedure: immediately following the procedure (red line), about 12 days later (green line) and about 30 days later (blue line). The increase in hot pixels due to on-orbit radiation damage is apparent, but the anneal procedures have been found to fix 80-90% of the hot pixels which accumulate over time. The hot pixel cutoff is shown

with a vertical line at 54 e^-/hr; at this threshold, the growth rate for WFC3 hot pixels is ~1000 pix/day.

Figure 6.15: Hot pixel histogram from CR-free pixels following an anneal procedure by 0 days (red), 12 days (green), and 30 days (blue).

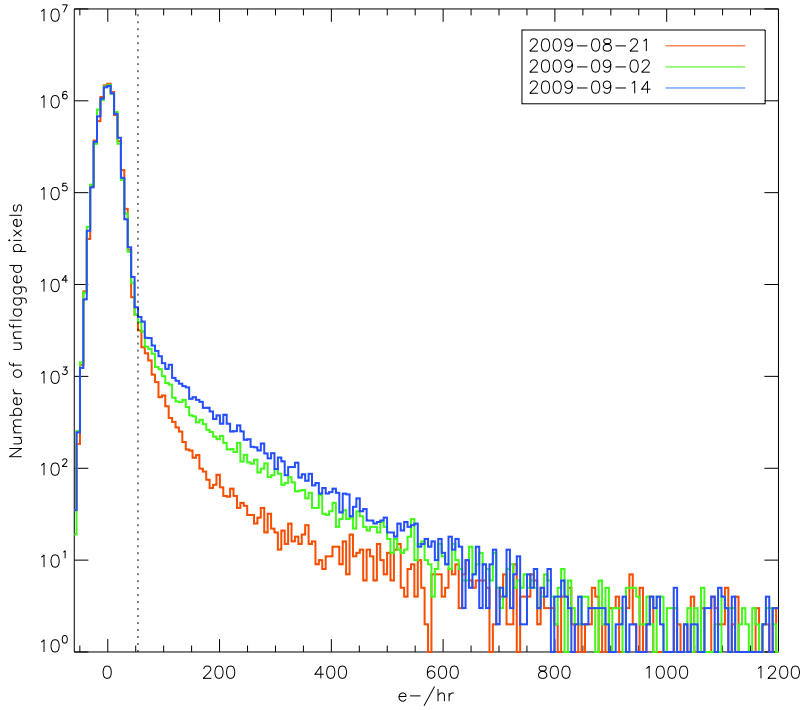

Due to radiation damage from the on-orbit environment, the number of hot pixels increases as a function of date and decreases after an anneal procedure (when the detector is warmed to fix hot pixels). Figure 6.16 shows the number of hot pixels as a function of time since the installation of WFC3 on *HST*, where the red vertical lines indicate the dates of the anneal procedures, the gold vertical lines represent the SIC&DH failures, when WFC3 was safed (prior to Oct. 2009, WFC3 safings warmed the chips to 20°C), and the brown vertical line is the switch between SMOV darks (1800 sec) and Cycle 17 darks (900 sec). Early on-orbit experience shows that about 90% of the hot pixels are "fixed" during an anneal procedure, though the fraction varies slightly from procedure to procedure. For ACS the hot pixel removal rate is ~82% for WFC and ~86% for HRC, where "hot" is classified as those pixels with dark rate 0.08e^-/pix/sec, or 288 e^-/pix/hr (see Section 4.3.5 of *ACS Instrument Handbook*).

Figure 6.16: Hot pixel growth between anneal taken during SMOV. Hot pixel anneal rate is >70%.

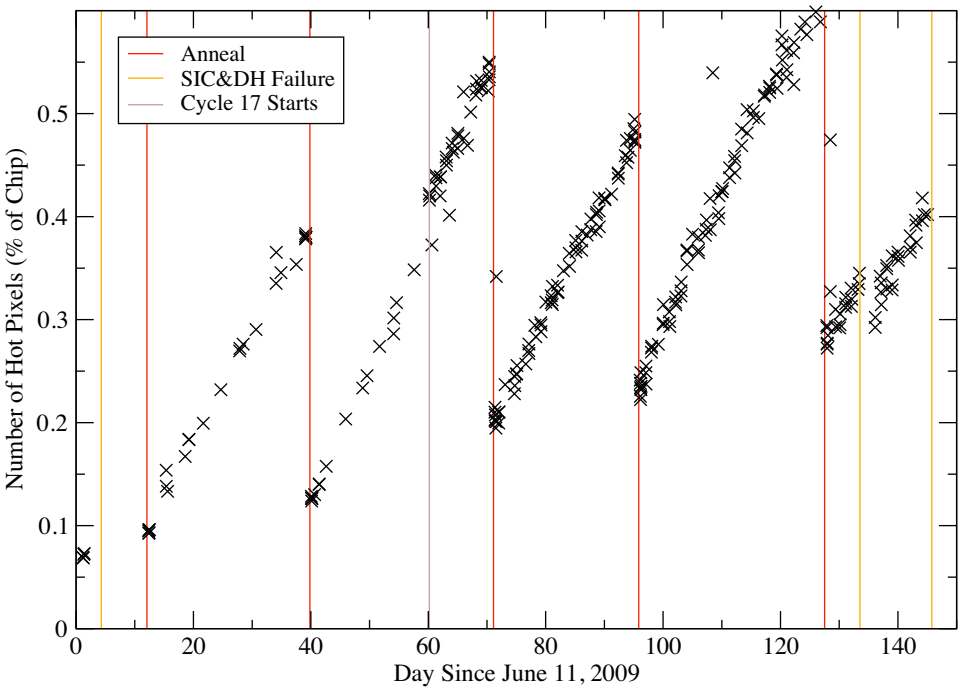

Radiation damage produces an overall higher dark current as well as an increase in the number of individual hot pixels. Based on a fit to the Cycle 17 900 sec dark frames, the median dark current (excluding hot pixels) is increasing by ~2 e^-/hr/pix/year. The number of permanent hot pixels, i.e., pixels that the anneals are unable to fix, is growing by 0.05-0.1% per month.

6.9.3 Charge-Transfer Efficiency

Ground-testing measurements of the charge-transfer efficiency (CTE) using the Extended Pixel Edge Response (EPER) technique for the WFC3 UVIS flight detector showed that CTE is 0.999999 for each CCD amplifier. Figure 6.17, from WFC3 ISR 2009-10, shows CTE as a function of signal level on the ground. But CTE will inevitably decline over time as on-orbit radiation damage creates charge traps in the detectors. The UVIS CCDs are large-format devices, similar in size to those in the ACS WFC, and thus require significantly more charge-shifting steps during readout compared to smaller devices like the STIS and WFPC2 CCDs. As a result, effects due to radiation-induced charge-transfer inefficiencies will be encountered earlier than for the smaller-format detectors.

Figure 6.17: UVIS CTE as inferred from EPER measurements. Red curve is the best power-law-fit.

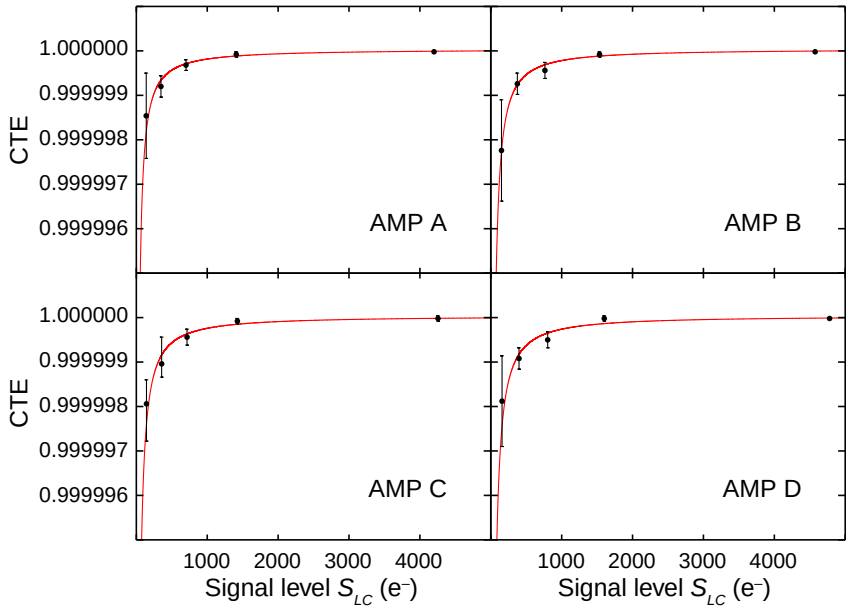

CTE losses can be mitigated by filling the charge traps; in WFC3, this can be done using a charge-injection capability, which inserts charge electronically. Charge injection is preferable to the traditional pre- or post-flash techniques that use light, because the associated noise is much lower. In ground tests of the WFC3 CCDs, the noise due to charge-injection levels of ~10,000 e^- was measured to be 12–13 e^-, much lower than the ~100 e^- Poissonian noise that would characterize a similar signal level achieved by exposure to light.

For Cycles 17 and 18, charge injection is not needed, and thus is unavailable to observers. In later cycles, observers will be provided the option to activate the charge-injection capability via an Optional Parameter for individual exposures in the Phase II observing proposal.

6.9.4 Image Persistence

No significant image-persistence effects following over-exposure were observed in instrument-level ground test or on-orbit data using the UVIS CCDs, as expected for back-illuminated devices.

6.9.5 Shutter-Induced Vibration

Shutter-induced vibration, or shutter jitter, affects only very short exposures. Shutter jitter causes slight blurring in image data and is not to be confused with exposure time deviation. Exposure time deviation is discussed in Section 6.7.1, and the UVIS shutter mechanism is described in Section 2.3.3.

The image quality analysis carried out during the third thermal-vacuum campaign revealed that vibrations of the UVIS shutter caused changes in the width and in the central pixel flux of point sources in short exposures. The analysis, and a schematic of the UVIS shutter mechanism, are given in WFC3 ISR 2008-44.

To test on-orbit performance, observations of the calibration standard star GD153 were acquired during SMOV. These confirmed that only the shortest exposures (0.5–3.0 sec) were significantly affected by the shutter vibrations. Furthermore, only side B of the shutter blade degrades the PSF. There is no noticeable degradation in exposures taken with side A of the shutter blade. Because the shutter blade always rotates in one direction, a series of short exposures show an odd/even effect, with exposures acquired with the shutter side B being blurred and shutter side A exposures being unaffected.

For the shortest exposures (0.5 sec), shutter vibrations produce a side-B PSF that is ~15% broader than the side-A PSF. At 1.0 sec, the difference in FWHM between the two shutter sides drops to 7%, and it is less then 1% for 10 sec exposure times. For images taken with side A shutter operation, no significant PSF width changes were seen between 0.5 sec and 350 sec exposures. No flux is lost due to shutter jitter, so the effect can be mitigated in point-source photometry by using big enough aperture (r>5 pixel) to measure the flux. The analysis of the shutter jitter effect using SMOV data is fully described in WFC3 ISR 2009-20.

6.9.6 Droplets

The outer window is contaminated, seemingly by a mineral residue introduced during acceptance testing of WFC3. These contamination features have been dubbed "droplets" due to their appearance at the time of discovery. In external flat-field images, these features have a strength of approximately ±0.5%. The droplets cause changes in PSF profile, such that flux in the core is redistributed to the near wings. In large-aperture (10 pixel radius) photometry of point sources stepped across a strong window feature, the feature does not significantly increase the photometric scatter. For small-aperture (3 pixel radius) photometry of point sources stepped across a strong window feature, the photometric scatter increases from ~0.5% to ~1%. Quadrant A has the lowest density of features. There are approximately 50, 129, 108, and 179 droplets in quadrants A, B, C, and D, respectively.

The best strategy for mitigating the flat-field features is an appropriate dither pattern. Although there are positions within a flat-field feature that cause systematic errors at the level of a few percent in point source photometry, other positions separated by 20 to 40 pixels show much smaller errors, suggesting that dithers on this scale would be sufficient for most photometric programs. To ensure a point source does not hit a particular feature twice requires larger dithers of approximately 100 pixels, which is the typical diameter of these features.

WFC3 2008-10 describes the characterization of the droplets and their photometric effects based on ground testing, and WFC3 ISR 2009-27 reports that about 30% of droplet positions have shifted by about 1 pixel after launch, but have been stable since then.

6.9.7 Optical Anomalies

In rare cases, the optical system causes stray light from sources outside the CCD FOV to be scattered into images.

Examples of stray light and other optical anomalies may be found on the WFC3 Web site:
http://www.stsci.edu/hst/wfc3/ins_performance/stray_light/

6.10 UVIS Observing Strategies

6.10.1 Dithering Strategies

For imaging programs, STScI generally recommends that observers employ dithering patterns. Dithering refers to the procedure of moving the telescope by pre-determined amounts between individual exposures on a target. The resulting images are subsequently combined via post-observation processing techniques using software such as *MultiDrizzle* (see the *MultiDrizzle Handbook*).

Use of dithering can provide improved sampling of the point spread function (PSF) and better correction of undesirable artifacts in the images (e.g., hot pixels, cosmic rays, the UVIS channel's inter-chip gap, and the UVIS "droplets"). Cosmic ray removal is more effective if more than 2 images are obtained, using CR-SPLIT exposures and/or dithers, especially for exposure times greater than 1000s. A sequence of offsets of a few pixels plus a fractional pixel in each coordinate is generally used to simultaneously remove hot pixels and cosmic rays and to sample the PSF. A larger offset along the image Y axis is needed to fill in the interchip gap in full-frame images (the WFC3-UVIS-MOS-DITH-LINE pattern uses a conservative step size of 2.4 arcsec). To ensure the best accuracy consider dithering to compensate for droplets (Section 6.9.6).

Larger offsets, up to sizes approaching the detector's field of view, can also be used to create mosaics. However, as a result of geometric distortion (Appendix B), some objects shift by an integer number of rows (or columns), while others shift by an integer plus some fraction of a pixel. The PSF is not resampled in that dimension in the former case, but is resampled in the latter case. Where the exposures overlap, the PSF is thus better sampled for some objects than for others. If PSF sampling is important, a combination of mosaic steps and small dither steps should therefore be used. Note that, in practice, mosaic steps must be contained within a diameter ~130 arcsec or less (depending on the availability of guide stars in the region) to use the same guide stars for all exposures. The rms pointing repeatability is significantly less accurate if different guide stars are used for some exposures (see Section 4.1 of the *MultiDrizzle Handbook*).

The set of Pattern Parameters in the observing proposal provides a convenient means for specifying the desired dither pattern of offsets. The pre-defined mosaic and dither patterns that have been implemented in APT to meet many of the needs outlined above are described in detail in the Phase II Proposal Instructions. The WFC3 patterns in effect in APT at the time of publication of this Handbook are summarized in Appendix C. Observers can define their own patters to tailor them to the amount of allocated observing time and the desired science goals of the program. Alternatively, they can use POSTARGs to implement dither steps (Section 6.4.3), but the exposures will then not be automatically associated and combined in the OPUS pipeline.

6.10.2 Parallel Observations

While the design of WFC3 precludes the simultaneous use of both the UVIS and IR channel, it is possible to use one or more of the other *HST* instruments in parallel with WFC3. Since each instrument covers a different location in the *HST* focal plane (see Figure 2.2), parallel observations typically sample an area of sky several arc minutes away from the WFC3 target. For extended targets such as nearby galaxies, parallel observations may be able to sample adjacent regions of the primary target. In other cases, the parallel observations may look at essentially random areas of sky.

For processing and scheduling purposes, *HST* parallel observations are divided into two groups: coordinated and pure.

A **coordinated parallel** is an observation directly related to (i.e., coordinated with) a specific primary observation, such as in the extended galaxy example above. A **pure parallel** is an observation typically unrelated to the primary observation, for example, parallel imaging scheduled during long spectroscopic observations. The primary restriction on parallel observations, both coordinated and pure, is that they must not interfere with the primary observations: they may not cause the primary observations to be shortened; and they must not cause the stored-command capacity and data-volume limits to be exceeded. The proposal software (APT) enforces these rules and notifies the observer when a specified parallel is not permitted.

In order to prolong the life of the *HST* transmitters, the number of parallels acquired during each proposal cycle is limited. Proposers must provide clear and strong justification in order to be granted parallel observing time. Please refer to the *HST Call for Proposals* for current policies and procedures concerning parallels.

CHAPTER 7:

IR Imaging with WFC3

In this chapter . . .

7.1 WFC3 IR Imaging

As described in Chapter 2, the optical design of WFC3 features two independent channels, each with its own separate optics, filters and grisms, and detectors. The **UVIS channel** is sensitive to UV and optical wavelengths (200-1000 nm), and the **IR channel** is sensitive to near-infrared wavelengths (800-1700 nm).

Only a single channel, either UVIS or IR, can be used at any one time. Thus they cannot be used in parallel, but they can be used sequentially.

A schematic diagram showing the locations of the fields of view of the UVIS and IR detectors in the *HST* focal plane is given in Figure 2.2.

This chapter describes the capabilities of the IR channel. The previous chapter, Chapter 6, describes the UVIS channel. Detailed characteristics of the detectors used in both channels are given in Chapter 5 and summarized in Table 5.1.

7.2 Specifying an IR Observation

In the *HST* proposal system, the parameters for an IR observation available to General Observers are:

1. **Configuration**: always **WFC3/IR.**
2. **Mode**: always **MULTIACCUM.**
3. **Aperture**: must be specified; **IR** selects the full detector area; for others see Section 7.4.5.
4. **Spectral Element**: must be specified for each exposure; see Section 7.5.
5. **Optional Parameters**: in the IR channel **SAMPSEQ** specifies a predefined sequence of times at which the detector is read out, and **NSAMP** specifies the total number of readouts (and thus the total exposure time); see Section 7.7. **SAMPSEQ** and **NSAMP** are required for IR observations.
6. **Special Requirements**: see the Phase II Proposal Instructions for details of Special Requirements related to the timing of visits and for dithering and mosaicking. Also available is the exposure-level Special Requirement **POS TARG** for offsetting the target from the default reference point of the aperture (see Section 7.4.3 for a discussion of the IR channel coordinate system).
7. **Number of Iterations and Time per Exposure**: in cases where two or more identical exposures are desired, the Number of Iterations may be set to 2 or more. In the IR channel, the Time per Exposure is fixed by the combination of **SAMPSEQ** and **NSAMP** (see item 5 above) and thus is not specified separately. Through various combinations it is possible to select times per exposure ranging from 2.93 to 2756 s (for readouts of the full detector array; considerably shorter exposures are possible using subarrays).

7.3 IR Channel Characteristics

The WFC3 IR channel has been optimized for observing over the wavelength range 800-1700 nm. All the IR reflective optics (except for the WFC3 pick-off mirror) are coated with a silver layer for maximum IR throughput.

A schematic mechanical diagram showing both channels of WFC3 is given in Figure 2.1. Components of the IR channel include: the Channel Select Mechanism (CSM), which directs on-axis light from the *HST* OTA to the IR channel; a flat folding mirror; a two-mirror mechanism for providing focus and alignment adjustments; the Refractive Corrector Plate (RCP), which applies the spherical-aberration correction; the IR filter wheel (FSM or Filter Selection Mechanism); and finally the HgCdTe IR detector package.

The WFC3 IR detector is a HgCdTe 1024×1024 array, with 18 micron pixels, bonded to a silicon multiplexer, with 1014×1014 pixels sensitive to incoming light. It is a direct descendant of the NICMOS 256×256 and Hawaii-1 1024×1024 arrays (more details on the detector are given in Chapter 5).

7.4 IR Field Geometry

7.4.1 Field of View and Pixel Size

The inner 1014×1014 pixels of the IR detector are exposed to incoming light. There are no gaps in the field (such as the gap between the two CCDs in the UVIS channel), or mechanical occultations (such as the coronagraphic spots in NICMOS camera 2).

The IR focal plane is tilted by ~22° with respect to the incoming beam. Thus the field of view as projected onto the sky is rectangular, with an aspect ratio of ~0.90. The pixels projected onto the sky are also rectangular, covering approximately 0.135×0.121 arcsec, with the shape varying slightly across the field. The field of view on the sky is 136×123 arcsec, or 4.65 arcmin^2.

7.4.2 Geometric Distortion

In addition to the rectangular field shape described above, the optical design of the IR channel also produces appreciable geometric distortion. Geometric distortions in both channels are discussed in more detail in Appendix B.

Distortion must be taken into account when exposures are flat-fielded, photometrically calibrated, used for astrometric measurements, or combined with other dithered exposures. The *MultiDrizzle* software appropriately carries out those operations using Calibration Database distortion polynomials (IDCTAB) and pixel area correction tables (PAM).

A pixel area map and coefficients for 4th-order polynomial coordinate transformations are available on the WFC3 Web site:
http://www.stsci.edu/hst/wfc3/pam/pixel_area_maps
http://www.stsci.edu/hst/wfc3/idctab_lbn

7.4.3 Coordinate Systems

Like the CCD, the IR channel requires multiple coordinate reference frames, each relevant for a specific goal. Readers may also wish to refer to Section 6.4.3, which

describes the coordinate systems for the UVIS channel. The coordinate systems used for the IR channel are illustrated in Figure 7.1 and are the following:

- **FITS image-based system** (AXIS1, AXIS2; units of pixels)
- **Proposal POS TARG system** (X-POSTARG, Y-POSTARG; units of arcsec)
- ***HST*-based system** (V2, V3 or U2, U3; units of arcsec)

Figure 7.1: WFC3 IR detector coordinates.

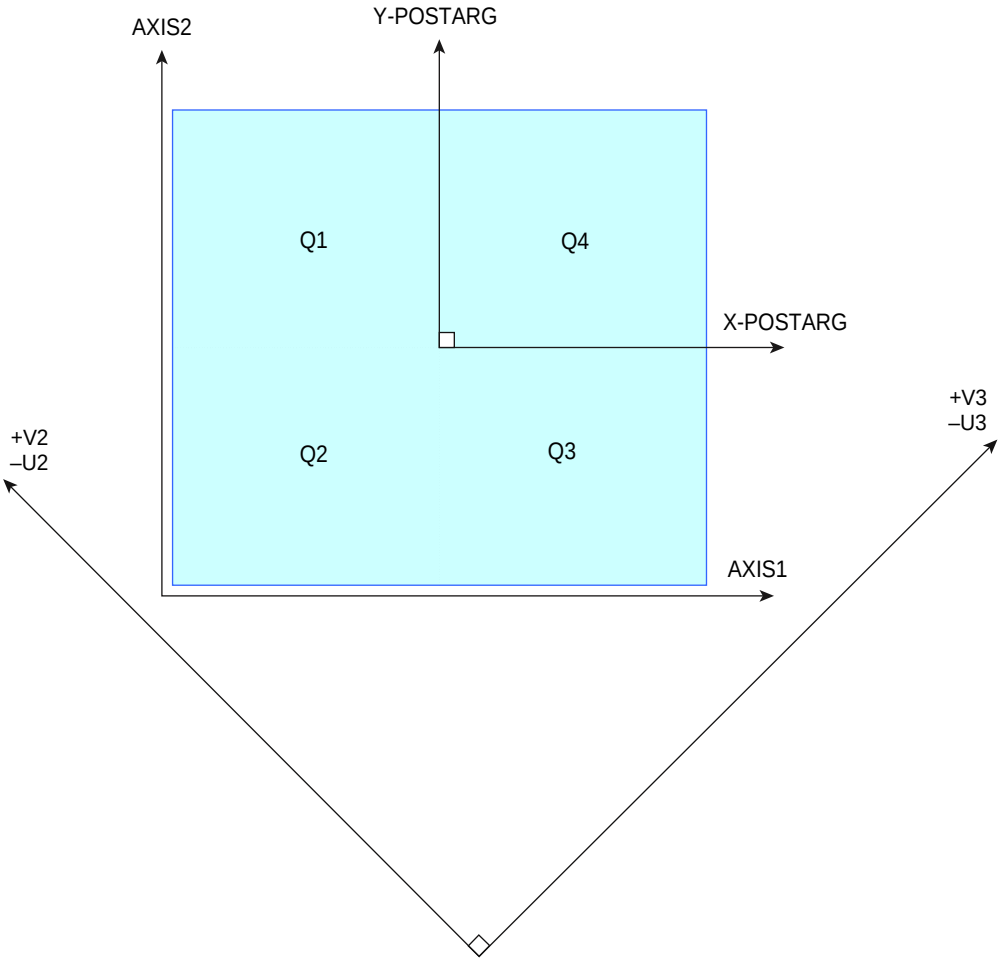

The **image-based coordinate system,** (AXIS1, AXIS2) in Figure 7.1, is a generic system used when an image is displayed on a computer screen. Here the origin of coordinates is at the lower left of the screen, the X axis increases to the right, and the Y axis to the top of the screen. Coordinates are expressed in pixel units. This system is used primarily by the generic conversion pipeline software, which creates science FITS files from the data telemetry coming from the telescope.

The **POS TARG reference frame**, (X-POSTARG, Y-POSTARG), is orthogonal on the sky, in units of arcseconds. It can be used to specify target placement at an offset location within the field of view, or for dithering or mosaicking purposes. In the IR channel, the POS TARG reference frame is designed to be virtually co-linear with the

AXIS reference frame, and it has its center located at the center of the chosen IR aperture. The transformation between the undistorted POS TARG (arcsec) frame and AXIS frame (pixels) contains non-linear distortion coefficients. For the IR detector, the POS TARG axes are almost exactly parallel to the detector edges. Note, however, that the IR X,Y POS TARG axes are not parallel to the UVIS X,Y POS TARG axes; the former are rotated a few degrees counterclockwise with respect to the latter.

The ***HST*-based**, or vehicle (V2, V3), system is an orthogonal reference frame tied to the telescope and is used operationally for alignment, pointing, and slewing purposes. The V1 axis lies along the optical axis while V2,V3 run parallel and perpendicular, respectively, to the solar-array rotation axis (see Figure 2.2). Note that the edges of the IR detector are rotated by approximately 45° with respect to the V2, V3 axes. Because WFC3 is on-axis, the origin of the V2,V3 system lies near the center of the WFC3 field of view. However, the V2,V3 coordinate axes have been shifted for clarity in Figure 7.1.

HST observers may be more familiar with the U2,U3 coordinate system than V2,V3; for example, the specification of the ORIENT angle Special Requirement in APT uses the position angle of the U3 axis. The U2,U3 coordinates are defined as U2 = –V2 and U3 = –V3, and are marked in Figure 7.1 as well.

7.4.4 Subarrays

In addition to obtaining standard full-field images, users can choose to read out smaller portions of the detector, called subarrays. Subarrays are useful to achieve reduced data volume, and/or to allow shorter exposure times. Shorter exposure times are especially important for the IR channel, because there is no physical shutter and the minimum integration time is limited by the time to read out the detector (2.9 s for full-frame readout). Very bright sources—including some of the primary "faint" IR photometric standards—may easily exceed the detector full-well of ~80,000 electrons in only a fraction of a second. Because the readout time is nearly proportional to the number of pixels read, subarrays can be used to reduce the effective integration time and make such observations feasible. This has been implemented in the IR channel with the RAPID readout mode, which in subarray mode runs at a speed nearly inversely proportional to the area of the subarray.

All of the IR subarrays are centered on the detector field of view. Four subarray sizes are supported, with pixel dimensions of 512×512, 256×256, 128×128, and 64×64. Note that the sizes of the subarrays refer to the actual active pixels, i.e., they do not include the reference pixels. (Of the 1024×1024 pixels of the WFC3 IR detector, only the inner 1014×1014 pixels are light-sensitive. The 5 rows and columns of pixels around the edge of the array use fixed capacitances to provide constant-voltage reference values.) The reference pixels, however, are still included in the output images, resulting in final images of 522×522, 266×266, 138×138, and 74×74 pixels. For subarray images, the reference pixels come from the same rows and columns of the subarray, with the 5×5 pixels at the subarray corners filled with the reference pixels at the corresponding corner of the detector (see Section 5.5 for details on reference pixels).

Beginning in Cycle 18, subarrays are available for grism spectroscopy, in addition to imaging. The actual selection of a subarray is accomplished by requesting one of the IR channel's subarry apertures, as described in Section 7.4.5.

Certain combinations of IR subarrays and sample sequences give rise to images containing an artifact. The artifact appears as a sudden jump in the overall background level of the image, with an amplitude of 3–5 DN. The jump occurs exactly at the vertical center of each quadrant of the image, such that the lower and upper quarters of the image have a different overall level than the middle of the image. So far we have seen the artifact in SPARS10/IRSUB256, SPARS25/IRSUB512, and STEP25/IRSUB512 modes.

The cause of the artifact is under investigation. If an operational solution can not be found, it may be possible to develop techniques to remove it during calibration.

Check the WFC3 Web site for information about IR subarray image artifacts:
http://www.stsci.edu/hst/wfc3/ins_performance/subarrays/

7.4.5 Apertures

The **APERTURE** parameter in the Phase II observing proposal defines two quantities: the active **region** of the detector to be read out (full frame or subarray), as well as the positioning of the target within the region (**reference point**). The default is to center the target at the chosen reference point, but a **POS TARG** Special Requirement may be added to offset the target from this position.

The available IR apertures are listed in Table 7.1. As with other *HST* instruments, there are two kinds of apertures with regard to their target reference position: "**fixed**" and "**optimum**." Apertures with their reference point at the geometric center of the array (or subarray) have "-FIX" appended of their name. These reference positions will never be adjusted during the *HST* mission. Apertures with their reference point at an "optimum" location (determined on the basis of best image quality, or detector cosmetics) have unadorned names. The reference point of these aperture may be optimized from time to time by STScI as circumstances warrant. At present, those reference points are offset from the boundaries of the amplifier quadrants.

For updates on subarray and aperture definitions, check the Science Instrument Aperture File (SIAF) page:
http://www.stsci.edu/hst/observatory/apertures/

Table 7.1: WFC3 IR Apertures.

Aperture Name	Reference point
IR	Optimum center of IR detector
IR-FIX	Geometric center of IR detector
IRSUB64	Optimum center of 64×64 subarray
IRSUB64-FIX	Geometric center of 64×64 subarray
IRSUB128	Optimum center of 128×128 subarray
IRSUB128-FIX	Geometric center of 128×128 subarray
IRSUB256	Optimum center of 256×256 subarray
IRSUB256-FIX	Geometric center of 256×256 subarray
IRSUB512	Optimum center of 512×512 subarray
IRSUB512-FIX	Geometric center of 512×512 subarray
G102-REF	G102 reference aperture for undispersed exposures
G141-REF	G141 reference aperture for undispersed exposures

7.5 IR Spectral Elements

7.5.1 Filter and Grism Summary

An overview of the IR spectral elements and of the process by which they were selected was given in Section 2.3. This section gives details of the IR filters and grisms. Table 7.2 lists the IR channel's filters, with a general description and fundamental parameters of each. Figures 7.5.2 and 7.3 show the effective throughput curves, including the filter transmission multiplied by the throughput of the OTA, WFC3 optics, and detector response.

More detailed information on the throughput curves of all of the filters is given in Appendix A; in particular, Section A.2.1 describes how to generate tabular versions of the throughput curves using ***synphot***. All measurements of the IR filters which involve wavelengths, as tabulated in Table 7.2 and plotted in Figures 7.5.2 and 7.3 and in Appendix A, were done in helium rather than vacuum. It should be noted that the laboratory measurements were done at a temperature of –30°C, whereas the filters are operated on orbit at –35°C; this may lead to wavelength shifts which are expected to be very small.

The IR channel is equipped with a single filter wheel with 18 slots, containing 15 passband filters, two grisms, and an opaque element (also referred to as the BLANK) for dark current measurements. The filter complement samples the spectral region between 800 and 1700 nm. All of the IR filter elements are full-sized, covering the entire field of view of the IR detector. Since all of the elements are mounted in a single wheel, only one element can be used at a given time.

The 900–1700 nm wavelength range is covered by a series of wide- and medium-band filters, with little wavelength overlap. Additional medium-band filters are centered on molecular bands and nearby continua, and several narrow-band filters are available for probing interstellar and nebular recombination lines.

The filter set is designed to include the most popular passbands used in extragalactic, stellar, and solar-system astronomy, as well as passbands similar to those already used in previous *HST* instruments.

Table 7.2: WFC3 IR Channel Filters and Grisms.

Name[1]	Description	Pivot[2] λ_p (nm)	Width[3] (nm)	Peak System Throughput
	IR Wide-Band (W) Filters			
F105W	Wide *Y*	1055.2	265.0	0.52
F110W	Wide *YJ*	1153.4	443.0	0.56
F125W	Wide *J*	1248.6	284.5	0.56
F140W	Wide *JH* gap; red grism reference	1392.3	384.0	0.56
F160W	WFC3 *H*	1536.9	268.3	0.56
	IR Medium-Band (M) Filters			
F098M	Blue grism reference	986.4	157.0	0.47
F127M	H_2O/CH_4 continuum	1274.0	68.8	0.54
F139M	H_2O/CH_4 line	1383.8	64.3	0.54
F153M	H_2O and NH_3	1532.2	68.5	0.55
	IR Narrow-Band (N) Filters			
F126N	[Fe II]	1258.5	15.2	0.50
F128N	Paschen β	1283.2	15.9	0.52
F130N	Paschen β continuum	1300.6	15.6	0.54
F132N	Paschen β (redshifted)	1318.8	16.1	0.52
F164N	[Fe II]	1640.4	20.9	0.47
F167N	[Fe II] continuum	1664.2	21.0	0.46
	IR Grisms (G)			
G102	"Blue" high-resolution grism	Useful range: 800–1150 nm[4]		0.41
G141	"Red" low-resolution grism	Useful range: 1075–1700 nm[4]		0.48

1. See Footnote 1 of Table 6.2 for naming conventions.
2. "Pivot wavelength" is defined as in Table 6.2 and Section 9.3. Filter transmissions were measured in helium but have been converted to vacuum wavelengths for this table.
3. Passband rectangular width, defined as in Table 6.2.
4. See Chapter 8 for IR Grism details.

Figure 7.2: Integrated system throughput of the WFC3 IR wide-band filters, presented in two panels for clarity. The throughput calculations include the *HST* OTA, WFC3 IR-channel internal throughput, filter transmittance, and the QE of the IR detector.

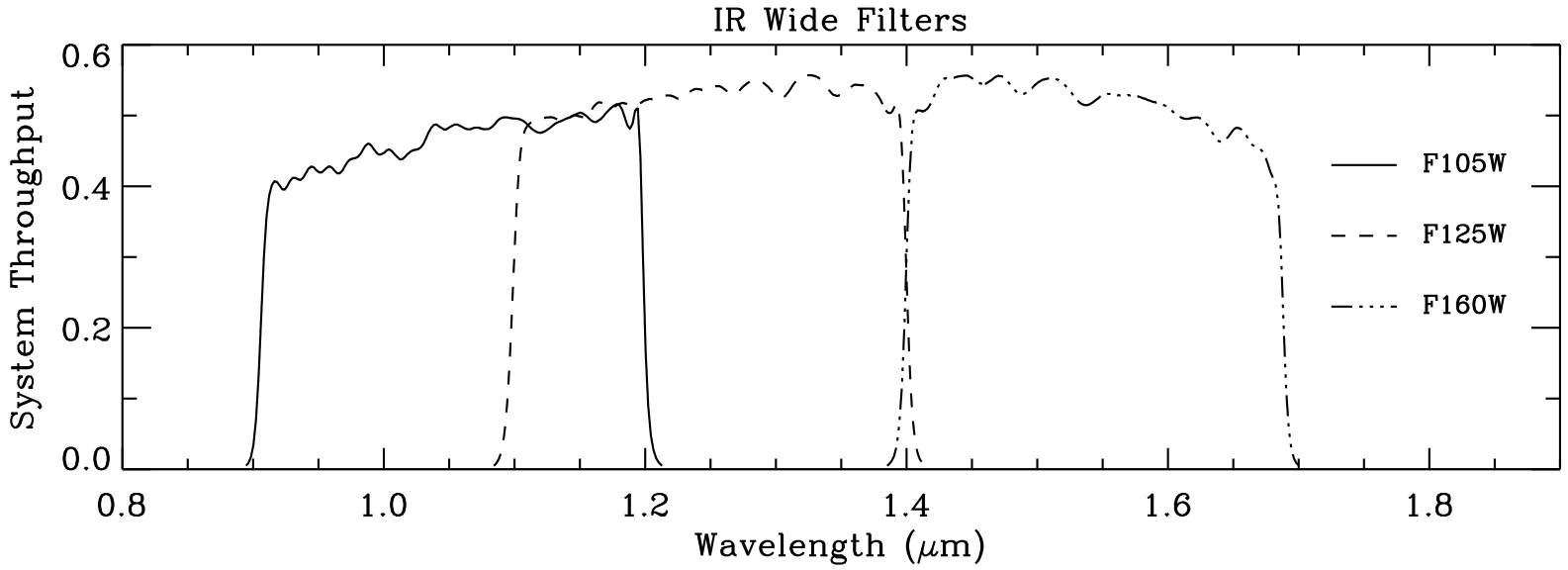

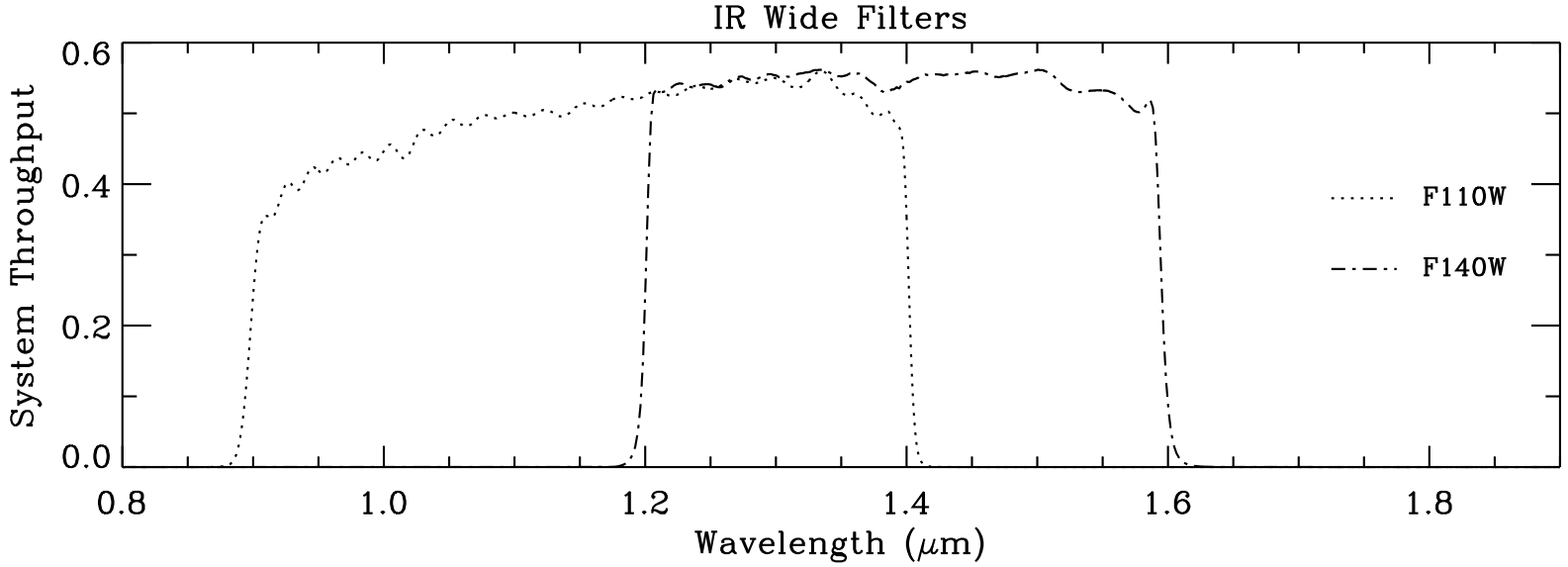

Figure 7.3: Integrated system throughput of the WFC3 IR medium-band filters (top panel) and narrow-band filters (bottom panel). The throughput calculations include the *HST* OTA, WFC3 IR-channel internal throughput, filter transmittance, and the QE of the IR detector.

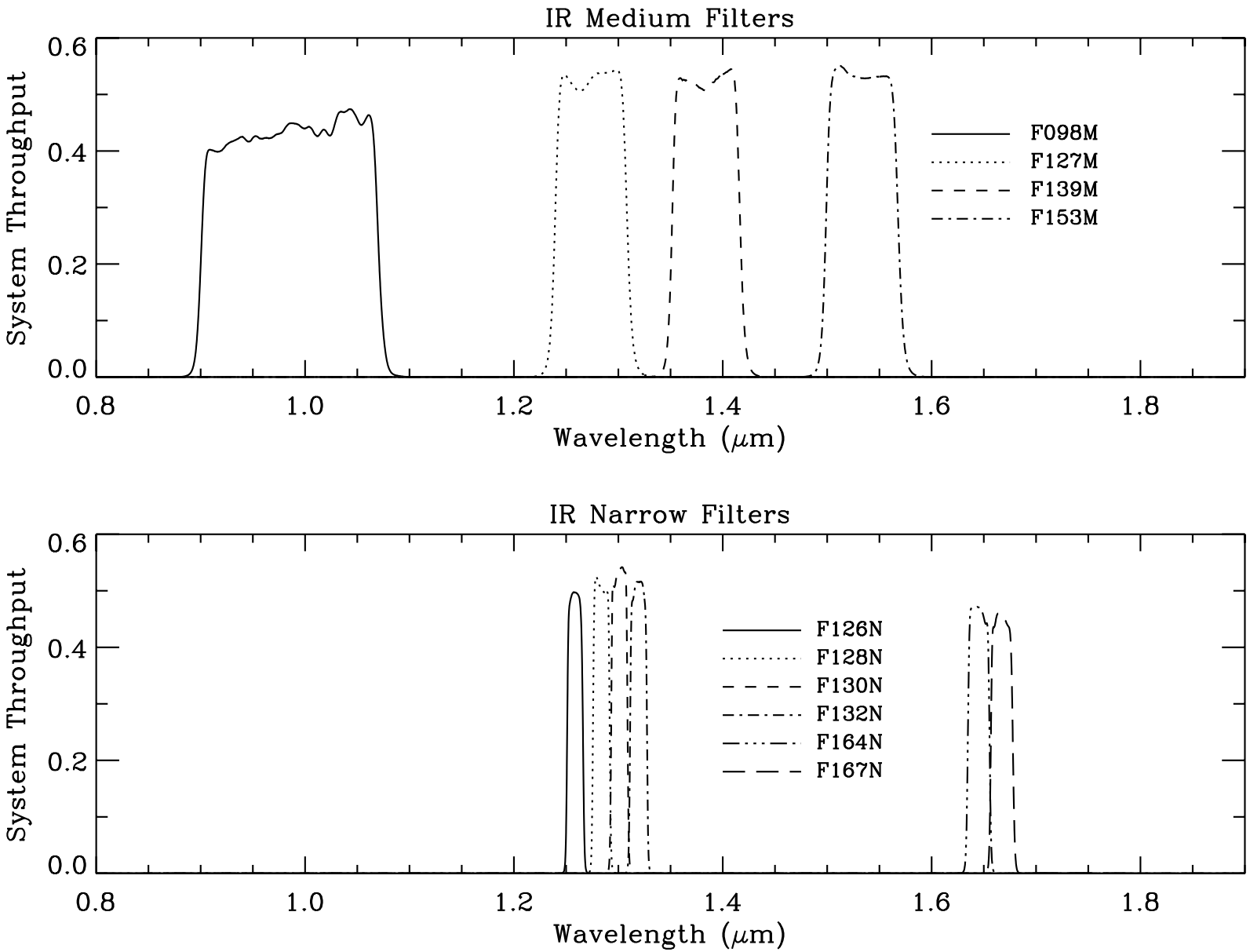

Wide-band Filters

The IR channel's versions of the ground-based *J* and *H* filters are F125W and F160W, respectively. The F125W filter has a width somewhat wider than that of a typical *J* passband used in ground-based cameras. The F160W filter's bandpass has been modified relative to ground-based *H* in order to give a better fit to the QE curve of the IR detector. Specifically, the WFC3 *H* filter's bandpass has been narrowed to approximately 1400-1700 nm, in order to limit thermal background and to have the filter define the bandpass on the red side rather than the detector sensitivity cutoff. By contrast, NICMOS *H* filter (NICMOS F160W) covers about 1400-1800 nm. This narrowing for WFC3 reduces photometric errors due to spatial variations in the detector's QE cutoff.

The wide F140W filter covers the gap between the *J* and *H* bands that is inaccessible from the ground. F105W has a central wavelength similar to ground-based *Y*, but is considerably wider. The IR channel also includes a very wide filter, F110W, spanning the ground-based *Y* and *J* bands. This filter can be used for deep imaging, with a bandpass fairly similar to that of the corresponding wide-band filter in NICMOS (also called F110W).

Medium-band filters

The F098M filter is useful as the G102 grism reference, allowing source selection and wavelength zero-point determination. It also complements the UVIS F845M filter, whose red 50% critical wavelength is ~900 nm. The overlap allows coverage over a continuous wavelength range across both WFC3 detectors.

The other medium filters span absorption bands of water and methane (F139M) and water and ammonia (F153M), with an adjacent continuum filter (F127M). These filters were intended for compositional studies of planets searching for water vapor (WFC3 ISR 2000-09). Solar system objects with visible inventories of these gas species are too bright to observe with the medium-band filters, and WFC3 lacks occulting hardware to access the high contrast ratios and small angular separations that would enable direct imaging of exoplanets. However, the high sensitivity of WFC3 enables compositional studies of the atmospheres of cool stars, brown dwarfs, and transiting exoplanets with the medium-band filters.

Narrow-band Filters

The IR channel includes six narrow-band filters which sample some of the most astrophysically important planetary, stellar, and nebular spectral features in the near-IR (e.g., [Fe II] and Paschen-β).

Cosmological emission lines can be detected across a range of redshifts within the bandpasses of the narrow-band filters. Table 7.3 lists the redshifts that can be probed using the specified emission lines. These redshift ranges are offered as a guide; exact values depend on the wavelengths of the filter cutoffs. Filter cutoffs used in Table 7.3 were defined using the passband rectangular widths (defined in Footnote 3 of Table 6.2). For consistency with Table 6.3, passband cutoffs were not centered on the filter pivot wavelengths λ_p (defined in Section 9.3). Instead, a central wavelength for each filter was determined by maximizing the wavelength-integrated product of a rectangular passband of the specified width with the actual system throughput for the

filter. For the IR narrow-band filters, these rectangular passband equivalent central wavelengths are within 0.3% of the pivot wavelengths.

Table 7.3: Nominal redshift ranges for WFC3/IR narrow-band filters.

Filter	Description	Filter λ_p (nm)	Filter Width (nm)	Line Rest Wavelength (nm)	Minimum *cz* (km/sec)	Maximum *cz* (km/sec)
F126N	[Fe II] on	1258.5	15.2	1256.7	-1312	2314
F128N	Pa β on or [Fe II] off	1283.2	15.9	1281.8	-1415	2304
F130N	*z* (Pa β) or Pa β off	1300.6	15.6	1281.8	2690	6338
F132N	[Fe II] off or Pa β off	1318.8	16.1			
F164N	[Fe II] on	1640.4	20.9	1643.6	-1632	2180
F167N	[Fe II] off	1664.2	21.0	1643.6	2371	6202

Grisms

The IR channel has two grisms that provide slitless spectra (see Chapter 8 for more details). The "blue" G102 grism provides a dispersion of 2.5 nm/pix (or a resolution of ~210) over the 800-1150 nm wavelength range. The "red" G141 grism has a dispersion of 4.7 nm/pix (resolution of ~130) over the 1100-1700 nm range. In most cases, a grism observation will be accompanied by a direct image, for source identification and wavelength calibration (see Section 8.3).

7.5.2 Filter Blue Leaks

All of the IR filters have been constructed using IR-transmitting colored glass with thin-film coatings to achieve the desired bandpasses. As with the UVIS filter designs, better in-band transmission generally means somewhat less suppression of out-of-band transmission. While the final IR filters have excellent in-band transmission (>90%), a few also have a small, narrow peak of transmission between 750-800 nm. After the filters were manufactured, a new IR detector was chosen which has appreciable sensitivity well down into the optical wavelength range see Figure 5.14). Some of the IR filters thus have a small amount of blue leak (i.e., a small amount of short-wavelength out-of-band light is detected). None of the IR filters have significant red leaks.

Table 7.4 presents estimates of the blue-leak effect, listing the fraction of detected count rate expected from 710 to 830 nm for each filter. The throughput calculation includes transmission of the filter, the throughputs of the *HST* OTA and the IR optics, and the QE of the IR detector.

As can be seen from the table, blue leaks in all the wide-band and some of the narrow- and medium-band filters are minimal; however, several filters, notably F126N, F128N, and F153M, have some blue leak (e.g., ~1% for objects with effective temperatures of 5000 K. In programs that may suffer adverse effects due to the blue

leaks, it may be useful to obtain UVIS images in the F763M filter, which covers the problematic wavelength region (750-800 nm).

Table 7.4: Fraction of detected count rate arising between wavelengths 710 to 830 nm as a function of effective temperature.

Filter	T_{eff} (K)										
	3500	**5000**	**10000**	**15000**	**20000**	**25000**	**30000**	**35000**	**40000**	**45000**	**50000**
F098M	3.8E-05	6.1E-05	8.4E-05	9.3E-05	9.8E-05	1.0E-04	1.0E-04	1.1E-04	1.1E-04	1.1E-04	1.1E-04
F105W	1.5E-05	2.2E-05	3.2E-05	3.5E-05	3.7E-05	3.9E-05	4.0E-05	4.1E-05	4.1E-05	4.1E-05	4.1E-05
F110W	8.8E-08	1.4E-07	2.4E-07	2.7E-07	2.9E-07	3.0E-07	3.1E-07	3.2E-07	3.2E-07	3.2E-07	3.2E-07
F125W	1.5E-07	2.4E-07	4.6E-07	5.3E-07	5.7E-07	6.1E-07	6.3E-07	6.5E-07	6.5E-07	6.5E-07	6.5E-07
F126N	6.4E-03	1.3E-02	2.6E-02	3.0E-02	3.3E-02	3.5E-02	3.6E-02	3.7E-02	3.8E-02	3.8E-02	3.8E-02
F127M	1.6E-03	3.2E-03	6.9E-03	8.0E-03	8.7E-03	9.2E-03	9.6E-03	9.8E-03	9.9E-03	1.0E-02	1.0E-02
F128N	5.7E-03	1.2E-02	2.7E-02	3.1E-02	3.3E-02	3.5E-02	3.6E-02	3.7E-02	3.7E-02	3.7E-02	3.7E-02
F130N	3.8E-04	6.7E-04	1.4E-03	1.6E-03	1.8E-03	1.9E-03	2.0E-03	2.0E-03	2.1E-03	2.1E-03	2.1E-03
F132N	3.7E-04	6.6E-04	1.4E-03	1.7E-03	1.8E-03	1.9E-03	2.0E-03	2.1E-03	2.1E-03	2.1E-03	2.1E-03
F139M	2.2E-03	3.9E-03	9.0E-03	1.1E-02	1.2E-02	1.3E-02	1.3E-02	1.4E-02	1.4E-02	1.4E-02	1.4E-02
F140W	6.3E-05	1.0E-04	2.4E-04	2.9E-04	3.2E-04	3.4E-04	3.5E-04	3.7E-04	3.7E-04	3.7E-04	3.7E-04
F153M	5.6E-03	9.9E-03	2.8E-02	3.3E-02	3.6E-02	3.9E-02	4.1E-02	4.2E-02	4.3E-02	4.3E-02	4.3E-02
F160W	9.4E-05	1.7E-04	4.8E-04	5.7E-04	6.3E-04	6.8E-04	7.1E-04	7.4E-04	7.4E-04	7.5E-04	7.5E-04
F164N	3.8E-03	8.0E-03	2.6E-02	3.1E-02	3.4E-02	3.7E-02	3.9E-02	4.0E-02	4.0E-02	4.1E-02	4.1E-02
F167N	3.3E-03	7.0E-03	2.2E-02	2.7E-02	3.0E-02	3.2E-02	3.4E-02	3.6E-02	3.6E-02	3.6E-02	3.6E-02

7.5.3 Ghosts

No significant optical ghosts are present in the IR channel.

7.6 IR Optical Performance

Following its alignment to the OTA, a series of observations through a variety of filters were obtained to demonstrate the WFC3 optical performance. The WFC3 IR channel meets or exceeds all image quality expectations. The following subsections summarize the measured flight optical performance for the IR channel, as described by its point-spread function (PSF), i.e., the spatial distribution of the flux in an image of a point source. The results shown are produced using an optical model which has been adjusted and correlated to the PSFs measured on-orbit and represent mean values averaged over the field. This PSF model includes the pupil geometry, including the

cold stop, residual aberration, the mid-frequency wavefront error of the OTA, the effect of the detector inter-pixel capacitive cross-talk, and first-order geometric distortion.

7.6.1 PSF width and sharpness

The IR channel PSFs are well approximated by Gaussian profiles. As was discussed in more detail for the UVIS channel in section 6.6.1, the PSFs can usefully be characterized by their FWHM or their sharpness (effectively the reciprocal of the number of pixels occupied by a point source, as defined in Section 6.6.1). Table 7.5 lists the FWHM of the model PSF core in units of pixel and arcsec and the sharpness parameter for 10 wavelengths. The sharpness range shown for each wavelength indicates the values for the PSF centered on the pixel corners and center. The monotonic increase in FWHM and decrease in sharpness with wavelength is due to diffraction.

Table 7.5: WFC3/IR PSF FWHM (pixels and arcseconds), and sharpness, vs. wavelength.

Wavelength (nm	FWHM (pix)	FWHM (arcsec)	Sharpness
800	0.971	0.124	0.127–0.197
900	0.986	0.126	0.118–0.182
1000	1.001	0.128	0.109–0.169
1100	1.019	0.130	0.100–0.156
1200	1.040	0.133	0.093–0.144
1300	1.067	0.137	0.087–0.132
1400	1.100	0.141	0.083–0.121
1500	1.136	0.145	0.080–0.112
1600	1.176	0.151	0.077–0.102
1700	1.219	0.156	0.074–0.093

Figure 7.4 plots the azimuthally-averaged model OTA+WFC3 PSF at three different IR wavelengths., indicating the fractional PSF flux per pixel at radii from 1 pixel to 5 arcsec.

Figure 7.4: Azimuthally averaged WFC3/IR PSF.

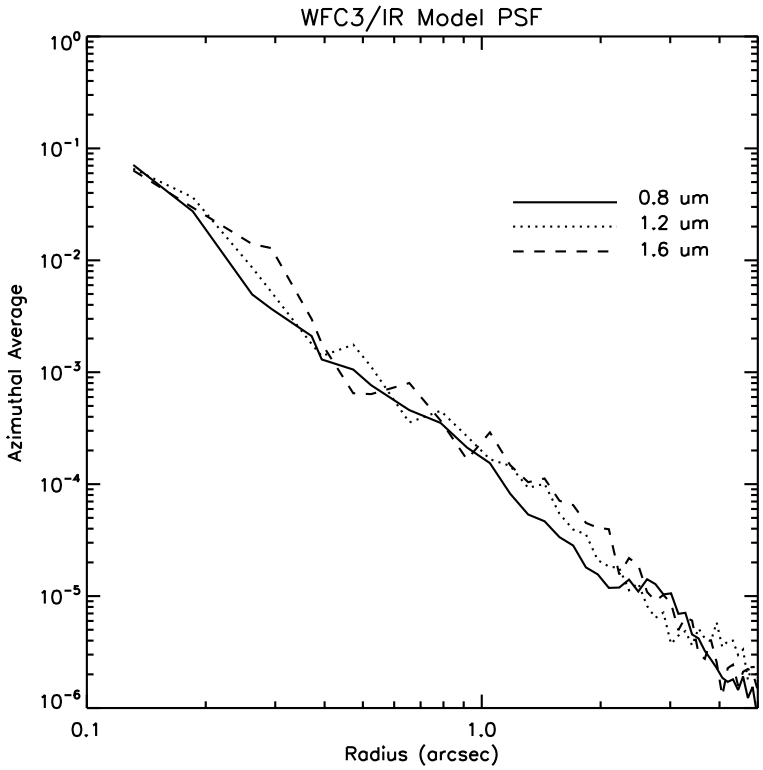

7.6.2 Encircled and Ensquared Energy

As described in more detail in section 6.6.2 for the UVIS channel, encircled energy, the fraction of light contained in a circular aperture, and ensquared energy, the fraction of energy falling within a certain number of pixels, are two other useful ways of characterizing well-behaved profiles.

Encircled-energy profiles for the IR channel at three representative wavelengths are plotted in Figure 7.5. The corresponding numerical values are presented in Table 7.6. The ensquared energy, which provides the flux per pixel, is presented in Table 7.7.

Figure 7.5: Encircled Energy for the WFC3/IR channel.

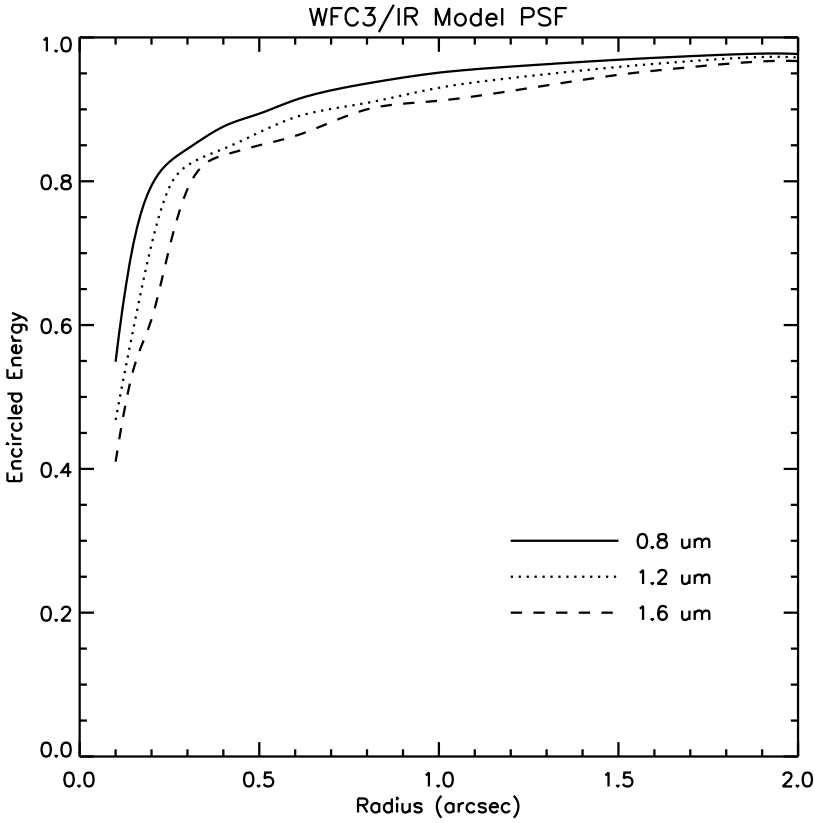

Table 7.6: WFC3/IR PSF Encircled Energy Fraction vs. Aperture Radius (arcsec).

Aperture radius (arcsec)	Wavelength (nm)										
	700	**800**	**900**	**1000**	**1100**	**1200**	**1300**	**1400**	**1500**	**1600**	**1700**
0.10	0.575	0.549	0.524	0.502	0.484	0.468	0.453	0.438	0.426	0.410	0.394
0.15	0.736	0.714	0.685	0.653	0.623	0.596	0.575	0.558	0.550	0.539	0.531
0.20	0.802	0.794	0.780	0.762	0.739	0.712	0.683	0.653	0.631	0.608	0.590
0.25	0.831	0.827	0.821	0.813	0.804	0.792	0.776	0.756	0.735	0.708	0.679
0.30	0.850	0.845	0.838	0.833	0.828	0.822	0.816	0.808	0.803	0.789	0.770
0.40	0.878	0.876	0.869	0.859	0.850	0.845	0.841	0.838	0.840	0.836	0.832
0.50	0.899	0.894	0.889	0.884	0.878	0.868	0.858	0.852	0.854	0.850	0.848
0.60	0.916	0.913	0.904	0.897	0.893	0.889	0.883	0.875	0.870	0.863	0.859
0.80	0.937	0.936	0.929	0.924	0.918	0.909	0.903	0.900	0.903	0.900	0.895
1.00	0.951	0.951	0.946	0.941	0.935	0.930	0.925	0.920	0.917	0.912	0.909
1.50	0.967	0.969	0.967	0.965	0.963	0.959	0.954	0.951	0.952	0.948	0.943
2.00	0.974	0.977	0.976	0.975	0.973	0.972	0.969	0.967	0.970	0.967	0.963

Table 7.7: WFC3/IR PSF Ensquared Energy Fraction vs. Aperture size (pixels), where the target is centered on the aperture. Row 1 indicates the maximal (PSF centered on the pixel) peak pixel fraction, useful for determining the exposure time at which saturation may occur.

Aperture size (pixels)	Wavelength (nm)										
	700	800	900	1000	1100	1200	1300	1400	1500	1600	1700
1×1	0.435	0.417	0.398	0.381	0.365	0.348	0.331	0.314	0.299	0.283	0.267
2×2[1]	0.728	0.707	0.679	0.648	0.618	0.592	0.571	0.554	0.545	0.534	0.524
3×3	0.815	0.811	0.802	0.790	0.776	0.757	0.733	0.706	0.682	0.655	0.631
5×5	0.872	0.868	0.858	0.849	0.844	0.840	0.836	0.830	0.830	0.826	0.821
7×7	0.905	0.900	0.894	0.888	0.882	0.872	0.862	0.855	0.856	0.854	0.852
9×9	0.927	0.924	0.917	0.909	0.904	0.898	0.893	0.888	0.886	0.876	0.868
11×11	0.941	0.939	0.934	0.928	0.921	0.914	0.910	0.905	0.905	0.901	0.897
13×13	0.951	0.951	0.946	0.941	0.936	0.930	0.924	0.917	0.919	0.915	0.911
15×15	0.957	0.958	0.955	0.951	0.946	0.942	0.936	0.931	0.931	0.925	0.921
17×17	0.961	0.963	0.962	0.958	0.955	0.950	0.945	0.942	0.942	0.938	0.933
19×19	0.964	0.967	0.966	0.964	0.961	0.958	0.954	0.949	0.951	0.947	0.942
21×21	0.967	0.969	0.969	0.967	0.965	0.963	0.960	0.956	0.957	0.953	0.950
23×23	0.970	0.972	0.971	0.970	0.969	0.967	0.964	0.961	0.964	0.960	0.956
25×25	0.972	0.974	0.973	0.972	0.971	0.970	0.968	0.965	0.968	0.965	0.962
51×51	0.993	0.993	0.991	0.990	0.988	0.987	0.986	0.985	0.988	0.987	0.986
101×101	0.998	0.999	0.998	0.998	0.997	0.997	0.996	0.996	0.998	0.997	0.997

1. For the 2×2 aperture, the target is located at the center of the array.

During SMOV, high-dynamic-range isolated star images were obtained through several filters. These are shown with a logarithmic stretch in Figure 7.6. The images appear slightly elongated vertically, due to the 24 degree tilt of the detector to the chief ray and the fact that a distortion correction has not been applied. Although the target was chosen to be isolated, a number of field galaxies appear in both the F098M and the F160W filter images; these are also seen in long wavelength UVIS channel images of the same target (Figure 6.13). Some detector artifacts, including cold and warm pixels and imperfectly removed cosmic ray hits are evident.

Figure 7.6: High dynamic range WFC3/IR star images through F098M (left) and F160W (right) subtending ~20 arcsec on each side near field center. No distortion correction has been applied. Stretch is logarithmic from 10^{-3} to 10^{3} e^{-} sec^{-1} $pixel^{-1}$. Faint galaxies appear in the background.

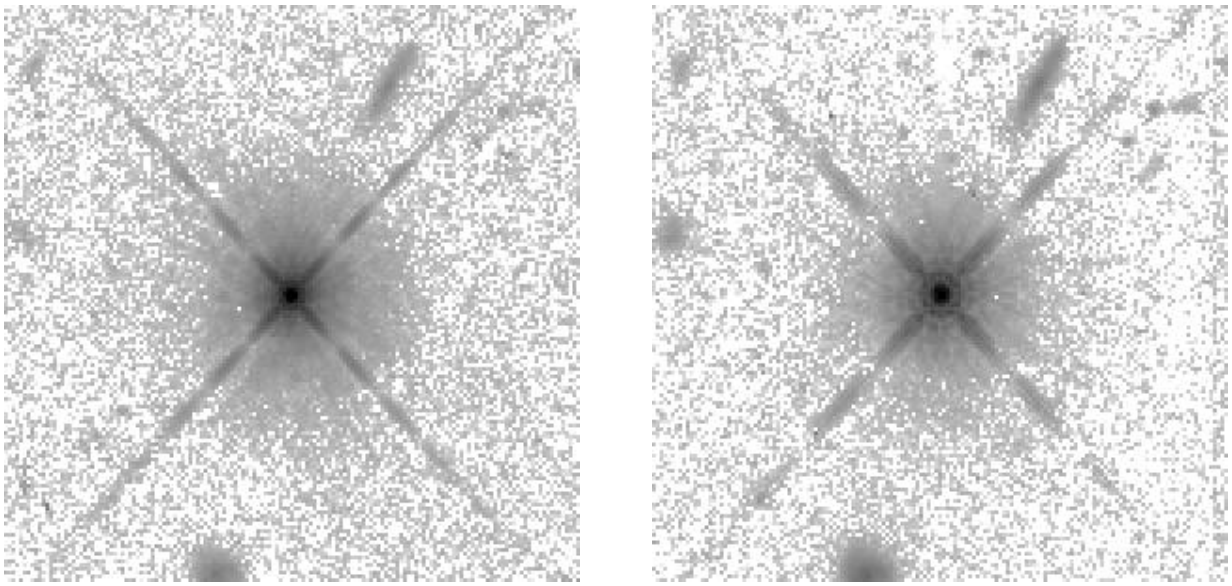

7.6.3 Other PSF Behavior and Characteristics

Temporal Dependence of the PSF: *HST* Breathing

As was discussed in section 6.6.3, short term focus variations, "breathing" arising from the changing thermal environment of *HST*, affect all *HST* observations to some degree. For the IR channel, breathing is expected to produce variations of ~0.3% and less than 0.1% in the FWHM of the PSF of WFC3/IR at 700 nm and at wavelengths longer than 1100 nm, respectively, on typical timescales of one orbit.

Intra-pixel Response

The response of a pixel of an IR detector to light from an unresolved source varies with the positioning of the source within the pixel due to low sensitivity at the pixel's edges and dead zones between pixels. For NICMOS, the intra-pixel sensitivity was found to be an important effect: it varies by as much as 40% (peak to valley). This effect has an impact on point sources which depends on the sampling, and therefore, for a given pixel scale, on the wavelength of the diffraction-limited images. Well-dithered exposures average out this effect, but photometric accuracy for stellar sources with few dither positions can be limited by uncertainties related to intra-pixel response.

For the WFC3/IR flight detector, no measurable intra-pixel sensitivity variation was found during ground testing (WFC3 ISR 2008-29). The smaller pixel size (18 μm vs. 40 μm) and the much higher WFC3/IR detector temperature (compared to NICMOS) are probably responsible for this improvement.

Inter-pixel Capacitance

The small pixel size, relative to that in NICMOS, increases the relevance of capacitive coupling between nearby pixels (see Brown et. al., 2006, *PASP*, **118**, 1443; Moore et. al., 2006, Opt. Eng., 076402). It affects the gain measurements and the PSF. The easiest method of estimating the inter-pixel capacitance is to measure the ratio of DNs in pixels adjacent to a "hot" (high-dark-current) pixel to the DNs in the hot pixel. In the WFC3 IR channel, on the order of 5% of electrons may leak to the adjacent pixels. WFC3 ISR 2008-26 describes a method for correcting inter-pixel capacitance using Fourier deconvolution, and demonstrates its effectiveness on WFC3/IR ground-testing data.

7.7 IR Exposure and Readout

The general operating modes of IR detectors have been described in Chapter 5. In this section we will detail the readout modes implemented in WFC3.

7.7.1 Exposure Time

Unlike the UVIS channel, the IR channel does not have a mechanical shutter. Integration times are thus determined purely electronically, by resetting the charge on the detector, and then accumulating signal until the exposure is completed. A second major difference from the UVIS channel is that the IR detector can be read out non-destructively as the exposure accumulates, as opposed to the single destructive readout at the end of a CCD exposure.

There is a set of pre-defined accumulation and readout sequences available to IR observers, which are used to set the total exposure time as described in the next subsection.

7.7.2 MULTIACCUM Mode

In IR observing it is possible, and desirable, to sample the signal multiple times as an exposure accumulates, and the MULTIACCUM mode accomplishes this. MULTIACCUM is the only observing mode available for the IR channel.

Multiple readouts offer three major advantages. First, the multiple reads provide a way to record a signal in a pixel before it saturates, thus effectively increasing the dynamic range of the final image. Second, the multiple reads can be analyzed to isolate and remove cosmic-ray events. Third, fitting to multiple reads provides a means for reducing the net effective read noise, which is relatively high for the IR detector.

The disadvantage of multiple readouts is that they are data-intensive. The HgCdTe detector array is 1024×1024 pixels, which is only about 1/16 by pixel number of the 4096×4102 UVIS array. However, since up to 16 IR readouts are used, the total data

volume of a single IR exposure approaches that of a single UVIS frame. A maximum of 32 IR readouts can be stored in the instrument buffer, after which the content of the buffer must be dumped to the *HST* Solid State Recorder (SSR). A buffer dump of 16 reads takes about 5.8 minutes.

MULTIACCUM readout consists of the following sequence of events:

1. **Array reset:** After a fast calibration of the Analog to Digital Converters, all pixels are set to the detector bias level, with two rapid reset cycles of the entire chip.
2. **Array read:** The charge in each pixel is measured and stored in the on-board computer's memory. This is done as soon as practical after the second array reset in step 1. In effect, given the short delay and the time needed to read the array, a very short-exposure image is stored in memory. This is known as the zero read.
3. **Multiple integration-read cycles:** The detector integrates for a certain amount of time and then the charge in each pixel is read out. This step can be repeated up to a total of 15 times during the exposure. All frames are individually stored in the on-board computer memory. Note that it takes a finite time (2.93 sec) to read the array, so there is a time delay between reading the first and last pixel. Since this delay is constant for each read, it cancels out in difference images.
4. **Return to idle mode:** the detector returns to idle mode, where it is continuously flushed in order to prevent charge build-up and to limit the formation of residual images.

All sequences start with the same “reset, reset, read” sequence, where the two reads are done as quickly as possible. This “double reset read” was originally implemented because the very first read after the reset may show an offset that does not reproduce in the following reads.

7.7.3 MULTIACCUM Timing Sequences: Full Array Apertures

There are 11 pre-defined sample sequences, optimized to cover a wide range of observing situations, available for the full-frame IR apertures. *(See Section 7.7.4 for a discussion of the sample sequences available for the IR subarray apertures. The same names are used for the sample sequences, but the times are different.)* The maximum number of reads during an exposure is 15, which are collected as the signal ramps up. It is possible to select less than 15 reads, thus cutting short the ramp and reducing the total exposure time. However, the timing of the individual reads within any of the 11 sequences cannot be adjusted by the user. This approach has been adopted because of experience with NICMOS, which indicates that optimal calibration of IR detectors requires a dedicated set of reference files (e.g., dark frames) for each timing pattern.

In summary, a WFC3/IR exposure is fully specified by choosing:

- one of the 11 available pre-defined timing sequences, and

- the total number of samples (NSAMP, which must be no more than 15), which effectively determines the total exposure time

The 11 timing sequences for the IR channel are:

- One **RAPID** sequence: the detector is sampled with the shortest possible time interval.
- Five linear (**SPARS**) sequences: the detector is sampled with uniform time intervals between reads, a so-called "linear sample up the ramp." ("SPARS" is a contraction of the word "sparse.")
- Five log-linear (**STEP**) sequences: the detector is initially sampled with reads spaced logarithmically in time. After a specified time, the sampling then becomes uniform until the last sample;

All 11 of the sequences above refer to readouts of the full 1024×1024 detector array. See Section 7.7.4 below for the timing sequences available for subarrays. Details of the sequences are in the following paragraphs. The timings of the individual reads are given in Table 7.8.

RAPID Sequence

The RAPID sequence provides linear sampling at the fastest possible speed. For the full array, this means one frame every 2.9 s, and the entire set of 16 reads completed in less than 44 s. The RAPID mode is mainly intended for the brightest targets. Due to the overheads imposed by buffer dumps (see Chapter 10), observations in this mode done continuously would have low observing efficiency.

SPARS Sequences

The SPARS sequences use evenly spaced time intervals. The five available SPARS sequences are designated SPARS10, SPARS25, SPARS50, SPARS100 and SPARS200, corresponding to sampling intervals of approximately 10, 25, 50, 100, and 200 s, respectively.

The SPARS modes can be regarded as the most basic readout modes, and they are applicable to a wide range of target fluxes. They provide flexibility in integration time and are well suited to fill an orbital visibility period with several exposures.

STEP Sequences

The five available logarithmic/linear sequences are STEP25, STEP50, STEP100, STEP200, and STEP400. They begin with logarithmic spacing up to the given number of seconds (e.g., 50 s for STEP50), and then continue with linear spacing for the remainder of the sequence.

The STEP mode is intended to provide a more uniform sampling across a wide range of stellar magnitudes, which is especially important for imaging fields containing both faint and bright targets. The faint targets require a long, linearly sampled integration, while the bright targets need to be sampled several times early in the exposure, before they saturate. Thus, the dynamic range of the final image is increased.

Figure 7.7: Example of STEP sequence with NSAMP=4. NSAMP+1 images are stored in the observer's FITS image.

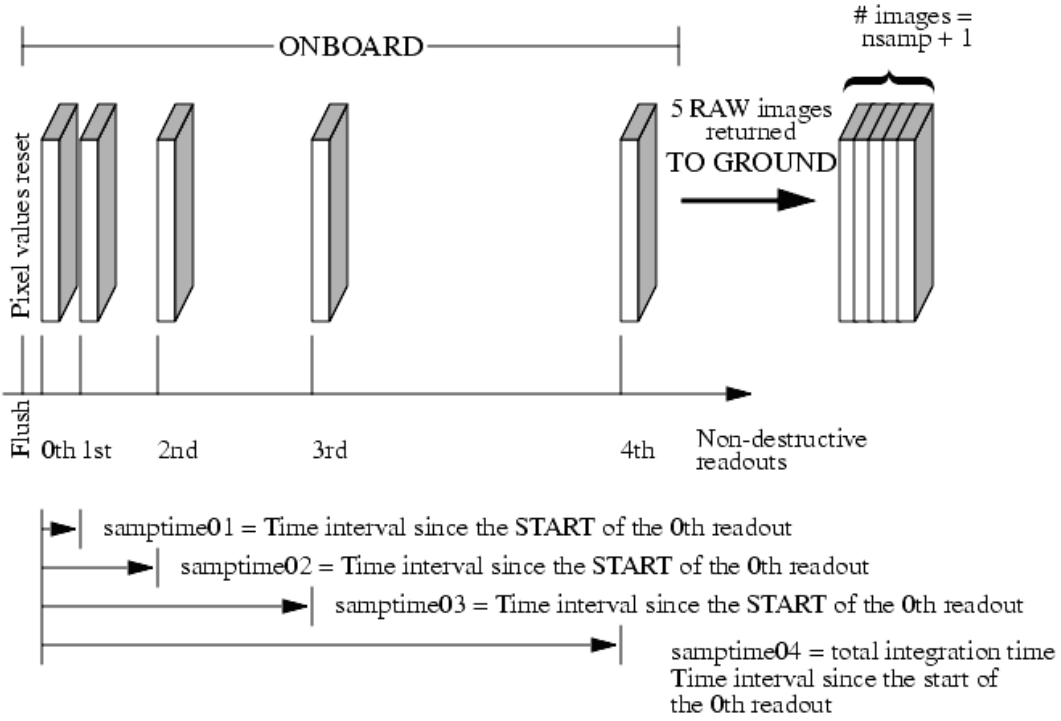

Table 7.8: Sample times of 1024×1024 MULTIACCUM readouts in seconds. The information in this table can also be found in Table 15.5 of the *Phase II Proposal Instructions*.

NSAMP	RAPID (sec)	SPARS (sec)					STEP (sec)				
		SPARS10	SPARS25	SPARS50	SPARS100	SPARS200	STEP25	STEP50	STEP100	STEP200	STEP400
1	2.932	2.932	2.932	2.932	2.932	2.932	2.932	2.932	2.932	2.932	2.932
2	5.865	12.933	27.933	52.933	102.933	202.932	5.865	5.865	5.865	5.865	5.865
3	8.797	22.934	52.933	102.933	202.933	402.932	8.797	8.797	8.797	8.797	8.797
4	11.729	32.935	77.934	152.934	302.933	602.932	11.729	11.729	11.729	11.729	11.729
5	14.661	42.936	102.934	202.934	402.934	802.933	24.230	24.230	24.230	24.230	24.230
6	17.594	52.937	127.935	252.935	502.934	1002.933	49.230	49.230	49.230	49.230	49.230
7	20.526	62.938	152.935	302.935	602.934	1202.933	74.231	99.231	99.231	99.231	99.231
8	23.458	72.939	177.936	352.935	702.935	1402.933	99.231	149.231	199.231	199.231	199.231
9	26.391	82.940	202.936	402.936	802.935	1602.933	124.232	199.232	299.231	399.231	399.231
10	29.323	92.941	227.937	452.936	902.935	1802.933	149.232	249.232	399.232	599.231	799.232
11	32.255	102.942	252.937	502.937	1002.936	2002.933	174.233	299.232	499.232	799.231	1199.232
12	35.187	112.943	277.938	552.937	1102.936	2202.933	199.233	349.233	599.232	999.231	1599.233
13	38.120	122.944	302.938	602.938	1202.936	2402.933	224.234	399.233	699.233	1199.231	1999.233
14	41.052	132.945	327.939	652.938	1302.936	2602.933	249.234	449.234	799.233	1399.231	2399.234
15	43.984	142.946	352.940	702.939	1402.937	2802.933	274.235	499.234	899.233	1599.231	2799.235

7.7.4 MULTIACCUM Timing Sequences: Subarray Apertures

As described in Section 7.4.4, subarrays are available in order to reduce data volume and enable short exposure times, defined in sample sequences. *For a given sample sequence name, the sample times are shorter for smaller subarrays.* However, only certain combinations of subarrays and sample sequences are supported by STScI. Other MULTIACCUM sequences can be used in principle but are not supported, and additional calibration observations would have to be made by the observer. The supported combinations are presented in Table 7.9. The exposure times may be found in Phase II Proposal Instructions, Chapter 14 (Wide Field Camera 3).

See Section 14.3.6 of the GO Phase II Proposal Instructions, Table 14.4, for the sample times associated with each combination of sample sequence and subarray size. Note that the sample times for a given sample sequence name are shorter for smaller subarrays.

Certain combinations of IR subarrays and sample sequences give rise to images containing a sudden low-level jump in the overall background level of the image. The cause of the artifact is under investigation (see Section 7.4.4).

Table 7.9: Supported subarray sample sequences.

Aperture	Sample Sequence			
	RAPID	SPARS10	SPARS25	STEP25
IRSUB64	yes	no	no	no
IRSUB64-FIX	yes	no	no	no
IRSUB128	yes	yes	no	no
IRSUB128-FIX	yes	yes	no	no
IRSUB256	yes	yes	yes	no
IRSUB256-FIX	yes	yes	yes	no
IRSUB512	yes	no	yes	yes
IRSUB512-FIX	yes	no	yes	yes

7.8 IR Sensitivity

7.8.1 Limiting Magnitudes

Table 7.10 presents the predicted limiting-magnitude performance of the WFC3 IR channel and compares it with that of the NIC3 camera. The calculations are based on a optimal extraction of a point source. The limiting ABMAG at a S/N of 10 was calculated for a 1-hour and a 10-hour exposure. The throughput curves for the WFC3 filters listed in column 2 were used; for NIC3, the most similar wide-band filter was used, and its name is given in column 3.

An Exposure Time Calculator (ETC) is available online. See Section 9.2.

Table 7.10: Limiting-magnitude performance of WFC3 compared with that of NIC3 based on on-orbit sensitivity from SMOV4. The table provides limiting ABMAGs at a S/N of 10 for the indicated WFC3 filters and for NIC3 with its most similar filters.

Band	Filter		Limiting magnitude in 1 hr		Limiting magnitude in 10 hrs	
	WFC3	NIC3	WFC3	NIC3	WFC3	NIC3
J	F110W	F110W	27.3	26.1	28.6	27.4
H	F160W	F160W	26.6	25.9	27.9	27.1

7.9 Other Considerations for IR Imaging

7.9.1 Gain and Full-well Saturation

Like the UVIS channel, the IR channel uses 16-bit Analog to Digital Converters (ADCs), providing a digital output signal in the range between 0 and 65,535 data numbers (DNs). The default gain setting for the IR channel is 2.5 electrons/DN and is the only one offered to observers.

The default gain is compatible with the full-well saturation level of the IR channel, which is about 78,000 electrons (~33,000 DN at the default gain), and with the detector readout noise, of order 20-22 electrons per correlated double sampling.

7.9.2 Cosmic Rays

Cosmic rays affect the image quality. On-orbit measurements indicate that cosmic ray events occur at a rate of 11 ± 1.5 CR/s for WFC3/IR. The use of MULTIACCUM mode makes it possible to filter out cosmic rays because it provides a series of intermediate non-destructive reads. The intermediate reads are used by the WFC3 data pipeline to identify cosmic ray hits, similarly to the use of CR-SPLITs in CCD observations.

Passages through the South Atlantic Anomaly (SAA) cause the highest number of cosmic ray hits. When the *HST* is within the predefined SAA exclusion zone, IR observations are not normally taken and the detector is set to auto-flush mode to minimize the effects of SAA passage on instrument performance. Unlike NICMOS, where the detector electronics must be switched off during SAA passage, it is possible to perform time-critical observations in the SAA with WFC3/IR.

7.9.3 On-orbit Degradation

Unlike the CCDs, minimal cosmic-ray damage to the IR detectors is anticipated. During ground testing using a particle accelerator, the WFC3/IR arrays have been subjected to radiation doses much higher than expected in their entire orbital lifetime, without sustaining significant long-term damage or measurable degradation in QE.

7.9.4 Image Persistence

The IR detector exhibits image persistence, particularly during and following observations of targets that saturate the detector by much more than the pixel full well depth. Characterization of image persistence is ongoing. The amount of image persistence depends on the brightness of the source and the amount of time the light from a the bright source is incident on the detector. Image persistence has been observed both within a set of dithered exposures in a single orbit and in observations where the target observed in a previous orbit was particular bright. Persistence appears to have at least two time scales, one of order 5 min and a second of order an orbit. All bright sources (50% of full well or greater) exhibit some persistence (typically 1/3 of a percent) immediately after an exposure. Many of the characteristics of the persistence are explained by the model of persistence described by Smith (SPIE 7021-22, Marseille 2008-06-24) for HgCd detectors.

The most common form of image persistence is due to bright stars in the field, which saturate or nearly saturate an observation. An example of this is shown in Figure 7.8, which is one of many dark exposures that have been obtained with WFC3/IR. In the previous 0.7 to 3 hours, a starfield containing a number of bright stars had been observed in a linear dither pattern. Residual images of the bright stars appear in the dark frame. The count rates observed an orbit later from the most saturated stars as large as 200 e^{-}/s in the flat field image. Close inspection of the images show that the shape of the residual images is less peaked than those of real stars; reflecting the fact that the persistence image is not a simple fraction of the initial count rate.

Figure 7.8: A dark exposure with the WFC3 IR channel affected by persistence images. The previous set of exposures with WFC3 IR contained several stars that were highly saturated. The linear dither pattern is clearly visible.

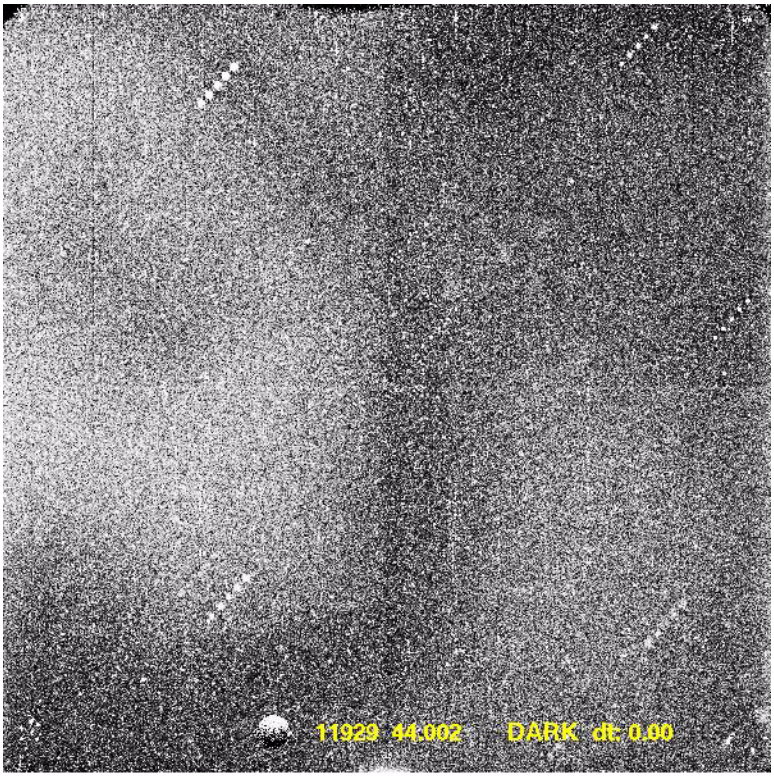

The presence of a few residual images in science data is a nuisance, but in most cases will not compromise the science you would expect to obtain from the IR channel of WFC3. Tools are being developed to help with the identification and removal of these features from the data. Observers can mitigate the problems of persistence within their own observations by taking care that bright or saturated sources within a field are not dithered across the same parts of the detector that record the highest science priority areas of the field.

Figure 7.9 shows a less common problem in which a bright extended source (a globular cluster) was observed in an orbit prior to the observation shown. Here the persistence image extends over much of the field, and may compromise the science from the program in question. The highly saturated observation was from a prior observer's program.

Figure 7.9: A observation of a fairly sparse field observed with WFC3 IR which shows the residual image of a globular cluster. The series of dithered exposures of the globular cluster had been obtained about 2 hours prior to this observation. The displayed image has been stretched to emphasize the residual image which has peak typical count rates of 0.4 electrons/sec, considerably less than 1% of the fluxes in the original exposures. The exposures of the globular cluster had numerous stars with typical fluxes corresponding to 1000 e^-/s.

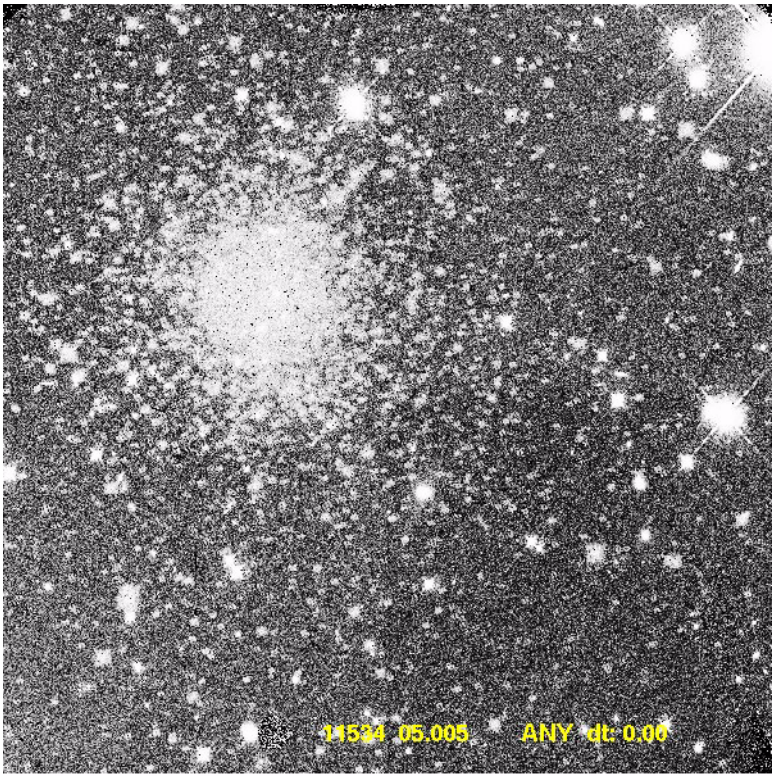

If observers suspect that prior saturated observations may have left residual images in their data, the *HST* History Search can be used to determine the timeline of observations just prior to the compromised data set. As the earlier observations are likely to be proprietary, observers may find it useful to display the same regions of the sky using images available from 2Mass or other archives.

STScI is working to avoid persistence problems at the planning stage and is also developing tools to help users remove artifacts from the data (as was done for NICMOS). Planning observations of dense fields, globular clusters, or very bright star formation regions may be complicated in instances where precise photometery or very large dynamic range are required. Trade-offs must be evaluated between dithering and persistence, depending on the effectiveness of the persistence correction tools currently being developed.

Online

Updates on persistence characterization and tools for persistence artifact removal will be posted on the WFC3 persistence page.
See: http://www.stsci.edu/hst/wfc3/ins_performance/persistence/

7.9.5 The IR Background

In space, the dominant sources of background radiation are zodiacal light and earthshine at shorter IR wavelengths, and the telescope thermal emission at longer wavelengths. For *HST*, the sum of these two background components has a minimum at about 1600 nm (roughly lying in the H band).

The surface brightness of zodiacal light is a function of the ecliptic latitude and longitude, and reaches a minimum ~120 degrees from the sun, i.e., near, but not at, the ecliptic poles increasing again to 180 degrees (anti-solar direction).

Figure 7.10 shows the observed background levels in the first few months of WFC3's operation (green), compared with values predicted from known instrument sensitivities and expected levels of zodiacal light. These preliminary values will be updated in the course of the Cycle 17 calibration campaign.

Figure 7.10: Infrared background levels for WFC3. The average, low and high zodiac points show the **synphot** predictions for three levels of zodicial light and no earth-shine. The observations selected include calibration and GO images of empty or sparsely populated fields, giving an accurate representation of early WFC3 observations but not covering all background conditions. Observational means (green points), ranges (error bars), and exposure counts are plotted..

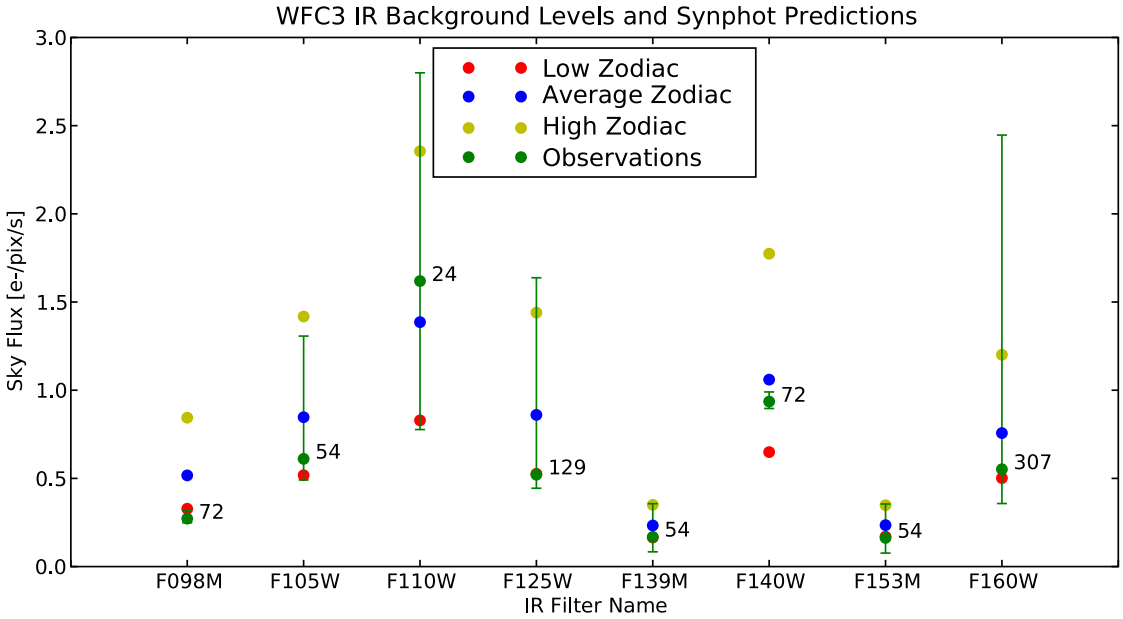

For pointings very close to the bright Earth limb, the zodiacal background may be exceeded by earth-shine. The brightness of the earth-shine falls very rapidly with increasing angle from the Earth's limb (due to the effectiveness of the *HST* baffles), and for most observations only a few minutes at the beginning and end of the target visibility period are significantly affected. The major exception to this behavior is a target in the continuous viewing zone (CVZ). Such targets are always be rather close to the Earth's limb, and so can sometimes see an elevated background for part of the orbit, even at shorter wavelengths where zodiacal emission ordinarily dominates.

For targets faint enough that the background level is expected to be much brighter than the target, the observer has two options when crafting the Phase II proposal:

(1) specify a non-standard Bright Earth Avoidance (BEA) angle, which increases the angle from the Earth's limb from 20° to 25° (note that this is an available mode and must be specially requested through a Contact Scientist), or (2) specify the LOW-SKY option, which restricts observations to targets more than 40° away from the Earth's limb and restricts scheduling to times when the zodiacal background is no greater than 30% above the minimum achievable level. The second option decreases the available observing (visibility) time during each orbit and implies scheduling constraints.

7.9.6 Optical Anomalies

Anomalous features are found in some IR detector images. For example, the optical system may cause stray light from sources outside the detector FOV to be scattered into images.

Examples of stray light features may be found on the WFC3 Web site. See:
http://www.stsci.edu/hst/wfc3/ins_performance/stray_light/

7.10 IR Observing Strategies

7.10.1 Dithering Strategies

For imaging programs, STScI generally recommends that observers employ dithering patterns. Dithering refers to the procedure of moving the telescope by small angle offsets between individual exposures on a target. The resulting images are subsequently combined in the pipeline or by the observer using software such as *MultiDrizzle* (see the *MultiDrizzle Handbook*).

Dithering is used to improve image quality and resolution. By combining multiple images of a target at slightly different positions on the detector, one can compensate for detector artifacts (blemishes, dead pixels, hot pixels, transient bad pixels, and plate-scale irregularities) that may not be completely corrected by application of the calibration reference files. Combining images, whether dithered or not, can also remove any residual cosmic ray flux that has not been well removed by the up-the-ramp fitting procedure used to produce flt images (see Section 7.7.2 and Appendix E). Effective resolution can be improved by combining images made with sub-pixel offsets designed to better sample the PSF. This is especially important for WFC3/IR, because the PSF is undersampled by a about factor of 2 (see Table 7.5).

Larger offsets are used to mosaic a region of sky larger than the detector field of view. (Large offsets can also be used for “chopping” to sample the thermal background. This has been recommended for NICMOS exposures at wavelengths

longer than 1.7 microns, where the telescope thermal background becomes increasingly dominant, but the thermal background is not a problem for WFC3/IR). In WFC3, all offsets must be accomplished by moving the telescope (whereas in NICMOS it is also possible to move the Field Offset Mirror). Dithers must be contained within a diameter ~130 arcsec or less (depending on the availability of guide stars in the region) to use the same guide stars for all exposures. The rms pointing repeatability is significantly less accurate if different guide stars are used for some exposures (see Section 4.1 of the *MultiDrizzle Handbook*). Mosaic steps and small dither steps are often combined to increase the sky coverage while also increasing resolution and removing artifacts. (See Section 6.10.1 for a discussion of the effect of geometric distortion on PSF sampling for mosaic steps).

The set of Pattern Parameters in the observing proposal provides a convenient means for specifying the desired pattern of offsets. The pre-defined mosaic and dither patterns that have been implemented in APT to meet many of the needs outlined above are described in detail in the Phase II Proposal Instructions. The WFC3 patterns in effect in APT at the time of publication of this Handbook are summarized in Appendix C. Observers can define their own patters to tailor them to the amount of allocated observing time and the desired science goals of the program. Alternatively, they can use POSTARGs to implement dither steps (Section 7.4.3), but the exposures are then not be associated and automatically combined in the OPUS pipeline.

7.10.2 Parallel Observations

Parallel observations, i.e., the simultaneous use of WFC3 with one or more other *HST* instruments, are the same for the IR channel as for the UVIS channel, previously described in Section 6.10.2.

7.10.3 Exposure Strategies

Given the variety of requirements of the scientific programs that are be executed with WFC3/IR, it is impossible to establish a single optimum observing strategy. In this section we therefore provide a few examples after guiding the reader through the main constraints that should be taken into account when designing an observation:

- Integrate long enough to be limited by background emission and not read noise. Dark current is rarely the limiting factor.
- Dither enough so that resolution can be restored to the diffraction limit and bad pixels and cosmic-ray impacts can be removed, while maintaining a homogeneous S/N ratio across the field.
- Split the MULTIACCUM ramps into as many reads as possible for readout noise suppression.

These constraints put contradictory requirements on the ideal observing strategy. It is clear that, given a certain amount of total observing time, the requirement of long

integrations for background limited performance is incompatible with a large number of dithering positions. Also, to split ramps for readout noise suppression decreases the observing efficiency, with a negative impact on the signal to noise ratio. Because the background seen by each pixel depends on the filter (Section 7.9.5), the optimal compromise must be determined on a case-by-case basis.

In this regard, it is useful to consider Table 7.11, which summarizes the total background seen by a pixel, including sky, telescope, and nominal dark current, and the time needed to reach 400 e^-/pixel of accumulated signal, corresponding to 20 e^-/pixel of Poisson-distributed background noise. This last value, higher than the expected readout noise of ~15 electrons after 16 reads, is used here to set the threshold for background-limited performance. The passage from readout-limited performance to background-limited performance can be regarded as the optimal exposure time for that given filter, in the sense that it allows for the largest number of dithered images without significant loss of S/N ratio (for a given total exposure time, i.e., neglecting overheads). For faint sources, the optimal integration time strongly depends on the background (zodiacal, Earth-shine thermal, and dark current) in each filter, ranging from just 220 s for the F110W filter to 2700 s for some of the narrow-band filters.

The optimal integration time shown in Table 7.11 can be compared with the integration times of the sampling sequences from Table 7.8. Table 7.12 synthesizes the results, showing for each filter which ramp (SPARS, STEP) most closely matches the optimal integration times for NSAMP=15.

Table 7.11: Background (e^-/pix/s) levels at the WFC3/IR detector. The columns show, from left to right: a) filter name; b) thermal background from the telescope and instrument; c) zodiacal background; d) earth-shine background; e) dark current; f) total background; g) integration time needed to reach background-limited performance, set at an equivalent readout noise of 20 electrons.

Filter	Thermal	Zodiacal	Earth-shine	Dark Current	Total	Optimal Integration Time (sec)
F105W	0.051	0.774	0.238	0.048	1.111	360
F110W	0.052	1.313	0.391	0.048	1.804	222
F125W	0.052	0.786	0.226	0.048	1.112	360
F140W	0.070	0.968	0.267	0.048	1.353	296
F160W	0.134	0.601	0.159	0.048	0.942	425
F098M	0.051	0.444	0.140	0.048	0.683	586
F127M	0.051	0.183	0.052	0.048	0.334	1198
F139M	0.052	0.159	0.044	0.048	0.303	1320
F153M	0.060	0.153	0.041	0.048	0.302	1325
F126N	0.051	0.037	0.011	0.048	0.147	2721
F128N	0.051	0.040	0.011	0.048	0.150	2667

Filter	Thermal	Zodiacal	Earth-shine	Dark Current	Total	Optimal Integration Time (sec)
F130N	0.051	0.041	0.011	0.048	0.151	2649
F132N	0.051	0.039	0.011	0.048	0.149	2685
F164N	0.065	0.036	0.009	0.048	0.158	2532
F167N	0.071	0.035	0.009	0.048	0.163	2454

The selection of which sample sequence type (RAPID, SPARS, STEP; Section 7.7.3) must take into account the science goals and the restrictions placed on their use. Here are some factors to consider when selecting a sample sequence:

- The RAPID ramp is a uniform sequence of short exposures. With its relatively short maximum exposure time, is suitable for a target consisting of bright objects that would saturate after a few reads in the other sequences. It is not appropriate for background-limited performance.
- SPARS ramps, with their uniform sampling, provide the most robust rejection of cosmic-ray events, and can be trimmed by removing a few of the final reads to fine-tune the integration time with little degradation of the achieved readout noise. Thus they are considered the standard sampling mode.
- STEP ramps are preferable where large dynamic range is needed; e.g., for photometry of stellar clusters. These ramps begin with a sequence of four uniform (RAPID) reads and end with a sequence of much longer uniform reads. The transition between the two uniform read rates is provided by a short sequence of logarithmically increasing read times. This design provides for correction of any non-linearities early in the exposure and allows for increased dynamic range for both bright and faint targets.

Table 7.12: Optimal exposure time for each WFC3/IR filter, along with the NSAMP=15 sequences that provide the closest match. The benefits and disadvantages of each sequence type are discussed in the accompanying text.

Filter	Optimal exposure time (sec)	SPARS	STEP
F105W	360	SPARS25	STEP50
F110W	222	SPARS25	STEP25
F125W	360	SPARS25	STEP50
F140W	296	SPARS25	STEP25
F160W	425	SPARS25	STEP50
F098M	586	SPARS50	STEP50
F127M	1198	SPARS100	STEP200
F139M	1320	SPARS100	STEP200
F153M	1325	SPARS100	STEP200
F126N	2721	SPARS200	STEP400
F128N	2667	SPARS200	STEP400
F130N	2649	SPARS200	STEP400
F132N	2685	SPARS200	STEP400
F164N	2532	SPARS200	STEP400
F167N	2454	SPARS200	STEP400

CHAPTER 8:

Slitless Spectroscopy with WFC3

In this chapter . . .

8.1 Grism Overview

WFC3 provides a slitless spectroscopy mode in both of its channels. The UVIS channel has a single grism and the IR channel two grisms, enabling low-resolution slitless spectroscopy over the entire field of view of both detectors.

In the UVIS channel, the G280 grism provides spectroscopy over a useful wavelength range of 200–400 nm, at a dispersion of about 1.4 nm per pixel in the first order. Reduced sensitivity and second-order contamination interfere with grism observations at wavelengths longer than 400 nm.

The two grisms for the IR channel cover the wavelength ranges 800–1150 nm (G102), and 1075 nm to 1700 nm (G141). The dispersions are 2.45 and 4.65 nm per pixel, respectively.

Table 8.1 summarizes the capabilities of the three WFC3 grisms in first-order mode. The resolving power is listed for each grism at a wavelength near the center of its range of coverage. The dispersion differs slightly between the two chips of the UVIS channel, and the mean value is listed. The tilt of the dispersion direction relative to the detector *x*-axis is also listed.

Table 8.1: WFC3 UVIS and IR Grisms.

Grism	Channel	Wavelength range (nm)	Resolving power[1]	Dispersion (nm/pixel)	Tilt (deg)[2]
G280	UVIS	200–400	70 @ 300 nm	1.4	–3
G102	IR	800–1150	210 @ 1000 nm	2.45[3]	+0.7
G141	IR	1075–1700	130 @ 1400 nm	4.65[3]	+0.5

1. Resolving power is based on the FWHM of the Gaussian image core measured in direction perpendicular to the dispersion.
2. Tilt of dispersion direction with respect to the positive *x*-axis of the image frame.
3. The dispersion varies over the field by ±4%; the tabulated value refers to the field center.

8.2 Slitless Spectroscopy with the UVIS G280 Grism

The G280 grism is a WF/PC1 spare. Figure 8.1 shows a spectrum of the wavelength calibration star WR14 observed as part of the Cycle 17 calibration program 11935. The circled spot shows the location of a direct image of the source obtained with a separate (undispersed) F300X filter exposure, but superposed on the grism image for illustrative purposes only. The prominent star-like feature near the center of the picture is the zeroth-order grism image, and the positive and negative higher orders extend towards the left and right of the zeroth order, respectively. The +1st order is defined to be the order with the higher throughput (due to the grating blaze), even though it falls at lower *x*-pixels than the position of the zeroth order. The +1st order extends to the left of the zeroth order a distance of about 1/4 of the image size. Further left there is heavy overlap with higher orders. Some prominent emission lines can be seen along the spectral trace.

Figure 8.1: Appearance of the G280 spectral orders on the detector. The circled source is the position of the direct image formed by summing an F300X image with the grism image. The stronger 1st order is to the left and the 0th order is in the center. Above the 1st orders, much weaker 2nd and 3rd orders are barely visible. The image shows the full extent of the detector in the *x*-axis and about 500 pixels in the *y*-axis.

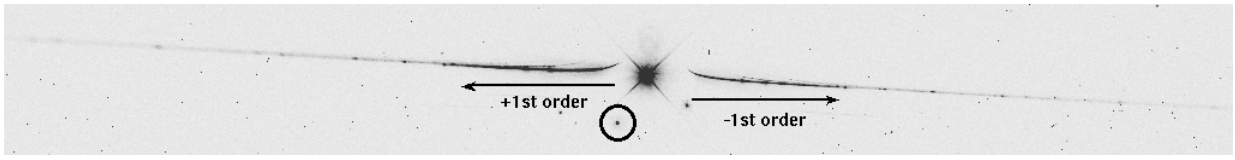

There are several features of this grism that differ, for example, from the G800L grism on ACS. There is an offset of about 160 pixels in the *y*-direction between the direct image and the spectra, the zeroth-order is relatively bright due to a lower grating efficiency and clear substrate, and there is curvature of the spectra at the blue ends of

the first orders (nearest the zeroth order). The amplitude of the curvature is about 30 pixels in the detector *y*-direction.

The dispersion has been measured during ground calibration and can be fitted by a fourth-order polynomial with an average dispersion of 1.4 and 1.5 nm/pixel in the +1st and −1st orders, respectively (WFC3 ISR 2009-01). The dispersion per pixel in the higher orders is higher by the approximate ratio of the orders; for example, in +3rd order it is 0.48 nm per pixel. These values were determined for UVIS Chip 1, and slight differences can be expected for Chip 2.

Figure 8.2 shows the absolute efficiency (including the instrument and CCD detector but not the telescope) for orders −2 through +3 as a function of wavelength, based on ground calibration data. The +1st order is more sensitive than the zeroth order at wavelengths less than 320 nm, but longward of this wavelength the zeroth order dominates. On deep exposures, orders out to at least −8 and +8 have been detected. The distortion of the spectral traces and the dispersion solution for at least the first few positive and negative orders have been calibrated to allow determination of absolute wavelengths to better than one pixel. The G280 grism will be calibrated in sensitivity during Cycle 17, allowing the determination of absolute fluxes to better than about 10% accuracy.

Figure 8.2: The absolute throughput of the G280 grism as a function of wavelength for the first few orders.

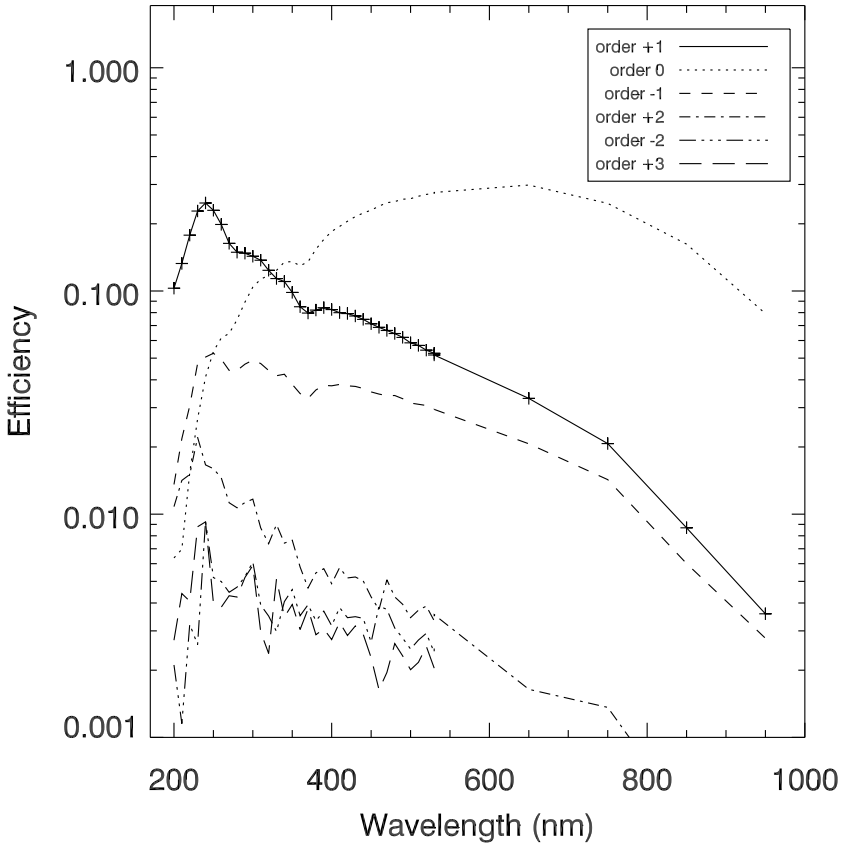

First-order spectra longward of 400 nm are likely to be overlapped by second-order light longward of 200 nm, for sufficiently hot sources.

Operationally, every grism exposure should always be accompanied by a direct image taken at the same guide-star pointing. This direct image allows the zero-point of the wavelength scale, and the size of the dispersed target, to be determined; the latter enables the size of the software extraction slit to be tuned to the object size (see Section 8.5). The 0th-order trace is slightly dispersed (making it difficult to centroid) and often saturated (making it impossible to centroid), so it cannot be used in place of a direct image for spatial and spectral calibration of the grism data. For slitless spectra, since the object takes the place of the slit in a conventional spectrograph, the spectral resolution is dependent on the object size, being lower for larger objects. The "natural" choice of a direct-imaging filter to provide the reference image for a grism exposure is F300X, since its response matches most closely the +1st-order grism response. However for fainter objects, or those with an unknown spectrum, the broader F200LP filter may be preferable.

For sufficiently bright objects, the multiple spectral orders may extend across the full field of view of the camera. This leads to overlapping of fainter spectra in the vicinity of the bright-object spectrum. Therefore, a careful determination of the optimum telescope roll angle is required to obtain non-overlapped spectra of faint objects in the vicinity of much brighter objects.

8.3 Slitless Spectroscopy with the IR G102 and G141 Grisms

8.3.1 IR G102

The G102 grism provides first-order spectra over the wavelength range from the grism short-wavelength cutoff at about 800 nm up to 1150 nm. The dispersion is high enough that only the positive first and second-order spectra, as well as the zeroth-order image, are visible on the detector when the positive first-order spectrum is centered in the field of view.

Figure 8.3 shows the disposition of the zeroth-order image and +1st-order spectrum (which has much higher sensitivity than the –1st order due to the grating blaze) for the G102 grism. The location of the direct image (superposed from an F098M undispersed exposure) is indicated in the figure.

Figure 8.3: G102 grism observation of the flux standard star GD153 (program 11552) with a F098M direct image (circled) superimposed to illustrate the relative positions. Spectral orders 0, +1, and +2 can be seen on the image. The image shows the full extent of the detector in the *x*-axis and about 200 pixels in the *y*-axis.

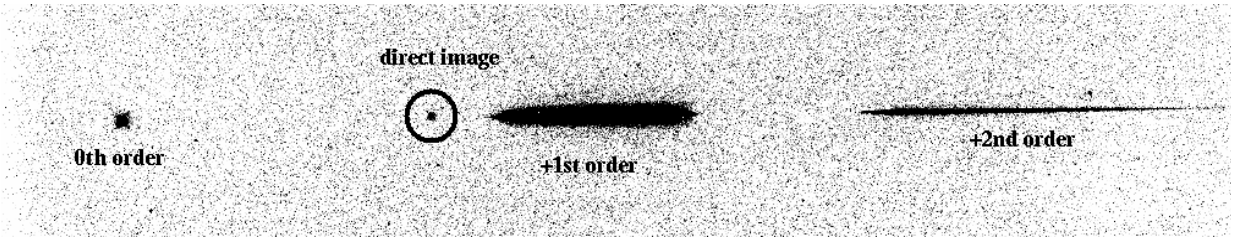

The trace of the first-order spectrum is well described by a first-order polynomial, however the offset and slope are a function of source position in the field. The tilt of the spectrum is 0.7° with respect to the detector *x*-axis. The total throughput (including *HST* optics) of the G102 grism has a maximum of 41.8% at 1100 nm in the positive first order and is above 10% between 800 and 1150 nm. The zeroth order and other negative and positive orders show much lower throughput (see Figure 8.4). The dispersion in the +1st order varies over the field from 2.36 to 2.51 nm/pixel; this variation was calibrated from both ground and on-orbit data to allow absolute wavelength calibration to better than one pixel. The absolute throughput of the G102 orders –1 to +3, including the instrument and the detector, is shown in Figure 8.4. Operationally, a grism exposure should always be accompanied by a direct image taken at the same guide star pointing. Suitable filters for the accompanying direct images for source selection and wavelength zero-point determination are F098M or F105W.

Figure 8.4: The absolute throughput of the G102 grism as a function of wavelength.

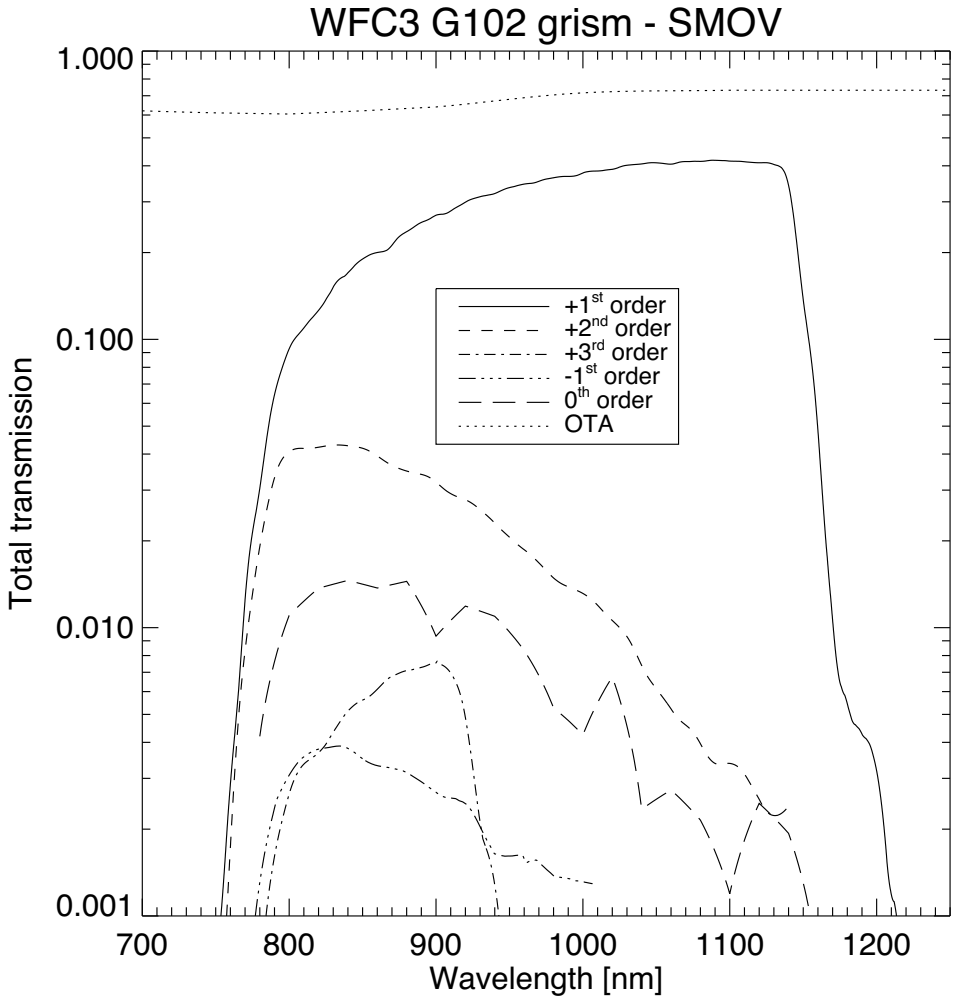

8.3.2 IR G141

For the lower-dispersion G141 grism, the zeroth-, first-, second-, and third-order spectra all lie within the field of view when the positive first-order is roughly centered. Figure 8.5 shows the appearance of the spectra on the detector, with the superposed direct image, for the G141 grism.The useful spectral range is from 1075 nm to about 1700 nm, limited in the red by the grism bandpass. Over most of the spectral range, more than 80% of the throughput is in the +1st-order spectrum. The trace of the first-order spectrum is well described by a first-order polynomial. The average tilt of the spectrum is 0.5 degrees with respect to the detector *x*-axis. The dispersion in the +1st-order varies over the field from 4.47 to 4.78 nm/pixel; this variation has been measured from both ground and on-orbit data to allow absolute wavelength calibration to better than one pixel. The total throughput (including *HST* optics) of the G141

grism reaches a maximum of 47.5% at ~1450 nm in the positive first order and is above 10% between 1075 and 1700 nm (see Figure 8.6).

Figure 8.5: G141 grism observation of the flux standard star GD153 (program 11552) with a F140W direct image (circled) superimposed to illustrate the relative positions. Spectral orders 0, +1, +2, and +3 can be seen in the image. The image shows the full extent of the detector in the *x*-axis and about 200 pixels in the *y*-axis.

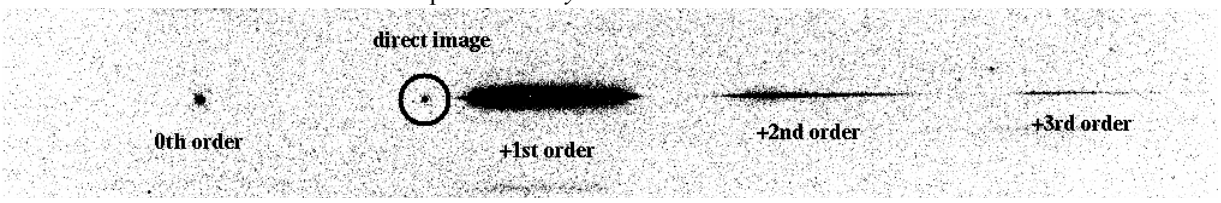

Figure 8.6: The absolute throughput of the G141 grism as a function of wavelength.

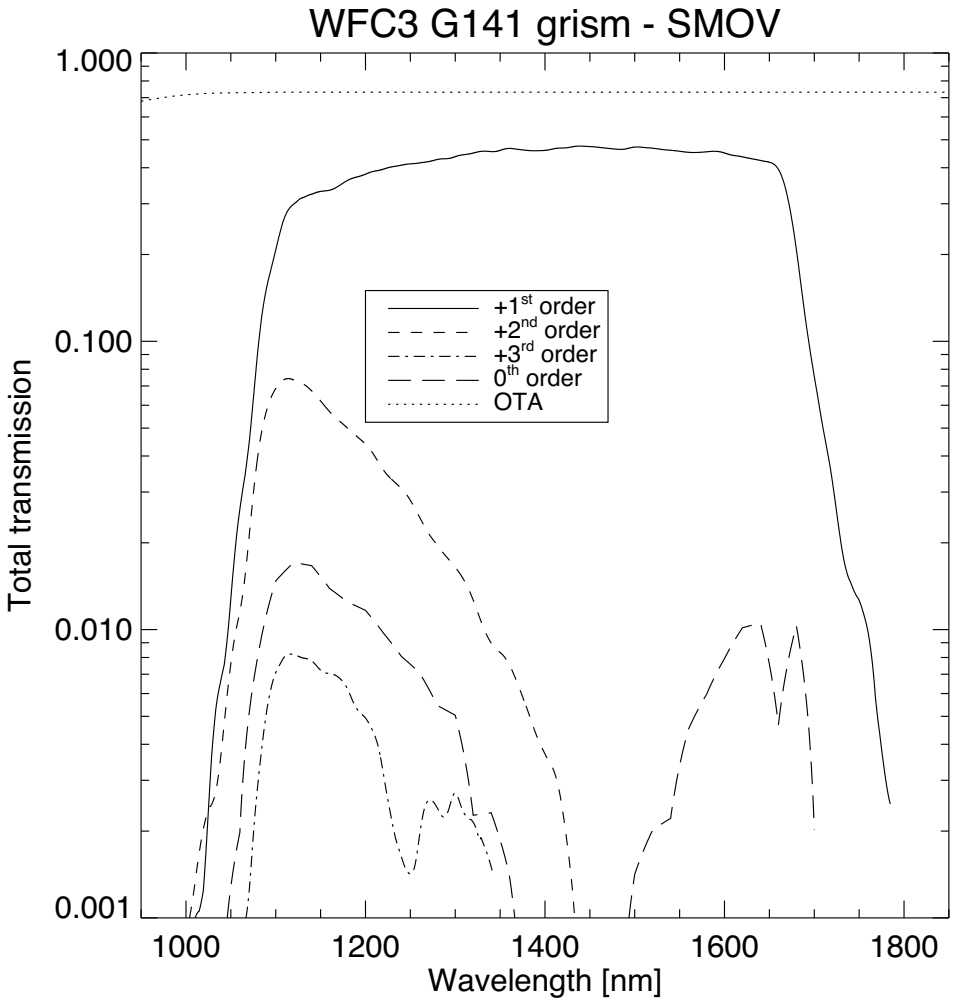

Operationally, a grism exposure should always be accompanied by a direct image taken at the same guide star pointing. Suitable filters for the accompanying direct images for source selection and wavelength zero-point determination are F140W or F160W in the case of extremely red sources.

8.4 Sensitivities and Exposure-Time Estimation

Table 8.2 lists current estimates of the detection limits for slitless spectroscopy with the UVIS and IR modes. The numbers in the table are the *V* magnitudes of sources for which a 1-hour exposure yields a spectrum with a S/N of 5 per resolution element, with extraction boxes of 1×5 and 1×3 pixels for the UVIS and IR, respectively. *V* magnitudes are given for three different assumed source spectral types.

Table 8.2: *V*-band detection limits for the WFC3 grism modes for 1-hour exposure and 5σ detection.

Mode	Spectral Type			Wavelength (nm)
	O3 V	A0 V (Vega)	G2 V	
UVIS/G280	24.8	21.8	18.2	250
IR/G102	21.3	21.9	22.9	1050
IR/G141	20.5	21.3	22.8	1550

For more accurate estimations of exposure times, observers should use the WFC3 Exposure Time Calculator (ETC). The ETC supports all three spectroscopic modes.

For more detailed simulations of WFC3 slitless data, a simulator is available that can generate 2D images (dispersed as well as direct) of synthetic target fields. The simulator package, aXeSIM, is available via a Web interface (reduced functionality) and as a stand-alone IRAF package (full functionality). For further information, see:

http://www.stecf.org/software/slitless_software/axesim/.

8.5 Extraction and Calibration of Spectra

Because there is no slit in the WFC3 grism mode, the PSF of the target determines the spectral resolution. In the case of non-stellar sources, it is the extent of the target in the direction of dispersion that limits the spectral resolution. The height of the software extraction slit is based on the object extent in the cross-dispersion direction of the direct image.

The dispersion of the grisms is well characterized, but in order to set the wavelength zero-point, it is necessary to know the position of the target in the direct image. The zeroth-order is generally too weak and is also slightly extended in a dispersed image to allow the wavelength zero-point to be set reliably. Given the typical spacecraft jitter, wavelength zero-points to ±0.5 pixels should be routinely achievable using a direct image taken just before or after the grism image.

A spectral extraction software package, called **aXe**, is available to extract, flat-field, wavelength- and flux-calibrate WFC3 grism spectra. Full details can be found at:

http://www.stecf.org/software/slitless_software/axe/.

The package is also available in STSDAS.

The spectral trace and dispersion solutions are a function of source position within the field of view. These 2-dimensional variations were determined during the ground calibration campaigns and from on-orbit data. The resulting reference and calibration files are used in the extraction software aXe and are also available from:

http://www.stecf.org/instruments/WFC3grism/.

For bright sources, the multiple spectral orders of the G280, G102 and G141 grisms may extend across the full detector extent. Therefore, a careful selection of the optimum telescope roll angle is required to obtain non-overlapping spectra of faint sources in the vicinity of brighter objects.

The quality of extracted spectra from single grism exposures can be degraded by bad pixels (e.g., dead, hot, strong cosmic ray hit). We therefore recommend a dithering strategy for grism exposures. The aXe software automatically takes dither steps into account by using the information in the image headers to produce a combined spectrum.

CHAPTER 9:

WFC3 Exposure-Time Calculation

In this chapter . . .

9.1 Overview

Chapter 4 of this *Handbook* describes the procedures for designing a Phase I WFC3 observing proposal. Two of the steps involved in this process are estimating the exposure times needed to achieve your scientific goals, and then combining these individual exposures with their associated overheads to derive the number of spacecraft orbits that you will request in your Phase I proposal.

This chapter gives guidance on estimating exposure times. The following chapter, Chapter 10, then describes how to include the various overheads so as to determine the total number of spacecraft orbits needed for your program.

You should also refer to the *Call for Proposals*, which includes information on policies and practices with respect to orbit-time requests. The *HST Primer* provides specific advice on orbit determination. Below, we provide a summary of the WFC3 sensitivities and give several examples that illustrate how to calculate your exposure times for Phase I Proposals.

9.2 The WFC3 Exposure Time Calculator (ETC)

In most cases, you will find it convenient to use the online WFC3 Exposure Time Calculator (ETC) to make estimates of the required exposure times for your project. The ETC is available from the WFC3 Web site at:

`http://www.stsci.edu/hst/wfc3/tools/etcs/`

The ETC calculates count rates for given source and background parameters. Once these are entered, the ETC then outputs signal-to-noise (S/N) ratios achieved for a given exposure time, or the exposure times required to achieve a given S/N ratio. The ETC supports both direct-imaging and spectroscopic (grism) observations. The aXeSIM tool is also available for simulation of grism observations (see Section 8.4). A variety of extraction apertures may be assumed in the ETC, both circular and square, allowing the user to select either a radius in arcseconds or a size in pixels. It is also possible to input a calibrated spectral-energy distribution (SED) of your source directly into the ETC. The ETC also outputs peak per-pixel count rates and total count rates, to aid in feasibility assessment. Warnings will appear if the source will saturate the detector, which would not only compromise CCD and IR observations, but might even affect subsequent exposures with the IR channel (see Appendix D). The ETC has extensive online help for its execution and interpretation of results.

It is also possible to use ***synphot*** in STSDAS to calculate count rates and the wavelength distribution of detected counts.

The remaining sections of this chapter give detailed information on the sensitivities of the UVIS and IR channels when combined with the various spectral elements, and the use of this information in the determination of count rates, for those who wish to understand the subject in depth.

9.3 Sensitivity Data

In this section, formulae appropriate for WFC3's imaging and spectroscopic modes are provided, from which one can calculate the expected count rates and the S/N ratio achieved in a given exposure time, based on the spectral energy distribution of a source. The formulae are given in terms of sensitivities, but we also provide transformation equations between throughput (QT) and sensitivity (S) for imaging and spectroscopic modes.

Throughputs are presented in graphical form as a function of wavelength for each of the imaging filters and grisms in Appendix A. Given the source characteristics and the sensitivity of the WFC3 configuration, calculating the expected count rate over a given number of pixels is straightforward. The additional information required is the encircled energy fraction (ε_f) in the peak pixel, the plate scale, and (for the spectroscopic modes) the dispersions of the grisms.

The sensitivity information is summarized in Tables 9.1 and 9.2. In these two tables, and in the following discussion, the filter transmission functions are denoted $T(\lambda)$, and the overall system response function (apart from the filter transmission) is

denoted $Q(\lambda)$. The terms "counts" and "count rates" always refer to the number of detected *electrons*, which is converted to data numbers, or DNs, according to the gain factors for the detectors. The measured gain is 1.6 e^-/DN for the UVIS channel and 2.4 e^-/DN for the IR channel (see Table 5.1).

In Tables 9.1 and 9.2, the following quantities are listed:

1. The filter or grism designation.
2. The "pivot wavelength" for that filter or grism, λ_p. Pivot wavelength is a source-independent measure of the characteristic wavelength of a bandpass, defined such that it is the same if the input spectrum is given in units of F_λ or F_ν (see A. Tokunaga & W. Vacca 2005, *PASP*, **117**, 421):

$$\lambda_p = \sqrt{\frac{\int Q(\lambda)T(\lambda)\lambda d\lambda}{\int Q(\lambda)T(\lambda)d\lambda/\lambda}}$$

3. The integral $\int Q_\lambda T_\lambda \, d\lambda/\lambda$, used to determine the count rate when given the astronomical magnitude of the source.
4. The ABmag zero-point, defined as the AB magnitude of a source with a flat F_ν that yields 1 count s^{-1} with the specified configuration.
5. The sensitivity integral, $\int S_\lambda \, d\lambda$, defined (see Section 9.4) as the count rate that would be detected from a flat F_λ source with a flux of 1 erg cm^{-2} s^{-1} $Å^{-1}$.
6. The ensquared energy, defined as the fraction of PSF flux enclosed in the default photometry aperture (5×5 pixels for the UVIS and 3×3 pixels for the IR).
7. The fraction of the total PSF flux in the central pixel for a centered stellar source, useful for determining the peak count rate to check for saturation (see also Appendix D).
8. The sky background count rate (electrons s^{-1}), which is the count rate that would be measured with average zodiacal background and average earth-shine. For the IR channel, this quantity also includes the thermal background from *HST* and the instrument. It does not include the contribution from the detectors themselves (i.e., dark current and read noise).

The next two sections describe how to calculate two quantities:

- The count rate in counts s^{-1}, C, from your source over some selected area on the detector containing N_{pix} pixels.
- The peak count rate in counts s^{-1} $pixel^{-1}$, P_{cr}, from your source, which is useful for avoiding saturated exposures.

We consider the cases of point sources and diffuse sources separately in each of the following imaging and spectroscopy sections.

Table 9.1: Sensitivity Data for WFC3/UVIS Channel.

Spectral Element	Pivot λ (Å)	$\int Q_\lambda T_\lambda d\lambda/\lambda$	ABMAG zero-point	$\int S_\lambda d\lambda$	Ensquared energy	Energy in central pixel	Background (sky) rate
F200LP	4970.9	0.3543	27.36	1.99E+19	0.75	0.17	0.1277
F218W	2230.6	0.0060	22.93	6.77E+16	0.70	0.13	0.0005
F225W	2373.6	0.0169	24.06	2.17E+17	0.71	0.14	0.0066
F275W	2710.1	0.0183	24.14	3.06E+17	0.74	0.15	0.0037
F280N	2833.5	0.0010	20.93	1.74E+16	0.74	0.16	0.0000
F300X	2822.1	0.0378	24.93	6.86E+17	0.74	0.16	0.0133
F336W	3354.8	0.0292	24.65	7.49E+17	0.77	0.17	0.0018
F343N	3435.2	0.0146	23.90	3.93E+17	0.77	0.17	0.0011
F350LP	5858.4	0.2425	26.95	1.90E+19	0.76	0.17	0.1077
F373N	3730.2	0.0024	21.94	7.63E+16	0.78	0.18	0.0003
F390M	3897.3	0.0115	23.63	3.97E+17	0.78	0.18	0.0017
F390W	3924.5	0.0567	25.37	1.99E+18	0.78	0.18	0.0098
F395N	3955.2	0.0047	22.67	1.68E+17	0.78	0.18	0.0008
F410M	4109.0	0.0112	23.61	4.31E+17	0.78	0.18	0.0028
F438W	4326.5	0.0345	24.83	1.47E+18	0.78	0.19	0.0099
F467M	4682.6	0.0122	23.70	6.10E+17	0.78	0.19	0.0046
F469N	4688.1	0.0021	21.81	1.07E+17	0.78	0.19	0.0008
F475W	4773.6	0.0763	25.69	3.96E+18	0.78	0.19	0.0278
F475X	4941.4	0.1173	26.16	6.52E+18	0.78	0.18	0.0444
F487N	4871.4	0.0031	22.22	1.68E+17	0.78	0.19	0.0012
F502N	5009.6	0.0034	22.31	1.93E+17	0.78	0.19	0.0014
F547M	5447.4	0.0312	24.72	2.11E+18	0.78	0.18	0.0148
F555W	5308.1	0.0835	25.79	5.36E+18	0.78	0.18	0.0377
F600LP	7451.3	0.0892	25.86	1.13E+19	0.72	0.16	0.0575
F606W	5887.5	0.1090	26.08	8.60E+18	0.77	0.18	0.0569
F621M	6218.6	0.0280	24.60	2.47E+18	0.76	0.18	0.0163
F625W	6241.4	0.0651	25.52	5.78E+18	0.76	0.18	0.0374
F631N	6304.3	0.0023	21.90	2.09E+17	0.76	0.18	0.0014
F645N	6453.6	0.0032	22.26	3.07E+17	0.75	0.17	0.0019
F656N	6561.4	0.0007	20.54	6.48E+16	0.75	0.17	0.0004

Spectral Element	Pivot λ (Å)	$\int Q_\lambda T_\lambda d\lambda/\lambda$	ABMAG zero-point	$\int S_\lambda d\lambda$	Ensquared energy	Energy in central pixel	Background (sky) rate
F657N	6566.6	0.0048	22.68	4.70E+17	0.75	0.17	0.0029
F658N	6584.0	0.0011	21.09	1.08E+17	0.75	0.17	0.0006
F665N	6655.9	0.0051	22.74	5.10E+17	0.75	0.17	0.0031
F673N	6765.9	0.0044	22.58	4.54E+17	0.74	0.17	0.0027
F680N	6877.4	0.0137	23.83	1.47E+18	0.74	0.17	0.0086
F689M	6876.4	0.0249	24.48	2.68E+18	0.74	0.17	0.0156
F763M	7613.6	0.0196	24.21	2.58E+18	0.71	0.16	0.0130
F775W	7648.3	0.0354	24.86	4.72E+18	0.71	0.16	0.0236
F814W	8029.9	0.0443	25.10	6.51E+18	0.70	0.15	0.0299
F845M	8437.6	0.0133	23.79	2.15E+18	0.68	0.14	0.0092
F850LP	9168.4	0.0123	23.71	2.35E+18	0.66	0.13	0.0086
F953N	9530.6	0.0005	20.34	1.14E+17	0.65	0.12	0.0004
FQ232N	2431.1	0.0005	20.13	6.12E+15	0.71	0.14	0.0000
FQ243N	2476.4	0.0007	20.52	9.10E+15	0.72	0.14	0.0000
FQ378N	3792.4	0.0052	22.78	1.70E+17	0.78	0.18	0.0006
FQ387N	3873.7	0.0015	21.44	5.21E+16	0.78	0.18	0.0002
FQ422M	4219.2	0.0050	22.73	2.02E+17	0.78	0.18	0.0013
FQ436N	4367.2	0.0019	21.67	8.16E+16	0.78	0.19	0.0005
FQ437N	4371.0	0.0014	21.32	5.92E+16	0.78	0.19	0.0004
FQ492N	4933.4	0.0058	22.90	3.23E+17	0.78	0.19	0.0023
FQ508N	5091.0	0.0066	23.03	3.89E+17	0.78	0.19	0.0028
FQ575N	5757.7	0.0007	20.64	5.51E+16	0.77	0.18	0.0004
FQ619N	6198.5	0.0025	21.99	2.20E+17	0.76	0.18	0.0015
FQ634N	6349.2	0.0026	22.02	2.38E+17	0.76	0.18	0.0015
FQ672N	6716.4	0.0007	20.61	7.30E+16	0.75	0.17	0.0004
FQ674N	6730.7	0.0005	20.22	5.09E+16	0.75	0.17	0.0003
FQ727N	7275.2	0.0018	21.65	2.21E+17	0.73	0.16	0.0012
FQ750N	7502.5	0.0017	21.57	2.19E+17	0.72	0.16	0.0011
FQ889N	8892.2	0.0011	21.05	1.91E+17	0.67	0.13	0.0007
FQ906N	9057.8	0.0010	20.94	1.79E+17	0.66	0.13	0.0007
FQ924N	9247.6	0.0008	20.70	1.50E+17	0.66	0.13	0.0005
FQ937N	9372.3	0.0007	20.53	1.31E+17	0.65	0.13	0.0005
G280	5047.0	0.3172	25.87	2.89E+18	0.81	0.27	0.1136

Table 9.2: Sensitivity Data for WFC3/IR Channel.

Spectral Element	Pivot λ (Å)	$\int Q_\lambda T_\lambda d\lambda/\lambda$	ABMAG zero-point	$\int S_\lambda d\lambda$	Ensquared energy	Energy in central pixel	Background (sky + thermal) rate
F098M	9864.7	0.0753	25.68	1.67E+19	0.79	0.38	0.6106
F105W	10551.0	0.1297	26.27	3.29E+19	0.78	0.37	1.0150
F110W	11534.4	0.2161	26.82	6.55E+19	0.76	0.36	1.6611
F125W	12486.1	0.1269	26.24	4.51E+19	0.74	0.34	0.9986
F126N	12584.6	0.0060	22.93	2.16E+18	0.74	0.34	0.0957
F127M	12740.2	0.0293	24.65	1.08E+19	0.74	0.34	0.2697
F128N	12831.5	0.0065	23.01	2.43E+18	0.74	0.33	0.0984
F130N	13005.4	0.0065	23.02	2.50E+18	0.73	0.33	0.0993
F132N	13187.5	0.0063	22.98	2.49E+18	0.73	0.33	0.0976
F139M	13837.5	0.0252	24.49	1.10E+19	0.71	0.32	0.2391
F140W	13922.8	0.1550	26.46	6.84E+19	0.71	0.32	1.1694
F153M	15321.9	0.0245	24.46	1.31E+19	0.67	0.29	0.2361
F160W	15369.1	0.0970	25.95	5.22E+19	0.67	0.29	0.8002
F164N	16403.1	0.0060	22.93	3.67E+18	0.65	0.28	0.1050
F167N	16641.1	0.0058	22.89	3.65E+18	0.64	0.27	0.1092
G102	9970.4	0.1110	26.10	2.51E+19	0.79	0.42	1.2040
G141	13860.0	0.1796	26.62	7.86E+19	0.73	0.34	1.8619

9.4 Count Rates (Imaging)

9.4.1 Point Source

For a point source, the count rate, *C*, can be expressed as the following integral over the bandpass of the filter:

$$C = A\int F_\lambda \frac{\lambda}{hc} Q_\lambda T_\lambda \varepsilon_f d\lambda = \int F_\lambda S_\lambda \varepsilon_f d\lambda$$

where:

- A is the area of an unobstructed 2.4-m telescope (i.e., 45,239 cm^2)
- F_λ is the flux from the astronomical source in erg cm^{-2} s^{-1} $Å^{-1}$.

- The factor λ/hc (where h is Planck's constant and c is the speed of light) converts ergs to photons.
- $Q_\lambda T_\lambda$ is the system fractional throughput, i.e., the probability of detecting a count per incident photon, including losses due to obstructions of the full 2.4-m OTA aperture. It is specified this way to separate out the instrument sensitivity Q_λ and the filter transmission T_λ.
- ε_f is the fraction of the point-source energy encircled within N_{pix} pixels.
- S_λ is the total imaging point-source sensitivity in units of counts s^{-1} $Å^{-1}$ per incident erg cm^{-2} s^{-1} $Å^{-1}$.

The peak counts s^{-1} $pixel^{-1}$ from the point source, C_{peak}, is given by the following integral over the bandpass:

$$C_{peak} = \int F_\lambda S_\lambda \varepsilon_f(1) d\lambda$$

where:

- F_λ, and S_λ are as above.
- $\varepsilon_f(1)$ is the fraction of energy contained within the peak pixel.

If the flux from the source can be approximated by a flat continuum (F_λ = constant) and ε_f is roughly constant over the bandpass, then:

$$C = F_\lambda \varepsilon_f \int S_\lambda d\lambda$$

We can now define an equivalent bandpass of the filter, B_λ, such that:

$$\int S_\lambda d\lambda = S_{peak} B_\lambda$$

where:

- S_{peak} is the peak sensitivity.
- B_λ is the effective bandpass of the filter.

The count rate from the source can now be written as:

$$C = F_\lambda \varepsilon_f S_{peak} B_\lambda$$

In Tables 9.1 and 9.2 above, we give the value of $\int S_\lambda d\lambda$ for each of the filters. Alternatively, we can write the count-rate equation in terms of V magnitudes:

$$C = 2.5 \times 10^{11} \varepsilon_f \left(\int QT d\lambda / \lambda\right) \times 10^{-0.4(V + AB_\nu)}$$

where V is the visual magnitude of the source, the quantity under the integral is the mean sensitivity of the detector+filter combination (also tabulated in Tables 9.1 and 9.2), and AB_ν is the filter-dependent correction for the deviation of the source spectrum from a constant F_ν spectrum. This latter quantity is tabulated for some representative astronomical spectra in Appendix A.

9.4.2 Diffuse Sources

For a diffuse source, the count rate, C, which is now per pixel, due to the astronomical source can be expressed as:

$$C = \int I_\lambda S_\lambda m_x m_y d\lambda$$

where:

- I_λ is the surface brightness of the astronomical source, in erg cm^{-2} s^{-1} Å^{-1} arcsec^{-2}.
- S_λ is as above.
- m_x and m_y are the plate scales in arcsec pixel^{-1} along orthogonal axes.

9.4.3 Emission-Line Sources

For a source where the flux is dominated by a single emission line, the count rate can be calculated from the equation

$$C = 2.28 \times 10^{12} \cdot (QT)_\lambda \cdot F(\lambda) \cdot \lambda$$

where C is the observed count rate in counts s^{-1}, $(QT)_\lambda$ is the system throughput at the wavelength of the emission line, $F(\lambda)$ is the emission-line flux in units of erg cm^{-2} s^{-1}, and λ is the wavelength of the emission line in angstroms. $(QT)_\lambda$ can be determined by inspection of the plots in Appendix A. See Section 9.9.3 for an example of count-rate estimation for an emission-line source.

9.5 Count Rates (Slitless Spectroscopy)

We now turn to estimation of count rates for slitless spectroscopy using the WFC3 grisms. In this case we are dealing with a dispersed image of the source.

For a point source with a continuous spectrum, the count rate, C, is calculated per pixel along the dispersed spectral trace, and is integrated over a fixed extraction height N_{spix} in the spatial direction perpendicular to the dispersion. The count rate is:

$$C = F_\lambda S'_\lambda \varepsilon'_{Nspix} = F_\lambda A \frac{\lambda}{hc} Q_\lambda T_\lambda \varepsilon'_{Nspix} d$$

where:

- S_λ is the total point source sensitivity in units of counts s^{-1} per incident erg cm^{-2} s^{-1} Å^{-1}; and $S'_\lambda = S_\lambda \cdot d$.
- d is the spectral dispersion in Å pixel^{-1}.

- ε'_{Nspix} is the fraction of the point-source energy within N_{spix} in the spatial direction.
- the other quantities are as defined in the previous section.

For a source with an unresolved emission line with a flux of F in units of erg cm^{-2} s^{-1}, the total count rate recorded over the N_{spix} extraction height is:

$$C = FS_{\lambda}\varepsilon'_{Nspix}$$

These counts will be distributed over pixels in the dispersion direction according to the instrumental line-spread function.

In contrast to the case of imaging sensitivity S_{λ}, the spectroscopic point source sensitivity calibration ($S'_{\lambda} \times \varepsilon'_{Nspix}$) for a default extraction height of N_{spix} was measured directly from observations of stellar flux standards during SMOV and Cycle 17 calibration programs 11934, 11936, and 11552. Therefore, the accuracy in laboratory determinations of T_{λ} for the WFC3 grisms are not crucial to the final accuracy of their sensitivity calibrations.

The peak counts s^{-1} pixel^{-1} from the point source is given by:

$$P_{cr} = \varepsilon'_{f}(1)F_{\lambda}S'_{\lambda}$$

where:

- $\varepsilon'_{f}(1)$ is the fraction of energy contained within the peak pixel.
- the other quantities are as above.

9.6 Estimating Exposure Times

9.6.1 S/N Reached in a Given Exposure Time

To derive the exposure time to achieve a given S/N ratio, or to derive the S/N ratio achieved in a given exposure time, there are four principal ingredients:

- Expected count rate C from your source over some area.
- The area (in pixels) over which those counts are received (N_{pix}).
- Sky background (B_{sky}) in counts s^{-1} pixel^{-1}.
- The detector background, or dark, (B_{det}) in counts s^{-1} pixel^{-1} and the read noise (R) in counts. (Section 9.7 provides information for determining the sky-plus-detector background.)

The S/N ratio Σ achieved in exposure time *t* seconds, is given by:

$$\Sigma = \frac{Ct}{\sqrt{Ct + N_{pix}(B_{sky} + B_{det})t + \frac{N_{pix}}{N_{bin}} N_{read} R^2}}$$

where:

- C = the signal from the astronomical source in counts s^{-1}. (Note that the actual output image uses DN, which will be equal to Ct/G, where G is the gain.)
- N_{pix} = the total number of detector pixels integrated over to achieve C.
- N_{bin} = the number of detector pixels binned to one read-out pixel when on-chip binning is used.
- B_{sky} = the sky background in counts s^{-1} $pixel^{-1}$.
- B_{det} = the detector dark current in counts s^{-1} $pixel^{-1}$.
- R = the read noise in electrons; 3.15 e^- for the UVIS channel and 12.5 e^- for the IR channel (this is the effective read noise achieved by fitting the ramp of IR readouts, if close to the full sequence of 16 readouts is used).
- N_{read} = the number of detector readouts.

The above equation assumes the optimistic (but often realistic) condition that the background zero-point level under the object that is subtracted could be well known (from integrating over many pixels) but is still noisy in N_{pix} and does not significantly contribute to the error budget; in crowded fields this may not be true.In general, C in the numerator should be the signal in N_{pix} from the component to be measured (e.g., the point source in an image or the line emission in a spectrum), while C in the denominator is the total astronomical signal in N_{pix} (e.g., including light from the underlying galaxy in the image or from the continuum in the spectrum).

9.6.2 Exposure Time to Reach a Given S/N

Observers normally take sufficiently long integrations that the read noise is not important. This condition is met when:

$$Ct + N_{pix}(B_{sky} + B_{det})t > 2\frac{N_{pix}}{N_{bin}} N_{read} R^2$$

In the regime where read noise is unimportant, and virtually all of the astronomical signal in N_{pix} comes from the component being measured, the integration time to reach a given signal-to-noise ratio Σ is:

$$t = \frac{\Sigma^2 [C + N_{pix}(B_{sky} + B_{det})]}{C^2}$$

If the source count rate is much higher than that of the sky plus detector backgrounds, then this expression reduces further to:

$$t = \frac{\Sigma^2}{C}$$

i.e., the usual result for Poisson statistics of $\Sigma = \sqrt{totalcounts}$.

More generally, the required integration time to reach a given S/N ratio is:

$$t = \frac{\Sigma^2[C + N_{pix}(B_{sky} + B_{det})] + \sqrt{\Sigma^4[C + N_{pix}(B_{sky} + B_{det})]^2 + 4\Sigma^2 C^2\left[\frac{N_{pix}}{N_{bin}} N_{read} R^2\right]}}{2C^2}$$

9.6.3 Exposure Time Estimates for Red Targets in F850LP

At long wavelengths, ACS CCD observations are affected by a red halo due to light scattered off the CCD substrate. An increasing fraction of the light as a function of wavelength is scattered from the center of the PSF into the wings. This problem affects particularly the very broad z-band F850LP filter, for which the encircled energy depends on the underlying spectral energy distribution the most. At the current time, it is thought that this problem has been fixed for WFC3, and so this should not be a concern for those planning WFC3 observations.

9.7 Sky Background

As noted in the previous section, the backgrounds from the sky and from the detector must be taken into account when calculating expected S/N ratios or exposure times.

Detector backgrounds (as well as read-out noise) for the CCDs and IR detector are discussed in Chapter 5. This section deals with the sky backgrounds that can affect WFC3 observations.

The most important sources of sky background are:

- Earthshine (ES).
- Zodiacal light (ZL).
- Geocoronal emission (GC).

The background in counts s^{-1} $pixel^{-1}$ for imaging observations can be computed as:

$$B_{sky} = \int I_\lambda S_\lambda m_x m_y d\lambda$$

where:

- I_λ is the surface brightness of the sky background, in erg cm^{-2} s^{-1} $Å^{-1}$ $arcsec^{-2}$.
- S_λ is the point-source sensitivity for the imaging mode.
- m_x and m_y are the plate scales in arcsec $pixel^{-1}$ along orthogonal axes.

In the case of slitless spectroscopy, the image of the sky through a disperser is not uniform, because some wavelengths fall off the detector for regions of sky near the edge of the field of view. The regions of lower sky background will be strips at the long- and short-wavelength edges of the field of view; a UVIS grism spectrum is roughly 270 pixels long, while an IR grism spectrum is roughly 170 pixels long. The maximum width of the strips from where the signal starts to decline to the edge, where the signal is down by roughly a factor of 2, will be about half the total length of a spectrum of a point source, i.e., roughly 135 pixels (UVIS) or 85 pixels (IR), in the case of a sky background with a continuum of wavelengths. These small strips of lower sky background are ignored in the following formulae. Furthermore, since the spectra do not lie along the direction of the anamorphic distortion, the plate scales of m_x and m_y above must be replaced by the plate scales m_s and m_λ in the orthogonal spatial and dispersion directions, respectively. Interior to the strips, a point on the detector sees a region of sky over the full wavelength coverage of the disperser. Thus, for **spectroscopic observations**:

$$B^{\lambda}_{sky} = \int I_\lambda S'_\lambda m_s m_\lambda d\lambda$$

For a **monochromatic** sky emission line at $\lambda = L$ like [O II] 2471, which will dominate the background through the UVIS/G280 grism:

$$B^{L}_{sky} = I_L S'_\lambda m_s m_\lambda / d$$

where

- I_L is the monochromatic intensity of a line at wavelength L in erg cm^{-2} s^{-1} $arcsec^{-2}$.

The total sky background is:

$$B_{sky} = B^{\lambda}_{sky} + B^{L}_{sky}$$

Figure 9.1 and Table 9.3 show "high" sky background intensity as a function of wavelength, identifying the separate components which contribute to the background. The "shadow" and "average" values of the earth-shine contribution in the WFC3

Exposure Time Calculator (ETC) correspond, respectively, to 0% and 50% of the "high" values in Figure 9.1 and Table 9.3. For the zodiacal sky background, the values in Figure 9.1 and Table 9.3 correspond to the high value of *V*-band surface brightness of 22.1 mag arcsec^{-2} from Table 9.4, while the "low" and "average" zodiacal light is scaled to *V* surface brightnesses of 23.3 and 22.7 mag arcsec^{-2}, respectively.

In Table 9.3 we present the "high" sky-background numbers, which are plotted in Figure 9.1. See the text and the caption of Figure 9.1 for more details. These high sky values are defined as the earth-shine at 38° from the limb and the high zodiacal light of $V = 22.1$ mag arcsec^{-2}.

Table 9.3: High sky backgrounds.

Wavelength (Å)	Earth-shine	Zodiacal light	Total background
		(erg cm^{-2} s^{-1} Å^{-1} arcsec^{-2})	
2000	7.69E-22	7.94E-20	8.02E-20
2500	1.53E-21	3.83E-19	3.84E-19
3000	1.43E-19	1.63E-18	1.77E-18
3500	8.33E-19	2.72E-18	3.55E-18
4000	1.66E-18	3.12E-18	4.78E-18
4500	2.59E-18	4.97E-18	7.57E-18
5000	2.63E-18	5.07E-18	7.70E-18
5500	2.55E-18	5.17E-18	7.72E-18
6000	2.42E-18	5.14E-18	7.56E-18
7000	1.95E-18	4.48E-18	6.42E-18
8000	1.56E-18	3.82E-18	5.38E-18
9000	1.23E-18	3.18E-18	4.40E-18
10000	9.97E-19	2.70E-18	3.70E-18
11000	8.02E-19	2.26E-18	3.06E-18
12000	6.65E-19	1.94E-18	2.61E-18
13000	5.58E-19	1.68E-18	2.24E-18
14000	4.70E-19	1.46E-18	1.93E-18
15000	3.97E-19	1.26E-18	1.66E-18
16000	3.35E-19	1.09E-18	1.43E-18
17000	2.79E-19	9.27E-19	1.21E-18

Figure 9.1: Sky background intensity as a function of wavelength.The total sky spectrum (black) for the "high-background" case adopted in the WFC3 ETC, along with the individual contributions from zodiacal light and earth-shine. These data correspond to a *V*-band surface brightness of 22.1 mag arcsec^{-2}. The only significant geocoronal emission line in the WFC3 spectral range is [O II] 2471 Å, shown as a line; it has a flux of 1.5×10^{-15} erg cm^{-2} s^{-1} arcsec^{-2}, extending beyond the upper limit of the plot.

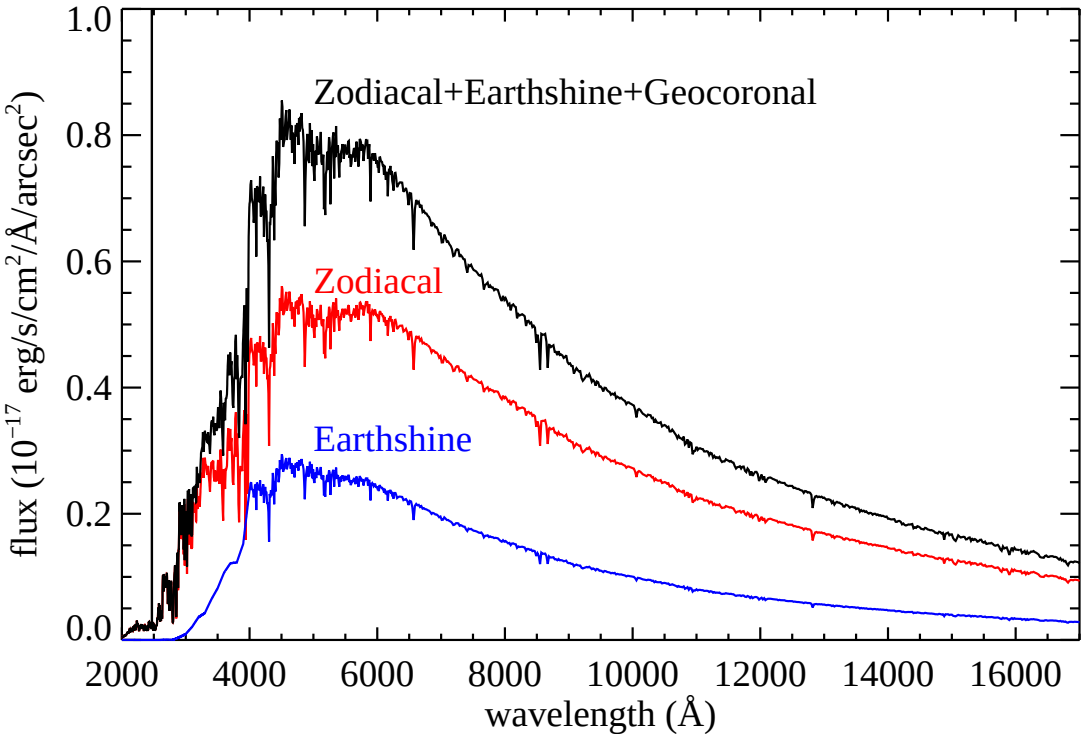

9.7.1 Background Variations and LOW-SKY

In the ultraviolet, the background contains a bright airglow line at 2471 Å, which varies in intensity from day to night and as a function of *HST* orbital position. The airglow line may be the dominant sky contribution in the UV both for imaging and spectroscopic observations. Away from the airglow line, at wavelengths shortward of ~3000 Å, the background is dominated by zodiacal light, where the small area of sky that corresponds to a pixel of the high-resolution *HST* instrumentation usually produces a signal that is much lower than the intrinsic detector background. The contribution of zodiacal light does not vary dramatically with time, but does vary by about a factor of about three throughout most of the sky as a function of distance from the Sun and ecliptic. Table 9.4 gives the variation of the zodiacal background as a function of ecliptic latitude and longitude relative to the Sun. For a target near ecliptic coordinates (50,0) or (–50,0), the zodiacal light is relatively bright at 20.9 mag arcsec^{-2}, i.e., about 9 times the faintest value of 23.3 mag arcsec^{-2}. Thus if you are considering deep imaging applications, you must carefully consider expected sky values.

On the other hand, earth-shine varies strongly depending on the angle between the target and the bright Earth limb. The variation of the earth-shine as a function of limb angle from the sunlit Earth is shown in Figure 9.2. The figure also shows the contribution of the moon, which is typically much smaller than the zodiacal contribution, for which the upper and lower limits are shown. For reference, the limb angle is approximately 24° when the *HST* is aligned toward its orbit pole (i.e., the center of the CVZ). The earth-shine contribution shown in Figure 9.1 and Table 9.3 corresponds to this position.

Figure 9.2: Background contributions in V magnitude per arcsec^2 due to the zodiacal light, Moon, and sunlit Earth, as a function of angle between the target and the limb of the Earth or Moon. The two zodiacal light lines show the extremes of possible values.

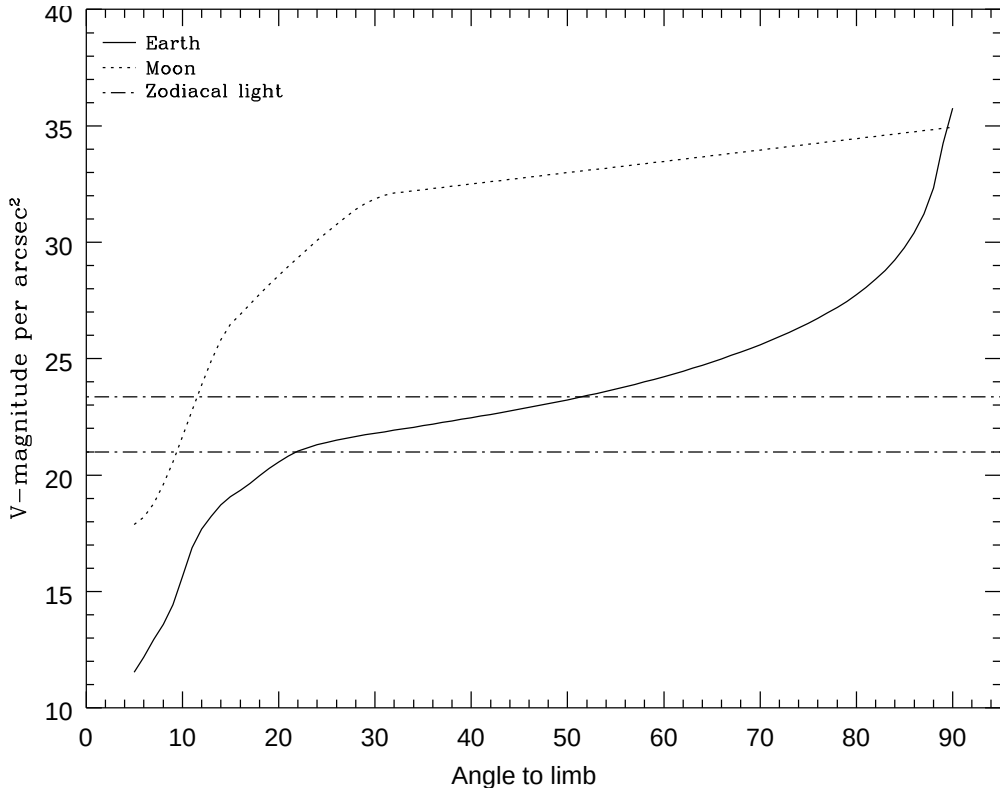

For observations taken longward of 3500 Å, earth-shine dominates the background at small (< 22°) limb angles. In fact, the background increases exponentially for limb angles < 22°. The background near the bright limb can also vary by a factor of ~2 on timescales as short as two minutes, which suggests that the background from earth-shine also depends upon the reflectivity of the terrain and the amount of cloud cover over which *HST* passes during the course of an exposure.

Table 9.4: Approximate zodiacal sky background as a function of ecliptic latitude and ecliptic longitude (in *V*-mag per arcsec^2). SA stands for Solar Avoidance zone, in which *HST* observations may not be made.

Ecliptic longitude (degrees)	Ecliptic latitude (degrees)						
	0	15	30	45	60	75	90
0	SA	SA	SA	SA	22.6	23.0	23.3
15	SA	SA	SA	SA	22.6	23.1	23.3
30	SA	SA	SA	22.3	22.7	23.1	23.3
45	SA	SA	22.1	22.5	22.9	23.1	23.3
60	21.3	21.9	22.4	22.7	23.0	23.2	23.3
75	21.7	22.2	22.6	22.9	23.1	23.2	23.3
90	22.0	22.3	22.7	23.0	23.2	23.3	23.3
105	22.2	22.5	22.9	23.1	23.3	23.3	23.3
120	22.4	22.6	22.9	23.2	23.3	23.3	23.3
135	22.4	22.6	22.9	23.2	23.3	23.4	23.3
150	22.4	22.6	22.9	23.1	23.3	23.4	23.3
165	22.3	22.5	22.8	23.0	23.2	23.4	23.3
180	22.1	22.4	22.7	23.0	23.2	23.4	23.3

Observations of the faintest objects may need the Special Requirement `LOW-SKY` in the Phase II observing program. `LOW-SKY` observations are scheduled during the part of the year when the zodiacal background light is no more than 30% greater than the minimum possible zodiacal light for the given sky position. `LOW-SKY` in the Phase II scheduling also invokes the restriction that exposures will be taken only at angles greater than 40° from the bright Earth limb to minimize earth-shine and the UV airglow lines. The `LOW-SKY` special requirement limits the times at which targets within 60° of the ecliptic plane will schedule, and limits visibility to about 48 minutes per orbit. The use of `LOW-SKY` must be requested and justified in the Phase I proposal.

The ETC provides the user with the flexibility to adjust separately both the zodiacal (low, average, high) and earth-shine (shadow, average, high) sky background components in order to determine if planning for use of `LOW-SKY` is advisable for a given program. However, the absolute sky levels that can be specified in the ETC may not be achievable for a given target; e.g., as shown in Table 9.4, the brightest zodiacal background for an ecliptic target is 21.3 V mag/arcsec^2, which is still brighter than both the low and average options with the ETC. By contrast, a target near the ecliptic pole would always have a zodiacal = low background in the ETC. The user is cautioned to carefully consider sky levels as the backgrounds obtained in *HST* observations can cover significant ranges.

9.7.2 Geocoronal Emission and SHADOW

Background due to geocoronal emission originates mainly from hydrogen and oxygen atoms in the exosphere of the Earth. In the far-UV spectral region, the strongest geocoronal emission lines are Lyman–α at 1216 Å, O I at 1304 Å, and O I] at 1356 Å, but WFC3 is of course not sensitive at these wavelengths. The only significant geocoronal emission line to which WFC3 is sensitive is [O II] 2471 Å, shown in Figure 9.1. In sunlight this line can be as bright as ~1.5×10^{-15} erg cm^{-2} s^{-1} arcsec^{-2}, while in Earth shadow it is much fainter, typically ~7.5×10^{-18} erg cm^{-2} s^{-1} arcsec^{-2}.

To minimize geocoronal emission the Special Requirement `SHADOW` can be requested. Exposures using this special requirement are limited to roughly 25 minutes per orbit, exclusive of the guide-star acquisition (or re-acquisition), and can be scheduled only during a small percentage of the year. `SHADOW` reduces the contribution from the geocoronal emission lines by roughly a factor of ten while the continuum earth-shine is set to zero. `SHADOW` requirements must be included and justified in your Phase I proposal (see the *Call for Proposals*).

9.8 Interstellar Extinction

Interstellar extinction can dramatically reduce the count rate detected from your source, particularly if you are working in the ultraviolet range but are inferring source brightnesses from optical data. Conversely, optically obscured objects may be much brighter in the IR than in the optical.

The Exposure Time Calculator includes the ability to correct exposure-time estimates for interstellar extinction based on the color excess $E(B–V)$. It may also be useful to refer to the standard references on interstellar extinction and its variations with location and metallicity, e.g., Fitzpatrick (1999, *PASP*, **111**, 63) and references therein.

9.9 Exposure-Time Calculation Examples

In the following sections you will find a set of examples for the two different channels and for different types of sources. The examples were chosen in order to present typical objects for the two channels and also to present interesting cases as they may arise with the use of WFC3.

9.9.1 Example 1: UVIS Imaging of a Faint Point Source

What is the exposure time needed to obtain a signal-to-noise of 10 for a point source of spectral type F0 V, normalized to $V = 27.5$, when using the UVIS F555W filter? Assume a photometry box size of 5×5 pixels, and average sky values.

The WFC3 Exposure Time Calculator (ETC) gives a total exposure time of 4419 s to obtain this S/N in a single exposure. Since such an exposure would be riddled with cosmic rays and essentially useless, it is necessary to specify how many exposures to split the observation into. WFC3/UVIS observations generally should be split if the exposure time is longer than about 5 minutes, but for multi-orbit observations, splitting into two exposures per orbit is generally sufficient.

For a typical object visibility of 53 minutes, after applying the requisite overheads, there is time for two exposures of approximately 1200 s per orbit. The required exposure time can thus be reached in 4 exposures, but re-running the ETC using `CR-SPLIT=4` raises the required exposure time to 4936 s (because of the extra noise introduced by the three extra readouts). To achieve the required exposure time would require `CR-SPLIT=5`, or three orbits; iterating the ETC one more time shows a total exposure time of 5089 s with this number of reads.

Using the pencil-and-paper method, Table 9.1 gives the integral $\int QTd\lambda/\lambda$ as 0.0835. An F0 V star has an effective temperature of 7,240 K; looking in Table A.1 the AB_V correction term for an effective temperature of 7,500 K is 0.03. According to Table 9.1, a 5×5 pixel square aperture encloses about 79% of the light from a star. The count rate can then be calculated from the equation

$$C = 2.5 \times 10^{11} \varepsilon_f \left(\int QTd\lambda/\lambda\right) \times 10^{-0.4(V + AB_v)}$$

or $2.5\times10^{11}*0.0835*0.79*10^{-0.4(27.5+0.03)} = 0.1604$ counts s^{-1}, which agrees with the ETC-returned value of 0.160. The exposure time can then be found by using the equation

$$t = \frac{\Sigma^2[C + N_{pix}(B_{sky} + B_{det})] + \sqrt{\Sigma^4[C + N_{pix}(B_{sky} + B_{det})]^2 + 4\Sigma^2 C^2\left[\frac{N_{pix}}{N_{bin}} N_{read} R^2\right]}}{2C^2}$$

to give $t = 5222$ s, which is close to the ETC-derived value of 5089 s. We have inserted the background rates of $B_{sky} = 0.0377$ (Table 9.1), $B_{det} = 0.00042$ (Chapter 5), a read noise of 3.1 e^- per read (Chapter 5), and 5 reads.

9.9.2 Example 2: IR Imaging of a Faint Extended Source

What is the exposure time needed to obtain a signal-to-noise of 10 for an elliptical galaxy that subtends an area of 1 $arcsec^2$ with an integrated V-magnitude of 26.7, when using the IR F140W filter? Assume a photometry box size of 9×9 pixels, and average sky values. Note that a 9×9 pixel box subtends 1.32 $arcsec^2$, so the equivalent

calculation would assume a surface brightness of 27.0 mag/arcsec^2 that uniformly fills this box. For simplicity we will assume a redshift of 0.

The WFC3 Exposure Time Calculator (ETC) gives a total exposure time of 1195 s to obtain this S/N in a single exposure. Although the non-destructive MULTIACCUM sequences on the IR channel can mitigate cosmic rays in a single read sequence, users are encouraged to dither their observations so that there are least 2 read sequences per field, to mitigate hot pixels and resample the point spread function. Re-running the calculation with 2 exposures gives an exposure time of 1309 s. If we assume (as in Example 1) that we can fit two 1200-second exposures in an orbit, this program fits within a single orbit. Two SPARS50 sequences, with 15 samples (703 s) per sequence should work well for this program.

Using the pencil-and-paper method, Table 9.2 gives the integral $\int QTd\lambda/\lambda$ as 0.1550. We will assume that the elliptical galaxy resembles an old (10 Gyr) burst of star formation; looking in Table A.2, the AB_v correction term is –1.41. We will assume that the 9×9 pixel box encloses all of the light for this object. The count rate can then be calculated from the equation

$$C = 2.5 \times 10^{11} \varepsilon_f \left(\int QTd\lambda/\lambda\right) \times 10^{-0.4(V+AB_v)}$$

or $2.5\times10^{11}*0.1550*1.0*10^{-0.4(26.7-1.41)} = 2.97$ counts s^{-1}, which is close to the ETC-returned value of 3.24. The exposure time can then be found by using the equation

$$t = \frac{\Sigma^2[C + N_{pix}(B_{sky} + B_{det})] + \sqrt{\Sigma^4[C + N_{pix}(B_{sky} + B_{det})]^2 + 4\Sigma^2 C^2\left[\frac{N_{pix}}{N_{bin}} N_{read} R^2\right]}}{2C^2}$$

to give t = 1116 s, which is close to the ETC-derived value of 1309 s. We have inserted the background rates of B_{sky} = 1.1694 (Table 9.2), B_{det} = 0.05 (Chapter 5), an effective read noise of 12.5 e$^-$ per read (Chapter 5, assuming we are fitting the MULTIACCUM sequence), and 2 reads.

9.9.3 Example 3: Imaging an HII region in M83 in Hα

What is the exposure time needed to obtain a signal-to-noise of 10 for an HII region in M83 in Hα which has a diameter of 2" and a flux F_λ in Hα of 5×10^{-16} ergs/cm^2/s? M83 has a redshift of 0.0017 so Hα appears at 6574 Å approximately. From an inspection of the throughput curves in Appendix A, we find the Hα (F656N) filter cuts off at too short a wavelength, so we elect to use the Wide Hα + [N II] (F657N) filter, which has a system throughput $(QT)_\lambda$ of 25% at 6574 Å.

We use the equation in Section 9.4.3 to estimate the total count rate C for the emission line to be 2.28×10^{12} * 0.25 * 5×10^{-16} * 6574 = 1.87 e$^-$/s. The source subtends approximately 2012 pixels, and the sky for this filter contributes 0.0029 e$^-$/s/pixel (Table 9.1) while the dark rate is 0.00042 counts per pixel (Chapter 5). Thus

the total background rate is 6.67 e^-/s. Assuming 2 reads, no binning and a read noise of 3.1 e^- per read (Chapter 5), we find using the same formula as in the previous section that the time to reach a S/N of 10 is 1195 s.

For comparison, using the ETC, specifying the size as 2" in diameter, entering the flux in ergs/cm^2/s/arcsec^2 as 1.59×10^{-16} at 6574 Å, and using a circular 1 arcsec radius extraction region we find similar results: an almost identical count rate and a slightly shorter exposure of 1145 s to reach the same S/N. We conclude, on the basis of these simple estimates that such bright HII regions are easily observed with *HST* and WFC3.

CHAPTER 10:

Overheads and Orbit Time Determinations

In this chapter . . .

10.1 Overview

This chapter provides information for Phase I proposers who plan to use WFC3 for some or all of their planned *HST* observations. Because your Phase I proposal must state a specific integer number of *HST* orbits that are requested for your program, it is important that this number be as accurate as possible.

After you establish a set of scientific exposures, as well as any additional calibration exposures required for your program, you are ready to determine the total number of orbits to request in your Phase I proposal. The time requested should include not only the total exposure time, but also the additional time for the observatory and instrument operations needed to support those exposures. Those operations usually include acquiring (and possibly re-acquiring) guide stars, configuring WFC3 in preparation for an exposure, transferring data, and possibly repositioning the target in the focal plane between exposures.

It will often be necessary or desirable to achieve the total exposure time through a sequence of shorter exposures. For example, an exposure totalling several hours will be interrupted by target occultations. Moreover, UVIS exposures will almost always be obtained as a sequence of shorter exposures, in order to remove cosmic-ray hits. For your Phase I proposal, you should plan the sequences of exposures and overhead

activities for each of the requested orbits. An overview of observation planning is given in Chapter 4.

Generally, you will need to compile the overheads for your individual exposures, having packed an integer number of exposures and their supporting activities into individual orbits. Some activities may be executed while the target is occulted by the Earth, allowing more efficient utilization of an orbit. Finally, you will tally the exposure times and resulting overhead times required during visibility of the target in order to determine the total number of orbits needed. This may be an iterative process as you refine your exposures to better use the targets' orbit visibility (for non-CVZ targets).

The Phase I *Call for Proposals* includes instructions on observatory policies and practices regarding orbit time requests; see

`http://www.stsci.edu/hst/hst/proposing/documents/cp/cp_cover.html`

The *HST Primer provides* additional specific advice on how to determine the number of required orbits for your scientific program; see

`http://www.stsci.edu/hst/proposing/documents/primer/primer_cover.html`

In the following sections, we provide a summary of the WFC3-specific overheads and give several examples that illustrate how to calculate your orbit request for a Phase I proposal.

The overheads presented below are approximate. These overhead times are to be used, in conjunction with the exposure times you determine and the instructions in the *HST* Primer, in order to estimate the total number of orbits for your Phase I proposal. If your *HST* proposal is accepted, you will then develop and submit a Phase II proposal to support the actual scheduling of your approved observations. At that time you will use the APT scheduling software (which employs more precise values for the various overheads) to craft exposure sequences that match orbital target visibility intervals and your allocation of orbits. Therefore, requesting sufficient time in your Phase I proposal for overhead operations is important; additional time to cover unplanned overhead will not be granted later.

10.2 Observatory Overheads

This section discusses the overheads involved in preparing the telescope for observations of a target. The next section describes the additional instrument-specific overheads involved in obtaining and storing the actual individual WFC3 exposures.

At the beginning of a sequence of WFC3 exposures, the telescope must acquire guide stars. The time required for this initial guide-star acquisition is 6 minutes. If the observations extend into the following orbit(s) following Earth occultation, you must also include the overhead for guide-star re-acquisition (another 5 minutes at the beginning of each new orbit). The only exception to this re-acquisition overhead occurs when you are observing a target in the Continuous Viewing Zone (CVZ; see the *HST Primer*), in which case guide-star re-acquisitions are unnecessary.

Following guide-star acquisition (or re-acquisition) and the first exposure during the orbit, it is likely that you will want to make a series of small telescope motions for the purpose of obtaining dithered observations. Each commanded movement of the telescope requires an amount of time ranging from 0.3 to 1.3 minutes, depending on the size of the motion. Furthermore, each time the telescope is moved more than 2 arcmin (e.g., for the purpose of constructing a mosaicked image), an additional guide-star acquisition will be necessary, requiring another 6 minutes.

When using WFC3's UVIS quad filters, it will often be necessary to repoint the telescope to place the target in the desired quadrant. This repositioning will require 1 minute. Due to the large field of view of WFC3/UVIS, offsets to different quadrants may require new guide stars to be acquired. Offsets between adjacent quadrants (e.g., A to B, or A to C) are small enough to maintain the same guide stars in many cases. However, offsets between diagonal quadrants (i.e., A to D, or B to C) are larger than 2 arcmin when using the "optimum" apertures, so the same guide stars cannot be used for diagonal quadrant offsets. For the "fixed" apertures, diagonal quadrant offsets are very close to 2 arcmin, so it is possible that the same guide stars may be used, depending on the placement of the particular guide stars. To determine whether quad filter observing sequences may require new guide star acquisitions, refer to Table 6.4 for quad filter positions, to Table 6.1 for aperture descriptions, and to the SIAF for aperture reference point definitions.

Table 10.1 summarizes the observatory-level overheads involved in WFC3 observing.

Table 10.1: Observatory Overhead Times.

Action	Overhead Time
Guide-star acquisition	6 minutes (first orbit)
Guide-star re-acquisitions	5 minutes at beginning of each new orbit for non-CVZ observing
	0 minutes for CVZ observing
New guide-star acquisition following dither of >2 arcmin	6 minutes
Spacecraft maneuvers	1 minute for offsets between 60 and 120 arcseconds
	0.8 minute for offsets between 28 and 60 arcseconds
	0.6 minute for offsets between 10 and 28 arcseconds
	0.5 minute for offsets between 1.25 and 10 arcseconds
	0.3 minute for offsets less than 1.25 arcsecond
	1 minute to offset to different UVIS quadrant (for quad filters)

10.3 Instrument Overheads

10.3.1 Exposure Overheads

The instrument-specific overhead times for WFC3 exposures are dominated by the time to move the filter wheels, to read out the detector, and especially to transfer and store the data. Although in a Phase II proposal the overheads computed with APT may prove to be smaller than the values given in this section, it is nevertheless important to plan your Phase I proposal using the conservative values given here in order to ensure the award of time adequate to attain your scientific goals.

Several kinds of overhead activities are associated with each exposure, and the specific activities depend on whether the exposure is a new one, or part of a series of identical ones. Identical exposures are defined as second and subsequent exposures on the same target, with the same filter.

For UVIS ACCUM exposures (i.e., CCD exposures), identical exposures are generated if the observer does any of the following: (1) specifies a CR-SPLIT number greater than 1; (2) does not specify the CR-SPLIT Optional Parameter, in which case it defaults to CR-SPLIT=2 for all exposures regardless of exposure time; (3) specifies the Special Requirement PATTERN (in order to dither, or to mosaic, a set of images); or (4) specifies a Number of Iterations greater than 1.

For IR MULTIACCUM exposures, CR-splitting is not used, and only items (3) and (4) in the preceding list apply. Furthermore, unless otherwise specified, a full 16-read (i.e., 15-sample, specified with NSAMP=15) sequence will be obtained for each IR MULTIACCUM exposure. The full set of samples (i.e., images) is considered to be one exposure.

At the end of each UVIS or IR exposure, images are read into WFC3's internal buffer memory, where they are stored until they are transferred to *HST*'s solid-state data recorder. The time needed to read a UVIS CCD image is 98 seconds. The time needed for a single read of an IR image is 3 seconds, leading to a total of 48 seconds for a full 16-read exposure. These times are included in the overhead times for the first and subsequent exposures presented in Table 10.2 below.

Dumping of the WFC3 buffer

The WFC3 buffer provides temporary storage of images read from the WFC3 detectors before they are dumped through the *HST* science data formatter (SDF) to the solid state recorder (SSR). The buffer can be dumped either between exposures (a "serial" dump), or during an exposure (a "parallel" dump), but cannot overlap any commands executed in WFC3, including the commands at the beginning or at the end of an exposure. The buffer may be dumped during pointing maneuvers, but not during acquisition of guide stars. The buffer may be dumped during target occultation, which does not deduct from the target visibility time. Switching channels (IR and UVIS) does not require dumping the buffer. Observers will generally prefer to use parallel dumps, in order to more fully utilize the time when a target is visible for science exposures. Although buffer dumps are typically forced by science data volume, a

buffer dump will also be forced whenever the buffer holds 100 image headers, regardless of the size of the images themselves. The 100-file limit is unlikely to be reached under typical conditions.

The rules for dumping the buffer in parallel with UVIS exposures differ in some respects from those for dumping in parallel with IR exposures. The two channels are considered separately in the following paragraphs.

UVIS parallel buffer dumps

The buffer can hold up to two full-frame UVIS images. A single full-frame image can be dumped in parallel with a UVIS exposure greater than 347 seconds, and two full-frame images can be dumped in parallel with a UVIS exposure greater than 663 seconds. When the buffer is dumped, all stored images must be dumped. Consequently, a sequence of 348-second (or longer) exposures will incur no overhead for dumping the buffer. Whether a sequence comprised of short exposures (less than 348 seconds) and long exposures (greater than 347 seconds) will require serial buffer dumps will depend upon the order of the long and short exposures and the duration of the long exposures. Dumping the buffer during a sequence of short and long exposures will be more efficient if the long exposures are 664 seconds (or longer). For example, an orbit with exposures with exposure times in the sequence 10-348-10-664-10-664-10 will incur no serial dump penalty. The observer will plan such sequences with APT in Phase 2. Sequences of full-frame, un-binned exposures less than 348 seconds will require the overhead of serial buffer dumps. For short exposures, using subarrays or binning may be advantageous in order to reduce the overhead of serial buffer dumps. The time to dump a subarray or binned exposure scales approximately with the number of pixels stored in the buffer.

IR parallel buffer dumps

The buffer can hold up to two full-frame, 15-sample IR images. To dump one such image in parallel with an IR exposure requires that exposure to be longer than 348 seconds. To dump two such images requires an exposure longer than 646 seconds. The rules for dumping IR exposures are somewhat more efficient than those for dumping UVIS exposures. For purposes of dumping IR exposures, each sample is treated individually; all samples in the buffer are not required to be dumped together; and samples can be dumped during the non-destructive read of the FPA. Sequences of full-frame, 15-sample exposures shorter than 349 seconds will require serial dumps after the second and subsequent exposures. Sequences of longer-exposure (i.e., greater than 348 seconds), full-frame, 15-sample exposures will incur no overhead for dumping the buffer. Sequences comprised of short (less than 349 seconds) full-frame, 15-sample exposures and long exposures (greater than 348 seconds) may incur overhead for serial dumps, depending upon the sequence of exposures and the duration of the long exposures. The observer will plan such sequences with APT in Phase 2. The time to dump an n-sample, full-frame exposure is approximately $39 + 19 \times (n + 1)$ seconds. Subarrays may also be used to reduce the overhead of serial buffer dumps.

Filter and channel select overheads

Both the UVIS and IR channels may be used during a single orbit, although not simultaneously. The time required to reconfigure between the two channels is 1 minute. If the buffer is not empty when switching channels, then time must also be taken to dump it before the exposure can begin with the other channel. Because the centers of the fields of view of the UVIS and IR channels are the same, acquisition of new guide stars is not required when changing channels to observe the same target.

The overhead for each exposure includes an allowance for the time required to position the filter or grism; however, selecting a UVIS quad filter requires an additional 1 minute of overhead to re-position the telescope, as indicated in Table 10.1.

Table 10.2 summarizes all of the instrument overheads described in this subsection.

Table 10.2: WFC3 Instrument Overhead Times.

Action	Overhead Time (minutes)
Reconfiguration between UVIS & IR channels during a single orbit	1.0
UVIS ACCUM Mode	
Single exposure or first exposure in a set of identical exposures (e.g., the first sub-exposure of a CR-SPLIT set)	2.6
Subsequent exposures in set of identical exposures (e.g., subsequent exposures in a CR-SPLIT set, or a dithered exposure set), per exposure	2.1
Buffer dump if exposure is not last one in an orbit, or if next exposure is less than 339 seconds	5.8
IR MULTIACCUM Mode	
Each exposure	1.0
Buffer dump if 16-read exposure is not last one in an orbit, or if next exposure is less than 346 seconds	5.8

10.3.2 Reducing Overheads with Subarrays and Binning

If your science program is such that a field of view smaller than the full detector size is adequate and you require many short exposures, then one way to reduce the frequency of buffer dumps, and hence their associated overheads, is to use a WFC3 subarray. Subarrays are described for the UVIS channel in Section 6.4.4, and for the IR channel in Section 7.4.4. When subarrays are used, only a small region of the detector is read out and stored in WFC3's buffer. The reduced data volume permits a larger number of exposures to be stored in the buffer before the memory fills and it becomes necessary to transfer them to the telescope's solid-state recorder. Use of subarrays reduces the amount of time spent dumping the buffer, and also reduces detector readout time. However, a dump is still required if the 100-file limit is reached before buffer memory is filled.

The available subarrays are specified for the UVIS and IR channels by apertures with "SUB" in their names. See Sections 6.4.4 and 7.4.4 further details**.**

The areas (A_{SA}) of the supported UVIS subarrays are 1/4, 1/16, or 1/64 of the area (A_{FF}) of a full-frame image. The areas of the IR subarrays are 1/4, 1/16, 1/64, or 1/256 of the area of a full-frame image. The number of subarray exposures that may be stored in the buffer, limited by image data volume, is $n = 2$ (A_{FF}/A_{SA}). For example, eight 1/4-area exposures may be stored in the buffer, which would allow eight 4-minute exposures to be taken and stored before having to dump the buffer. If the exposures were full-frame, the buffer would have to be dumped after each pair of observations, thus leading very low observing efficiency.

The 100-file limit must also be considered in optimizing buffer dumps. For UVIS exposures, the limit will almost never be encountered. For IR exposures, each read (not each exposure) counts against the limit. The number of IR exposures that can be stored before a buffer dump is forced is therefore n = 100/(NSAMP +1), or six exposures for NSAMP = 15.

In the IR channel, certain combinations of subarrays and sample sequences give rise to images containing a sudden low-level jump in the overall background level of the image. The cause of the artifact is under investigation (see Section 7.4.4).

Data volume and overhead time can also be reduced for UVIS images by using on-chip binning of adjacent pixels, as described in Section 6.4.4. By using 2×2 pixel binning, the data volume is reduced by a factor of 4, although the readout time is only reduced by about a factor of 2 to 50 sec. For 3×3 pixel binning it is reduced by a factor of 9, and the readout time by a factor of 4 to 23 s. IR readouts cannot be binned, but data volume may be reduced by taking less than the default 15 samples during an exposure.

10.4 Orbit Use Examples

The easiest way to learn to estimate total orbit time requests is to work through a few examples. Below we provide five different examples:

1. A simple UVIS CR-SPLIT image using one filter.
2. A set of short UVIS exposures that require large overheads associated with buffer dumps.
3. A one-orbit IR observation using two different filters.
4. A two-orbit UVIS observation using dithering.
5. A one orbit IR grism spectroscopic observation.

These examples represent fairly typical usage scenarios of WFC3. However, it should be noted that in several of the examples we have used un-dithered images. In most actual cases, observers are advised to use dithering. Furthermore, although observers can use the shadow or low-sky target visibility restrictions, the examples

below are all for the standard (i.e., unrestricted) target visibility (see the *HST Primer*, Section 6.3, for further discussion).

10.4.1 Example 1: UVIS, 1 orbit, 1 filter

Consider a target to be imaged with UVIS in a given filter in one orbit. Let us suppose that, by using the Exposure Time Calculator (ETC) (see Chapter 9), we find that we need a total exposure time of 2400 s (40 minutes) to reach the desired S/N. Given that we desire the observation to be split into two exposures for cosmic-ray removal (using the default CR-SPLIT=2), we map the overheads and the science exposure times onto the orbit as follows:

Table 10.3: Orbit Calculation for Example 1

Action	Time (minutes)	Explanation
Guide-star acquisition	6.0	Needed at start of observation of new target
UVIS overhead for first sub-exposure	2.6	Includes filter change, camera set-up, and readout
First science sub-exposure	20.0	
UVIS overhead for second sub-exposure	2.1	Includes readout
Second science sub-exposure	20.0	Total exposure time is 40 min
Total time used	50.7	

Thus, with a total time of nearly 51 minutes, this set of observations would fit into all unrestricted *HST* orbits. The exposure time could, if needed, be adjusted so as to fill the actual target visibility interval (which depends on several factors, including the date and target location in the sky, as described in Chapter 6 of the *HST Primer*). The time needed to dump the buffer following the second sub-exposure incurs no overhead in this example, because it can be performed during target occultation.

It should be noted that this simple sequence of two fairly long, non-dithered exposures would produce an image with a gap between the two CCD chips (see Section 6.3), and that cosmic-ray removal might not be optimal (see Section 5.4.10).

10.4.2 Example 2: UVIS, 1 orbit, short exposures

This example illustrates the impact of short exposures on the useful time in the orbit. Suppose we intend to use one orbit to observe a target with UVIS in two filters, F606W and F814W. The observation consists of two sequences, each one with two identical CR-SPLIT exposures, for a total of four individual sub-exposures. Suppose that the ETC shows that the exposure time must be 540 seconds for each of the filters,

so each of the CR-SPLIT sub-exposures must be at least 270 seconds long. For the target declination, which in this example is –35°, we find that the unrestricted visibility time is 55 minutes. The time budget for the orbit is as follows:

Table 10.4: Orbit Calculation for Example 2

Action	Time (minutes)	Explanation
Guide-star acquisition	6.0	Needed at start of observation of new target
UVIS overheads for first sub-exposures in both series	2 × 2.6 = 5.2	Includes filter change, camera set-up, and readouts
UVIS overheads for subsequent sub-exposures in both series	2 × 2.1 = 4.2	Includes readouts
Buffer dump after 2nd sub-exposure	2 × 5.8 = 11.6	Full buffer must be dumped in target visibility in order to obtain last two exposures, which are too short to accommodate dump (270 sec < 339 sec).
Science exposures	4 × 4.5 = 18.0	
Total time used	45.0	

Compared with Example 1, we see that the efficiency is very low due to the large overheads associated with buffer dumps. We have achieved only 18 minutes of exposure time during 45 minutes of target visibility, whereas in Example 1 we obtained 40 minutes of exposure time during 51 minutes of visibility. Of course, this is caused by the short exposures of this example, versus the long exposures of Example 2, where “short” and “long” are relative to the time to dump the buffer, 339 seconds. This time that is “lost” to dumping the buffer can be recovered by sufficiently increasing the exposure time. For example, if the 540-second exposure time is required to obtain a minimum S/N (and not to avoid saturation), then increasing the exposure times to 720 s will improve the S/N and require the same amount of target visibility time, 45 min.

Alternatively, if compatible with the scientific goals, a subarray could have been used to read out only a fraction of the detector area, allowing more frames to be stored in the buffer before requiring a dump. In this example, using UVIS 2k×2k subarrays for 4 short (<339 seconds) exposures would save about 8 minutes of readout time and 12 minutes of dump time.

10.4.3 Example 3: IR, 1 orbit, 2 filters

The third example demonstrates the orbit calculation for a simple IR observation. We want to obtain full-frame images of a target in two filters, F110W and F160W. Suppose that the ETC has shown that the exposure times adequate for our scientific goals are 10 minutes in F110W and 20 minutes in F160W. These times can be

achieved with the up-the-ramp MULTIACCUM sequences SPARS50 (11.7 min) and SPARS100 (23.4 min), respectively. From the orbit visibility table (see Chapter 6 of the *HST Primer*), suppose that we find that at the target declination (here assumed to be 0°) the unrestricted target visibility time is 54 minutes. The orbit calculation goes like this:

Table 10.5: Orbit Calculation for Example 3

Action	Time (minutes)	Explanation
Guide-star acquisition	6.0	Needed at start of observation of new target
IR overheads for 2 exposures	2 × 1.0 = 2.0	Includes filter changes, camera set-ups, and readouts
Science exposure in F110W	11.7	
Science exposure in F160W	23.4	
Total time used	43.1	

The total time used in the orbit shows that our target can indeed be imaged in the selected filters within one orbit. Furthermore, the first exposure can be dumped from the buffer during the second exposure. The ~9 minutes of unused time could be used for an additional exposure, during which the second exposure would be dumped.

10.4.4 Example 4: UVIS, dithering, 2 orbits, 1 filter

This example illustrates the orbit calculation for a UVIS observation with a WFC3 UVIS box dithering pattern, which implements imaging at four pointings. The goal of the observation is to obtain a dithered image of a field in such a way that would allow us to bridge the ~1.2 arcsec inter-chip gap between the UVIS CCDs in the combined image. As indicated in Table 10.1, for a 2-arcsec offset maneuver, the three dithers will take 0.5 minutes each. Suppose we have determined that the exposure time necessary to reach the desired S/N ratio is 80 minutes, and that the visibility time at our target declination, assumed to be +53°, is 58 minutes. Furthermore, we will use the cosmic-ray removal provided by the dither data-reduction package, and therefore set CR-SPLIT=1. As a result, the orbit calculation will involve a sequence of four exposures of 20-minutes duration (i.e., one exposure at each of the four dither pointings). These observations will be distributed across two *HST* orbits, as shown in the following Table 10.6.

Table 10.6: Orbit Calculation for Example 4.

Action	Time (minutes)	Explanation
	Orbit 1	
Guide-star acquisition	6.0	Needed at start of observation of new target
UVIS overhead for first exposure	2.6	Includes filter change, camera set-up, and readout
UVIS overhead for second exposure	2.1	Includes readout
Spacecraft maneuver	0.5	To offset from first to second dither pointing
Two science exposures	2 × 20 = 40.0	Exposures at the first two pointings in the dither pattern
Total time used in orbit 1	51.2	
	Orbit 2	
Guide-star re-acquisition	5.0	Needed at start of new orbit to observe same target
UVIS overheads for 3rd and 4th exposures	2 × 2.1 = 4.2	Includes readouts
Spacecraft manaeuvers	2 × 0.5 = 1.0	To offset to the 3rd and 4th dither pointings
Two science exposures	2 × 20 = 40.0	Exposures at the final two pointings in the dither pattern
Total time used in orbit 2	50.2	

No overhead is incurred to dump the exposures, because they are all longer than 339 seconds. Thus the desired exposures can be accomplished within the two orbits, and in fact there are ~7-8 minutes of unused visibility time per orbit that could be used to increase the exposure times.

10.4.5 Example 5: IR, 1 orbit, grism

This example illustrates the orbit calculation for an IR G102 grism spectroscopic observation. We will use the full-frame, up-the-ramp MULTIACCUM sequence SPARS200 with NSAMP=13, requiring 40 minutes to expose. We will also obtain undispersed images to calibrate target positions and wavelengths, using a SPARS10 (2.4-minute) exposure before and after the grism exposure. The overhead calculations are presented in Table 10.7.

Table 10.7: Orbit Calculation for Example 5.

Action	Time (minutes)	Explanation
Guide-star acquisition	6.0	Needed at start of observation of new target
IR overheads for 3 exposures	3 × 1.0 = 3.0	Includes filter changes, camera set-ups, and readouts
Science exposure (undispersed)	2 × 2.4 = 4.8	SPARS10, NSAMP=15
Science exposure (grism)	40.0	SPARS200, NSAMP=13
Total time used	53.8	

The buffer dumps incur no overhead because the first undispersed exposure can be dumped during the long grism exposures, and the last two can be dumped during the subsequent target occultation. Thus, since at least 54 minutes of target visibility are available at any target's declination, this set of observations can be obtained in one orbit.

APPENDIX A:

WFC3 Filter Throughputs

In this appendix . . .

A.1 Introduction

This appendix contains plots of throughputs and sensitivities for each WFC3 filter. It is organized by *detector* and *filter*. For each imaging mode the following are provided:

- Plots of integrated system throughput for each filter as a function of wavelength.
- Plots of the time needed to achieve a desired signal-to-noise ratio vs. magnitude for each filter for a point-source and for a 1"×1" extended source.
- Tables of color corrections AB_V to go from Johnson V magnitude to AB magnitude for stellar spectra (as a function of effective temperature) and composite populations (as a function of age). The stellar spectra come from the Lejeune et al. (1997, *A&AS*, **125**, 229) grid, and assume a surface gravity of log g = 5 and solar metallicity. The composite populations come from the "instantaneous burst" and "continuous star formation" models of Bruzual & Charlot (1993, *ApJ*, **405**, 539), updated in 1995, assuming a Salpeter IMF spanning 0.1 to 125 solar masses.

A.2 Throughputs and S/N Ratio Data

A.2.1 Sensitivity Units and Conversions

This appendix contains plots of throughputs for each WFC3 filter. Section 9.3 explains how to use these throughputs to calculate expected count rates from your source.

The first figure for each filter gives the integrated system throughput based on on-orbit observations of spectrophotometric standards. This is the combination of the efficiencies of the detector and of the optical elements in the light path. The throughput is defined as the number of detected counts/second/cm^2 of telescope area relative to the incident flux in photons/cm^2/s. For both the UVIS and IR channels, "counts" is the number of electrons detected. In both channels the detected counts obey Poisson statistics, except that at short wavelengths in the UVIS channel, a single incoming photon has a finite chance of producing multiple electrons in the CCD. Section 5.4.2 describes this phenomenon, which was measured to have a much smaller effect in the UVIS detectors compared to theoretical predictions. The plots in this appendix have been corrected to remove multiple electrons generated by UV photons, using a correction that is intermediate between the theoretical and measured UVIS "quantum yields." The throughput includes all obscuration effects in the optical train (e.g., due to the *HST* secondary).

All wavelength measurements for the UVIS and IR channel filters were done in a gaseous medium: air for UVIS measurements and helium for IR measurements. The results have been converted to vacuum wavelengths using the indices of refraction of the gaseous media. The UVIS laboratory measurements were done at a temperature of 20°C, whereas the filters are operated on orbit at 0°C; this may lead to wavelength shifts which are expected to be small. The IR laboratory measurements were done at a temperature of –30°C, whereas the filters are operated on orbit at –35°C; this may lead to wavelength shifts which are expected to be very small.

Note that the tables in the ***synphot*** package and the WFC3 Exposure Time Calculator all assume vacuum wavelengths for both the UVIS and IR filter transmission data.

Because we have applied a correction to the throughputs for quantum yield in order to derive appropriate counting statistics for the source, the sensitivity calculations shown here are conservative in background- or read-noise-dominated regimes; the additional signal electrons from the enhanced UV quantum yield will increase the detection of faint sources in the 200-300 nm range somewhat vs. these sample calculations.

To recalculate the throughput with the most recent detector QE tables in ***synphot***, you can create total-system-throughput tables (instrument plus OTA) using the ***synphot calcband*** task. ***calcband*** takes any valid ***obsmode*** command string as input and produces a table with two columns of data called “wavelength” and “throughput” as its output. For example, to evaluate the throughput for the F475W filter and the UVIS detector, Chip 1, you would use the command ***calcband wfc3,uvis1,f475w sdssg_thpt***. The resulting throughput table is stored in an IRAF table, ***sdssg_thpt***. The table can be converted to standard text format with ***tdump "sdssg_thpt" datafile="sdssg_thpt.txt" columns="wavelength,throughput"***.

A.2.2 Signal-to-Noise Ratio

For each imaging mode, plots are provided to estimate the signal-to-noise ratio (S/N) for a representative source. The first figure shows S/N for point sources. The second figure shows S/N for uniform extended sources of area 1 arcsec^2.

The different line styles in the S/N figures delineate regions where different sources of noise dominate. If the total noise from backgrounds (read noise, sky, thermal, dark) is larger than the noise from the source, the observation is considered to be background-dominated, and the line style reflects which background source is largest. Note that for the WFC3 detectors, the dark current can never be the largest source of noise when a source is background-dominated, because the read noise is always larger than the dark count noise when exposures are 1000 s or less. The point- and extended-source S/N figures assume average sky levels. These plots also indicate where an observation will saturate the full well of the detector.

For point sources, an aperture size of 5×5 pixels has been used for the UVIS channel, while an aperture size of 3×3 pixels has been used for the IR channel. For extended sources, a 1 arcsec^2 aperture was used. The read noise has been computed

assuming a number of readouts NREAD= integer (t / 1000 s), where t is the exposure time, with a minimum NREAD=2.

In situations requiring more detailed calculations (non-stellar spectra, extended sources, other sky background levels, unknown target V magnitude, etc.), the WFC3 Exposure Time Calculator should be used.

Follow these steps to use the signal-to-noise plots:

1. Determine the AB magnitude of your source at the wavelength of interest. There are several ways to do this.
   - Examine Tables A.1, A.2, or A.3 and find AB_ν for the desired spectral type and filter. Sum the V magnitude of the target and AB_ν derived from the table.
   - Alternatively, compute ABMAG (=V+AB_ν) from the source flux, using the relation $ABMAG = -2.5\log f_\nu - 48.60$, or $ABMAG = -2.5\log f_\lambda - 5\log\lambda - 2.406$.
2. Find the appropriate plot for the filter in question, and locate V+AB_ν on the horizontal axis. Then read off the signal-to-noise ratio for the desired exposure time, or vice-versa.

Note that the plots show the S/N as a function of source magnitude for exposure times as short as 0.1 s, although the minimum exposure time for the UVIS channel is actually 0.5 s.

UVIS/F200LP

Description

Clear.

Figure A.1: Integrated system throughput for F200LP.

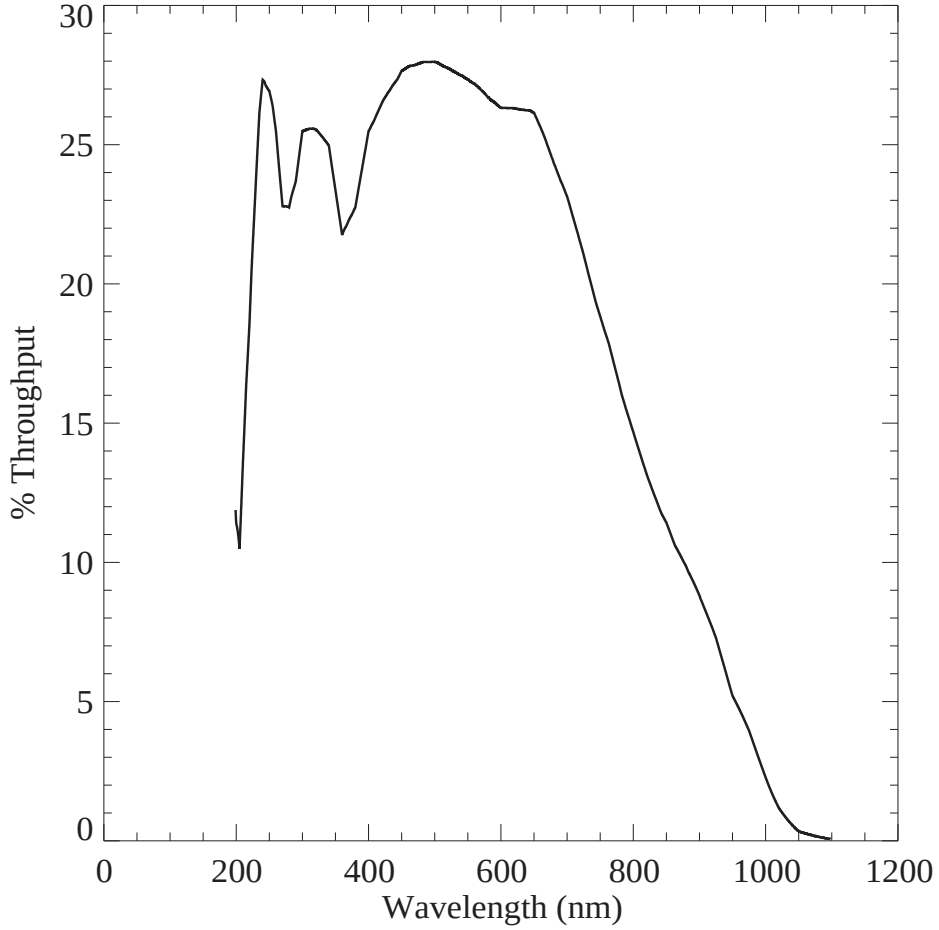

Figure A.2: Point source S/N vs. V+AB$_\nu$ for the F200LP filter, assuming high sky backgrounds and a 5×5 pixel aperture.

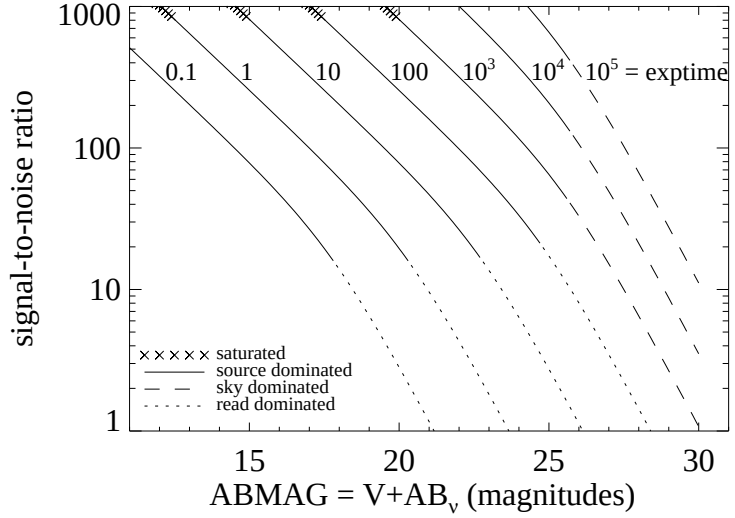

Figure A.3: Extended source S/N vs. V+ABν for the F200LP filter, assuming high sky backgrounds and a source uniformly filling a 1 arcsec^2 aperture.

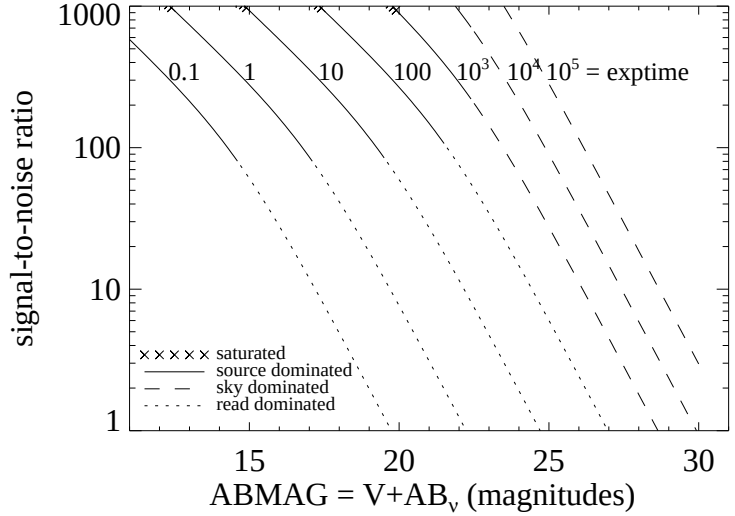

UVIS/F218W

Description

ISM feature filter.

Figure A.4: Integrated system throughput for F218W.

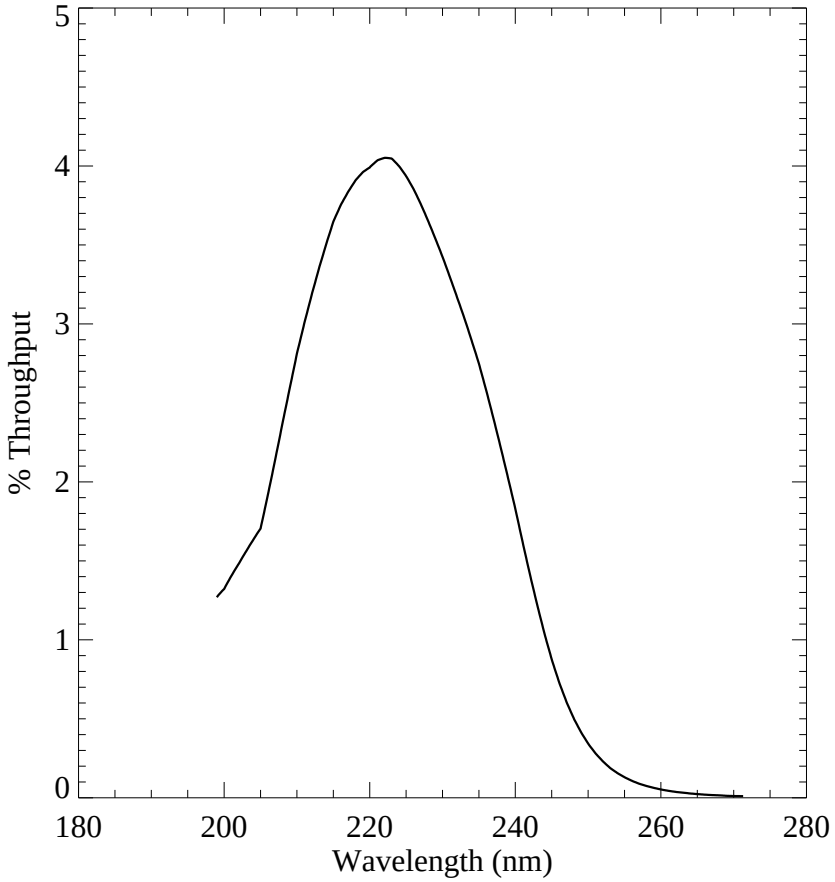

Figure A.5: Point source S/N vs. V+ABν for the F218W filter, assuming high sky backgrounds and a 5×5 pixel aperture.

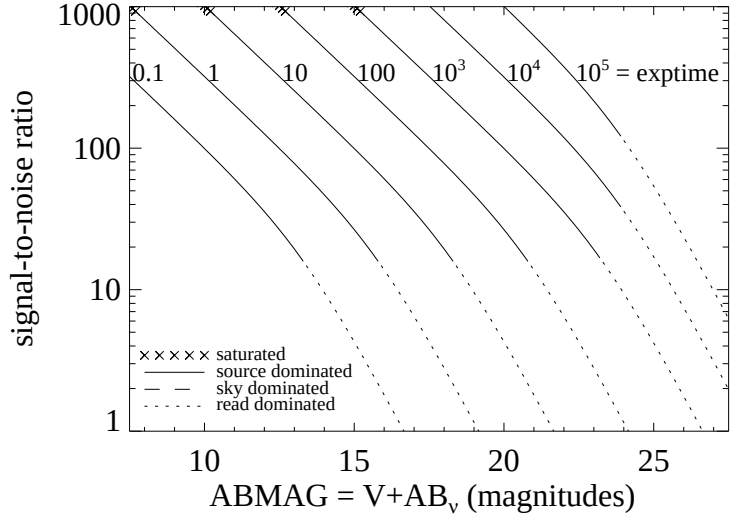

Figure A.6: Extended source S/N vs. V+ABν for the F218W filter, assuming high sky backgrounds and a source uniformly filling a 1 arcsec^2 aperture.

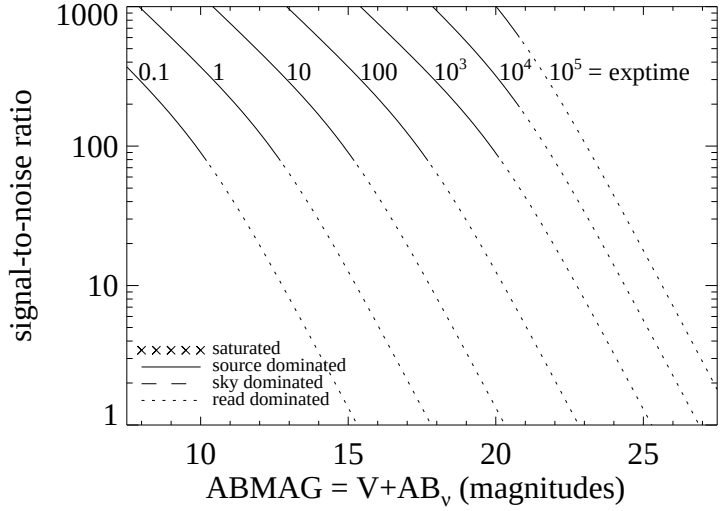

UVIS/F225W

Description

UV wide filter.

Figure A.7: Integrated system throughput for F225W.

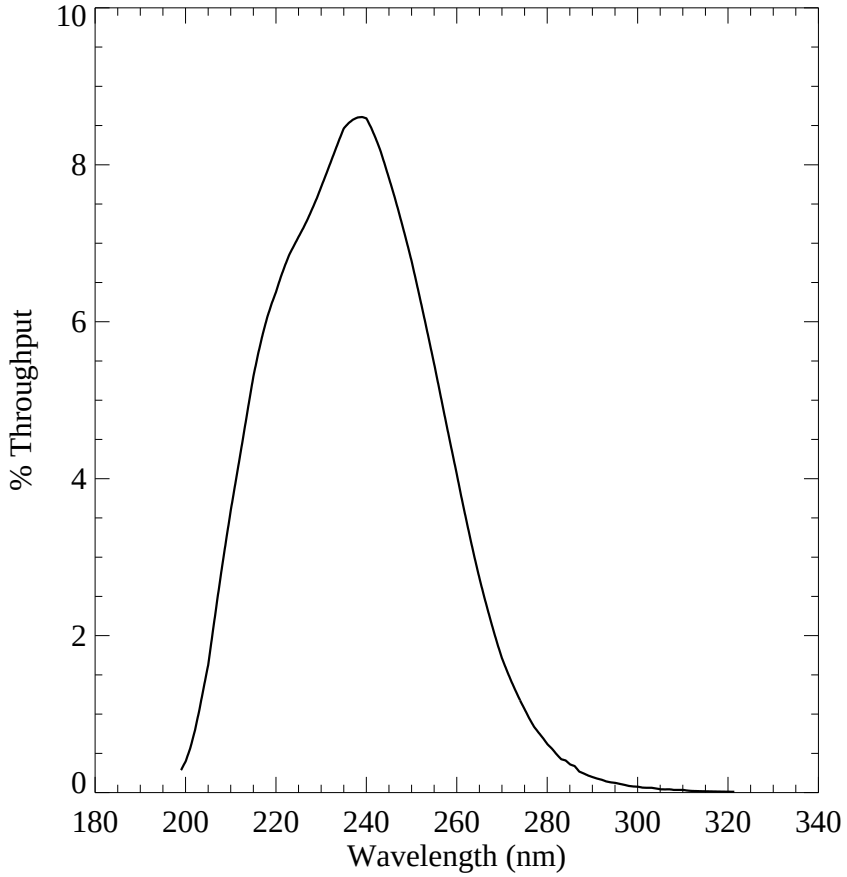

Figure A.8: Point source S/N vs. V+ABν for the F225W filter, assuming high sky backgrounds and a 5×5 pixel aperture.

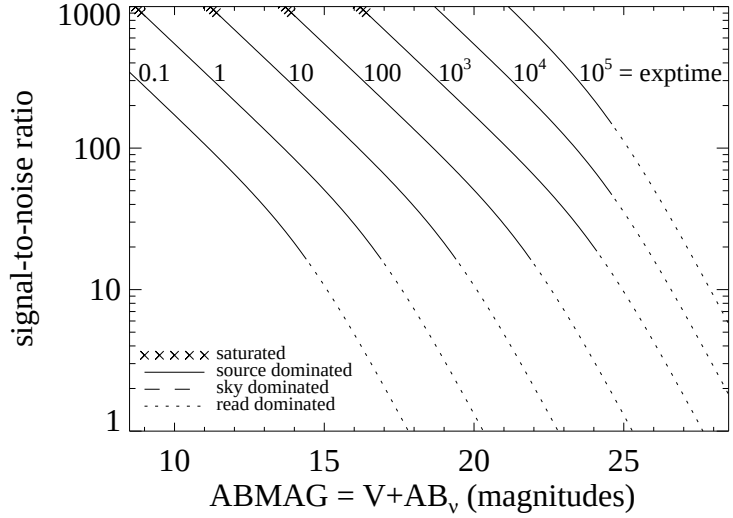

Figure A.9: Extended source S/N vs. V+ABν for the F225W filter assuming high sky backgrounds and a source uniformly filling a 1 arcsec^2 aperture.

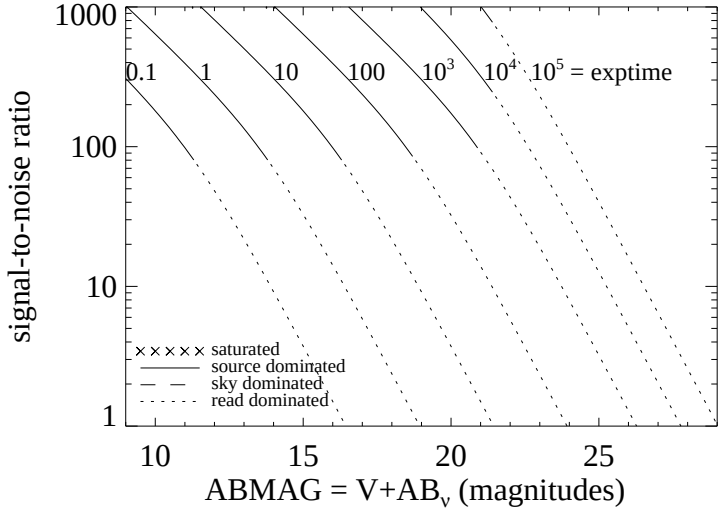

UVIS/F275W

Description

UV wide filter.

Figure A.10: Integrated system throughput for F275W.

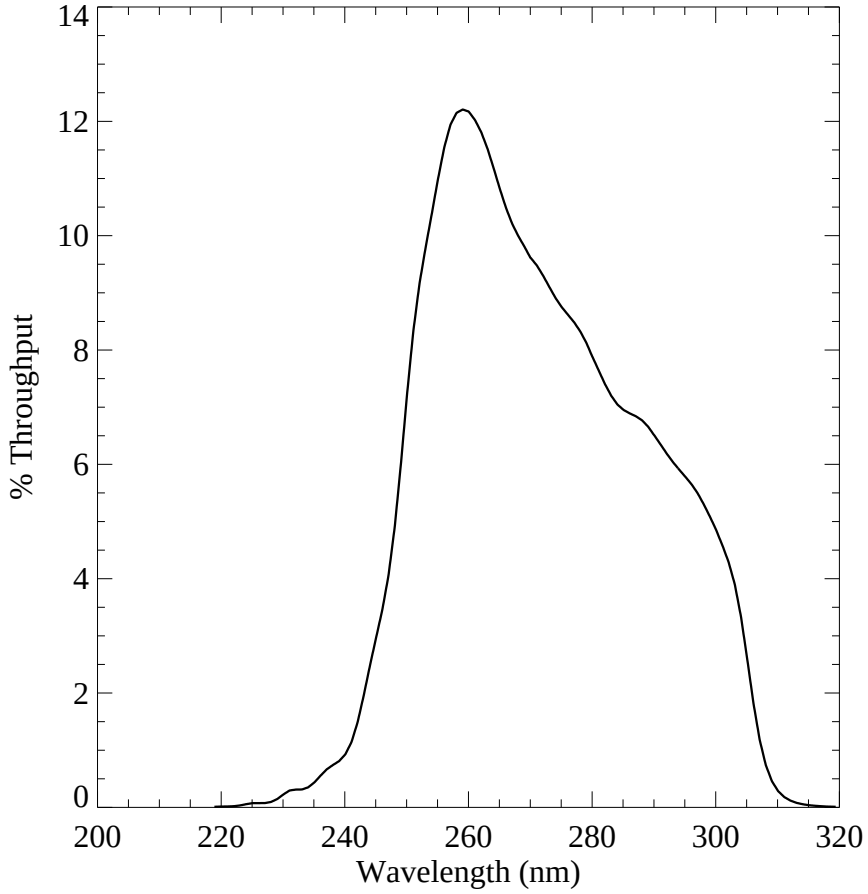

Figure A.11: Point source S/N vs. V+ABν for the F275W filter, assuming high sky backgrounds and a 5×5 pixel aperture.

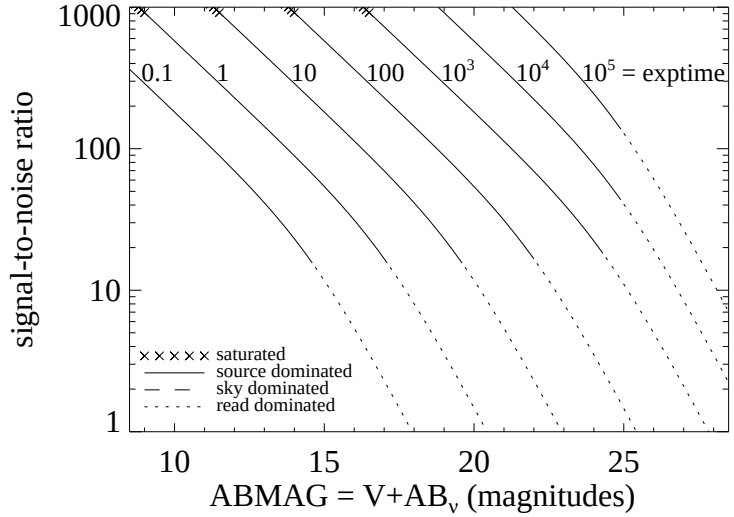

Figure A.12: Extended source S/N vs. V+ABν for the F275W filter, assuming high sky backgrounds and a source uniformly filling a 1 arcsec^2 aperture.

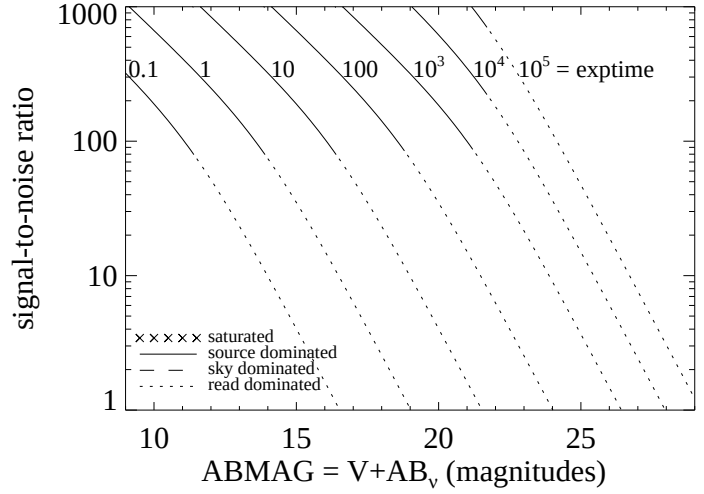

UVIS/F280N

Description

Mg II 2795/2802 filter.

Figure A.13: Integrated system throughput for F280N.

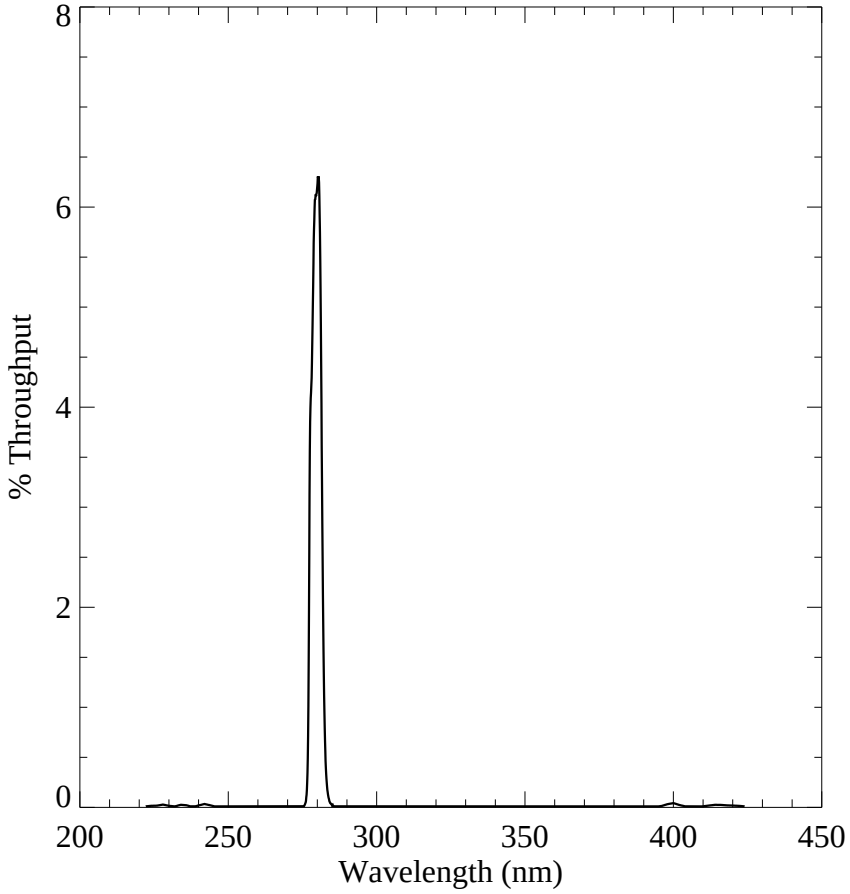

Figure A.14: Point source S/N vs. V+ABν for the F280N filter, assuming high sky backgrounds and a 5×5 pixel aperture.

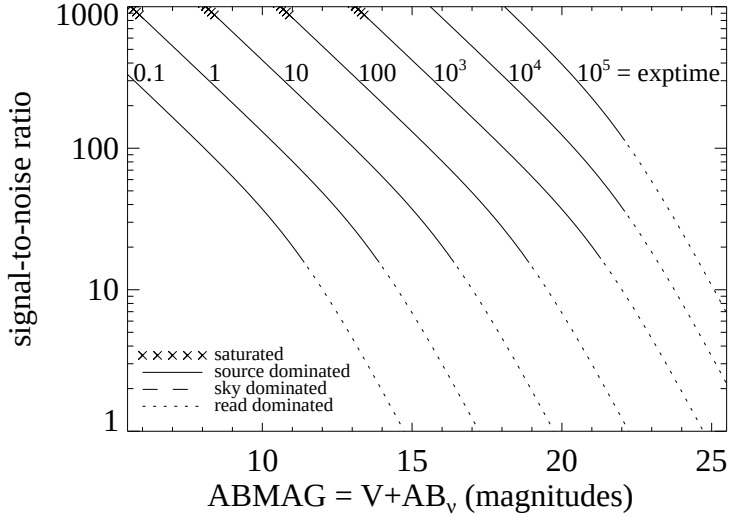

Figure A.15: Extended source S/N vs. V+ABν for the F280N filter, assuming high sky backgrounds and a source uniformly filling a 1 arcsec^2 aperture.

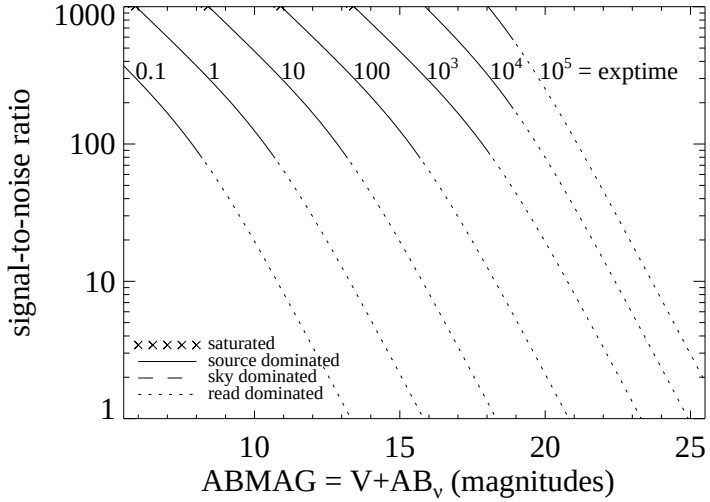

UVIS/F300X

Description

Extremely wide UV filter; grism reference.

Figure A.16: Integrated system throughput for F300X.

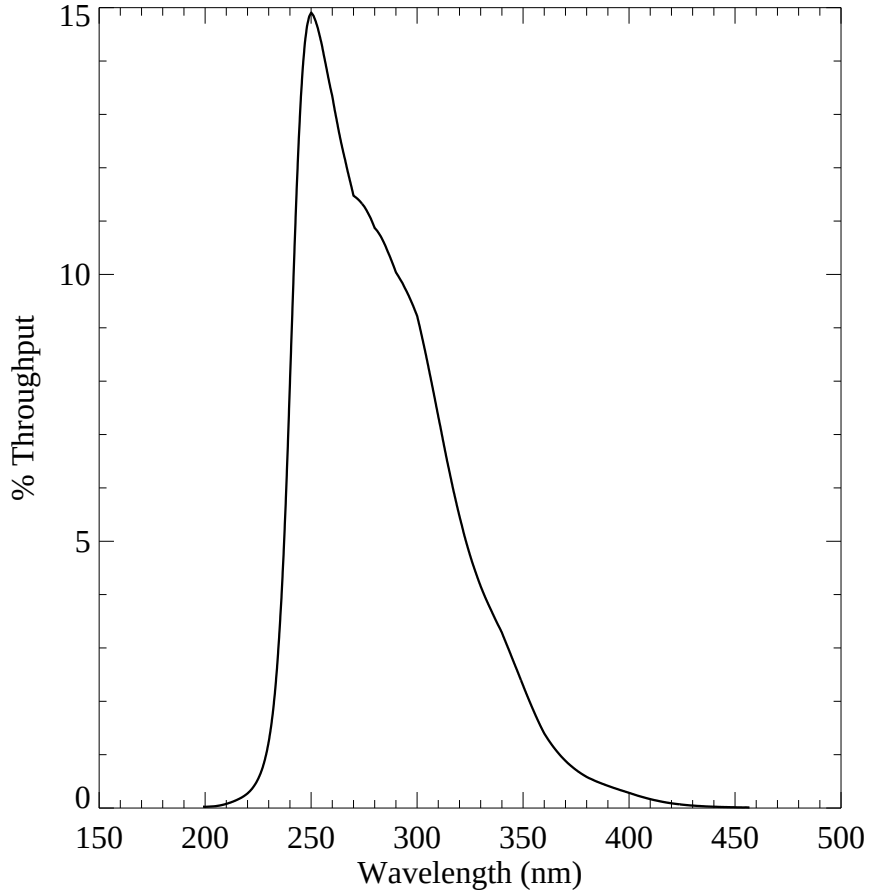

Figure A.17: Point source S/N vs. V+ABν for the F300X filter, assuming high sky backgrounds and a 5×5 pixel aperture.

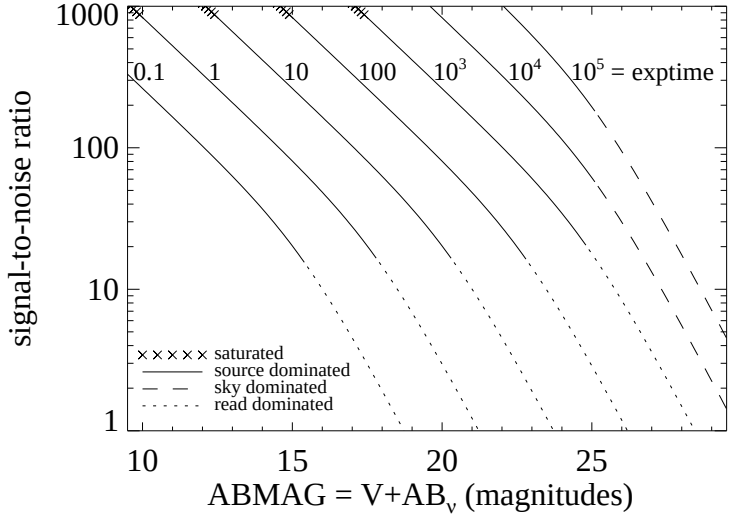

Figure A.18: Extended source S/N vs. V+ABν for the F300X, assuming high sky backgrounds and a source uniformly filling a 1 arcsec^2 aperture.

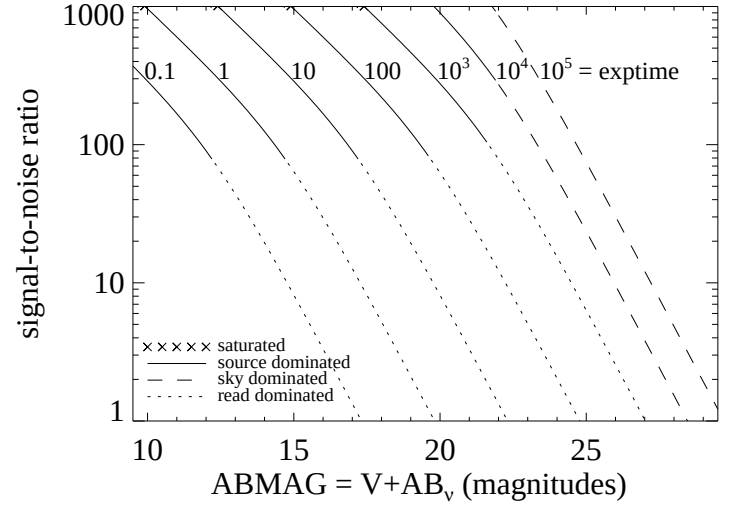

UVIS/F336W

Description

U, Strömgren *u* filter.

Figure A.19: Integrated system throughput for F336W.

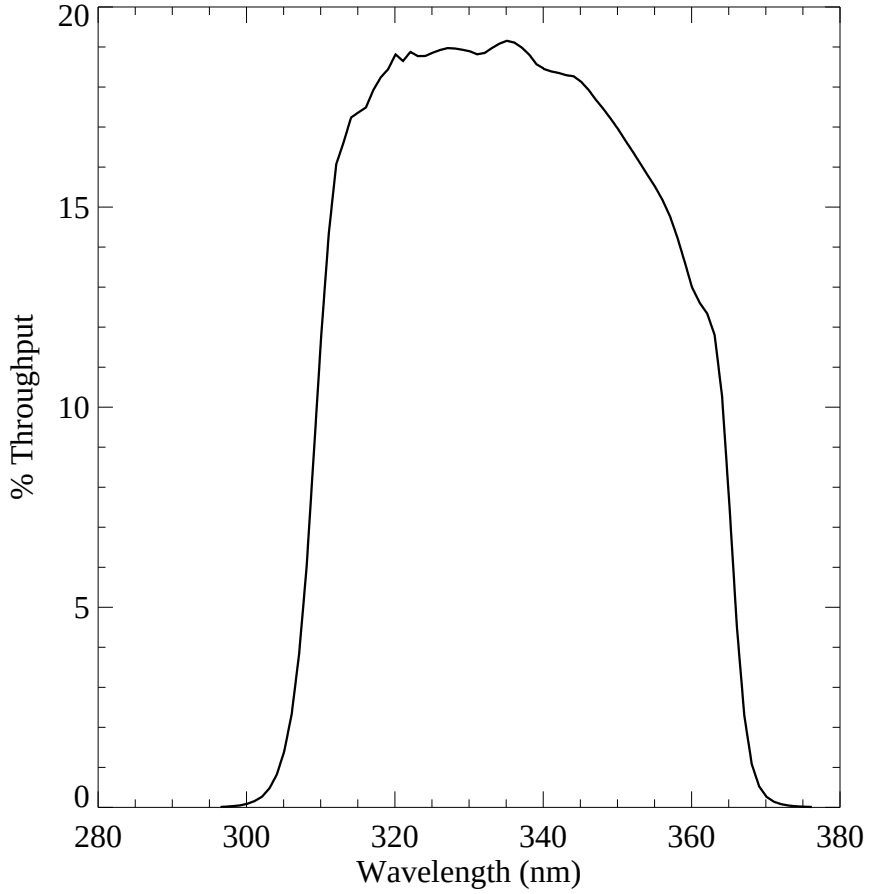

Figure A.20: Point source S/N vs. V+ABν for the F336W filter, assuming high sky backgrounds and a 5×5 pixel aperture.

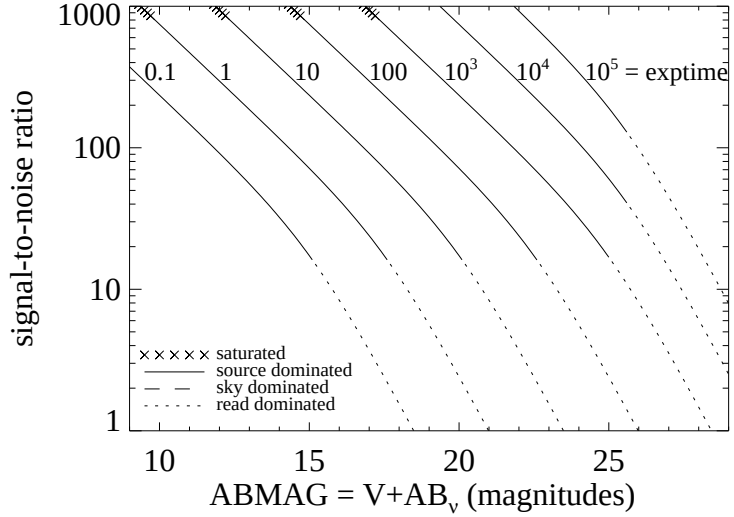

Figure A.21: Extended source S/N vs. V+ABν for the F336W filter, assuming high sky backgrounds and a source uniformly filling a 1 arcsec^2 aperture.

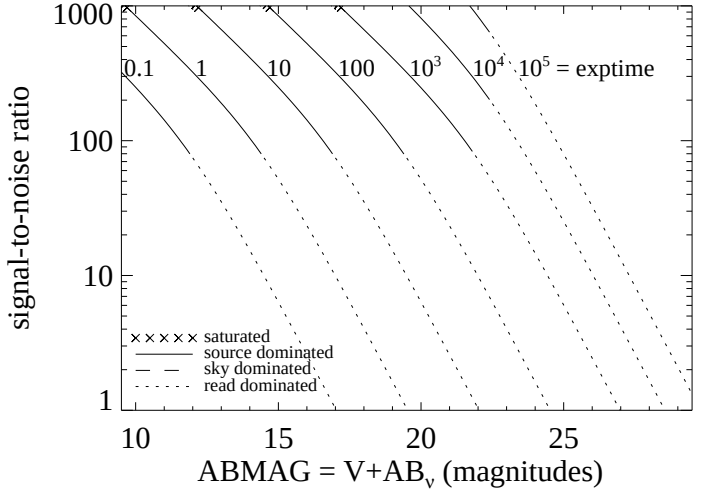

UVIS/F343N

Description

[Ne V] 3426 filter.

Figure A.22: Integrated system throughput for F343N.

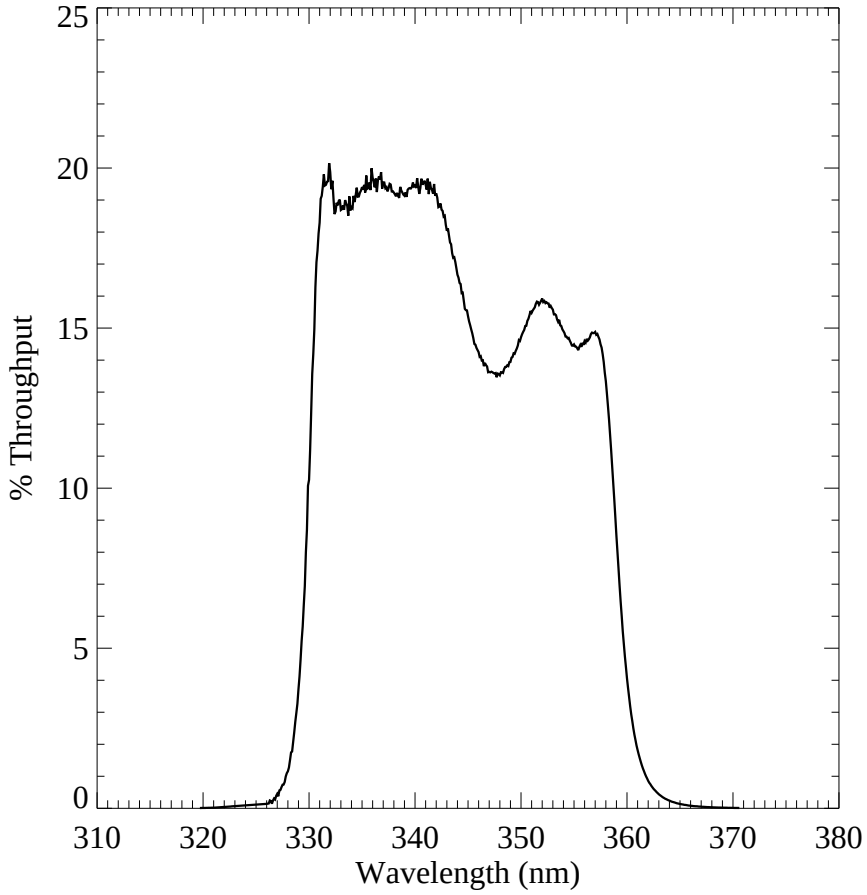

Figure A.23: Point source S/N vs. V+ABν for the F343N filter, assuming high sky backgrounds and a 5×5 pixel aperture.

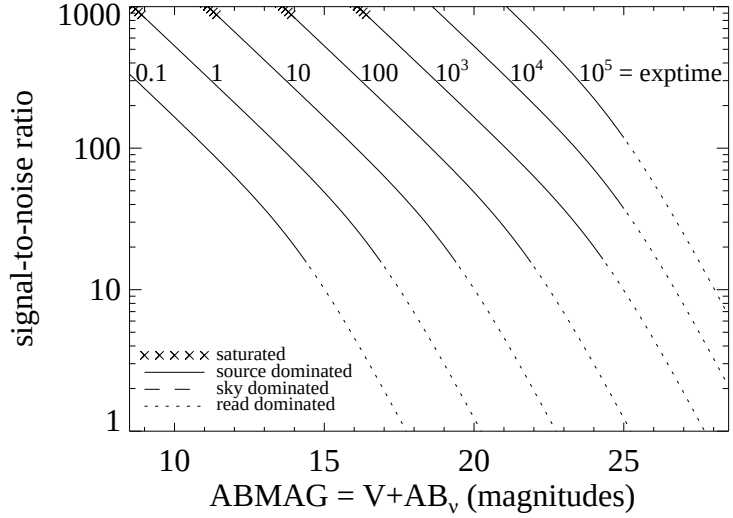

Figure A.24: Extended source S/N vs. V+ABν for the F343N filter, assuming high sky backgrounds and a source uniformly filling a 1 arcsec^2 aperture.

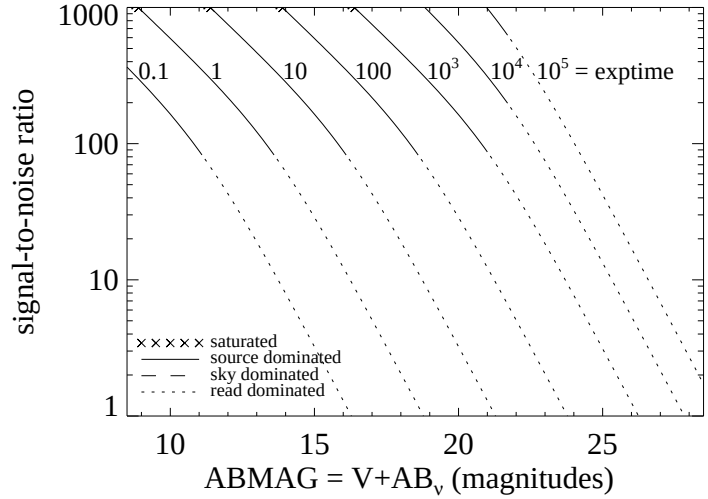

UVIS/F350LP

Description

Long pass filter.

Figure A.25: Integrated system throughput for F350LP.

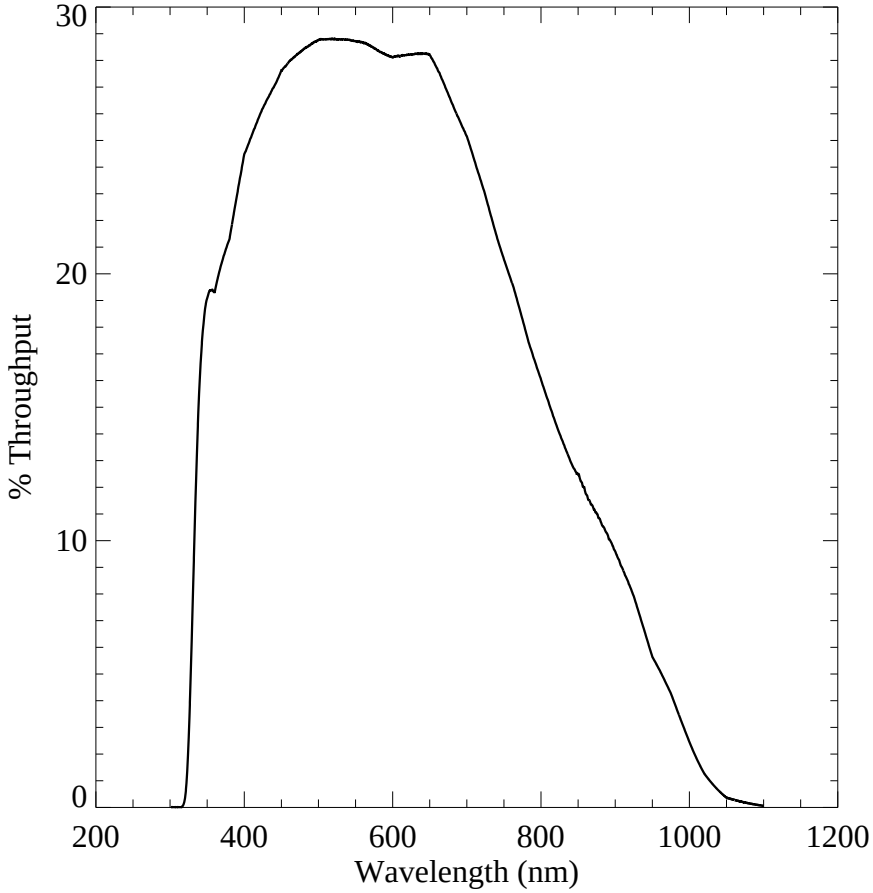

Figure A.26: Point source S/N vs. V+ABν for the F350LP filter, assuming high sky backgrounds and a 5×5 pixel aperture.

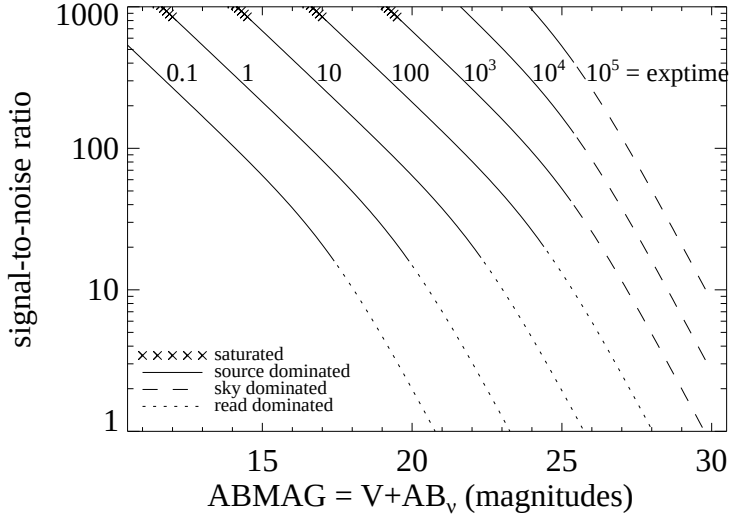

Figure A.27: Extended source S/N vs. V+ABν for the F350LP filter, assuming high sky backgrounds and a source uniformly filling a 1 arcsec^2 aperture.

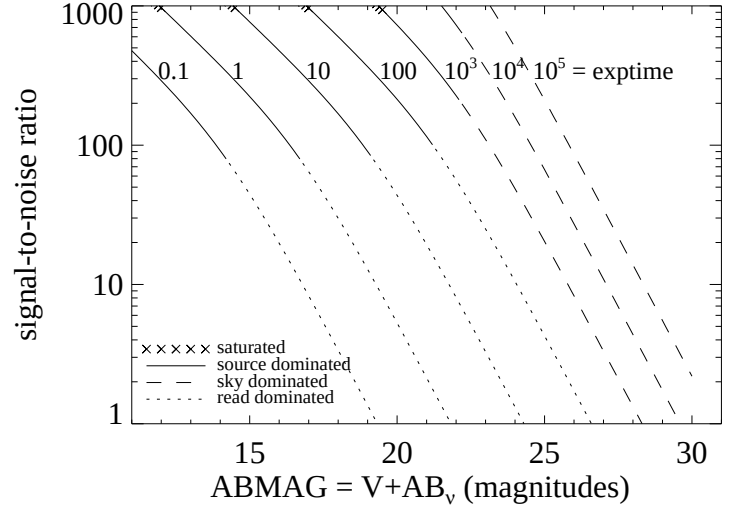

UVIS/F373N

Description

[O II] 3726/3728 filter.

Figure A.28: Integrated system throughput for F373N.

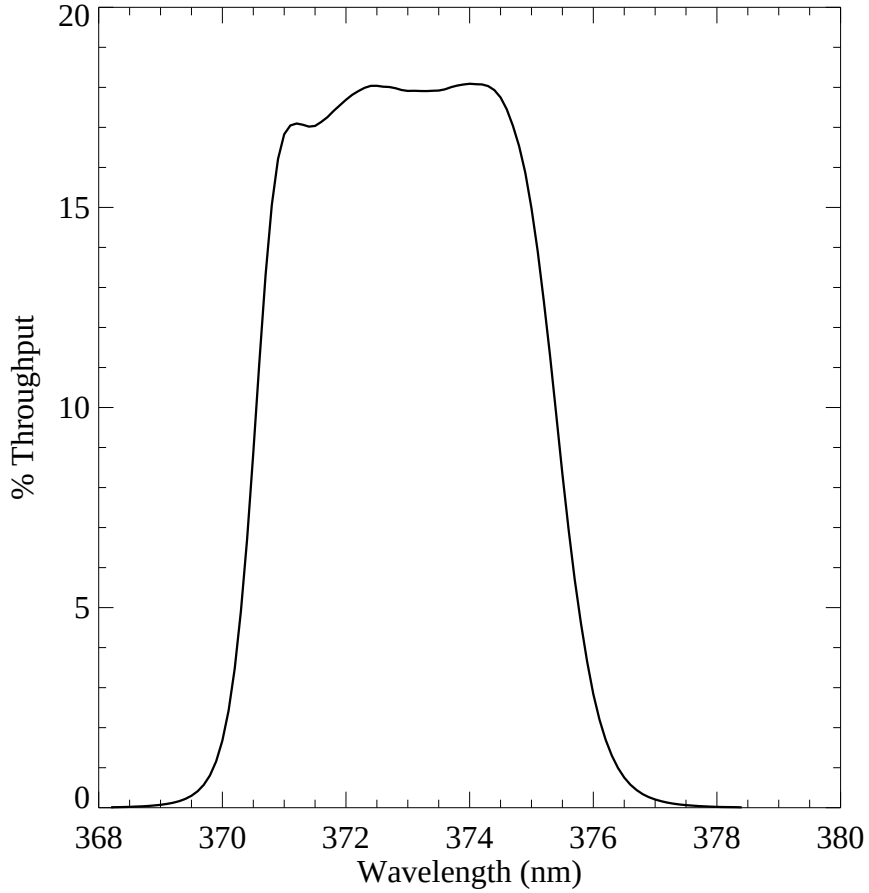

Figure A.29: Point source S/N vs. V+ABν for the F373N. filter, assuming high sky backgrounds and a 5×5 pixel aperture.

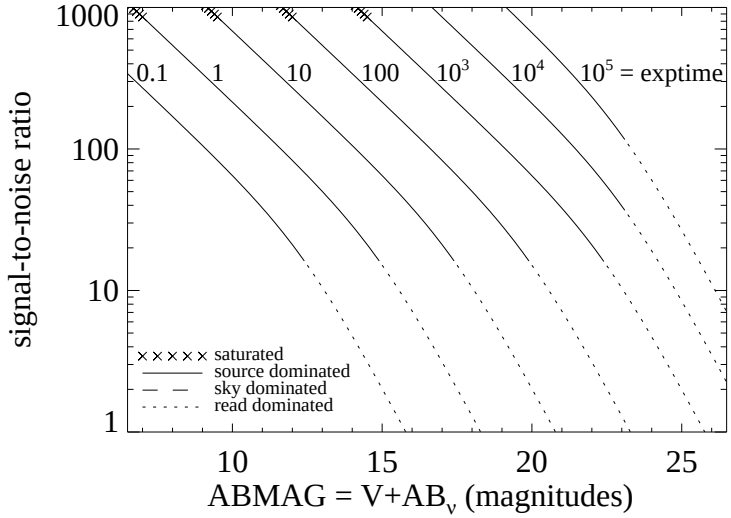

Figure A.30: Extended source S/N vs. V+ABν for the F373N. filter, assuming high sky backgrounds and a source uniformly filling a 1 arcsec^2 aperture.

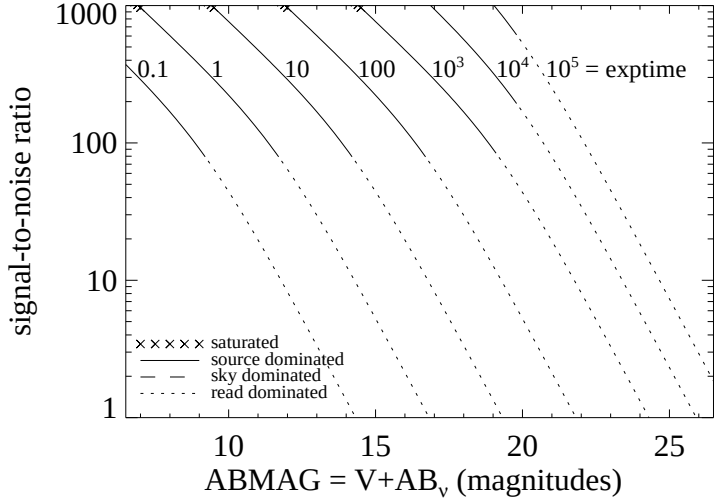

UVIS/F390M

Description

Ca II continuum filter.

Figure A.31: Integrated system throughput for F390M.

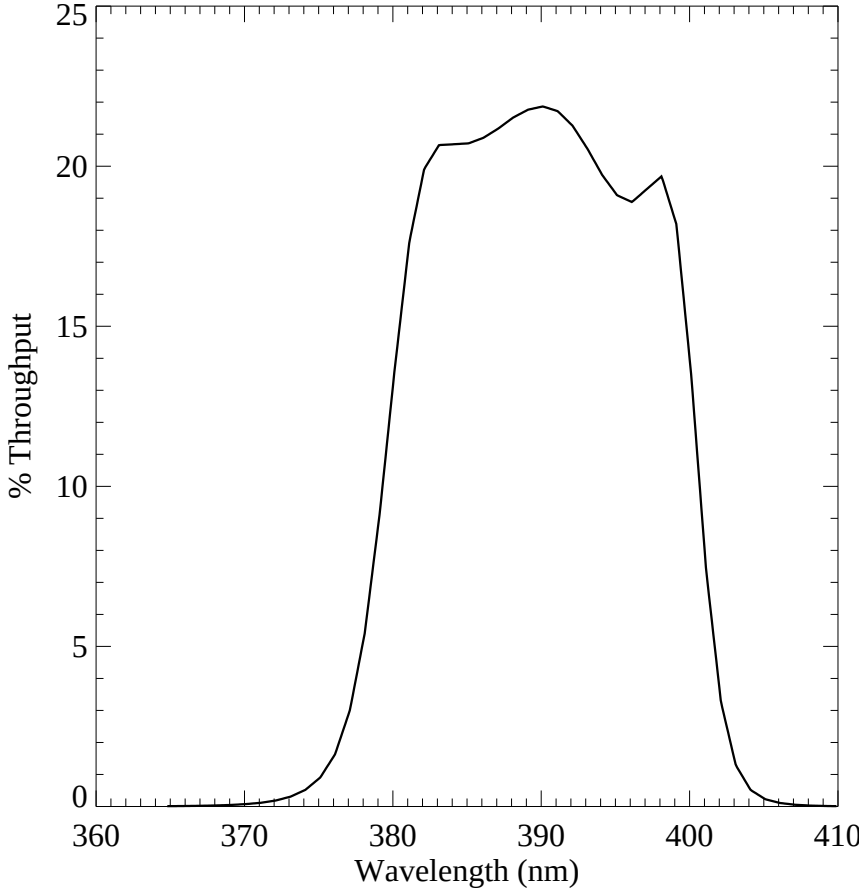

Figure A.32: Point source S/N vs. V+ABν for the F390M filter, assuming high sky backgrounds and a 5×5 pixel aperture.

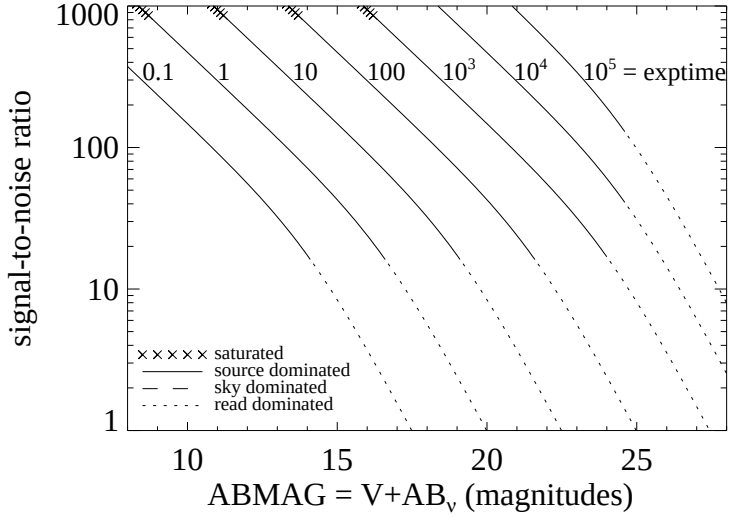

Figure A.33: Extended source S/N vs. V+ABν for the F390M filter, assuming high sky backgrounds and a source uniformly filling a 1 arcsec^2 aperture.

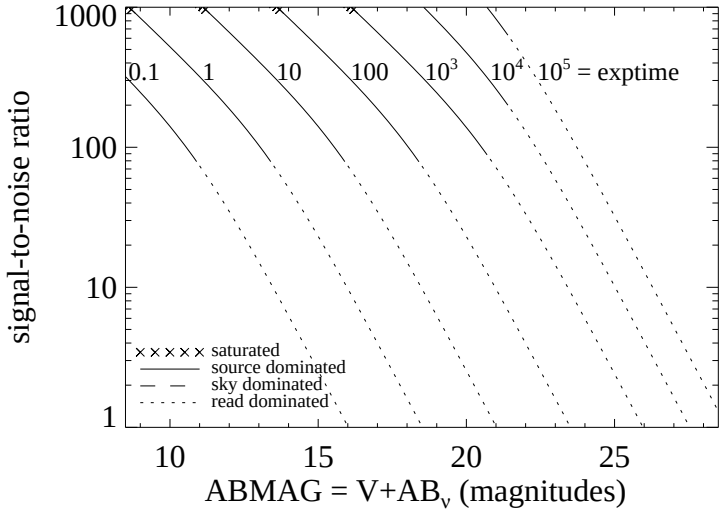

UVIS/F390W

Description

Washington *C* filter.

Figure A.34: Integrated system throughput for F390W.

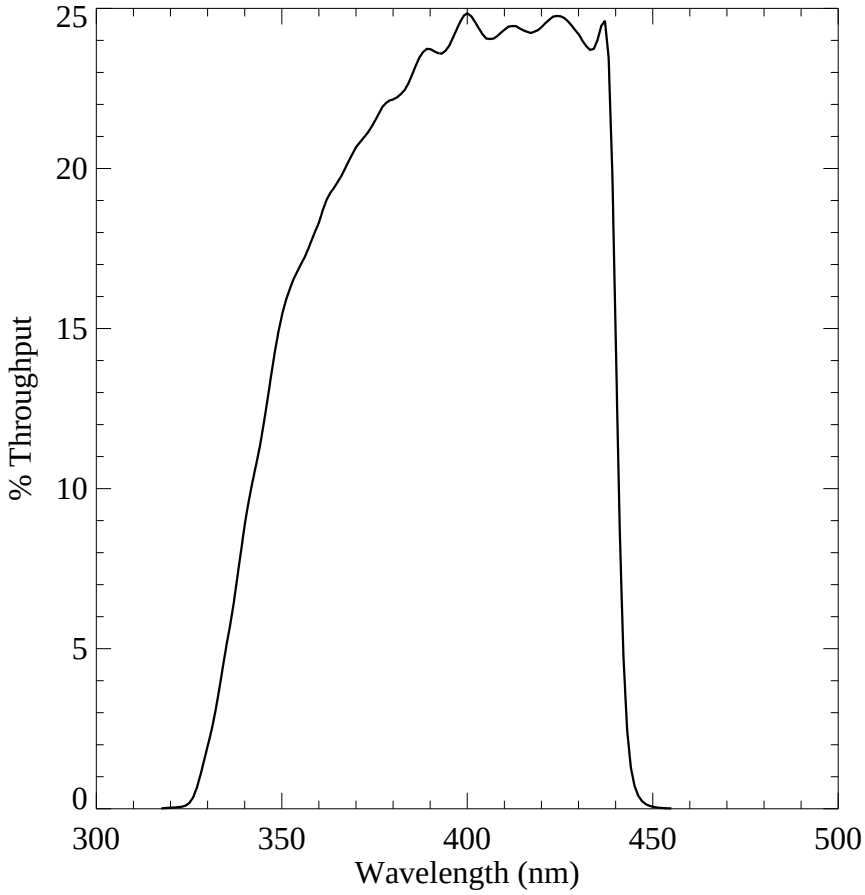

Figure A.35: Point source S/N vs. V+ABν for the F390W filter, assuming high sky backgrounds and a 5×5 pixel aperture.

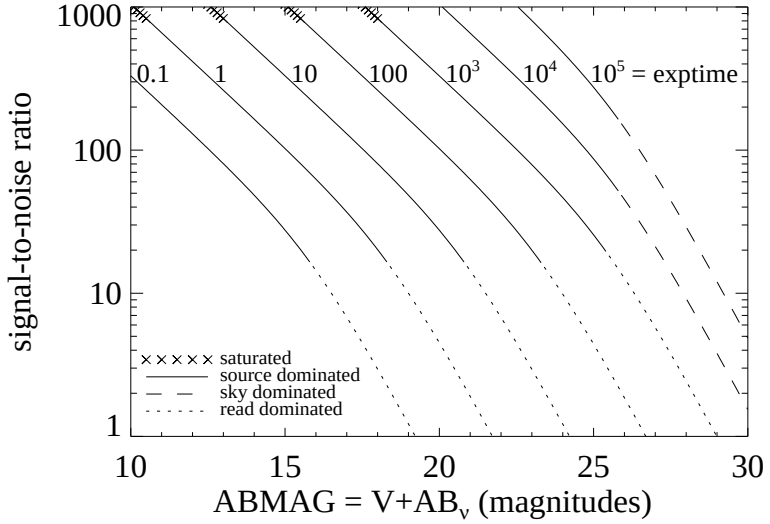

Figure A.36: Extended source S/N vs. V+ABν for the F390W filter, assuming high sky backgrounds and a source uniformly filling a 1 arcsec^2 aperture.

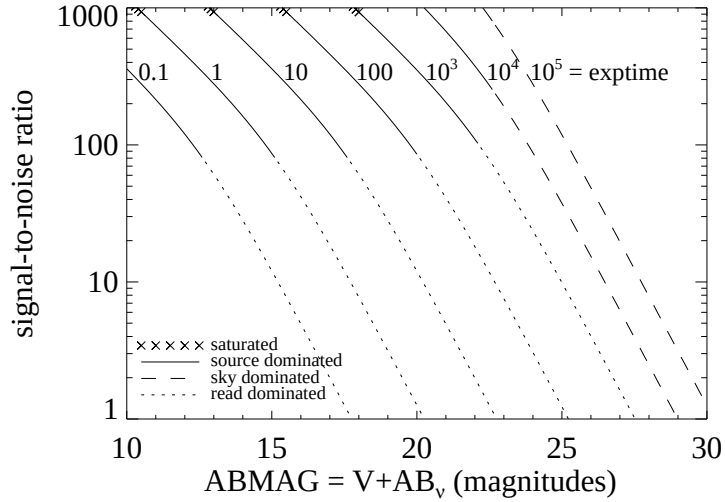

UVIS/F395N

Description

Ca II 3933/3968 filter.

Figure A.37: Integrated system throughput for F395N.

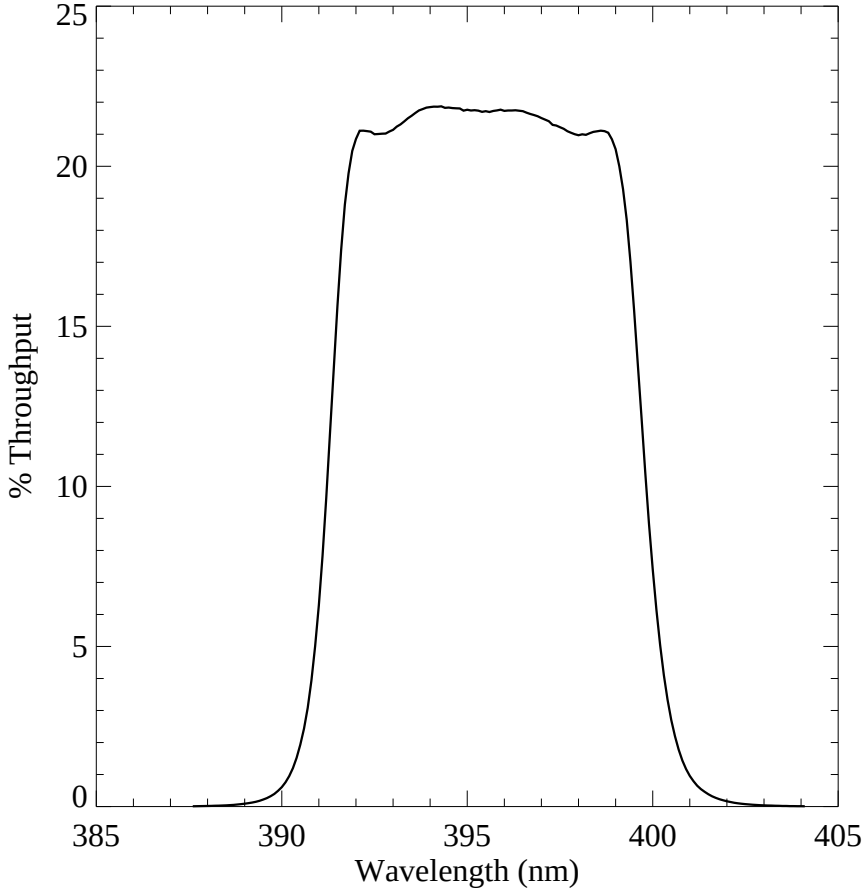

Figure A.38: Point source S/N vs. V+ABν for the F395N filter, assuming high sky backgrounds and a 5×5 pixel aperture.

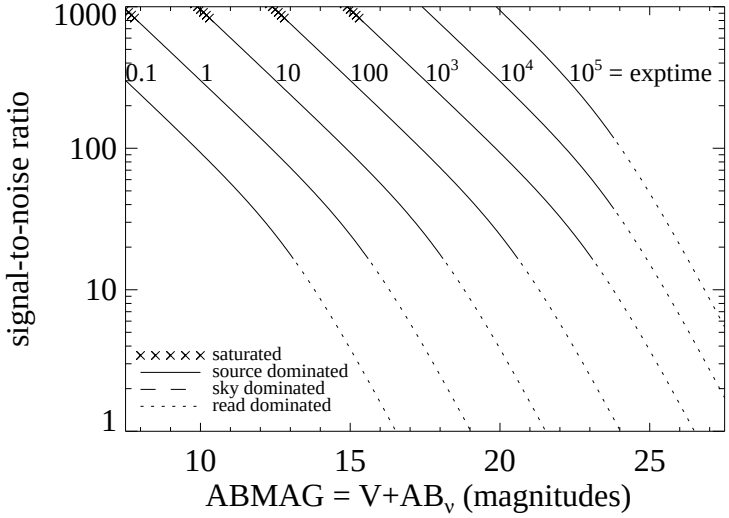

Figure A.39: Extended source S/N vs. V+ABν for the F395N filter, assuming high sky backgrounds and a source uniformly filling a 1 arcsec^2 aperture.

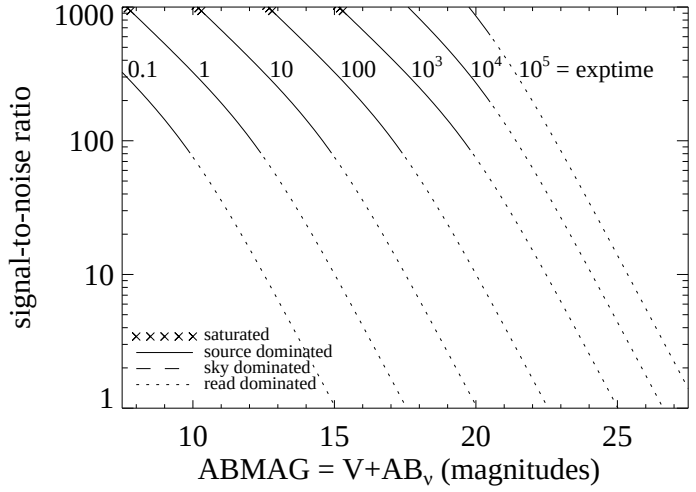

UVIS/F410M

Description

Strömgren *v* filter.

Figure A.40: Integrated system throughput for F410M.

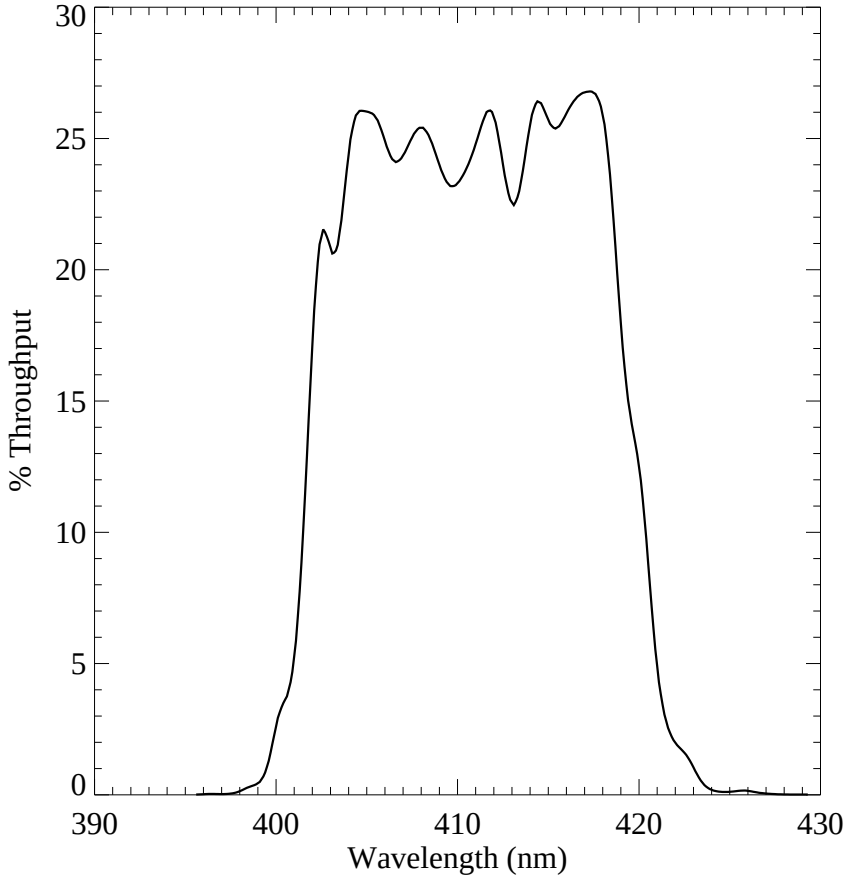

Figure A.41: Point source S/N vs. V+ABν for the F410M filter, assuming high sky backgrounds and a 5×5 pixel aperture.

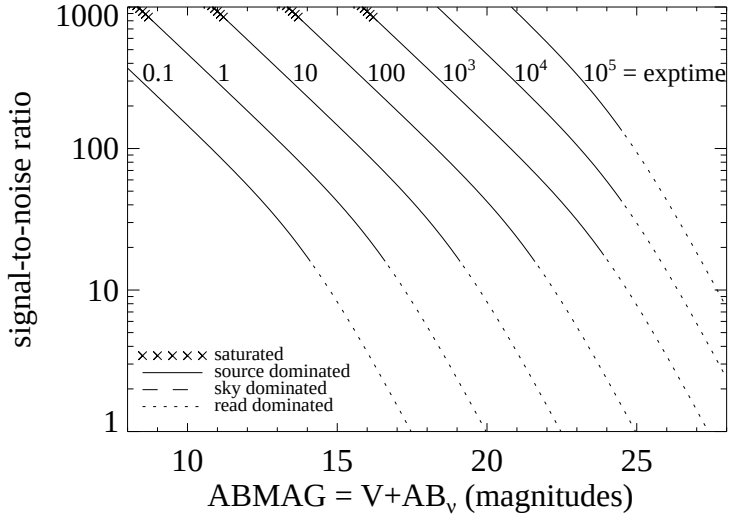

Figure A.42: Extended source S/N vs. V+ABν for the F410M filter, assuming high sky backgrounds and a source uniformly filling a 1 arcsec^2 aperture.

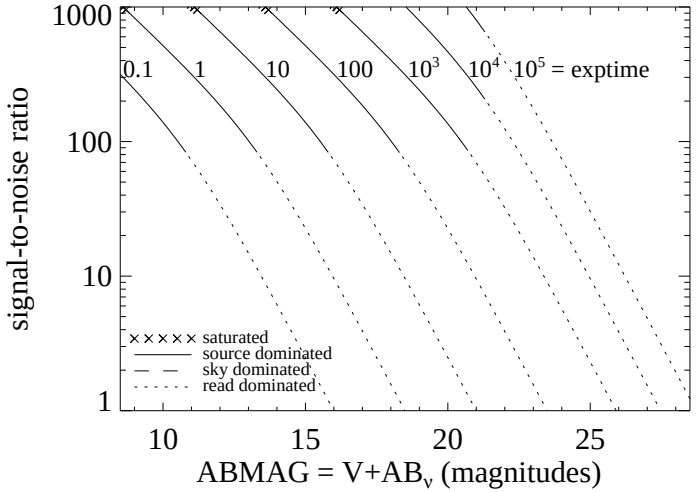

UVIS/F438W

Description

WFPC2 *B* filter.

Figure A.43: Integrated system throughput for F438W.

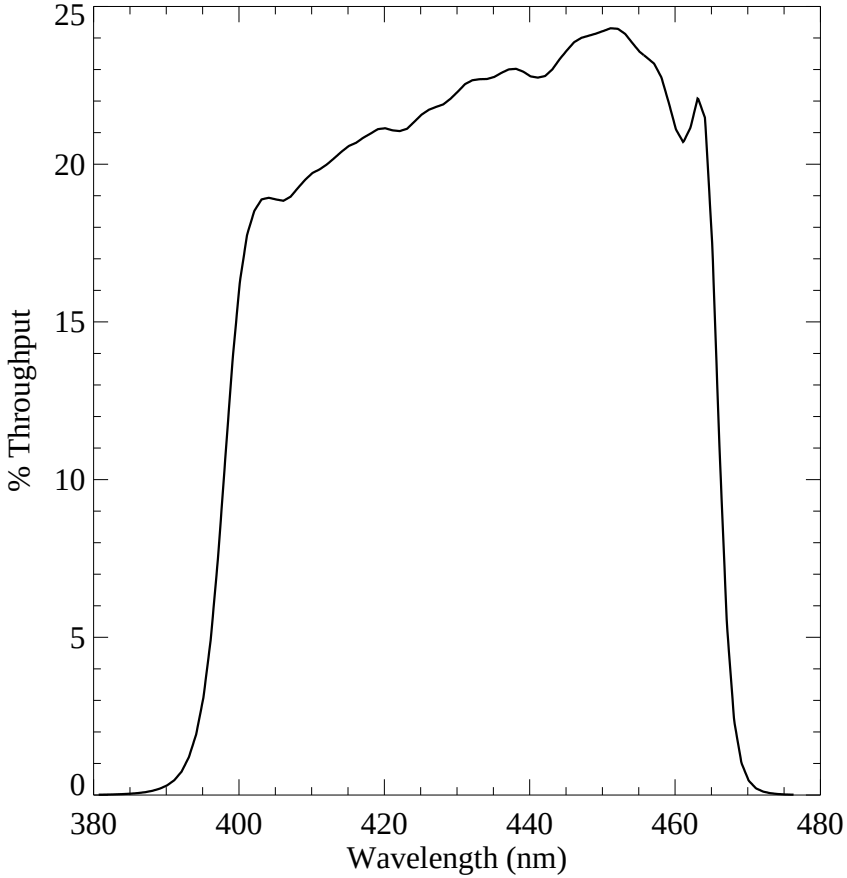

Figure A.44: Point source S/N vs. V+ABν for the F438W filter, assuming high sky backgrounds and a 5×5 pixel aperture.

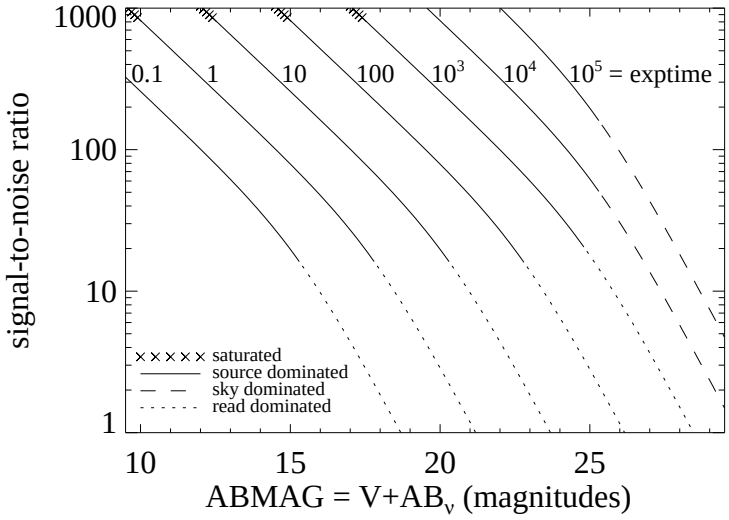

Figure A.45: Extended source S/N vs. V+ABν for the F438W filter, assuming high sky backgrounds and a source uniformly filling a 1 arcsec^2 aperture.

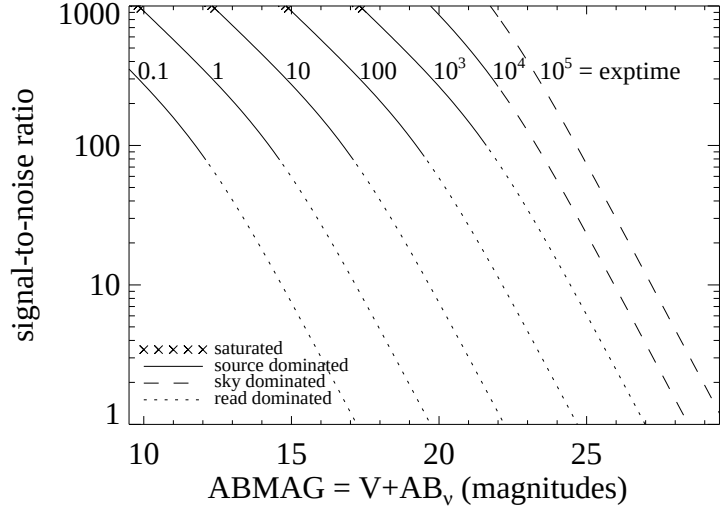

UVIS/F467M

Description

Strömgren *b* filter.

Figure A.46: Integrated system throughput for F467M.

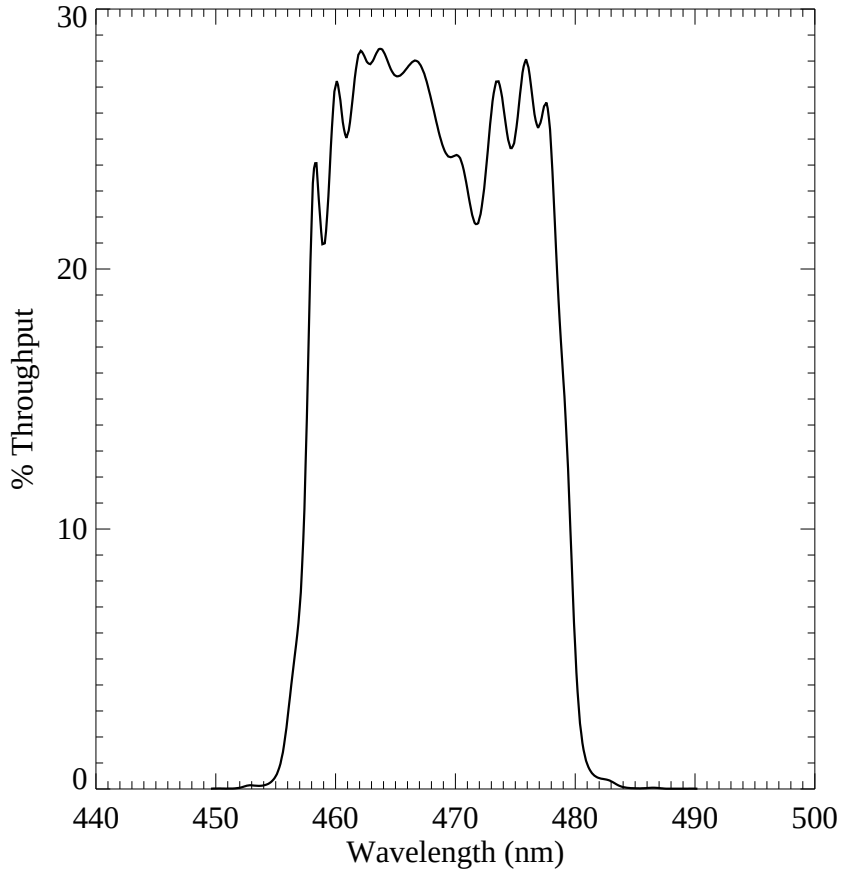

Figure A.47: Point Source S/N vs. V+ABν for the F467M filter, assuming high sky backgrounds and a 5×5 pixel aperture.

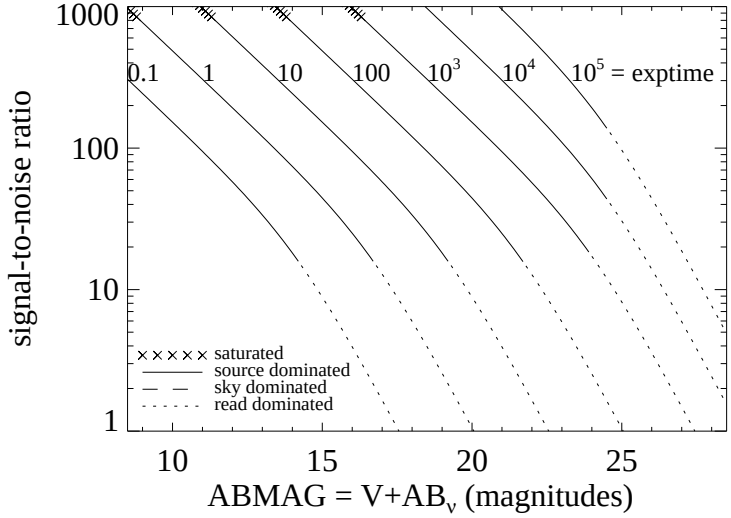

Figure A.48: Extended Source S/N vs. V+ABν for the F467M filter, assuming high sky backgrounds and a source uniformly filling a 1 arcsec^2 aperture.

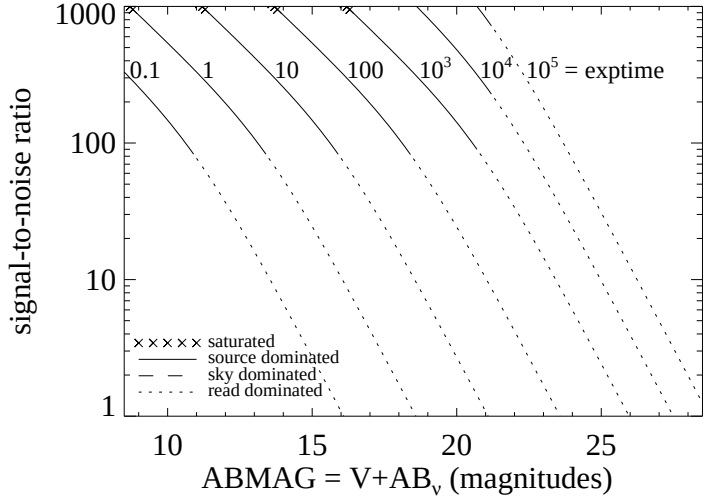

UVIS/F469N

Description

He II 4686 filter.

Figure A.49: Integrated system throughput for F469N.

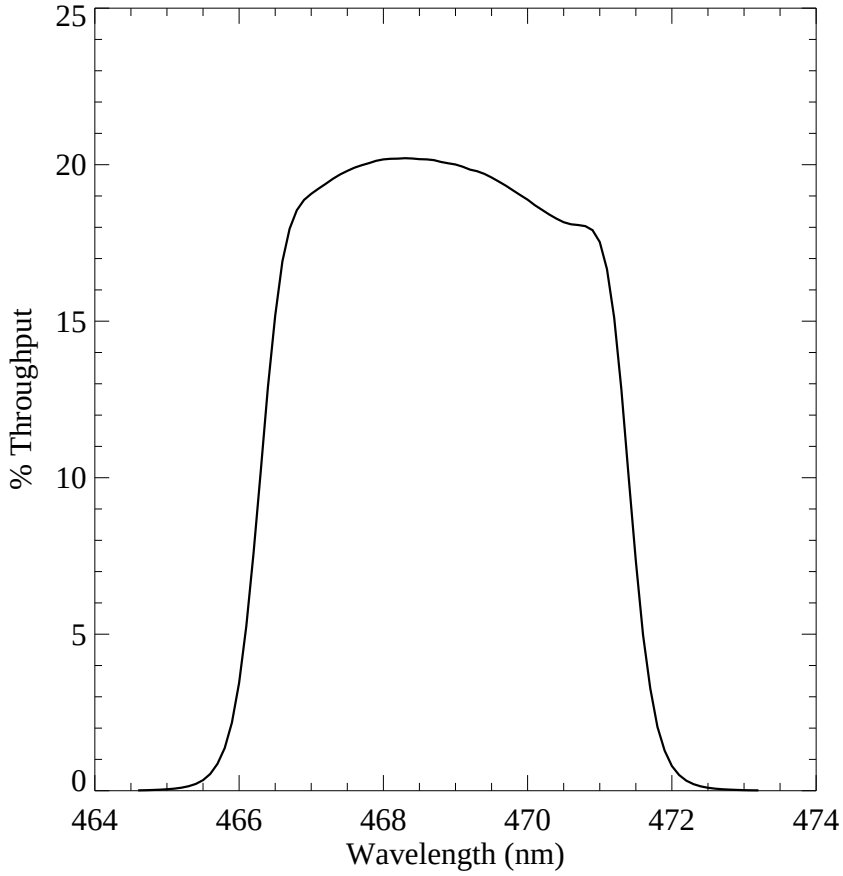

Figure A.50: Point source S/N vs. V+ABν for the F469N filter, assuming high sky backgrounds and a 5×5 pixel aperture.

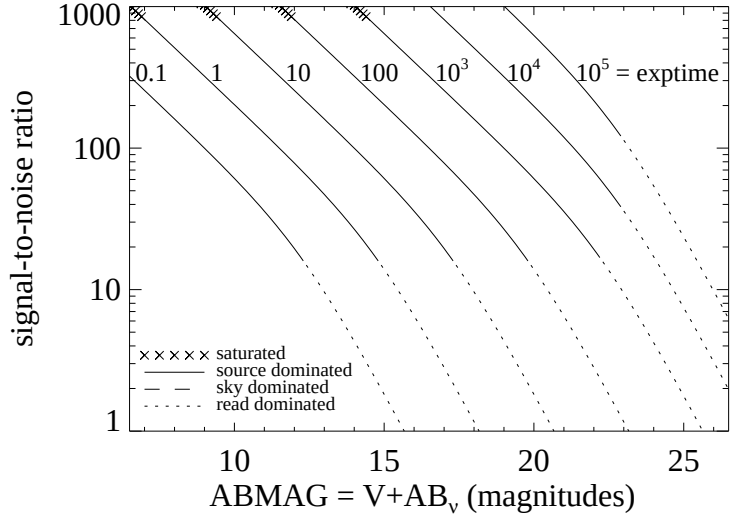

Figure A.51: Extended source S/N vs. V+ABν for the F469N filter, assuming high sky backgrounds and a source uniformly filling a 1 arcsec^2 aperture.

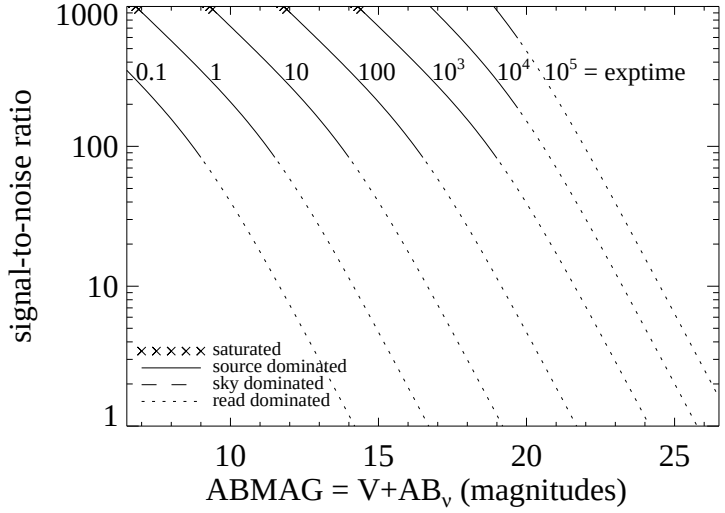

UVIS/F475W

Description

Sloan Digital Sky Survey *g*′ filter.

Figure A.52: Integrated system throughput for F475W.

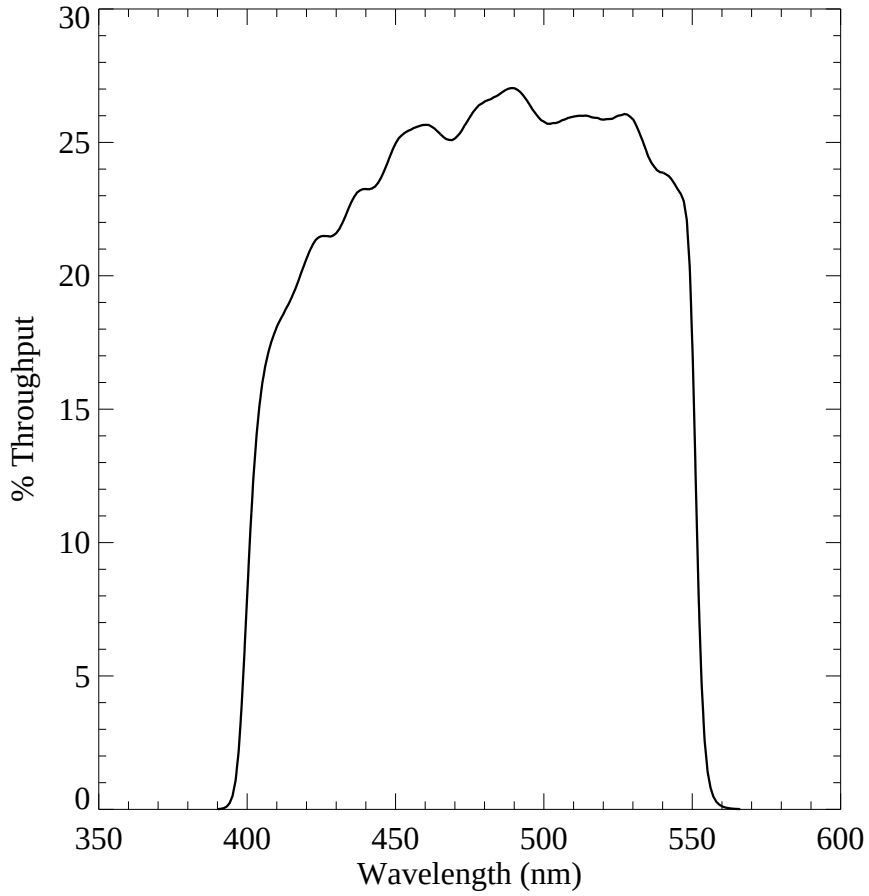

Figure A.53: Point source S/N vs. V+ABν for the F475W filter, assuming high sky backgrounds and a 5×5 pixel aperture.

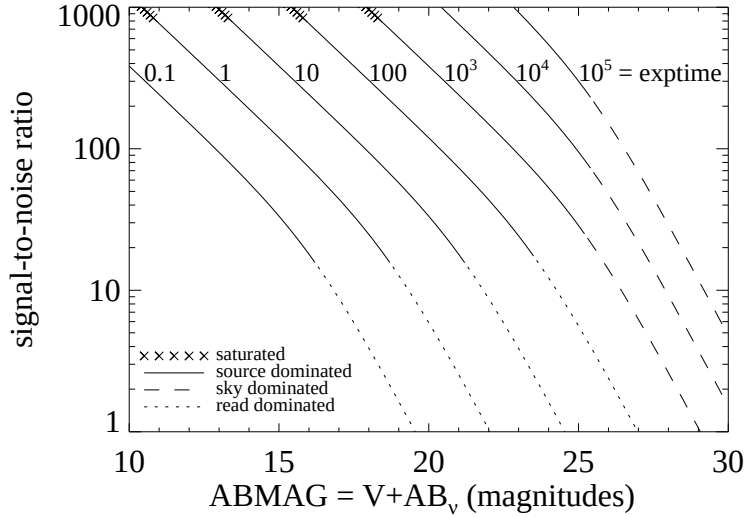

Figure A.54: Extended source S/N vs. V+ABν for the F475W filter, assuming high sky backgrounds and a source uniformly filling a 1 arcsec^2 aperture.

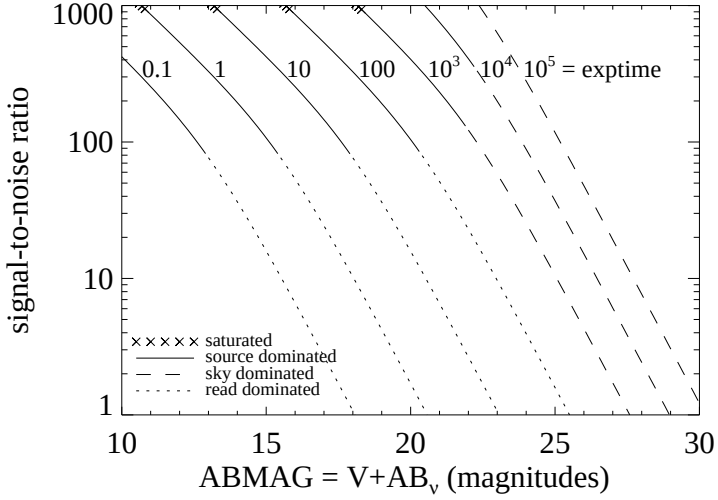

UVIS/F475X

Description

Extremely wide blue filter.

Figure A.55: Integrated system throughput for F475X.

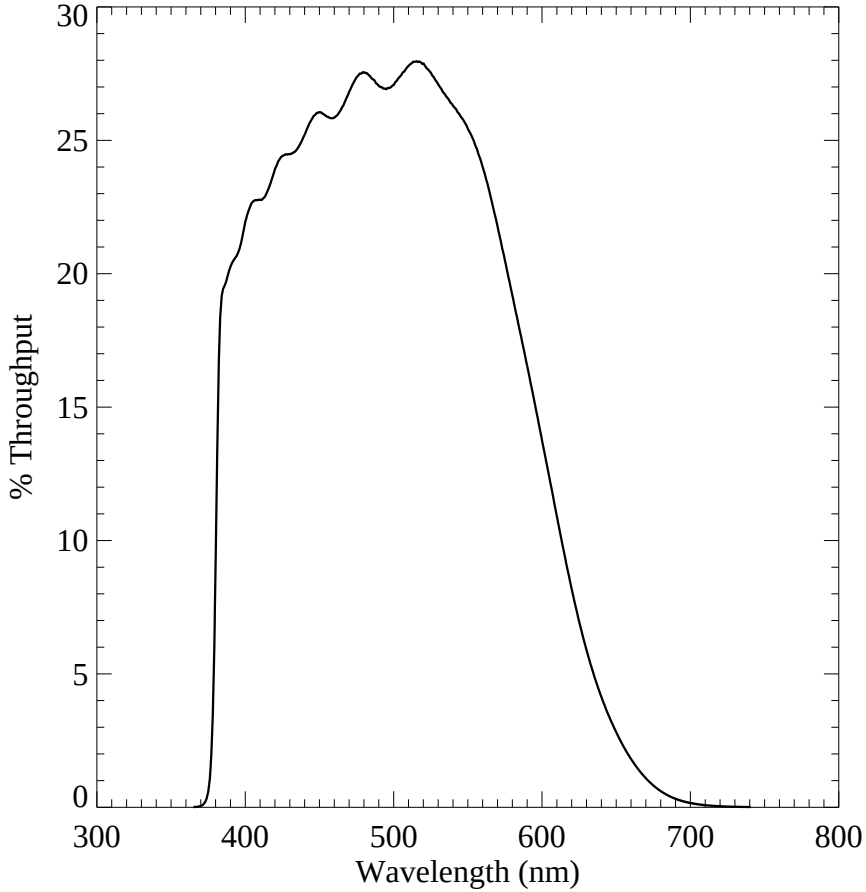

Figure A.56: Point source S/N vs. V+ABν for the F475X filter, assuming high sky backgrounds and a 5×5 pixel aperture.

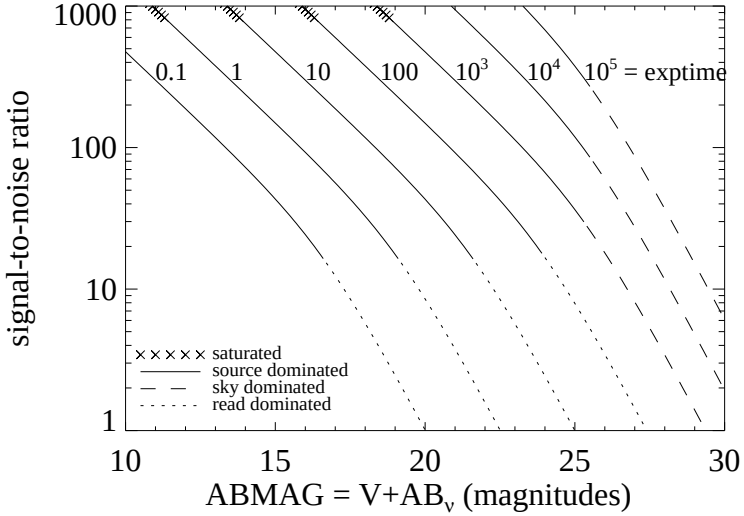

Figure A.57: Extended source S/N vs. V+ABν for the F475X filter, assuming high sky backgrounds and a source uniformly filling a 1 arcsec^2 aperture.

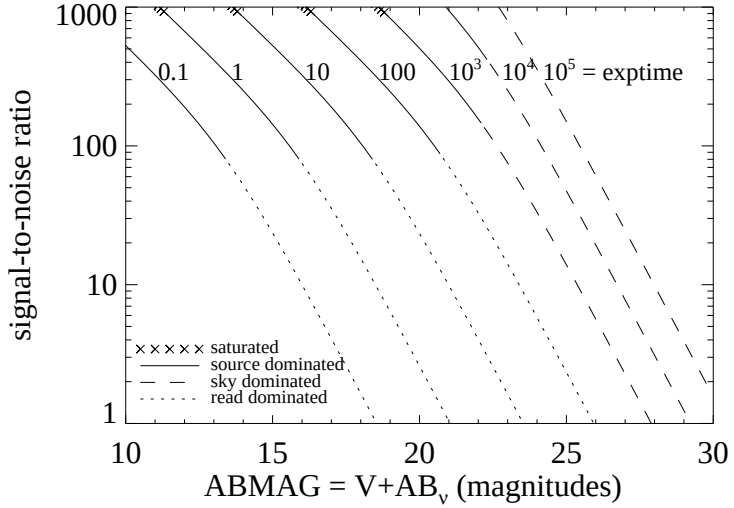

UVIS/F487N

Description

Hβ 4861 filter.

Figure A.58: Integrated system throughput for F487N.

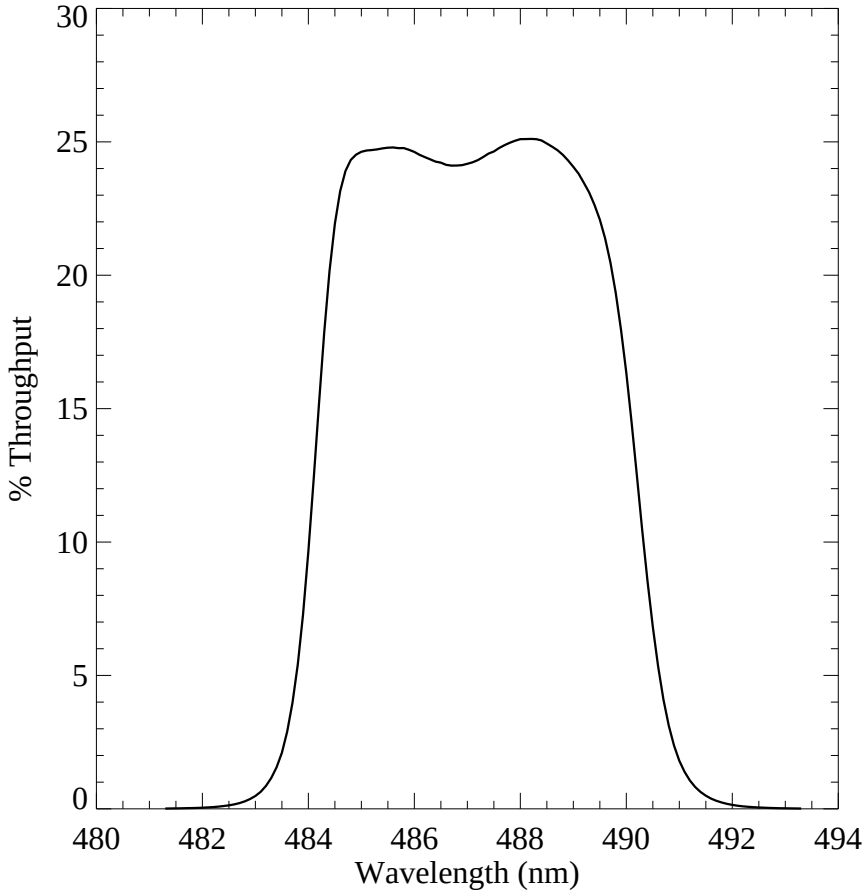

Figure A.59: Point source S/N vs. V+ABν for the F487N filter, assuming high sky backgrounds and a 5×5 pixel aperture.

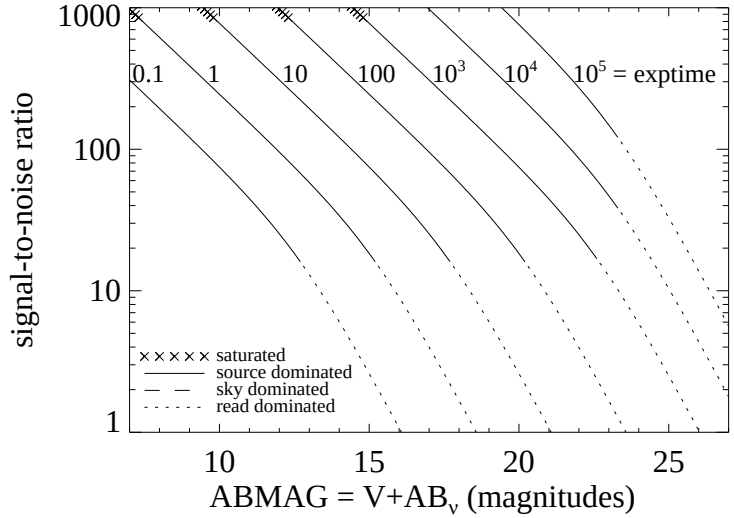

Figure A.60: Extended source S/N vs. V+ABν for the F487N filter, assuming high sky backgrounds and a source uniformly filling a 1 arcsec^2 aperture.

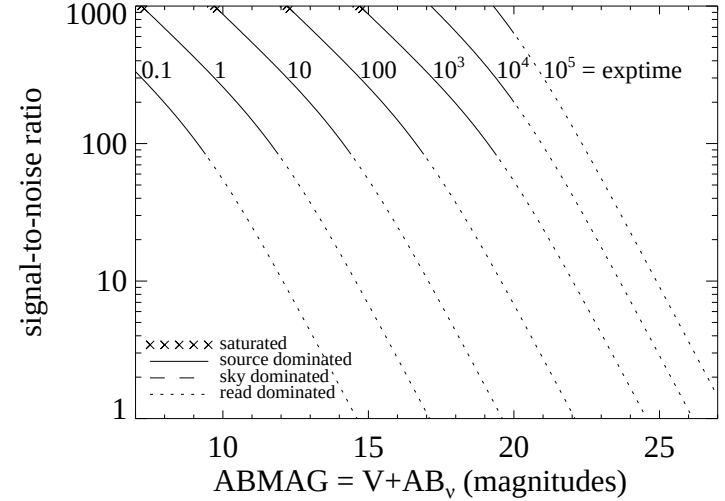

UVIS/F502N

Description

[O III] 5007 filter.

Figure A.61: Integrated system throughput for F502N.

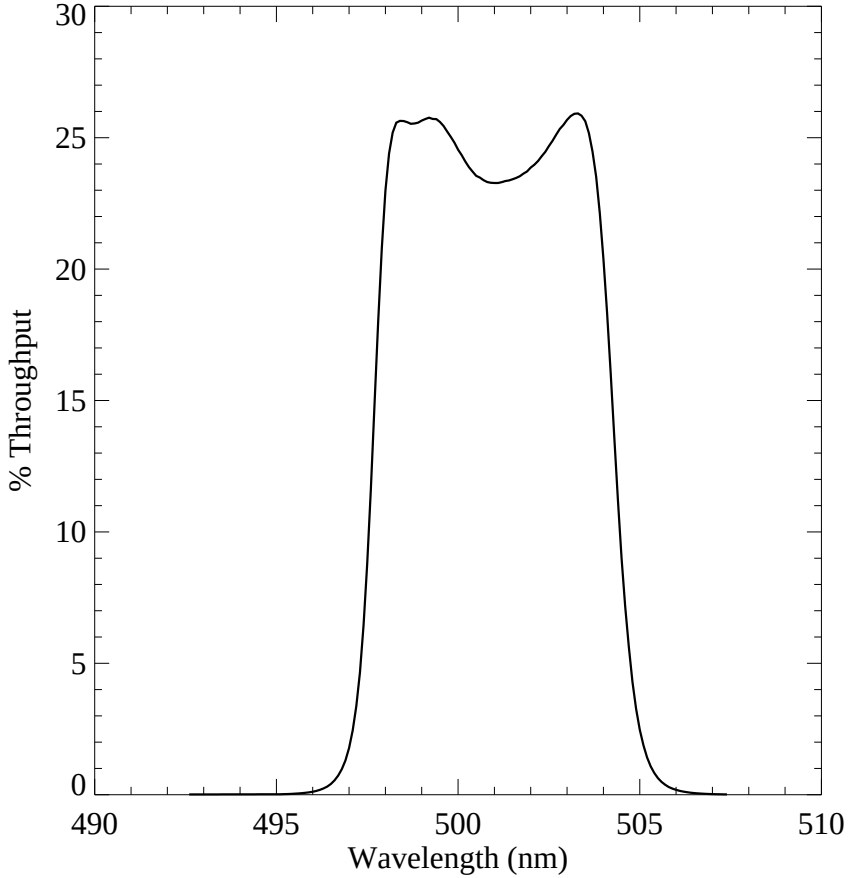

Figure A.62: Point source S/N vs. V+ABν for the F502N filter, assuming high sky backgrounds and a 5×5 pixel aperture.

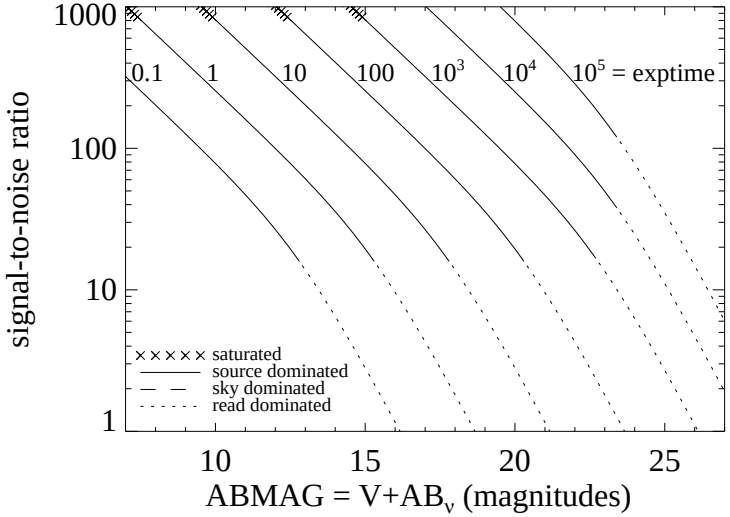

Figure A.63: Extended source S/N vs. V+ABν for the F502N filter, assuming high sky backgrounds and a source uniformly filling a 1 arcsec^2 aperture.

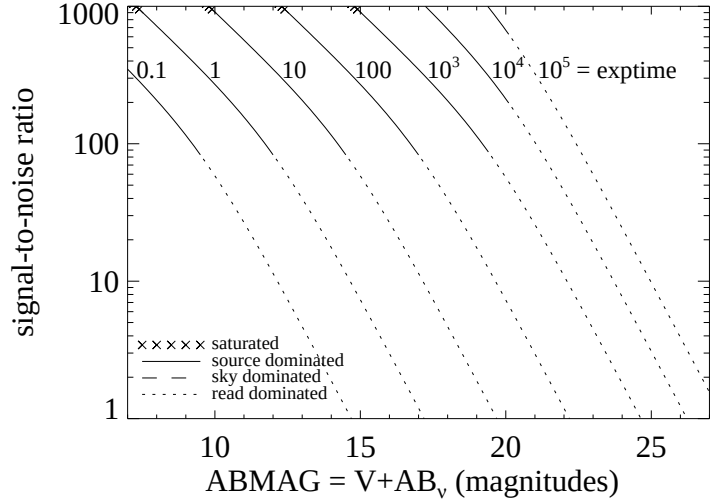

UVIS/F547M

Description

Strömgren *y* filter.

Figure A.64: Integrated system throughput for F547M.

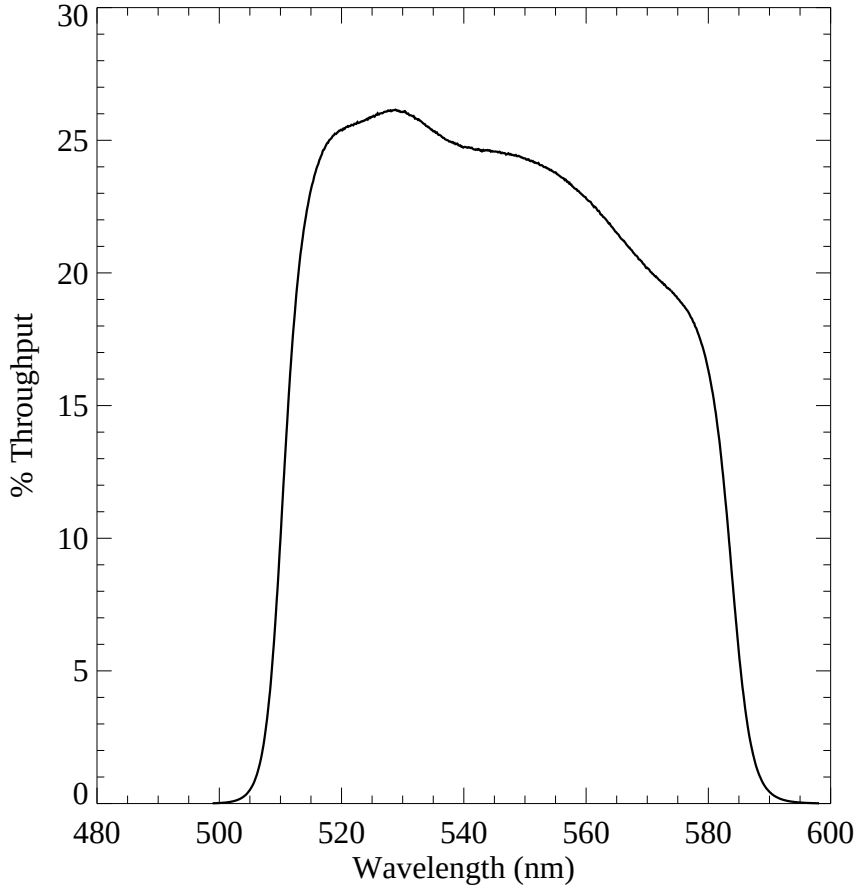

Figure A.65: Point source S/N vs. V+ABν for the F547M filter, assuming high sky backgrounds and a 5×5 pixel aperture.

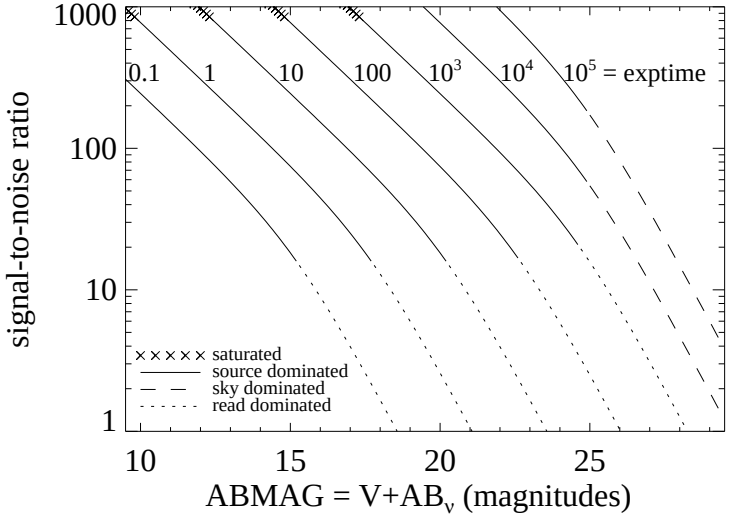

Figure A.66: Extended source S/N vs. V+ABν for the F547M filter, assuming high sky backgrounds and a source uniformly filling a 1 arcsec^2 aperture.

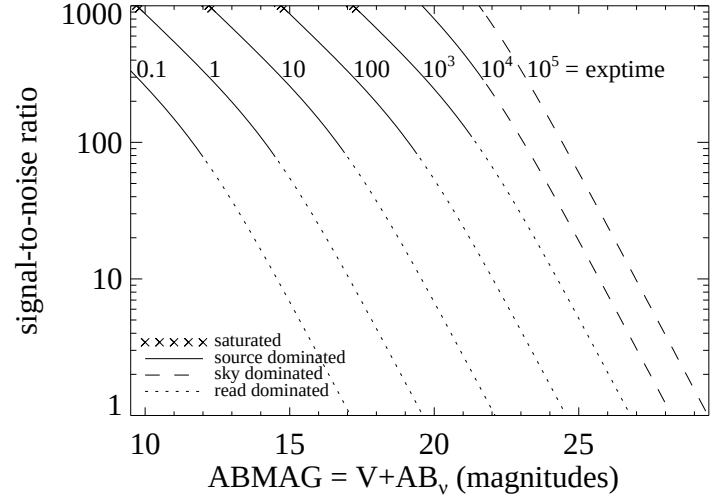

UVIS/F555W

Description

WFPC2 *V* filter.

Figure A.67: Integrated system throughput for F555W.

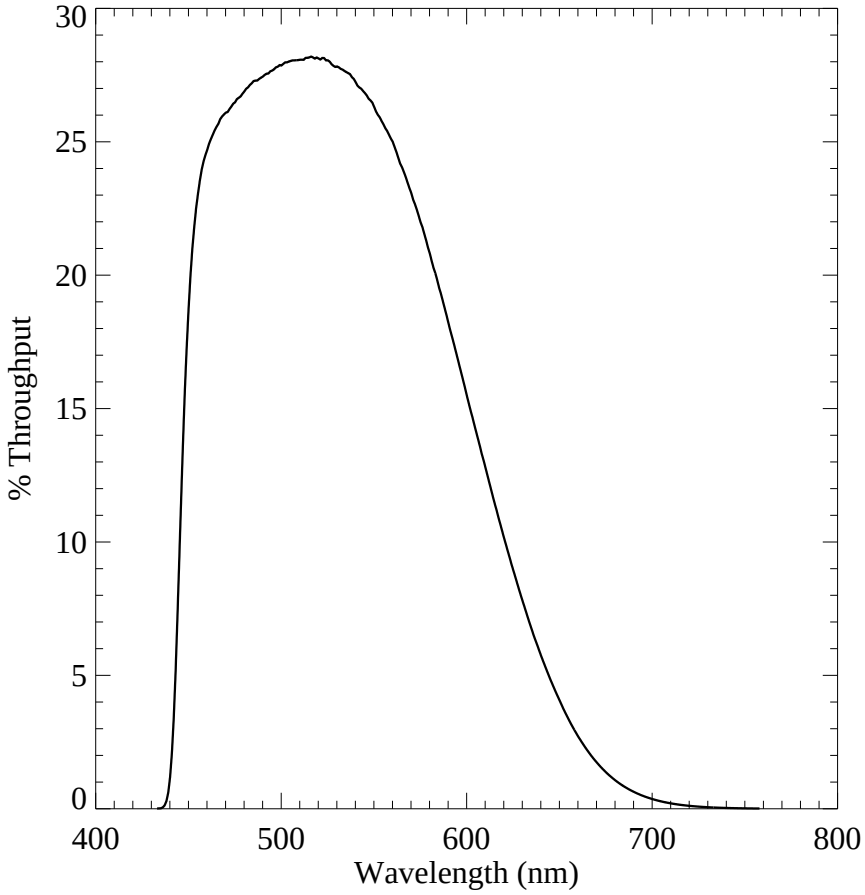

Figure A.68: Point source S/N vs. V+ABν for the F555W filter, assuming high sky backgrounds and a 5×5 pixel aperture.

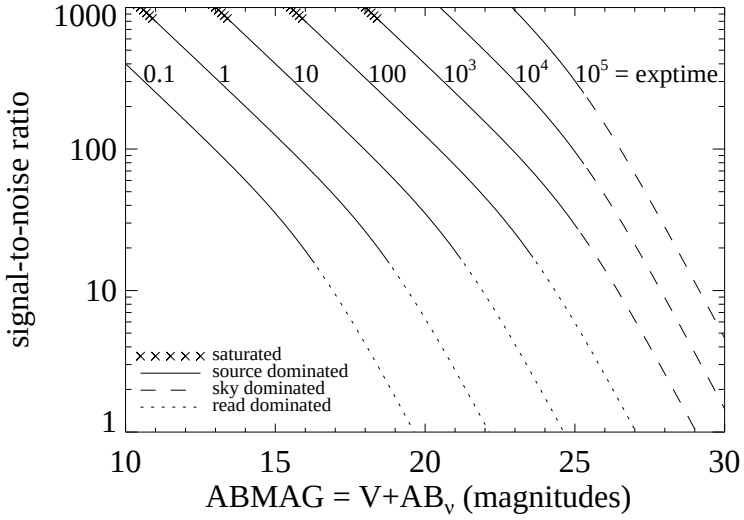

Figure A.69: Extended source S/N vs. V+ABν for the F555W filter, assuming high sky backgrounds and a source uniformly filling a 1 arcsec^2 aperture.

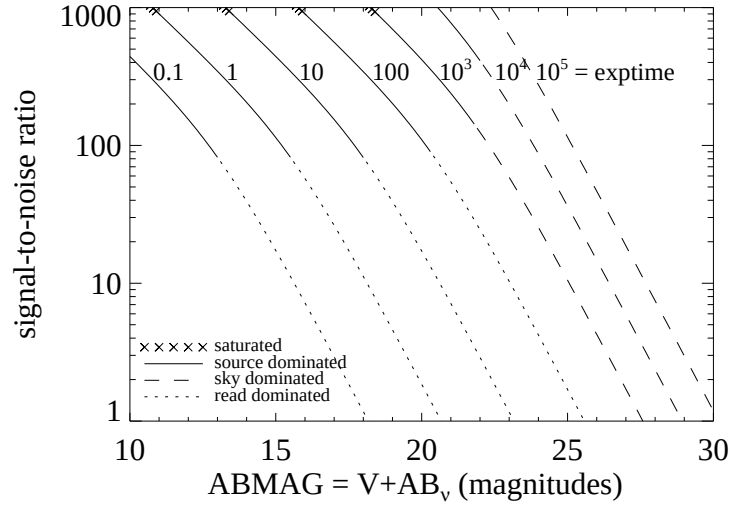

UVIS/F600LP

Description

Long-pass filter.

Figure A.70: Integrated system throughput for F600LP.

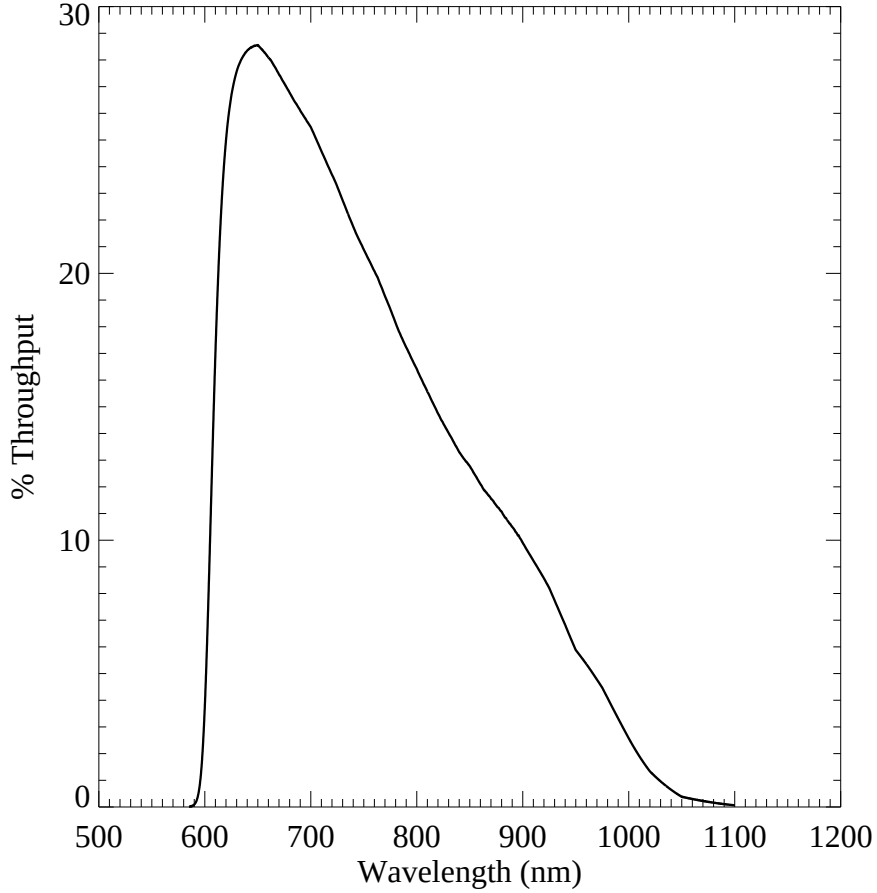

Figure A.71: Point source S/N vs. V+ABν for the F600LP filter, assuming high sky backgrounds and a 5×5 pixel aperture.

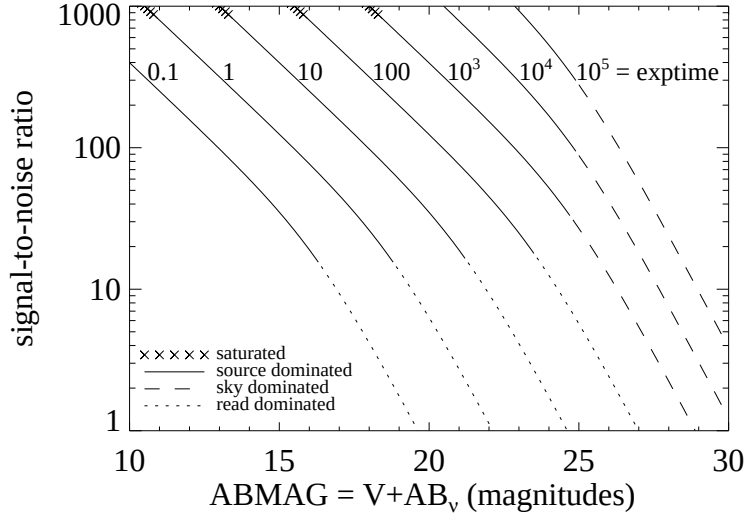

Figure A.72: Extended source S/N vs. V+ABν for the F600LP filter, assuming high sky backgrounds and a source uniformly filling a 1 arcsec^2 aperture.

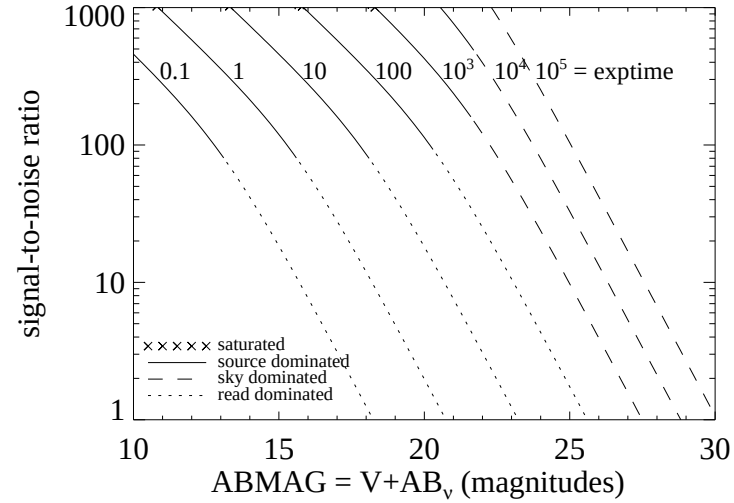

UVIS/F606W

Description

WFPC2 Wide *V* filter.

Figure A.73: Integrated system throughput for F606W.

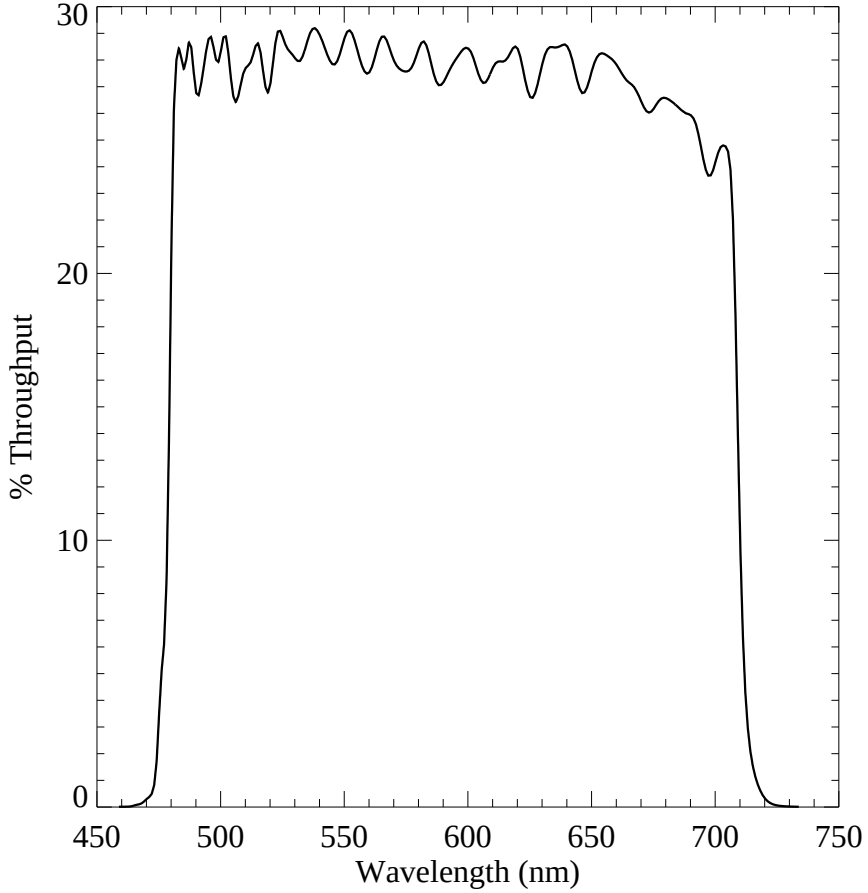

Figure A.74: Point source S/N vs. V+ABν for the F606W filter, assuming high sky backgrounds and a 5×5 pixel aperture.

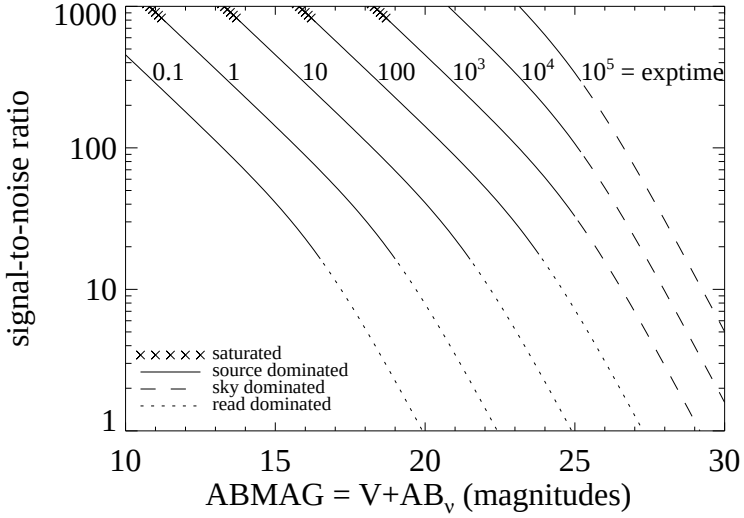

Figure A.75: Extended source S/N vs. V+ABν for the F606W filter, assuming high sky backgrounds and a source uniformly filling a 1 arcsec^2 aperture.

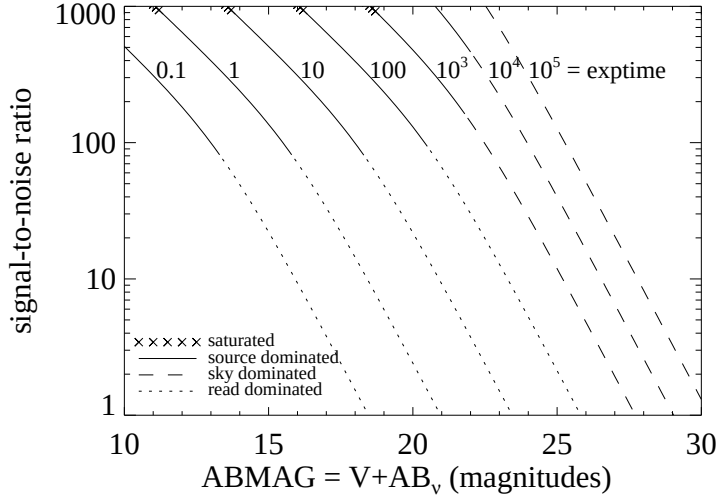

UVIS/F621M

Description

11% passband filter.

Figure A.76: Integrated system throughput for F621M.

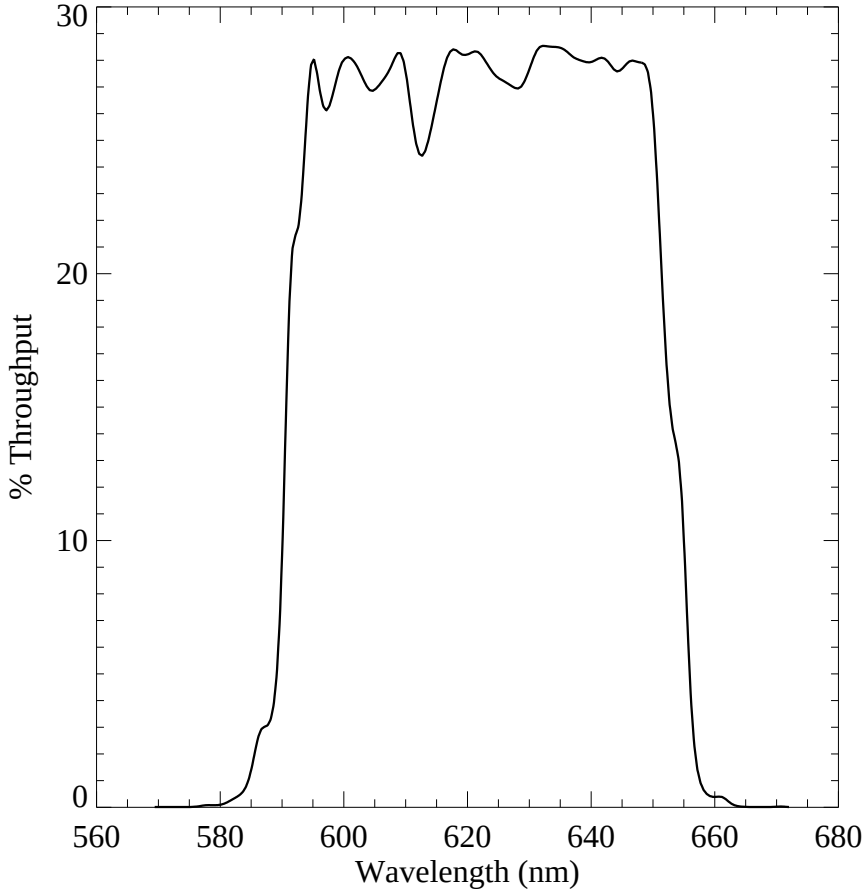

Figure A.77: Point source S/N vs. V+ABν for the F621M filter, assuming high sky backgrounds and a 5×5 pixel aperture.

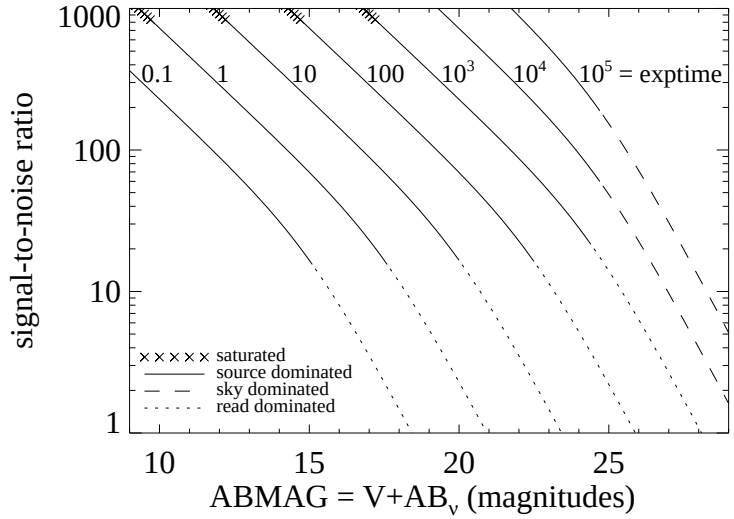

Figure A.78: Extended source S/N vs. V+ABν for the F621M filter, assuming high sky backgrounds and a source uniformly filling a 1 arcsec^2 aperture.

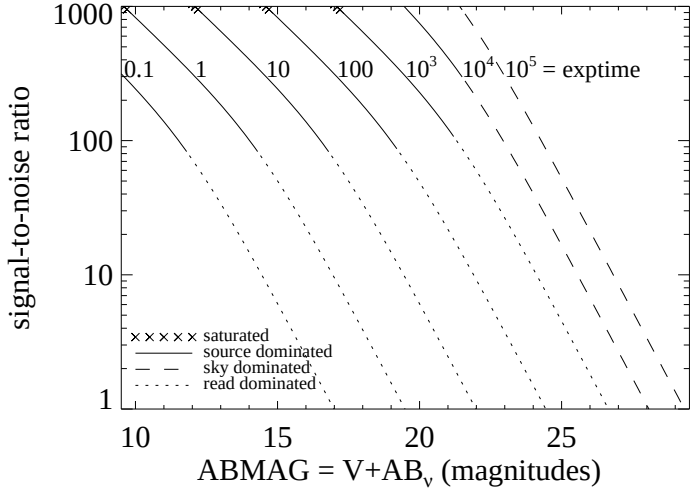

UVIS/F625W

Description

Sloan Digital Sky Survey *r′* filter.

Figure A.79: Integrated system throughput for F625W.

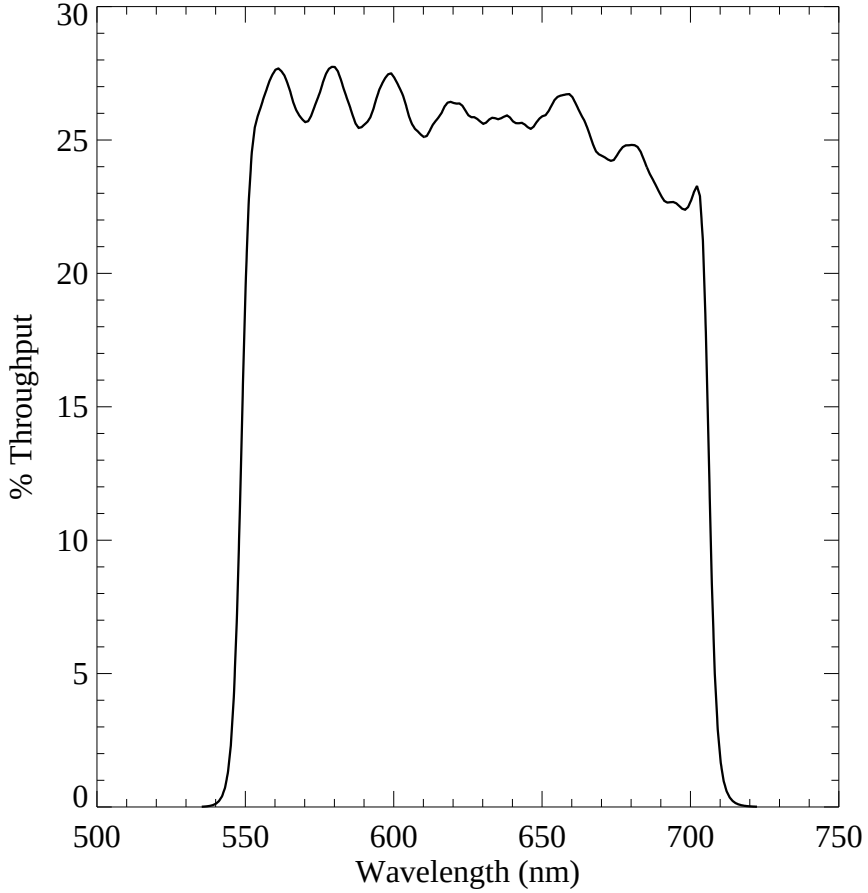

Figure A.80: Point source S/N vs. V+ABν for the F625W filter, assuming high sky backgrounds and a 5×5 pixel aperture.

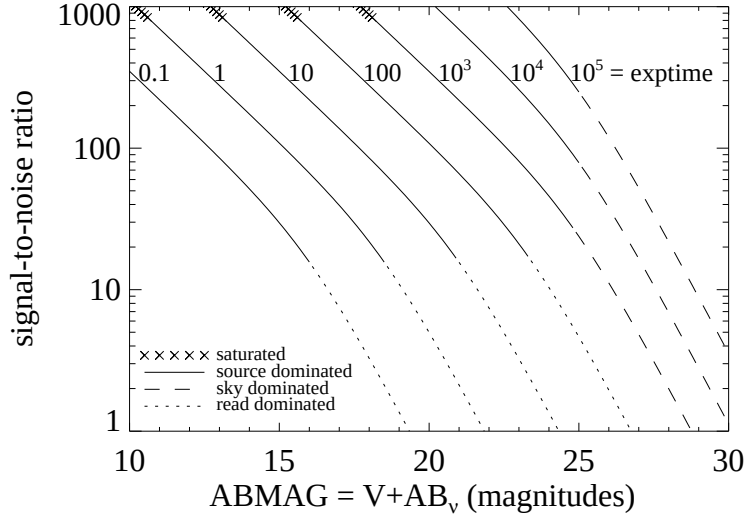

Figure A.81: Extended source S/N vs. V+ABν for the F625W filter, assuming high sky backgrounds and a source uniformly filling a 1 arcsec^2 aperture.

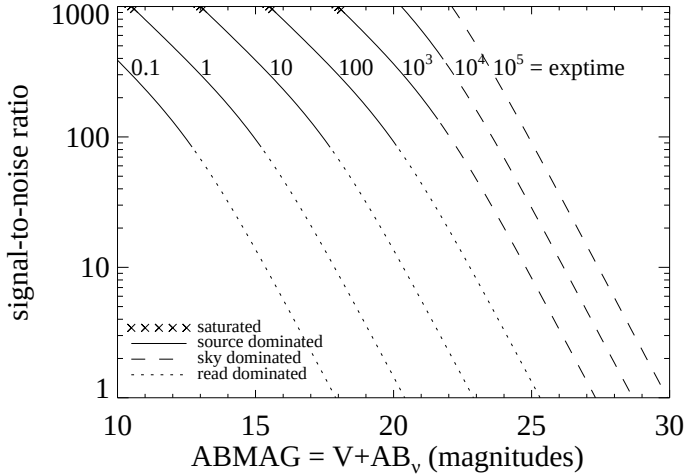

UVIS/F631N

Description

[O I] 6300 filter.

Figure A.82: Integrated system throughput for F631N.

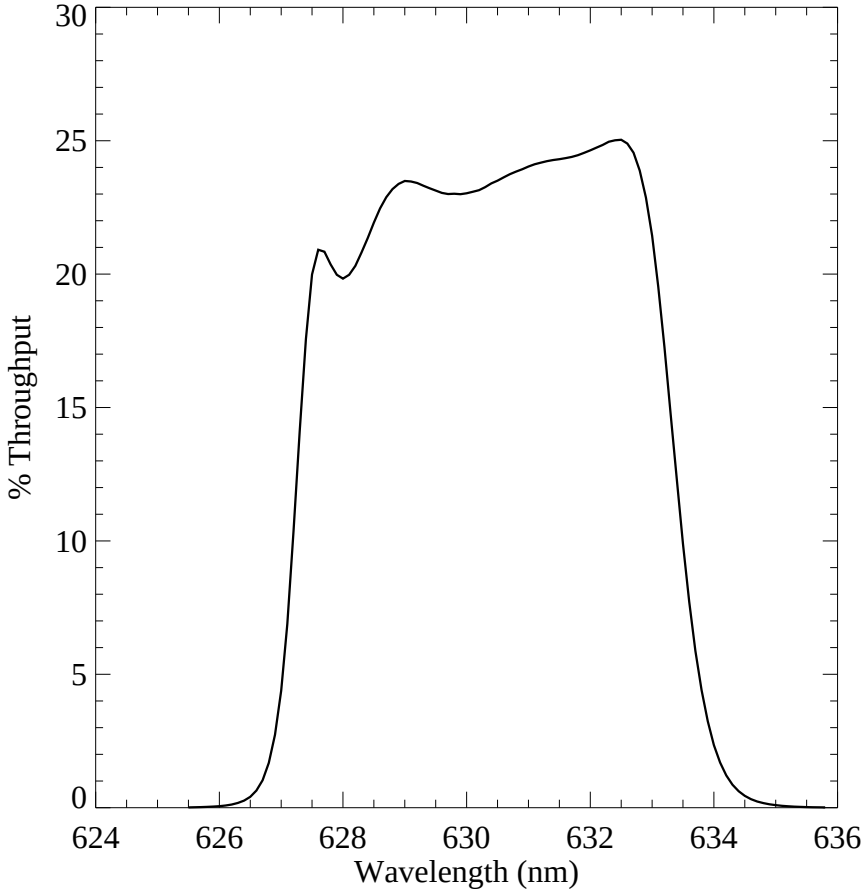

Figure A.83: Point source S/N vs. V+ABν for the F631N filter, assuming high sky backgrounds and a 5×5 pixel aperture.

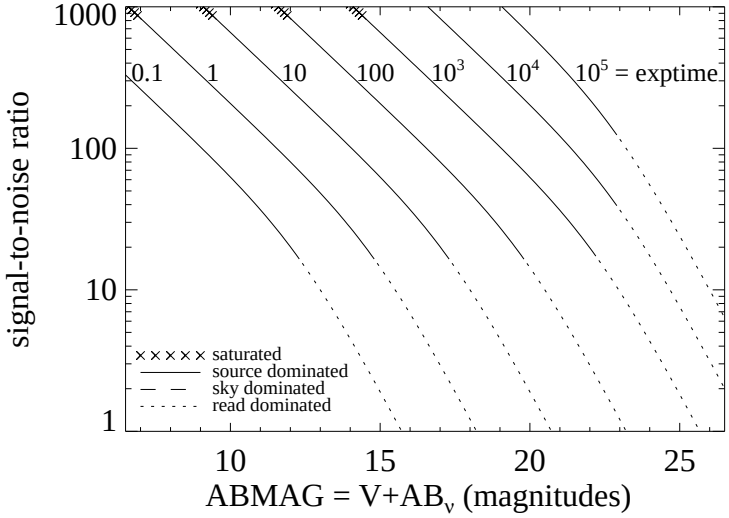

Figure A.84: Extended source S/N vs. V+ABν for the F631N filter, assuming high sky backgrounds and a source uniformly filling a 1 arcsec^2 aperture.

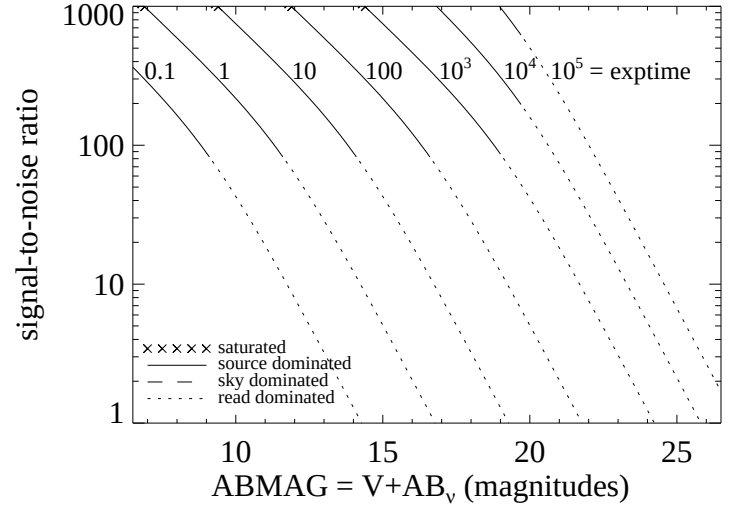

UVIS/F645N

Description

Continuum filter.

Figure A.85: Integrated system throughput for F645N.

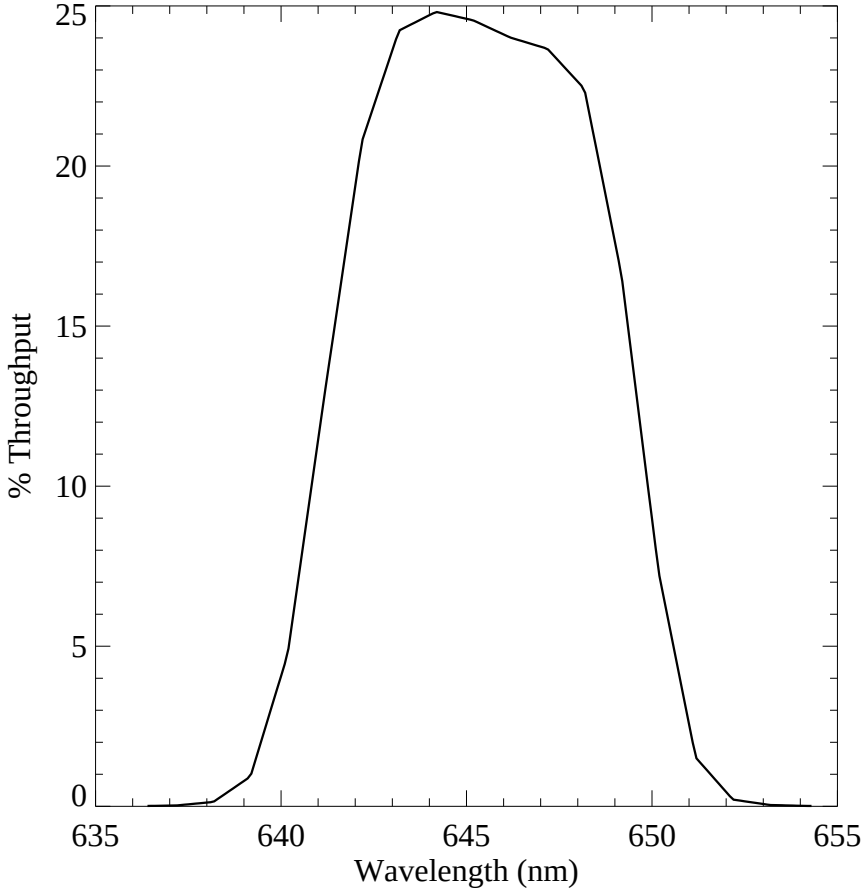

Figure A.86: Point source S/N vs. V+ABν for the F645N filter, assuming high sky backgrounds and a 5×5 pixel aperture.

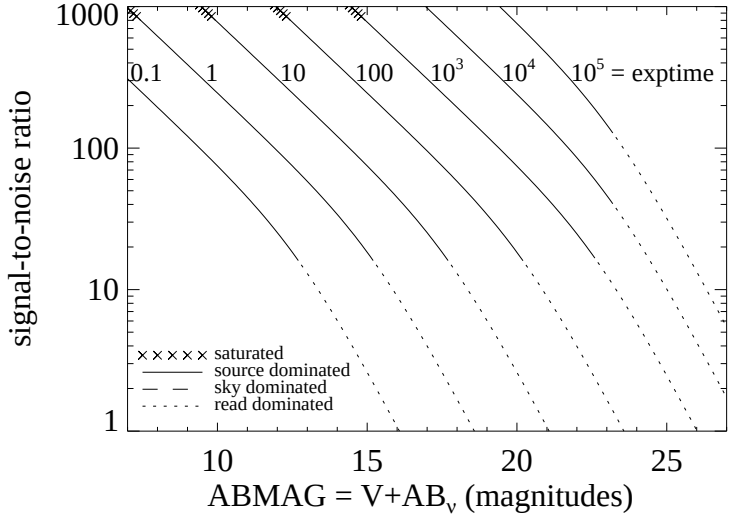

Figure A.87: Extended source S/N vs. V+ABν for the F645N filter, assuming high sky backgrounds and a source uniformly filling a 1 arcsec^2 aperture.

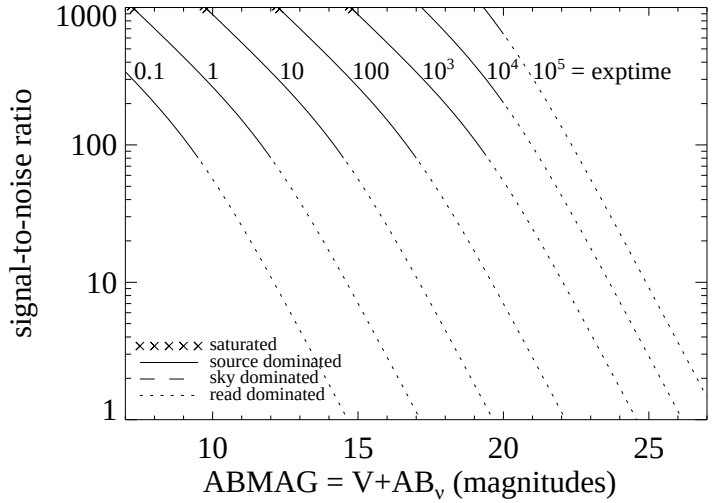

UVIS/F656N

Description

Hα 6562 filter.

Figure A.88: Integrated system throughput for F656N.

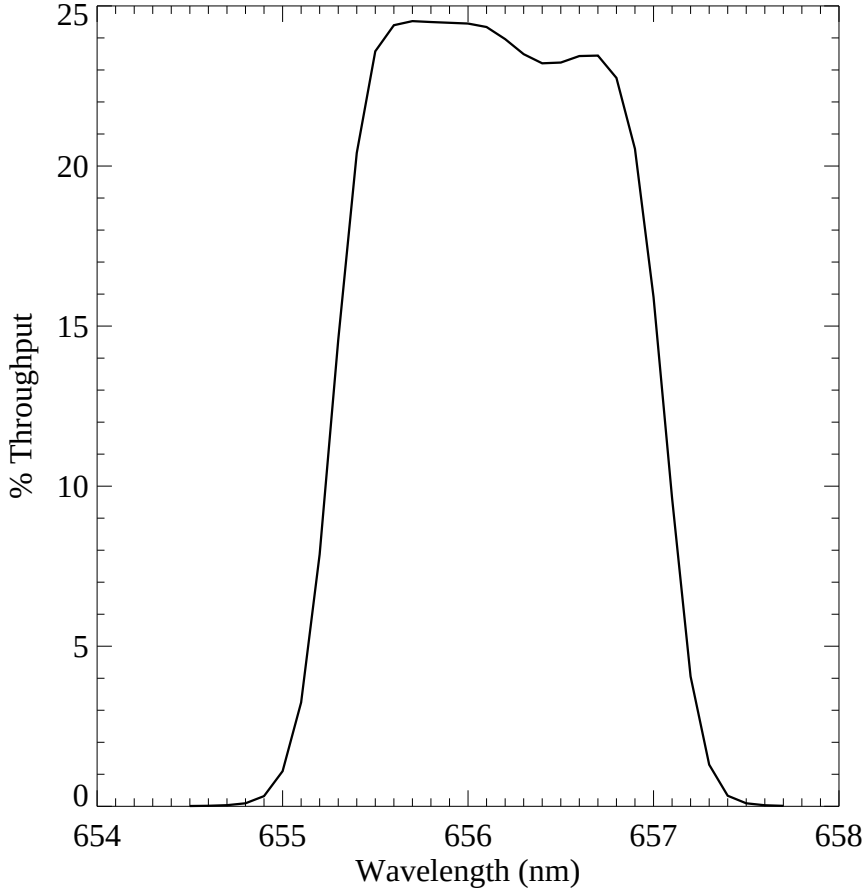

Figure A.89: Point source S/N vs. V+ABν for the F656N filter, assuming high sky backgrounds and a 5×5 pixel aperture.

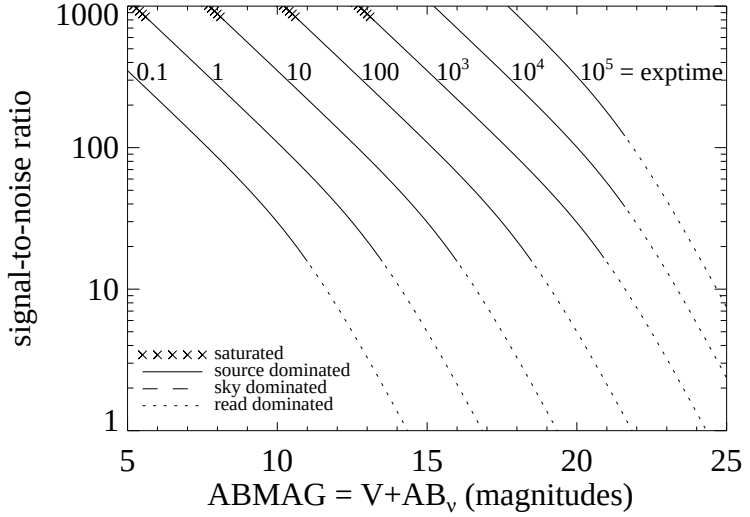

Figure A.90: Extended source S/N vs. V+ABν for the F656N filter, assuming high sky backgrounds and a source uniformly filling a 1 arcsec^2 aperture.

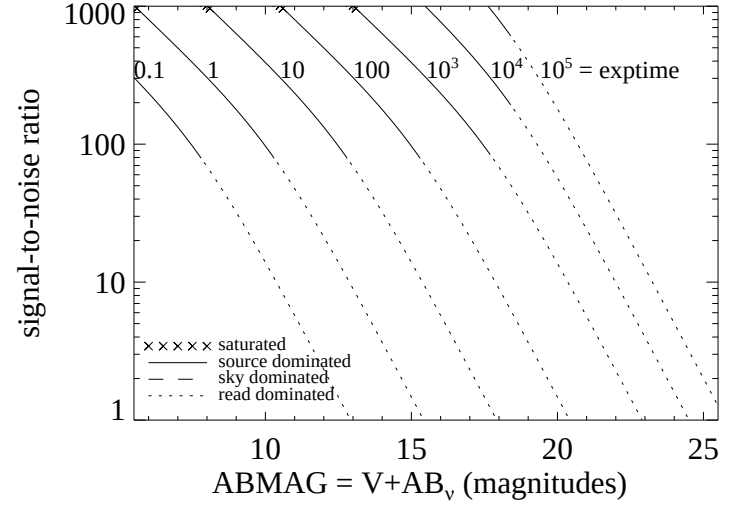

UVIS/F657N

Description

Wide Hα + [N II] filter.

Figure A.91: Integrated system throughput for F657N.

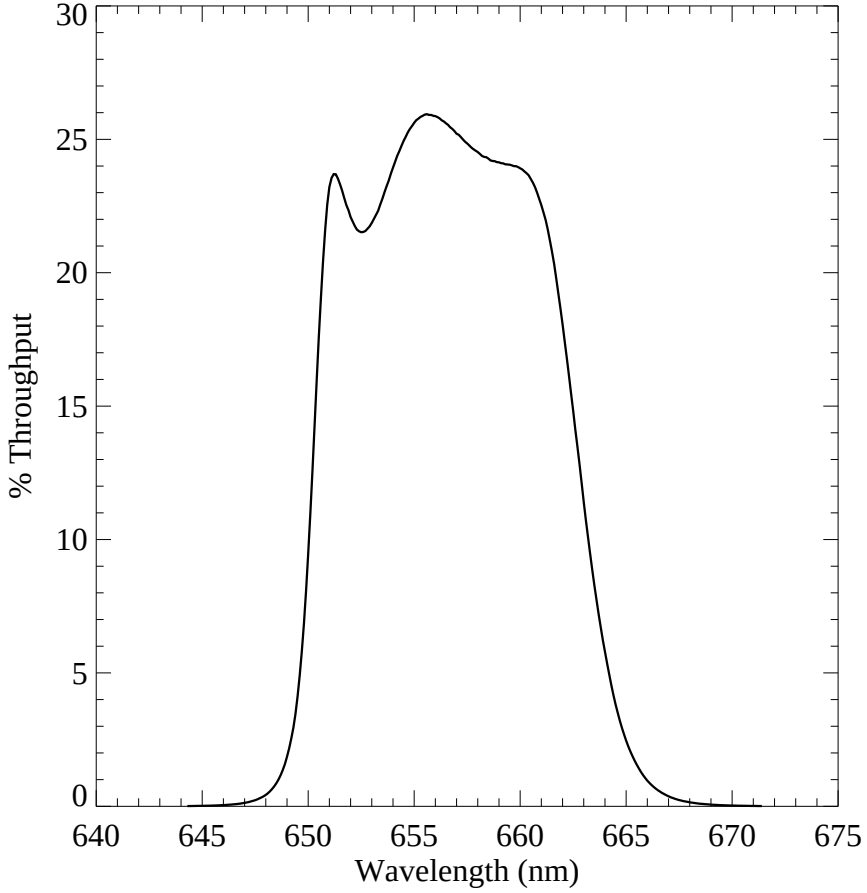

Figure A.92: Point source S/N vs. V+ABν for the F657N filter, assuming high sky backgrounds and a 5×5 pixel aperture.

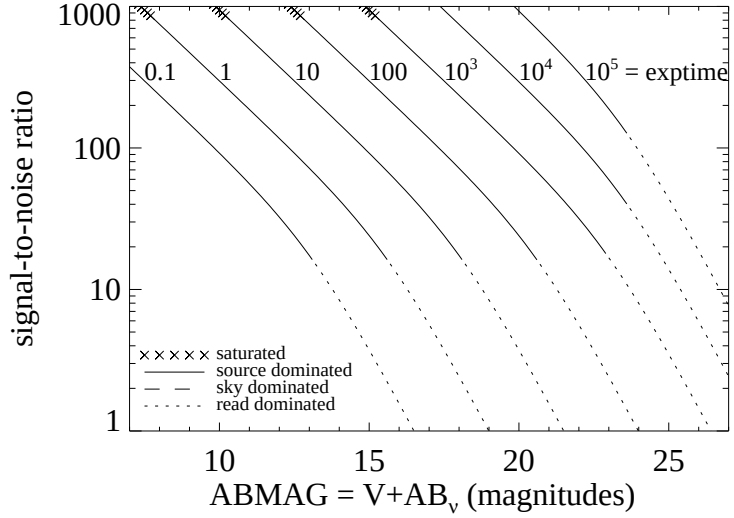

Figure A.93: Extended source S/N vs. V+ABν for the F657N filter, assuming high sky backgrounds and a source uniformly filling a 1 arcsec^2 aperture.

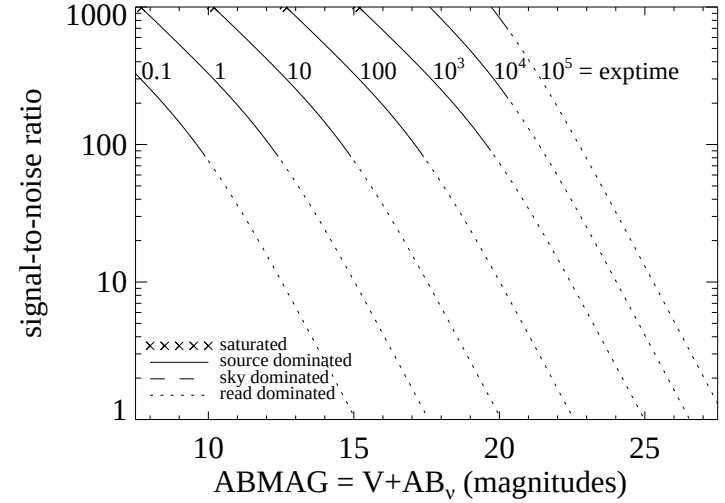

UVIS/F658N

Description

[N II] 6583 filter.

Figure A.94: Integrated system throughput for F658N.

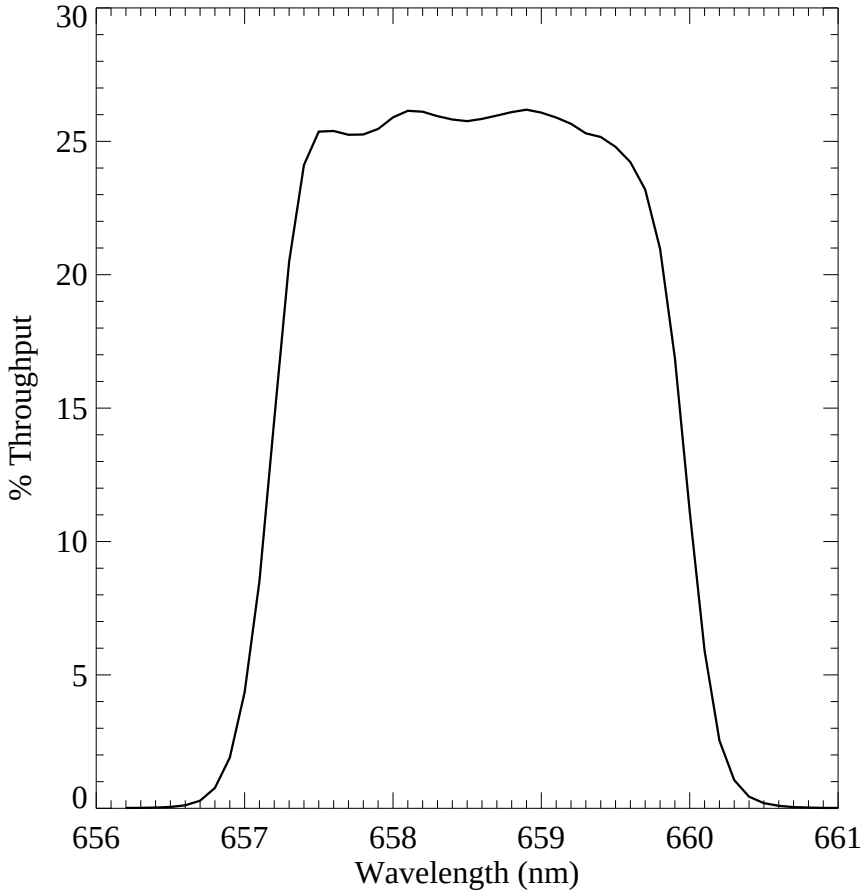

Figure A.95: Point source S/N vs. V+ABν for the F658N filter, assuming high sky backgrounds and a 5×5 pixel aperture.

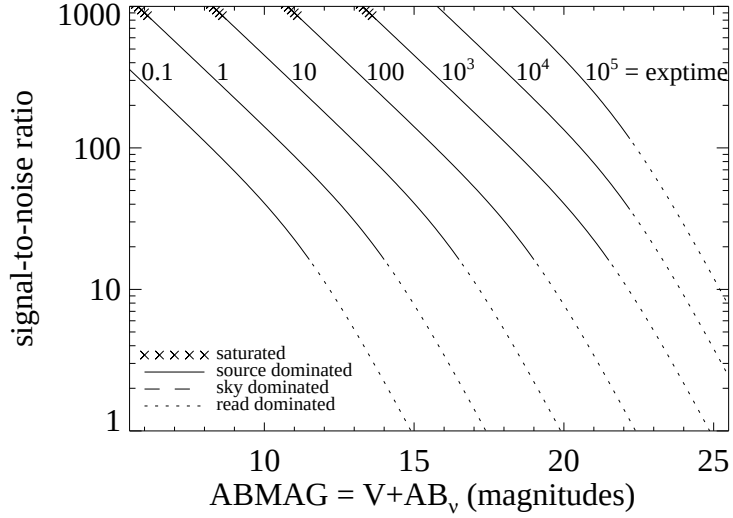

Figure A.96: Extended source S/N vs. V+ABν for the F658N filter, assuming high sky backgrounds and a source uniformly filling a 1 arcsec^2 aperture.

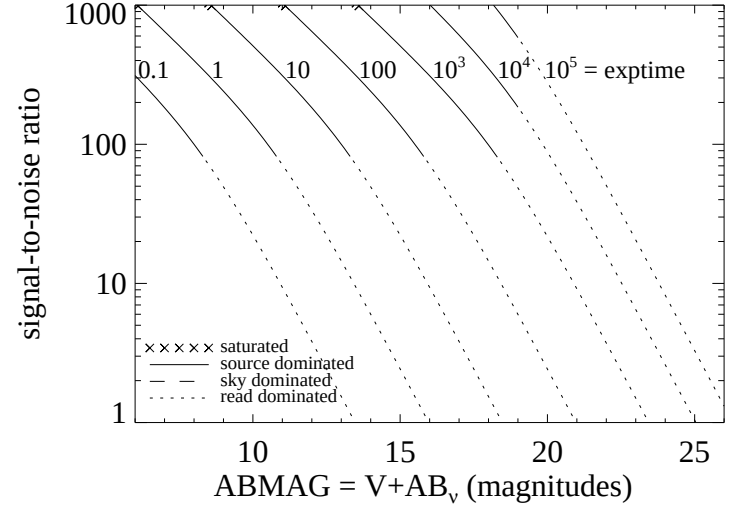

UVIS/F665N

Description

z (Hα + [N II]) filter.

Figure A.97: Integrated system throughput for F665N.

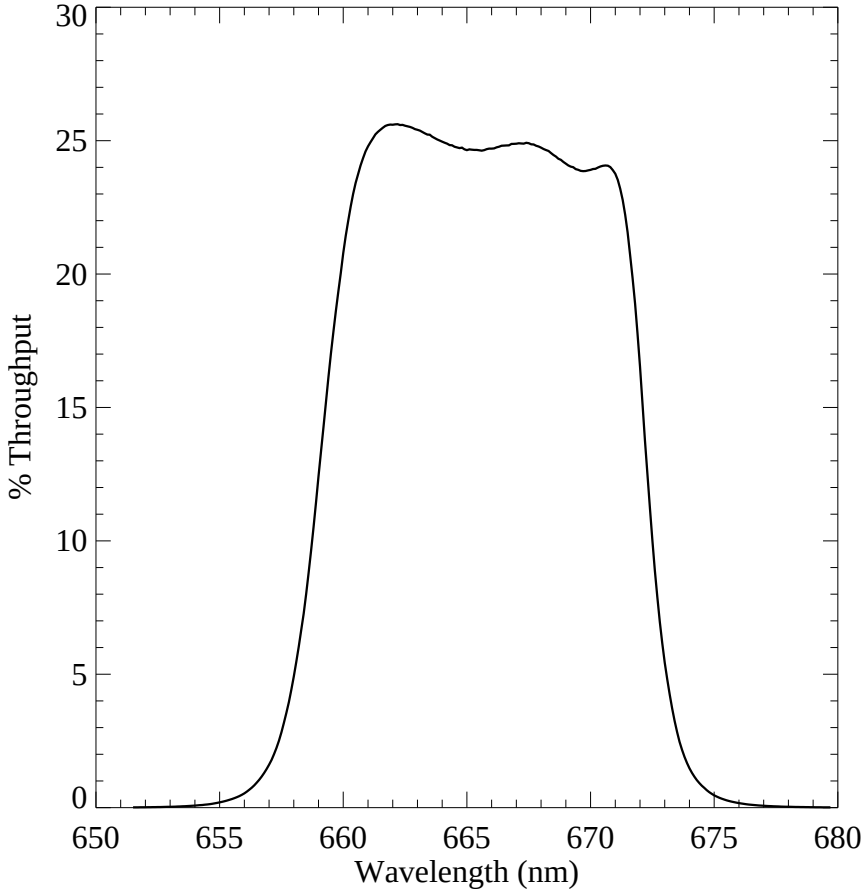

Figure A.98: Point source S/N vs. V+ABν for the F665N filter, assuming high sky backgrounds and a 5×5 pixel aperture.

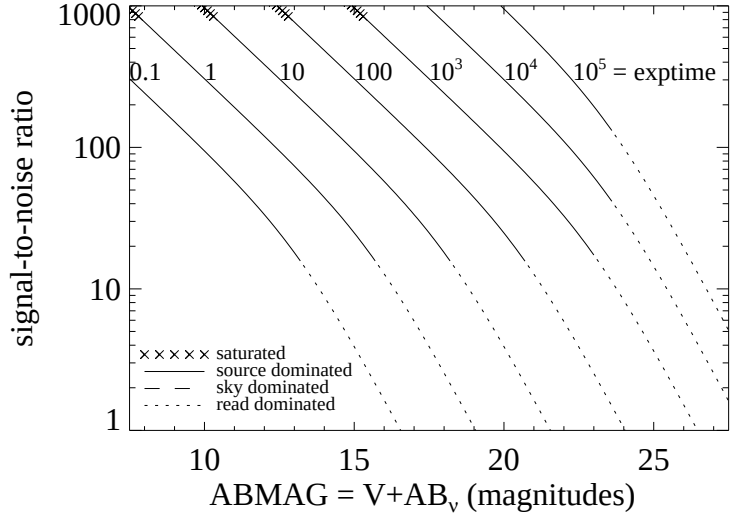

Figure A.99: Extended source S/N vs. V+ABν for the F665N filter, assuming high sky backgrounds and a source uniformly filling a 1 arcsec^2 aperture.

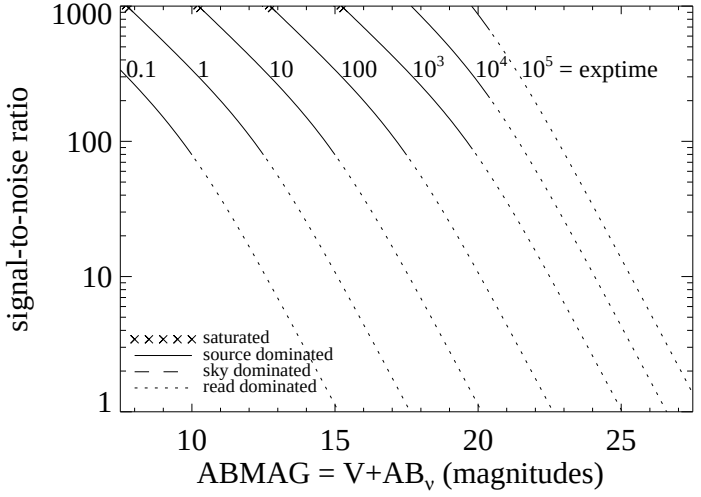

UVIS/F673N

Description

[S II] 6717/6731 filter.

Figure A.100: Integrated system throughput for F673N.

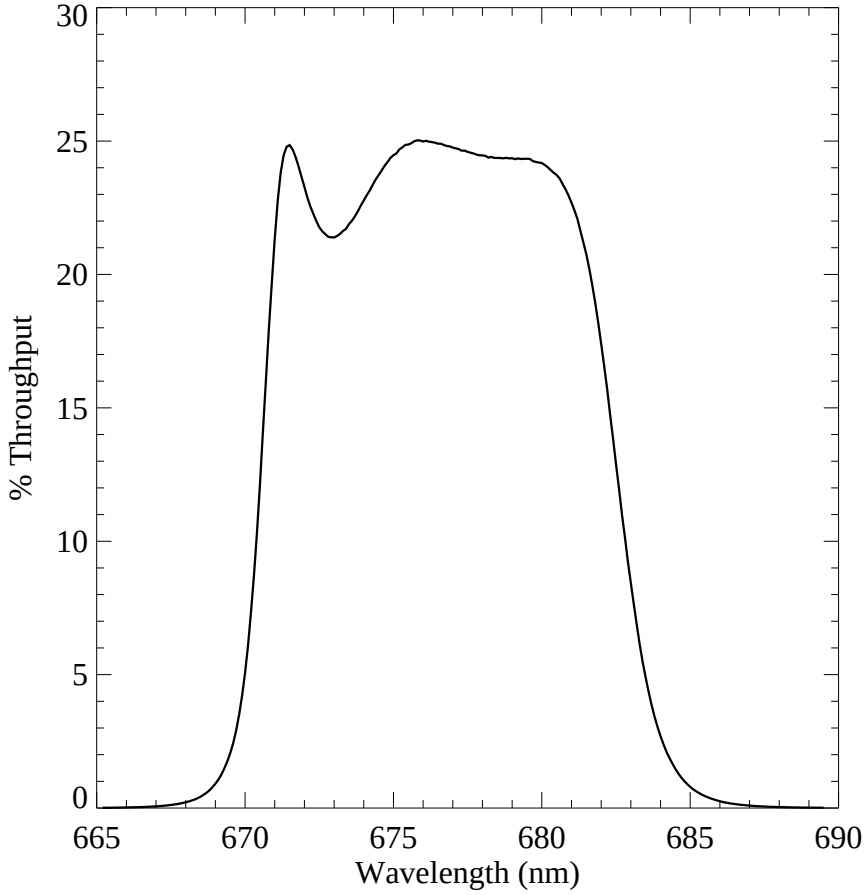

Figure A.101: Point source S/N vs. V+ABν for the F673N filter, assuming high sky backgrounds and a 5×5 pixel aperture.

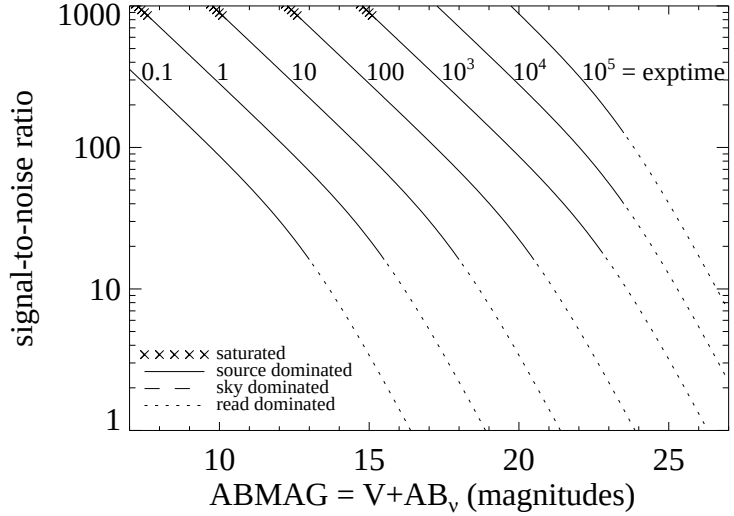

Figure A.102: Extended source S/N vs. V+ABν for the F673N filter, assuming high sky backgrounds and a source uniformly filling a 1 arcsec^2 aperture.

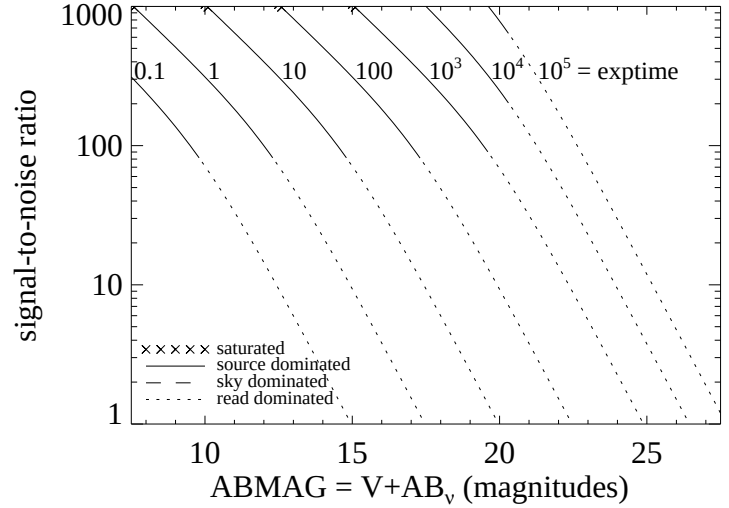

UVIS/F680N

Description

z (Hα + [N II]) filter.

Figure A.103: Integrated system throughput for F680N.

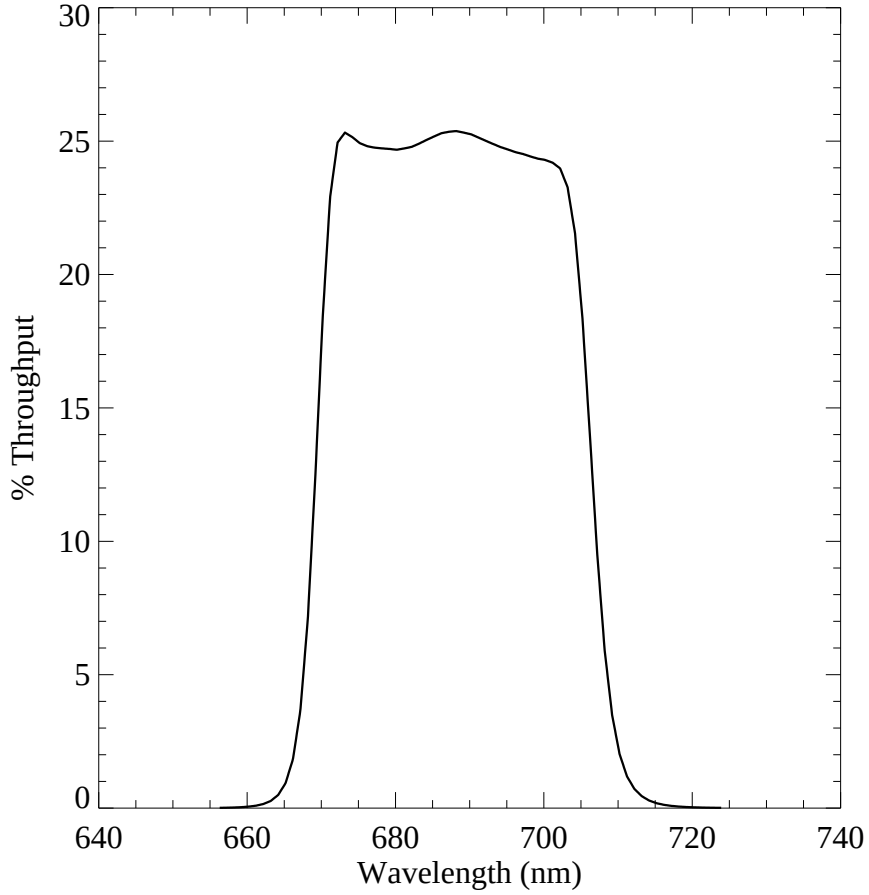

Figure A.104: Point source S/N vs. V+ABν for the F680N filter, assuming high sky backgrounds and a 5×5 pixel aperture.

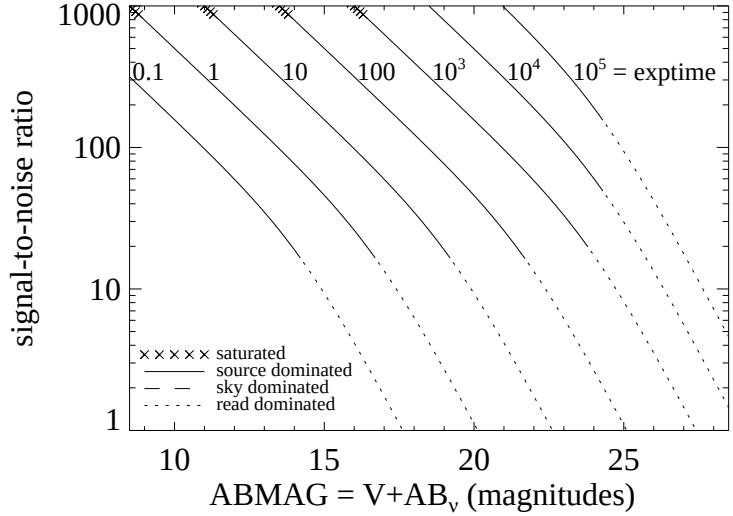

Figure A.105: Extended source S/N vs. V+ABν for the F680N filter, assuming high sky backgrounds and a source uniformly filling a 1 arcsec^2 aperture.

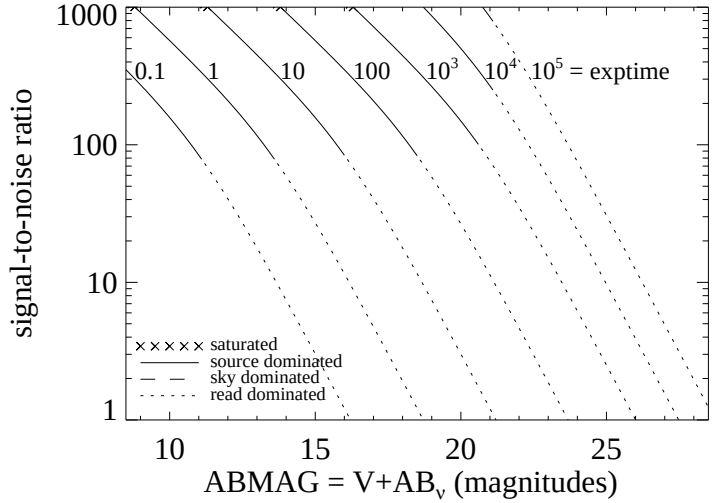

UVIS/F689M

Description

11% passband filter.

Figure A.106: Integrated system throughput for F689M.

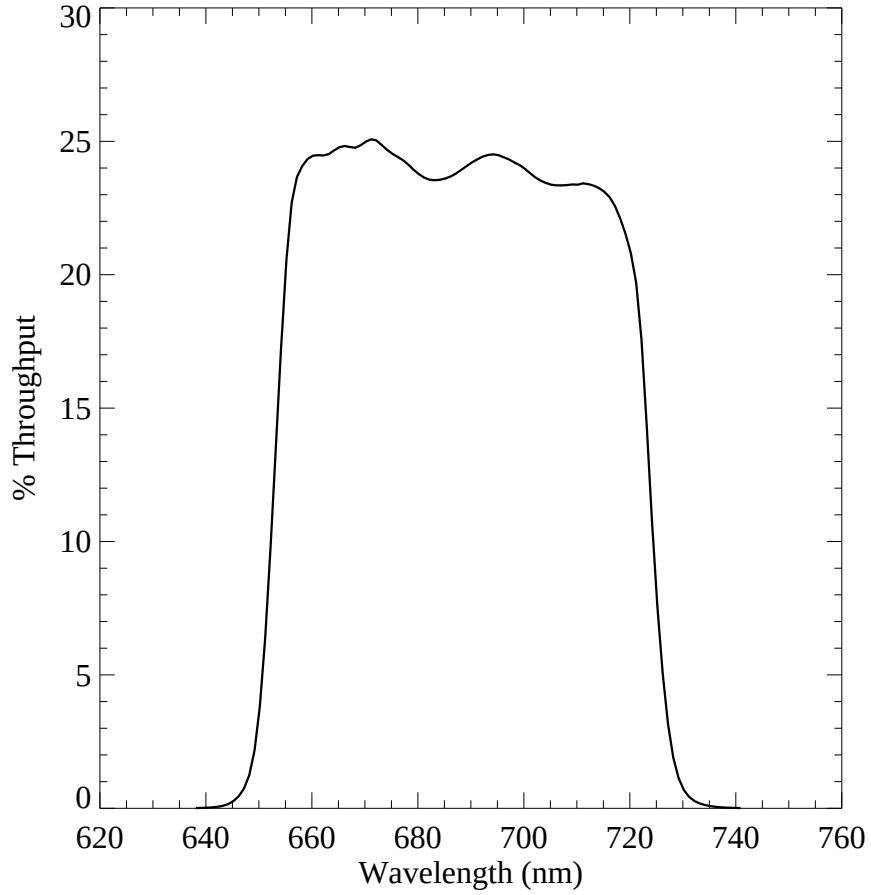

Figure A.107: Point source S/N vs. V+ABν for the F689M filter.Top curves are for low sky; bottom curves are for average sky.

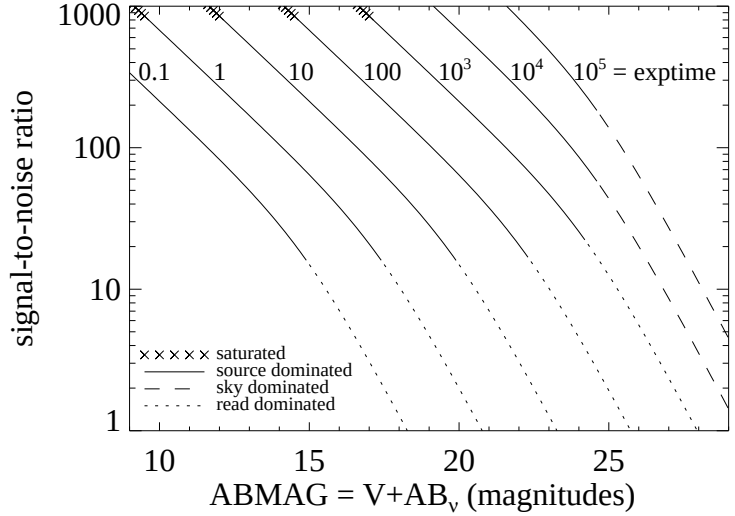

Figure A.108: Extended source S/N vs. V+ABν for the F689M filter, assuming high sky backgrounds and a source uniformly filling a 1 arcsec^2 aperture.

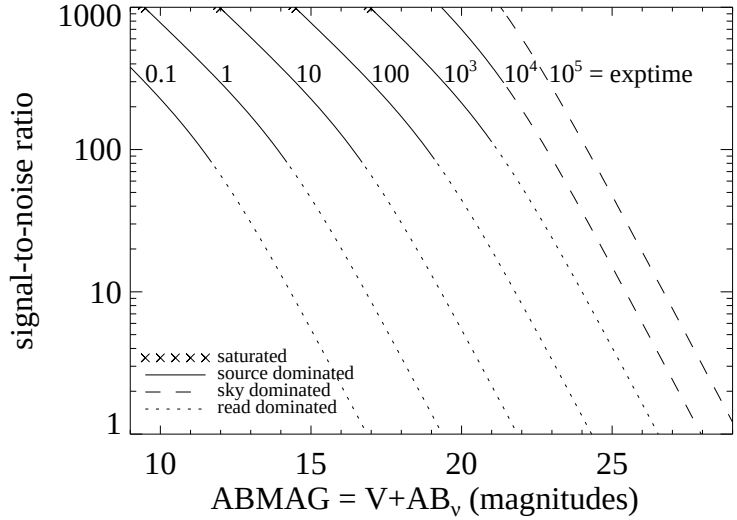

UVIS/F763M

Description

11% passband filter.

Figure A.109: Integrated system throughput for F763M.

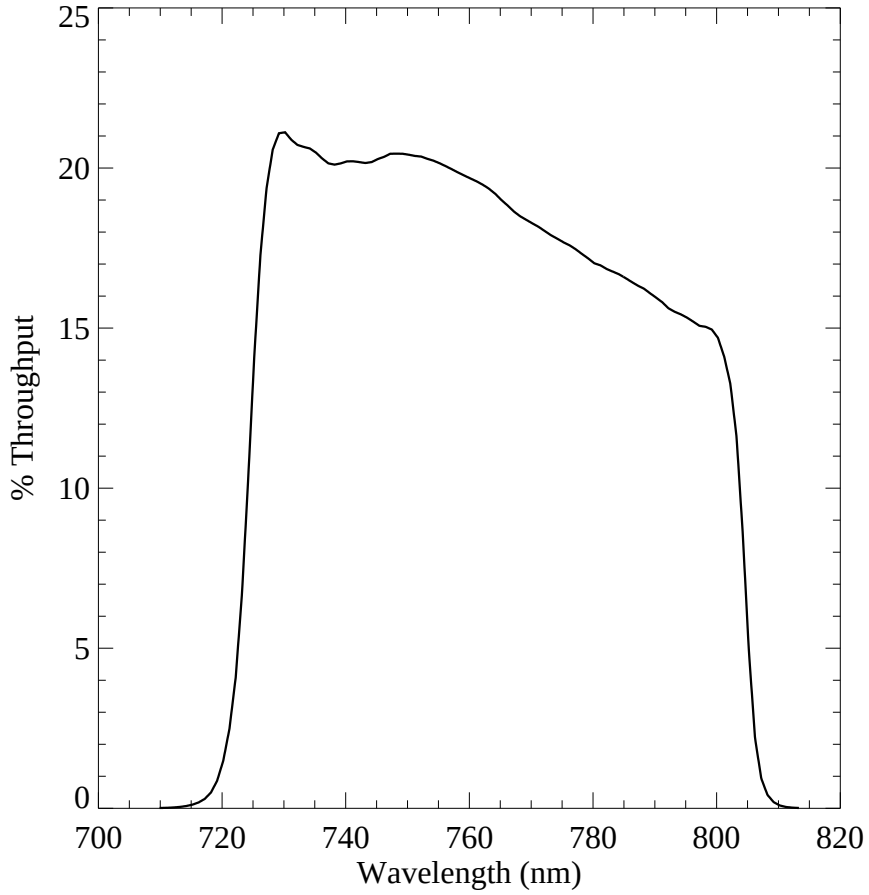

Figure A.110: Point source S/N vs. V+ABν for the F763M filter.Top curves are for low sky; bottom curves are for average sky.

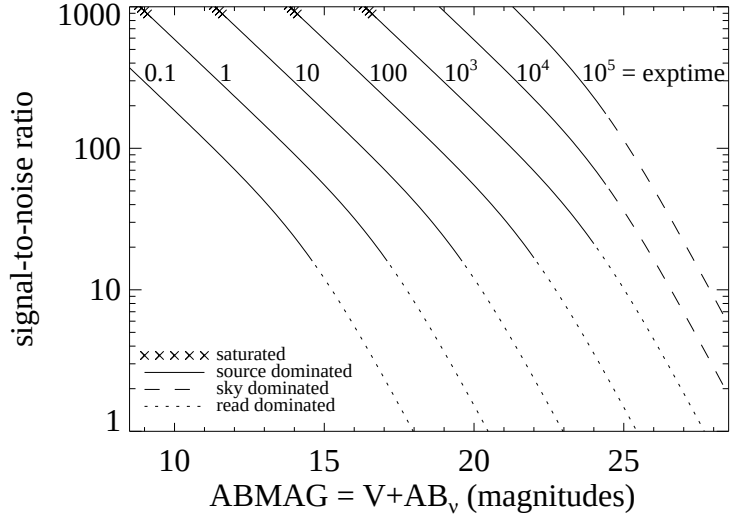

Figure A.111: Extended source S/N vs. V+ABν for the F763M filter, assuming high sky backgrounds and a source uniformly filling a 1 arcsec^2 aperture.

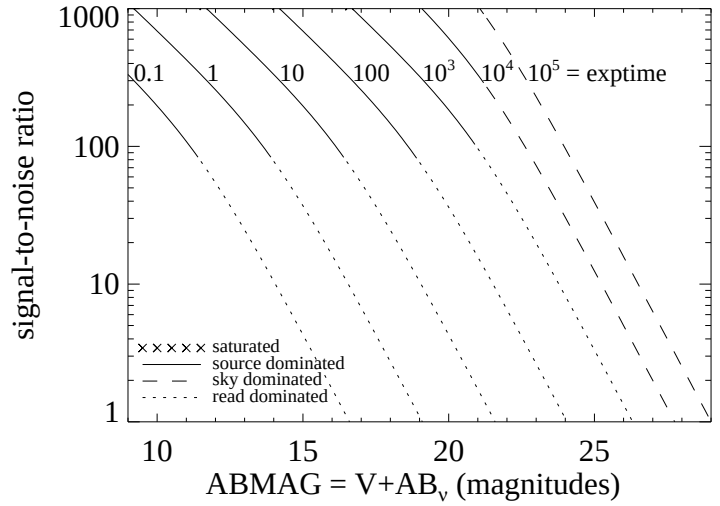

UVIS/F775W

Description

Sloan Digital Sky Survey *i′* filter.

Figure A.112: Integrated system throughput for F775W.

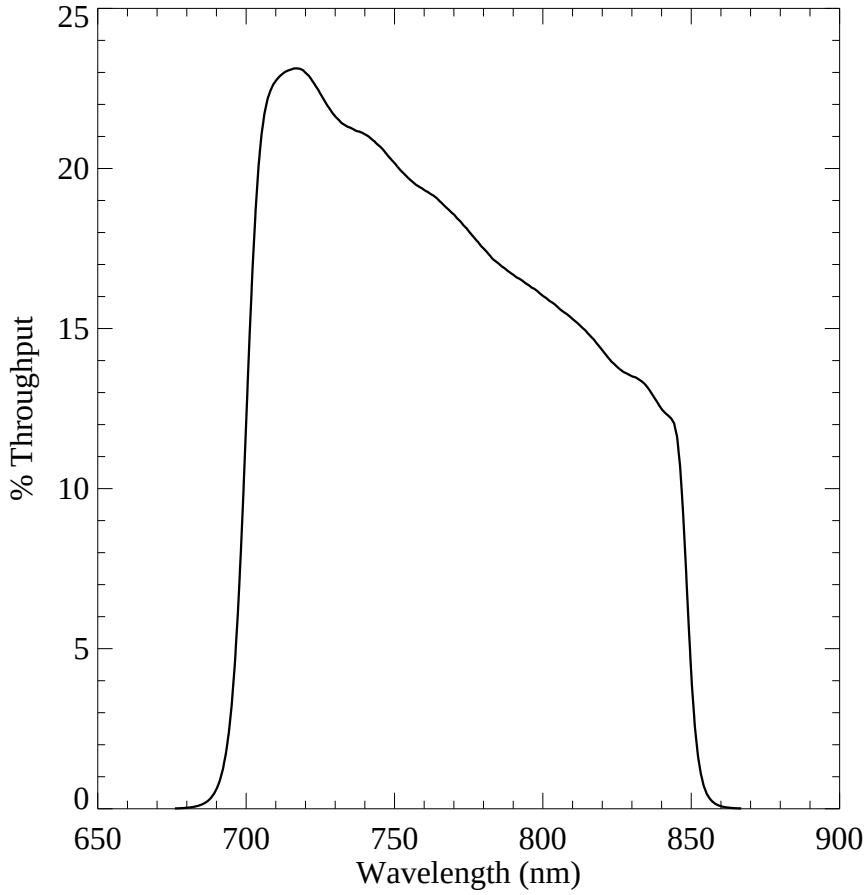

Figure A.113: Point source S/N vs. V+ABν for the F775W filter, assuming high sky backgrounds and a 5×5 pixel aperture.

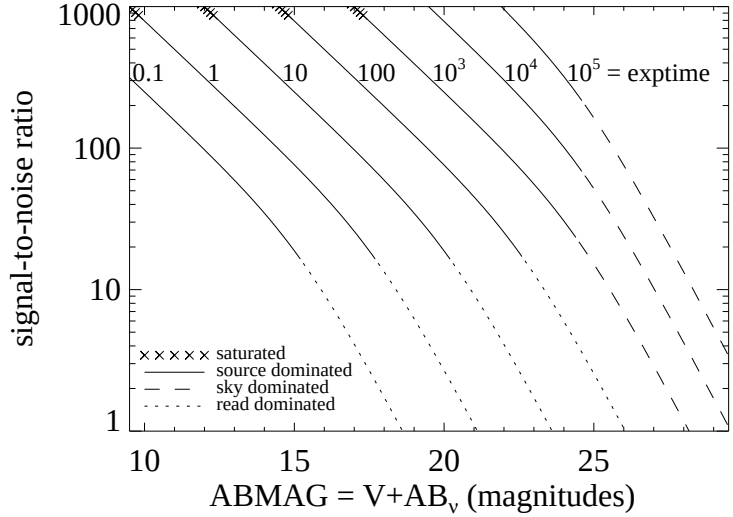

Figure A.114: Extended source S/N vs. V+ABν for the F775W filter, assuming high sky backgrounds and a source uniformly filling a 1 arcsec^2 aperture.

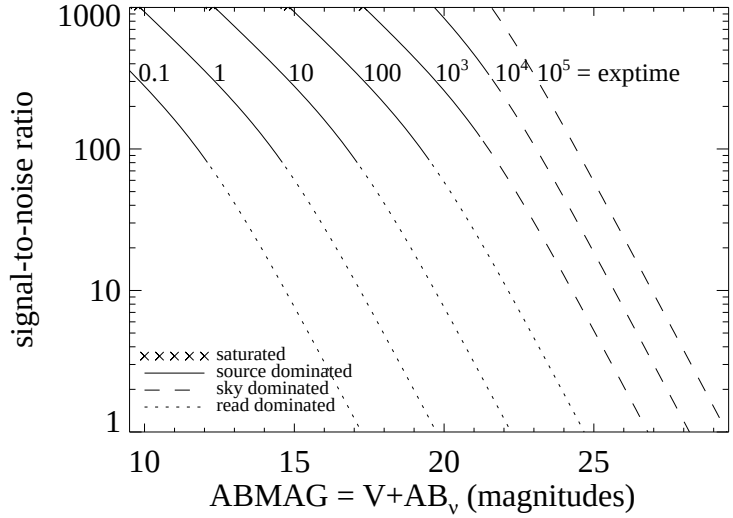

UVIS/F814W

Description

WFPC2 Wide *I* filter.

Figure A.115: Integrated system throughput for F814W.

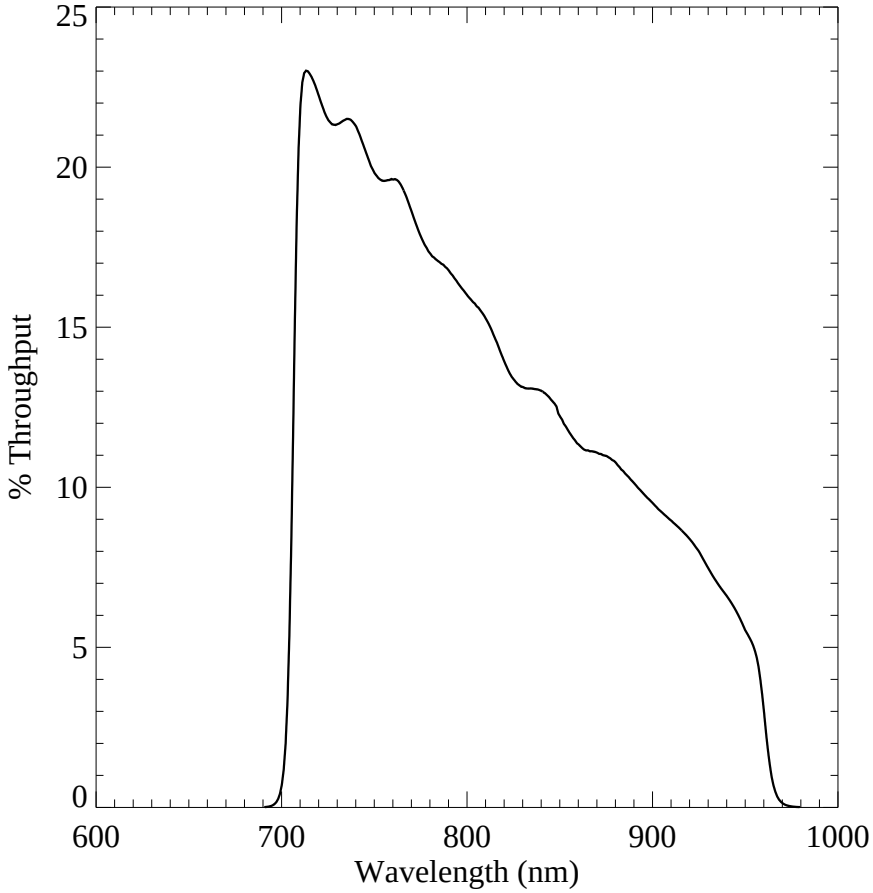

Figure A.116: Point source S/N vs. V+ABν for the F814W filter, assuming high sky backgrounds and a 5×5 pixel aperture.

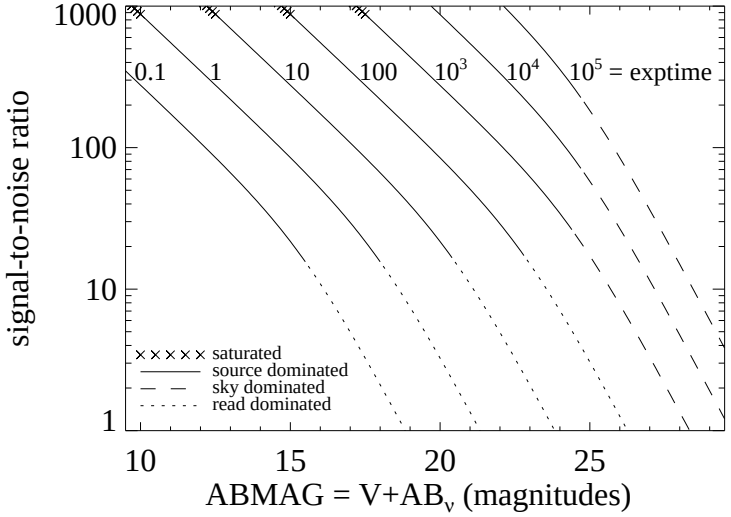

Figure A.117: Extended source S/N vs. V+ABν for the F814W filter, assuming high sky backgrounds and a source uniformly filling a 1 arcsec^2 aperture.

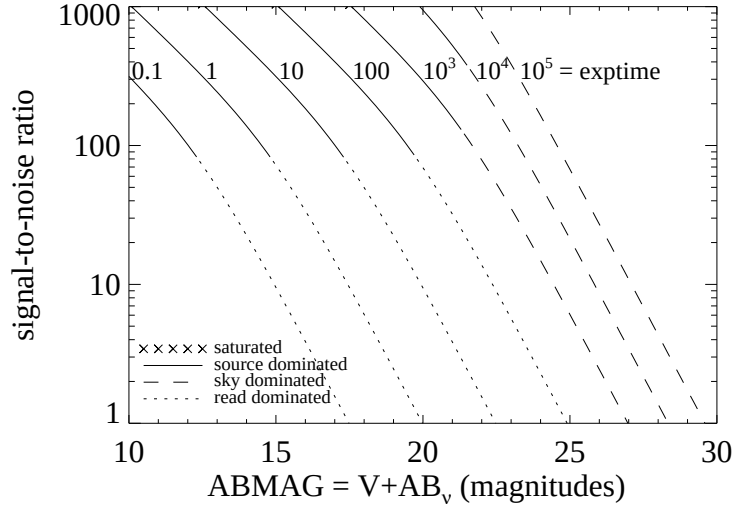

UVIS/F845M

Description

11% passband filter.

Figure A.118: Integrated system throughput for F845M.

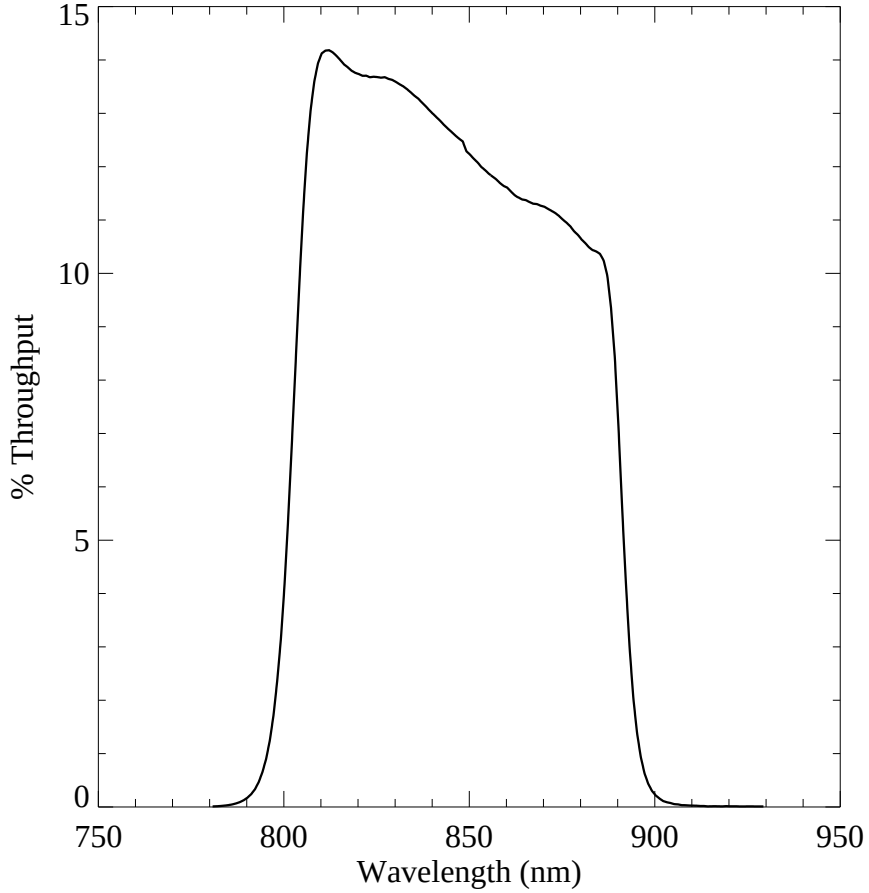

Figure A.119: Point source S/N vs. V+ABν for the F845M filter, assuming high sky backgrounds and a 5×5 pixel aperture.

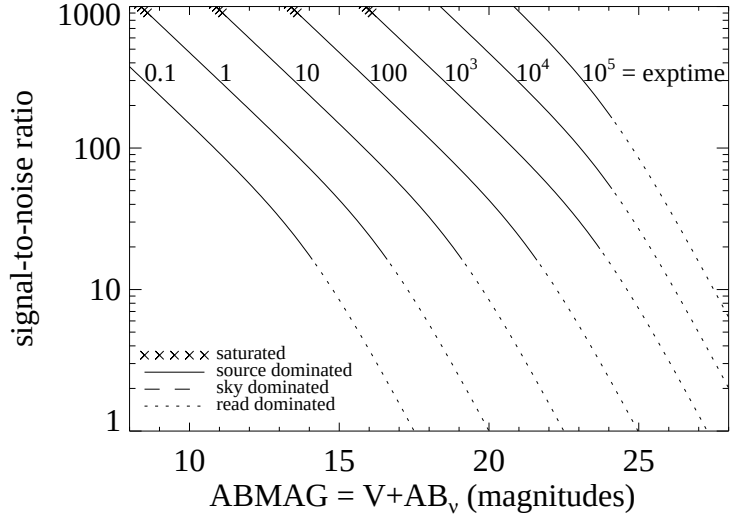

Figure A.120: Extended source S/N vs. V+ABν for the F845M filter, assuming high sky backgrounds and a source uniformly filling a 1 arcsec^2 aperture.

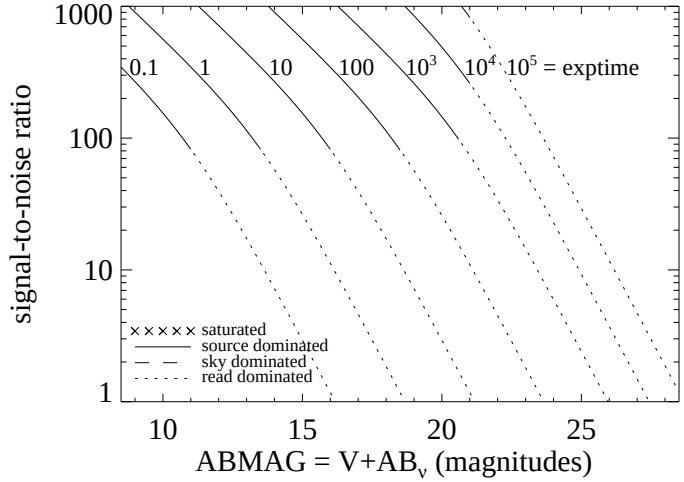

UVIS/F850LP

Description

Sloan Digital Sky Survey z' filter.

Figure A.121: Integrated system throughput for F850LP.

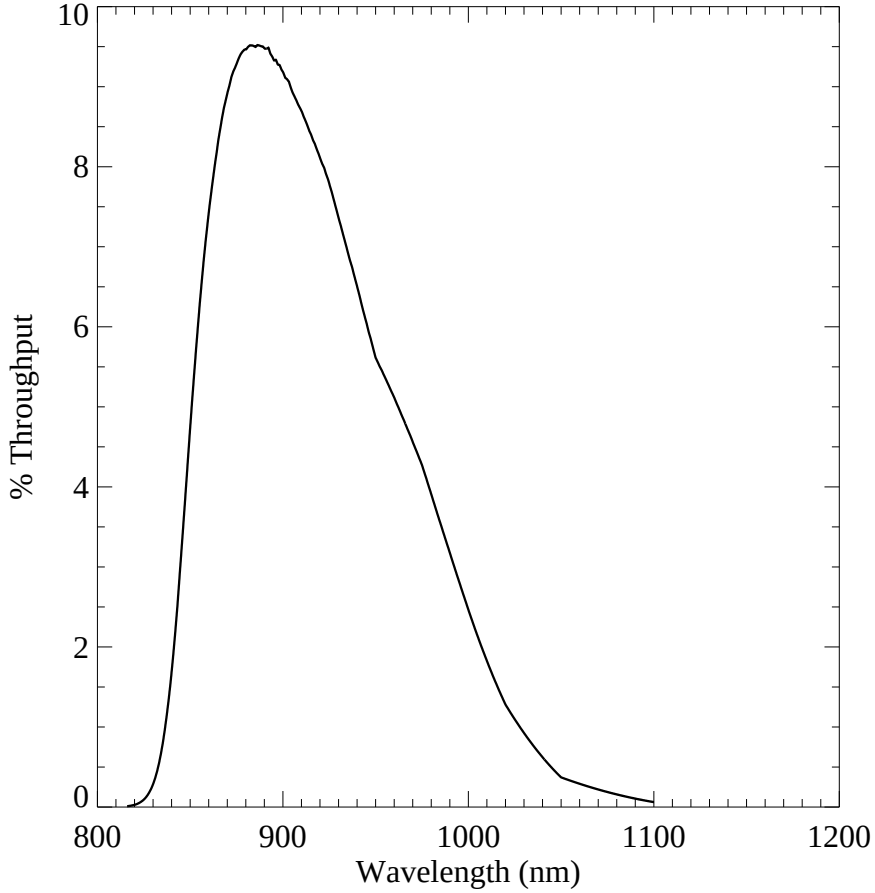

Figure A.122: Point source S/N vs. V+ABν for the F850LP filter.Top curves are for low sky; bottom curves are for average sky.

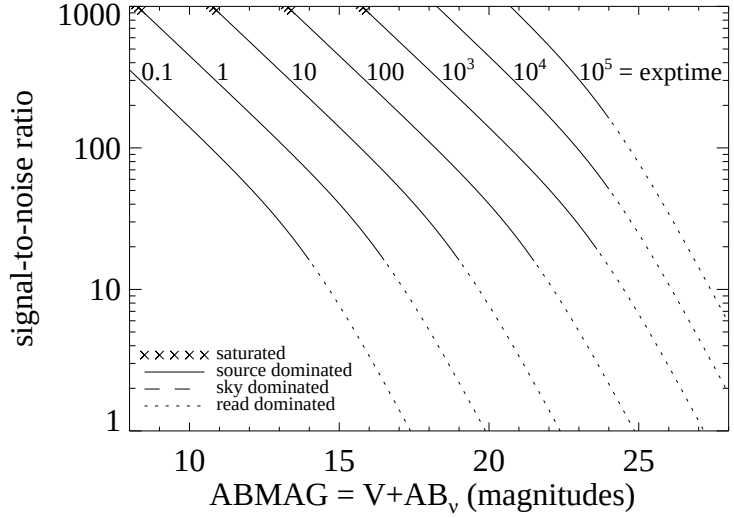

Figure A.123: Extended source S/N vs. V+ABν for the F850LP filter, assuming high sky backgrounds and a source uniformly filling a 1 arcsec^2 aperture.

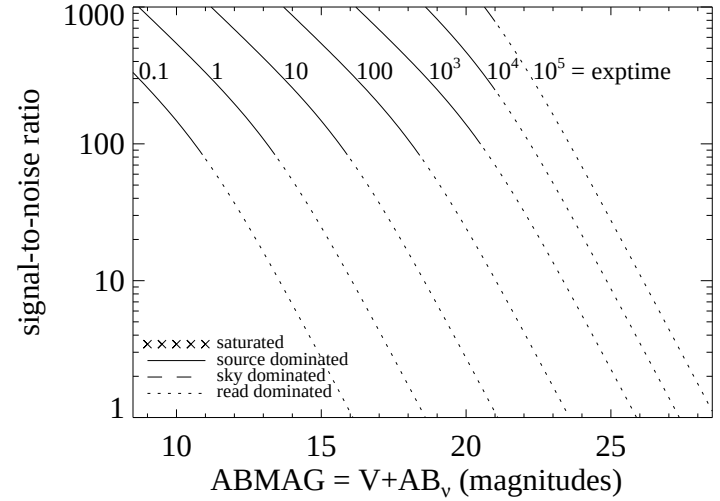

UVIS/F953N

Description

[S III] 9532 filter.

Figure A.124: Integrated system throughput for F953N.

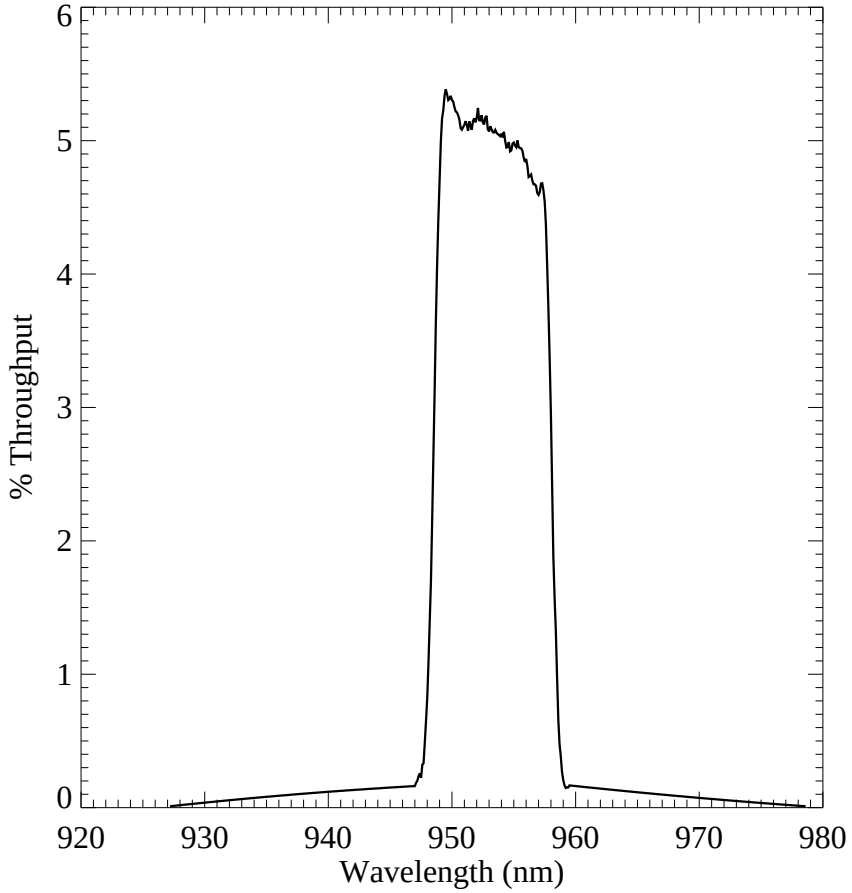

Figure A.125: Point source S/N vs. V+ABν for the F953N filter, assuming high sky backgrounds and a 5×5 pixel aperture.

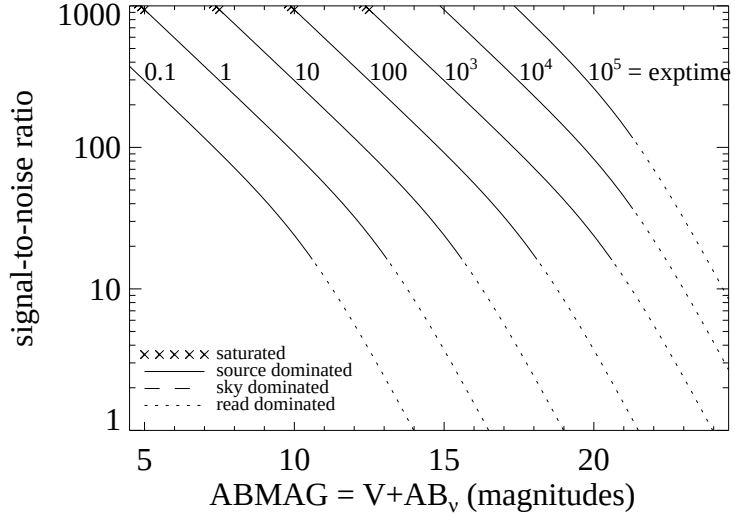

Figure A.126: Extended source S/N vs. V+ABν for the F953N filter, assuming high sky backgrounds and a source uniformly filling a 1 arcsec^2 aperture.

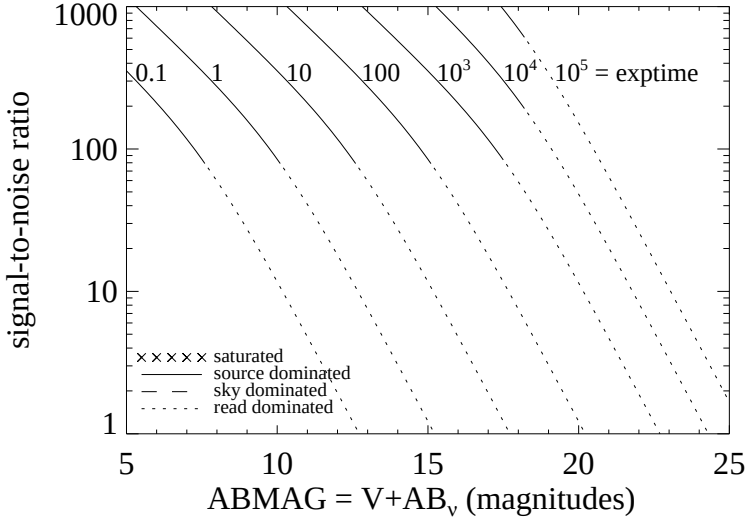

UVIS/FQ232N

Description

C II] 2326 filter.

Figure A.127: Integrated system throughput for FQ232N.

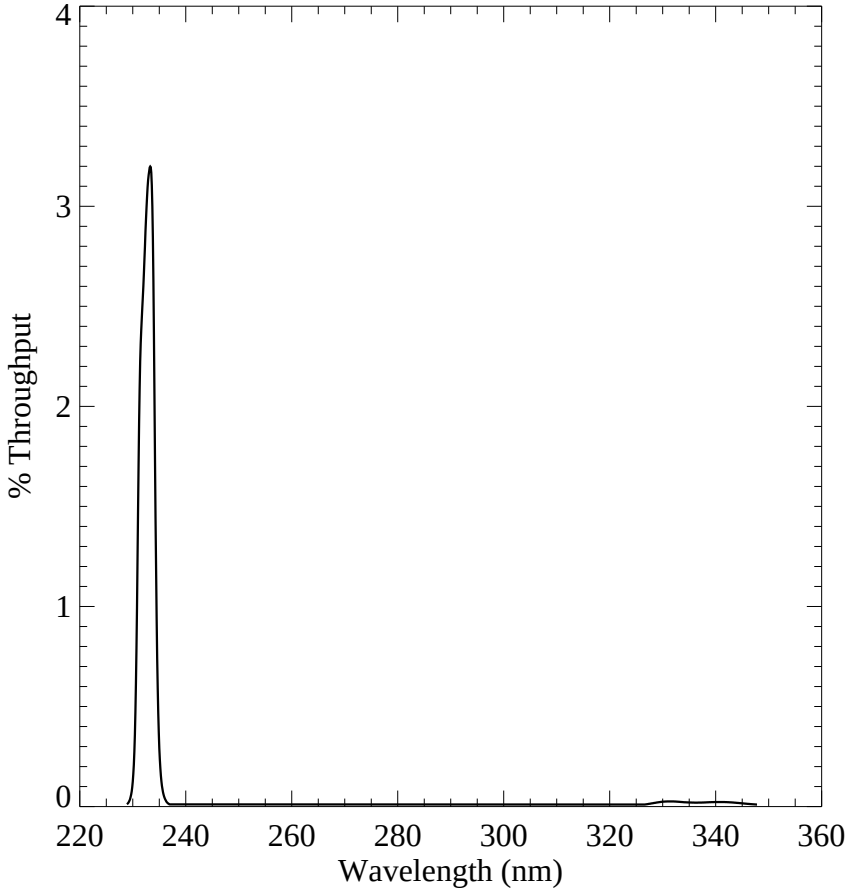

Figure A.128: Point source S/N vs. V+ABν for the FQ232N filter, assuming high sky backgrounds and a 5×5 pixel aperture.

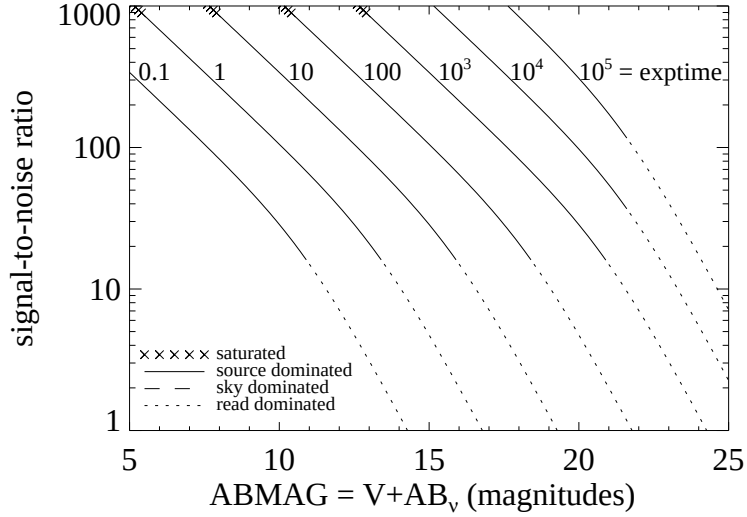

Figure A.129: Extended source S/N vs. V+ABν for the FQ232N filter, assuming high sky backgrounds and a source uniformly filling a 1 arcsec^2 aperture.

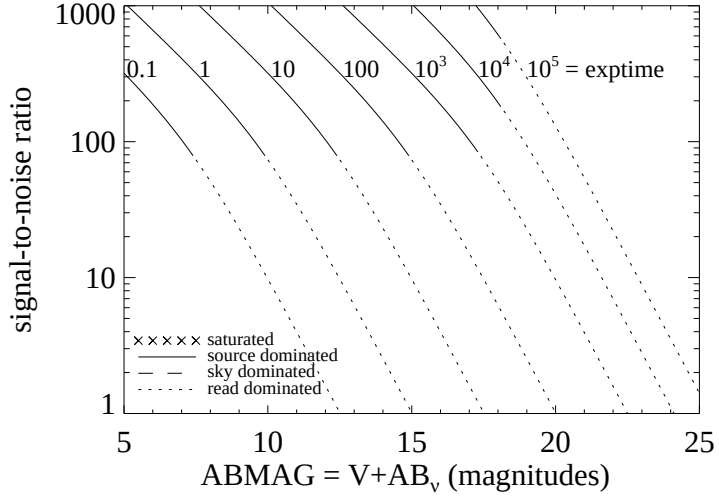

UVIS/FQ243N

Description

[Ne IV] 2425 filter.

Figure A.130: Integrated system throughput for FQ243N.

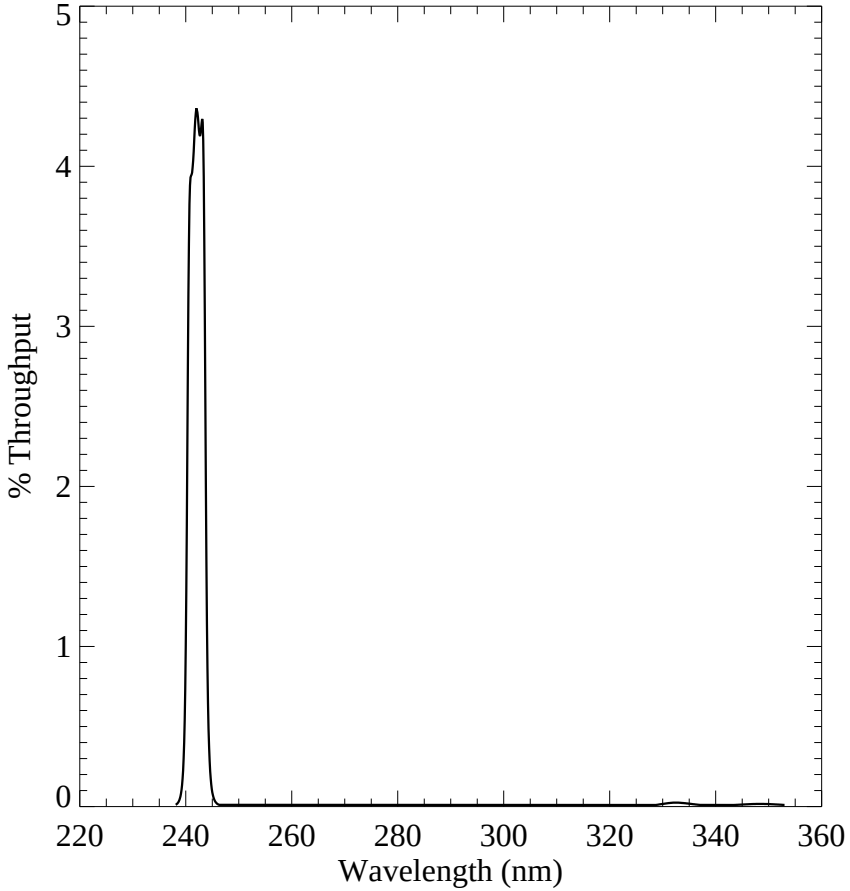

Figure A.131: Point source S/N vs. V+ABν for the FQ243N filter, assuming high sky backgrounds and a 5×5 pixel aperture.

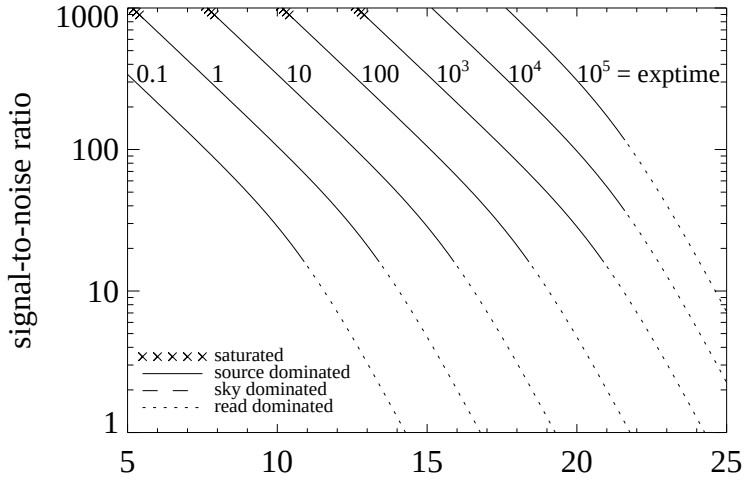

Figure A.132: Extended source S/N vs. V+ABν for the FQ243N filter, assuming high sky backgrounds and a source uniformly filling a 1 arcsec^2 aperture.

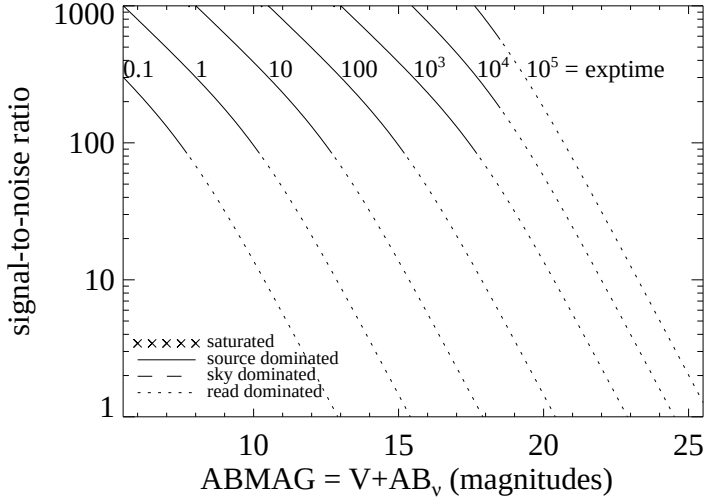

UVIS/FQ378N

Description

z ([O II] 3726) filter.

Figure A.133: Integrated system throughput for FQ378N.

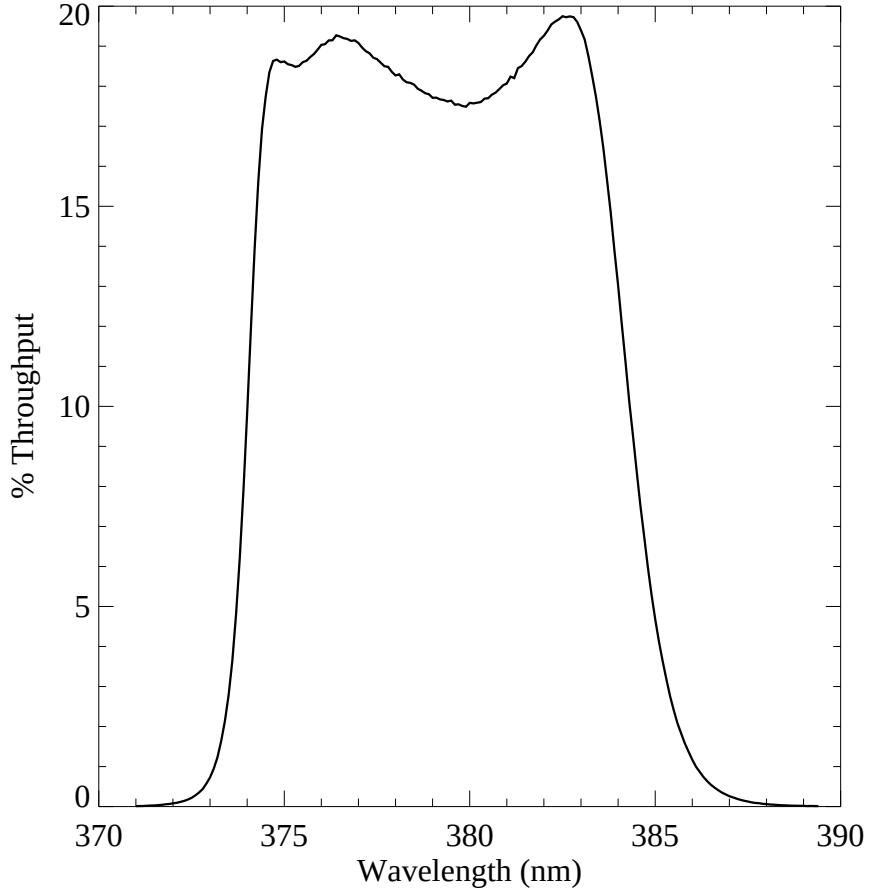

Figure A.134: Point source S/N vs. V+ABν for the FQ378N filter, assuming high sky backgrounds and a 5×5 pixel aperture.

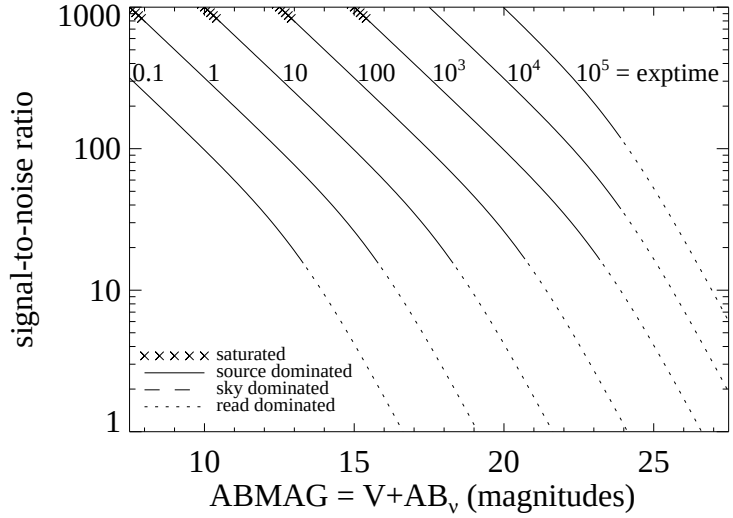

Figure A.135: Extended source S/N vs. V+ABν for the FQ378N filter, assuming high sky backgrounds and a source uniformly filling a 1 arcsec^2 aperture.

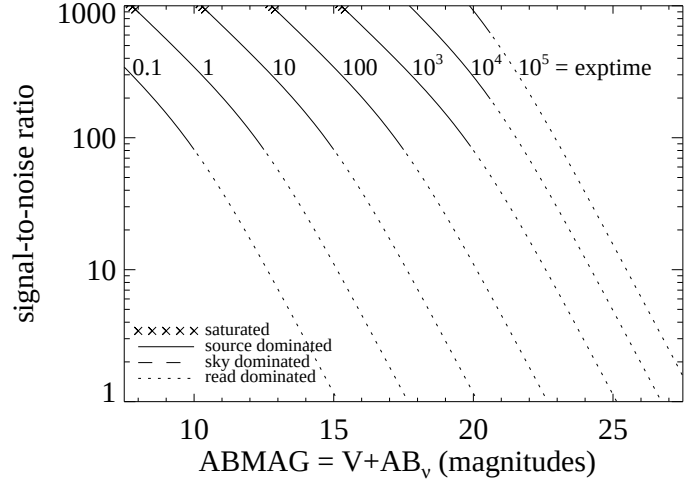

UVIS/FQ387N

Description

[Ne III] 3868 filter.

Figure A.136: Integrated system throughput for FQ387N.

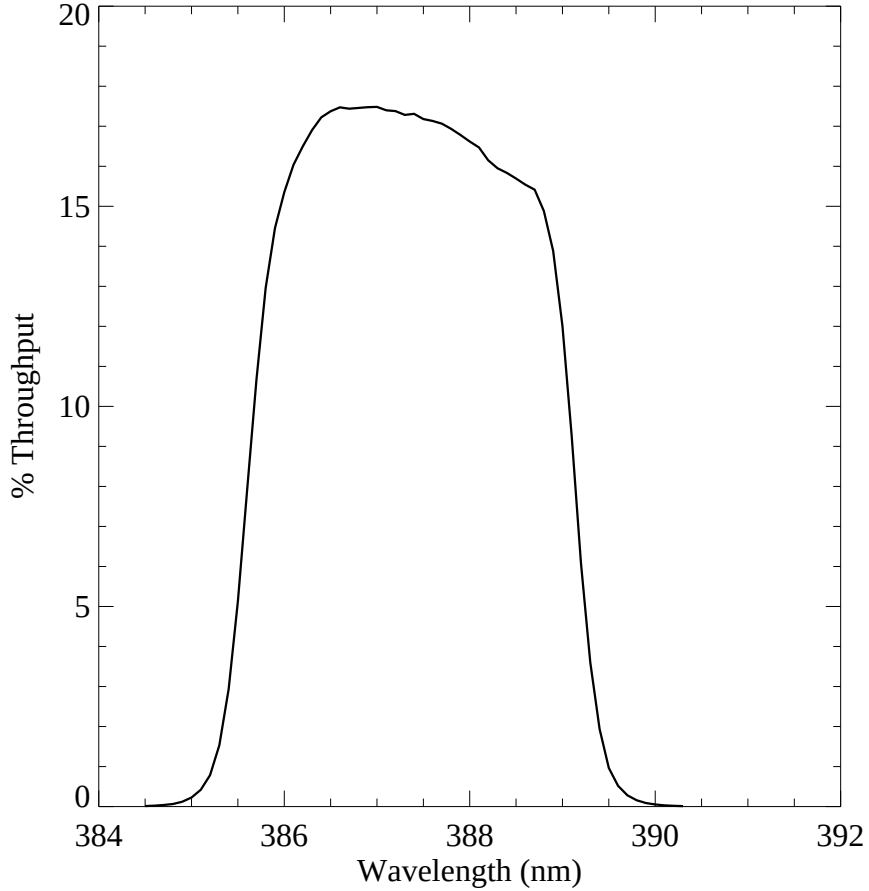

Figure A.137: Point source S/N vs. V+ABν for the FQ387N filter, assuming high sky backgrounds and a 5×5 pixel aperture.

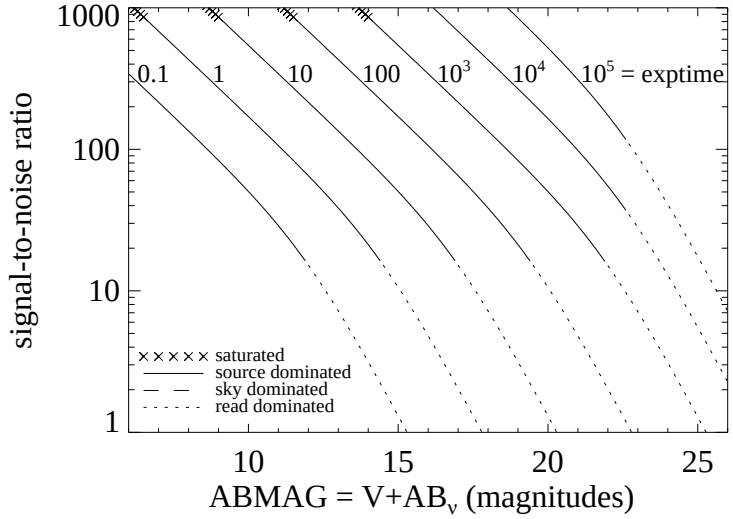

Figure A.138: Extended source S/N vs. V+ABν for the FQ387N filter, assuming high sky backgrounds and a source uniformly filling a 1 arcsec^2 aperture.

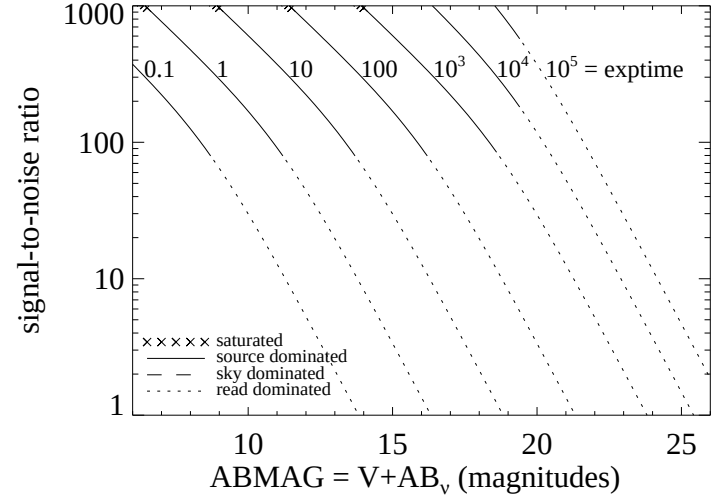

UVIS/FQ422M

Description

Blue continuum filter.

Figure A.139: Integrated system throughput for FQ422M.

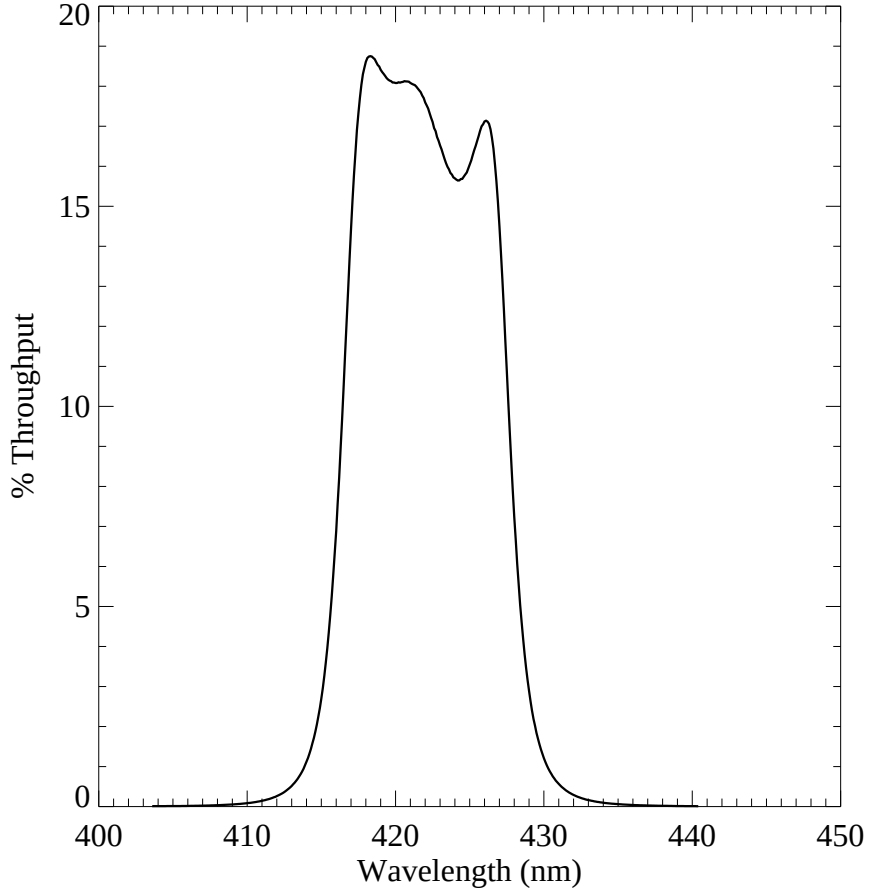

Figure A.140: Point source S/N vs. V+ABν for the FQ422M filter, assuming high sky backgrounds and a 5×5 pixel aperture.

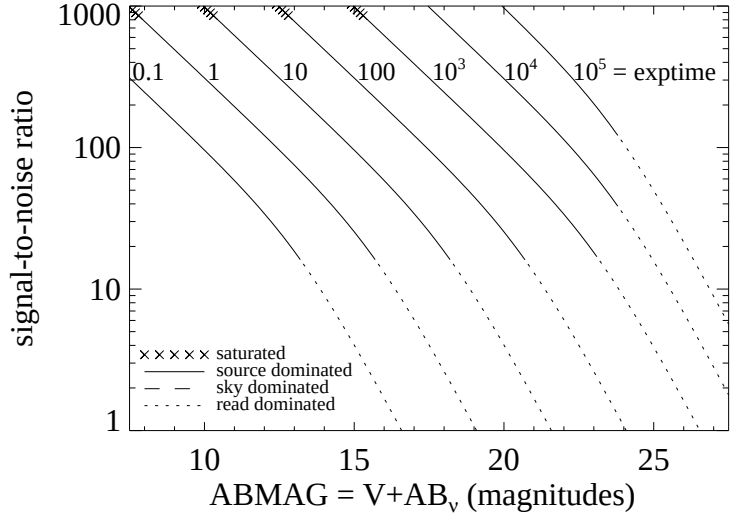

Figure A.141: Extended source S/N vs. V+ABν for the FQ422M filter, assuming high sky backgrounds and a source uniformly filling a 1 arcsec^2 aperture.

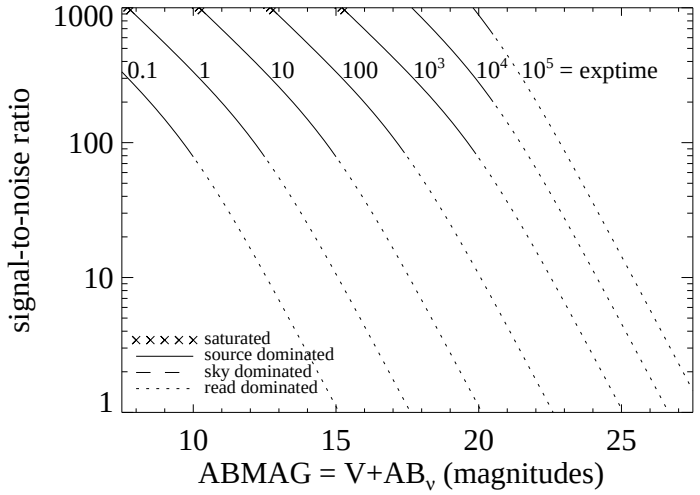

UVIS/FQ436N

Description

Hγ 4340 + [O III] 4363 filter.

Figure A.142: Integrated system throughput for FQ436N.

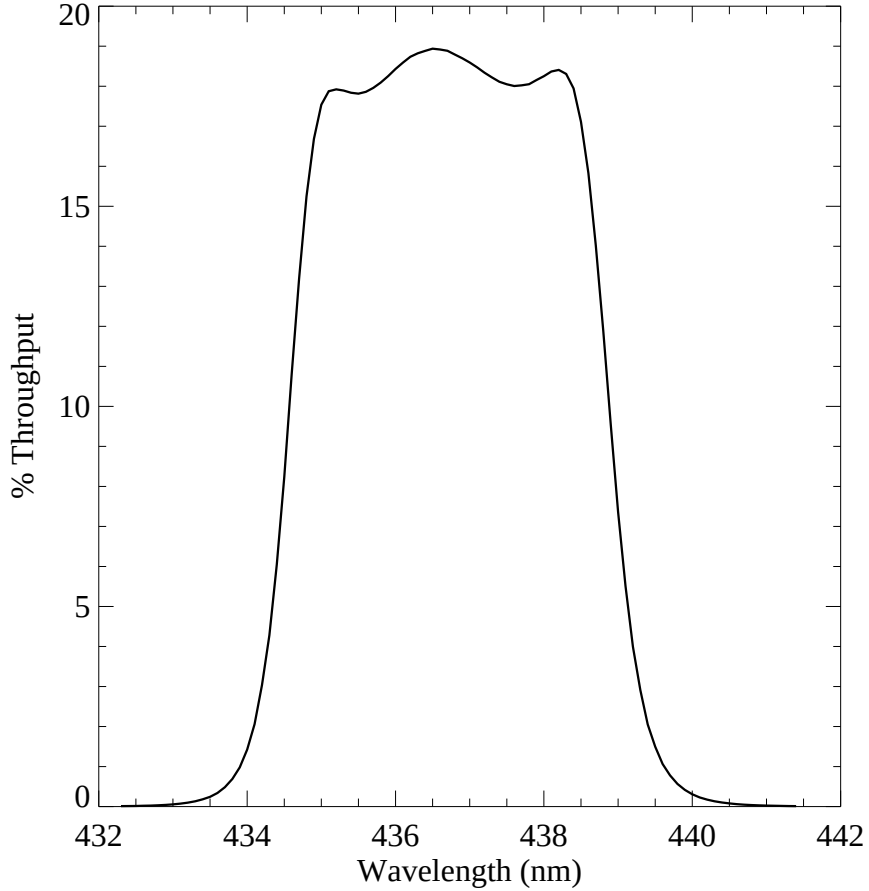

Figure A.143: Point source S/N vs. V+ABν for the FQ436N filter, assuming high sky backgrounds and a 5×5 pixel aperture.

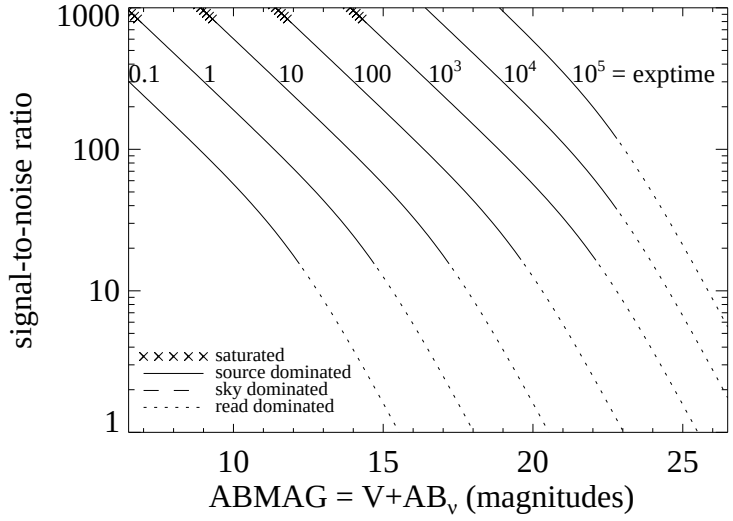

Figure A.144: Extended source S/N vs. V+ABν for the FQ436N filter, assuming high sky backgrounds and a source uniformly filling a 1 arcsec^2 aperture.

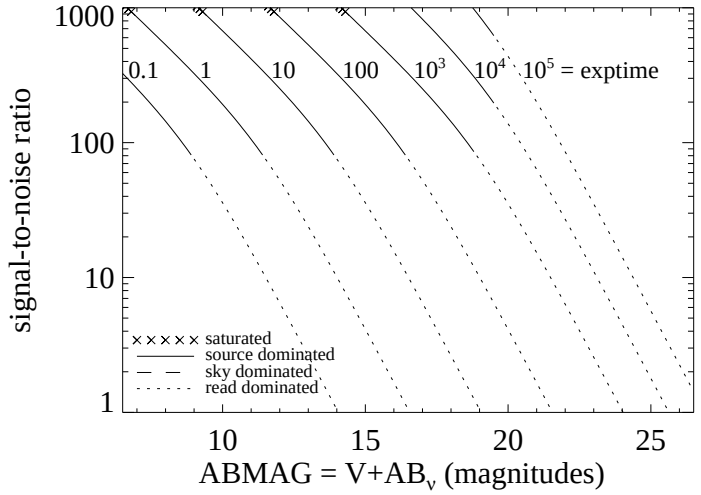

UVIS/FQ437N

Description

[O III] 4363 filter.

Figure A.145: Integrated system throughput for FQ437N.

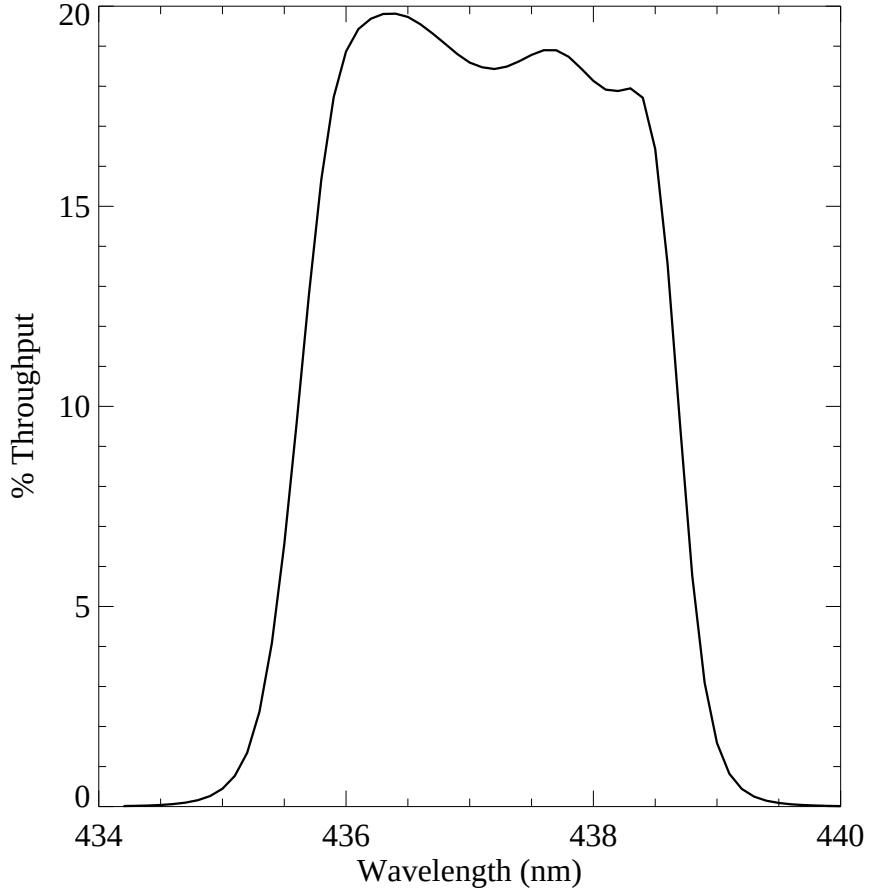

Figure A.146: Point source S/N vs. V+ABν for the FQ437N filter, assuming high sky backgrounds and a 5×5 pixel aperture.

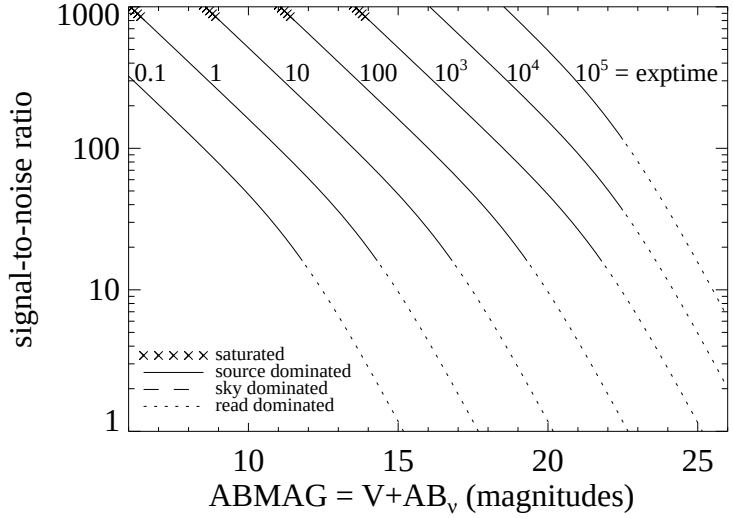

Figure A.147: Extended source S/N vs. V+ABν for the FQ437N filter, assuming high sky backgrounds and a source uniformly filling a 1 arcsec^2 aperture.

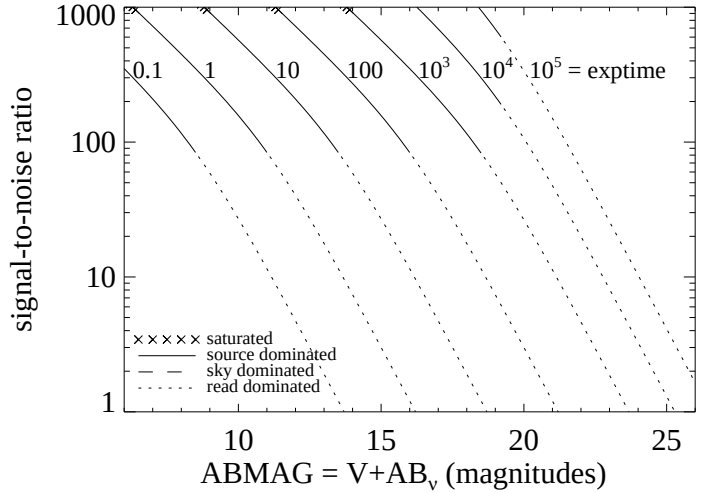

UVIS/FQ492N

Description

z (Hβ) filter.

Figure A.148: Integrated system throughput for FQ492N.

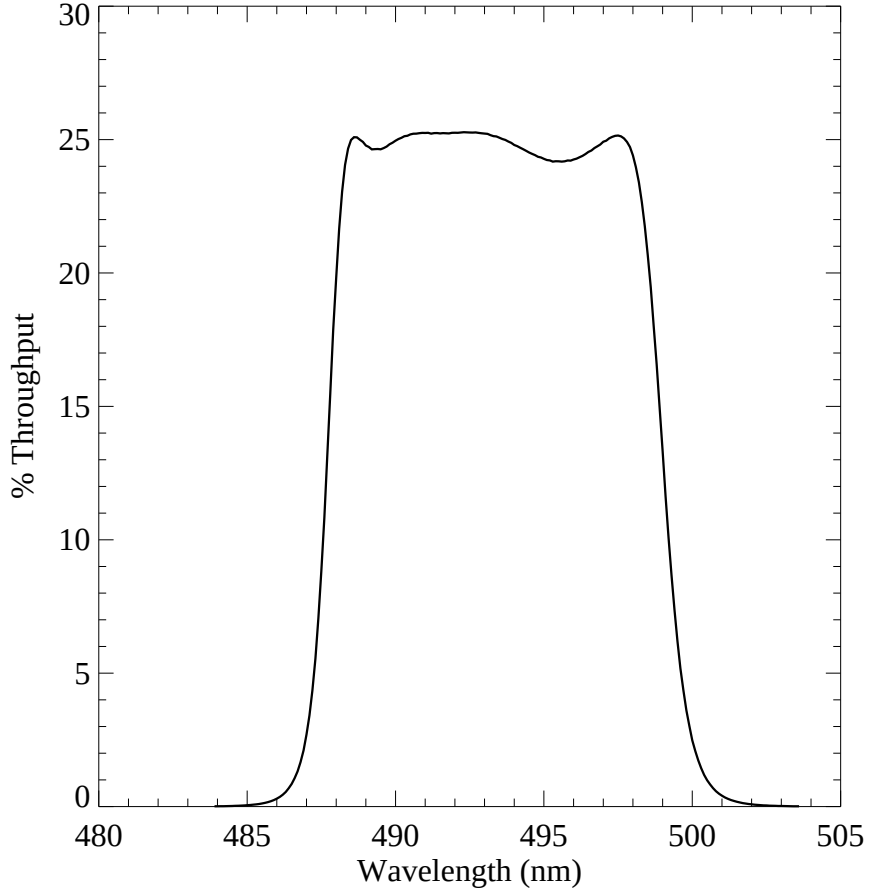

Figure A.149: Point source S/N vs. V+ABν for the FQ492N filter, assuming high sky backgrounds and a 5×5 pixel aperture.

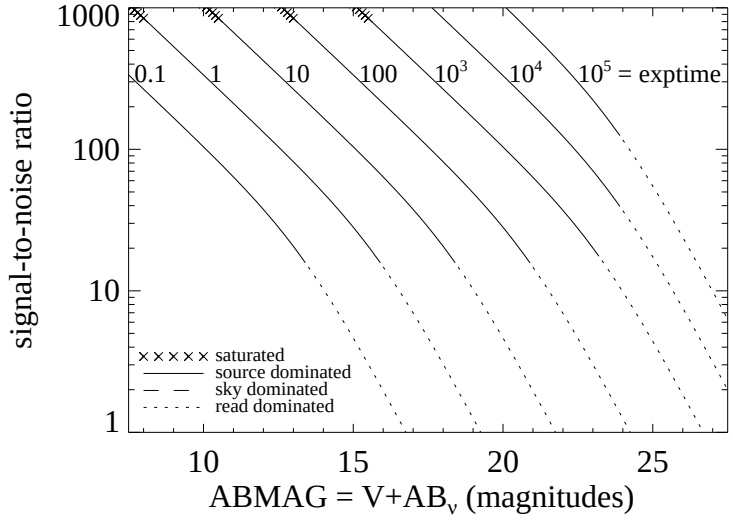

Figure A.150: Extended source S/N vs. V+ABν for the FQ492N filter, assuming high sky backgrounds and a source uniformly filling a 1 arcsec^2 aperture.

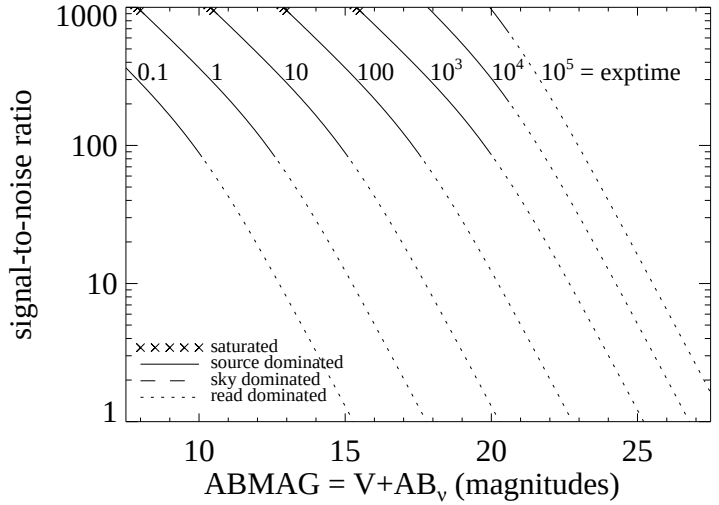

UVIS/FQ508N

Description

z ([O III] 5007) filter.

Figure A.151: Integrated system throughput for FQ508N.

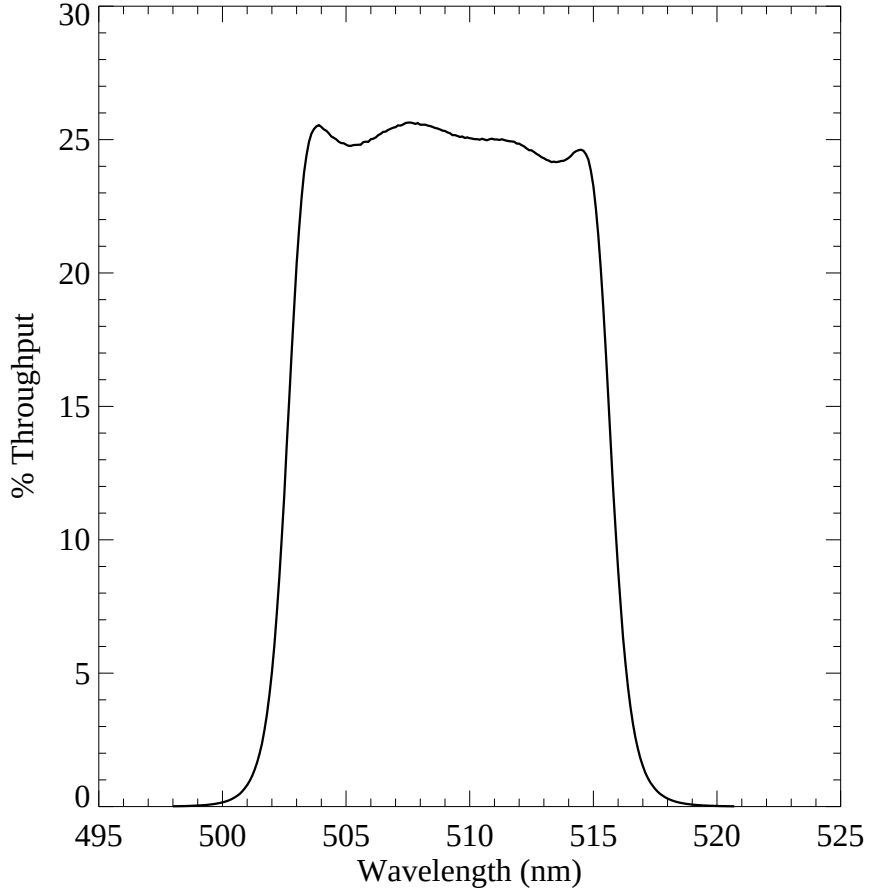

Figure A.152: Point source S/N vs. V+ABν for the FQ508N filter, assuming high sky backgrounds and a 5×5 pixel aperture.

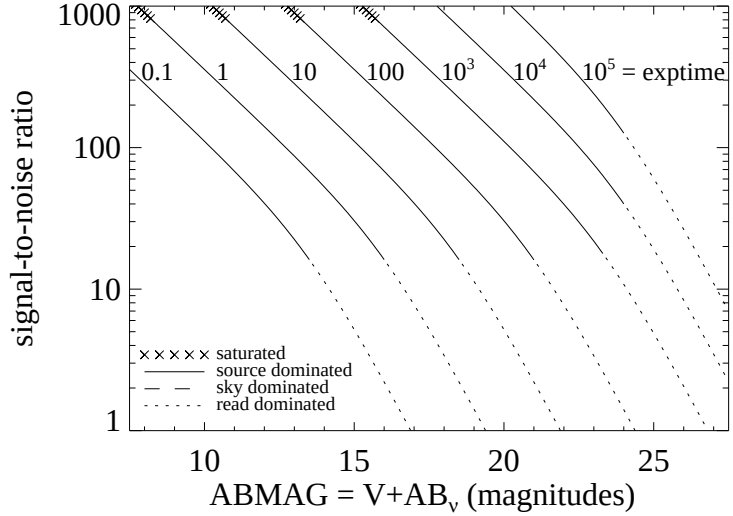

Figure A.153: Extended source S/N vs. V+ABν for the FQ508N filter, assuming high sky backgrounds and a source uniformly filling a 1 arcsec^2 aperture.

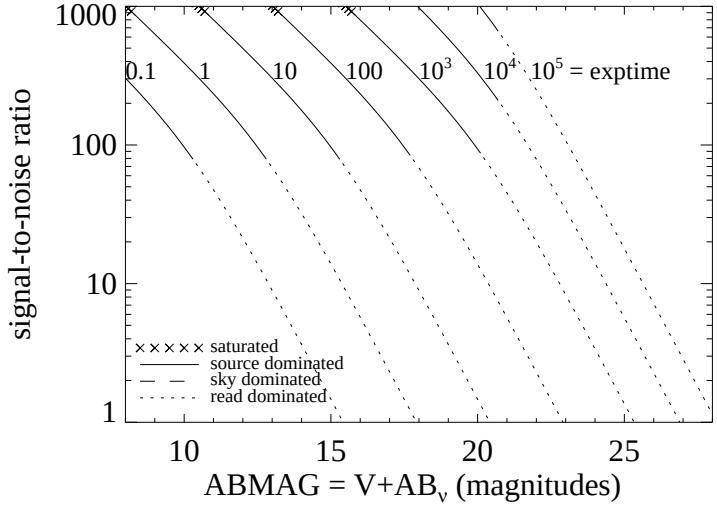

UVIS/FQ575N

Description

[N II] 5754 filter.

Figure A.154: Integrated system throughput for FQ575N.

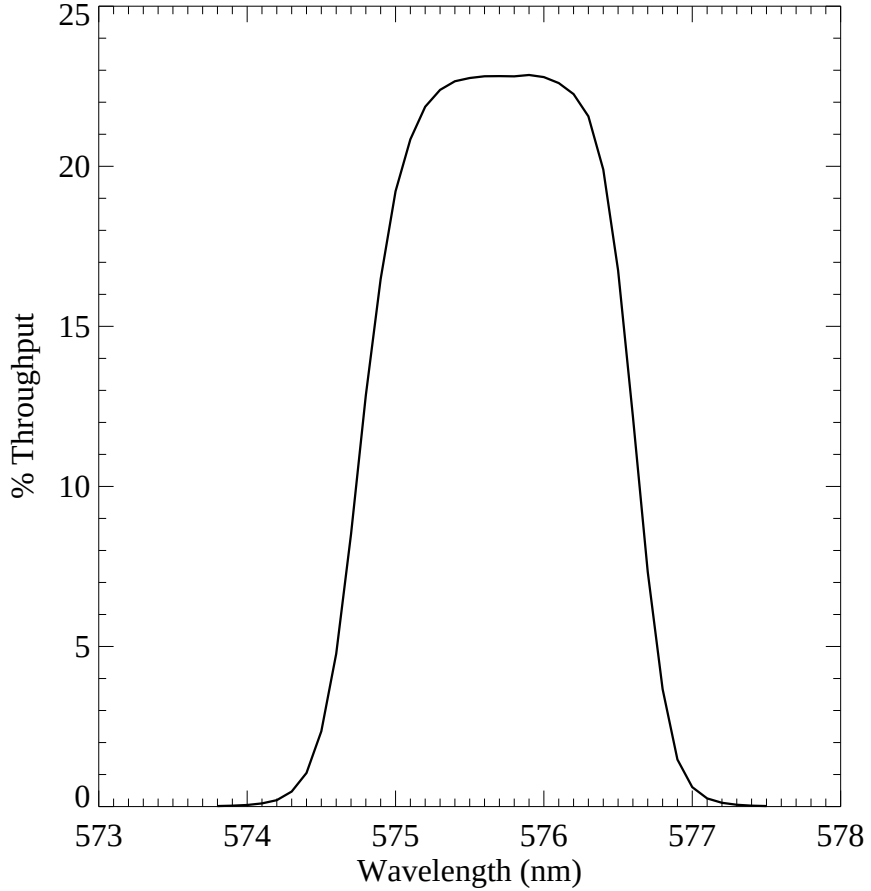

Figure A.155: Point source S/N vs. V+ABν for the FQ575N filter, assuming high sky backgrounds and a 5×5 pixel aperture.

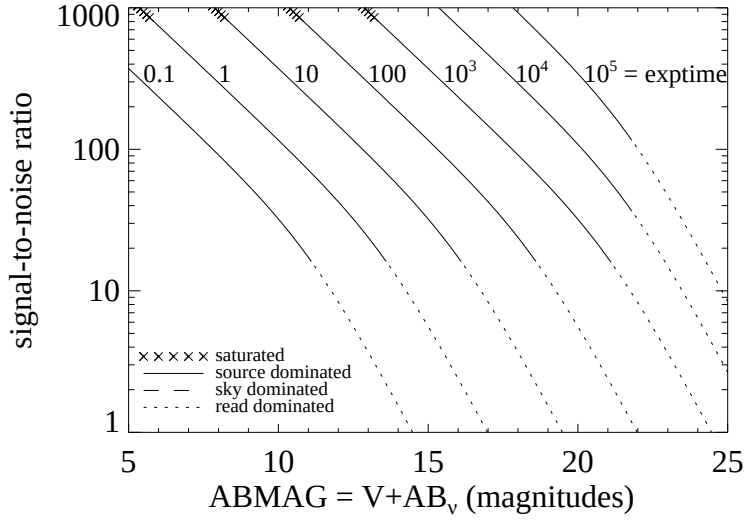

Figure A.156: Extended source S/N vs. V+ABν for the FQ575N filter, assuming high sky backgrounds and a source uniformly filling a 1 arcsec^2 aperture.

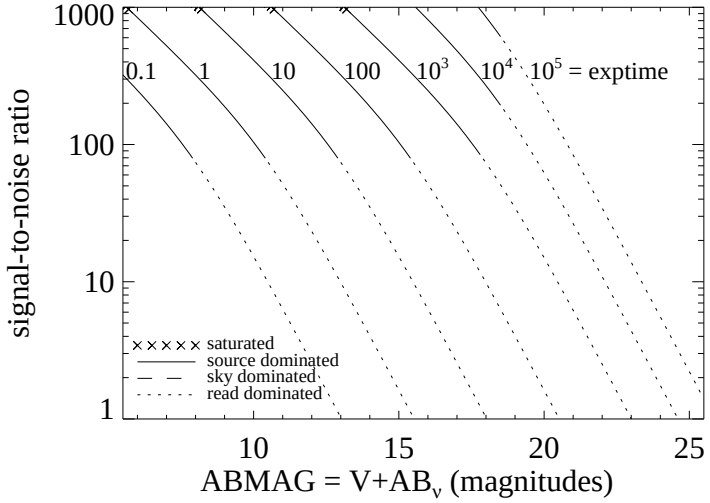

UVIS/FQ619N

Description

CH_4 6194 filter.

Figure A.157: Integrated system throughput for FQ619N.

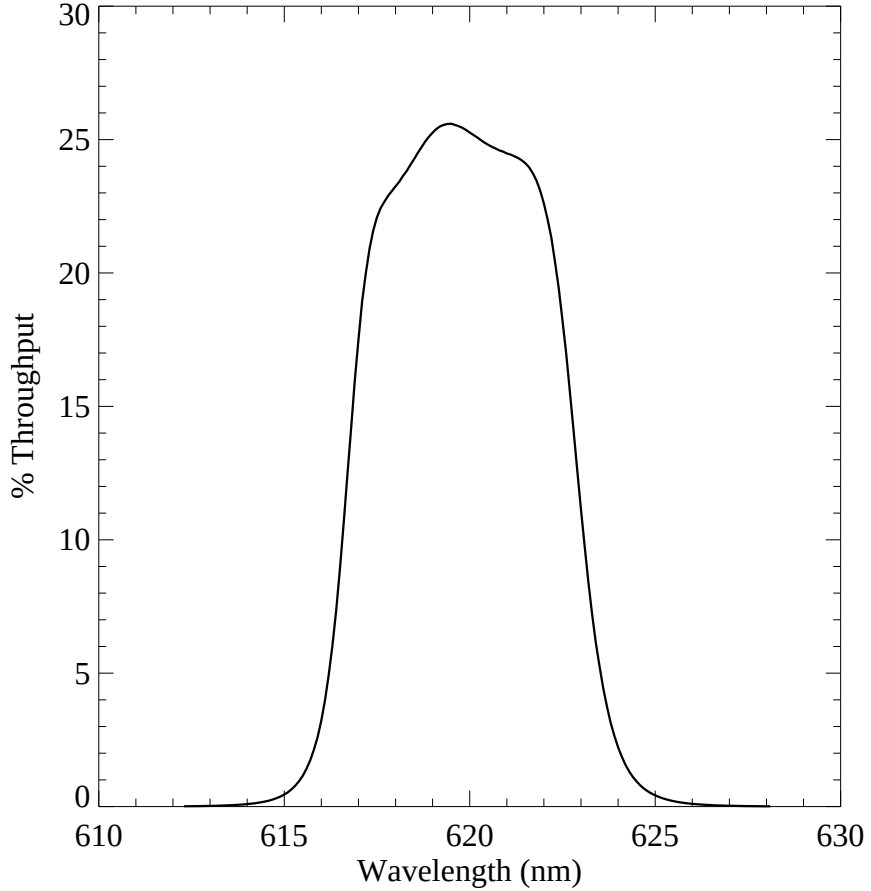

Figure A.158: Point source S/N vs. V+ABν for the FQ619N filter, assuming high sky backgrounds and a 5×5 pixel aperture.

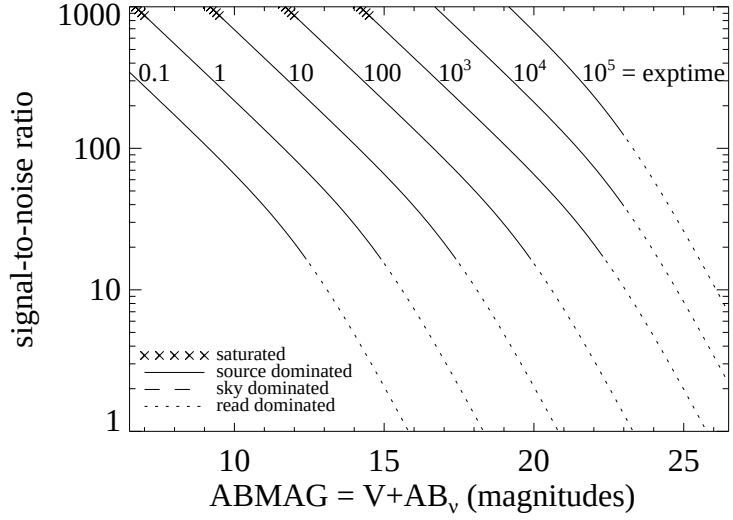

Figure A.159: Extended source S/N vs. V+ABν for the FQ619N filter, assuming high sky backgrounds and a source uniformly filling a 1 arcsec^2 aperture.

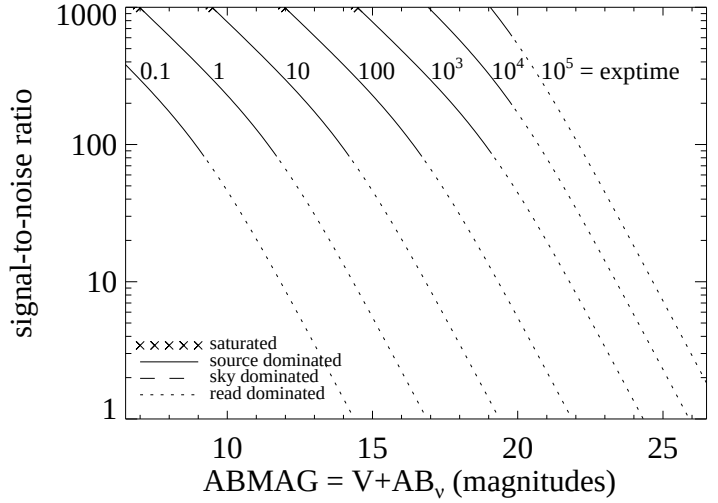

UVIS/FQ634N

Description

6194 continuum filter.

Figure A.160: Integrated system throughput for FQ634N.

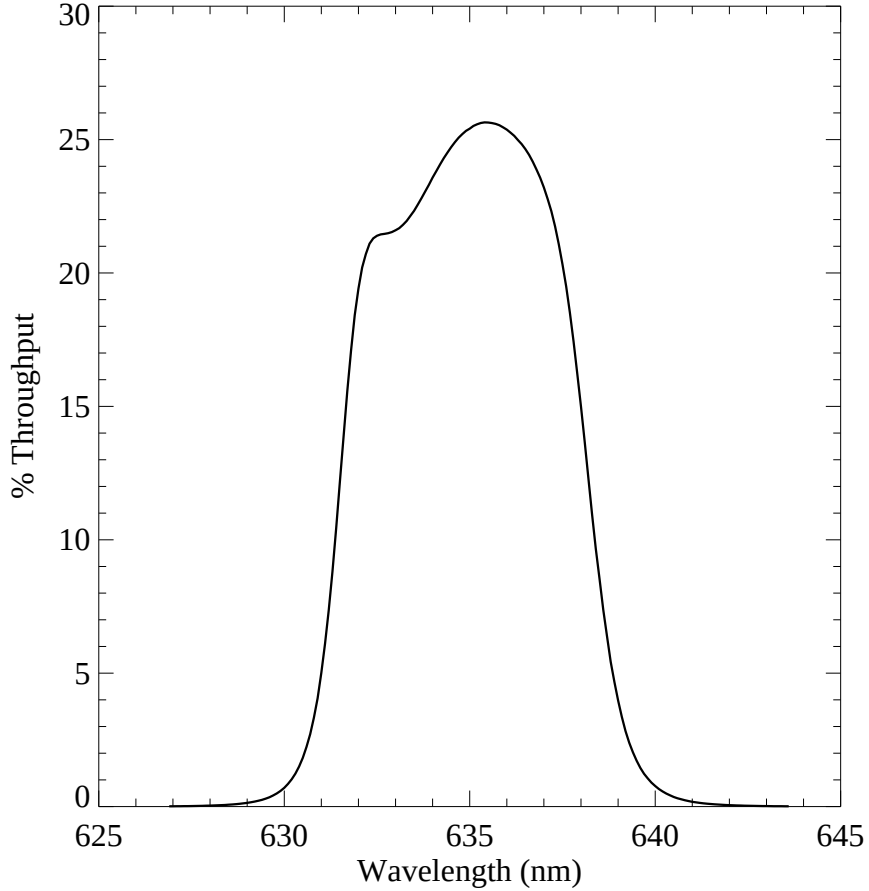

Figure A.161: Point source S/N vs. V+ABν for the FQ634N filter, assuming high sky backgrounds and a 5×5 pixel aperture.

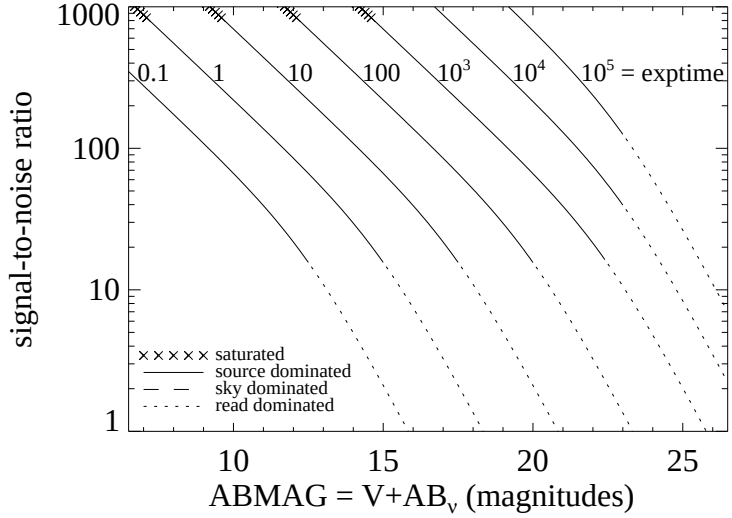

Figure A.162: Extended source S/N vs. V+ABν for the FQ634N filter, assuming high sky backgrounds and a source uniformly filling a 1 arcsec^2 aperture.

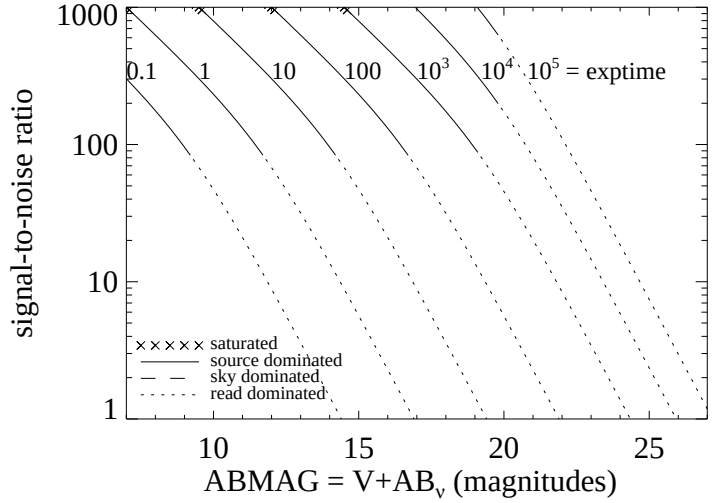

UVIS/FQ672N

Description

[S II] 6717 filter.

Figure A.163: Integrated system throughput for FQ672N.

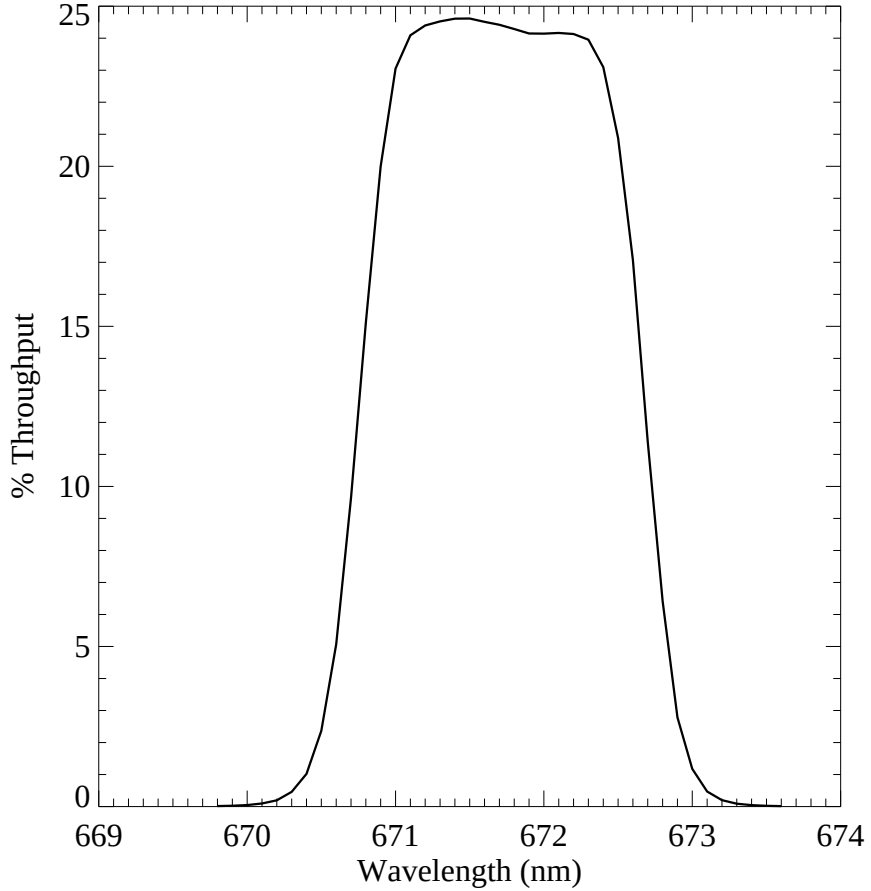

Figure A.164: Point source S/N vs. V+ABν for the FQ672N filter, assuming high sky backgrounds and a 5×5 pixel aperture.

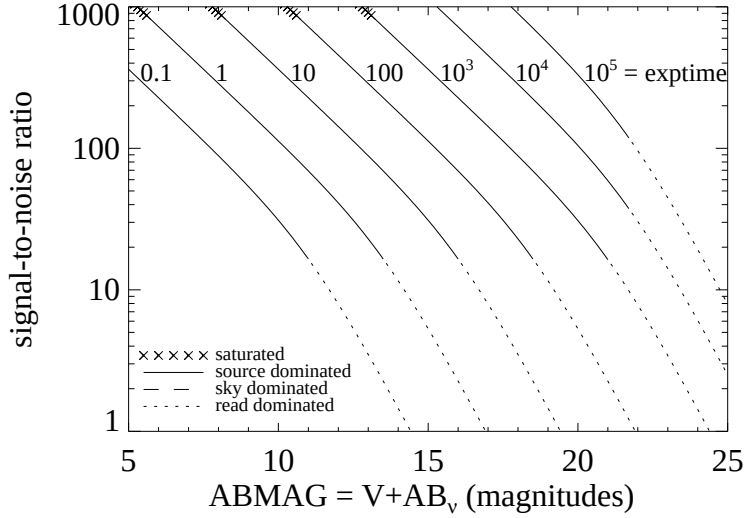

Figure A.165: Extended source S/N vs. V+ABν for the FQ672N filter, assuming high sky backgrounds and a source uniformly filling a 1 arcsec^2 aperture.

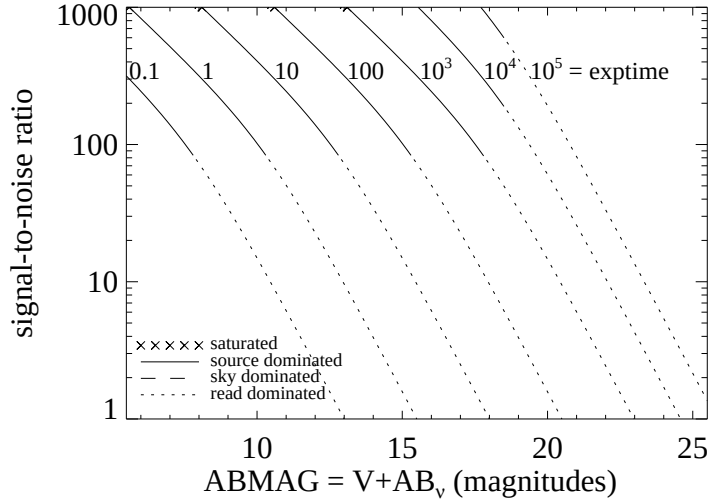

UVIS/FQ674N

Description

[S II] 6731 filter.

Figure A.166: Integrated system throughput for FQ674N.

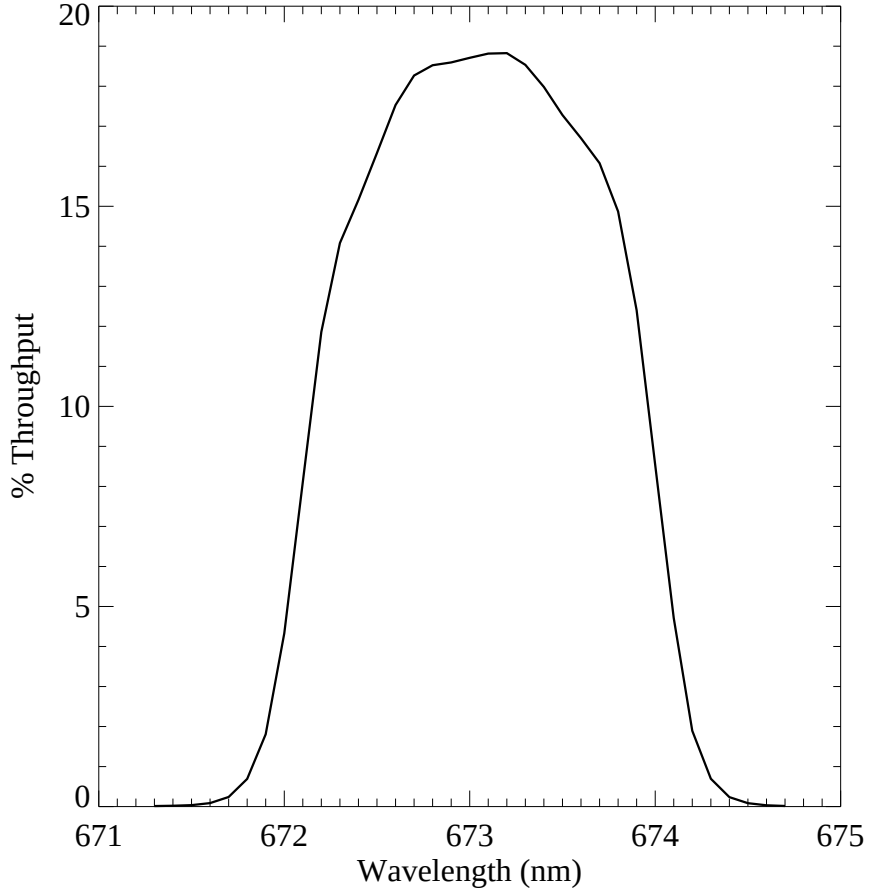

Figure A.167: Point source S/N vs. V+ABν for the FQ674N filter, assuming high sky backgrounds and a 5×5 pixel aperture.

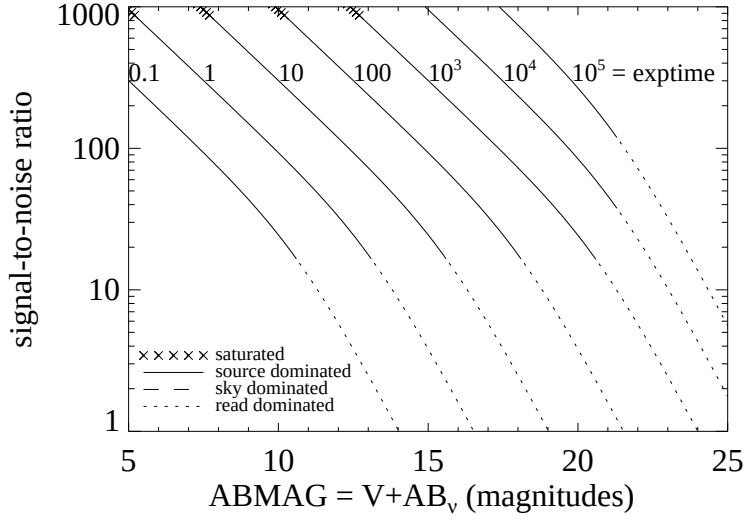

Figure A.168: Extended source S/N vs. V+ABν for the FQ674N filter, assuming high sky backgrounds and a source uniformly filling a 1 arcsec^2 aperture.

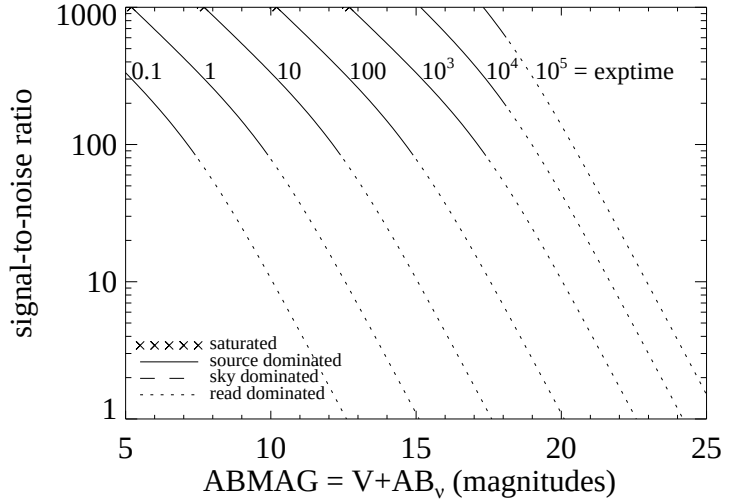

UVIS/FQ727N

Description

CH_4 7270 filter.

Figure A.169: Integrated system throughput for FQ727N.

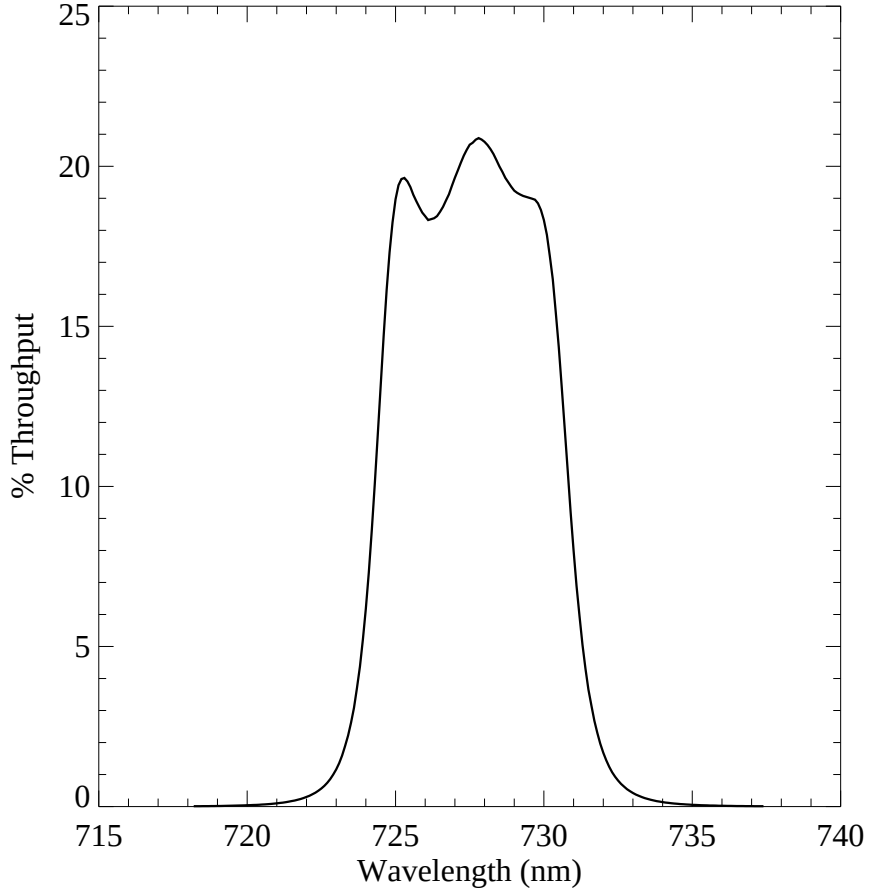

Figure A.170: Point source S/N vs. V+ABν for the FQ727N filter, assuming high sky backgrounds and a 5×5 pixel aperture.

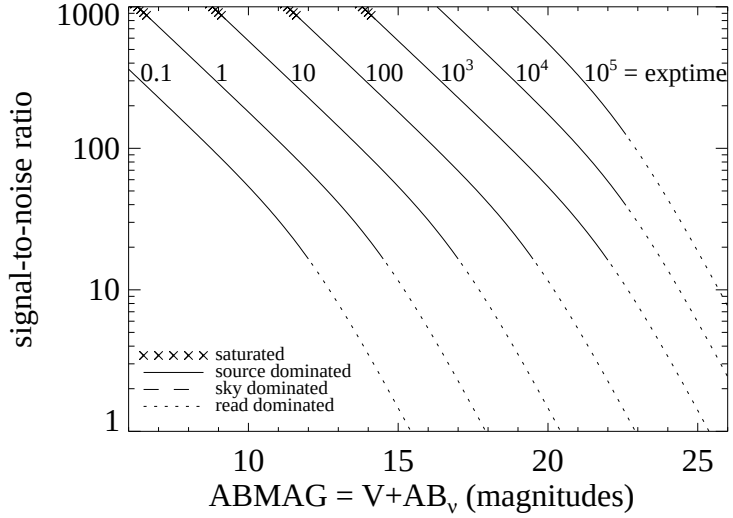

Figure A.171: Extended source S/N vs. V+ABν for the FQ727N filter, assuming high sky backgrounds and a source uniformly filling a 1 arcsec^2 aperture.

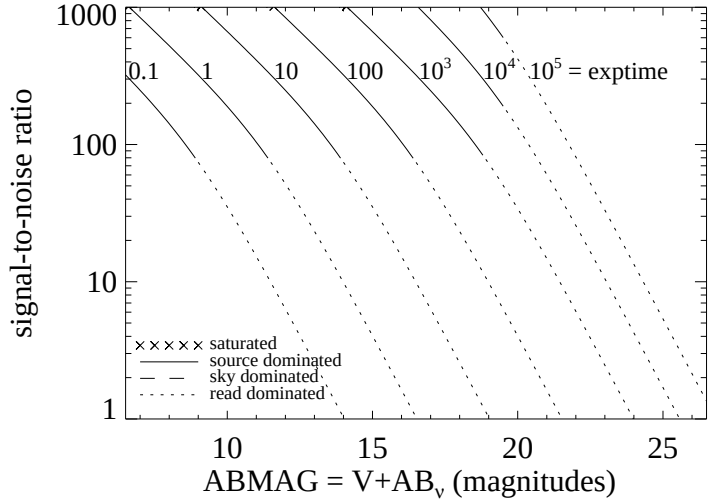

UVIS/FQ750N

Description

7270 continuum filter.

Figure A.172: Integrated system throughput for FQ750N.

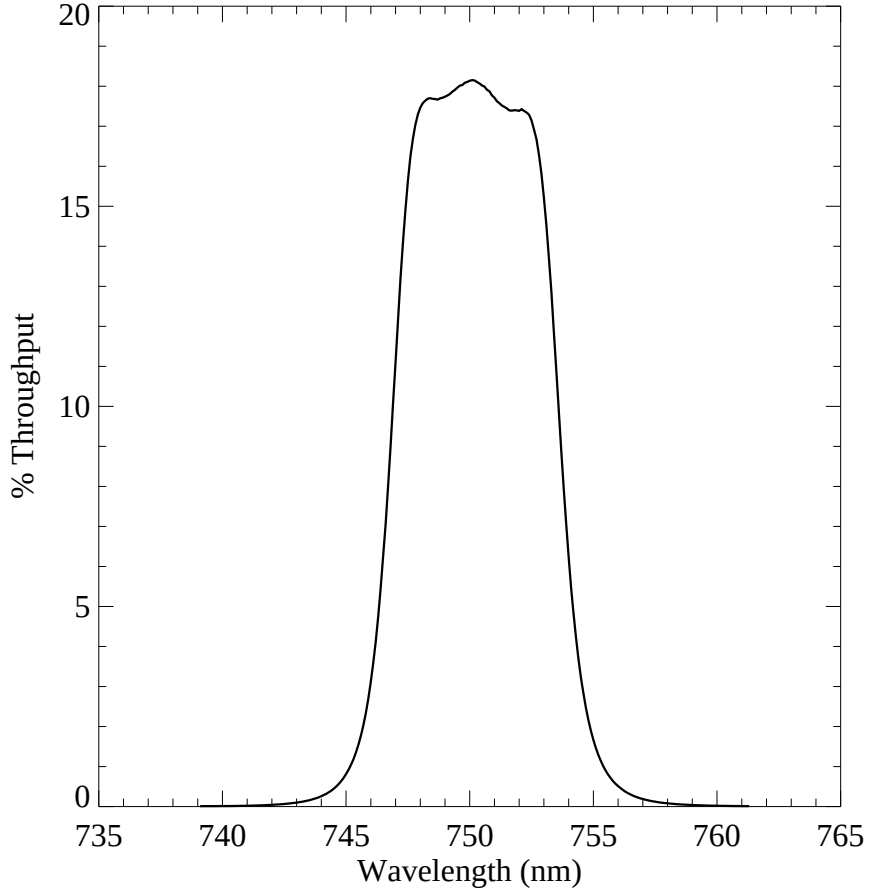

Figure A.173: Point source S/N vs. V+ABν for the FQ750N filter, assuming high sky backgrounds and a 5×5 pixel aperture.

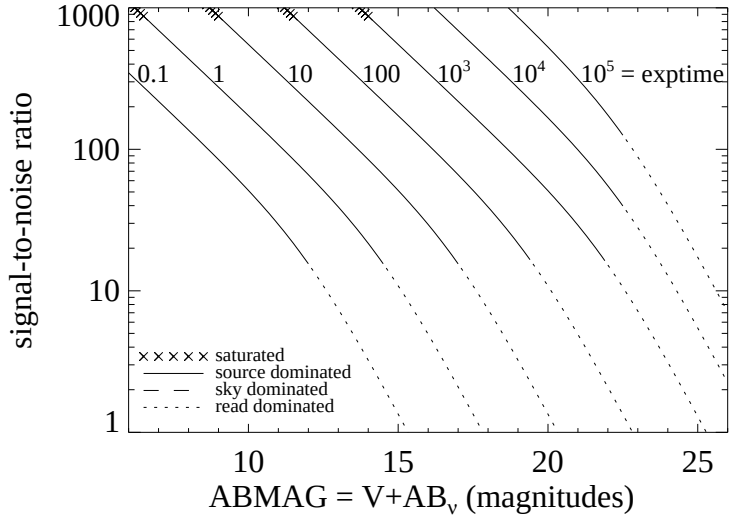

Figure A.174: Extended source S/N vs. V+ABν for the FQ750N filter, assuming high sky backgrounds and a source uniformly filling a 1 arcsec^2 aperture.

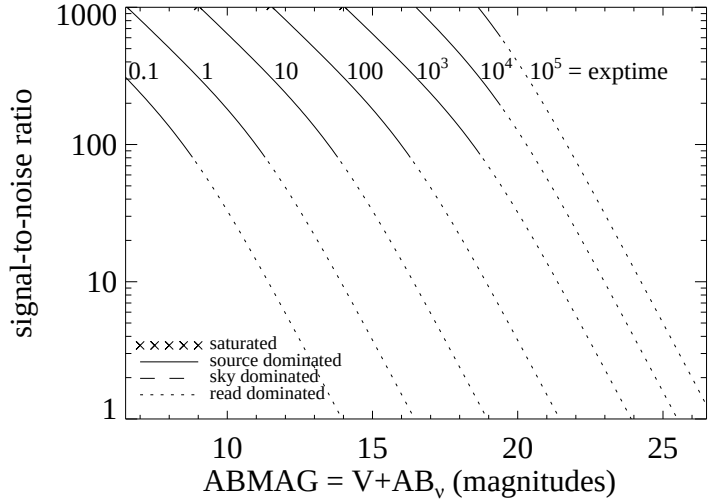

UVIS/FQ889N

Description

CH_4 25 km-agt filter.

Figure A.175: Integrated system throughput for FQ889N.

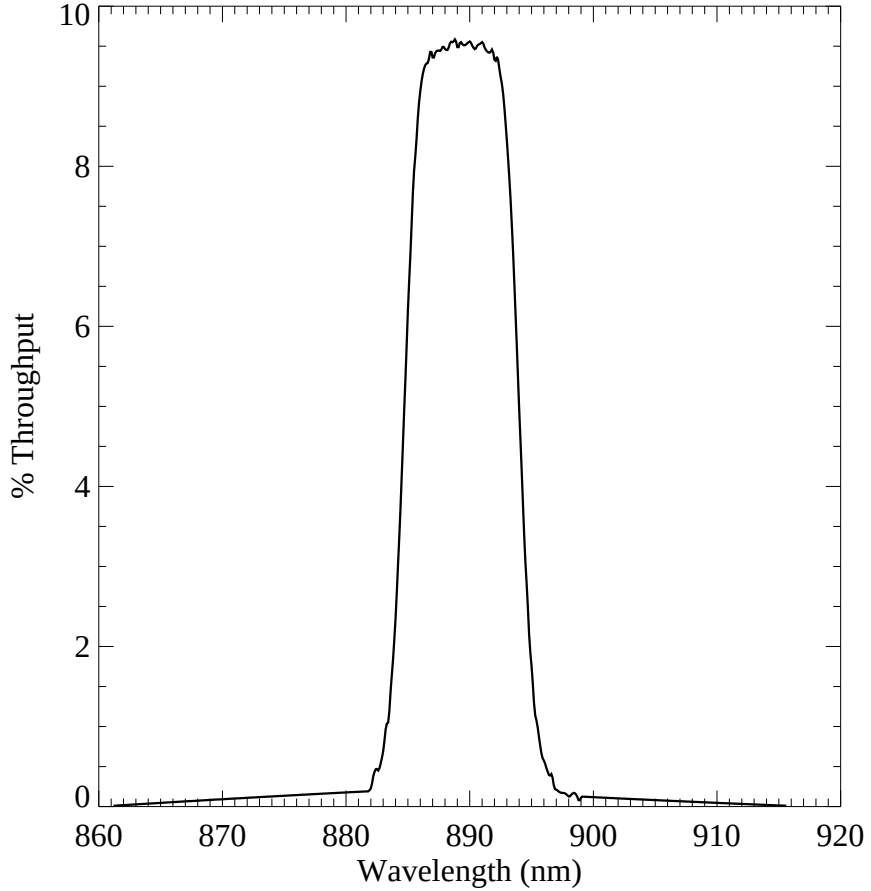

Figure A.176: Point source S/N vs. V+ABν for the FQ889N filter, assuming high sky backgrounds and a 5×5 pixel aperture.

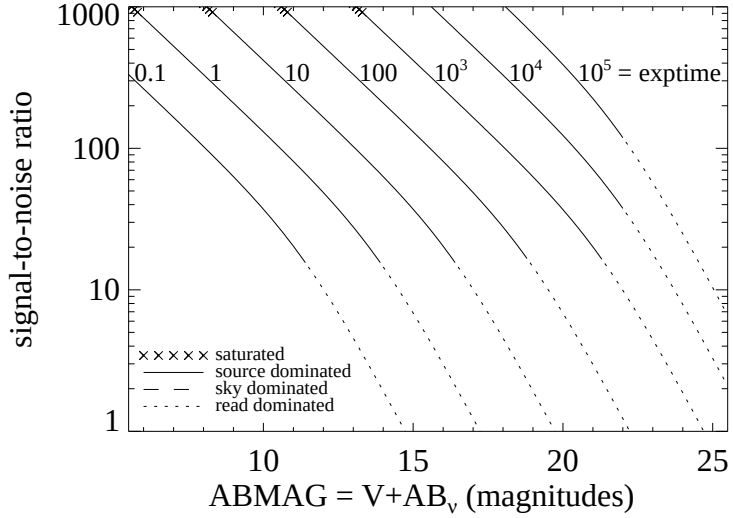

Figure A.177: Extended source S/N vs. V+ABν for the FQ889N filter, assuming high sky backgrounds and a source uniformly filling a 1 arcsec^2 aperture.

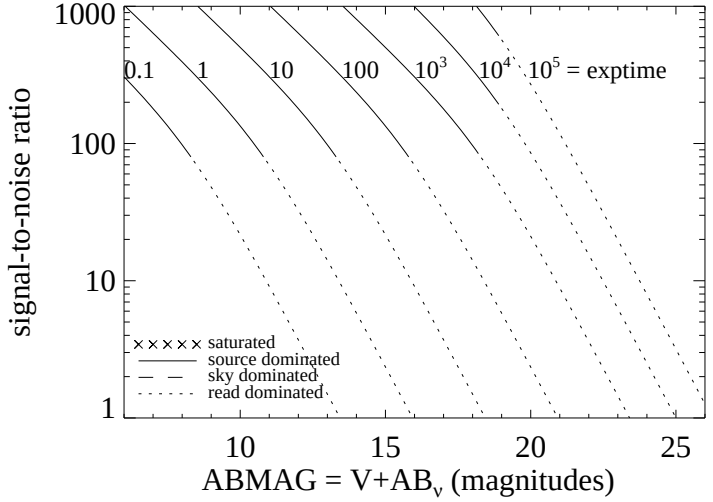

UVIS/FQ906N

Description

CH_4 2.5 km-agt filter.

Figure A.178: Integrated system throughput for FQ906N.

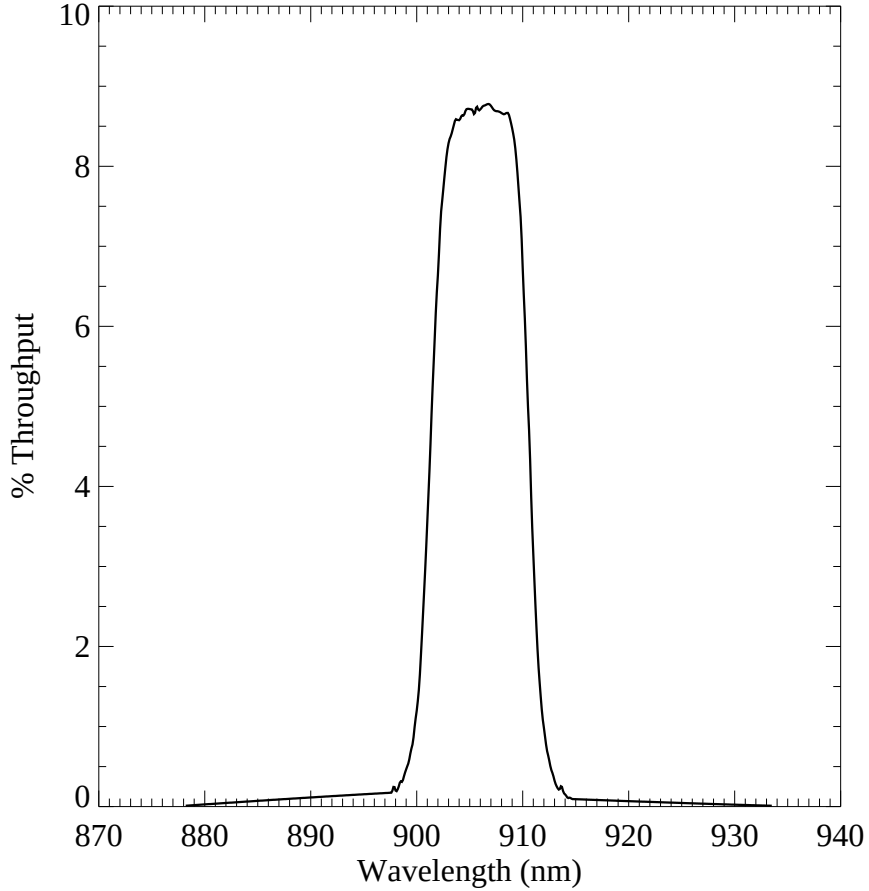

Figure A.179: Point source S/N vs. V+ABν for the FQ906N filter, assuming high sky backgrounds and a 5×5 pixel aperture.

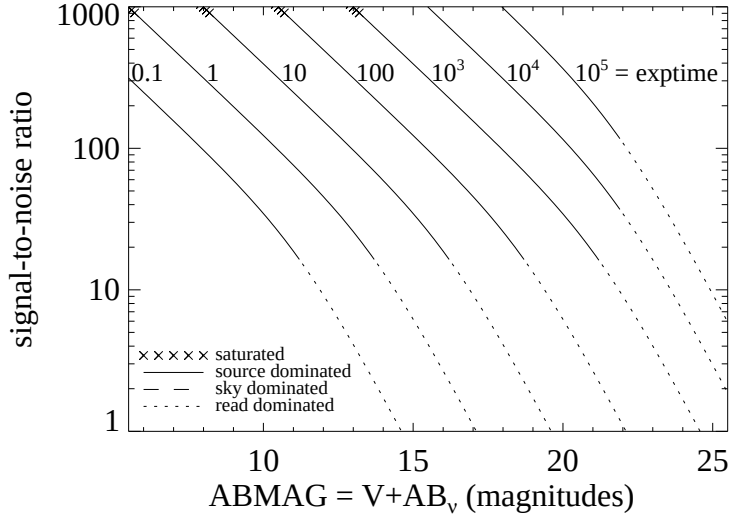

Figure A.180: Extended source S/N vs. V+ABν for the FQ906N filter, assuming high sky backgrounds and a source uniformly filling a 1 arcsec^2 aperture.

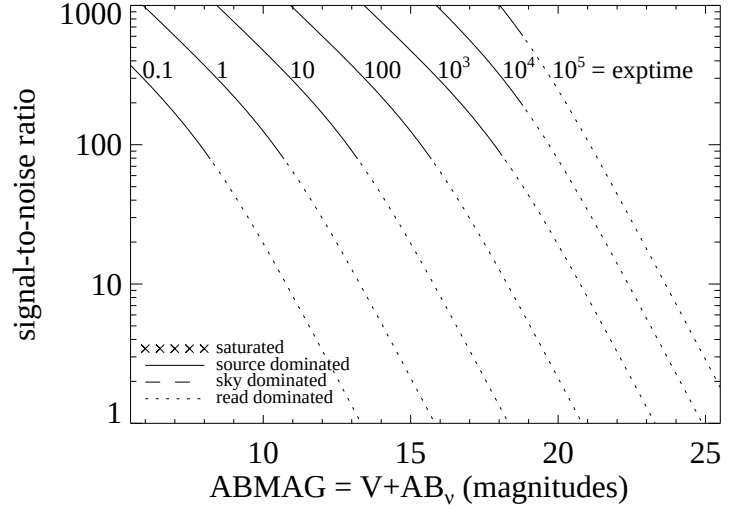

UVIS/FQ924N

Description

CH_4 0.25 km-agt filter.

Figure A.181: Integrated system throughput for FQ924N.

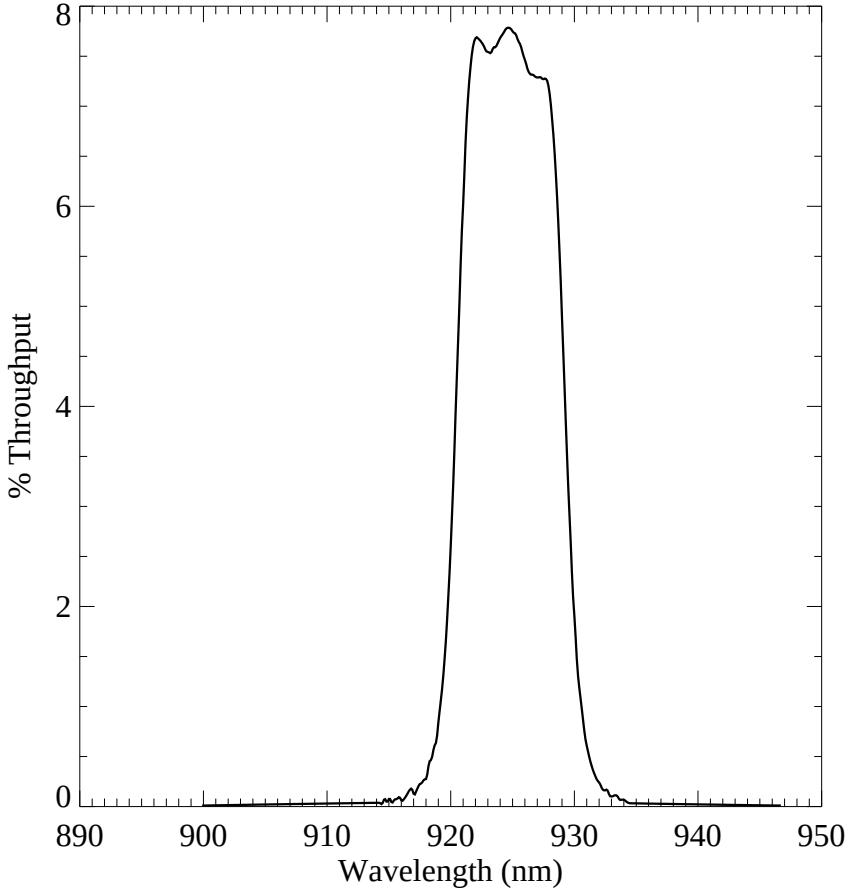

Figure A.182: Point source S/N vs. V+ABν for the FQ924N filter, assuming high sky backgrounds and a 5×5 pixel aperture.

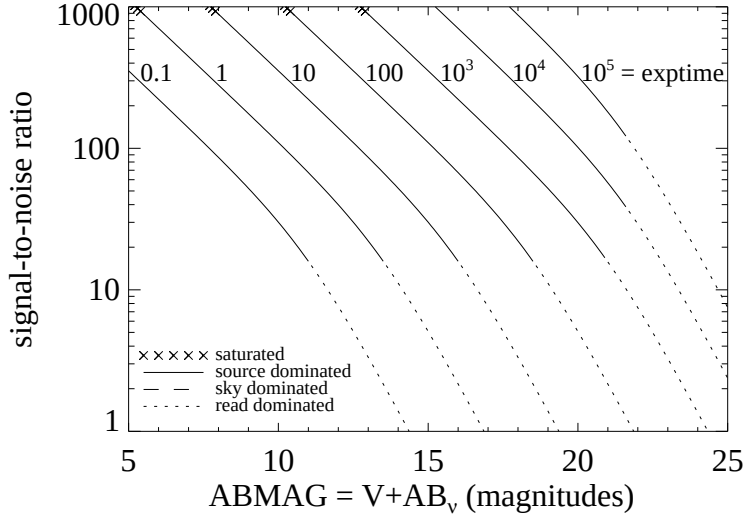

Figure A.183: Extended source S/N vs. V+ABν for the FQ924N filter, assuming high sky backgrounds and a source uniformly filling a 1 arcsec^2 aperture.

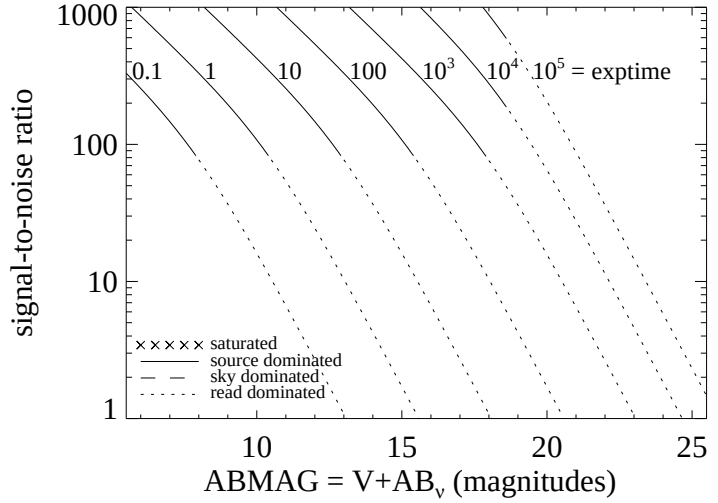

UVIS/FQ937N

Description

CH_4 0.025 km-agt filter.

Figure A.184: Integrated system throughput for FQ937N.

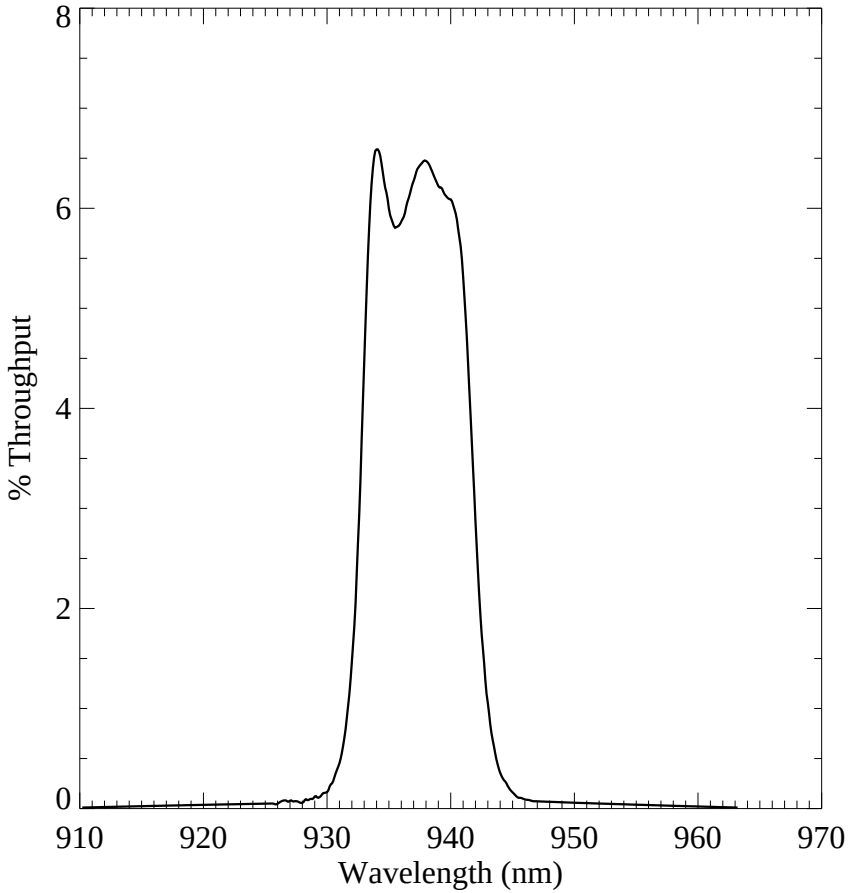

Figure A.185: Point source S/N vs. V+ABν for the FQ937N filter, assuming high sky backgrounds and a 5×5 pixel aperture.

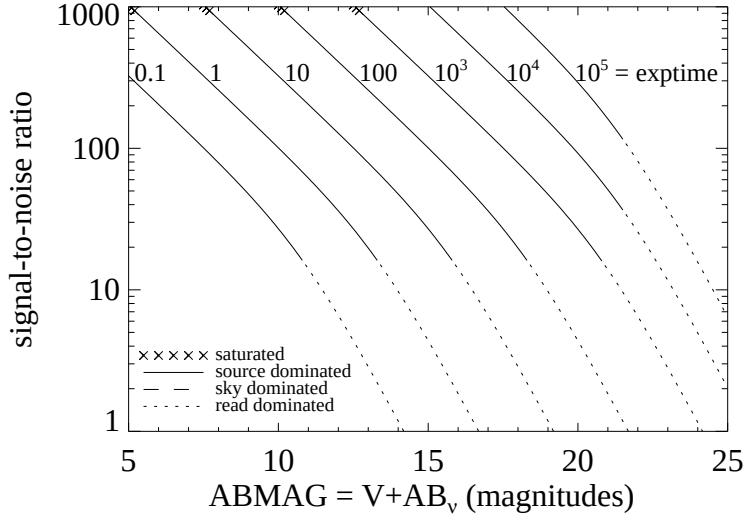

Figure A.186: Extended source S/N vs. V+ABν for the FQ937N filter, assuming high sky backgrounds and a source uniformly filling a 1 arcsec^2 aperture.

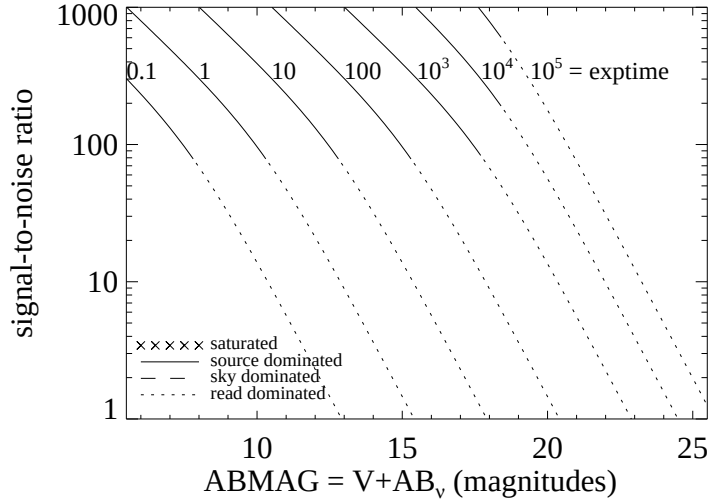

IR/F098M

Description

Blue grism reference filter.

Figure A.187: Integrated system throughput for F098M.

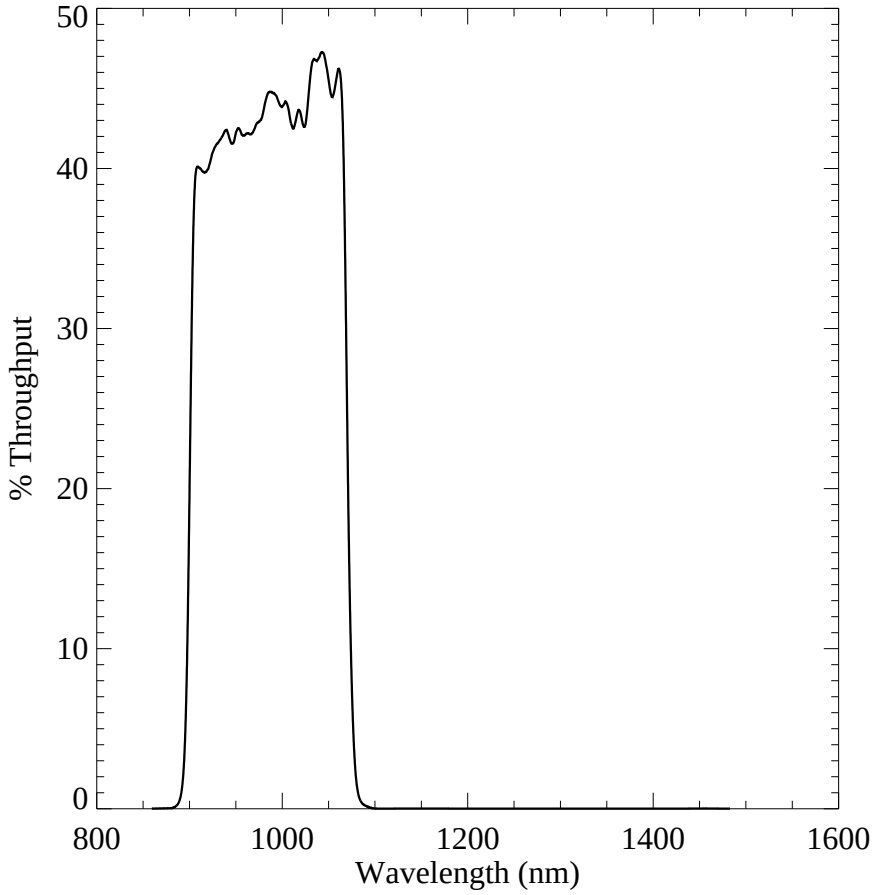

Figure A.188: Point source S/N vs. V+ABν for the F098M filter, assuming high sky backgrounds and a 3×3 pixel aperture.

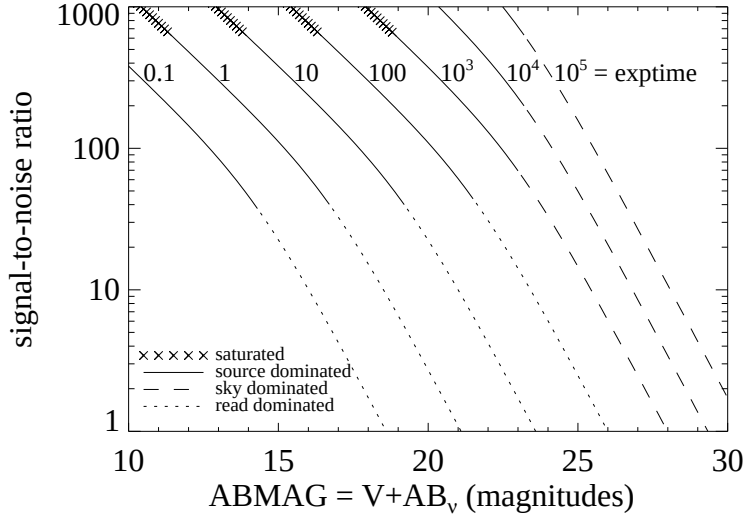

Figure A.189: Extended source S/N vs. V+ABν for the F098M filter, assuming high sky backgrounds and a source uniformly filling a 1 arcsec^2 aperture.

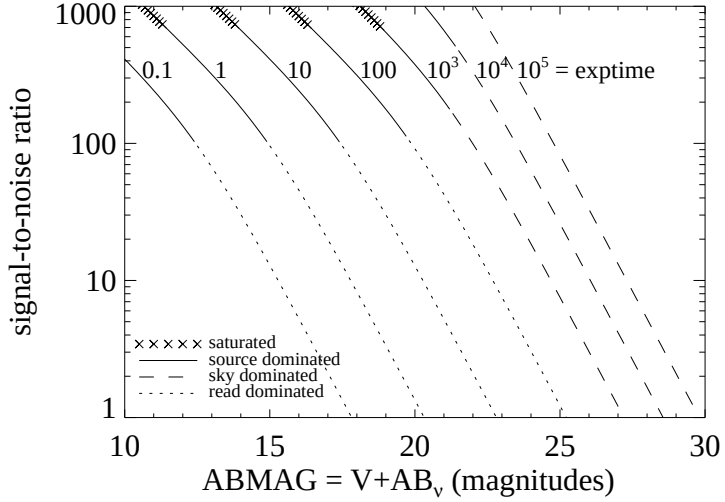

IR/F105W

Description

Wide *Y* filter.

Figure A.190: Integrated system throughput for F105W.

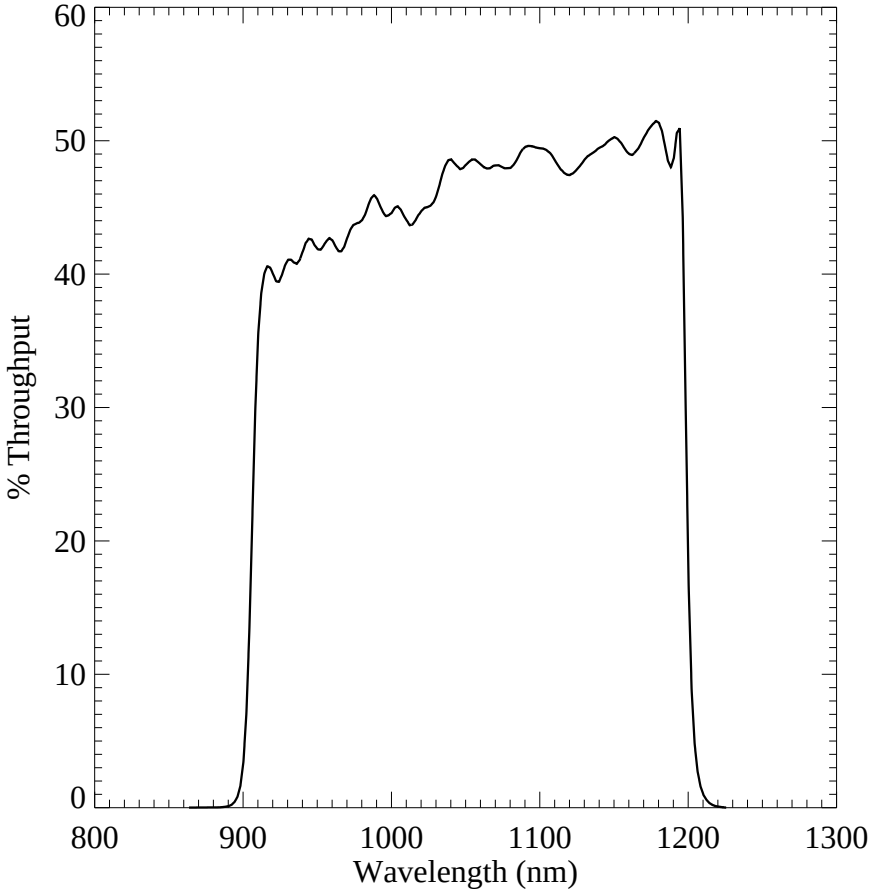

Figure A.191: Point source S/N vs. V+ABν for the F105W filter, assuming high sky backgrounds and a 3×3 pixel aperture.

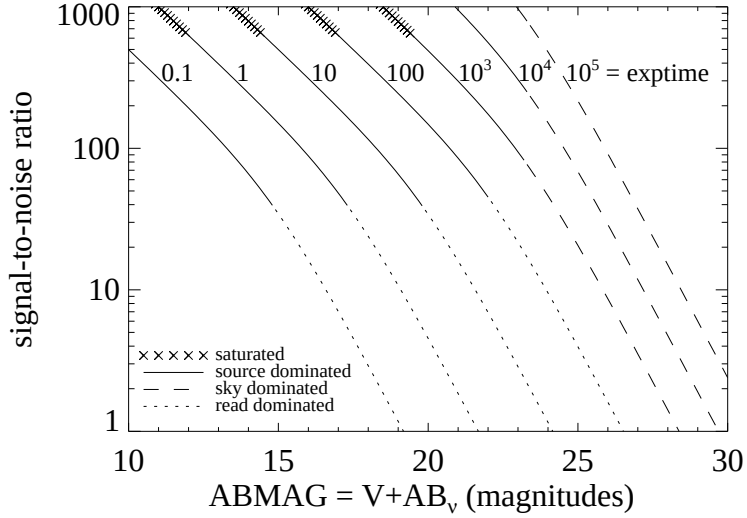

Figure A.192: Extended source S/N vs. V+ABν for the F105W filter, assuming high sky backgrounds and a source uniformly filling a 1 arcsec^2 aperture.

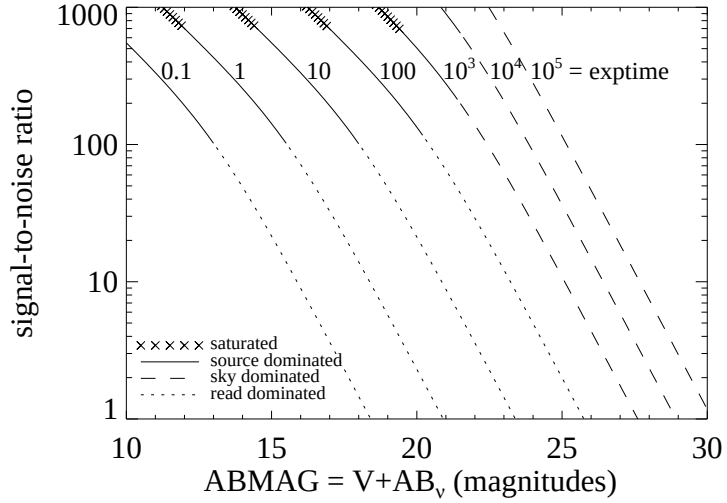

IR/F110W

Description

Wide *YJ* filter.

Figure A.193: Integrated system throughput for F110W.

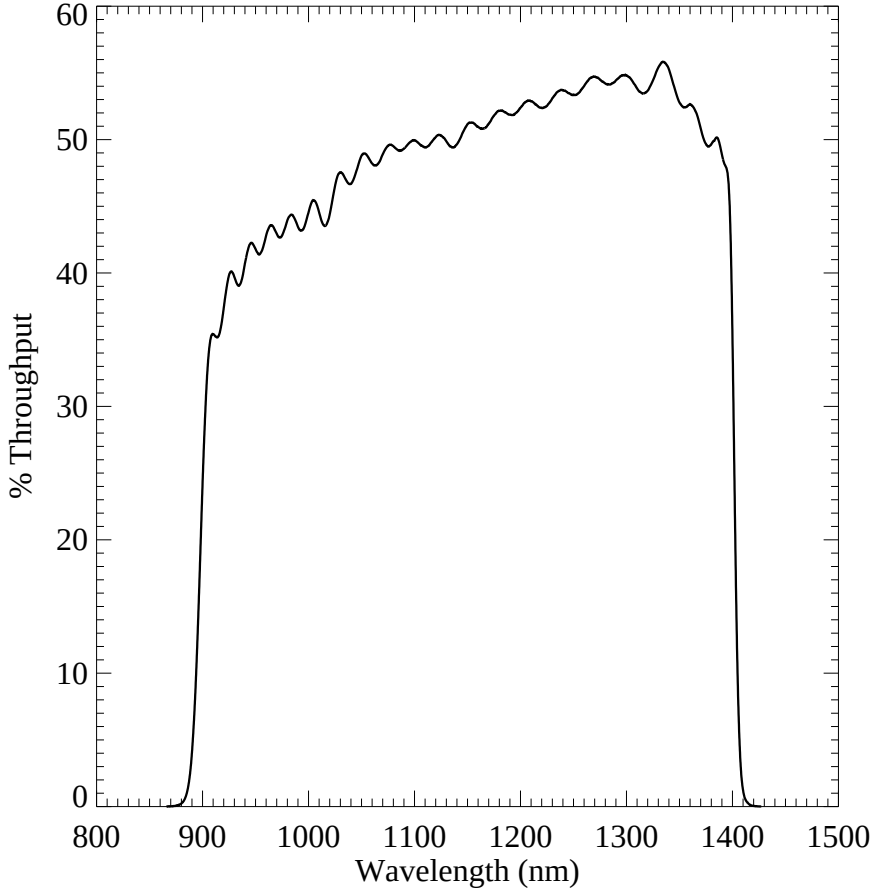

Figure A.194: Point source S/N vs. V+ABν for the F110W filter, assuming high sky backgrounds and a 3×3 pixel aperture.

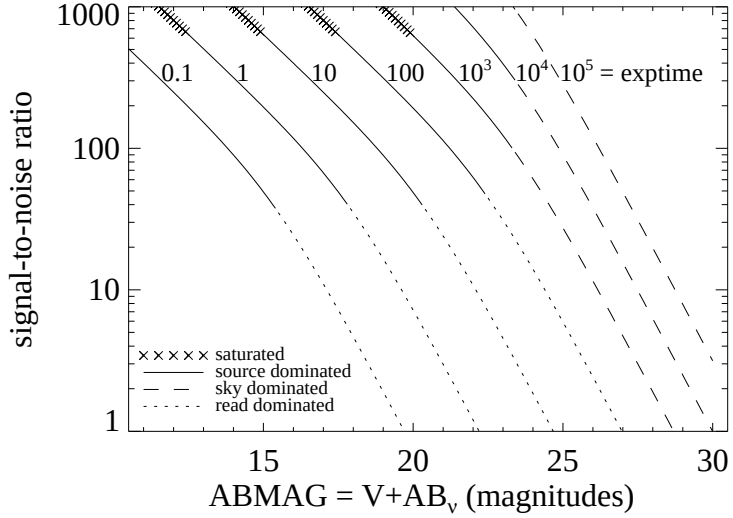

Figure A.195: Extended source S/N vs. V+ABν for the F110W filter, assuming high sky backgrounds and a source uniformly filling a 1 arcsec^2 aperture.

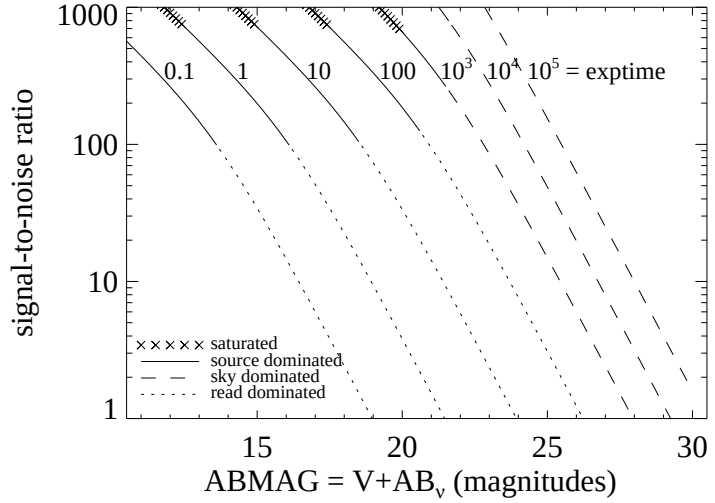

IR/F125W

Description

Wide *J* filter.

Figure A.196: Integrated system throughput for F125W.

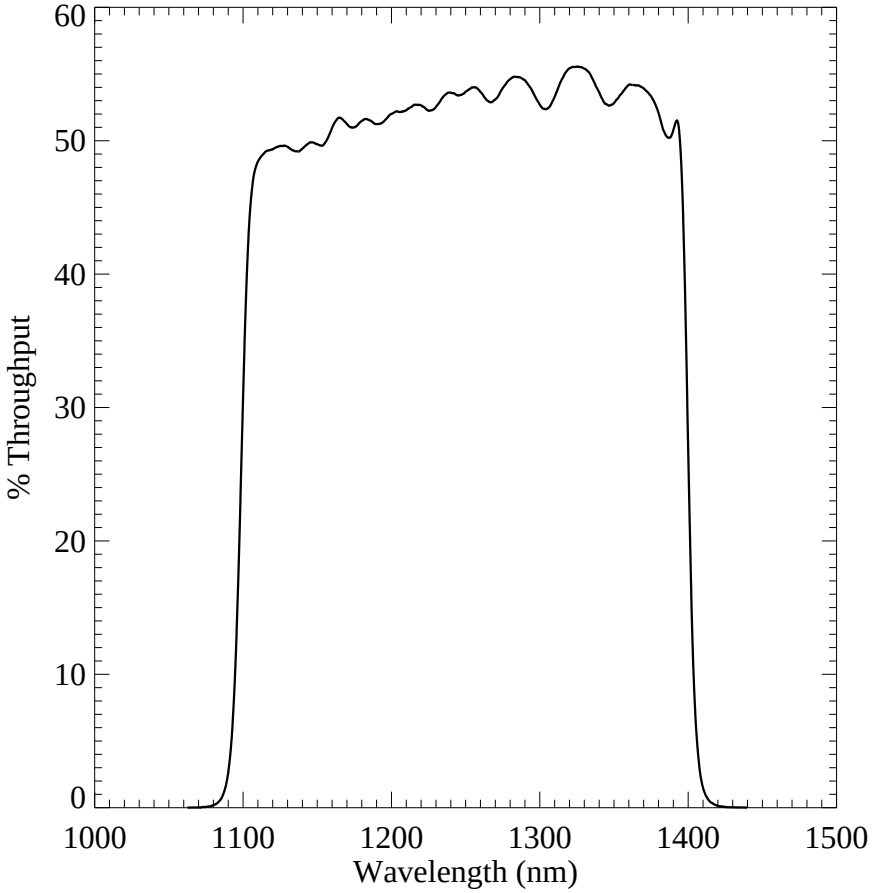

Figure A.197: Point source S/N vs. V+ABν for the F125W filter, assuming high sky backgrounds and a 3×3 pixel aperture.

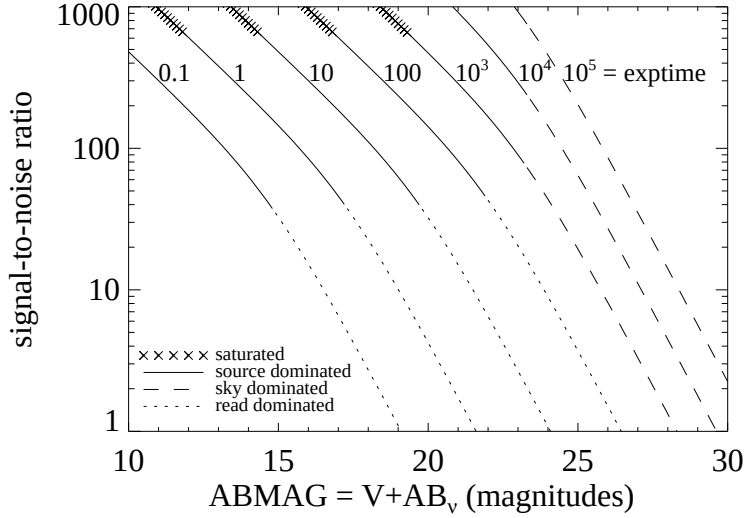

Figure A.198: Extended source S/N vs. V+ABν for the F125W filter, assuming high sky backgrounds and a source uniformly filling a 1 arcsec^2 aperture.

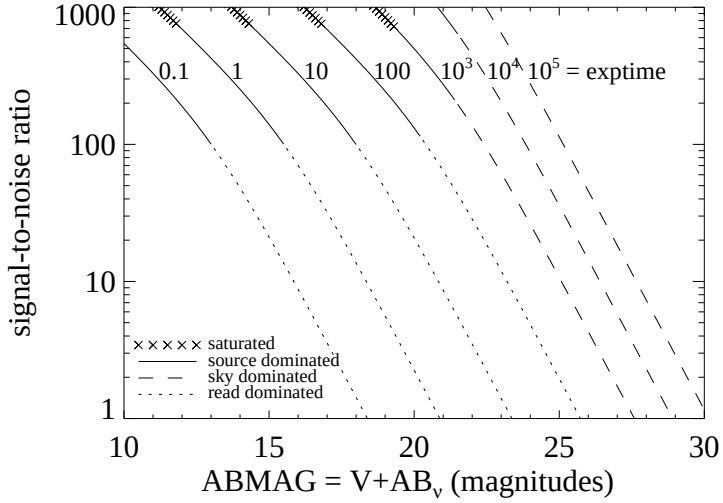

IR/F126N

Description

[Fe II] filter.

Figure A.199: Integrated system throughput for F126N.

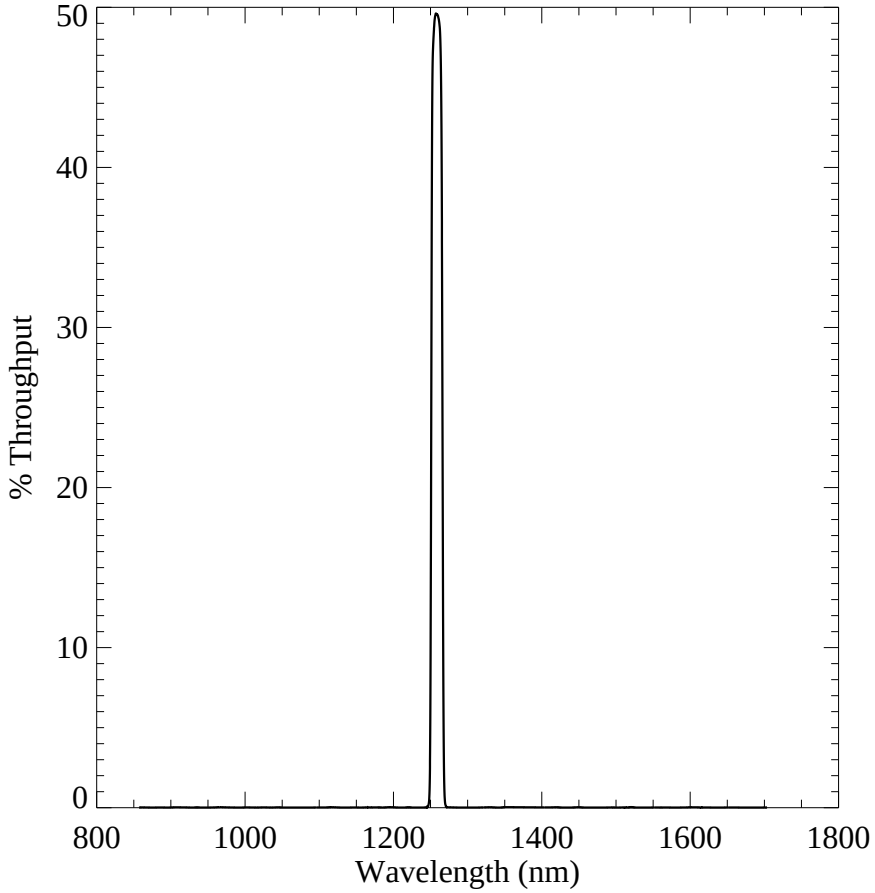

Figure A.200: Point source S/N vs. V+ABν for the F126N filter, assuming high sky backgrounds and a 3×3 pixel aperture.

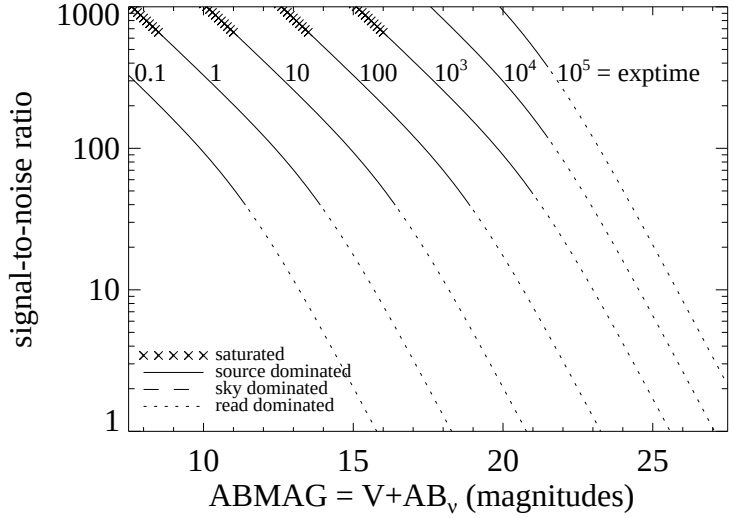

Figure A.201: Extended source S/N vs. V+ABν for the F126N filter, assuming high sky backgrounds and a source uniformly filling a 1 arcsec^2 aperture.

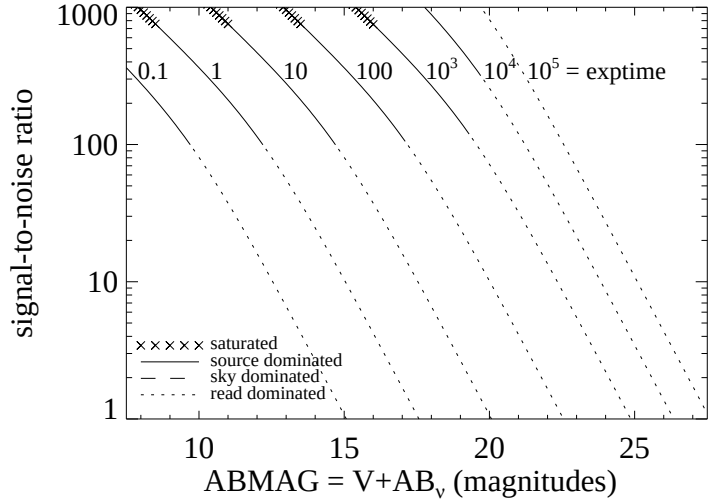

IR/F127M

Description

H_2O/CH_4 continuum filter.

Figure A.202: Integrated system throughput for F127M.

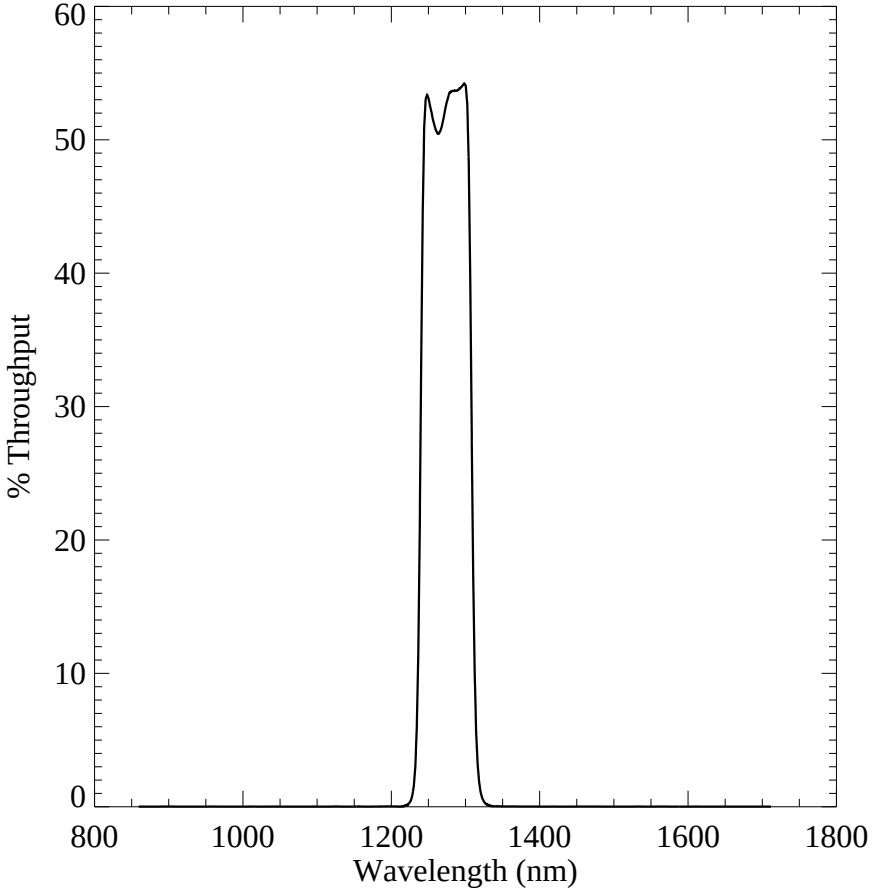

Figure A.203: Point source S/N vs. V+ABν for the F127M filter, assuming high sky backgrounds and a 3×3 pixel aperture.

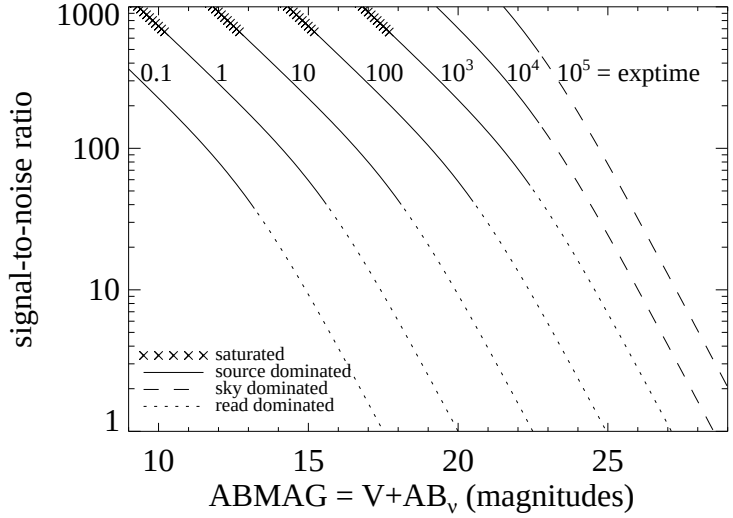

Figure A.204: Extended source S/N vs. V+ABν for the F127M filter, assuming high sky backgrounds and a source uniformly filling a 1 arcsec^2 aperture.

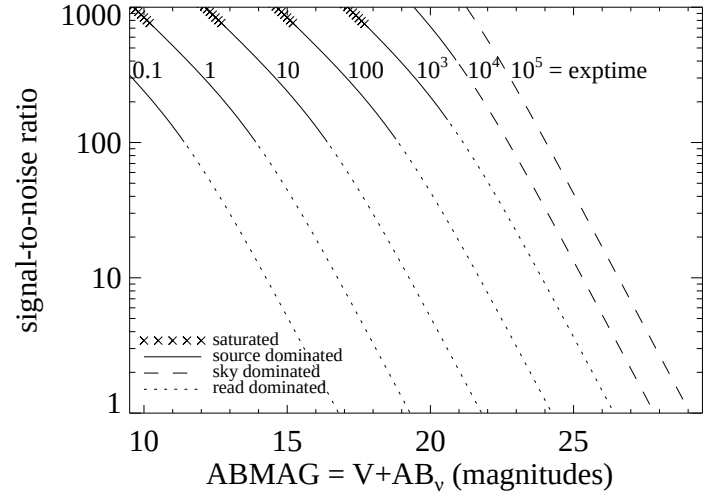

IR/F128N

Description

Paschen β filter.

Figure A.205: Integrated system throughput for F128N.

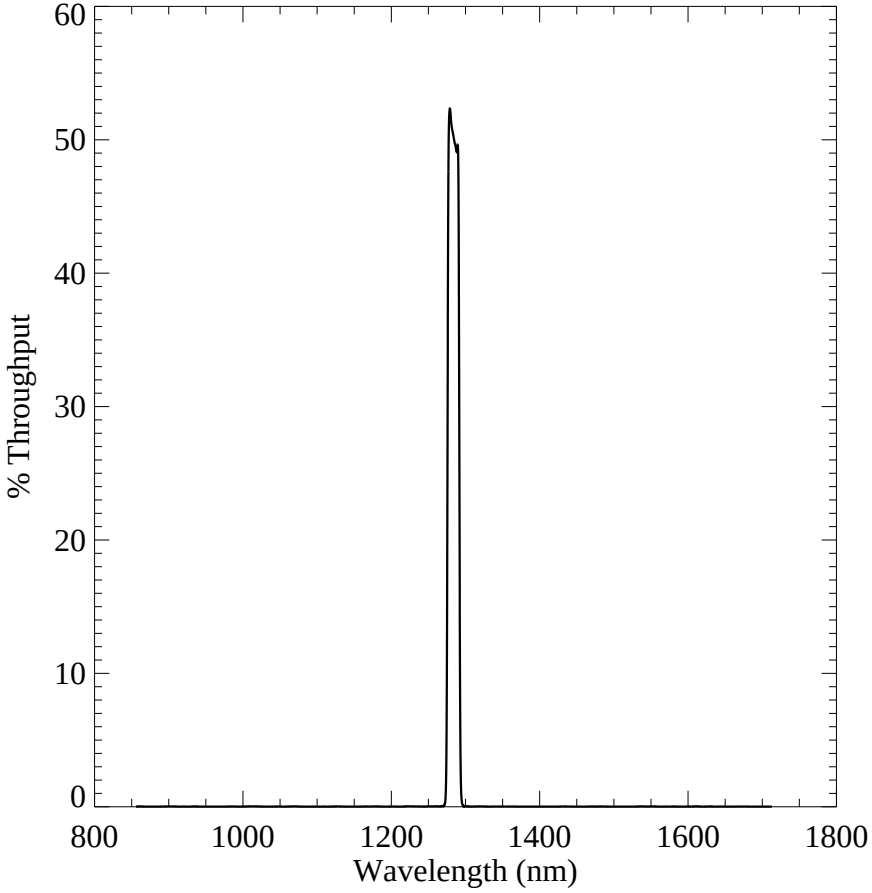

Figure A.206: Point source S/N vs. V+ABν for the F128N filter, assuming high sky backgrounds and a 3×3 pixel aperture.

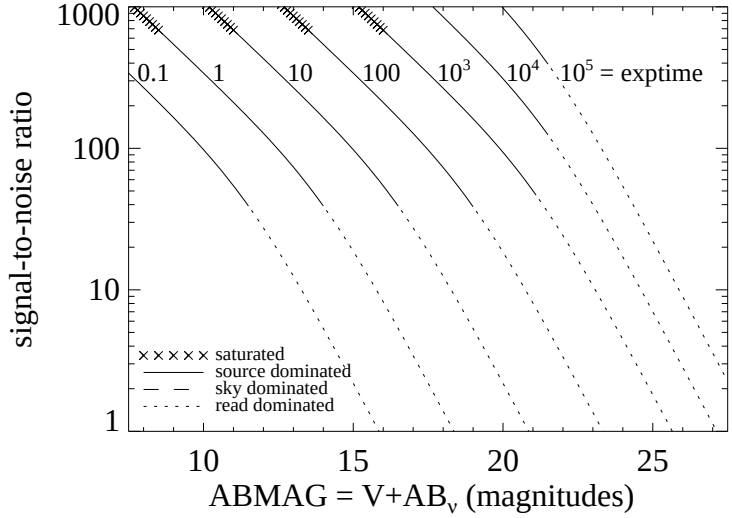

Figure A.207: Extended source S/N vs. V+ABν for the F128N filter, assuming high sky backgrounds and a source uniformly filling a 1 arcsec^2 aperture.

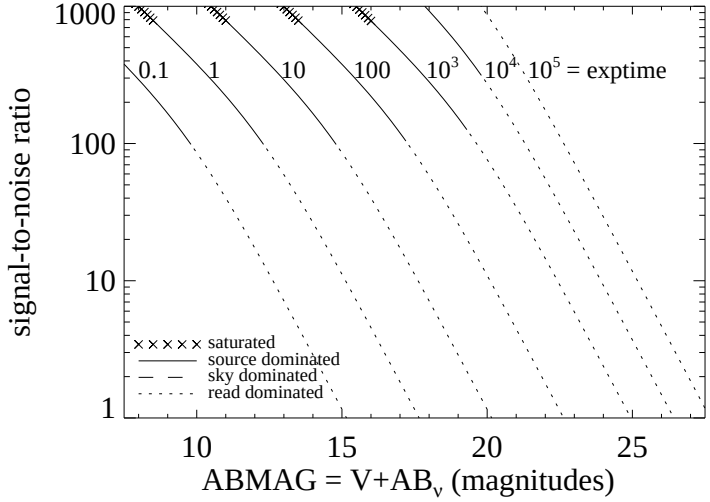

IR/F130N

Description

Paschen β continuum filter.

Figure A.208: Integrated system throughput for F130N.

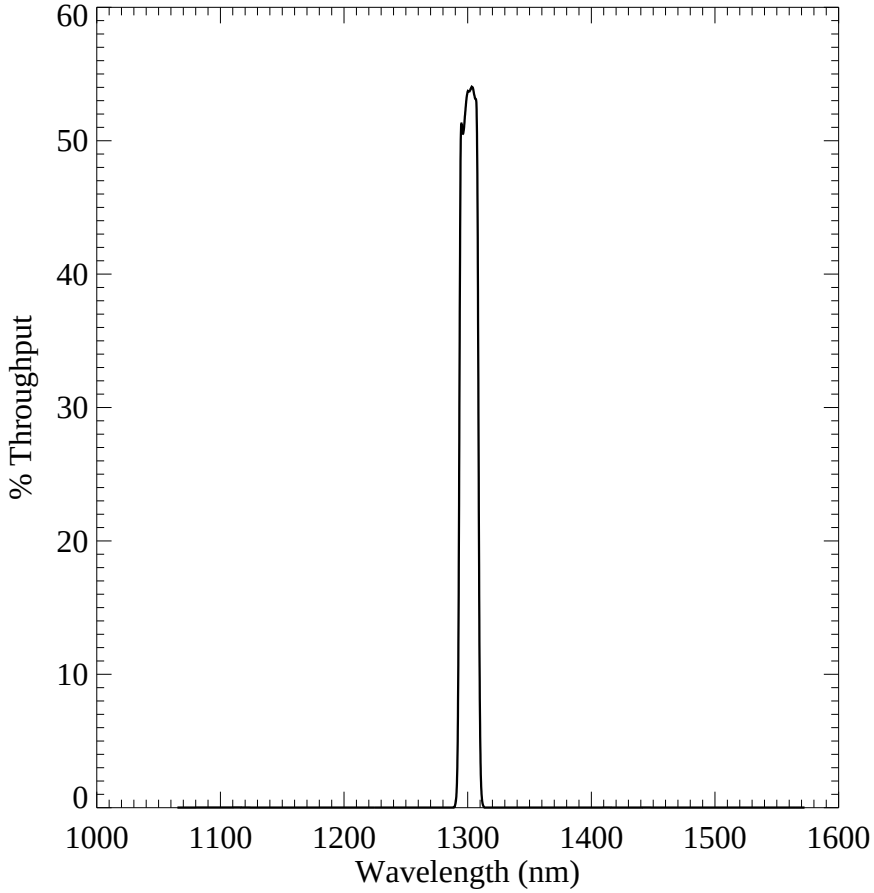

Figure A.209: Point source S/N vs. V+ABν for the F130N filter, assuming high sky backgrounds and a 3×3 pixel aperture.

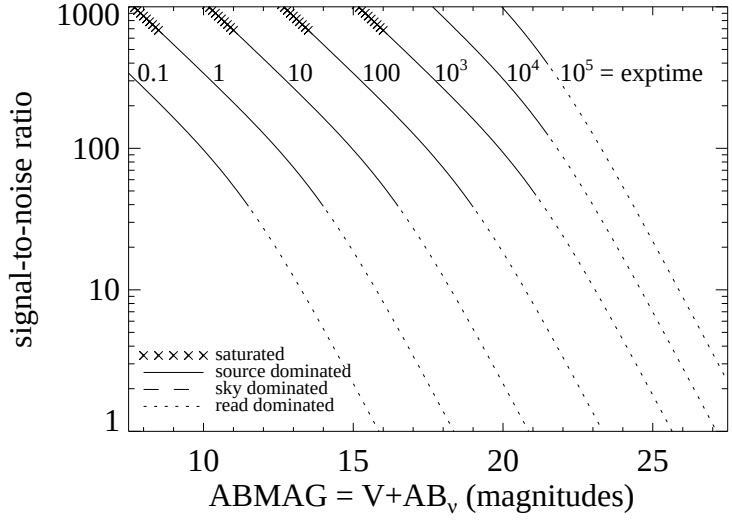

Figure A.210: Extended source S/N vs. V+ABν for the F130N filter, assuming high sky backgrounds and a source uniformly filling a 1 arcsec^2 aperture.

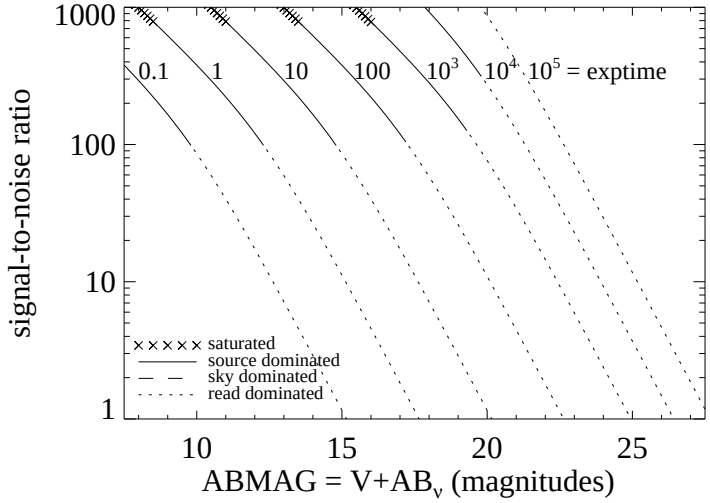

IR/F132N

Description

Paschen β (redshifted) filter.

Figure A.211: Integrated system throughput for F132N.

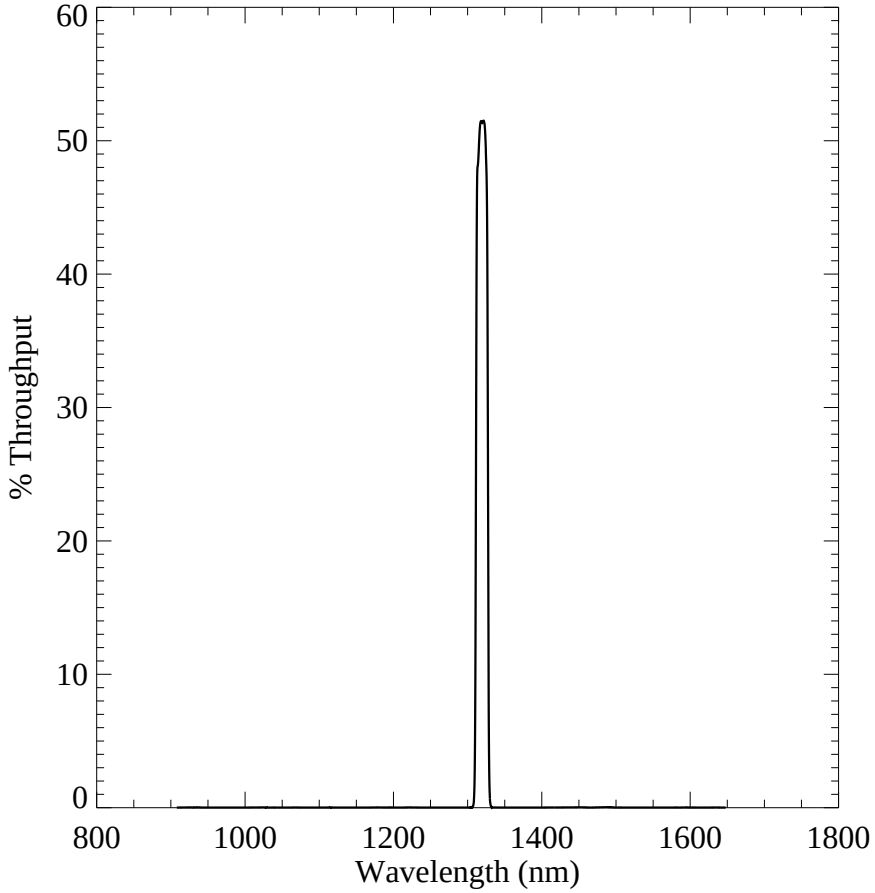

Figure A.212: Point source S/N vs. V+ABν for the F132N filter, assuming high sky backgrounds and a 3×3 pixel aperture.

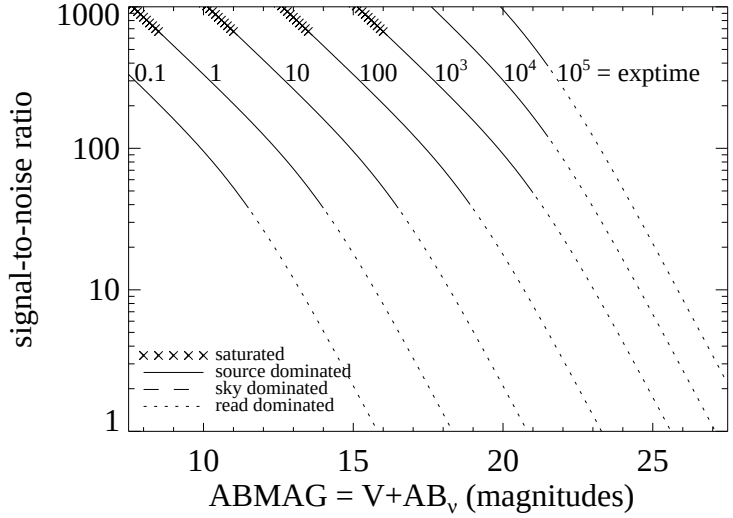

Figure A.213: Extended source S/N vs. V+ABν for the F132N filter, assuming high sky backgrounds and a source uniformly filling a 1 arcsec^2 aperture.

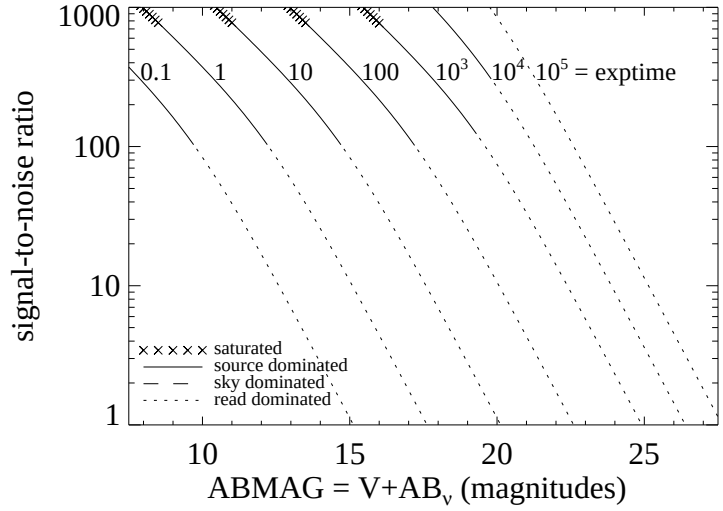

IR/F139M

Description

H_2O/CH_4 line filter.

Figure A.214: Integrated system throughput for F139M.

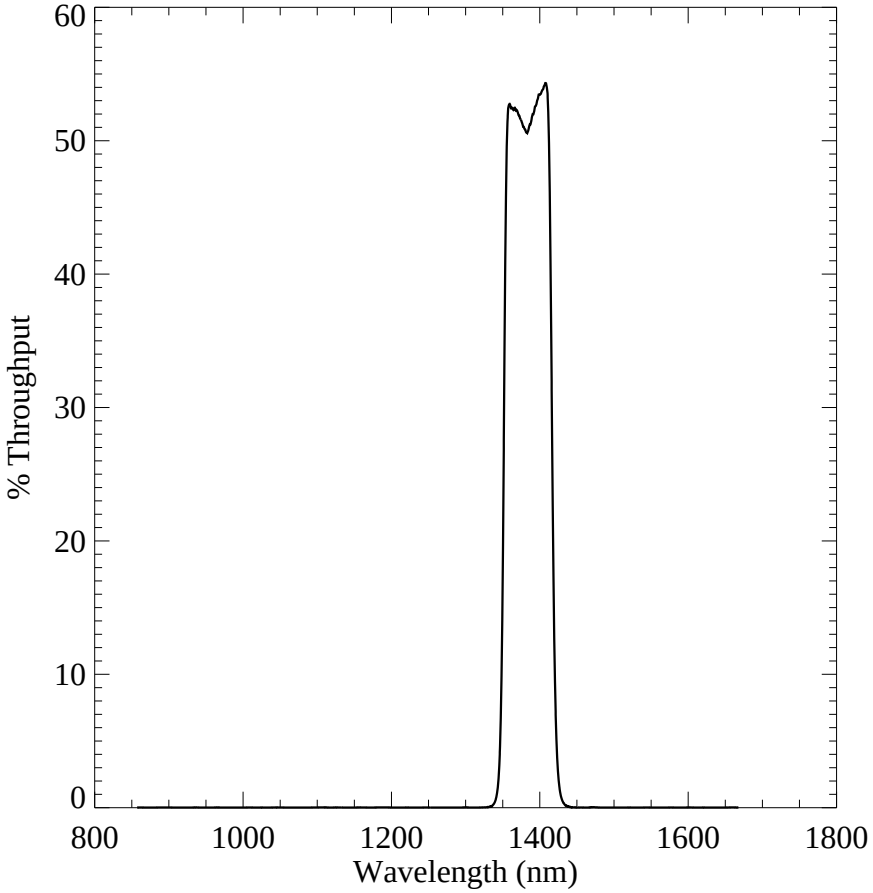

Figure A.215: Point source S/N vs. V+ABν for the F139M filter, assuming high sky backgrounds and a 3×3 pixel aperture.

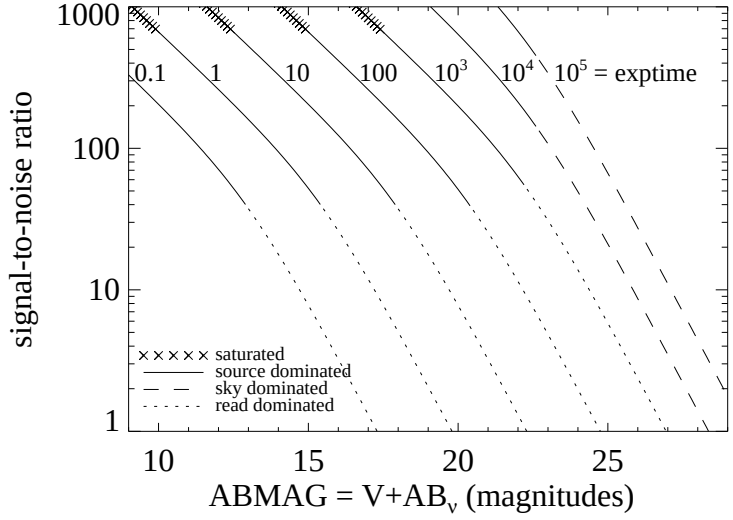

Figure A.216: Extended source S/N vs. V+ABν for the F139M filter, assuming high sky backgrounds and a source uniformly filling a 1 arcsec^2 aperture.

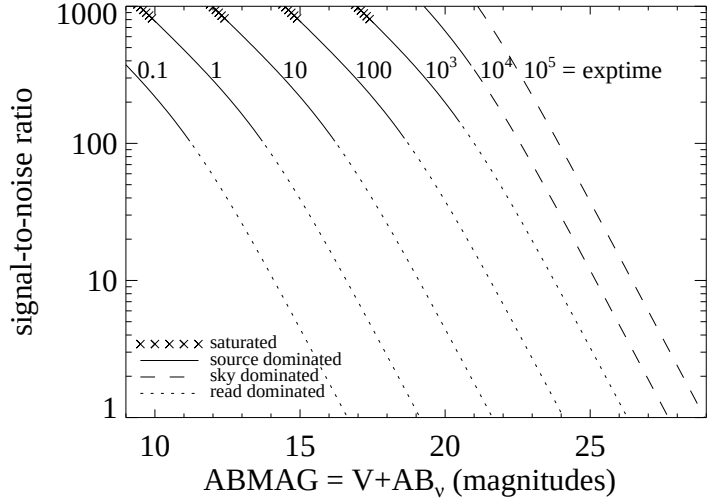

IR/F140W

Description

Wide *JH* gap; red grism reference filter.

Figure A.217: Integrated system throughput for F140W.

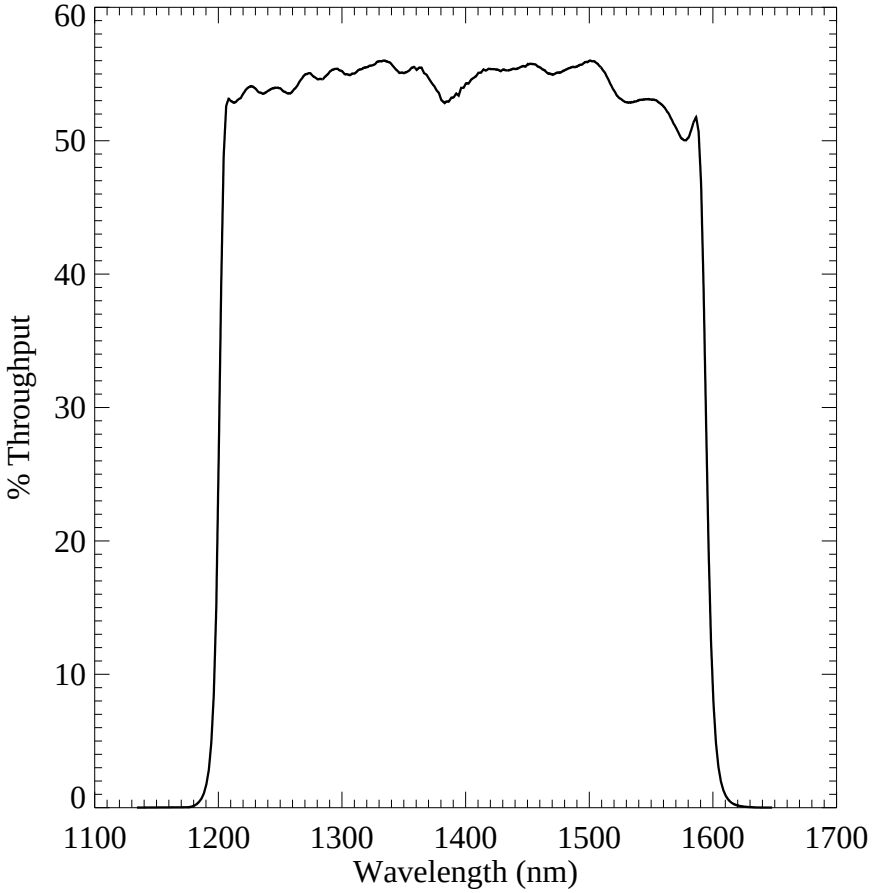

Figure A.218: Point source S/N vs. V+ABν for the F140W filter, assuming high sky backgrounds and a 3×3 pixel aperture.

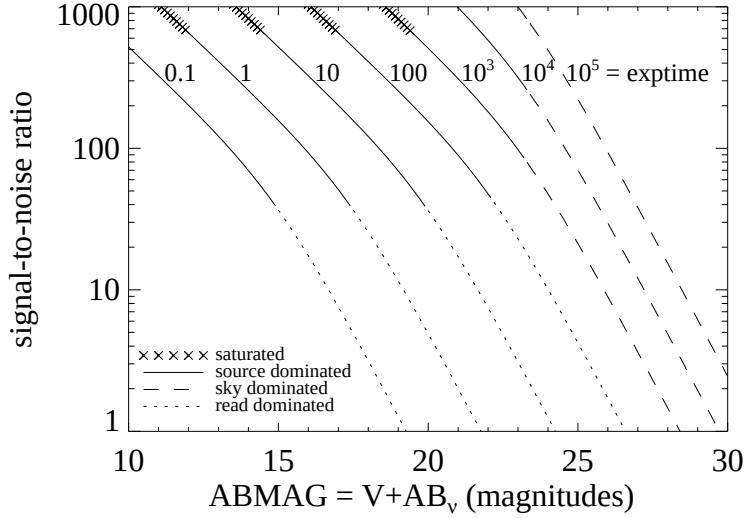

Figure A.219: Extended source S/N vs. V+ABν for the F140W filter, assuming high sky backgrounds and a source uniformly filling a 1 arcsec^2 aperture.

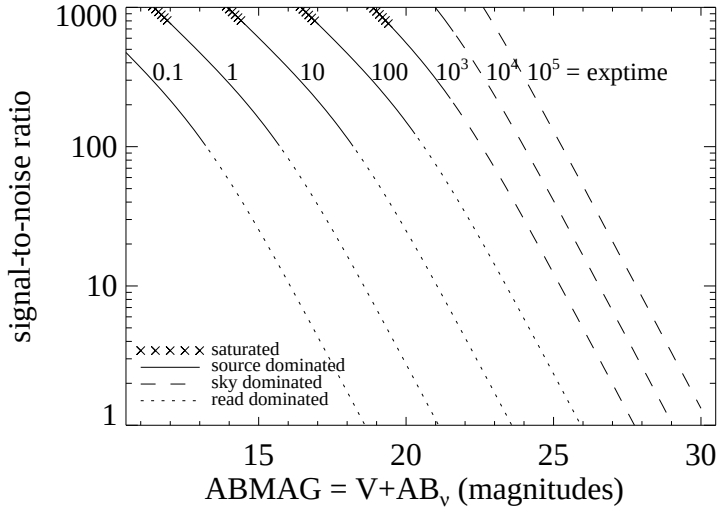

IR/F153M

Description

H_2O and NH_3 filter.

Figure A.220: Integrated system throughput for F153M.

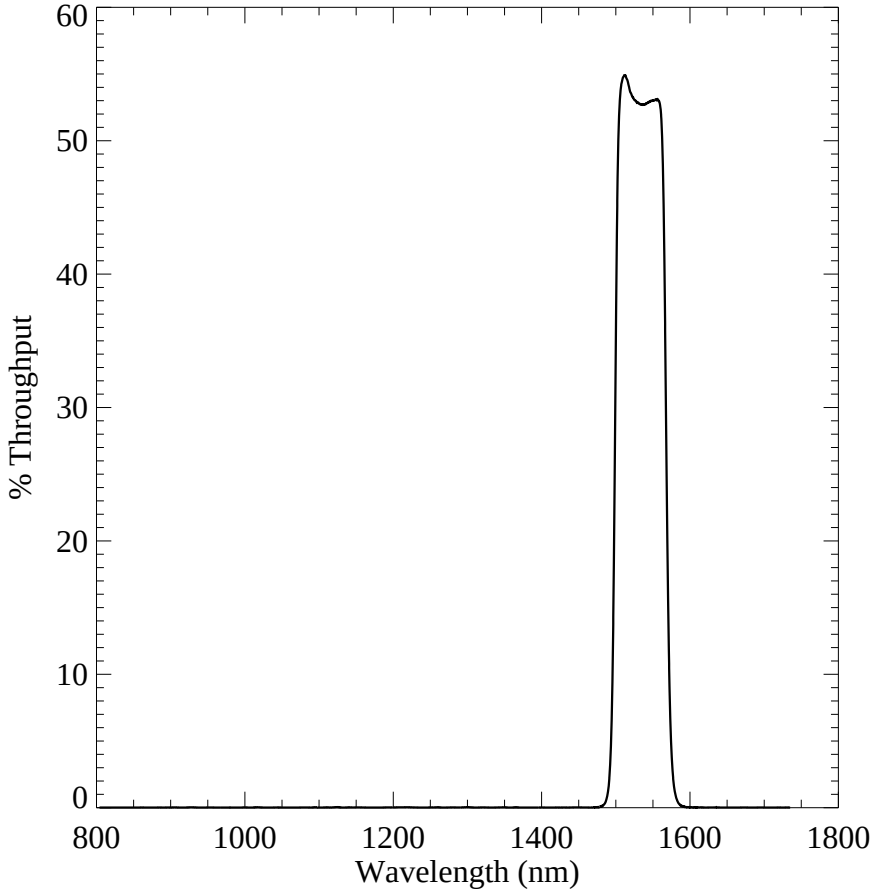

Figure A.221: Point source S/N vs. V+ABν for the F153M filter, assuming high sky backgrounds and a 3×3 pixel aperture.

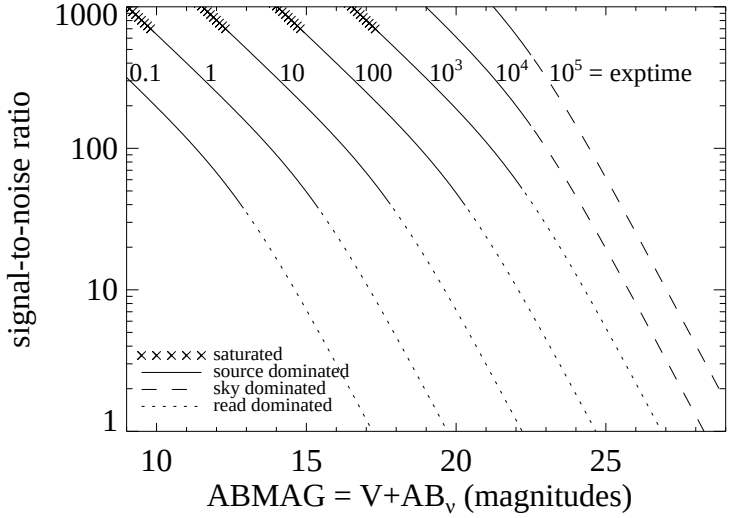

Figure A.222: Extended source S/N vs. V+ABν for the F153M filter, assuming high sky backgrounds and a source uniformly filling a 1 arcsec^2 aperture.

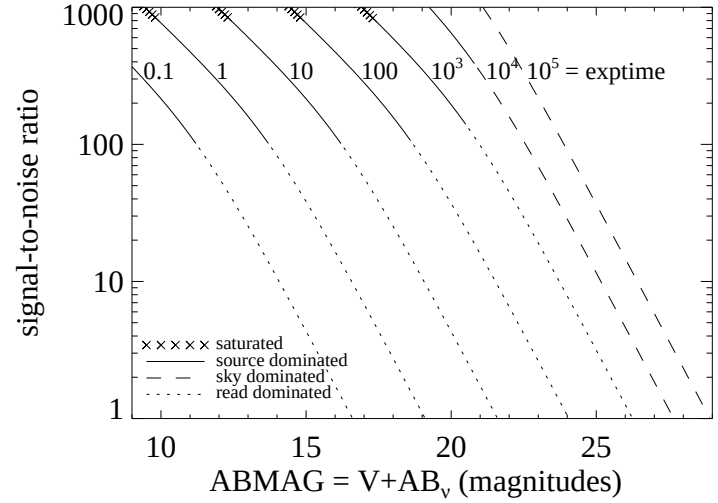

IR/F160W

Description

WFC3 *H* filter.

Figure A.223: Integrated system throughput for F160W.

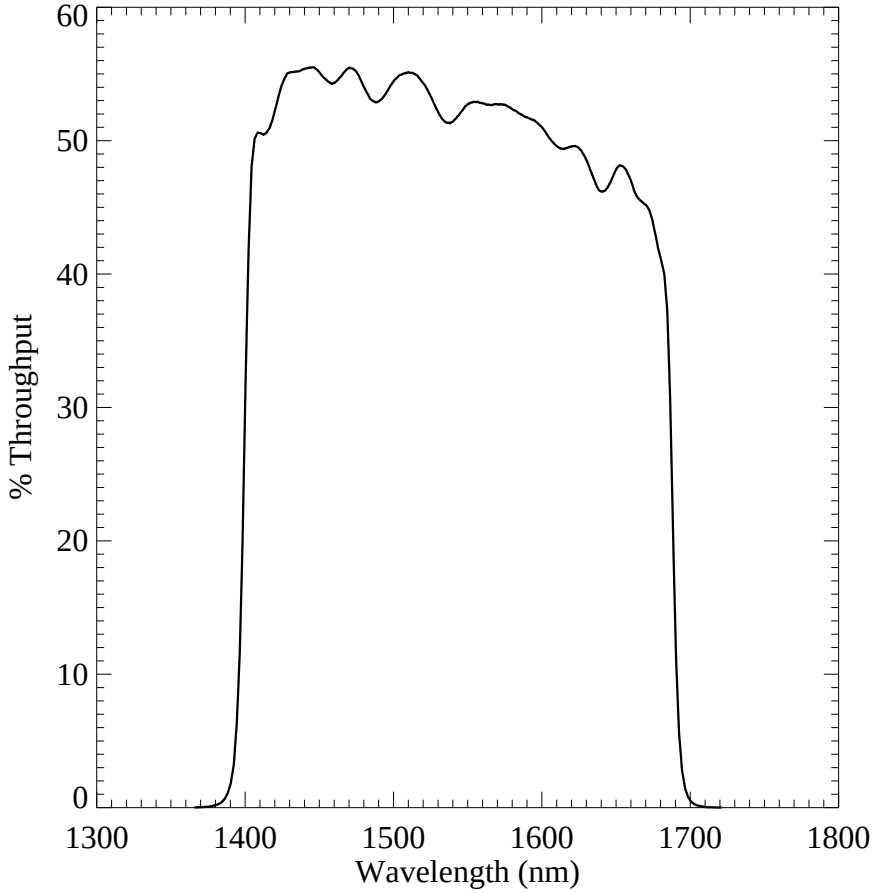

Figure A.224: Point source S/N vs. V+ABν for the F160W filter, assuming high sky backgrounds and a 3×3 pixel aperture.

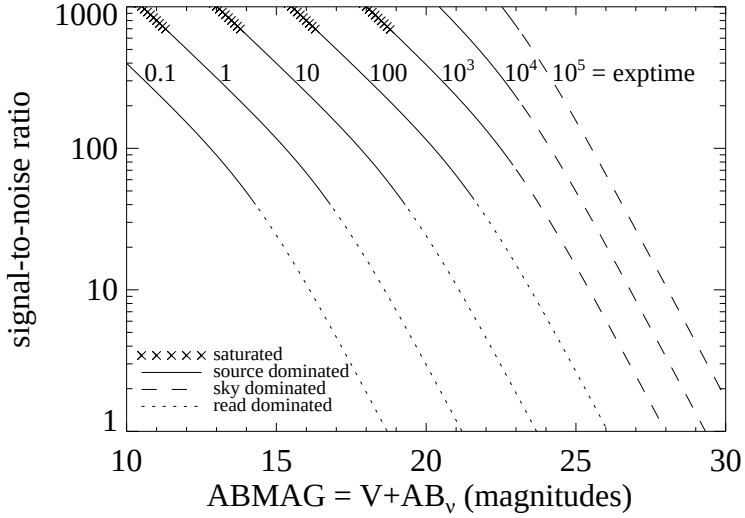

Figure A.225: Extended source S/N vs. V+ABν for the F160W filter, assuming high sky backgrounds and a source uniformly filling a 1 arcsec^2 aperture.

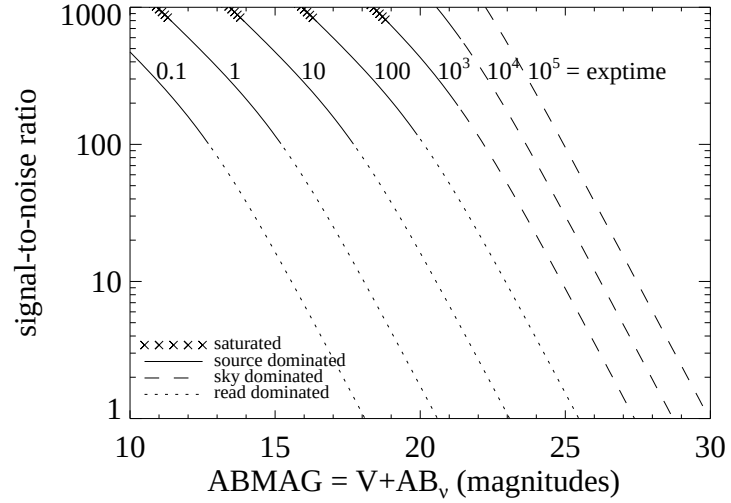

IR/F164N

Description

[Fe II] filter.

Figure A.226: Integrated system throughput for F164N.

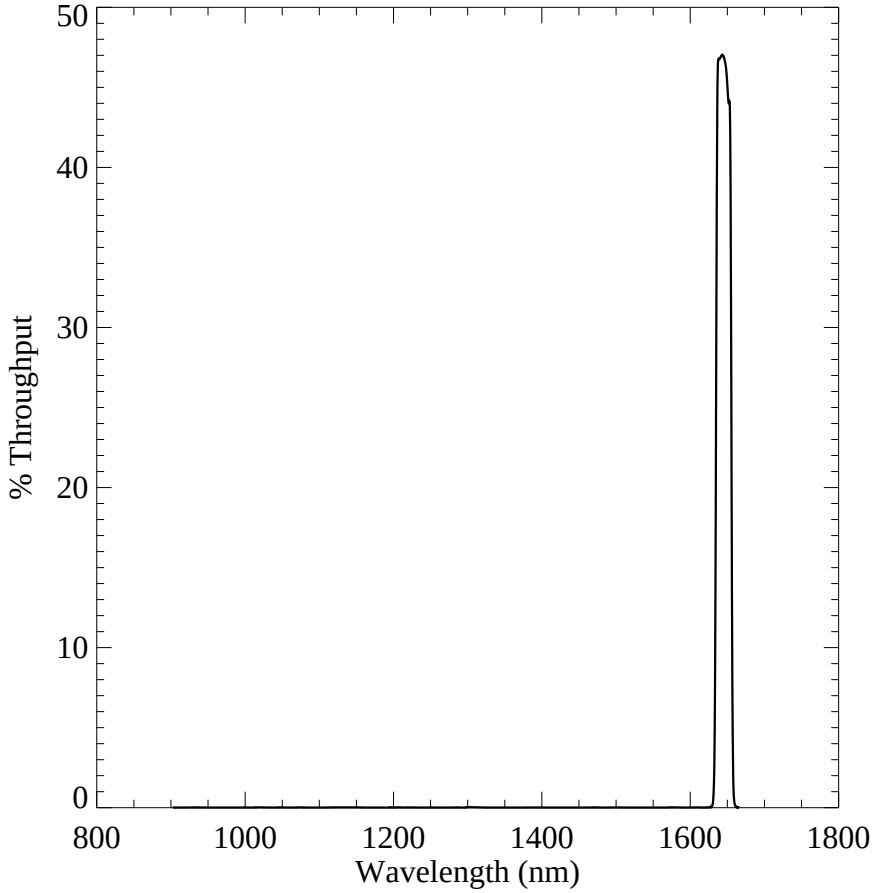

Figure A.227: Point source S/N vs. V+ABν for the F164N filter, assuming high sky backgrounds and a 3×3 pixel aperture.

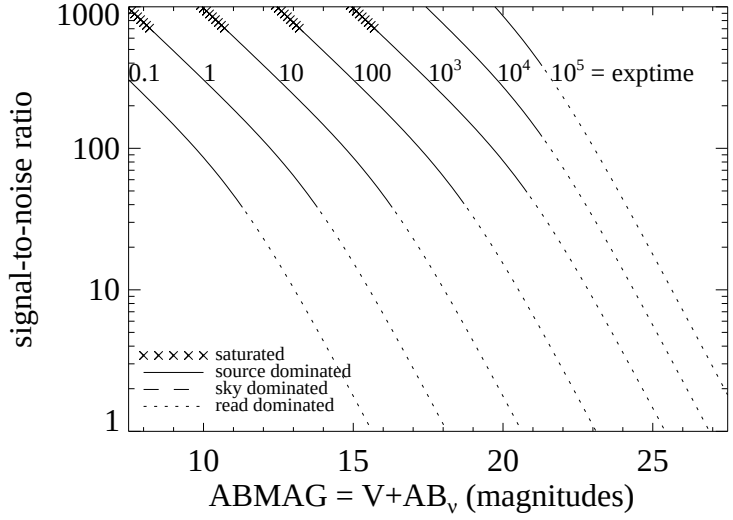

Figure A.228: Extended source S/N vs. V+ABν for the F164N filter, assuming high sky backgrounds and a source uniformly filling a 1 arcsec^2 aperture.

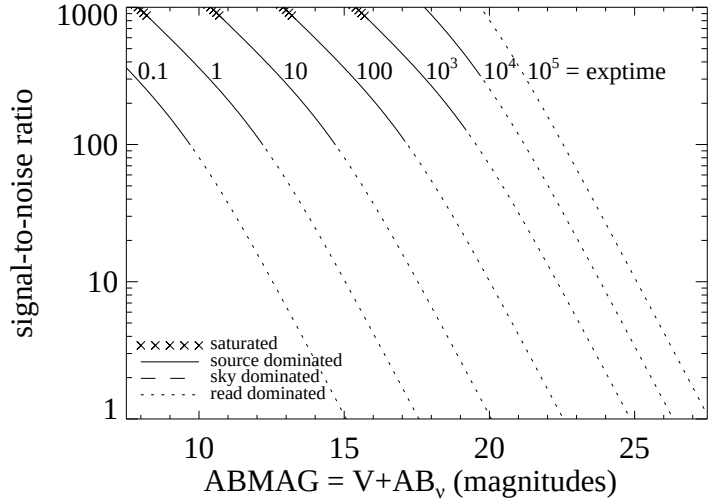

IR /F167N

Description

[Fe II] continuum filter.

Figure A.229: Integrated system throughput for F167N.

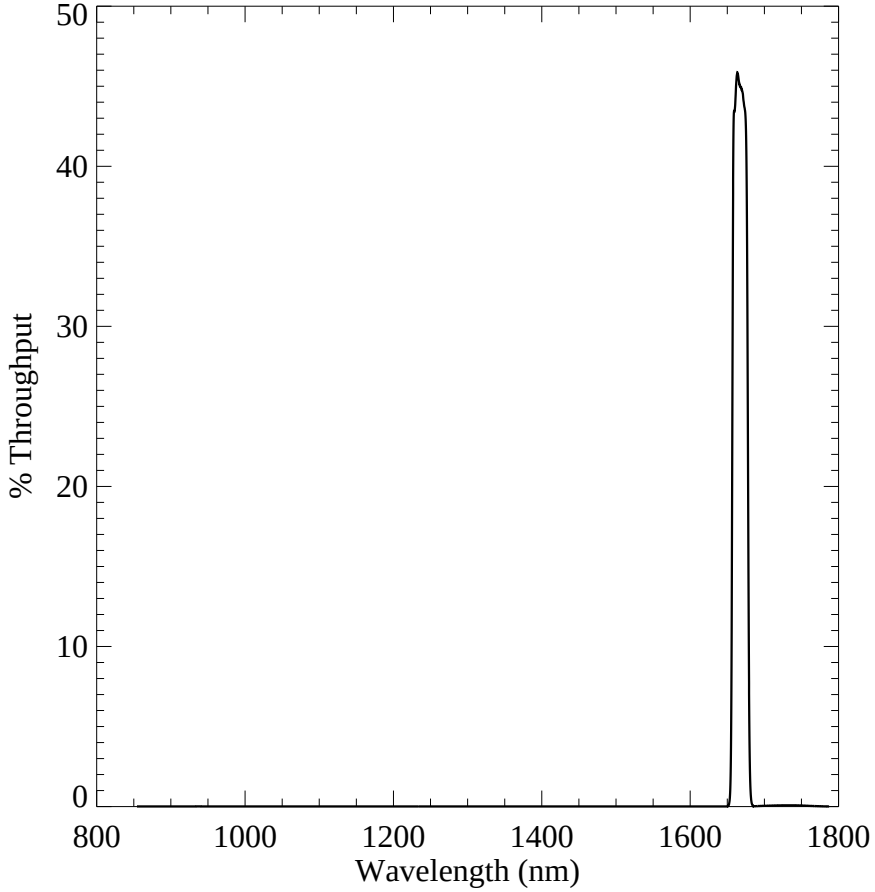

Figure A.230: Point source S/N vs. V+ABν for the F167N filter, assuming high sky backgrounds and a 3×3 pixel aperture.

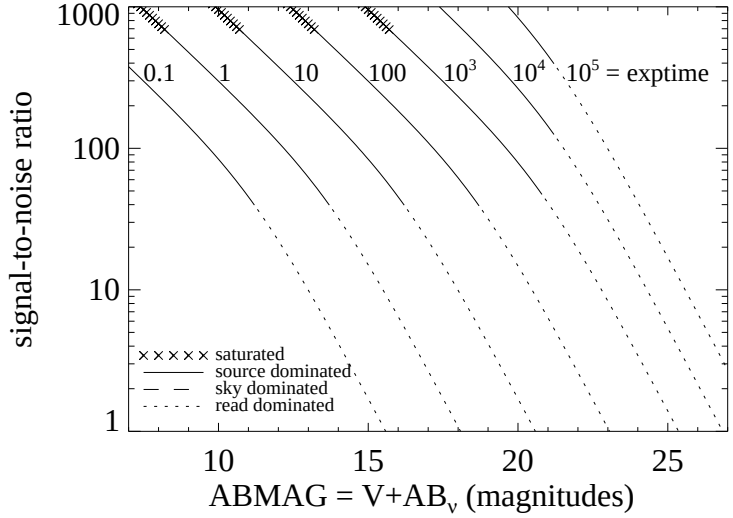

Figure A.231: Extended source S/N vs. V+ABν for the F167N filter, assuming high sky backgrounds and a source uniformly filling a 1 arcsec^2 aperture.

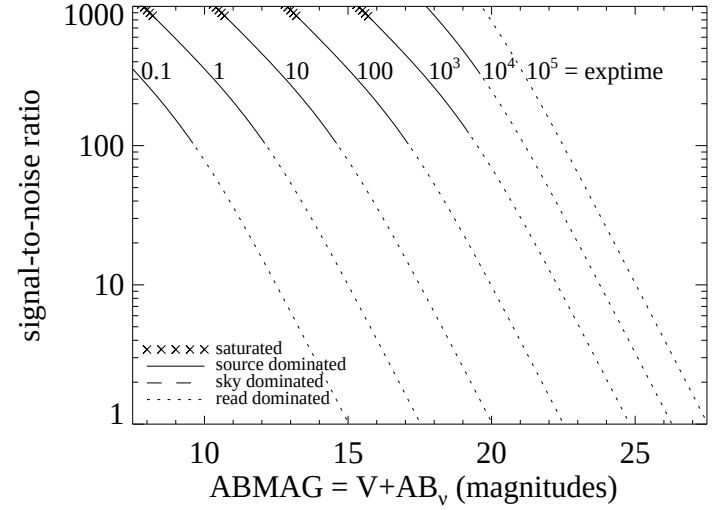

Table A.1: Color corrections AB_ν to go from Johnson V magnitude to AB magnitude for WFC3 as a function of stellar effective temperature.

	T_{eff}							
Mode	**2500K**	**5000K**	**7500K**	**10000K**	**15000K**	**20000K**	**30000K**	**50000K**
UVIS/F200LP	–2.22	0.45	0.48	0.40	0.08	–0.12	–0.40	–0.57
UVIS/F218W	7.21	7.82	2.95	1.51	0.09	–0.53	–1.22	–1.55
UVIS/F225W	6.07	7.22	2.84	1.51	0.12	–0.49	–1.15	–1.46
UVIS/F275W	7.30	5.30	2.27	1.35	0.10	–0.42	–0.96	–1.24
UVIS/F280N	3.29	4.49	2.50	1.44	0.13	–0.40	–0.90	–1.17
UVIS/F300X	5.96	4.05	1.98	1.26	0.10	–0.39	–0.91	–1.19
UVIS/F336W	4.98	2.71	1.31	1.00	0.10	–0.26	–0.64	–0.86
UVIS/F343N	4.74	2.62	1.24	0.97	0.11	–0.24	–0.60	–0.82
UVIS/F350LP	–2.64	0.07	0.18	0.18	0.09	0.04	–0.02	–0.07
UVIS/F373N	7.03	2.53	1.10	0.94	0.21	–0.09	–0.43	–0.65
UVIS/F390M	4.25	2.08	0.67	0.25	–0.20	–0.33	–0.48	–0.60
UVIS/F390W	3.80	1.63	0.59	0.26	–0.14	–0.29	–0.47	–0.60
UVIS/F395N	3.91	1.92	0.67	0.15	–0.27	–0.37	–0.49	–0.58
UVIS/F410M	2.96	1.16	0.29	–0.10	–0.32	–0.39	–0.46	–0.52
UVIS/F438W	2.28	0.86	0.18	–0.12	–0.28	–0.33	–0.39	–0.43
UVIS/F467M	1.74	0.34	0.02	–0.15	–0.22	–0.24	–0.26	–0.27
UVIS/F469N	1.64	0.33	0.03	–0.14	–0.21	–0.24	–0.26	–0.26
UVIS/F475W	1.23	0.44	0.09	–0.07	–0.17	–0.20	–0.24	–0.26
UVIS/F475X	0.61	0.35	0.12	–0.01	–0.12	–0.15	–0.19	–0.23
UVIS/F487N	1.47	0.29	0.20	0.28	0.06	–0.02	–0.11	–0.17
UVIS/F502N	2.32	0.32	0.02	–0.07	–0.11	–0.12	–0.14	–0.15
UVIS/FQ508N	1.07	0.32	0.01	–0.06	–0.08	–0.10	–0.11	–0.12
UVIS/F547M	0.08	0.03	0.02	0.01	0.01	0.01	0.01	0.02
UVIS/F555W	0.15	0.09	0.03	–0.01	–0.03	–0.04	–0.05	–0.06
UVIS/F600LP	–3.71	–0.42	0.09	0.34	0.47	0.52	0.57	0.60
UVIS/F606W	–0.83	–0.11	0.04	0.10	0.12	0.12	0.13	0.13
UVIS/F621M	–1.23	–0.26	0.03	0.16	0.22	0.25	0.27	0.28
UVIS/F625W	–1.17	–0.25	0.04	0.16	0.22	0.24	0.26	0.27

Table A.1: Color corrections AB_V to go from Johnson V magnitude to AB magnitude for WFC3 as a function of stellar effective temperature.

	T_{eff}							
Mode	**2500K**	**5000K**	**7500K**	**10000K**	**15000K**	**20000K**	**30000K**	**50000K**
UVIS/F631N	–0.33	–0.28	0.03	0.17	0.24	0.27	0.30	0.31
UVIS/F645N	–2.20	–0.29	0.04	0.20	0.28	0.31	0.35	0.35
UVIS/F656N	–1.99	–0.26	0.36	0.63	0.56	0.54	0.52	0.45
UVIS/F657N	–2.31	–0.31	0.14	0.37	0.39	0.41	0.42	0.41
UVIS/F658N	–2.04	–0.31	0.18	0.42	0.42	0.43	0.44	0.41
UVIS/F665N	–1.30	–0.35	0.06	0.26	0.34	0.38	0.42	0.42
UVIS/F673N	–0.69	–0.37	0.04	0.24	0.35	0.39	0.44	0.45
UVIS/F680N	–1.61	–0.38	0.05	0.26	0.38	0.42	0.47	0.48
UVIS/F689M	–1.69	–0.37	0.06	0.28	0.39	0.43	0.47	0.48
UVIS/F763M	–3.09	–0.45	0.09	0.37	0.53	0.59	0.65	0.69
UVIS/F775W	–3.60	–0.45	0.09	0.38	0.54	0.59	0.65	0.70
UVIS/F814W	–4.14	–0.48	0.12	0.43	0.60	0.67	0.74	0.79
UVIS/F845M	–4.56	–0.51	0.16	0.51	0.70	0.77	0.84	0.91
UVIS/F850LP	–5.03	–0.56	0.21	0.56	0.79	0.89	0.98	1.06
UVIS/F953N	–5.52	–0.59	0.27	0.68	0.91	1.00	1.10	1.16
UVIS/FQ232N	2.15	4.54	2.68	1.53	0.20	–0.43	–1.12	–1.46
UVIS/FQ243N	2.84	5.10	2.76	1.52	0.18	–0.44	–1.11	–1.40
UVIS/FQ378N	4.90	2.32	0.86	0.61	0.01	–0.20	–0.44	–0.62
UVIS/FQ387N	6.34	2.42	0.61	0.25	–0.21	–0.34	–0.49	–0.61
UVIS/FQ422M	5.05	1.17	0.18	–0.22	–0.36	–0.41	–0.46	–0.48
UVIS/FQ436N	2.64	0.84	0.23	0.08	–0.16	–0.24	–0.31	–0.39
UVIS/FQ437N	2.59	0.83	0.18	0.00	–0.21	–0.28	–0.34	–0.40
UVIS/FQ492N	0.91	0.27	0.04	–0.02	–0.10	–0.13	–0.16	–0.17
UVIS/FQ575N	–0.58	–0.18	0.01	0.07	0.10	0.11	0.13	0.13
UVIS/FQ619N	0.72	–0.25	0.03	0.15	0.22	0.24	0.27	0.27
UVIS/FQ634N	–0.96	–0.28	0.03	0.18	0.26	0.29	0.32	0.32
UVIS/FQ672N	–0.77	–0.35	0.04	0.23	0.34	0.38	0.42	0.44
UVIS/FQ674N	–0.39	–0.37	0.04	0.24	0.35	0.39	0.43	0.44
UVIS/FQ727N	–2.81	–0.41	0.07	0.32	0.46	0.52	0.57	0.60

Table A.1: Color corrections AB_V to go from Johnson V magnitude to AB magnitude for WFC3 as a function of stellar effective temperature.

	T_{eff}							
Mode	**2500K**	**5000K**	**7500K**	**10000K**	**15000K**	**20000K**	**30000K**	**50000K**
UVIS/FQ750N	–3.06	–0.44	0.08	0.36	0.51	0.57	0.63	0.66
UVIS/FQ889N	–4.98	–0.55	0.20	0.57	0.78	0.86	0.95	1.01
UVIS/FQ906N	–5.15	–0.56	0.21	0.57	0.79	0.88	0.98	1.05
UVIS/FQ924N	–4.89	–0.57	0.26	0.66	0.87	0.95	1.04	1.10
UVIS/FQ937N	–5.19	–0.58	0.19	0.48	0.77	0.89	1.01	1.11
IR/F098M	–5.40	–0.60	0.25	0.60	0.88	1.00	1.12	1.21
IR/F105W	–5.68	–0.62	0.31	0.69	0.98	1.11	1.24	1.34
IR/F110W	–5.77	–0.64	0.39	0.80	1.12	1.25	1.39	1.49
IR/F125W	–5.91	–0.67	0.48	0.94	1.28	1.43	1.58	1.69
IR/F126N	–5.99	–0.67	0.49	0.96	1.31	1.46	1.61	1.72
IR/F127M	–6.04	–0.67	0.52	1.01	1.35	1.49	1.65	1.75
IR/F128N	–6.08	–0.67	0.59	1.11	1.41	1.55	1.69	1.78
IR/F130N	–6.13	–0.68	0.53	1.02	1.37	1.52	1.68	1.79
IR/F132N	–6.04	–0.67	0.54	1.03	1.39	1.55	1.71	1.82
IR/F139M	–5.64	–0.69	0.60	1.11	1.49	1.64	1.81	1.92
IR/F140W	–5.89	–0.69	0.61	1.12	1.49	1.64	1.80	1.92
IR/F153M	–6.03	–0.71	0.73	1.29	1.69	1.85	2.02	2.14
IR/F160W	–6.05	–0.70	0.74	1.30	1.69	1.85	2.02	2.15
IR/F164N	–6.39	–0.70	0.84	1.42	1.82	1.99	2.16	2.28
IR/F167N	–6.32	–0.69	0.84	1.41	1.83	2.00	2.18	2.31

Table A.2: Color corrections AB_V to go from Johnson V magnitude to AB magnitude for WFC3 as a function of age in an instantaneous burst population.

	Age				
Mode	**10 Gyr**	**1 Gyr**	**100 Myr**	**10 Myr**	**1 Myr**
UVIS/F200LP	0.38	0.48	0.29	0.02	–0.48
UVIS/F218W	6.11	3.89	1.06	0.15	–1.22
UVIS/F225W	5.83	3.76	1.03	0.16	–1.15

Table A.2: Color corrections AB_V to go from Johnson V magnitude to AB magnitude for WFC3 as a function of age in an instantaneous burst population.

	Age				
Mode	**10 Gyr**	**1 Gyr**	**100 Myr**	**10 Myr**	**1 Myr**
UVIS/F275W	4.75	3.14	0.93	0.19	–0.97
UVIS/F280N	4.32	3.03	0.89	0.21	–0.92
UVIS/F300X	3.95	2.80	0.89	0.20	–0.94
UVIS/F336W	2.69	1.98	0.77	0.27	–0.67
UVIS/F343N	2.55	1.89	0.76	0.28	–0.63
UVIS/F350LP	–0.09	0.04	0.06	–0.06	–0.04
UVIS/F373N	2.28	1.57	0.66	0.34	–0.49
UVIS/F390M	2.03	1.12	0.22	0.14	–0.50
UVIS/F390W	1.63	1.00	0.27	0.15	–0.50
UVIS/F395N	1.88	1.03	0.14	0.11	–0.49
UVIS/F410M	1.23	0.64	0.02	0.02	–0.47
UVIS/F438W	0.90	0.48	0.01	0.02	–0.39
UVIS/F467M	0.44	0.22	–0.03	–0.01	–0.26
UVIS/F469N	0.46	0.23	–0.02	–0.01	–0.25
UVIS/F475W	0.48	0.27	0.02	0.04	–0.23
UVIS/F475X	0.38	0.24	0.03	0.03	–0.20
UVIS/F487N	0.36	0.27	0.12	0.10	–0.14
UVIS/F502N	0.33	0.17	0.02	0.08	–0.12
UVIS/F547M	0.04	0.03	0.03	0.03	0.02
UVIS/F555W	0.11	0.07	0.02	0.01	–0.05
UVIS/F600LP	–0.72	–0.38	–0.04	–0.27	0.54
UVIS/F606W	–0.17	–0.08	0.01	–0.04	0.13
UVIS/F621M	–0.33	–0.18	0.00	–0.10	0.26
UVIS/F625W	–0.33	–0.18	–0.00	–0.10	0.26
UVIS/F631N	–0.34	–0.19	0.00	–0.10	0.29
UVIS/F645N	–0.43	–0.23	–0.02	–0.15	0.33
UVIS/F656N	–0.45	–0.18	0.06	–0.16	0.37
UVIS/F657N	–0.47	–0.22	0.00	–0.18	0.37
UVIS/F658N	–0.47	–0.22	0.00	–0.18	0.37

Table A.2: Color corrections AB_V to go from Johnson V magnitude to AB magnitude for WFC3 as a function of age in an instantaneous burst population.

	Age				
Mode	**10 Gyr**	**1 Gyr**	**100 Myr**	**10 Myr**	**1 Myr**
UVIS/F665N	–0.48	–0.26	–0.03	–0.18	0.39
UVIS/F673N	–0.49	–0.28	–0.02	–0.15	0.42
UVIS/F680N	–0.54	–0.30	–0.02	–0.17	0.45
UVIS/F689M	–0.53	–0.29	–0.02	–0.18	0.45
UVIS/F763M	–0.77	–0.40	–0.05	–0.32	0.64
UVIS/F775W	–0.78	–0.41	–0.05	–0.31	0.64
UVIS/F814W	–0.89	–0.47	–0.07	–0.36	0.71
UVIS/F845M	–1.00	–0.53	–0.09	–0.41	0.82
UVIS/F850LP	–1.18	–0.65	–0.13	–0.47	0.96
UVIS/F953N	–1.27	–0.71	–0.12	–0.50	1.06
UVIS/FQ232N	4.48	3.43	1.03	0.17	–1.14
UVIS/FQ243N	4.88	3.62	0.98	0.14	–1.10
UVIS/FQ378N	2.24	1.37	0.42	0.22	–0.51
UVIS/FQ387N	2.27	1.16	0.23	0.14	–0.51
UVIS/FQ422M	1.16	0.55	–0.03	0.01	–0.44
UVIS/FQ436N	0.86	0.49	0.04	0.05	–0.36
UVIS/FQ437N	0.86	0.46	0.00	0.03	–0.37
UVIS/FQ492N	0.31	0.17	0.01	0.05	–0.15
UVIS/FQ508N	0.31	0.17	0.04	0.12	–0.09
UVIS/FQ575N	–0.18	–0.08	0.00	–0.06	0.12
UVIS/FQ619N	–0.28	–0.16	0.02	–0.06	0.26
UVIS/FQ634N	–0.37	–0.21	–0.01	–0.12	0.30
UVIS/FQ672N	–0.47	–0.27	–0.02	–0.16	0.40
UVIS/FQ674N	–0.48	–0.27	–0.02	–0.16	0.41
UVIS/FQ727N	–0.65	–0.34	–0.01	–0.26	0.56
UVIS/FQ750N	–0.81	–0.43	–0.07	–0.33	0.61
UVIS/FQ889N	–1.12	–0.61	–0.14	–0.46	0.91
UVIS/FQ906N	–1.22	–0.68	–0.15	–0.49	0.94
UVIS/FQ924N	–1.21	–0.65	–0.12	–0.48	1.00

Table A.2: Color corrections AB_V to go from Johnson V magnitude to AB magnitude for WFC3 as a function of age in an instantaneous burst population.

	Age				
Mode	**10 Gyr**	**1 Gyr**	**100 Myr**	**10 Myr**	**1 Myr**
UVIS/FQ937N	–1.16	–0.65	–0.11	–0.47	1.00
IR/F098M	–1.35	–0.74	–0.15	–0.51	1.10
IR/F105W	–1.39	–0.74	–0.14	–0.54	1.22
IR/F110W	–1.38	–0.70	–0.11	–0.57	1.36
IR/F125W	–1.39	–0.67	–0.08	–0.60	1.57
IR/F126N	–1.37	–0.64	–0.07	–0.62	1.60
IR/F127M	–1.38	–0.64	–0.07	–0.62	1.62
IR/F128N	–1.39	–0.64	–0.07	–0.63	1.64
IR/F130N	–1.40	–0.65	–0.07	–0.63	1.66
IR/F132N	–1.40	–0.64	–0.07	–0.62	1.69
IR/F139M	–1.37	–0.62	–0.05	–0.60	1.78
IR/F140W	–1.41	–0.65	–0.06	–0.64	1.77
IR/F153M	–1.49	–0.69	–0.07	–0.70	1.98
IR/F160W	–1.49	–0.68	–0.07	–0.70	1.97
IR/F164N	–1.59	–0.75	–0.11	–0.79	2.10
IR/F167N	–1.58	–0.74	–0.10	–0.78	2.13

Table A.3: Color corrections AB_V to go from Johnson V magnitude to AB magnitude for WFC3 as a function of age in a population with constant star formation.

	Age				
Mode	**10 Gyr**	**1 Gyr**	**100 Myr**	**10 Myr**	**1 Myr**
UVIS/F200LP	0.31	0.24	0.03	–0.15	–0.48
UVIS/F218W	1.39	0.79	0.08	–0.48	–1.22
UVIS/F225W	1.39	0.79	0.09	–0.44	–1.15
UVIS/F275W	1.35	0.78	0.12	–0.36	–0.97
UVIS/F280N	1.34	0.77	0.14	–0.33	–0.92
UVIS/F300X	1.31	0.76	0.13	–0.34	–0.93
UVIS/F336W	1.15	0.71	0.19	–0.21	–0.66

Table A.3: Color corrections AB_V to go from Johnson V magnitude to AB magnitude for WFC3 as a function of age in a population with constant star formation.

	Age				
Mode	**10 Gyr**	**1 Gyr**	**100 Myr**	**10 Myr**	**1 Myr**
UVIS/F343N	1.13	0.71	0.20	–0.18	–0.62
UVIS/F350LP	0.00	0.03	–0.01	–0.01	–0.04
UVIS/F373N	1.04	0.66	0.24	–0.11	–0.49
UVIS/F390M	0.67	0.28	–0.00	–0.25	–0.50
UVIS/F390W	0.64	0.30	0.03	–0.23	–0.49
UVIS/F395N	0.60	0.21	–0.04	–0.27	–0.49
UVIS/F410M	0.37	0.07	–0.11	–0.30	–0.47
UVIS/F438W	0.29	0.05	–0.09	–0.25	–0.39
UVIS/F467M	0.14	–0.00	–0.08	–0.18	–0.26
UVIS/F469N	0.15	0.00	–0.07	–0.17	–0.25
UVIS/F475W	0.18	0.04	–0.03	–0.14	–0.23
UVIS/F475X	0.16	0.05	–0.02	–0.11	–0.20
UVIS/F487N	0.21	0.14	0.05	–0.05	–0.14
UVIS/F502N	0.13	0.04	0.01	–0.06	–0.13
UVIS/F547M	0.03	0.03	0.03	0.03	0.02
UVIS/F555W	0.05	0.02	–0.00	–0.03	–0.05
UVIS/F600LP	–0.36	–0.13	–0.05	0.22	0.54
UVIS/F606W	–0.06	–0.00	0.01	0.07	0.13
UVIS/F621M	–0.14	–0.03	0.01	0.13	0.26
UVIS/F625W	–0.14	–0.03	0.01	0.12	0.26
UVIS/F631N	–0.15	–0.03	0.02	0.14	0.29
UVIS/F645N	–0.19	–0.05	–0.01	0.15	0.33
UVIS/F656N	–0.16	0.01	0.02	0.19	0.37
UVIS/F657N	–0.20	–0.04	–0.01	0.16	0.37
UVIS/F658N	–0.20	–0.04	–0.02	0.16	0.37
UVIS/F665N	–0.23	–0.07	–0.02	0.16	0.39
UVIS/F673N	–0.23	–0.06	0.01	0.19	0.42
UVIS/F680N	–0.26	–0.07	0.00	0.20	0.45
UVIS/F689M	–0.25	–0.07	–0.01	0.20	0.45

Table A.3: Color corrections AB_V to go from Johnson V magnitude to AB magnitude for WFC3 as a function of age in a population with constant star formation.

	Age				
Mode	**10 Gyr**	**1 Gyr**	**100 Myr**	**10 Myr**	**1 Myr**
UVIS/F763M	–0.39	–0.13	–0.06	0.25	0.64
UVIS/F775W	–0.39	–0.14	–0.06	0.25	0.64
UVIS/F814W	–0.46	–0.18	–0.08	0.26	0.71
UVIS/F845M	–0.53	–0.22	–0.12	0.28	0.82
UVIS/F850LP	–0.66	–0.31	–0.14	0.30	0.96
UVIS/F953N	–0.72	–0.34	–0.15	0.32	1.06
UVIS/FQ232N	1.37	0.79	0.10	–0.43	–1.14
UVIS/FQ243N	1.37	0.78	0.08	–0.43	–1.10
UVIS/FQ378N	0.85	0.46	0.10	–0.20	–0.50
UVIS/FQ387N	0.70	0.29	0.01	–0.25	–0.51
UVIS/FQ422M	0.32	0.02	–0.12	–0.30	–0.44
UVIS/FQ436N	0.31	0.08	–0.06	–0.22	–0.37
UVIS/FQ437N	0.28	0.05	–0.09	–0.24	–0.38
UVIS/FQ492N	0.12	0.03	–0.01	–0.09	–0.15
UVIS/FQ508N	0.14	0.06	0.04	–0.03	–0.09
UVIS/FQ575N	–0.07	–0.01	–0.00	0.06	0.13
UVIS/FQ619N	–0.12	–0.01	0.03	0.14	0.26
UVIS/FQ634N	–0.17	–0.04	0.00	0.14	0.30
UVIS/FQ672N	–0.22	–0.06	–0.00	0.18	0.40
UVIS/FQ674N	–0.22	–0.06	0.00	0.19	0.41
UVIS/FQ727N	–0.31	–0.09	–0.03	0.23	0.56
UVIS/FQ750N	–0.42	–0.16	–0.08	0.23	0.61
UVIS/FQ889N	–0.62	–0.28	–0.15	0.28	0.91
UVIS/FQ906N	–0.69	–0.34	–0.17	0.27	0.94
UVIS/FQ924N	–0.67	–0.30	–0.14	0.31	1.00
UVIS/FQ937N	–0.65	–0.30	–0.14	0.31	0.99
IR/F098M	–0.76	–0.37	–0.16	0.33	1.10
IR/F105W	–0.78	–0.37	–0.17	0.36	1.22
IR/F110W	–0.76	–0.33	–0.17	0.39	1.36

Table A.3: Color corrections AB_V to go from Johnson V magnitude to AB magnitude for WFC3 as a function of age in a population with constant star formation.

	Age				
Mode	**10 Gyr**	**1 Gyr**	**100 Myr**	**10 Myr**	**1 Myr**
IR/F125W	–0.74	–0.30	–0.17	0.44	1.57
IR/F126N	–0.73	–0.29	–0.18	0.45	1.60
IR/F127M	–0.73	–0.29	–0.18	0.45	1.62
IR/F128N	–0.74	–0.29	–0.18	0.45	1.64
IR/F130N	–0.74	–0.29	–0.18	0.46	1.66
IR/F132N	–0.74	–0.28	–0.17	0.47	1.69
IR/F139M	–0.71	–0.25	–0.14	0.49	1.78
IR/F140W	–0.75	–0.28	–0.17	0.47	1.77
IR/F153M	–0.81	–0.32	–0.20	0.47	1.97
IR/F160W	–0.80	–0.32	–0.21	0.46	1.97
IR/F164N	–0.88	–0.39	–0.27	0.43	2.10
IR/F167N	–0.88	–0.38	–0.26	0.44	2.13

APPENDIX B:

Geometric Distortion

In this appendix . . .

B.1 Overview

WFC3 images exhibit significant geometric distortion, similar to that seen in ACS images. The required folding, with powered optics, of the light paths in both channels to fit within the instrument's optical-bench envelope results in substantial tilts of the focal surfaces with respect to the chief rays. The WFC3 UVIS detector is tilted at ~21° about one of its diagonals, producing a rhomboidal elongation of ~7%. The IR detector has a ~24° tilt about its *x*-axis, creating a rectangular elongation of ~10%.

If these were the only distortions they would not present much difficulty: their impacts on photometry, mosaicking, or dithering could be computed simply. More problematic, however, is the variation of plate scale across each detector. For the WFC3 UVIS and IR channels, this variation in plate scale amounts to a change of 3.5% and 2%, respectively, over the full field. Hence the area on the sky covered by an UVIS pixel varies by about 7% from corner to corner, and about 8% for the IR channel. Allowance for this change in plate scale must be made in photometric reductions of WFC3 data that have not been corrected for distortion. Further details are available at the pixel area map section of the WFC3 Web site:

http://www.stsci.edu/hst/wfc3/pam

Dithering and mosaicking are complicated by the fact that an integer pixel shift near the center of the detector translates into a non-integer displacement for pixels in other locations. Even this is not a fundamental difficulty, but implies some computational complexity in registering and correcting images. All of these considerations make it necessary to obtain accurate measurements of the distortions.

The orientations of the WFC3 detector edges for both detectors are at approximately 45° with respect to the V2 and V3 coordinate axes of the telescope. Figure 2.2 shows the WFC3 apertures in the telescope's V2,V3 reference frame. For a telescope roll angle of zero this would correspond to an on-sky view with the V3 axis aligned with north and the V2 axis with east.

The first on-orbit measurements of the geometric distortion for the WFC3 detectors were made during SMOV (Servicing Mission Observatory Verification). Astrometric fields in 47 Tuc (NGC 104) and the LMC were observed with multiple offsets in programs 11444 (UVIS, filter F606W) and 11445 (IR, filter F160W). Geometric distortion solutions have been derived from this data and entered into IDCTAB files at:

`http://www.stsci.edu/hst/wfc3/idctab_lbn`

(see WFC3 ISR 2009-33, WFC3 ISR 2009-34) to support the use of MultiDrizzle to produce distortion-corrected images (see the *MultiDrizzle Handbook*). In the initial IDCTAB files, the solutions for filters F606W and F160W have been applied to all UVIS and IR filters, respectively. Because there are small filter-dependent differences in distortion, exposures made with other filters during SMOV and in subsequent calibration programs will be used to derive solutions for the more commonly used filters.

B.2 UVIS Channel

Figure B.1 illustrates the shape of the UVIS channel field of view as projected onto the sky. As noted above, its rhomboidal shape is due primarily to the diagonal tilt of the CCD focal plane with respect to the chief ray (see the schematic mechanical drawing of the instrument in Figure 2.1). The angle between the *x*- and *y*-axes is ~86.1°. The field diagonals are tilted slightly from the V2 and V3 axes. There is a ~1.2 arcsec gap between the two CCD chips. The crosses in the diagram indicate where points in the image would be located without non-linear distortion, and the vectors, scaled up by a factor of 10, indicate the actual locations of the points on the sky, including the non-linear distortion components.

The corner displacements are about 30 pixels, corresponding to 1.3 arcsec. The principal effect is the diagonal variation of scale. At the center of UVIS1 (CCD Chip 1), the scale in the *x*-direction is 0.0396 arcsec/pixel, and 0.0393 arcsec/pixel in the *y*-direction. For UVIS2 (CCD Chip 2), these scales are 0.0400 arcsec/pixel, and 0.0398 arcsec/pixel, respectively. Between the corner of the UVIS image nearest to Amp A and the diagonally opposite corner near Amp D, the overall scale increases by 3.5%. UVIS1 forms a slightly distorted rectangle 162×81 arcsec in size, while UVIS2 subtends 164×81 arcsec.

The resulting variation of the projected pixel area on the sky requires corrections to photometry of point sources using images that have not been distortion-corrected. A contour plot of relative pixel size across the UVIS image, normalized at the

photometric reference pixel, is shown in Figure B.2. The ratio of maximum to minimum pixel area over the detector is 1.074.

See http://www.stsci.edu/hst/wfc3/pam/pixel_area_maps for a fits file of the pixel area map and a discussion of its normalization and application for photometry.

Figure B.1: Linear components (crosses) and non-linear components (vectors, magnified by 10) of geometric distortion on the WFC3/UVIS detector.

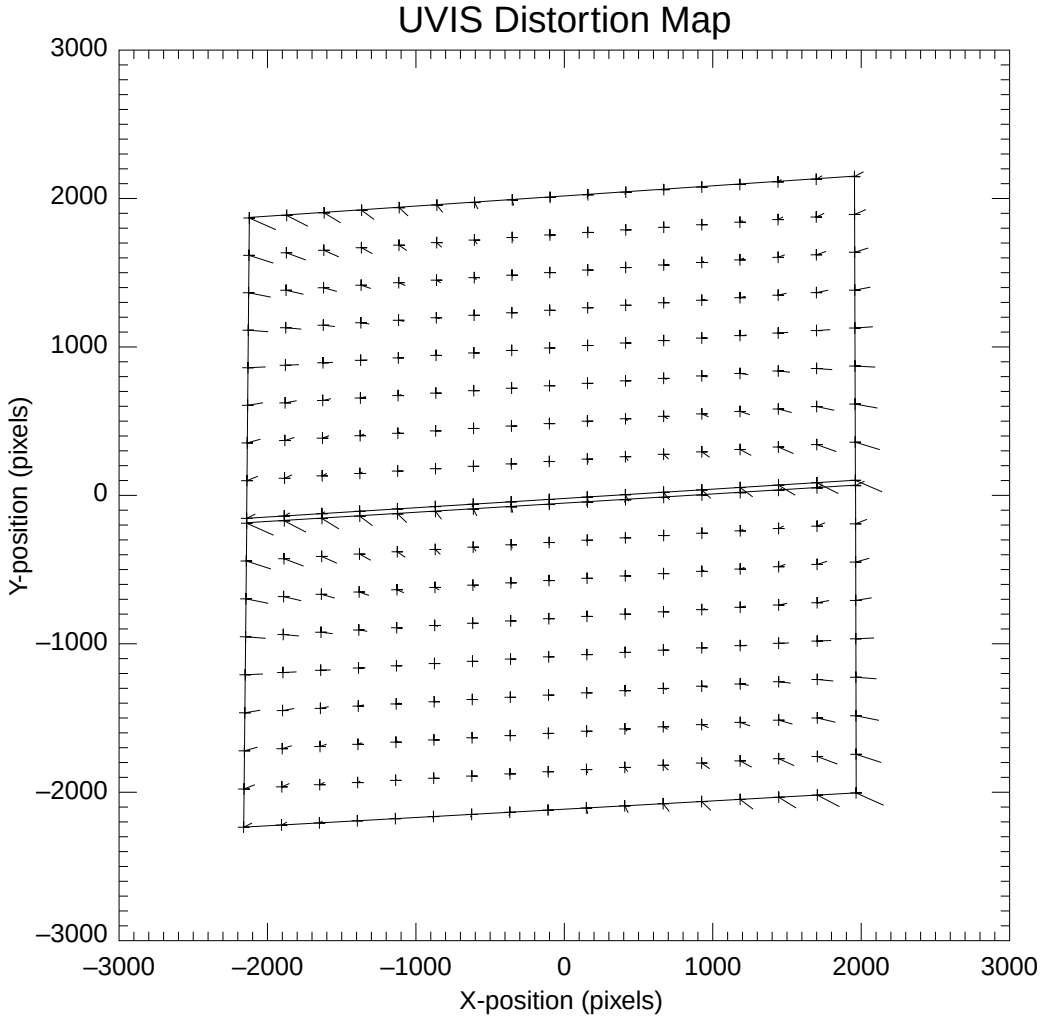

Figure B.2: Variation of the effective pixel area with position on the UVIS detector. Darker shading indicates pixels with smaller area. Contours are drawn at 1% increments.

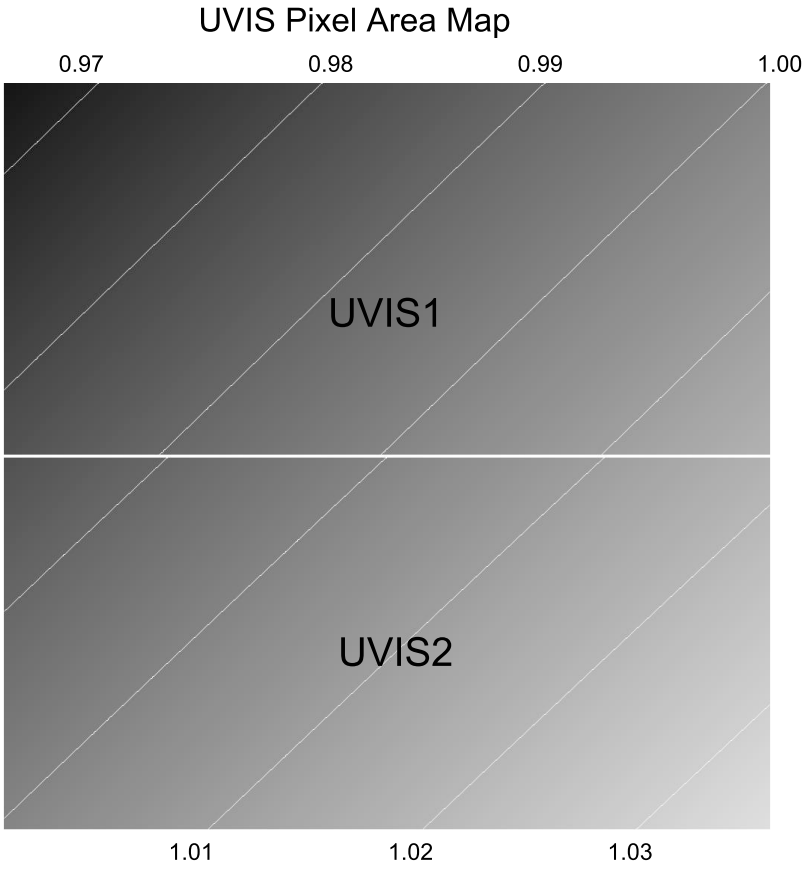

B.3 IR Channel

The IR detector field of view is nominally concentric with the UVIS field, but subtends a somewhat smaller area on the sky, 136×123 arcsec. The detector tilt is about the x-axis (AXIS1 in Figure 7.1), so the projected aperture shape is nearly a rectangle, with the angle between the x- and y-axes on the sky nearly 90°, as shown by the outline in Figure B.3. At field center, the x- and y-scales are 0.135 and 0.121 arcsec/pixel, respectively. A vector plot of the deviation from linearity is given in Figure B.3. The deviations have been magnified by a factor of 10, as in Figure B.1. The largest deviation is 10 pixels, corresponding to about 1.4 arcsec.

Figure B.3: Linear components (crosses) and non-linear components (vectors, magnified by 10) of the geometric distortion on the WFC3/IR detector.

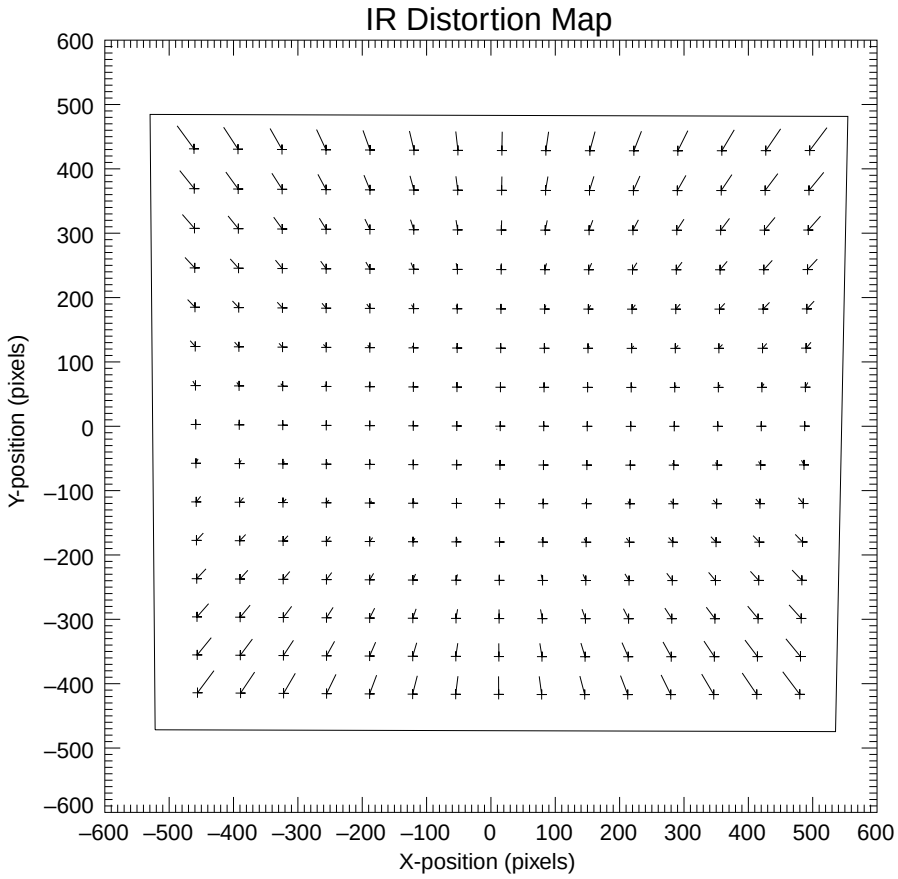

A map of the variation of pixel area across the IR detector to be used for correction of point-source photometry from images that have not been distortion-corrected (see http://www.stsci.edu/hst/wfc3/pam/pixel_area_maps) is shown in Figure B.4. The ratio of maximum to minimum pixel area is 1.090.

Figure B.4: Variation of the effective pixel area with position on the IR detector. Darker shading indicates pixels with smaller area. Contours are drawn at 2% increments.

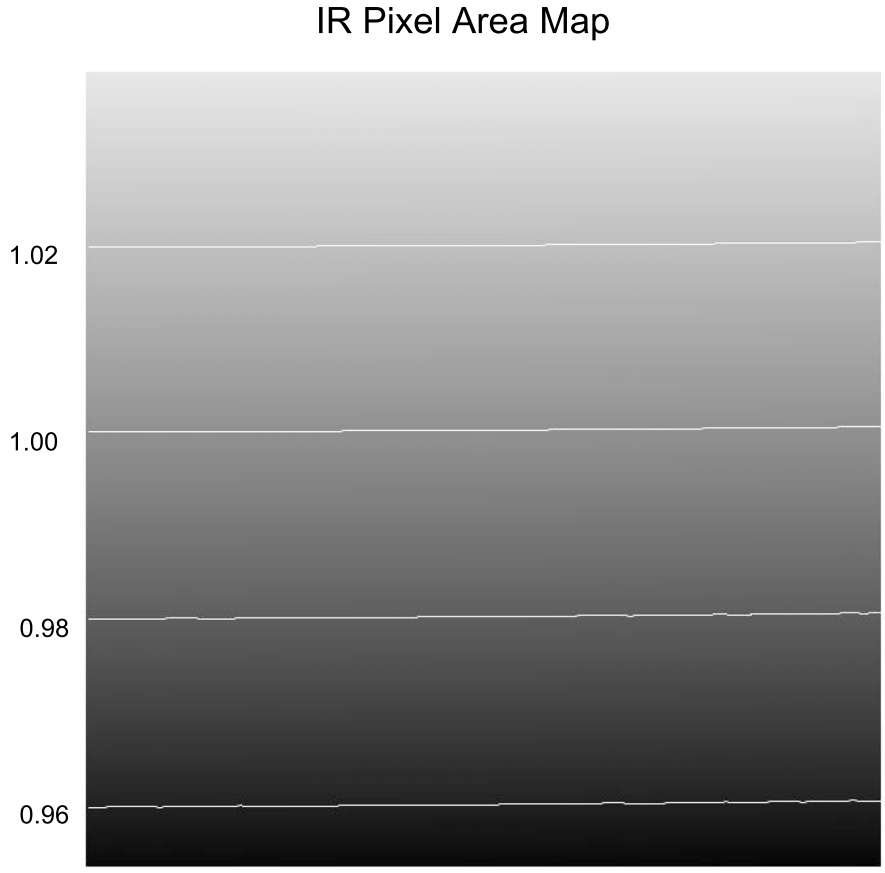

B.4 Summary

Images produced by both WFC3 channels are affected by considerable geometric distortion, dominated by a linear anamorphism introduced by the tilt of the image surface with respect to the chief ray. This is compounded by non-linear terms that produce changes across the field of view in both plate scale and area subtended by the pixels. Distortion solutions derived from data taken during SMOV with UVIS filter F606W and IR filter F160W are presented here. They have been entered into IDCTAB files to support the use of MultiDrizzle to produce distortion-corrected images. The corresponding pixel area maps, also presented here, have been made available for photometric calibration.

APPENDIX C:

Dithering and Mosaicking

In this appendix . . .

C.1 Why Mosaicking and Dithering are Needed

The sizes of telescope pointing offsets between successive exposures can be very different, depending on whether the purpose is "**mosaicking**" and "**dithering**." Mosaicking is done with the aim of increasing the area of sky covered by a particular set of exposures, usually with the goal of providing a seamless joining of contiguous frames. The angular offsets used when mosaicking are generally large, up to the size of the field of view. Only programs observing targets larger than the field of view of the detector need to use mosaicked exposures.

Dithering generally involves much smaller telescope offsets, often just a few pixels in size. Most imaging programs are advised to use dithering for several reasons, including:

- removal of hot pixels and other detector blemishes (Section 6.9.2)
- improving sampling of the PSF (Sections 6.10.1 and 7.10.1)
- improving photometric accuracy by averaging over flat-fielding errors (Sections 5.4.3, 5.7.4, and 6.10.1)
- bridging over the gap between the chips in the UVIS channel (Section 5.2.2).

Dithered and mosiaced exposures can be combined using software such as MultiDrizzle (see the *MultiDrizzle Handbook*). MultiDrizzle is produced by STScI, and is expected to be implemented in the OPUS pipeline for WFC3 in January 2010. Note that it is sometimes necessary to use software like MultiDrizzle to combine even

CR-SPLIT or repeat exposures, when pointing drift causes slight misalignment of exposures and differences in how PSFs are pixelated, or when gradual changes in focus over the course of an orbit produce changes in the observed PSF.

In some programs, especially those observing time-variable phenomena, combining dithered exposures to correct for cosmic rays and transient bad pixels may be scientifically infeasible. In such cases, single-image based methods must be used. These methods use statistical properties of cosmic-ray brightness or sharpness to identify and interpolate across cosmic rays. Single-image cosmic ray rejection schemes are not available through the standard WFC3 calibration pipeline.

C.2 WFC3 Patterns

A number of different types of patterns are available to support dithered and mosaicked WFC3 observations. The pre-defined patterns that have been implemented in APT are described in the Phase II Proposal Instructions. The WFC3 patterns in effect in APT at the time of publication of this Handbook are summarized here. Observers can adjust the parameters of these patterns to suit the needs of their programs, or can use them as a model for user-defined patterns; for example, to add a secondary dither pattern to a primary mosaic pattern. Due to geometric distortion (Appendix B), a large mosaic step shifts some objects by an integer number of rows (or columns), and others by an integer plus some fraction of a pixel. The PSF is thus not evenly sampled in the overlap region of the two exposures, so a PSF-sampling dither should be added if spatial resolution is important.

Use of patterns, rather than POSTARG offsets, has the advantage of allowing exposures to be associated and combined automatically during ***calwfc3*** pipeline processing, as long as the same guide stars have been used for all exposures. Pointings must be contained within a diameter ~130 arcsec or less (depending on the availability of guide stars in the region) to use the same guide stars. Note that the rms pointing repeatability is significantly less accurate if different guide stars are used for some exposures. (See Section 4.1 of the *MultiDrizzle Handbook*).

The names and purposes of the patterns in effect in APT at the time of publication are given in Table C.1. (The initially adopted names of patterns have been preserved for continuity, although they do not always correspond to the distinction between dither steps and mosaic steps outlined above.) The small BOX dither patterns are designed to optimally sample the PSF when 4 steps are used. Since time constraints do not always permit visits to be broken into multiples of 4 steps, LINE dither patterns are also given. For a full discussion of patterns that optimally sample the PSF for different numbers of steps, see Section 2.5.2 of the *MultiDrizzle Handbook*. Note that PSF sampling generally produces a more significant improvement for IR images than for UVIS images (see Section 6.6.1 and Section 7.6.1) The remainder of the patterns in Table C.1 are special-purpose mosaic patterns that are expected to be commonly needed. We have not defined patterns to deal with specific features in flats—notably, the circular dead spot on the IR detector (WFC3 ISR 2008-08) and the UVIS "droplets" (WFC3 ISR 2008-10)—but the characteristics, locations, and impact of these features are discussed in the ISRs.

Table C.1:Dithering and Mosaicking Patterns for WFC3.

Pattern Name	Description
	WFC3 IR Patterns
WFC3-IR-DITHER-BOX-MIN	Samples the PSF.
WFC3-IR-DITHER-BOX-UVIS	Produces an IR mosaic (despite the name) covering the same area as the UVIS-CENTER aperture.
WFC3-IR-DITHER-LINE	Samples the PSF.
	WFC3 UVIS Patterns
WFC3-UVIS-DITHER-BOX	Samples the PSF and produces spacings of >1 column to move hot columns
WFC3-UVIS-DITHER-LINE	Samples the PSF and produces spacings of >1 column to move hot columns
WFC3-UVIS-MOS-BOX-LRG	Produces a mosaic that can generally be executed with a single set of guide stars.
WFC3-UVIS-MOS-DITH-LINE	Combines a primary gap-stepping pattern with an optional dither at each primary position.
WFC3-UVIS-MOSAIC-LINE	For full-frame UVIS with ACS/WFC in parallel; steps the gap on both detectors.

The default specifications of the patterns are summarized in table C.2. The equivalent POSTARG moves are summarized in table C.3, along with the approximate number of pixels corresponding to these moves. The number of pixels was computed using only the linear distortion terms with coefficients measured at the center of each detector. This is an excellent approximation for small moves and for objects that remain in the central region of the detector. (See Figure B.1 and B.3 in Appendix B.)

Table C.2:Default values of the parameters that define the WFC3 convenience patterns.

Pattern	No. of Points	Point Spacing (arcsec)	Line Spacing (arcsec)	Pattern Orient (degrees)	Angle between Sides (degrees)	Center Pattern
WFC3-IR-DITHER-BOX-MIN	4	0.572	0.365	18.528	74.653	no
WFC3-IR-DITHER-BOX-UVIS	4	23.020	35.212	0.713	89.287	yes
WFC3-IR-DITHER-LINE	2	0.636		41.788		no
WFC3-UVIS-DITHER-BOX	4	0.173	0.112	23.884	81.785	no
WFC3-UVIS-DITHER-LINE	2	0.145		46.840		no
WFC3-UVIS-MOS-BOX-LRG	4	79.400	77.500	5.550	95.300	yes
WFC3-UVIS-MOS-DITH-LINE						
primary pattern	3	2.400		85.754		yes
secondary pattern	2	0.119		33.606		no
WFC3-UVIS-MOSAIC-LINE	2	3.264		63.697		no

Table C.3:Steps in arcsec in the POS TARG frame and in detector pixels for the WFC3 convenience patterns.

Pattern Name	POS TARG X (arcsec)	POS TARG Y (arcsec)	x (pixels)	y (pixels)
WFC3-IR-DITHER-BOX-MIN	0.000	0.000	0.0	0.0
	0.542	0.182	4.0	1.5
	0.339	0.485	2.5	4.0
	-0.203	0.303	-1.5	2.5
WFC3-IR-DITHER-BOX-UVIS	-11.071	-17.744	-81.7	-146.5
	11.947	-17.457	88.2	-144.2
	11.071	17.744	81.7	146.5
	-11.947	17.457	-88.2	144.2
WFC3-IR-DITHER-LINE	0.000	0.000	0.0	0.0
	0.474	0.424	3.5	3.5
WFC3-UVIS-DITHER-BOX	0.000	0.000	0.0	0.0
	0.158	0.070	4.0	1.5
	0.099	0.165	2.5	4.0
	-0.060	0.095	-1.5	2.5
WFC3-UVIS-DITHER-LINE	0.000	0.000	0.0	0.0
	0.099	0.106	2.5	2.5
WFC3-UVIS-MOS-BOX-LRG	-39.611	-42.120	-1000.0	-997.0
	39.611	-36.860	1000.0	-1001.0
	39.611	42.120	1000.0	997.0
	-39.611	36.860	-1000.0	1001.0
WFC3-UVIS-MOS-DITH-LINE	-0.178	-2.393	-4.5	-60.2
	-0.079	-2.328	-2.0	-58.7
	0.000	0.000	0.0	0.0
	0.099	0.066	2.5	1.5
	0.178	2.393	4.5	60.2
	0.277	2.459	7.0	61.7
WFC3-UVIS-MOSAIC-LINE	0.000	0.000	0.0	0.0
	1.446	2.926	36.5	71.5

For the IR detector, the linear relation between POSTARGs and pixels is simply

$$\text{POSTARGX} = a_{11} * x$$

$$\text{POSTARGY} = b_{10} * y$$

where a_{11} ~ 0.1355 arcsec/pixel and b_{10} ~ 0.1211 arcsec/pixel near the center of the detector. For the UVIS detector, there is a cross-term that takes into account the fact that the projected axes are not perpendicular:

$$\text{POSTARGX} = a_{11} * x$$

$$\text{POSTARGY} = b_{11} * x + \text{b}_{10} * y$$

where a_{11} ~ 0.0396 arcsec/pixel, b_{11} ~ 0.0027 arcsec/pixel, and b_{10} ~ 0.0395 arcsec/pixel near the center of the detector. This relationship is illustrated in Figure C.1.

Figure C.1: Transformation between image x,y coordinates (in pixel units) and X,Y coordinates (in arcsec) in the POSTARG frame. See also Figure 6.1.

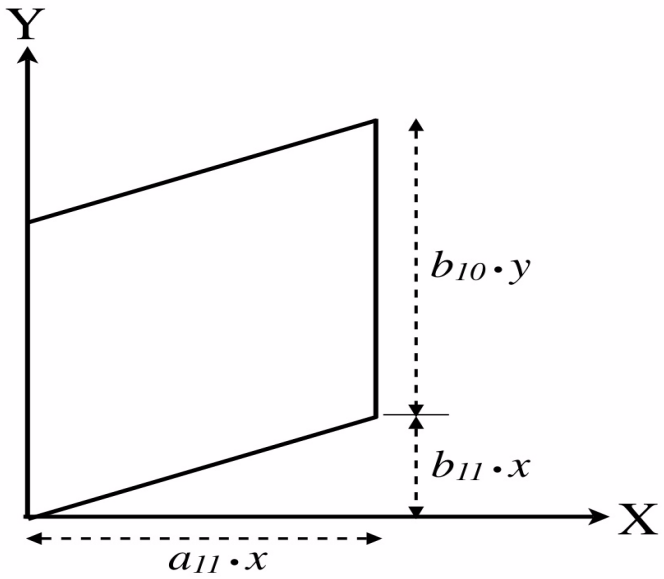

APPENDIX D:

Bright-Object Constraints and Image Persistence

In this appendix . . .

D.1 UVIS Channel

The UVIS channel's CCDs have no bright-object constraints. Overexposures on very bright targets do not have any adverse health and safety issues, nor should they affect subsequent exposures. As for any CCD, there can be some bleeding into adjacent rows and columns surrounding the bright object. This however is generally quite modest assuming the bright object is not itself the science target. From a scientific perspective, the largest problem with bright targets in the field is likely to arise from window or filter ghosts (See Section 6.5.3).

D.2 IR Channel

The IR channel likewise has no bright-object constraints that are imposed due to instrument safety concerns. However, observers should bear in mind that there is a potential for image-persistence effects that could compromise observations made immediately following an exposure on a bright target. Such observations contain "afterglow" images at the location of the overexposed object, which gradually fades away over an interval of several hours. The afterglow has both a short and long term

component. The short-term component is important for exposures obtained within an orbit while the longer term component affects subsequent observations (within the visit or some other observer's subsequent visit).

The WFC IR channel has a field of view seven times larger than NICMOS Camera 3 and higher sensitivity. This combination means that for WFC3/IR images it is impossible to avoid some saturated portions of the image. The amount of afterglow depends on the level of saturation and the length of time the IR detector is exposed to the bright source. Unfortunately, from this perspective, since WFC3 IR channel has no shutter, the time the detector is exposed to light is not the exposure time in the science image. Various efforts are underway to develop procedures to mitigate the effects of afterglow. Operationally, for Cycle 17, a list of observations have been identified that are likely to cause the worst problems and procedures have been put in place to prevent prime observation taking place with WFC3 IR soon after the bright observation. It is likely that this procedure will be enhanced for Cycle 18; there is however a trade-off associated with this, since these kinds of constraints make all observations with *HST* harder to schedule.

If you are planning a sequence of IR observations that may contain severely overexposed images, you may wish to estimate the degree of overexposure. An IR observer might expect that the Two Micron All Sky Survey (2MASS) would be the appropriate catalog for examining the frequency of WFC3/IR saturation, but in fact the 2MASS catalog is generally not deep enough for this purpose. Although the depth of the survey varies across the sky, the faint limit is typically near 15th mag in J, H, and Ks (the formal Level 1 requirements on limiting magnitudes of the 2MASS catalog are J = 15.8, H = 15.1, and Ks = 14.3). Stars near this faint limit saturate the WFC3/IR detector in a relatively short time (of order 100 s in some of the wide IR bandpasses). The STScI Guide Star Catalog (GSC), currently at version 2.3, generally goes much fainter (down to 22nd mag in V), but the extrapolation from the optical into the infrared depends on the accuracy of the spectral type implied by the optical colors and the assumed extinction (a large source of systematic errors along sightlines of high extinction).

As described in Chapter 9, the WFC3 Exposure Time Calculator (ETC) can be used to estimate the count rate in the central pixel for a given astronomical source. However, as a rough guideline, below we present tables of the count rates to reach S/N = 10 for two cases: a "hot star" with spectral type O3V, $T_{\rm eff}$ = 45,000 K, [Fe/H] = 0, and log g = 4.0; and a "cool star" with spectral type M5V, $T_{\rm eff}$ = 3500 K, [Fe/H] = 0, and log g = 5.0.

Tables D.1, D.2, D.3, and D.4 give the results for the cases where one normalizes to Johnson *J, K, V,* and Bessel *H,* as stated in the table captions. In each case a magnitude of 15 in the respective bandpass is assumed. The count rates are given in electrons/s for the central pixel of a star centered in a WFC3 IR pixel. These tables give the most reliable results when normalizing to a ground-based bandpass that overlaps with the WFC3 bandpass, regardless of the assumed spectral energy distribution. However, when normalizing to Johnson *V,* one must know the underlying spectral energy distribution to high accuracy in order to predict the count rate in the WFC3/IR bandpasses.

The Bright Object Tool (BOT) in the Astronomer's Proposal Tool (APT) can provide a list of saturated objects for a potential WFC3/IR observation, given a Phase II proposal. Because the 2MASS survey is sufficiently deep for objects that would severely oversaturate the detector (by more than a factor of 100), the BOT uses 2MASS data where they are available, and the GSC2 where no 2MASS data are available.

Table D.1: Count Rates (e^-/s) for source with J=15 renormalized to Johnson/J.

WFC3 IR filter	Cool star[1]	Hot star[1]
F098M	2542.9	1876.2
F105W	4541.3	3572.4
F110W	7610.7	6754.8
F125W	4570.8	4484.4
F126N	226.4	215.0
F127M	1108.7	1068.2
F128N	244.9	238.8
F130N	246.9	243.5
F132N	235.2	240.0
F139M	790.2	1030.2
F140W	5136.5	6336.3
F153M	749.4	1144.6
F160W	3021.0	4527.5
F164N	204.0	301.0
F167N	197.4	295.3

1. See text for definition of "cool" and "hot" star.

Table D.2: Count Rates (e^-/s) for source with H=15 renormalized to Bessell/H.

WFC3 IR filter	Cool star[1]	Hot star[1]
F098M	1540.5	5141.9
F105W	2751.2	7706.9
F110W	4610.7	10850.3
F125W	2769.1	4982.5
F126N	137.2	226.2
F127M	671.7	1065.4
F128N	148.3	229.7
F130N	149.6	224.8
F132N	142.5	210.3
F139M	478.7	744.7
F140W	3111.8	4652.4
F153M	454.0	554.7
F160W	1830.2	2202.0
F164N	123.6	112.3
F167N	119.6	104.0

1. See text for definition of “cool” and “hot” star.

Table D.3: Count Rates (e^-/s) for source with K=15 renormalized to Johnson/K.

WFC3 IR filter	Cool star[1]	Hot star[1]
F098M	1402.6	5684.4
F105W	2504.9	8520.0
F110W	4197.8	11995.0
F125W	2521.2	5508.2
F126N	124.9	250.1
F127M	611.5	1177.8
F128N	135.1	253.9
F130N	136.2	248.5
F132N	129.7	232.4
F139M	435.9	823.3
F140W	2833.2	5143.2
F153M	413.3	613.2
F160W	1666.3	2434.3
F164N	112.5	124.0
F167N	108.9	115.0

1. See text for definition of “cool” and “hot” star.

Table D.4: Count Rates (e^-/s) for source with V=15 renormalized to Johnson/V.

WFC3 IR filter	Cool star[1]	Hot star[1]
F098M	52334.0	2291.8
F105W	93463.6	3435.0
F110W	156631.7	4836.1
F125W	94070.7	2220.8
F126N	4660.4	100.8
F127M	22818.0	474.8
F128N	5039.4	102.4
F130N	5081.7	100.2
F132N	4840.2	93.7
F139M	16262.9	331.9
F140W	105713.1	2073.6
F153M	15422.3	247.1
F160W	62174.0	981.5
F164N	4197.5	50.0
F167N	4062.2	46.4

1. See text for definition of “cool” and “hot” star.

APPENDIX E:

Reduction and Calibration of WFC3 Data

In this appendix . . .

E.1 The STScI Reduction and Calibration Pipeline

In this appendix, we summarize the basic reductions and calibrations that are performed in the STScI WFC3 pipeline. The material in this appendix is intended to provide only enough background to develop robust observing proposals. The WFC3 Data Handbook provides more detailed information needed for analyzing your data.

Science data taken by WFC3 are received from the Space Telescope Data Capture Facility and sent to the STScI OPUS pipeline, where the data are unpacked, keyword values are extracted from the telemetry stream, and the science data reformatted and repackaged into raw (uncalibrated) FITS files by the generic conversion process. All WFC3 science data products are two-dimensional images that are stored in FITS image-extension files. Like ACS and STIS images, WFC3 UVIS channel exposures are stored as triplets of FITS image extensions, consisting of science (SCI), error (ERR), and data quality (DQ) arrays. There is one triplet of image extensions for each CCD chip used in an exposure. Full-frame exposures, using both chips, therefore have two triplets of SCI, ERR, and DQ extensions in a single FITS file. UVIS subarray exposures, which use only one CCD chip, have a single triplet of extensions in their FITS files.

WFC3 IR channel exposures use the NICMOS file structure, which are quintuplets of FITS image extensions, consisting of science (SCI), error (ERR), data quality (DQ),

number of samples (SAMP), and integration time (TIME) arrays. There is one quintuplet of extensions for each of the non-destructive detector readouts that make up an IR exposure. Using the maximum number of readouts (16) in an IR exposure therefore results in a single FITS file containing a total of 80 image extensions.

The raw, uncalibrated FITS files are processed through ***calwf3***, the software task that calibrates the data for individual exposures, producing calibrated FITS files. Exposures that are obtained as part of an associated set, such as dithered images, have ***calwf3*** calibration applied to the individual exposures before being processed as a set for the purpose of image combination. All calibrated images will be processed further with the STScI MultiDrizzle software, for the purpose of removing geometric distortions from individual exposures and for combining associated exposures.

The FITS file name suffixes given to WFC3 raw and calibrated data products are described in Table E.1 and closely mimic the suffixes used by ACS and NICMOS. The initial input files to ***calwf3*** are the raw (RAW) files from generic conversion and the association (ASN) table, if applicable, for the complete observation set. For WFC3/UVIS images, a temporary file, with the suffix "BLV_TMP," is created by ***calwf3*** once bias levels have been subtracted and the overscan regions trimmed. This file is renamed using the "FLT" suffix after the remaining standard calibrations (dark subtraction, flat fielding, etc.) have been completed. For exposures taken as part of a UVIS CR-SPLIT or REPEAT-OBS set, a parallel set of processing is performed, using the BLV_TMP files as input to an image combination and cosmic ray rejection routine. The resulting CR-combined image, with a temporary file name suffix of "CRJ_TMP", then receives the remaining standard calibrations, after which it is renamed using the "CRJ" suffix.

Table E.1: WFC3 File Name Suffixes.

File Suffix	Description	Units
_RAW	Raw data	DN
_ASN	Association file for observation set	
_SPT	Telemetry and engineering data	
_TRL	Trailer file with processing log	
_BLV_TMP	Bias subtracted individual UVIS exposure	DN
_CRJ_TMP	Uncalibrated, CR-rejected combined UVIS image	DN
_IMA	Calibrated intermediate IR exposure	e^-/s
_FLT	Calibrated individual exposure	e^- (UVIS) e^-/s (IR)
_CRJ	Calibrated, CR-rejected, combined UVIS image	e^-
_DRZ	Calibrated, geometrically-corrected, dither-combined image	e^-/s

Processing of WFC3/IR exposures results in an intermediate MULTIACCUM (IMA) file, which is a file that has had all calibrations applied (dark subtraction, linearity correction, flat fielding, etc.) to all of the individual readouts of the IR exposure. A final step in ***calwf3*** processing of WFC3/IR exposures produces a combined image from the individual readouts, which is stored in an FLT output product file.

The UVIS processing portion of ***calwf3*** is based on ***calacs*** calibrations of ACS/WFC CCD images, while the ***calwf3*** IR processing is very similar to ***calnica*** processing of NICMOS images. ***Calwf3*** performs the following basic science data calibrations:

- Bad pixel flagging
- Bias level subtraction (UVIS); Reference pixel subtraction (IR)
- Bias image subtraction (UVIS); Zero-read subtraction (IR)
- Dark current subtraction
- Non-linearity correction
- Flat field correction and gain calibration
- Shutter shading correction (UVIS only)
- Up-the-ramp fitting (IR only)
- Photometric calibration (keyword updates only)
- CR-SPLIT/REPEAT-OBS image combination

As noted in the list above, the details of some calibration steps differ for UVIS and IR exposures, while others do not apply at all. The process of bias subtraction, in particular, differs for UVIS and IR exposures. The UVIS channel CCDs include regions of overscan, which are used for measuring and subtracting the overall bias level from each CCD exposure. A bias reference image is also subtracted from each science exposure to remove spatial variations in the bias. For IR exposures, the reference pixels located around the perimeter of the detector are used to track and remove changes in the overall bias level between readouts, while the image from the initial ("zeroth") readout of the exposure is subtracted from all subsequent readouts to remove spatial bias structure.

UVIS shutter shading correction is in principle only necessary for very short duration exposures. Note, however, that testing has shown that the shading amounts to only a 0.2-0.3% variation across the field and therefore this step is normally not applied.

Up-the-ramp fitting is applied to IR exposures to determine a final signal rate for each pixel in the image. This process not only determines the best-fit rate from the individual readouts of the exposure, but also detects and removes effects due to cosmic-ray hits. This process is also capable of recovering a useful signal for pixels that go into saturation during the exposure by using only the non-saturated readouts to compute the fit.

WFC3 grism observations are handled in a special way by the pipeline. Grism observations require a special flat-fielding procedure, where the flat-field value for each pixel is based on the wavelength of the detected signal. ***Calwf3*** processing of grism images therefore uses an "identity" flat-field reference image (an image filled with values of 1.0 at each pixel), which allows for the gain calibration part of the flat-fielding step to still be applied without actually flat-fielding the science image. A separate software package, aXe, which was developed at ST-ECF and previously used for processing NICMOS and ACS spectral observations, is used to extract and calibrate one-dimensional spectra from WFC3 grism exposures (see Section 8.5). The aXe software is available in STSDAS via PyRAF. The aXe software is used to locate and extract spectra of individual sources from calibrated images and performs wavelength calibration, background subtraction, flat fielding, and absolute flux calibration for the extracted spectra.

Table E.2 shows the values assigned to pixels in the DQ arrays of calibrated images, which indicate anomalous conditions and are frequently used in downstream processes to reject a pixel value. If more than one data quality condition applies to a pixel, the sum of the values is used. Note that some flag values have different meanings for UVIS and IR images.

Table E.2: WFC3 Data Quality Flags.

FLAG Value	**Data Quality Condition**	
	UVIS	**IR**
0	OK	OK
1	Reed-Solomon decoding error	Reed-Solomon decoding error
2	Data replaced by fill value	Data replaced by fill value
4	Bad detector pixel	Bad detector pixel
8	(unused)	Unstable in zero-read
16	Hot pixel	Hot pixel
32	CTE tail	Unstable photometric response
64	Warm pixel	Warm pixel
128	Bad pixel in bias	Bad reference pixel
256	Full- well saturation	Full-well saturation
512	Bad or uncertain flat value	Bad or uncertain flat value
1024	Charge trap	(unused)
2048	A-to-D saturation	Signal in zero-read
4096	Cosmic ray rejected by MultiDrizzle	Cosmic ray rejected by MultiDrizzle
8192	Cosmic ray detected during CR-SPLIT or REPEAT-OBS combination	Cosmic ray detected during up-the-ramp fitting
16384	Pixel affected by ghost or crosstalk	Pixel affected by crosstalk

E.2 The SMOV Calibration Plan

The Servicing Mission Observatory Verification (SMOV) plan for WFC3 was executed following its successful installation in *HST* in May, 2009. The calibration plan consisted of engineering, alignment, and calibration activities whose principal goal was to verify that the instrument would be ready for science at the beginning of Cycle 17 in August, 2009. WFC3's SMOV activities began on 25 May 2009 with the Activation Test. The first set of SMOV imaging data were acquired on 11 June 2009, and the last in the first week of September. Because of the short duration, only a critical subset of WFC3's imaging and spectroscopic modes were calibrated. All of the 44 activities are presented in Table E.3. Most of these activities have an associated Instrument Science Report, published in 2009, and are available on the WFC3 Web site at:

http://www.stsci.edu/hst/wfc3/documents/ISRs/.

Cycle 17 calibration programs will provide improved photometric, spectroscopic, flat field, and geometric distortion values as well as additional on orbit detector characterization.

Table E.3: SMOV4 Calibration Programs.

Proposal ID	Title
11454	Activation Test
11357	Memory Test
11358	Sci Data Buffer Test
N/A	UVIS CCD Cooldown
N/A	IR Detector Cooldown
11419	UVIS Det Functional
11420	IR Det Functional
11421	CSM Test
11422	UVIS SOFA Test
11529	UVIS Spare Tungsten Lamp
11423	IR FSM Test
11543	IR Spare Tungsten Lamp
11424	UVIS Initial Alignment
11425	IR Initial Alignment
11426	UVIS Contam Monitor

Proposal ID	Title
11427	UVIS Shutter Test
11428	D2 Cal Lamp Test
N/A	UVIS TEC Performance
N/A	IR TEC Performance
11431	UVIS Hot Pixel Anneal
11432	UVIS Int Flats
11433	IR Int Flats
11434	UVIS Fine Alignment
11435	IR Fine Alignment
11436	UVIS Image Quality
11437	IR Image Quality
11438	UVIS PSF Wings
11439	IR PSF Wings
11549	UVIS & IR Pointing Stability
11442	FGS-UVIS Update
11443	FGS-IR Update
11444	UVIS Plate Scale
11445	IR Plate Scale
11446	UVIS Dark, Noise, Backgnd
11447	IR Dark, Noise, Backgnd
11448	UVIS SAA Passage
11449	IR SAA Passage
11450	UVIS Phot Zero Points
11451	IR Phot Zero Points
11452	UVIS Flat Field Uniformity
11453	IR Flat Field Uniformity
11552	IR Grisms
11798	UVIS PSF Core Modulation
11808	UVIS Bowtie Monitor

Glossary

The following terms and acronyms are used in this Handbook.

ADU: Analog-to-digital Unit

ADC: Analog to digital Converter

ABMAG: –2.5 log (F_ν) – 48.60 where F_ν is the flux from the source in erg cm^{-2} sec^{-1} Hz^{-1}

AB$_\nu$: Correction to ABMAG to account for the fact that the source spectrum is not constant in F_ν (ABMAG=V+AB_ν)

ACS: Advanced Camera for Surveys

APT: Astronomer's Proposal Tool

aXe: Spectroscopic Data Extraction Software

BOP: Bright Object Protection

calwf3: WFC3 calibration pipeline software

CCD: Charge Coupled Device. Solid-state, light detecting device

CDS: Correlated Double Sampling

COS: Cosmic Origins Spectrograph

CP: Call for Proposals

CR: Cosmic ray

CR-SPLIT: Division of a CCD exposure into shorter exposures to be used for cosmic ray rejection

CSM: Channel select mechanism

CTE: Charge transfer efficiency

CVZ: Continuous viewing zone

DCL: Detector Characterization Laboratory at NASA GSFC

DN: Data number

DQ: Data quality

EE: Encircled energy

ETC: Exposure Time Calculator. ETCs are Web-based tools which can be accessed through the WFC3 Web pages.

FET: Field-effect Transistor

FGS: Fine Guidance Sensors

FITS: Flexible Image Transport System

FOV: Field of view

FPA: Focal-Plane Array

FSM: Filter select mechanism

FWHM: Full width at half maximum

GO: General Observer

GSC: Guide Star Catalog

GSFC: NASA's Goddard Space Flight Center

Help Desk: Facility for getting help on *HST* related topics via email. help@stsci.edu.

HRC: High Resolution Channel of ACS (non-operational)

HST: Hubble Space Telescope

IPT: Integrated Product Team

IR: Infrared; also IR channel of WFC3

IRAF: Image Reduction and Analysis System. The environment in which STSDAS operates.

ISR: Instrument Science Report. Available at the WFC3 Web site.

K: Degree Kelvin

MBE: Molecular-beam Epitaxial

MPP: Multi Pinned Phased, a CCD mode that reduces dark current rate

MTF: Modulation Transfer Function

MUX: Multiplexer

NICMOS: Near-Infrared Camera and Multi-Object Spectrograph

NUV: Near ultraviolet (~2000 to 4000 Å)

OTA: Optical Telescope Assembly

PASP: Publications of the Astronomical Society of the Pacific

Phase I proposal: A proposal for observing time on *HST*

Phase II program: An approved *HST* program; includes precise detail of how program is to be executed

PI: Principal investigator

POM: Pick- off Mirror

PRF: Pixel Response Function

PSF: Point-spread function.

PyRAF: version of IRAF implemented in the Python language

QE: Quantum Efficiency

ramp: A sequence of non-destructive readouts comprising a single IR exposure

rms: Root mean square

SAA: South Atlantic Anomaly

SBC: Solar-Blind Channel of ACS

SDSS: Sloan Digital Sky Survey

SED: Spectral-energy Distribution

SIAF: Science Instrument Aperture File

SM4: Servicing Mission 4

SMOV: Servicing Mission Observatory Verification

S/N: signal-to-noise ratio

SOFA: Selectable Optical Filter Assembly

SOC: Scientific Oversight Committee

ST-ECF: Space Telescope European Coordinating Facility

STIS: Space Telescope Imaging Spectrograph

STScI: Space Telescope Science Institute

STSDAS: Space Telescope Science Data Analysis System. The complete suite of IRAF data analysis and calibration routines used to process *HST* data.

synphot: STSDAS synthetic photometry (IRAF) software package

TAC: Telescope Allocation Committee

TEC: Thermal Electric Coolers

UV: Ultraviolet

UVIS: Ultraviolet and Visual (CCD channel of WFC3)

WFC: Wide-Field Channel of ACS

WFC3: Wide Field Camera 3

WF/PC-1: Wide Field Planetary Camera-1. Original on-axis *HST* camera.

WFPC2: Wide Field Planetary Camera 2. Replacement for WF/PC-1 installed during first servicing mission of December 1993.

Index

E

F